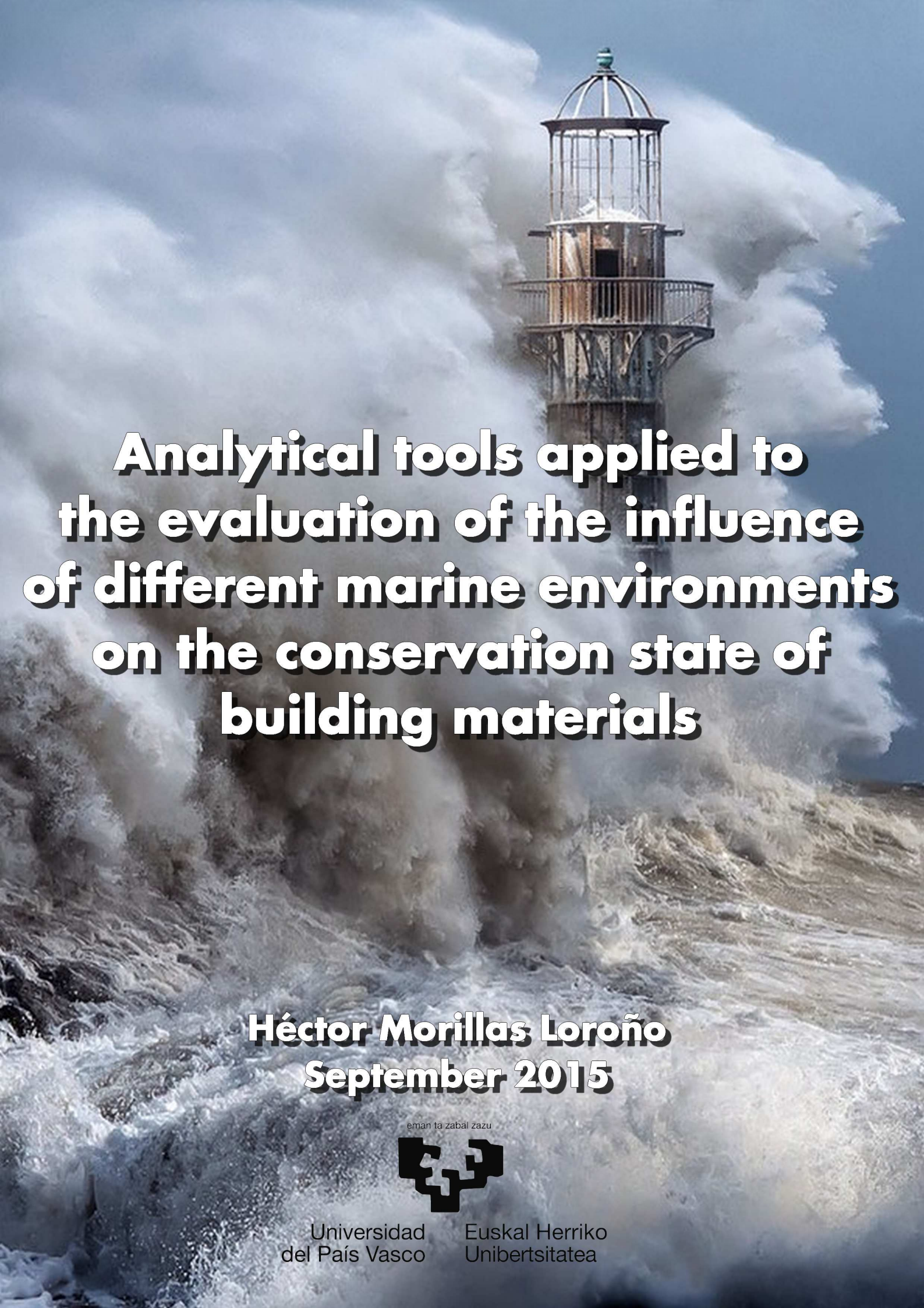

Analytical tools applied to the evaluation of the influence of different marine environments on the conservation state of building materials

Héctor Morillas Loroño

September 2015

eman ta zabal zazu

Universidad del País Vasco

Euskal Herriko Unibertsitatea

Analytical tools applied to the evaluation of the influence of different marine environments on the conservation state of building materials

This PhD Thesis has been developed in the Analytical Chemistry Department from the University of the Basque Country
(Faculty of Science and Technology, Leioa, Spain)

Héctor Morillas Loroño

Leioa, SEPTEMBER 2015

(c)2015 HECTOR MORILLAS LOROÑO

ACKNOWLEDGEMENTS

The author of this PhD Thesis thanks to the University of the Basque Country (EHU/UPV) and mainly to the action UFI 11-26 Global Change and Heritage, who funded his pre-doctoral contract.

The research work carried out in the present PhD project has been financially supported by IMDICOGU (ref.BIA2008-06592) project funded by the Spanish MICINN; DEMBUMIES (ref.BIA2011-28148) project funded by the Spanish Ministry of Economy and Competitiveness (MINECO), DISILICA-1930 (ref. BIA2014-59124) project funded by the Spanish Ministry of Economy and Competitiveness (MINECO) and the Regional Development Fund (FEDER).

He also gratefully acknowledgements the possibility of the three months stay in the Université Pierre et Marie Curie (UPMC), in Paris, to the UNESCO Chair of Cultural Landscape and Heritage (EHU/UPV).

Primeramente quisiera agradecer a mis dos directores de Tesis Doctoral, Juan Manuel Madariaga y Maite Maguregui el apoyo incondicional prestado a lo largo de todo este largo camino. A ti Juanma agradecerte la confianza que depositaste en mi dándome la oportunidad de realizar esta Tesis Doctoral. Sin tus consejos y ánimos así como todos los momentos sufridos pero a la vez disfrutados, esta tesis no hubiera sido lo misma. A Maite, por saber guiarme y darme las pautas necesarias para realizar los diferentes estudios, así como el sufrimiento derivado de todas las correcciones a lo largo de la tesis. Gracias de verdad a los dos.

Thanks to Professor Philippe Colomban, for being so kind with me during my stay in Paris. I would like to extend this acknowledgement also to the whole MONARIS research group. Especially, to Ludovic and Celine, for their personal support during my stay in Paris.

Thanks each and every one of “Paris Connection” team: Feas, Marine, Betta and Tomas. I don´t know how to give you thanks and explain the lived experience in that 3 months in Paris, but it was really great and I will never forget it. Feas thank you so much for everything, thank you for your tolerance, for your Buda´s phrases and most of all, for joining us!! 100%!!. Marine, merci pour ton hospitalité, pour ta cuisine exceptionnelle, et pour ton sens de l'humour. Tu es spéciale et ne change jamais !! Bonne chance dans ta nouvelle étape!! ELEVENNN!! Betta, grazie mille per tutto, grazie per la tua gentilezza e grazie

dolcissima amica per tua vera amicizia. PATATA!!. Finalmente quisiera dar las gracias a Tomas, gracias de todo corazón, primeramente por la vivencia compartida en Paris, en la que de una manera u otra nos supimos apoyar el uno en el otro y compartimos buenos momentos y cervezas arreglando el mundo y sobre todo posteriormente en ese mes en Chile, donde aparte de enseñarme mucho en el trabajo, me abriste la puerta primero de tu casa y también de tu familia. Recuerdos a Caro!!. Realmente he conocido poca gente como tú, y sé que pese a la distancia y el tiempo tendré un amigo para siempre. Dale Chungungo!! And finally thanks to the Mayflower barman for the best beers in Paris.

Gracias también a todas las personas que forman parte del grupo de investigación IBeA (profesores, técnicos de laboratorio, doctores, doctorando y secretaria), tanto en Leioa como en Zamudio porque quien mas quien menos ha colaborado también en este trabajo. Eskerrik asko!

Primeramente gracias a Josu, por tu positividad, entusiasmo y compañerismo en todo momento. Has sido un pilar muy importante y un hombro donde apoyarme. Eskerrik asko!

Como ocurre en muchos casos, lo último es lo que queda, y por eso empezaré dando las gracias a la nueva "hornada de químicos" y fichajes top Cristina e Iker. Cristina desde que has llegado a Zamudio, todo se ve de otra manera. Gracias por prestarte para ayudarme sobre todo en este último período y alegrarme en muchos momentos la escritura. Gracias también por ser cómo eres y sobre todo absolutamente nunca cambies pese a quien le pese, eres única. A Iker, darle las gracias también por los consejos y ayuda que me ha prestado también en este último período y por las conversaciones musicales y futbolísticas tan amenas, ¡La Beca es tuya crack!.

Gracias a Olivia, Leti, Ane, Ilaria y Claudia. A Olivia primeramente por la compañía y conversaciones en esos viajes interminables en la época de Máster; y por el apoyo que me has podido dar en estos 4 años. A Leti por todos los momentos tan amenos que nos has hecho vivir a todos, a Ane gracias también por la amabilidad que en todo momento me has brindado. A Ilaria también por el apoyo de este ultimo año y que ojala consigas la beca. Y finalmente a Claudia porque aunque fueron 2 meses conectamos muy bien, te esperamos para la próxima! Brava!. También agradecer a Marco, Iratxe, Arri, Nagore, Julene y Nikole por las horas compartidas en Zamudio.

Quisiera agradecer también a mis amigos y la cuadrilla en general por todo el apoyo prestado. Quizá esta última temporada os he tenido abandonados. Espero que de ahora en

adelante pueda volver a seguir disfrutando de buenos momentos y anécdotas con vosotros. Eskerrik asko peña!!.

En este punto quiero dar las gracias a mis padres y a Patri. Gracias por el apoyo y compresión prestada, los valores inculcados, el respeto y la educación hacia las personas y los consejos recibidos a lo largo de toda la vida. Os quiero, gracias de corazón!

Por último, quisiera dar las gracias nuevamente a una persona muy especial e indispensable para mí en la vida. Han pasado muchos años desde que nos conocimos y siempre has estado ahí, para los buenos y para los malos momentos; para las risas y para los llantos; para animarme y para apoyarme; para aconsejarme y también para abrirme los ojos cuando estaba equivocado. Por todo ello gracias de todo corazón. Gracias porque aunque quizá sea un poco tópico has sido, eres y espero que seas mi guía, y sé que sin ti todo esto no hubiera sido posible. Gracias por todo el esfuerzo realizado. Sé que al igual que yo has sufrido mi estrés y agobio sobre todo al final de la tesis, gracias por haber sabido siempre estar ahí.

Eskerrik asko Maite!!

Table of contents

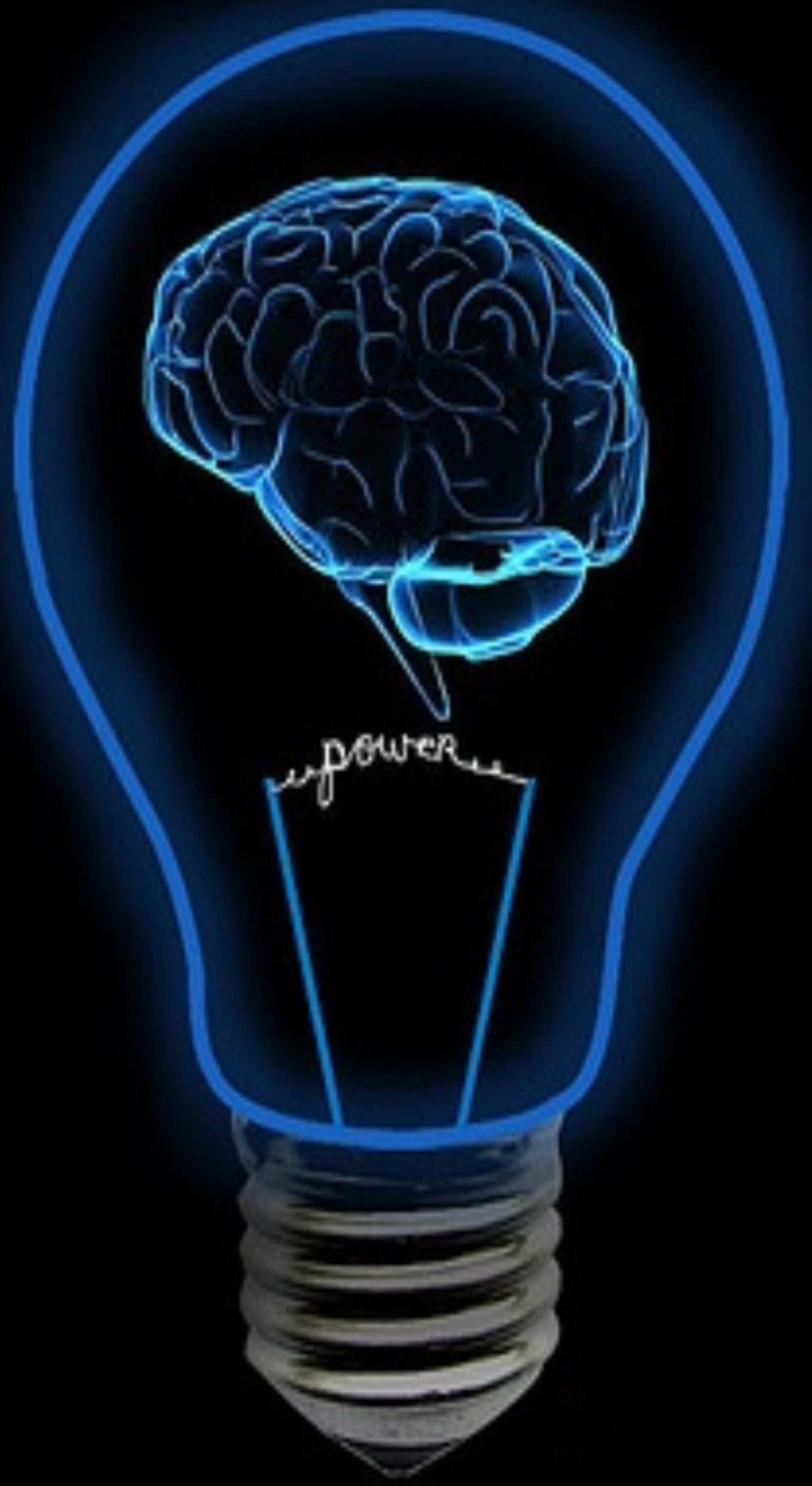

Chapter 1:
Introduction

CHAPTER 1.

INTRODUCTION

Cultural Heritage is an expression of the ways of living developed by a community and passed on from generation to generation, including customs, practices, places, objects, artistic expressions and values. Cultural Heritage is often expressed as either Intangible Cultural Heritage (ICH) or Tangible Cultural Heritage (TCH) [1]. ICH is the counterpart of culture which is intangible or untouchable, whereas intangible culture includes song, music, drama, skills, cuisine, annual festivals, crafts, and the other parts of culture that can be recorded but cannot be touched and interacted with. TCH includes buildings (houses, churches, castles, military fortifications, etc.) and historic places, monuments, artefacts, etc., which are considered worthy of preservation for the future. These include also objects significant to the archaeology, architecture, science or technology.

Inside TCH, the Built Heritage (BH) term is included. BH can be considered as one of the most important cultural assets, representing the historical layers of our built environment in places made of different types of materials (mud, brick, plaster, wood, metal, stone etc.). The importance of BH resides in the fact that it can contribute to the feelings of connectedness, a community pride and confidence. Built Heritage can excite curiosity about our past and enrich our daily lives.

Apart from buildings like cathedrals, houses, factories etc., BH includes areas, precincts and streetscapes. Of course, it is the physical evidence of our cultural development, giving a key to the understanding of our shared history, but the surrounded environment has also great importance. In this way, a new global term should be included along with BH: Landscape and Heritage (LH). LH represents inseparable concepts that allow the simultaneous assessment of all the elements that describe landscape (built heritage and surrounded environment). In recent years, different multidisciplinary groups belonging to UNESCO (archaeologists, chemists, geologists etc.) constituted a research platform that contributes to put into value the LH. For that purpose, scientific tools are being created. An example of this

type of platforms is the new “UNESCO Chair on Cultural Landscape and Heritage” [2]. This PhD is going to be focused on the characterization of the BH, but taking into account also the global influence of the LH.

1.1 From ancient natural rocks to actual building materials

To go deeper on the Built Heritage term, it is indispensable to understand the history of the materials used to create constructions and buildings. The use of natural materials inside constructions started in the prehistory. The natural rocks (mainly sandstones and limestone) accessible from the surrounding settlements helped to start constructing small structures in caves that serve as a refuge and as a place to live. During time, toward the year 3000 BC, the most traditional building materials started using: for example, wood and stone for structures and enclosures; skin as waterproofing in rainy places and absorbent tissues and absorbent soil in desert areas. As Swenson and Cheng reported [3], the building materials history is diverse and very extensive. Moreover, brick walls, clay and lime have been widely used to enclosure walls and floors. Around 600 BC, the Romans introduced a new binder agent in mortars, the pozzolanic materials (Pozzuoli soil), and the use of iron as stone reinforcement (Pont Salarius on the Tiber). In 180 BC, air mortar was widely used (without lime and sandstone in the ratio 1: 2). Around 150 BC, the first hydraulic mortar based on the use of burnt lime, brick dust and pozzolanic material coming from Vesuvius volcano was introduced by Romans. This recipe can be considered the first cement-type material used that hardens with humidity (hydrolysis, setting and hardening). They start using it in arches and vaults from constructions.

Towards 100 BC, the Syrians transformed the Sidon glass into transparent. The interest of the Romans about the transparent glass and the proliferation of doubtful quality workshops gave rise to the constitution of the first brand in the history: “CCAA” (Cologne Agruppinensis Claudia Augusta) responsible of the manufacturing of this type of glass. In the 100 AC, Romans invented the hollow bricks to conduct the hot air in the roman heating systems of their houses. Towards the 880 AC, the colored glass was improved. In that period, the window glass fragments were achieved with large diameter containers (with slight curve). In 1330, the lunar glass was developed which approximates to flat glass getting round or crescent large plates, which cut into squares to form the window glass.

In 1741 steel was used for first time as material for a hanging bridge in England. In 1790 James Keir discovers the “Corten” steel, that is protected from oxidation with a superficial oxide layer that stops the progress of steel oxidation. In 1796, Parker subject to cooking the hydraulic lime obtaining a special binder that he called "Roman cement". In 1824, Aspdin

obtained the first artificial cement burning chalk and lime mortar. This artificial cement was called Portland cement because its final color was similar to the natural stones of Portland (an English town). In 1849, Joseph Monier, developed the reinforced concrete. In 1882, Abbot tested various alloys, culminating in 1913 with the discovering of the stainless steel. In 1892 also, Kühlewein developed the asbestos cement; it is an impermeable material which allows the manufacture of cover plates, reservoirs, etc. In 1899, Hennebique built the first reinforced concrete building. In 1933, the ICI British Chemical discovered polyethylene. This discovery allowed to develop different types of plastics useful as building materials. In 1973, Delaware College built the first equipped house with solar panels and finally in 1980, the recycling materials started to be used as building materials.

Considering the building materials history through years, it has always tried to optimize the technological knowledge, when it was possible, to give solutions to the main construction problems. Naturally, there were differences between cities and rural areas as well as between the capital cities (large resources consumers) and secondary cities. The thing that characterizes our time from ancient is the refined exploitation, making materials such as glass and ceramics, which were indispensables to become cement or steel indispensable at the present.

1.2 Buildings close to the sea and its associated pathologies

The wide majority of the buildings show the indelible time footprint, manifested in the deterioration of the materials used in its constructions. The alteration of building materials is caused by a set of either anthropogenic and/or natural processes. In this way, the buildings indirectly show the effect of climate, environment and even the damage caused by humans.

The anthropogenic effects are taking special importance in recent years due to the increased presence of pollutants in the atmosphere. In general, all the atmospheric pollutants affect to all of the construction materials in a higher or lower way. As we will see later, different types of pathologies associated with anthropogenic sources can be numbered.

Apart from anthropogenic sources, there also exist natural sources that can affect the integrity of the building materials and depending the location different types can be present.

In this PhD buildings close to the sea that experiment particular types of pathologies (coming from anthropogenic and/or natural sources) are going to be considered. In the literature, many examples of deterioration processes on buildings close to the sea can be

found. Most of them focused their attention on the chemical alterations of the materials used in the specific constructions [4, 5].

1.2.1 Atmospheric Pollutants

The percentage of the main components on the air is fairly constant from ground levels to an altitude of about 100 km, where variations due to solar and cosmic radiation appear. As it s shown in Figure 1.1, Nitrogen and Oxygen are the major components of the air.

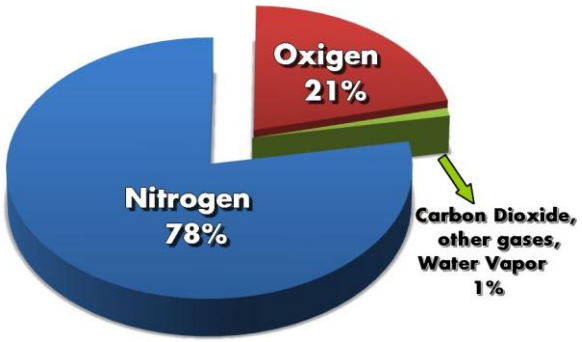

Figure 1.1. Chemical composition of the air from the terrestrial atmosphere.

Others, such as carbon dioxide (CO_2) or argon (Ar), are in a much lower ratio than the previous two ones, as can be seen in Table 1.1. Finally, a number of different compounds (NH_3, NO_2 and SO_2 etc.) whose presence is very low (trace levels) comparing to the other ones, are also present. However, its presence cannot be ignored because its harmful properties.

Apart from the classification of components depending on their concentration, it is possible to classify them according to their dwell time in the atmosphere. The dwell time is defined as the half-life of the molecules of a gas calculated by the relationship between the atmospheric concentration of a species and the emission rate thereof. According to this classification, permanent gases (higher living time), variable gases and highly variable gases (shorter living time) can be distinguished. Moreover these types of gases can also be found in different kind of atmospheres, such as marine or urban /industrial ones [6].

Table 1.1. Air chemical composition in ground level proximities.

GASES	% IN VOLUME	DWELL TIME
PERMANENTS		
Nitrogen (N_2)	78.08	10^6 Years
Oxigen (O_2)	20.95	$5 \cdot 10^3$ Years
Argon (Ar)	0.93	-
Helium (He)	0.00052	10^7 Years
Neon (Ne)	0.00018	-
Kripton (Kr)	0.0001	-
Xenon (Xe)	0.000008	-
VARIABLES		
Carbon Dioxide (CO_2)	0.03	15 Years
Metane (CH_4)	0.00015	5 Years
Hydrogen (H_2)	0.00005	7 Years
Dinitrogen monoxide (N_2O)	0.00002	8 Years
Ozone (O_3)	0.000002	2 Years
VERY VARIABLES		
Water (H_2O)	0-5	10 Days
Carbon Monoxide (CO)	0.00001	1/2 Year
Ammonia (NH_3)	0.0000006	7 Days
Nitrogen Dioxide (NO_2)	0.0000001	6 Days
Sulfur Dioxide (SO_2)	0.00000002	3 Days
Hydrogen Sulfide (H_2S)	0.00000002	2 Days

As it can be observed, the composition of the atmosphere is very diverse and its natural components can influence on building materials in a different ways depending on the type of materials. Thus, in recent years the concept of atmospheric acid gases (AAG) is taking particular importance. These AAG began to have influence in the atmosphere since the Industrial Revolution (end of 19th century) and increase in the atmosphere with the technological development, due to different types of emissions coming from different sources like road traffic, ships fuel combustion emissions, industry, etc. Among AAG, the most known ones are O_3 (oxidant), CO_2, SO_x and NO_x. These acid gases can react with alkaline building materials giving rise to different pathologies which affect their integrity. At this point, it is necessary to highlight that these anthropogenic pollutants (aerosols and/or

particle) can be deposited following two processes: Dry or wet depositions (DD and WD respectively).

On the one hand, in the DD, the AAG can react with both the porous material surface and the aerosol particles suspended in the atmosphere [7]. Moreover, the increase of some factors such as pollutant concentrations, air direction and turbulence can favor the dry deposition process [8]. The deposited salts and/or metallic particles can be accumulated in specific areas depending on the distance from the pollution source, the regularity of wetting and wet-drying cycles and of course the prevailing or preferential wind direction [9].

On the other hand, in the WD, the decay pathway starts with the transformation of the atmospheric pollutants (CO_2, SO_x, NO_x) into their respective acids (H_2CO_3, H_2SO_4, HNO_3) by interaction with the rainwater or even humidity [10, 11]. The formation of acids increases the acidity of natural rainwater, promoting the reaction between these acids and some original components of alkaline nature present in building materials giving as a result the formation of different salts (nitrates, sulfates, carbonates), depending on the original composition of the impacted building material and the acid type that interact with it [12].

1.2.2 Particulate Matter

In all around the world, there exists a type of pollution related with very small size particles, called Particulate Matter (PM). Usually PM is a mixture of solid particles and liquid droplets or clusters which can be found in the air. Some particles, such as dust, dirt, soot or smoke, are big enough to be seen at the naked eye. Others are so small that they can only be detected using an electron microscope.

According to their size, different types of particles can be mentioned. Particles with diameters between 2.5 and 10 micrometers are called PM_{10} and particles with diameters around 2.5 micrometers or smaller are called $PM_{2.5}$ respectively. Figure 1.2 illustrates graphically the relative size of these particles against a human hair.

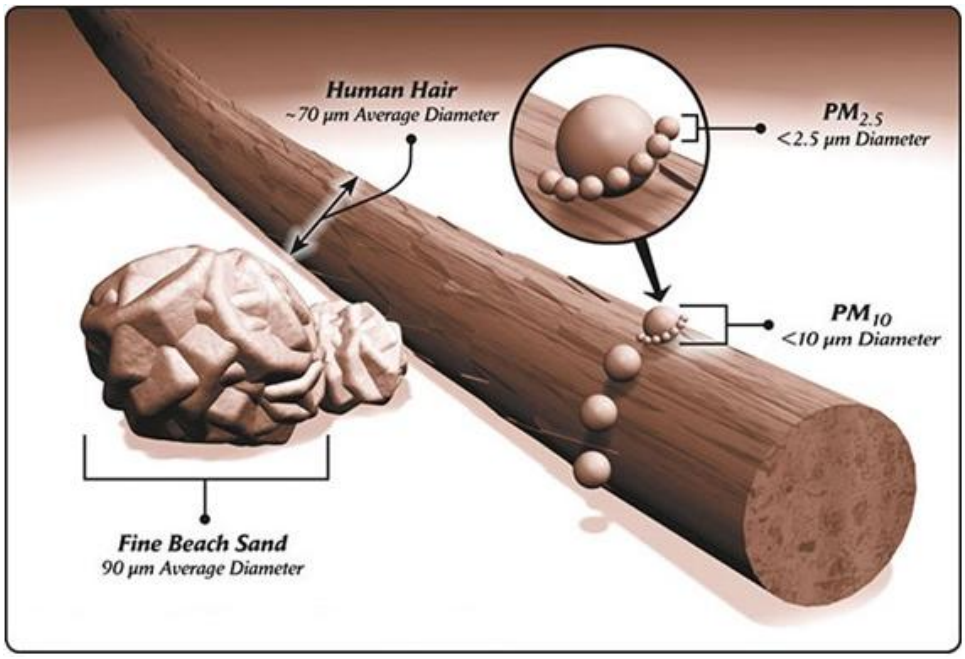

Figure 1.2. $PM_{2.5}$ and PM_{10} size particles compared with a human hair diameter size (source: US Environmental Protection Agency [13]).

The sources of these types of particulate matters are very variable and usually are closely related to the surrounded environment. Most of these particles can be found as a result of the release of different chemicals. In this way, two types of particulate matter can be found: (a) the so-called primary particles (PP), which are emitted directly from a source, such as construction places, paving roads, smokestacks or fires, etc. and (b) the so-called secondary particles (SP), which can form in the atmosphere as a consequence of the chemical reaction between the PP and the chemical compounds such as nitrogen oxides and sulfur dioxides coming from the emission of power plants, industries, road traffic etc. The PP can be of natural origin (e.g. crustal particles coming from the erosion of surrounding natural rocks, beach sands, sodium chloride from marine aerosol, etc.) or they can come also from anthropogenic sources. An example of this last could be the metallic particles emitted from the industry, road traffic, etc. The SPs are the most common pollution particles around the world. For this reason, the works that study the relation between PP and SP and its influence, in the conservation state of historical buildings, are gaining importance in the scientific research field [14-17].

1.2.3 Reactivity between Atmospheric Acid Gases (AAG) and building materials

As it has been mentioned before, the chemical composition of the atmosphere is very variable and the compounds present on it (gases and particles) can affect the building materials following a wet or a dry deposition. The wet deposition is usually known by the popular name of acid rain. Any rain is acid since the moment when the carbon dioxide from the atmosphere is dissolved. The CO_2 dissolved in the rain acidifies its pH up to 5.6. Additionally, sulphur dioxide also present in the atmosphere becomes its pH still lower. In the urban-industrial atmospheres and due to the high concentrations of SO_2 acid gas among others (NOx), this pH can decrease below 5.0. These gases are closely related with anthropogenic combustion processes; that is why their presence is more abundant in industrial areas or areas exposed to a polluted environment. Furthermore, natural combustion processes such as volcanic eruptions, fires, etc. can also contribute to increase the concentration of certain acid aerosols [18]. When these acid gases are incorporated in the rain, they can be dissolved giving as a result their respective acids in the rainwater. When these acids are deposited on the surface of building materials, they can react with their original components (mainly carbonates). The wet deposition of atmospheric pollutants is more damaging than the one following a dry deposition process (mainly particulate matter but also acid gases), since the atmospheric pollutants can penetrate easily the material by capillarity [11, 19-22].

The most common reactions that can take place between the building material and the emissions of CO_2 and SO_2 are summarized in reactions 1-9. In those reactions, M represents the cation of the main carbonate present in the building material (calcareous material) that it is being impacted by these kinds of wet depositions. Sometimes, a smaller concentration of carbonate is also enough to observe the deterioration products formed due to this reactions. A clear example of this situation is the case of sandstones with a certain percentage of calcium carbonate as the binder agent [23]. The formation of sulfate and nitrate compounds requires the presence of the respective carbonate because the direct reaction of H_2SO_4 or HNO_3 with the metal oxide M_2O_m (s) stops at a certain point due to the formation of a passivation layer that inhibits the quantitative transformation to sulfate or nitrate.

SO_2 (g) + ½ O_2 (g) → SO_3 (g) **(1)**

SO_3 (g) + H_2O → H_2SO_4 **(2)**

NO (g) + ½ O_2 (g) → NO_2 (g) **(3)**

$3NO_2$ (g) +H_2O → $2HNO_3$ + NO (g) **(4)**

CO_2 + H_20 → H_2CO_3 (s) **(5)**

M_2O_m (s) + H_2O → $2M(OH)_m$ (s) **(6)**

$2M(OH)_m$ (s) + mH_2CO_3 → $M_2(CO_3)m \cdot nH_2O$ (s) **(7)**

$M_2(CO_3)_m$ (s) + mH_2SO_4 → $M_2(SO_4)m \cdot nH_2O$ (s) **(8)**

$M_2(CO_3)_m$ (s) + $MHNO_3$ → $M(NO_3)m \cdot nH_2O$ (s) **(9)**

1.2.4 Weathering Crust Formation

In the Cultural Heritage field, historical buildings and monuments can act also as repositories of airborne pollutants, which can accumulate at the surfaces even in zones frequently soaked by rainwater but not washed out. For example, organic pollutants that can be present in the atmosphere are usually trapped in these crusts. It is well-known that the $PM_{2.5}$ and PM_{10} play also a key role in the formation of these types of crusts [24]. These weathering crusts formed in building surfaces can be considered as indicators of the surrounded pollution giving an idea of the pollution levels from a specific environment. Apart from the importance of the accumulation of these pollutants for human health, these crusts during time can contribute also to soiling process of stone surfaces promoting the losing material. Two types of crusts can be formed on the surface of building materials: White and Black Crusts.

1.2.4.1 White Crusts

The white crusts are usually carbonate-rich coatings and its presence is influenced by diverse factors such as building design, mortar composition and its water content. These white crusts can be formed on diverse building materials such as limestones, igneous rocks, concrete, tiles and even glasses [25]**.** Although a priori the white crusts look like crusted efflorescence, they cannot be considered efflorescences. Its main feature lies in its stability over time (see Figure 1.3). The white crusts do not suffer dissolution/crystallization cycles related to moisture regimes, they are not easily removed by rain-wash and they are also difficult to clean [26].

Figure 1.3. Example of white crust formed over building surface.

In many mortars, cements, etc. setting, calcium oxide (CaO) is usually used as main component. Therefore, calcium carbonate can be formed due to a previous hydration process of the corresponding calcium oxide, and its subsequent carbonation due to the influence of the atmospheric CO_2 (reaction 10). This calcium carbonate can react with CO_2 at high humidity values given free calcium and bicarbonate ions. When the water ecaporates, the calcium carbonate precipitates again (reaction 11). If these reactions take place and if they are repetitive during time, a re-precipitation process takes place, giving rise to large areas of white crusts over the material of building surface (see reactions 10 and 11).

$$CaO\,(s) + H_2O \leftrightarrows Ca(OH)_2\,(s) + CO_2\,(g) \leftrightarrows CaCO_3\,(s) + H_2O \quad \textbf{(10)}$$

$$CaCO_3\,(s) + CO_2\,(g) + H_2O \leftrightarrows Ca^{2+} + 2HCO_3^- \rightarrow CaCO_3\,(s) \quad \textbf{(11)}$$

In some cases, these white crusts (calcite as main component) can be the precursor of the subsequent black crust formations.

1.2.4.2 Black Crusts, soiling and deposits

The terms soiling, black crust and also deposit have been often used to mean different alterations that can takes place in building materials. According to the ICOMOS glossary [27], they are defined as follows:

Black crust: *Kind of crust developing generally on areas protected against direct rainfall or water runoff in urban environment. Black crusts usually adhere firmly to the substrate. They are composed mainly of particles from the atmosphere, trapped into a gypsum matrix ($CaSO_4{\cdot}2H_2O$).*

***Soiling**: Deposit of a very thin layer of exogenous particles (e.g. soot) giving a dirty appearance to the stone surface. With increasing adhesion and cohesion, soiling can transform into a crust. Soiling may originate from atmospheric pollutants (industrial, domestic or car exhaust products) or from particles transported by running water or heating convection.*

***Deposit**: Accumulation of exogenic material of variable thickness. Some examples of deposits: splashes of paint or mortar, sea salt aerosols, atmospheric particles such as soot or dust, remains of conservation materials such as cellulose poultices, blast materials etc. Not to be confused with: Crust, which has a visible thickness and deposit, which has a visible thickness and not systematically a dirty appearance."*

Therefore, black crusts are a particular kind or stage of soiling, which are due to form in atmospheric polluted environments, over non-washed surfaces and they will likely be formed especially in those construction materials with fractions of calcium carbonate (e.g. marbles, limestone, sandstones, mortars, frescoes, etc.), since this compound promotes the formation of gypsum. Meanwhile, the soiling, which may be transformable in a black crust, refers to the dirty appearance of the surfaces due to depositions of exogenous particles not always by atmospheric agents, leading to a confusion with the term deposit, which as soiling does not need to be formed necessarily by atmospheric agents, but in this case nor have a dirty appearance.

The black crusts are a black-grayish type of deterioration that appears on the materials surfaces. Generally, they are present in the building faces less exposed to rainfalls due to atmospheric pollutants dry deposition.

According to most of the works that can be found in the literature, in first stage gypsum layer in formed over the stone surface and then the deposition of the airborne particles takes place.

Gypsum is formed starting from the calcium carbonate from the stone itself. This carbonate can experiment a partial solubilization process due to the action of an acid, i.e. the dissolved CO_2 in the atmospheric aerosols or rain (reaction 12). After that, when the free (Ca^{2+}) ions reacts with the SO_4^{2-} present in the surrounded polluted atmosphere (SO_2 acid aerosol incorporated in the rainwater in the form H_2SO_4) gives rise to gypsum ($CaSO_4 \cdot 2H_2O$) and CO_2 gas. This sulfate starts to grow after dissolution-crystallization cycles (reaction 13).

$$CaCO_3\,(s) + H_2CO_3\,(dis) \leftrightarrows Ca^{2+} + 2HCO_3^- \quad \textbf{(12)}$$

$$Ca^{2+} + SO_4^{2-} \leftrightarrows CaSO_4\,(dis) \leftrightarrows CaSO_4 \cdot 2H_2O\,(s) \quad \textbf{(13)}$$

$$2HCO_3^- + 2H^+ \leftrightarrows 2CO_2\,(g) + 2H_2O \quad \textbf{(14)}$$

According to the mechanism of black crust formation described by Moropoulou et al. [28], on those areas protected from intensive washout, SO_2 and water vapor or rainwater diffuse at a high rate through the pores towards the $CaCO_3$-gypsum interface. Thus, new porous gypsum film layers must be formed at the $CaCO_3$-gypsum interface. As the thickness of the gypsum crust increases, the number and length of the pores decrease due to the larger molecular volume of gypsum compared with that of $CaCO_3$ and finally, at approximately 30 nm gypsum thickness, the pores cease to exist. Depending on the immediate environment (e.g. low relative humidity or higher temperatures, etc.), gypsum can be dehydrated losing a water molecules of hydration and providing a gypsum hemihydrate ($CaSO_4 \cdot 1/2H_2O$) or anhydrite ($CaSO_4$). These hydration-dehydration cycles actually play an important role in the deterioration of the porous stones as it generates inward migrations, causing a change in the volume of the carbonate mineral which can lead to the cracking or even breaking of the material itself.

The gypsum crust also increases the porosity, the specific surface area and the roughness of the surface, turning into the original stone in a good accumulator of (marine) aerosol particles (salts mainly), organic particles such as soot and unburned plant material, organic compounds (organic carbon, polycyclic aromatic hydrocarbons, volatile organic compounds, etc.), metallic particulate matter, microbial biomass with their metabolic products and/or biogenic pigments, etc. For instance, the accumulation of NaCl coming from the marine aerosol shifts the initial solubility of the gypsum at 42ºC to lower temperatures [29].

Figure 1.4 shows different examples of black crusts. The chemical composition of these black crusts can vary depending on the building geographic location. Thus, black crusts on buildings close to the sea will have different chemical composition than others located in rural or urban areas, depending on the compounds present in the atmosphere, which can be trapped in the porous matrix of the black crust. Although a priori, a location close to the sea can be free of pollutants, if in the surrounded environment, industry and ships traffic are present, these pollutants can be potentially accumulated on the black crusts. In the recent years because of the increased use of diesel fuels, a considerable increase of NO_X in the atmosphere has been registered. The acid aerosol can react with the primary particles emitted to the atmosphere, giving rise to nitrate particles as secondary particles, which can be also deposited and accumulated in the black crusts.

Figure 1.4. Examples of black crusts formed over A) limestone building surface in Germany, B) limestone building surface in Chile, C) sandstone building surface in U.S.A, D) limestone building corner surface in United Kingdom, E) sandstone building surface in France, F) brick wall.

Therefore, black crusts can be considered as natural passive samplers useful to determine the pollution of a specific environment. Considering that sometimes high concentrations of metals and organic pollutants can be trapped in this kind of matrix, preventive measurements must be taken if the building materials; where those black crusts are present, are going to be manipulated (e.g. restorations processes, demolish and clear-up works in old buildings.).

As it has been mentioned before, apart from being unaesthetic, black crust can also cause serious consequences on the physical integrity of materials where they grow up. However, sometimes it is better to leave these crusts on the material where they have been formed, instead of removing them, because their removal can cause the losing of the original material, because of the strong physicochemical joining of the black crusts to the surface of the building material itself.

1.2.5 Infiltration waters

Another common pathology that can be found in Built Heritage is the negative influence of infiltration waters. Depending on the area where the building is located, building materials can experiment different types of pathologies associated with water infiltrations. Normally, the reactions unchained by infiltration waters can happen in a synergistic way, together with other physical and chemical processes. The water infiltrations can reach the surface material by capillary action, favouring the ionic migrations (salts carried in these waters to the pores of the building materials), giving as a result the formation of new minerals. In this way, the infiltration waters coming from the ground can reach different heights depending on the porosity of the material, the evaporation rate and the critical water content of the soil. Once the water access to the inner part of the material, the formation of soluble salts by condensation takes place, and consequently the loss of material can occur. When ions transported by infiltration waters react with the original components of the building materials, the formation of new salts on the porous materials take place [30]. The crystallization of salts takes place when the saline phase from the infiltration reaches to supersaturation, and the thermodynamic characteristics of the media are suitable for the formation of crystalline nucleus from which crystals of the salts grow up [31]. Considering this observation, the principal decay sign on building materials which suffer from the impact of infiltration waters is the formation of soluble salts (carbonates, sulfates, nitrates and chloride salts) [32,33].

In the literature, many examples of historical buildings that suffer from the impact of infiltration waters can be found [34, 35]. As an example, a possible source of infiltration waters in a historical building could be a river annexed to it [34, 35]. Additional sources of infiltration waters rich in (salts) ions are gardens and agricultural soils annexed to the buildings [36, 37]. In this case, the salts input could come from the irrigation waters, which usually transport enough concentrations of nitrates and sulfates, arising from the use of ammonium fertilizers such as (NH_4NO_3 or $KNH_4(NO_3)_2$ and $(NH_4)_2SO_4$) [38, 39]. The ions coming from this kind of sources can penetrate through the pores of the building materials. Concretely, the ammonium cation (NH_4^+) from this kind of salts can react with the carbonates present in calcareous materials (reactions 15 and 16), giving as a result the crystallization of nitrate salts.

$$CaCO_3\,(s) + 2NH_4^+ \leftrightarrows Ca^{2+} + NH_3(g) + HCO_3^- + NH_4^+ \quad \textbf{(15)}$$

$$Ca^{2+} + 2NO_3^- \leftrightarrows Ca(NO_3)_2 \cdot 4H_2O \quad \textbf{(16)}$$

This newly crystallized salt can be formed inside the building material (sub-efflorescences) or on its surface (efflorescences) that can be later dissolved by the rain wash. In the Figure 1.5, a representation of water infiltrations and subsequent salts crystallizations is represented. In a first step, soluble salts migration from the infiltration waters to the building material itself takes place. The second step is the formation of salts preferentially on the external parts of the material (see Figure 1.5 B). After the formation of the efflorescences, a loss of material process start by rain dissolution, promoting also little cracks (see Figure 1.5 C). Finally these first small cracks give raise to the formation of bigger cracks and also to the loss of material, promoting in the worst cases, the wall or even building collapse (Figure 1.5 D).

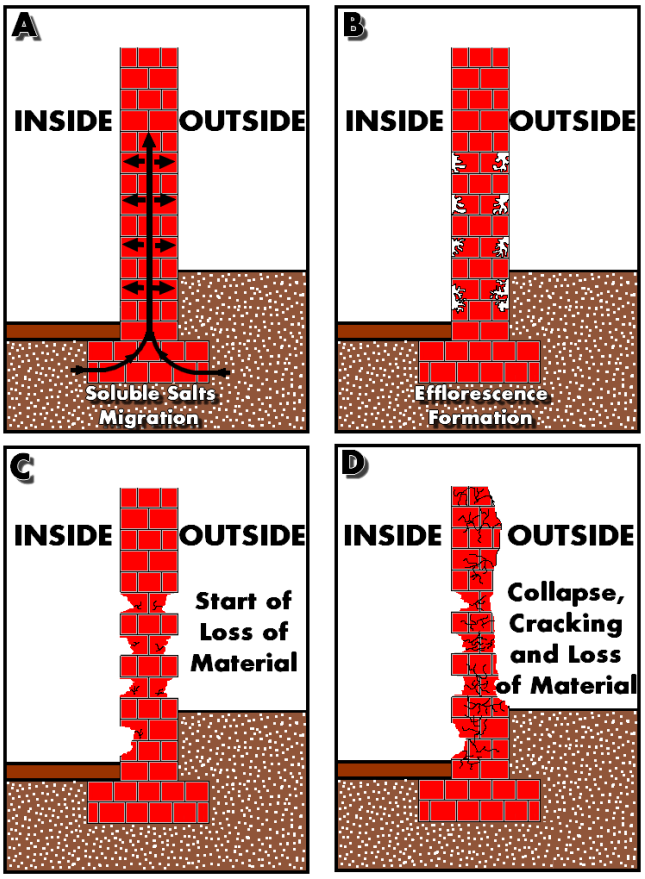

Figure 1.5. Water infiltration process and its affection to the building material.

1.2.6 Efflorescences

The efflorescences are saline aggregates, which are formed by the precipitation of the soluble salts present in the material itself or due to a reaction between original components of the building materials with salts coming from infiltration waters, or acid aerosols coming from the atmosphere. As it has previously mentioned, if the salts crystallize on the porous of the material and under the surface, they are called subeflorescences. On the contrary, if they

crystallize more internally, they are called cryptoeflorescences. Figure 1.6 shows an image of halite (NaCl) cryptoefflorescences acquired using scanning electron microscopy (SEM). Finally, the salts which crystallize on the outer part of the material are called efflorescences.

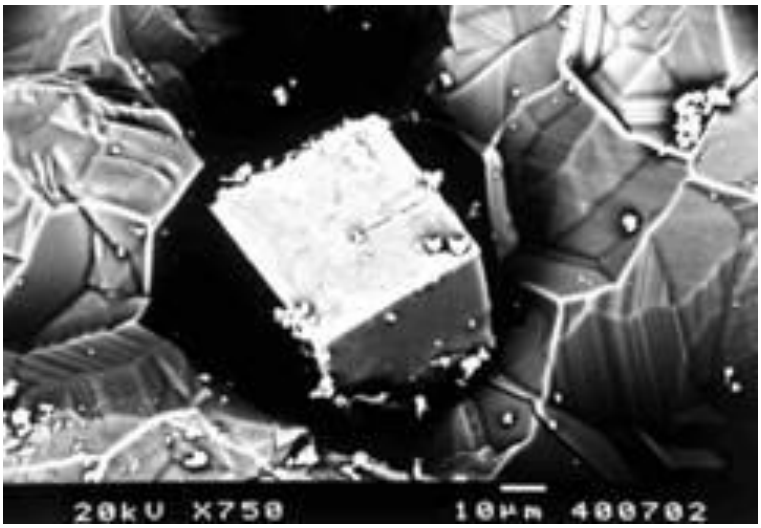

Figure 1.6. A SEM image of an halite (NaCl) cryptoefflorescence (source: University of Pablo Olavide, Seville (Spain). [40]).

An example of the formation of salts crystallizations inside the building materials is explained in the Figure 1.7. The crystallization process inside the pores follows several steps. In the first one, crystals are formed inside pores. Lower size pores are not held by these crystallized salts. This phenomenon takes place as a consequence of the porous material drying process, in which water is evaporated firstly in the biggest cavities, and then flows to smaller cavities. After that, pores are full of solutions of saturated or supersatured salts (Figure 1.7 A). In the second step, the crystals size increases, exceeding the building materials pore size and originating pressures on the pores of building materials. This pressure leads a perpendicular stress to the external part of the building material surface. This stress causes fissures which affect the integrity of the porous material (Figure 1.7 B). In the third step, salts crystallizations are concentrated on the open fissures, because the water evaporation is easier in those areas. Therefore, new crystals can grow in those areas, increasing the opening of the fissures (see Figure 1.7 C). Finally, while the fissures are opened and the saline solution is flowing, the contact area between the new formed crystals and the solution is higher, causing detachments of the superficial parts of the material or even the collapse of the material (Figure 1.7 D).

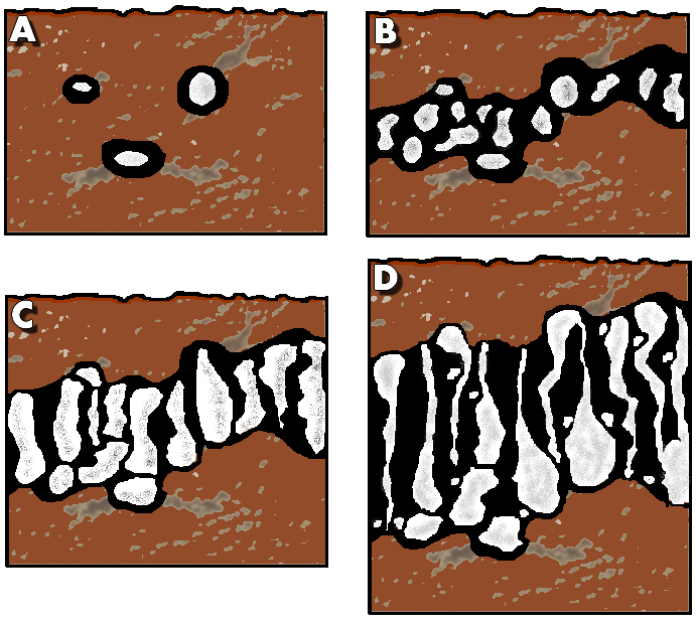

Figure 1.7. Steps of porous building materials decay after the salts crystallizations on their pores.

In the marine and surrounded environment, apart from the material itself, different types of sources can promote the generation of efflorescences. Marine aerosol carries different kind of salts which can be deposited on the pores of the material surface, promoting the accumulation and also the precipitation of new salts in the surface of the building material. Sometimes, the salts carried by the marine aerosol can be dissolved, penetrating through the inner areas of the material to suffer a subsequent re-crystallization on the inner pores of the material [41-43].

1.2.7 Is the biocolonization dangerous for buildings materials?

Biodeterioration and bioprotection are in an unstable equilibrium which can be unbalanced by environmental conditions, the substratum and the type of organisms colonizing the material. The influence of microorganisms colonizations on the conservation state of building materials has been widely studied. Most of the building materials exposed to the environment are susceptible to suffer biological colonizations and therefore to undergo their respective associated transformations. Microorganisms do not only inhabit on the surface of building materials, they can also penetrate into the material itself, to depths of several millimeters or even centimeters [44-46]. Biological growths can exercise influence over the physical and chemical properties of the building material where they grow up, accelerating its weathering and deterioration process.

One of the most important environmental factors that allow the growth of microorganisms on the building material is the water available on the media. Apart from that, relative

humidity percentage (%RH), ambient temperature, pressure on the material, the composition of the material itself, the building location and the orientation where the building material is placed, are important factors for the developing of biological colonizations [47]. Moreover, these factors determine in some cases which type of microorganisms can grow. Among the microorganisms or higher biological organisms that can colonize building materials the following ones can be cited.

1.2.7.1 Macroscopically Visible Organisms

Beside higher plants (e.g. ivy), which can induce a negative effect in the conservation state of building materials (e.g. material losing), lichens, mosses and algae are also macroscopically evident because they can cover building material surfaces. The growing of these organisms usually comes together with an aesthetic alteration of the building surfaces, since biological patinas or biofilms of specific colors (green, reddish, yellow, etc.) can be formed. Moreover, they induce a corrosive effect on the building substrate, because they excrete acid metabolites and also chelating agents that promote the solubilization and disintegration of the support were they grow up [48]. For example, lichens can provoke physical and chemical damages due to the penetration of their hyphae, which can be expanded or contracted, causing a volume change in the building material itself, propoting fissures, cracks and even holes. According to the chemical reactions that can take place, the acid metabolites secreted by this colonizers (e.g. carbonic acid) can solubilize the building material. The term *biodeterioration* suggest that biologically induced substrate weathering and mineral loss at significant depths and rates is taking place. However, lichen can have influence, for the majority of species and porous substrates, only in the upper millimeters of the material surface, leaving evidences of their biophysical and biochemical activity only in this superficial area.

Many researchers point out that lichens can also play a role of the building material surface protection. To evaluate if lichens can act as protectors of those materials, several factors must be evaluated: their attachment way to the substrate, its binding and waterproofing role and consider if their thallus provides and effective shield. Passive protection may be induced by the formation of an insoluble encrustation at the lichen-building material interface. Frequently, these kinds of encrustation are formed on stones, and not in building materials such as plasters and cements. These insoluble encrustations are usually made of calcium oxalate. The reaction of oxalic acid secreted by many lichen with the minerals (Ca^{2+}) of the rocks leads to the precipitation of oxalates [49]. As it is reported in the literature, the oxalate crystals are formed intracellularly, within the wall of the hyphae, and, when they

increase in length, theirs distal ends protrude through the hyphal wall [50, 51]. Among the different calcium oxalates that can be formed, weddellite ($CaC_2O_4 \cdot 2H_2O$) and whewellite ($CaC_2O_4 \cdot H_2O$) can be mentioned. Weddellite is the metastable form and whewellite the stable phase of the system, since the first one is transformed into the second one trough dissolution of the polyhydrate crystals. As an example of the positive effect of an oxalate layer formation on building materials, the work of Ariño et al. can be mentioned. In this work, the presence of lichens on the sandstone from the Baelo Claudia forum pavement (Spain) retards rainwater absorption, and it also prevents the abrasive action produced by airborne sands particles [52]. Other authors also suggest that lichens had an important moisture-controlling function for the environmental stressed stones such as the ones of a temple located in Angkor Wat (Camboia) [53].

In order to reproduce this natural protective oxalate patina, some researchers began to synthesize artificial calcium oxalate patinas to preserve the integrity of stones, mainly on marbles, 25 years ago [54].

Algae are other kind of colonizers which can also promote the physical damage and biocorrosion of the building materials where they grow up. But, according to some authors these colonizers can also act as protective agents for building materials. Concretely, Cutler et al. reported that sandstone from central Belfast heritage structures, exposed for around 100 years and colonized by green algae biofilms, showed less weathered surfaces [55].

1.2.7.2 Microorganisms

Microorganisms are defined as organisms not visible to the naked eye. According to the literature it is well known that those microorganisms are involved in rocks and mineral substrates decay. In this sense, a very wide number and variety of microorganisms can be present. Although in the materials many autotrophic and heterotrophic bacteria, algae and fungi are present, only some of them are involved in the deterioration of building materials. Among them, those which are able to excrete under stress or upon lysis some compounds from their cells that serve as nutrients for other heterotrophic decay microorganism, or interact directly with the material.

1.2.7.3 Phototropic microorganisms

One of the most common associations that can be found in colonized building materials is lichen and cyanobacteria communities. These kinds of communities usually can appear together with green, red algae and diatoms [56]. Depending of the location, the temperature, relative humidity, as well as the level of UV radiation, some microorganisms are predominant among others. Cyanobacteria and green or red algae growing on porous surfaces are well adapted to survive in regions with low levels of radiation [57]. Concretely, cyanobacteria can be thrived on the surface or several millimeters deep on the porous substrate.

The phototropic systems composed by cyanobacteria and alga can form biofilms on building surfaces that are deep or bright green in color and in conditions of higher relative humidity percentage they become deep black, pointing out that these systems are in a necrosis state. Apart from the aesthetic damage (color change), physical and chemical deterioration of the material surface also take place. Cyanobacteria are able to excrete different biogenic pigment and are also able to excrete organic acids and sugar derived carbonic acids, which are able to react with the original components from the material, promoting as a consequence fissures and cracks on it. Examples of cyanobacteria which are able to perforate strongly the materials are the endolithic cyanobacteria. Finally in general terms, algae are eukaryotic phototrophs and they can also have a negative influence on the conservation state of materials when they are associated with fungi or creating symbiotic system with lichens. Figure 1.8 shows an example of Phototropic system between algae and cyanobacteria.

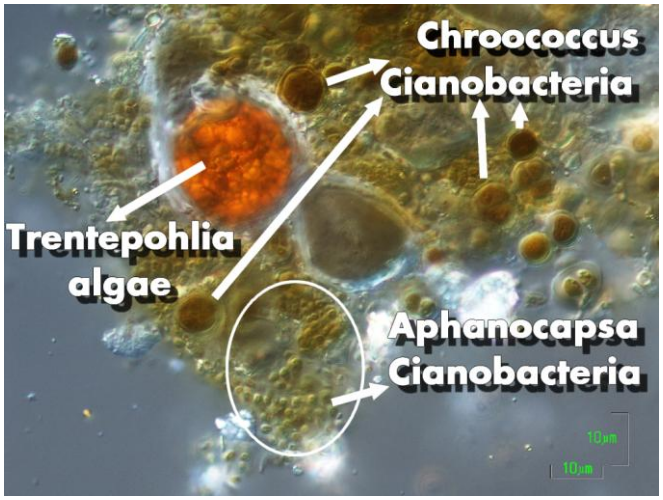

Figure 1.8. Example of a phototropic system extracted from a reddish biopatina on lime plaster showing the presence of a red algae (*Trentepohlia* Genus) and two types of cyanobacteria (*Aphanocapsa* and *Chroococcus*).

1.2.7.4 Chemolithotrophic microorganisms

Nitrifying bacteria is one of the most common chemolithotropic microorganisms that can colonize building materials. These bacteria are usually found on deteriorated surfaces of rocks. These kinds of bacteria are able to oxidize ammonium or nitrite compounds, which can be deposited on the material itself coming from infiltration waters or from the acid aerosols on the atmosphere respectively, into nitrates. These newly formed nitrates can be transformed into nitric acid. This last acid compound is able to react with the porous building material (mainly calcareous materials containing calcium carbonate):

$$NH_4^+ + 3/2\ O_2 \rightarrow 2H^+ + NO_2^- + H_2O \quad \textbf{(17)}$$

$$NO_2^- + 1/2\ O_2 \rightarrow NO_3^- \quad \textbf{(18)}$$

In the reaction 17, the oxidation of ammonium is usually catalyzed mainly by *Nitrosomonas*, *Nitrosococcus*, *Nitrosovibrio* and *Nitrospira* bacteria. Reaction 18 explains the oxidation of nitrite. In this case, this reaction is catalyzed mainly by *Nitrobacter*, *Nitrococcus* and *Nitrospira* bacteria [58].

The formed nitrate ions could react with calcium cations, from previously dissolved calcareous material, giving rise to more soluble compounds than the original materials, such as calcium nitrate tetrahydrate ($Ca(NO_3)_2 \cdot 4H_20$). These compounds can be dissolved, becoming the material more porous or even giving rise to cracks and material loss.

1.2.7.5 Chemoheterotrophic microorganisms

Chemoheterotrophic bacteria can also grow on building materials. These kinds of bacteria need organic carbon sources to grow. Normally, they usually take nutrients from the organic compounds from the atmosphere, animal droppings and from organic compounds that sometimes are present also in the material itself. These chemoheterotrophs can metabolize a wide variety of chemical compounds, such as polycyclic aromatic hydrocarbons (PAHs) derived from maritime traffic, road traffic or even from resins or waxes used for material consolidations. Normally chemoheterotrophic microorganisms are able to produce organic pigments and different types of organic acids. Examples of these types of bacteria are the filamentous bacteria *Actinomycetes* that cause serious damage on stone materials [59].

1.2.8 Loss of Material

One of the consequences of the pathologies described in the previous sections and promoted by anthropogenic and/or natural sources is the loss of building material.

According to salts formation, if those salts tend to accumulate in certain areas of the materials, they can promote the spalling of the material, starting a common pathology called *delamination*.

Another pathology related with the loss of material is the formation of *alveolizations* or *honeycombs.* This kind of pathologies can be found on many different building materials such as limestones, sandstones, volcanic stones, among others. These cavernous-like forms on stones are widely common in coastal environments, but also in other regions. In the literature, several mechanisms have been proposed to explain their origin. In their formation, different physical-chemical processes are involved: freeze-thaw cycles [60], chemical weathering [61, 62]**,** thermal changes [63], variation in moisture content in clay-rich rocks [64], erosion accelerated by the wind [65], erosion of large clasts [66] and salt weathering [67-69].

Where *alveoli*, *honeycombs* and *tafoni* (small cave-like features) are formed, salts can be usually found. This observation suggests that salt weathering is closely related with the presence of these formations [70]. Salt weathering is, as it has been explained before, one of the major pathologies that can take place in different kind of materials and in many types of environments [71, 72]. The newly formed salts may also contribute to the development of the cavernous and honeycomb weathering induced by chemical weathering [73, 74] or by thermal expansion [75]. In some works [76], honeycomb weathering process was experimentally reproduced in an unaltered and homogeneous stone. Thanks to these experiments, it was asses that in a first step, the saline solution is evaporated due to the effect of the wind, small cavities on the material. After that, heterogeneous wind flow induces a more rapid evaporation of the saline solution within the initial cavities, favoring the formation of deeper cavities due to the physical action of the new salts crystallized on the material (volume changes originating contractions and expansions of the material).

In the Figure 1.9 an example of alveolizations or honeycombs formed on a sandstone wall can be observed.

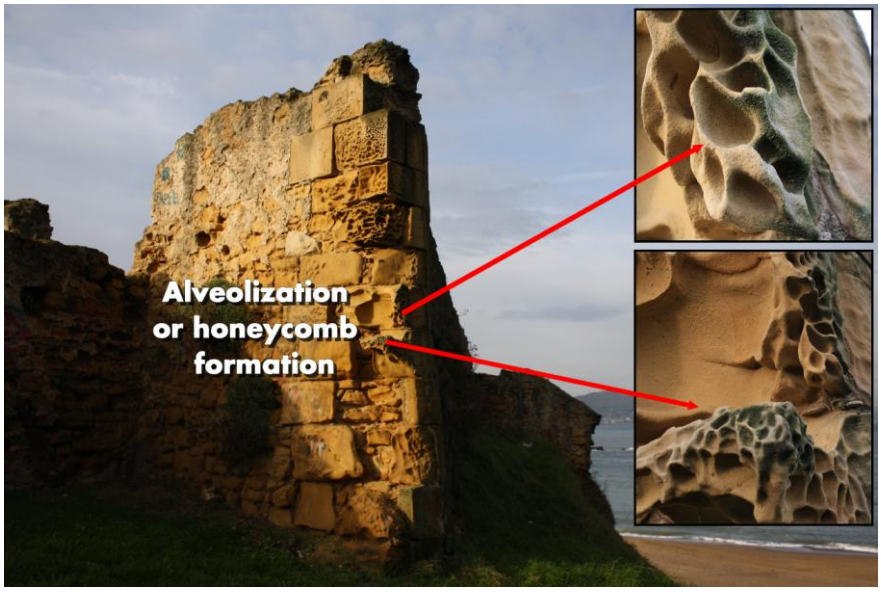

Figure 1.9. Example of alveolization or honeycomb formations on a wall, remain of an ancient fortification building of Getxo (Basque Country, north of Spain).

1.3 Marine Aerosol

The marine aerosol constitutes one of the most important natural aerosols from the Earth. It contributes significantly to the Earth's radioactive budget, biogeochemical cycling and even to the air quality. The marine aerosol comprises primary and secondary aerosol components.

1.3.1 Primary Marine Aerosol (PMA)

The primary marine aerosol (PMA) is formed due to the interaction of the wind on the ocean surface. The result of this interaction is the mechanical production of the sea spray (inorganic sea salt and organic matter). Sea spray, is produced when the bubbles from the generated whitecap burst. This process originates a jet of saline drops commonly known as sea spray aerosol (SSA). This aerosol carries particles of submicrometre size and up to a few micrometres [77]. It is estimated that whitecap formation occurs when the wind reaches the speed of $4 m \cdot s^{-1}$. One of the physical characteristics of the sea aerosol is the size of its suspended particles (>1 μm), which depends on the wind speed, sea-air water transfer, etc. [78]. The global annual mass emission of primary marine particles (PMP), or sea aerosol, is estimated to range from $2 \cdot 10^{12}$ to $1 \cdot 10^{14}$ $Kg \cdot year^{-1}$, which is comparable to that of dust aerosol [79].

Apart from this, the SSA has a key role in chemical reactions such as the coupled cycles of sulfate-sea salt [80, 81] and nitric acid-sea salt [82]. Apart from that, other authors focused their attention in the study of SSA role in climate change [83]. SSA has also been linked to the marine boundary layer (MBL) cycle through the activation of halogens, leading to ozone depletion [84-86].

1.3.2 Secondary Marine Aerosol (SMA)

The secondary marine aerosol (SMA) production consists on cluster particle formation resulting from gas to solid particle conversion [78]. The sulfur species present in the atmosphere and coming from the anthropogenic emissions are closely related with the SMA formation. The SMA formation occurs in two steps. The first step consists in the new particle formation via the nucleation of 0.5–1nm stable clusters. Once these clusters are formed, they can grow to larger sizes via condensation. The second step consists in the clusters growing via different heterogeneous reactions and aqueous phase oxidation of dissolved gases in existing aerosol particles. In terms of the sulfur cycle, dimethylsulphide (DMS), a waste produced by phytoplankton, is released from the ocean into the atmosphere where it undergoes oxidation by the OH radical to form SO_2, which is further oxidized to form H_2SO_4 [87]. H_2SO_4 is thought to participate in binary homogeneous nucleation with H_2O, and in ternary nucleation with H_2O and NH_3. Apart from this, in coastal zones where regular and significant particle nucleation takes place, iodine oxides have a key role in the clusters nucleations and growth [88].

1.3.3 Clusters sizes

In general, all the aerosol particles (AP) present in the environment have different diameters that are in the range from 1 nm to several hundred of microns. They are larger than typical atmospheric ions but can be as large as cloud droplets or ice crystals. In contrast to cloud droplets or ice crystals, they are rather homogeneously mixed in the atmosphere and do not just occur in isolated entities, such as clouds. AP are usually classified according to their diameters (see Table 1.2).

Table 1.2. Classification of aerosol particles accoding to their diameters.

Nucleation mode: 10^{-3} µm - 10^{-2} µm
Aitken mode: 10^{-2} µm – 0.1 µm
Accumulation mode: 0.1 µm – 1 µm
Coarse mode: Particles >1 µm

Aerosol particles larger than 10 μm are also referred as giant aerosol particles and all particles below 1 μm are sometimes summarized as fine particles. The middle term particles PM10 (10 μm >θ > 2.5 μm) and PM2.5 (2.5 μm> θ >1.0 μm) are the most abundant ones.

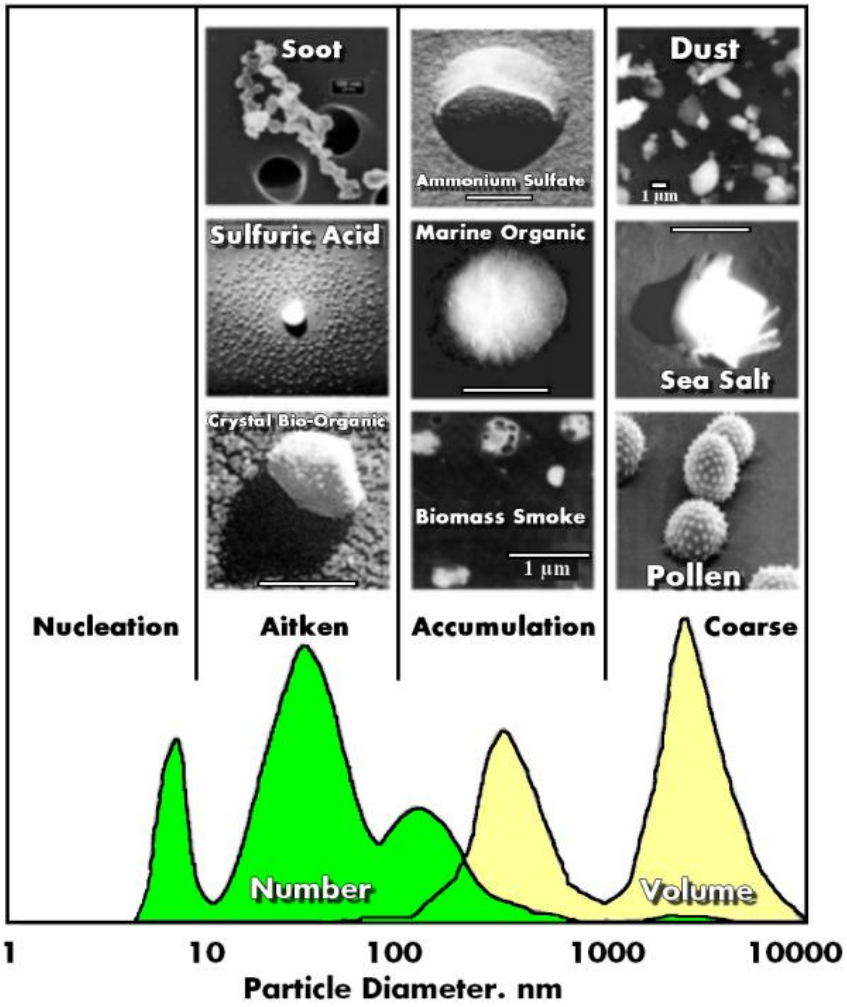

Figure 1.10. Images of different aerosol particles using an electron microscope as a function of the aerosol mode together with the typical number and volume distributions (source: Heintzenberg et al. [89]).

Each AP type depends of the specific source from where it comes (natural or anhropogenic) and the surrounded environment. Each AP can be present in higher or lower amount depending on the specific atmosphere. An example of this situation can be found in the Table 1.3.

Table 1.3. Types of aerosol particles and their sources as a function of a comparison between nowadays and pre-industrial times (source: reference [89]).

Species	Natural Processes	Anthropogenic Processes	Present day particle burden compared to pre-industrial time	Potential changes in the climatic conditions
PRIMARY PARTICLES				
Mineral dust	Wind erosion	Land use change and Industrial dust emissions	Dust increase	Changes in the winds and precipitations
Sea salt	Wind	-	-	Changes in the winds
Biological particles	Wind, Biochemical processes	Agriculture	?	Changes in the winds
Carbonaceous particles	Vegetation fires	Fossil fuel & Biomass Burning	Carbonaceous particles increase	Changes in the precipitations (droughts, etc.)
PRECURSORS OF SECONDARY PARTICLES				
Dimethyl-sulfide	Phytoplankton degradation	Increased oxidation capacity	Sulfates increase	Changes in the winds and air-sea
SO_2	Volcanic emissions	Fossil fuel combustion	Sulfates increase	
NH_3	Microbial activity	Agriculture	Ammonium nitrate increase	
NOx	Lightning	Fossil fuel combustion	Nitrate increase	Change in convective activities (e.g. lightning)
Volatile organic compounds	Emission from vegetation	Increased oxidation capacity and Industrial processes	Organic aerosol increase	-

1.3.4 The Chemical Composition of marine aerosol and its Influence on the Conservation State of Buildings close to the sea

In the literature, several works that describe the negative influence of marine aerosol on the conservation state of building materials from constructions located close to the sea [90, 91] can be found [92, 93].

Although the main mass fraction of marine aerosol is inorganic sea salt, organic matter is present and can also contribute to the overall mass [94]. Usually marine aerosol carries organic residue from the decomposition of algae, plankton and salts. The most abundant salt carried on marine aerosol is sodium chloride, but other types of chemical compounds like sulfates and nitrates can be also present [95, 96]**.**

Apart from chlorides, sulfates and nitrates other ions are also present in a suspended way such as Ca^{2+}, K^{+}, Mg^{2+}, Fe^{3+}, Al^{3+}, Sr^{2+}, NH_4^{+}, HCO_3^{-} and Br^{-}. Usually, organic matter has also a high importance because it represents around the 10% of marine aerosol [97, 98]. Additionally, $P.M_{2.5}$ and $P.M_{10}$ airborne particulate matter can be transported by the marine aerosol including metals such as Pb, Cd, Cr, Mn, Cu, Mo, Rh, Ni, As, Ti, V and Hg [99].

The source of these heavy metals can reside in the influence of maritime traffic, port activities and also industry or even road traffic [100]. Taking into account the physical properties of marine aerosol, where all the ions are suspended, historical buildings close to the sea can experiment their dry and wet depositions (explained in previous sections). Especially for buildings close to the sea, chloride and sulfate salts, can cause different kinds of pathologies [101, 102]. According to the literature, the most common soluble salts found in historical buildings often appear as efflorescences and subefflorescences. Among them, the most common ones are carbonates, sulfates, chlorides and nitrates with different numbers of crystallization waters.

1.4 Trends in Analytical Chemistry to evaluate the influence of marine aerosol on buildings close to the sea

In Spain, different research groups develop works related to the evaluation of the conservation state of historical buildings. In this way, different researchers from different fields working on thisfield are grouped in the "National Network of Science and Technology for the Conservation of Cultural Heritage: TecnoHeritage". This network is formed by 15 research groups of the CSIC, 30 research groups of Spanish Universities, 12 Cultural Institutions and 8 Private Companies. Specific research groups inside this network have focused their studies in the evaluation of biological colonizations or bioimpacts (Cesareo Saiz Jiménez research group, IRNA-CSIC, Sevilla), in the geological aspects of the materials (Sergio Sanchez-Moral research group (MNCN-CSIC, Madrid), Rafael Fort research group (ICM-CSIC/UCM, Madrid), Eduardo Sebastián research group (Granada University), etc.), in the resistance and behavior of materials (Angel Justo research group (INM-CSIC, Sevilla), María Teresa Varela research group (CEMAPA-Eduardo Torroja-CSIC, Madrid)), in the behavior of metallic alloys exposed to different kind of environments (Emilio Cano research group (CENIM, Madrid), in the application of lasers in the analysis of objects belonging to Cultural Heritage (Marta Castillejo research group (LANAPAC-Rocasolano-CSIC, Madrid)), in the elemental analysis of the materials using X-Ray Fluorescence (Clodoaldo Roldán research group, University of Valencia) and LIBS (Javier Laserna research group, University of Malaga).

IBeA (Analytical Research and Innovation) research group from the Analytical Chemistry Department of the University of the Basque Country UPV/EH, where this PhD Thesis was developed, is also member of the TechnoHeritage Network.

Concerning Spain, apart from these research groups members of the TechnoHeritage Network, additional research groups focused their attention on the study of the influence or interaction of marine aerosol on the Built Heritage. An example of that is the research group of Dr. Carolina Cardell from the Mineralogy and Petrology Department (Faculty of Science, University of Granada). Regarding the analytical techniques used to develop their works, SEM-EDS, XRD, XRF, Raman spectroscopy, infrared spectroscopy, etc. can be mentioned [103, 104].

Among Europe, during the 90´s decade, one of the research group pioneer in the study of the marine aerosol influence on building materials (mainly sandstones and limestones) was the group of the Doctors Fulvio Zezza and Fabio Macri, belonging to the Geotechnical Applied Geology Institute, Faculty of Engineering, in the Polytechnic University of Bari (Italy). This group combined different analytical techniques (SEM-EDS, X-Ray Fluorescence, EPMA, infrared spectroscopy, XRD, ion chromatography, atomic spectrometry, etc.) in order to understand the problems occurred in different historical buildings due to the marine aerosol [101, 102].

Another research group that studies the interaction between the atmosphere and historical buildings is the research group "Natural environmental and Anthropic hazards of Cultural Heritage" of the Professor Cristina Sabbioni and Dr. Alessandra Bonazza belongin to the Institute of Atmospheric Sciences and Climate of National Research Center (CNR-ISAC), in Bologna (Italy). This group combines chromatographic techniques with other analytical techniques such as infrared spectroscopy, X-Ray Diffraction, ICP-LA-MS etc., to characterize the pathologies present on Built Heritage as a consequence of the interaction between the environmental stressors and the building materials [5, 105-109].

Another example of that, is the research group of the Professor Christodoulos Pilinis belonging to the Department of Environment in the University of the Aegean (Greece). This research group is mainly involved in research projects dealing with acid depositions, indoor pollution and long range transport of pollutants and its influence in building materials. Inside their analytical methodology, analytical techniques such as SEM-EDS and also data treatment using chemometric tools were also included. With this last data treatment they try to explain the influence of different environmental stressors on the conservation state of historical buildings.

In South America, the research group (Departamento de Geologia/Lagemar- Universidade Federal Fluminense in Rio de Janeiro) of Dr. Maria Augusta M. Silva which evaluates the environmental influence on the soiling process and other deterioration process on stones used in buildings from Rio de Janeiro in Brazil. For that purpose, their use different analytical techniques such as SEM-EDS and Ion Chromatography

In Asia, the Professor Peter Brimblecombe leads a research group in the School of Energy and Environment from the City University of Hong Kong. Their main objective are to evaluate the long-term changed in urban air pollution and its effects on the building materials and also to evaluate the impact of climate change on historic sites.

Historically, from the 1990 to 1994, the Framework Programmes (FP) from the European Union/European Comission funded 18 projects, through two calls for proposals, related with the evaluation of salt marine spray influence on Mediterranean monuments made up of stone. In the context of the following FP4 (1994-1998), several projects were developed to complete the scientific information of the environmental degradation of Built European Heritage. Among the different tasks, one of them was to evaluate the effects of marine salts on Mediterranean/Atlantic coastal monuments and the impact of urban atmosphere pollution on modern and ancient mortars. From 2001 to 2004 and inside the FP, an European project ASSET project was developed leaded by the Professor Rob van Hees from the Delft University of Technology. In this project, conservation treatments were developed to isolate sea-salts trapped in the pores of European historic buildings that may be exposed to sea-salts (sea floodings, rising damp and marine spray) and also to prevent further penetration of those salts in the building materials from historic buildings [110].

Inside Horizon 2020, the Joint Programming Initiatives (JPI) related with the Cultural Heritage and Global Change must be mentioned. Currently, nine projects are officially running inside this JPI. Among others, EMERISDA and KISADAMA projects can be mentioned. The main objective of EMERISDA (Effectiveness of Methods against Rising Damp in Building) project is to evaluate the effectiveness of different methods against rising damp in Built Heritage [111]. On the contrary, the main objective of KISADAMA (Kinetic of Salt Crystallization and Mechanical Damage in Historic Masonry) project is to develop an integrate approach for modeling and analysis of the decay mechanism of masonry structures, made by fired clay or sandstone brick, due to salt crystallization [112]. Although different projects related with the salts crystallization are considered inside this JPI action related with Cultural Heritage and Global change, there is no specific mention to the influence of marine aerosol on the formation of salts in building materials.

1.5 References

[1] ICOMOS, International Cultural Tourism Charter. Principles And Guidelines For Managing Tourism At Places Of Cultural And Heritage Significance. ICOMOS International Cultural Tourism Committee (2002).

[2] http://www.catedraunesco.eu/en/ [last acceded June 2015].

[3] A. Swenson, P. C. Chang, Building Construction, Encyclopaedia Britannica (2008).

[4] S. McCabe, B. J. Smith, P. A. Warke, An holistic approach to the assessment of stone decay: Bonamargy Friary, Northern Ireland, Geological Society Special Publication (Building Stone Decay (2007) 271: 179-188.

[5] I. Ozga, N. Ghedini, C. Giosue, F. Tittarelli, C. Sabbioni, A. Bonazza, Assessment of air pollutant sources in the deposit on monuments by multivariate analysis, Science of the total environment (2014) 490: 776-784.

[6] C. O. Barrenetxea, A. P. Serrano, N. G. Delgado, F. R. Vidal, J. A. Blanco, Contaminación Ambiental. Una Visión desde la Química, Ed. Thompson, Madrid (2006) 306.

[7] D. Watt, B. Colston, Investigating the effects of humidity and salt crystallisation on medieval masonry, Building & Environment (2000) 35: 737–749.

[8] A. E. Charola, R. Ware, Acid deposition and the deterioration of stone: a brief review of a broad topic,Natural Stone, Weathering Phenomena, Conservation Strategies and Case Studies, Geological Society, London, Special Publications (2002) 205: 393-406.

[9] M. Maguregui, A. Sarmiento, I. Martínez-Arkarazo, M. Angulo, K. Castro, G. Arana, N. Etxebarria, J. M. Madariaga, Analytical Diagnosis Methodology to Evaluate Nitrate Impact on Historical Building Materials, Analytical & Bioanalytical Chemistry (2008) 391: 1361–1370.

[10] M. Pérez-Alonso, K. Castro, M. Álvarez, J. M. Madariaga, Scientific analysis versus restorer's expertise for diagnosis prior to a restoration process: the case of Santa Maria Church (Hermo, Asturias, North of Spain), Analytica Chimica Acta (2004)524: 379–389.

[11] G. C. Allen, A. El-Turki, K. R. Hallam, D. McLaughlin, M. Stacey, Role of NO_2 and SO_2 in degradation of Limestone, British Corrosion Journal (2000) 35: 35–38.

[12] H. Bravo, A. R. Soto, E. R. Sosa, A. P. Sánchez, J. A. L. Alarcón, J. Kahl, B. J. Ruíz (2006) Effect of acid rain on building material of the El Tajín archaeological zone in Veracruz, Mexico, Environmental Pollution (2006) 144: 655–660.

[13] http://www.epa.gov/ [last accessed 15 June 2015].

[14] I. Ozga, N. Ghedini, A. Bonazza, L. Morselli, C. Sabbioni, The importance of atmospheric particle monitoring in the protection of cultural heritage, WIT Transactions on Ecology and the Environment, Air Pollution XVII (2009) 123: 259-269.

[15] J. Watt, D. Jarret, R. Hamilton, Dose-response functions for the soiling of heritage materials due to air pollution exposure, Science of the Total Environment (2008) 400: 415-424.

[16] J. Sanjurjo-Sanchez, C. Alves, Decay effects of pollutants on stony materials in the built environment, Environmental Chemistry Letters (2012) 10: 131-143.

[17] P. Ortiz, M. A. Vazquez, R. Ortiz, J. M. Martin, T. Ctvrtnickova, M. P. Mateo, G. Nicolas, Investigation of environmental pollution effects on stone monuments in the case of Santa Maria La Blanca, Seville (Spain), Applied Physics A: Materials Science & Processing (2010) 100: 965-973.

[18] E. Ilyinskaya, A. Aiuppa, B. Bergsson, R. Di Napoli, T. Fridriksoon, A. A. Oladottir, F. Oskarsson, F. Grassa, M. Pfeffer, K. Lechner, R. Yeo, G. Giudice, Degassing regime of Hekla volcano 2012-2013, Geochimica et Cosmochimica Acta (2015) 159: 80-99.

[19] A.E. Charola, Review of the Literature on the Topic of Acidic Deposition on Stone, The National Center for Preservation Technology and Training, New York, USA (1998).

[20] A. Sarmiento, M. Maguregui, I. Martinez-Arkarazo, M. Angulo, K. Castro, M. A. Olazabal, L. A. Fernandez, M. D. Rodriguez-Laso, A. M. Mujika, J. Gómez, J. M. Madariaga, Raman spectroscopy as a tool to diagnose the impacts of combustion and greenhouse acid gases on properties of Built Heritage, Journal of Raman Spectroscopy (2008) 39: 1042-1049.

[21] J. A. Van Aardenne, G. R. Carmichael, H. Levy, D. Streets, L. Hordijk, Anthropogenic NO_x emissions in Asia in the period 1990-2020, Atmospheric Environment (1999) 33: 633-646.

[22] E. Dotsika, D. Psomiadis, D. Poutoukis, B. Raco, P. Gamaletsos, Isotopic analysis for degradation diagnosis of calcite matrix in mortar, Analytical & Bioanalytical Chemisty (2009) 395: 2227-2234.

[23] Q. Yongan, W. Min, Z. Wei, L. Da, Calcite cements in burrows and their influence on reservoir property of the Donghe sandstone, Tarim Basin, China, Journal of Earth Science (2012) 23: 129-141.

[24] A. Török, T. Licha, K. Simon, S. Siegesmund, Urban and rural limestone weathering; the contribution of dust to black crust formation, Environmental Earth Sciences (2010) 63: 675-693.

[25] C. Alves, White Crusts on Recent Buildings, Materials Science Forum (2010) 636-637: 1300-1305.

[26] C. Beall, Masonry Design and Detailing For Architects and Contractors, McGraw-Hill Professional, New York, USA, (2003).

[27] ICOMOS-ISCS, Illustrated glossary on stone deterioration patterns (2008)

[28] A. Moropoulou, K. Bisbikou, K. Torfs, R. Van Grieken, F. Zezza, F. Macri , Origin and growth of weathering crusts on ancient marbles in industrial atmosphere, Atmospheric Environment (1998) 32: 967-982.

[29] E. Bock, On the solubility of anhydrous calcium sulphate and of gypsum in concentrated solutions of sodium chloride at 25^{0}C, 30^{0}C, 40^{0}C and 50^{0}C, Canadian Journal of Chemistry (1961) 39: 1746-1751.

[30] F. Moreno, S. A. G. Vilela, A. S. G. Antunes, C. C. S Alvares, Capillary-rising salt pollution and granitic stone erosive decay in the parish church of Torre de Moncorvo (NE Portugal), implications for conservation strategy, Journal of Cultural Heritage (2006) 7: 56-66.

[31] G. Torroca, Porous building materials, Materials science of architectural conservation, ICCROM, Rome, Italy, (1998).

[32] E. S. Larsen, C. B. Nielsen, Decay of bricks due to salt, Materials & Structures (1990) 23: 16-25.

[33] P. Cardiano, S. Ioppolo, C. De Stefano, A. Pettignano, S. Sergi, O. Piraino, Study and characterization of the ancient bricks of monastery of San Filippo di Fragala (Sicily), Analytica Chimica Acta (2004) 519: 103-111.

[34] O. Gómez-Laserna, M. A. Olazabal, H. Morillas, N. Prieto-Taboada, I. Martinez-Arkarazo, G. Arana, J. M. Madariaga, In-situ spectroscopic assessment of the conservation state of building materials from a Palace house affected by infiltration water, Journal of Raman Spectroscopy (2013) 44: 1277-1284.

[35] O. Gómez-Laserna, N. Prieto-Taboada, H. Morillas, I. Arrizabalaga, M. A. Olazabal, G. Arana, J. M. Madariaga, Analytical study to evaluate the origin and severity of damage caused

by salt weathering in a historical Palace House: the attack of infiltration water, Analytical Methods (2015) 7: 4608-4615.

[36] M. Veneranda, M. Irazola, M. Díez, A. Iturregui, J. Aramendia, K. Castro, J. M. Madariaga, Raman spectroscopic study of the degradation of a middle age mural painting: the role of agricultural activities, Journal of Raman Spectroscopy (2014) 45: 1110-1118.

[37] V. Matovic, S. Eric, A. Kremenovic, P. Colomban, D. Sreckovic-Batocanin, N. Matovic, The origin of syngenite in black crusts on the limestone monument King´s Gate (Belgrade Fortress, Serbia)-the role of agriculture fertilizer, Journal of Cultural Heritage (2012) 13: 175-186.

[38] J. M. Sanchez Perez, I. Antiguedad, I. Arrate, C. Garcıa-Linares, I. Morell, The influence of nitrate leaching through unsaturated soil on groundwater pollution in an agricultural area of the Basque country: a case study, Science of the Total Environment (2003) 317: 173-187.

[39] L. F. Du, T. Zhao, C. Zhang, Z. An, Q. Wu, B. Liu, P. Li, M. Ma, Investigations on Nitrate Pollution of Soil, Groundwater and Vegetable from Three Typical Farmlands in Beijing Region, China, Agricultural Science in China (2011) 10: 423-430.

[40] http://www.upo.es/tym/WebCT/Medioambiente/page_12.htm [last accessed 30 June 2015].

[41] R. Sirbu, T. Negreanu-Pirjol, M. Sirbu, E. M. Cadar, Aggressivity of the marine medium on some buildings from the Romanian Black Sea coast, Journal of Environmental Protection and Ecology (2006) 7: 59-68.

[42] M. Azeroual, B. Baghdad, M. Bounakhla, A. Doukkali, M. El Wartiti, The atmospheric pollution and the marine aerosols impact on the monumental stone of the Sale surrounding wall´s entrances (Morroco), Physical & Chemical News (2007) 33: 59-64.

[43] E. A. L. Costa, V. P. Campos, L. C. P. da Silva Filho, H. A. Greven, Evaluation of the aggressive potential of marine chloride and sulfate salts on mortars applied as renders in the Metropolitan Region of Salvador-Bahia, Brazil, Journal of Environmental Management (2008) 90: 1060-1068.

[44] S. P. Gupta, K. Sharma, The role of fungi in biodeterioration of sandstone with reference to Mahadev temple, Bastar, Chhtisgarh, Recent Research in Science and Technology (2012) 4: 18-21.

[45] N. Schiavon, T. De Caro, A. Kiros, A. T. Caldeira, I. E. Parisi, C. Riccucci, G. E. Gigante, A multianalytical approach to investigate stone biodeterioration at a UNESCO world heritage

site: the volcanic rock-hewn churches of Lalibela, Northern Ethiopia, Applied Physics A: Materials Science Processing (2013) 113: 843–854.

[46] S. E. Favero-Longo, C. Gazzano, M. Girlanda, D. Castelli, M. Tretiach, C. Baiocchi, R. Piervittori, Physical and chemical deterioration of Silicate and Carbonate rocks by Meristematic Microcolonial Fungi and Endolithic Lichens (Chaetothyriomycetidae), Geomicrobiology Journal (2011) 28: 732–744.

[47] B. O. Ortega-Morales, C. Gaylarde, A. Anaya-Hernandez, M. J. Chan-Bacab, S. C. De la Rosa-García, D. Arano-Recio, J. Montero-M, Orientation affects Trentepohlia-dominated biofilms on Mayan monuments of the Rio Bec style, International Biodeterioration & Biodegradation (2013) 84: 351–356.

[48] J. Chen, H. P. Blume, L. Beyer, Weathering of rocks induced by lichen colonization- a review, Catena (2000) 39: 121-146.

[49] M. Maguregui, U. Knuutinen, J. Trebolazabala, H. Morillas, K. Castro, I. Martinez-Arkarazo, J. M. Madariaga, Use of in situ and confocal Raman spectroscopy to study the nature and distribution of carotenoids in brown patinas from a deteriorated wall painting in Marcus Lucretius House (Pompeii), Analytical & Bioanalytical Chemistry (2012) 402: 1529–1539.

[50] D. Pinna, Fungal physiology and the formation of calcium oxalate films on stone monuments, Aerobiologia (1983) 9: 157-167.

[51] B. B. Polynov, The first stages of soil formation on massive crystalline rocks, Pochcowdenie (1945) 7: 327–339 (Israel program for technical translations. Cat. No. 1350).

[52] X. Ariño, J. J. Ortega-Calvo, A. Gomez-Bolea, C. Saiz-Jimenez, Lichen colonization of the Roman pavement at Baelo Claudia (Cadiz, Spain): biodeterioration vs bioprotection, Science of the Total Environment (1995) 167: 353-363.

[53] T. Warscheid, H. Leisen, Microbiological studies on stone deterioration and development of conservation measures at Angkor wat, Biocolonization of Stone : Controland Preventive Methods, Proceedings from the MCI Workshop Series, Vol.2, eds A. E. Charola, C. McNamara and R. J. Koestler (Washington, DC USA) Smithsonian Institution Scholarly Press) (2011) 1-18.

[54] A. Bralia, M. Matteini, A. Moles, G. Sabatini, La sintesi degli ossalati di calcio nella interpretazione delle patine presenti sui marmi esposti all'aperto. Risultati Preliminari. Le

pellicole ad ossalati: Origine e significato nella conservazione delle opere d'arte, Milano 1989.

[55] N. A. Cutler, H. A. Viles, S. Ahmad, S. McCabe, B. J. Smith, Algal "greening" and the conservation of stone heritage structures, Science of the Total Environment (2013) 442: 152-164.

[56] N. T. Eriksen, Heterotrophic microalgae in biotechnology, Microalgae (2012) 347-412.

[57] D.M. John, Algal growths on buildings: a general review and methods of treatment, Biodeterioration Abstracts (1988) 2: 81-102.

[58] R. L. Mancinelli, The nature of nitrogen: an overview, Life support & biosphere science: International journal of earth space (1996) 3: 17–24.

[59] M. Saarela, H.L. Alakomi, M. L. Suihko, L. Maunuksela, L. Raaska, T. Mattila-Sandholm, Heterotrophic microorganisms in air and biofilm samples from Roman catacombs, with special emphasis on actinobacteria and fungi, International Biodeterioration & Biodegradation (2004) 54: 27-37.

[60] A. Cailleux, Taffonis et érosion alveolaire, Cahiers géologiques de Thoiry (1953) 16–17: 130–133.

[61] E. D. Gill, E. R. Segnit, N. H. McNeill, 1981, Rate of formation of honeycomb weathering features (small scale tafoni) on the Otway Coast, S. E. Australia, Royal Society of Victoria Proceedings (1981) 92: 149–154.

[62] D.N. Mottershead, K. Pye, 1994, Tafoni on coastal slopes, South Devon, U.K., Earth Surface Processes and Landforms (1994) 19: 543–563.

[63] W. Klaer, Verwitterungsformen in Granit auf Korsika, Petermanns Geographische Mitteilungen (1956) 261: 1-146.

[64] D. Dragovich, The origin of cavernous surfaces (tafoni) in granitic rocks of southern South Australia, Zeitschrift für Geomorphologie (1969) 13: 163–181.

[65] K. Futterer, Ueber Windkorrasion am Heidelberg Schlossturm, Mitteilungen der gross herzoglichen badischen geologisches Landesanstalt (1899) 5: 471–495.

[66] I. Schattner, Weathering phenomena in the crystalline of the Sinai in the light of current notions, Research Council of Israel Bulletin (1961) 10: 247–266.

[67] I. S. Evans, Salt crystallization and rock weathering: A review, Revue Géomorphologie Dynamique, (1970) 19: 153–177.

[68] W. C. Bradley, J. T. Hutton, C. R. Twidale, Role of salts in development of granitic tafoni, South Australia, Journal of Geology (1978) 86: 647–654.

[69] G. E. Mustoe, The origin of honeycomb weathering, Geological Society of America Bulletin (1982) 93: 108–115.

[70] D. N. Mottershead, Spatial variations in intensity of alveolar weathering of a dated sand- stone structure in a coastal environment, Weston-super-Mare, UK, Rock weathering and landform evolution: John Wiley and Sons, Chichester (1994) 151–174.

[71] A. S. Goudie, H. Viles, Salt weathering hazards, John Wiley and Sons, Chichester, (1997) 241 p.

[72] I. S. Evans, Salt crystallization and rock weathering: A review, Revue Géomorphologie Dynamique (1970) 19: 153–177.

[73] P. K. Weyl, Pressure solution and the force of crystallization: A phenomenological theory, Journal of Geophysical Research (1959) 64: 2001–2025.

[74] J. P. McGreevy, A preliminary scanning electron microscope study of honeycomb weathering of sandstone in a coastal environment, Earth Surfaces Processes and Landforms (1985) 10: 509–518.

[75] A. R. Young, Salt as an agent in the development of cavernous weathering: Geology (1987) 15: 962–966.

[76] C. L. Johannessen, J. J. Feiereisen, A. N. Wells, Weathering of ocean cliffs by salt expansion in a mid-latitude coastal environment: Shore and Beach (1982) 50: 26–34.

[77] C. Rodriguez-Navarro, E. Doehne, E. Sebastian, Origins of honeycomb weathering: The role of salts and wind, GSA Bulletin (1999) 111: 1250–1255.

[78] C. D. O'Dowd, G. de Leeuw, Marine aerosol production: a review of the current knowledge, Philosophical Transactions of Royal Society A (2007) 365: 1753-1774.

[79] C. Textor, M. Schulz, S. Guibert, S. Kinne, Y. Balkanski, S. Bauer, T. Berntsen, T. Berglen, O. Boucher, M. Chin, F. Dentener, T. Diehl, R. Easter, H. Feichter, D. Fillmore, S. Ghan, P. Ginoux, S. Gong, J. E. Kristjansson, M. Krol, A. Lauer, J. F. Lamarque, X. Liu, V. Montanaro, G. Myhre, J. Penner, G. Pitari, S. Reddy, O. Seland, P. Stier, T. Takemura, X. Tie, Analysis and

quantification of the diversities of aerosol life cycles within AeroCom, Atmospheric Chemistry and Physics (2006) 6: 1777-1813.

[80] C.D. O'Dowd, J.A. Lowe, M.H. Smith, Coupling sea-salt and sulphate interactions and its impact on predicting cloud droplet concentrations, Geophysical Research Letters (1999) 26: 1311–1314.

[81] C. D. O'Dowd, J. A. Lowe, N. Clegg, S. L. Clegg, M. H. Smith, Modelling heterogeneous sulphate production in maritime stratiform clouds, Journal of Geophysical Research (2000) 105: 7143–7160.

[82] L. L. Sørensen, S. Pryor, G. de Leeuw, M. Schulz, Flux divergence for nitric acid in the marine atmospheric surface layer, Journal of Geophysical Research (2005) 110: D15306.

[83] Intergovernmental Panel on Climate Change (IPCC) In Climate change 2001: the scientific basis (eds J. T. Houghton, Y. Ding, D. J. Griggs, M. Noguer, P. J. van der Linden & D. Xiaosu), Cambridge University Press, New York, USA, (2001).

[84] C. D. O'Dowd, J. A. Lowe, M. H. Smith, A. D. Kaye, The relative importance of sea-salt and nss-sulphate aerosol to the marine CCN population: an improved multi-component aerosol-droplet parameterization, Quarterly Journal of the Royal Meteorological Society (1999) 125: 1295–1313.

[85] R. Vogt, P. J. Crutzen, R. Sander, A mechanism for halogen release from sea salt aerosol in the remote marine boundary layer, Nature (1996) 383: 327–330.

[86] G. McFiggens, J. M. C. Plane, B. J. Allan, L. J. Carpenter, H. Coe, C. D. O'Dowd, A model study of Iodine chemistry in the marine boundary layer, Journal of Geophysical Research (2000) 105: 14371–14386.

[87] R. J. Charlson, J. E. Lovelock, M. O. Andreae, S. G. Warren, Oceanic phytoplankton, atmospheric sulfur, cloud albedo and climate, Nature (1987) 326: 655–661.

[88] kela, L. Pirjola, M. Kulmala, S. G. Jennings, H. Berresheim, H.C. Hansson, G. de Leeuw, G. J. Kunz, A. G. Allen, C. N. Hewitt, A. Jackson, Y. Viisanen, T. Hoffmann, A dedicated study of new particle formation and fate in the coastal environment (PARFORCE): overview of objectives and initial achievements, Journal of Geophysical Research (2002) 107: 8108.

[89] J. Heintzenberg, F. Raes, S. Schwartz, Atmospheric Chemistry in a Changing World, Chapter 4. Tropospheric Aerosols, Springer-Verlag, New York, USA, (2003).

[90] E. A. L. Costa, V. P. Campos, L. C. P. da Silva Filho, H. A. Greven, Evaluation of the aggressive potential of marine chloride and sulfate salts on mortars applied as renders in the Metropolitan Region of Salvador - Bahia, Brazil, Journal of Environmental Management (2008) 90: 1060-1068.

[91] M. Vendrell-Saz, M. Garcia-Valles, S. Alarcon, J. Molera, Environmental impact on the Roman monuments of Tarragona, Spain, Environmental Geology (1996) 27: 263-269.

[92] N. A. Stefanis, P. Theoulakis, C. Pilinis, Dry deposition effect on marine aerosol to the building stone on the medieval city of Rhodes, Greece, Building and Environment (2009) 44: 260-270.

[93] K. M. Anwar Hossain, S. M. Easa, M. Lachemi, Evaluation of the effect of marine salts on urban built infrastructure, Building and Environment (2009) 44: 713-722.

[94] M. Claeys, W. Wang, R. Vermeylen, I. Kourtchev, X. Chi, Y. Farhat, J. D. Surratt, Y. Gómez-González, J. Sciare, W. Maenhaut, Chemical characterisation of marine aerosol at Amsterdam Island during the austral summer of 2006–2007, Journal of Aerosol Science (2010)41: 13-22.

[95] Y. Zhao, Y. Gao, Acidic species and chloride depletion in coarse aerosol particles in the US east coast, Science of the Total Environment (2008) 407: 541-547.

[96] S. S. Abdalmogith, R. M. Harrison, R. G. Derwent, Particulate sulphate and nitrate in Southern England and Northern Ireland during 2002/3 and its formation in a photochemical trajectory mode, Science of the Total Environment (2006) 368: 769-780.

[97] W. L. Chameides, A. W. Stelson, Aqueous-phase chemical processes in deliquescent sea salt aerosols: A mechanism that couples the atmospheric cycles of S and sea salts, Journal of Geophysical Research (1992) 97: 565-580.

[98] H. Tervahattu, J. Juhanoja, V. Vaida, A. F. Tuck, J. V. Niemi, K. Kupiainen, M. Kulmala, H. Vehkamäki, Fatty acids on continental sulfate aerosol particles, Journal of Geophysical Research-Atmospheric (2005) 110: 1984-1991.

[99] A. Arruti, I. Fernandez-Olmo, A. Irabien, Regional evaluation of particulate matter composition in an Atlantic coastal area (Cantabria region, northern Spain): Spatial variations in different urban and rural environments, Atmospheric Research (2011) 101: 280-293.

[100] E. T. Gomez, T. Sanfeliu, J. Rius, M. M. Jordan, Evolution, Sources and Distribution of Mineral Particles and Amorphous Phase of Atmospheric Aerosol in An Industrial and Mediterranean Coastal Area, Water Air & Soil Pollution (2005) 167: 311-330.

[101] F. Zezza, F. Macri, Marine aerosol and stone decay, Science of the Total Environment (1995) 167: 123-143.

[102] K. Torfs, R. van Grieken, R. Zezza, N. García, F. Macri, The catedral of Bari, Italy: evaluation of environmental effects on stone decay phenomena, Studies in Conservation (1997) 42: 193-206.

[103] B. Horemans, C. Cardell, L. Bencs, V. Kontozova-Deutsch, K. de Wael, R. Van Grieken, Evaluation of airborne particles at the Alhambra monument in Granada, Spain, Microchemical Journal (2011) 99: 429-438.

[104] C. Cardell, T. Rivas, M. J. Mosquera, J. M. Birginie, A. Moropoulou, B. Prieto, B. Silva, R. van Grieken, Patterns of damage in igneous and sedimentary rocks under conditions simulating sea-salt weathering, Earth Surface Processes and Landforms (2003) 28: 1-14.

[105] D. Barca, V. Comite, C. M. Belfiore, A. Bonazza, M. F. La Russa, S. A. Ruffolo, G. M. Crisci, A. Pezzino, C. Sabbioni, Impact of air pollution in deterioration of carbonate building materials in Italian urban environments, Applied Geochemistry (2014) 48: 122-131.

[106] N. Ghedini, I. Ozga, A. Bonazza, M. Dilillo, H. Cachier, C. Sabbioni, Atmospheric aerosol monitoring as a strategy for the preventive conservation of urban monumental heritage: The Florence Baptistery, Atmospheric Environment (2011) 45: 5979-5987.

[107] I. Natali, P. Tomasin, F. Becherini, A. Bernardi, C. Ciantelli, M. Favaro, O. Favoni, V. J. Forrat-Perez, I. D. Olteanu, M. A. Romero-Sanchez, A. Vivarelli, A. Bonazza, Innovative consolidating products for stone materials: field exposure tests as a valid approach for assessing durability, Heritage Science (2015) 3: 6.

[108] S. A. Ruffolo, V. Comité, M. F. La Russa, C. M. Belfiore, D. Barca, A. Bonazza, G. M. Crisci, A. Pezzino, C. Sabbioni, An analysis of the black crusts from the Seville Cathedral: A challenge to deepen the understanding of the relationship among microstructure, microchemical features and pollution sources, Science of the Total Environment (2015) 502: 157-166.

[109] C. M. Belfiore, D. Barca, A. Bonazza, V. Comité, M. F. Russa, A. Pezzino, S. A. Ruffolo, C. Sabbioni, Application of spectrometric analysis to the identification of pollution sources

causing cultural heritage damage, Environmental Science and Pollution Research (2013) 20: 8848-8859.

[110] A. Hacquebord, B. Lubelli, R. van Hess, T. Nijland, Youth in Conservation of Cultural Heritage, YOCOCU 2012, Evaluation of Spreading and Effectiveness of Injection Products against Rising Damp in Mortar/Brick Combinations, Procedia Chemistry (2013) 8: 139-149.

[111] http://www.emerisda.eu/about-project/project-description/summary/ [last accessed 11 July 2015].

[112] http://www.kisadama.eu/node/1 [last accessed 11 July 2015].

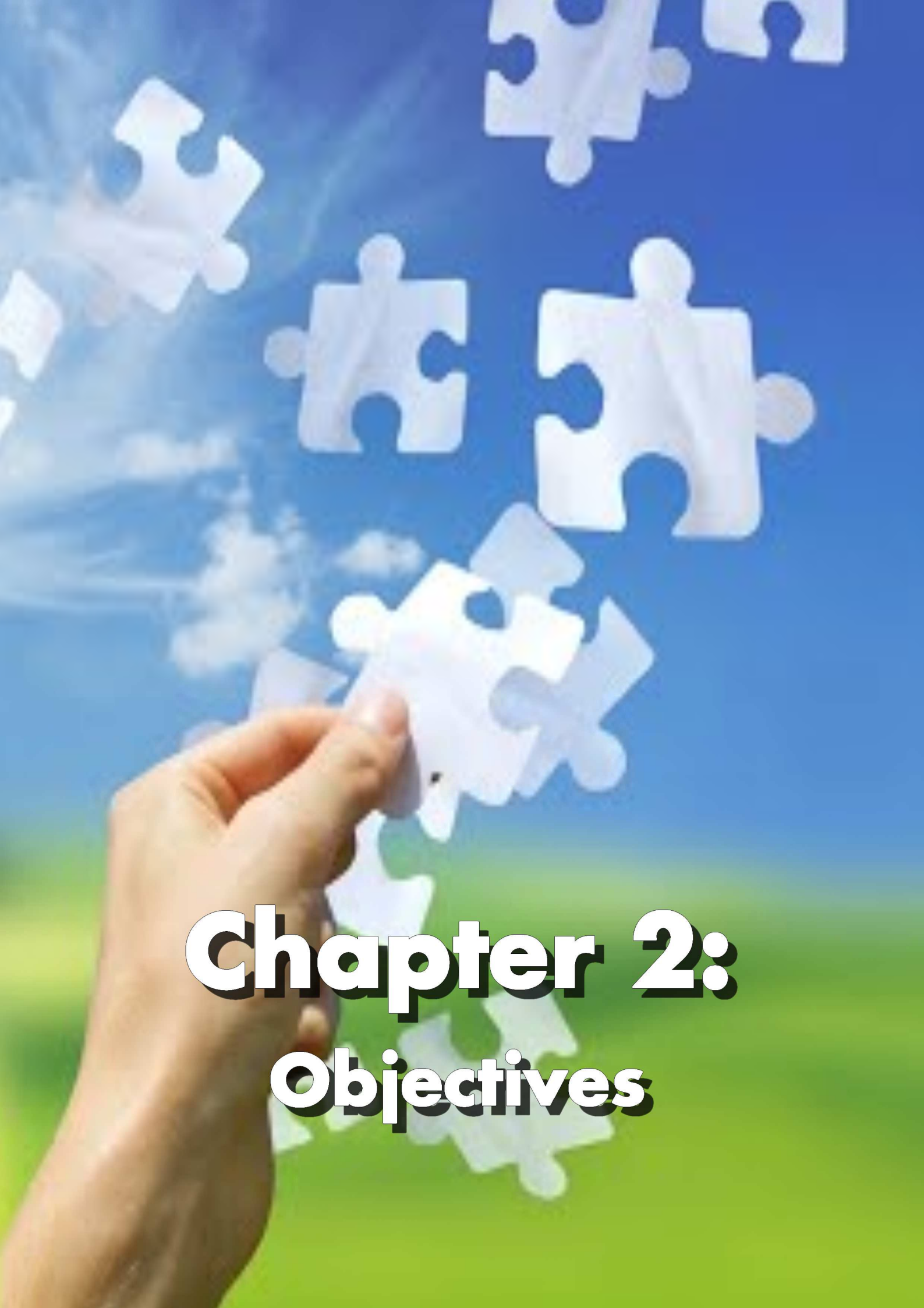

Chapter 2:
Objectives

CHAPTER 2.

OBJECTIVES

The main objective of this PhD Thesis was to apply a diagnosis protocol based on the use of a multianalytical methodology valid to characterize the deterioration compounds present on the pathologies from different kind of building materials used mainly on historical constructions, which are negatively influenced by the marine aerosol and other natural and/or anthropogenic environmental stressors, which can be present in different kind of marine environments. Three different marine scenarios, which can have negative influence in the conservation state of the building materials included in different constructions, have been considered as representative of the European coastal areas: (1) the direct impact of the marine aerosol without the influence of the urban-industrial pollution on the Igueldo lighthouse (San Sebastian, Basque Country, north of Spain), (2) the diffuse influence of marine aerosol, together with the diffuse influence of the urban-industrial pollution on several detached houses of newly construction (Berango, Basque Country, north of Spain), (3) the direct impact of marine aerosol and the direct impact of urban-industrial pollution on La Galea Fortress (Getxo, Basque Country, north of Spain).

To attain the main objective proposed, ten operational objectives were defined to be developed on this PhD work:

1. To evaluate the usefulness of portable/hand-held analytical techniques, such as Raman spectroscopy and energy dispersive X-Ray fluorescence (ED-XRF), in order to obtain a first approach of the original building materials composition and the nature of the compounds/elements present in the pathologies identified, without any previous sampling.

2. To diagnose the influence of marine aerosol (in a direct or diffuse way), with or without the influence of anthropogenic environmental stressors coming from urban-industrial areas using the a multianalytical methodology based on the use

of elemental and molecular non-invasive spectroscopic techniques (punctual analysis and imaging analysis in some cases), together with destructive analyses of the extracted samples, in order to determine the concentration of the salts and metals formed and deposited respectively on the materials. Chemometric and chemical/thermodynamic modellings will be also applied using these quantitative data, to ascertain the decaying pathways proposed to explain the deterioration processes, according to the formation of the experimentally observed compounds.

3. To characterize outdoor and indoor materials from the Igueldo Lighthouse, in order to asses if, apart from the salts present in the material itself, the environmental stressors coming from the marine environment in where this building is immersed, can affect the conservation state of not only the external building materials, but also the conservation state of the materials from the indoor areas of this construction.

4. To study the rainwater composition and its influence on building materials from detached houses of newly constructions, by the action of wet depositions and water infiltrations. Moreover, the use of additives in the setting of building materials will be also tested to search if they have a key role in their conservation state.

5. To study the composition of the original Primary Marine Aerosol particles (PMAP) coming from seawater.

6. To develop a home-made passive sampler in order to trap and characterize the composition of the Secondary Marine Aerosol particles (SMAP) formed in the atmosphere from La Galea site, due to the reaction between the PMAP and the acid gases present in this atmosphere.

7. To asses if the PMAP, SMAP, crustal particles and metallic airborne particulate matter identified in the atmosphere from La Galea site, can be deposited on the sandstone from La Galea Fortress following wet deposition processes.

8. To perform an in-depth characterization of the sandstone from La Galea Fortress, in order to evaluate which are the pathologies responsible of the bad conservation state of this material; and also to evaluate the role of the wind and additional natural and anthropogenic environmental stressors coming from the

marine environment surrounding La Galea site, in the conservation state of the sandstone.

9. To characterize the sandstone from the NW orientation of La Galea Fortress, which is in a better conservation state than the one from other orientations, and to correlate this observation with the characterization of the reddish biofilm or biopatina present on the sandstone from this orientation, in order to evaluate possible bioprotective role of this biological patina.

10. To characterize the composition of the black crusts and the biological colonizations below them, formed on the sandstone from La Galea Fortress and to perform an in-depth characterization of the crustal and metallic particles trapped in those crusts, according to the orientation of the black crusts in the building.

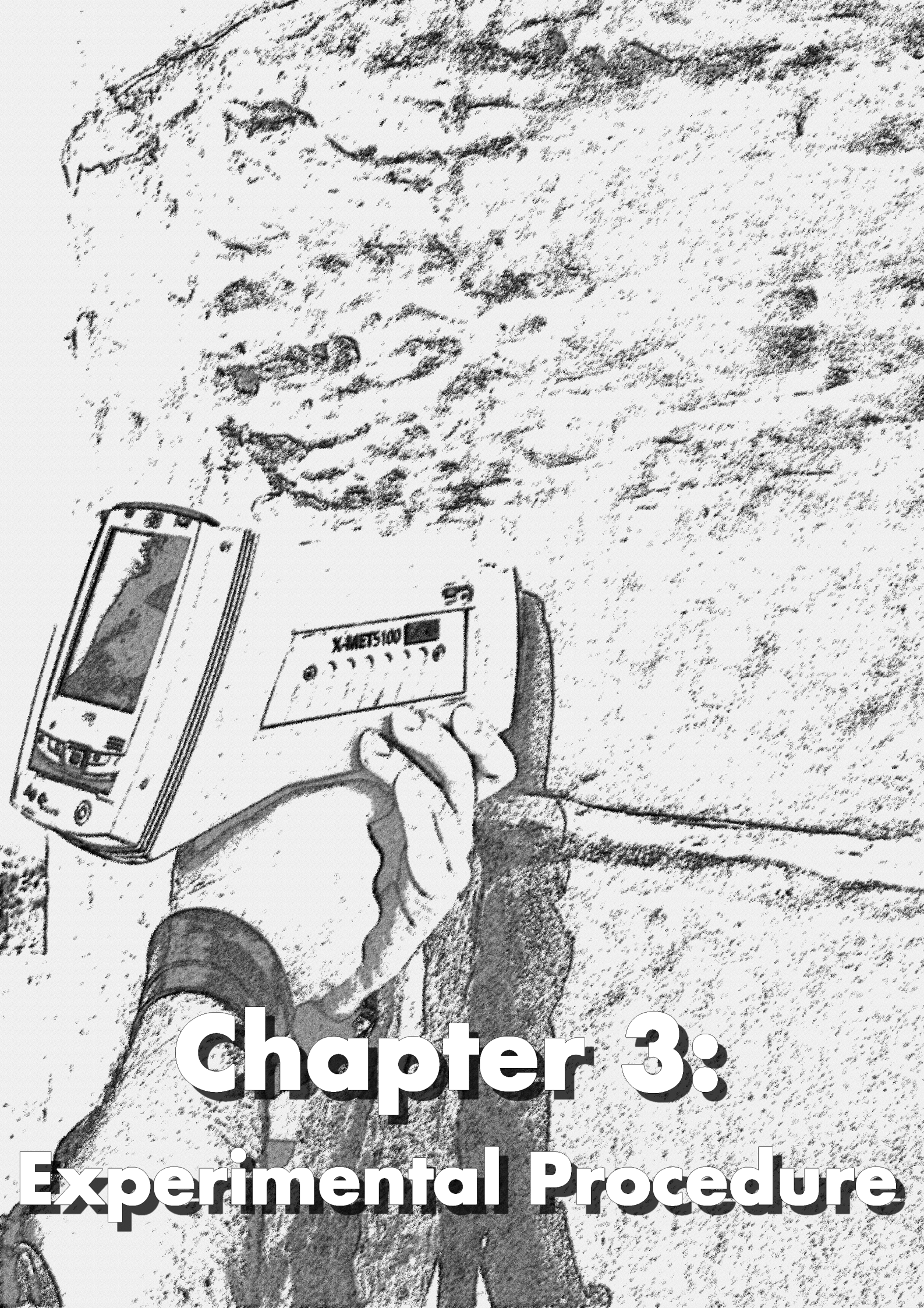

Chapter 3:
Experimental Procedure

CHAPTER 3.

EXPERIMENTAL PROCEDURE

This PhD Thesis was developed using different analytical techniques. Among all of them, vibrational spectroscopic techniques were mainly used because they provide very suitable and valuable results on the molecular composition of the samples. Spectroscopic tools or techniques are described as the basis for analytical methods in the field of Cultural Heritage (historical building materials, art items, archaeology etc.) [1]. During time, thanks to these types of instruments, the scientific community has achieved valuable information to preserve the state of conservation of many historical buildings.

Among all the vibrational spectroscopic techniques which are going to be described in this PhD Thesis, Raman spectroscopy was the most used technique in all the presented individual studies. In general, Raman micro-spectroscopy has been recognized as powerful instrumental technique for compositional and structural elucidation of a wide range of materials in numerous research areas, such as medical [2], biology [3], physics applications [4], chemistry [5], even in archaeological [6] and cultural heritage fields [7]. Apart from this, Raman spectroscopy has been established as a reliable tool for the non-invasive analysis of a wide variety of inorganic and organic compounds present in materials from Built Heritage, art and archaeological fields, presenting unique advantages over other molecular analytical techniques (no sample preparation, polymorphs differentiation, no sample consume, etc.)[8]. Besides, it has a high sensitivity and specificity enabling analysis in situ, in a non-invasive way, at relatively short times, and with excellent spatial resolution of a wide variety of materials [9].

Infrared Spectroscopy (IR), a complementary vibrational technique to Raman spectroscopy, has also a wide applicability in the analysis of this kind of materials [1]. This technique was also included in the multianalytical methodology applied in this PhD Thesis to obtain

additional or complementary molecular information of the samples (original and decay compounds).

X-Ray Diffraction (XRD), the classical technique of structural analyses, has also high applied to the analyses of building materials [10]. Normally the combined use of XRD with other molecular techniques (such as Raman spectroscopy and Infrared Spectroscopy) is very helpful. In this way we have to highlight that XRD hardly detect compounds which are under the 5% of the total composition in the sample and/or are amorphous. Therefore, the combined use of XRD and vibrational spectroscopic techniques is proven to be an adequate analytical methodology to avoid inaccurate assignments regarding the molecular composition of the sample, which can be done only using one of those techniques.

Apart from the molecular and structural characterization, it is highly convenient to complete the analytical characterization of the samples under study with a proper elemental analysis. X-Ray fluorescence spectroscopy (XRF) is a well-known technique which offers good results in the elemental characterization of samples belonging to the cultural heritage [11]. In this work, a Hand-held X-Ray Fluorescence Spectrometer (HH-XRF) was used to perform the preliminary screening of the materials on-site and micro Energy Dispersive X-Ray Fluorescence Spectrometer (μ-ED-XRF) for the in-depth characterization of the selected samples in the laboratory; although this instrument can be considered portable, it allowed us to characterize the samples following a point-by-point strategy (individual measurements) and also a mapping strategy. With the aim of characterizing small particles and also to improve the detection of lighter elements in some samples, an energy dispersive X-ray spectrometer (EDS) was used coupled to a scanning electron microscope (SEM-EDS). In this case, light elements detection can be improved, since the sample is introduced in a chamber under vaccum. Nevertheless, the detection limits for heavier elements are lower with the HH-XRF or with the μ-ED-XRF instruments that with the EDS. Therefore, all the information extracted from the three instruments was combined. Apart from point-by-point elemental spectra, elemental distribution maps of an specific screened area were also obtained in some of the analysis. Scanning Electron Microscope (SEM) coupled to the EDS allows identifying, focusing and taking a microscopic image of the area under study.

Apart from the elemental mapping achieved with the μ-ED-XRF spectrometer, the confocal Raman microscope used in this work also provides surface molecular mappings. With this option, it is possible to obtain a distribution map of all the molecular species present in the mapped area. In some studies of this PhD manuscript, a combination of Raman imaging, XRF

imaging and SEM imaging is presented. As will be see later, this combination is very helpful to understand better the decaying processes that take place in the characterized materials.

Moreover, apart from the use of laboratory XRD and Raman, Infrared spectroscopy, SEM-EDS and XRF instruments, portable or handheld devices were also used to perform in situ characterizations. An example of these is the use of portable Raman spectrometer and the HH-XRF previously described, in the study of the nature and origin of white efflorescences over different materials such as mortar, bricks and artificial stones.

Most of the building materials included in this PhD manuscript, suffer from the effect of soluble salts crystallization. In order to study the impact and the extended of the deterioration caused by the crystallization of soluble salts, the use of analytical techniques which offer quantitative results of the composition of these soluble salts was considered. Ion Chromatography (IC) is a good tool to quantify the anions and cations concentrations in the aqueous sample obtained after extracting the soluble salts from the solid materials sampled. Besides, inductively coupled plasma-mass spectrometry (ICP-MS) was also used to quantify in the collected samples, soluble cations and also extractable metals under acid conditions.

Prior to the quantification of cations and anions present in the samples, it was necessary to have a proper methodology to extract all these ions to the aqueous phase. All the soluble salt tests included in this PhD Thesis were performed using ultrasound-assisted extraction methods, an alternative to the obsolete Italian NORMAL 13/83 recommendation and actual UNI 11087 Italian standard method UNI 11087/2002 to extract soluble salts [12]. In Europe, the European Commission have developed the newly EN 16455/2012 norm in order to establish a standard for the soluble salts extraction from building materials.

Apart from the use of analytical techniques to obtain experimental results from samples, numerical data were also treated using chemometric tools. Chemometrics offers complementary and additional information about the decay of mortars, plasters, bricks, sandstone, limestone etc. Besides, thermodynamic modellings were performed using, academic free software, useful to predict the probable formation of decay compounds and soluble salts crystallizations identified using the multianalytical methodology. Chemometric and chemical/thermodynamic calculations were used in this work to reinforce the reactions of the proposed decay pathways.

3.1 Materials, reactives and general purpose instruments

3.1.1 Material Cleaning

Previous to the development of any of the quantitative analyses all the glassware and non volumetric plastic material used in the experimental procedure was exhaustively washed with water and acetone. For the cleaning, Milli-Q water (18.2 MΩ.cm, Millipore, Billerica, Massachusetts, USA) and acetone (Merck KGaA, Darmstadt, Germany) were used. In addition, the glassware was immersed in a 10% HNO_3 (69%, Merck) bath for 24 h, exhaustively rinsed twice with Elix (Millipore, USA) quality water and finally soaked again with Milli-Q water and dried in a laminar airflow hood or in a heater at 50ºC and was stored until next use.

3.1.2 Reactives

The reactives used to prepare the mobile phase used in the ion chromatograph, to determine soluble ions concentrations on building samples were: sodium hydroxide (NaOH) 50% sol (J.T Baker Center Valley, U.S.A.) analyzed, sodium carbonate (Na_2CO_3) Suprapur 99.99% (Merck, KGaA, Darmstadt, Germany) and sodium bicarbonate ($NaHCO_3$) p.a 99% (Merck, KGaA, Darmstadt, Germany) and methanesulfonic acid (CH_4O_3S) puriss (> 99.0%) (Fluka Analytical actually Sigma Aldrich, St. Louis, U.S.A.).

The standard solutions used to prepare the calibrates for each ion were the following: fluoride, chloride, nitrate, sulfate and oxalate standard (Fluka Analytical actually Sigma Aldrich, St. Louis, U.S.A.) solutions (1000 ppm). Ammonium standard trace CERT solution for ion chromatography (Fluka Analytical actually Sigma Aldrich, St. Louis, U.S.A.) and 1000 ppm multielemental (Ba, Ca, K, Li, Na, Mg and Sr) CertiPUR standard solution (Merck, KGaA, Darmstadt, Germany).

The HNO_3 (69%) and the HCl (36%) used for microwave digestion and ICP-MS analysis were of Tracepur grade and supplied by Merck (Merck® Millipore KGaA, Darmstadt, Germany).

3.1.3 Gringing (Agate mortar with pestle)

The samples used for quantitative analysis (Ion Chromatograpy and ICP-MS) and for XRD analyses were homogenized in an agate mortar with pestle. This step is very important in order to obtain homogenized samples with lower particles size (See Figure 3.1).

Figure 3.1. Agate mortar with pestle.

3.1.4 Weighing

Samples were weighed using an AJ150L analytical balance (Mettler Toledo, Ohio, USA) with ± 0.0001 g of precision for the quantitative analyses and when a lower precision was enough a PB6025 top loading balance (Metter Toledo, Ohio, USA) with a precision of ± 0.01 g was used (see Figure 3.2).

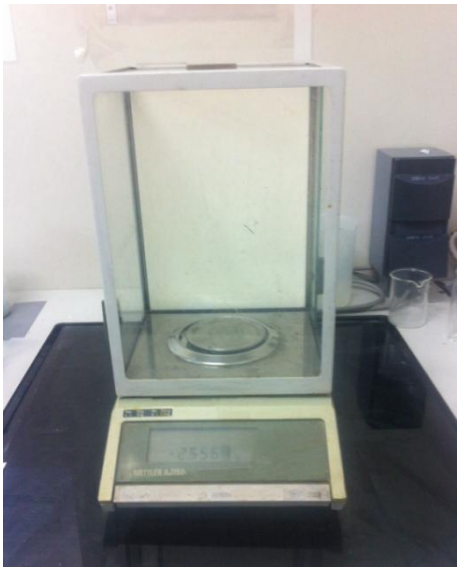

Figure 3.2. AJ150L analytical balance (Mettler Toledo, Ohio, USA).

3.1.5 pH Meter/VoltMeter

In this PhD Thesis, for the analysis of pH and redox potential of the rainwater samples (see Chapter 5), a Crison microph 2000 (Crison Instruments S.A. Alella, Barcelona, Spain) instrument was used (see Figure 3.3). In this instrument, depending on the variable to be measured (pH or redox potential), the measuring electrode was selected. On one hand, for the calibration of pH meter, a diary calibration using two buffer solutions was carried out. Firstly the pH 7.00 buffer solution (Crison pH 7.00 @ 25^0C buffer solution CRI9464.99) was used. Secondly the pH 4.01 buffer solution (Crison pH 4.01 @ 25^0C buffer solution CRI9463.99) was used. Both of them were measured at 25^0C. On the other hand for the calibration of the voltmeter, a diary calibration using a Hamilton Redox Bufer 475± 5mV which is certified traceable to N.I.S.T and P.T.B (N.I.S.T: National Institute of Standards and Technology, USA and P.T.B: Physikalich-Technische Bundesanstalt, Germany) was used.

Figure 3.3. pH meter / VoltMeter Crisonmicroph 2000.

3.1.6 Phase Contrast Microscope

A Nikon Eclipse 80i PCM (Phase Contrast microscope) provided with 20×, 40×, and 60× objective lenses was used to obtain microphotographs of the red biofilm from Chapter 6 (see Figure 3.4). For the preparative process of the sample, special tweezers were used to sample the main colonizer from the red biofilm, under the view of a microscope. After the extraction of the main colonizer, it was placed on a slide and a drop of oil was also added to avoid spherical aberration with the highest numerical aperture lenses, promoted by the different indexes of refraction of the specimen and the objective lenses.

Figure 3.4. Nikon Eclipse 80i Phase Contrast Microscopy

3.2 Analytical techniques to determine the molecular composition of the materials in the laboratory

3.2.1 Raman spectroscopy

3.2.1.1 Renishaw RA100 spectometer

For an exhaustive analysis of the samples in the laboratory a Renishaw RA 100 Raman spectrometer (Renishaw, Gloucestershire, UK) (see Figure 3.5) coupled to a fibre optic microprobe with an excitation diode laser of 785 nm, a Peltier cooled CCD detector and the Wire 3.2 software (Renishaw, Gloucestershire, UK) package for data obtaining. The nominal power is 150 mW at the source and neutral filters allow working at 1% (5 mW at the source and 1 mW at the sample), 10 % (50 mW at the source and 10 mW at the sample) and 100 % (150 mW at the source and 30 mW at the sample) of the total power.

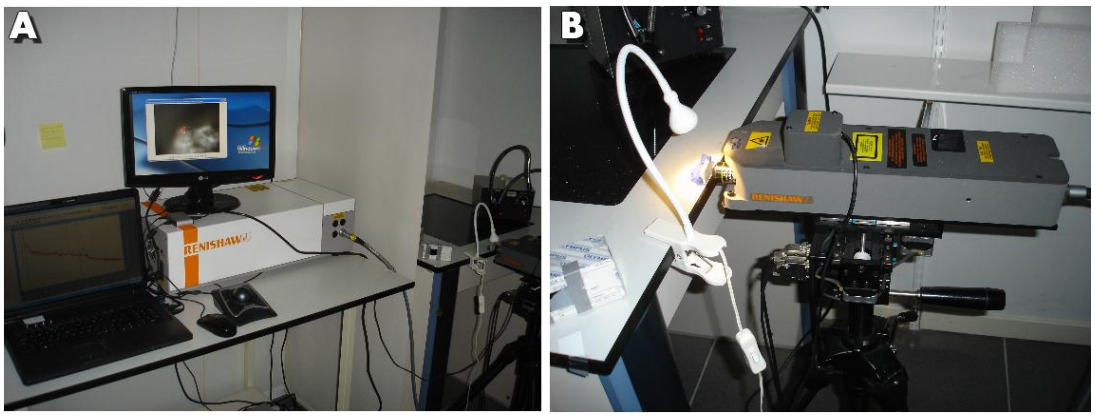

Figure 3.5. A) Renishaw RA 100 Raman spectrometer (Renishaw, Gloucestershire, UK) B) Raman microprobe mounted on a tripod.

The Raman microprobe mounted on a tripod (see Figure 3.5 B) can incorporate long range 4x, 20x and 50x objectives (10 µm, 5 µm and 2 µm of lateral resolution respectively) and has a video-camera which allow focusing the laser beam in the range of 10-200 µm at the sample (depending on the objective lens used). The instrument is positioning is controlled by a micrometric stage which permits a perfect focusing of the areas of interest. The spectra were acquired in the range of 100-3250 cm^{-1} with a resolution of 2 cm^{-1}.

3.2.1.2 Bruker Senterra micro-Raman spectrometer

For micro-Raman spectroscopy and Raman Imaging, a Senterra spectrometer (Bruker Optics, Karlsruhe, Germany) equipped with a Peltier-cooled charge-coupled device detector CCD working at -65°C and implementing 10x and 50x long working distance Olympus objectives was used to collect the Raman spectra excited under a 785 nm light from a diode laser. OPUS© 7.0 (Bruker Optik GmbH, Ettlingen, Germany (2011)) software was used for Raman Imaging; and Omnic 7.2 (Nicolet) and Wire 2.0 (Renishaw) software for spectral treatment and assignation (see Figure 3.6).

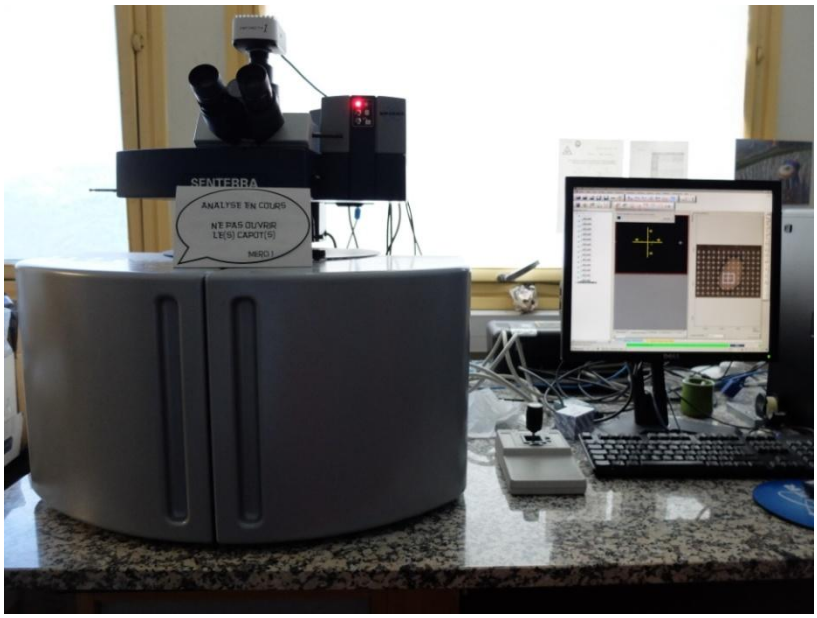

Figure 3.6. Senterra micro-Raman spectrometer.

3.2.1.3 Renishaw inVia Confocal Raman microscope

The instrument was relevant for a more in depth analysis of the samples, since the system can be used with different laser excitation sources and detectors. Renishaw InVia confocal micro Raman microscope (Renishaw, Gloucestershire, UK) is provided with a 514 nm and a 785 nm lasers as excitation sources (at highest powers, the nominal laser powers at the

source are 50 mW and 350 mW for each of the laser beam, and at the samples 20 mW and 150 mW respectively), and a Peltier cooled CCD detector (-70ºC) (see Figure 3.7).

The spectrometer is coupled to a DMLM Leica microscope (Bradford, UK) and for visualization and first focusing 5x PLAN (0.12 aperture) objective and 20x N PLAN EPI (0.40 aperture) lens were used. The spectra were acquired using 50x PLAN (0.75 aperture, lateral resolution of 2 μm) and 100x (lateral resolution of 1 μm) long-range objectives. At high magnifications, the laser spot was reduced to around 1 μm. The microscope implements a Prior Scientific motorized XYZ positioning stage with a joystick and is equipped with a micro-camera. The spectra were acquired between 100-4000 cm^{-1} with a resolution of 1 cm^{-1} using the Wire 3.2 software (Renishaw, Gloucestershire, UK).

Figure 3.7. The Renishaw inVia confocal Raman microscope.

Moreover, the equipment is installed on an antivibratory table inside a temperature controlled chamber. Furthermore, the developments in spectroscopic detector technologies combined with multispectral image-processing strategies, have enabled spectral as well as spatial information to be recorded simultaneously resulting on the creation of false-colour Raman chemical imaging analyses. As a result, thousands of spectra can be collected, outlining the distribution of several chemical components in a spatial location of any sample.

In order to obtain Raman chemical image acquisitions of specific areas, the StreamLine (Renishaw) technology device was used with the 785 nm laser as excitation source (the spectral resolution was around 1 cm^{-1}). Laser was set at low power (not more than 1 mW at the sample) in order to avoid thermal decomposition. The software used for the data collection was also the Renishaw Wire 3.2 (Renishaw, Gloucestershire, UK). The inVia equipment implements a motorized microscope stage which moves the sample under the lens, to be the line raster across the area of interest. As the line moves across the sample,

data are swept synchronized across the StreamLine UVDD CCD detector and read out continuously. The spectra were obtained with the 20x N PLAN EPI objective. For higher magnifications using objective lens such as 50x and 100x, significant defocusing was observed which precluded mapping experiments. The Raman spectra for the spectral imaging were recorded in 1-3 s (depending on the sample) and 1 accumulation in a spectral range of 135-1650 cm^{-1}. The acquisitions varied depending on each chemical map (from 2244 to 11016 spectra) and the step size was set in 3.5 μm resulting on a high-sampling frequency along both directions, giving higher spectral content and thus, more accurate information on chemical behavior and borders of particle and cement domains. In the data collected for each map it was carried out a cosmic ray removal and a noise filter based on Principal Component Analysis (PCA). After performing the baseline correction, the spectra were filtered based on the integration of the main Raman bands for each molecular phase in order to represent their chemical image in the selected mapping area. In the case of mineral phases sharing band positions, secondary Raman bands were taken into account for peak integration.

3.2.1.4 Considerations for Raman micro-spectroscopic measurements

The quality of measurements of the different Raman equipments used was guaranteed by means of an internal calibration and a diary calibration using the Raman signal of Si at 520.7 cm^{-1} of a crystalline silicon chip. All the Raman spectroscopic measurements were carried out in darkness, due to the fact that the artificial light protons and sunlight can reach the spectrometer detector and their signal can be confused with the Raman signals from the sample. Even with that, occasionally cosmic rays were observed.

To avoid laser induced thermal degradation and phase transitions of the samples, the intensity of the laser powers was varied by neutral density filters from 0% to 100% depending on the analyzed matrix, ensuring a good signal to noise ratio. The acquisition of the spectra was developed following a protocol mainly consisting on starting at lower laser powers and then increasing it until a good signal to noise ratio was obtained. Nevertheless, when analyzing ferruginous mineral phases, the laser power was usually kept at 20% or lower, to avoid sample degradation. After recording each spectrum, a visual inspection through a micro-video camera was performed on the measurement an on the microscope stage in order to detect any phase transitions caused by the laser.

The spectra were taken in different ranges, the integration time and the scans were also set to optimum in each of the selected areas (1-30 s, 1-60accum.) in order to ensure a good signal to-noise ratio and to accomplish well-resolved Raman spectra. To assume that an

specific compound is present in a sample, repetitive spectra must be recorded in each selected area (normally, more than 20).

The analysis and the treatment of the Raman spectra were performed using the Omnic 7.2 software (Thermo-Nicolet, Madison, USA) which basically consisted on spike removal and sometimes baseline correction or smoothing was used to a greater or lesser extent in order to correct fluorescence or noise interferences. When broadening effects of the peaks were observed, deconvolutions were performed with the Grams 8.0 software (Thermo Fisher Scientific INC, Waltham, USA) based on Lorentzian and Gaussian functions. Furthermore, the interpretation of the results was performed by comparison with reference standard Raman spectra from the e-VISARCH, e-VISART [13], e-VISNICH [14] (an on-line Raman Spectra Database of Natural, Industrial and Cultural Heritage compounds) libraries and with other on-line available spectral databases such as RRUFF [15].

3.2.2 FTIR Spectroscopy

The infrared spectra were acquired using a Bruker Equinox 55 FTIR spectrometer in Attenuated Total Reflectance (ATR) mode (see Figure 3.8). The infrared source of this instrument is a heated silicon carbide filament that emits radiation in the mid infrared. The ATR measurements were performed using a Golden Gate (Specac, Kent, U.K) ATR unit equipped with a diamond crystal (refractive index of 2.4than 1000 cm^{-1}), with incidence angle of 45°.Asystemof zinc selenide (ZnSe) mirrors and lenses focuses the infrared beam on the diamond crystal which is transmitted to the sample. The detector used is a DTGS (acid sulfate Triglycine deuterated). The sample is placed in contact with the crystal by a sapphire anvil on which is applied a maximum pressure of 0.1GPa.The area analyzed on the samples is about 0.8mm^2. The spectra were acquired between 600-6500cm^{-1} (narrow spectral range to low wavenumbers due to the presences of ZnSe lenses), with a standard resolution of4 $cm^{-1}$and each spectrumaccumulated16times.

Figure 3.8. Bruker Equinox 55 spectrometer (top) and ATR unit from Golden Gate (bottom).

3.2.3 X-Ray Diffraction (XRD)

To contrast, confirm and complement the information given by Raman and infrared spectroscopies, XRD analyses were carried out on the X-ray Service from SGIker of UPV/EHU. Previous to the analyses each of the samples was powdered and homogenized manually using an agate mortar. The XRD analyses were performed using a PANalytical Xpert PRO powder diffractometer equipped with a copper tube ($\lambda Cu_{K\alpha media}$ = 1.5418 Å, $\lambda Cu_{K\alpha 1}$ = 1.54060 Å, $\lambda Cu_{K\alpha 2}$ = 1.54439 Å), vertical goniometer (Bragg–Brentano geometry), programmable divergence aperture, automatic interchange of samples, secondary graphite monochromator, and PixCel detector. The operating conditions for the Cu tube were 40 kV and 40 mA, with an angular range (2θ) scanned between 5 and 70º (see figure 3.9). The treatment of the diffractograms and the identification of the mineral phases present were carried out using the specific X'pert HighScore (PANalytical) software in combination with the specific Powder Diffraction File (PDF2) database (International Centre for Diffraction Data – ICDD, Pennsylvania, USA).

Figure 3.9. PANalyticalXpert PRO powder X-ray diffractometer

3.3 Laboratory instruments for elemental characterization of the samples

For the elemental characterization of building material samples energy dispersive X-Ray Fluorescence spectroscopy and SEM-EDS were used.

3.3.1 Portable micro-energy dispersive X-Ray fluorescence spectroscopy (μ-ED-XRF)

In this PhD Thesis, apart from point-by-point analyses, elemental maps were also acquired using a lower lateral resolution (650 μm) thanks to the use of a lower diameter collimator implemented in a secondμ-ED-XRF instrument, the portable ARTAX μ-ED-XRF from Röntec (currently Bruker Nano GmbH, Berlin, Germany). Each elemental map was constructed according to the net areas of XRF lines. This spectrometer implements a low-power metal-ceramic-type MCBM 50 X-Ray tube with molybdenum target as excitation source. The molybdenum anode spot size in the instrument is 70 x 50 μm, and it can be used at a maximum voltage of 50 kV and at a maximum current of 700 μA (maximum power of 35 W). The radiation-protecting tube housing is equipped with an electrical shutter and safety functions externally controlled by a PC. The X-Ray Fluorescence radiation is detected by means of an electro-thermally cooled Xflash® detector, which is a silicon drift detector with high-speed low-noise electronics. The detector has an active area of 5 mm^2 and a 8 μm-thick Dura-beryllium window. The geometry between primary beam, sample, and detector is fixed at 0º/40º relative to the perpendicular of the sample surface. The X-Rays were collimated by a tantalum collimator with a diameter of 0.65 mm and the beam diameter in the sample surface is around 200 mm^2. An integrated CCD camera provides an image of the sample region under investigation (8 mm x 8 mm). In the vibration-damped swivel arm from the instrument, a motor-driven XYZ positioning stage is directly mounted, which consists of three equal modules with a maximum travel of 50 mm in each direction. This motor unit allows focusing on different parts of the sample

Figure 3.10. Artax μ-XRF portable instrument by Röntec (currently Bruker).

3.3.2 M4 TORNADO micro-energy dispersive X-Ray fluorescence spectroscopy (μ-ED-XRF)

For the measurements in the millimeter scale, the M4 Tornado (Bruker Nano GmbH, Berlin, Germany) μ-ED-XRF instrument was used (see Figure 3.11). With this instrument punctual measurements, line scans and HyperMaps were acquired. The X-Ray tube implemented in this instrument is a micro-focus side window Rh tube powered by a low-power HV generator and cooled by air. Thanks to the implemented collimator, spot sizes of 1 mm were measured. The X-ray tube can work at a maximum voltage of 50 kV and at a maximum current of 700 μA, which were the conditions considered for the spectra acquisition in this work. The detection of the fluorescence radiation was performed by an XFlash® silicon drift detector with 30 mm^2 sensitive area and energy resolution of 145 eV for Mn-Kα. In order to improve the detection of the lightest elements (Z>11), filters were not used and measurements were acquired under vacuum (20 bar). To achieve the vacuum, a diaphragm pump MV 10 N VARIO-B was used. The live time used for each punctual measurement was 200 seconds. For the focusing of the area under study, two video-microscopes were used, one of them to explore the sample under a low magnification (1 cm^2 areas), and the other one to perform the final focusing (1 mm^2 areas). Apart from punctual measurements and line scans, HyperMaps were also acquired. The elemental maps showed in this PhD manuscript were obtained after a previous assignation of the elements, deconvolution and application of Fundamental Parameters based-method regarding the quantitative information of each element on each point from the mapped area. The spectral data acquisition and treatment was performed using the M4 TORNADO software and the quantification was done thanks to the M-Quant software package

Figure 3.11. M4 Tornado μ-EDXRF by Bruker.

3.3.3 Scanning electron microscopy-energy dispersive X-Ray spectrometry (SEM-EDS)

SEM-EDS was used to determine the elemental composition of smaller areas and particles inside the samples. SEM-EDS analyses were carried out in the UPV/EHU Singular Laboratory of hyphenated multispectroscopic techniques (Raman-LASPEA) of SGIker.

Previous SEM-EDS analyses, sample pretreatment was carried out. In this way, different building materials samples (around 1cm aprox.) were mounted in special aluminium pin stubs which were partially covered by an adhesive carbon tape where the samples were fixed. Subsequently, in some cases, to improve the quality of the SEM images, samples were coated with a gold film (< 20 μm) in an Emitech K550X sputter coater vacuum chamber (Quorum Technologies $_{LTD}$, Sussex, UK) (see Figure 3.12)

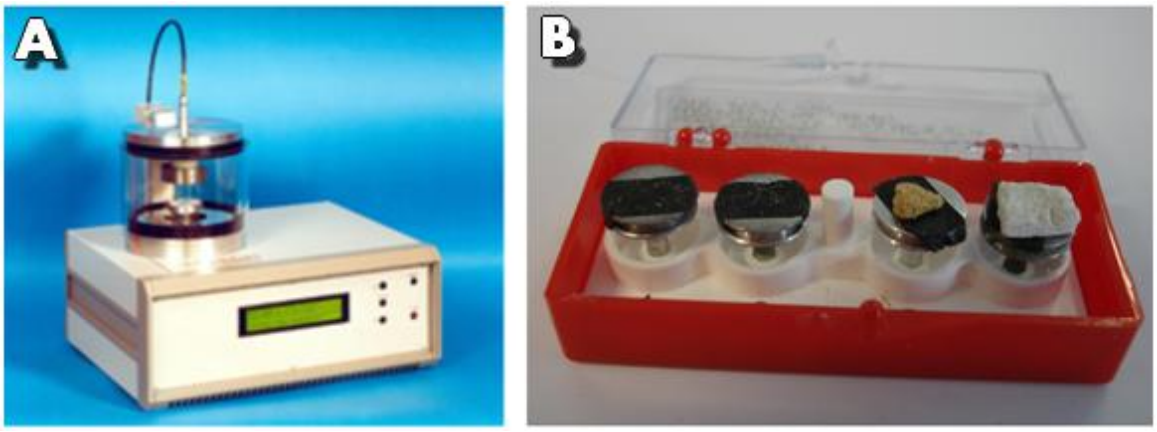

Figure 3.12. A) The Emitech K550X vaccum chamber, B) different samples fixed on the adhesive carbon tape and mounted on the Aluminium pin stubs.

The electron image acquisitions and elemental composition determinations (point-by-point spectra and elemental mappings) were conducted by means of an EVO®40 Scanning Electron Microscope (Carl Zeiss NTS GmbH, Oberkochen, Germany) coupled to an Oxford INCA 350 X-Max Energy-Dispersive X-Ray Spectrometer (Oxford Instruments, Oxfordshire, UK) (see Figure 3.13).

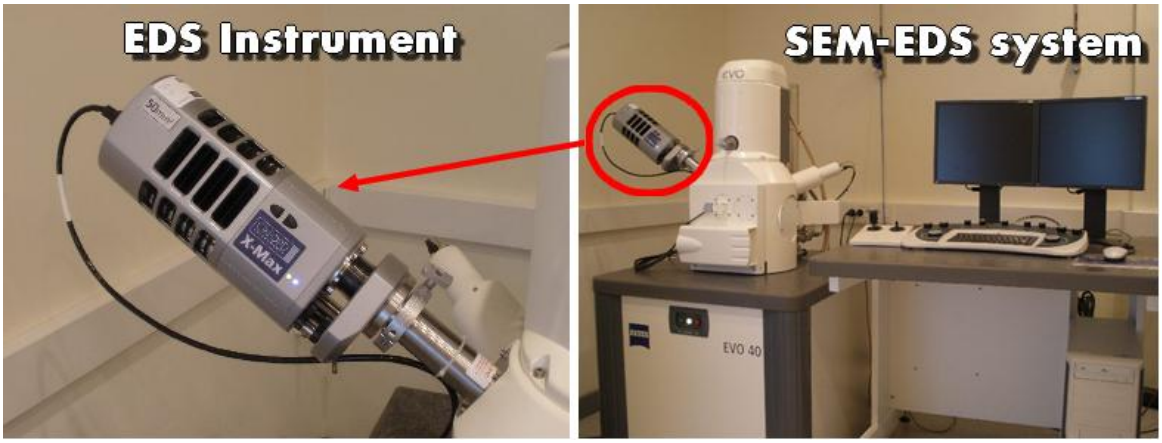

Figure 3.13. SEM-EDS sytem with EVO®40 Scanning Electron Microscope (Carl Zeiss NTS GmbH, Oberkochen, Germany) coupled to an Oxford INCA 350 X-Max Energy-Dispersive X-ray Spectrometer (Oxford Instruments, Oxfordshire, UK).

Apart from qualitative spectral information, EDS also provides semi-quantitative elemental information of the analyzed surfaces. The equipment is also installed on an antivibratory table inside a temperature controlled room. SEM images were acquired at high vacuum employing an acceleration voltage of 20-30 kV and 6-13 mm working distance. Magnifications up to 10.000x were reached using a Secondary Electron (SE) detector for image acquisitions. Moreover, elemental mappings and punctual analyses were performed with the EDS using a 8.5 mm working distance, a 35º take-off angle, 10 scans, an acceleration voltage of 20 kV and an integration time of 50 s to maximize the signal-to-noise ratio. Finally, the analysis and the treatment of the data were performed with the INCA Microanalysis Suite 4.3 software (Oxford Instruments, Oxfordshire, UK).

3.4 Hand-held/portable instrumentation

As it has been mentioned before, for the elemental composition a HH-XRF was used and for the molecular characterization two portable Raman spectrometers were selected.

3.4.1 Hand-held energy dispersive X-Ray fluorescence spectrometer (HH-ED-XRF)

A hand-held ED-XRF XMET5100 spectrometer (Oxford Instruments, UK) equipped with a Rh tube as X-Ray source was used (see Figure 3.14). This device can work at maximum of 45 KV and the size of the emitted radiation X-Ray beam is 9 mm. The analyzer includes a silicon drift detector (SDD) of high resolution that is able to provide an energetic resolution of 150 eV (calculated for the Mn Kα line at -20 ˚C) and a spectral resolution of 20 eV. The analyzer contains a PDA to control the spectrometer and also to the obtained spectra and the semi-

quantitative information (both in .txt format) save. This device contains different methods to perform the measurements and to obtain the semi-quantitative results. To extract the spectral information of the heavier elements (from iron, Z ≥ 20) on the characterized surfaces or samples, SOIL FP method was used. With this method, the operating parameters were 45 kV (tube voltage) and 15 μA (tube current). Moreover, between the primary beam and the sample, a 500 μm Al filter was placed to remove the "pinches" Bremsstrahlung and to removes 3rd Generation peaks. Each spectrum was acquired during 50 seconds. To determine the presence of the lighter elements in the analyzed areas, the MINING LE FP method was used. In this case, the test measurement was done during 50 seconds. During those seconds two spectra were acquired, one of them during 36 seconds at 13 kV and 45 μA (without any filter) and the second one during 14 seconds at 40 kV and 10 μA (using the 500 μm Al filter). With the first spectrum, acquired at lower voltage and higher current, the presence of light elements (between Al (Z=13) and Ca (Z=20)) was evaluated. The spectra for the heavier elements obtained running the MINING LE FP method was also compared with the one obtained using the tube conditions fixed in the SOIL FP method. Both quantification methods are based on fundamental parameters (FP). The quantitative information offered by both methods was only used as indicative values, no data treatments were performed with the concentration values offered. Only spectral information and normalized net areas of certain lines from the detected elements are presented in this manuscript.

To ensure the possible contribution of certain signals arising from the XRF set-up (e.g. detector, specific pieces, etc.) or from possible particles penetrated in the sampling head, two instrument blanks (a polytetrafluorethylene (PTFE) block and a methylcellulose pellet) were used. In order to ensure that PTFE block was free from superficial contamination, it was placed in a 20 % nitric acid bath during 24 hours. Then, the PTFE block was rinsed with Milli-Q water and air-dried before its use. 10 repetitive measurements (with the same tube conditions and measurement test times described from the surfaces/samples under study) on each instrument blank were performed, to extract the background of the instrument and possible external contaminations.

Figure 3.14. Handheld ED-XRF XMET5100 (Oxford Instruments, UK).

3.4.2 Portable Raman spectrometers

Two portable Raman spectrometers were used as a first screening to obtain a preliminary characterization of the different building materials under study. Both spectrometers belong to innoRam™ model (see Figure 3.15 and 3.16) ($B_{\&}WTEK_{INC}$, Newark, USA). The first one implements a 785 nm diode excitation laser, a Charge Coupled Device (CCD) detector (Peltier cooled). The equipment implements a laser power software controller from 0% to 100%, being at 100% of laser power the nominal laser power of the instrument at the source 330 mW ± 15% and at the surface of the analyzed sample 255 mW ±15%. The spectral range is 65-3000 cm^{-1} with an average of 4 cm^{-1} of spectral resolution.

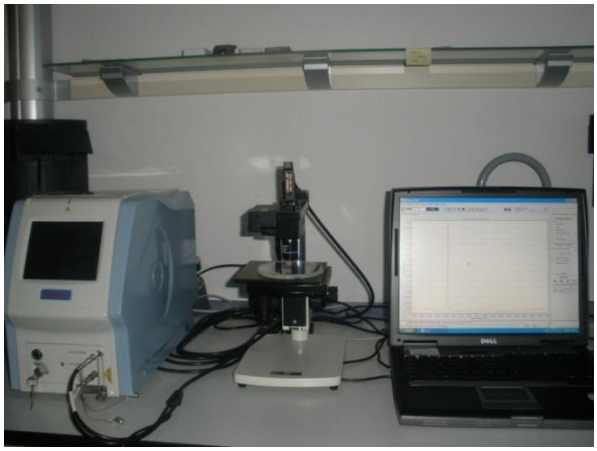

Figure 3.15. Portable innoRam™ spectrometer (785nm) with the probe coupled to a micro-video camera also from $B_{\&}WTEK_{INC}$.

The microprobe (about 0.1 mm of focus) can be used directly on the surface under study. The Raman probe was also used in the laboratory to perform microscopic analyses on selected samples, mounting the probe on a video-camera where different objectives (20x and 50x long-range in this case) can be coupled to perform micro-Raman measurements.

The other Raman instrument was the hand-held innoRam™ BWS445-532S Spectrometer ($B_{\&}WTEK_{INC.}$, Newark, USA). In this case, this Raman instrument implements 532 nm diode excitation laser (33 mW laser output power) and the Raman signals were collected by a CCD detector refrigerated by Peltier effect. The spectral range of the Raman instrument is 65-3750 cm^{-1} with an average spectral resolution of 5 cm^{-1}. For this case, the raman probe was also used in the laboratory performing microscopic analyses on selected samples, using a video-camera with different objectives (20x and 50x long-range) that can coupled to perform micro-Raman measurements. The spectra for the two instruments were acquired using the $B_{\&}WTEK_{INC}$ 3.26 software ($B_{\&}WTEK_{INC}$, Newark, USA).

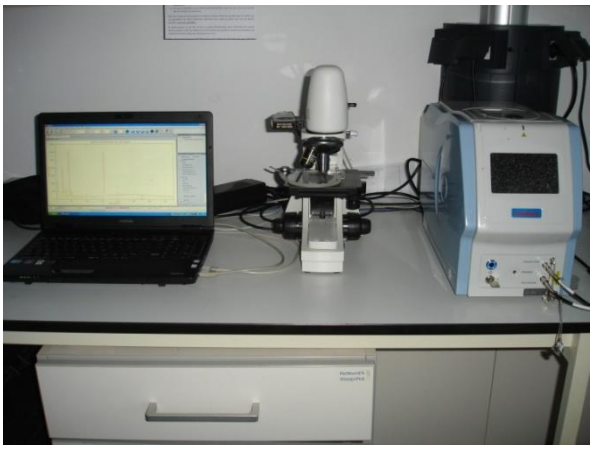

Figure 3.16. Portable innoRam™ spectrometer (532nm) with the probe coupled to a micro-video camera also from $B_{\&}WTEK_{INC}$.

3.5 Destructive analyses

Building materials samples were destroyed in order to determine the concentration of the soluble salts (ions) and in some cases metals present on them.

3.5.1 Soluble Salts Quantification

3.5.1.1 Ultrasound-Assisted Extraction method for soluble salts quantification

As it was mentioned previously, an ultrasound-assisted extraction method was used to carry out the soluble salt test for porous materials (cementitious materials, limestones and

sandstones). An alternative method to the Italian NORMAL 13/83 recommendation (now UNI 11087 Italian standard method and EN 16455/2012) for the extraction of soluble salts from non-soluble materials such as stones, cements, mortars was applied. Cementitious materials, limestones and sandstones, were subjected to the following sample pre-treatment before the salts extraction. In most of the research works presented in this PhD manuscript, a previous separation of external and internal parts of the porous materials was conducted by using a scalpel. The scrapped samples were crushed in an agate mortar with pestle in order to obtain a fine powder. After that, samples were dried on a heater at 100-105 ºC until constant weight. At this point, samples were ready for the extraction procedure. The extraction was performed in an ultrasound bath for 120 min, using 100 ml of deionised water (milli-Q quality) and 100 mg sample. In some cases, lower deionised water volumes were considered because a high quantity of water can dilute in excess the ions, making impossible the detection of these cations/anions present in the samples. The solution after extraction was filtered through a 0.45 µm syringe filter of polyamide CHROMAFIL® Xtra PA-45/25 (Macherey-Nagel, Düren, Germany) to obtain the final solution ready for quantification. This method was optimized as an alternative to the mentioned NORMAL 13/83 and UNI 11087/2003 standardized methods [16].

3.5.1.2 Ion chromatography (IC) coupled to a conductimetric detector with postcolumn suppression for soluble salts quantification

In this work, an ion chromatograph coupled to a conductimetric detector with postcolumn suppression was used:

a) To evaluate the soluble salt contents on mortars and cementitious materials from historical building (Igueldo Lighthouse) exposed to the open air suffering from different impacts (infiltration waters, marine aerosol, etc.)

b) To evaluate the salts concentration on sandstones, limestones and gypsum plaster from interior areas from Igueldo Lighthouse, in order to observe the influence of the surrounded marine environment.

c) To evaluate the concentrations of anions in rainwater from different areas of Metropolitan Bilbao

In all situations, cations and anions involved in each soluble salts were quantified by means of a Dionex ICS 2500 ion chromatograph connected to a conductimetric detector (ED50 Dionex conductimetric detector) with postcolumn suppression (Dionex Corporation, Sunnyvaley, California, USA) (see Figure 3.17).

For the anions separation, theDIONEX IONPAC® AS23 (4 x 250 mm) 60 µm particle size column, and DIONEX IONPAC® AG23 (4 x 50 mm) guard column were used. The self-regenerating suppressor for anions used was the suppressed conductivity DIONEX AERS 500 4mm RFIC™. As mobile phase a mixture of 4.5 mM Na_2CO_3 - 0.8 mM $NaHCO_3$ flowing at 1.0 ml min^{-1}. For the suppression, 25 mA current was used.

For cations separation a DIONEX IONPAC™ CG12A RFIC™ (4 x 250 mm) 9 µm particle size column and a DIONEX IONPAC™ CG12A RFIC™ (4 x 50 mm) cation guard column and a suppressed conductivity DIONEX CERS 500 4mm self-regenerating suppressor (59 mA suppression current) was used. 20 mM methanesulfonic acid as mobile phase at 1.0 ml min^{-1} flow was used (see chromatographic details in Table 3.1).

Table 3.1. General chromatographic conditions for the quantification of anions and cations.

CONDITIONS	ANIONS	CATIONS
Type of GuardColumn	DIONEX IONPAC® AG23 4x50 mm	DIONEX IONPAC™ CG12A RFIC™ 4x50 mm
Type of Column	DIONEX IONPAC® AS23 4x250 mm	DIONEX IONPAC™ CG12A RFIC™ 4x250 mm
Suppresor	DIONEX AERS 500 4mmRFIC™	DIONEX CERS 500 4mm
Currentapplied to suppresor	25 mA	59 mA
Mobile Phase	4,5 mM Na_2CO_3/0,8 mM$NaHCO_3$	MethaneSulfonicAcid 20mM
Flow	1,0 mL/mi	1,0 mL/min
InjectionVolume	25 µL	25 µL

The chromatograph is coupled to an autosampler AS40 from Dionex which makes possible an automatic analysis of sample series. The acquisition and data-handling was performed using the Chromaleon 6.60-SPIa software (Dionex Corporation).

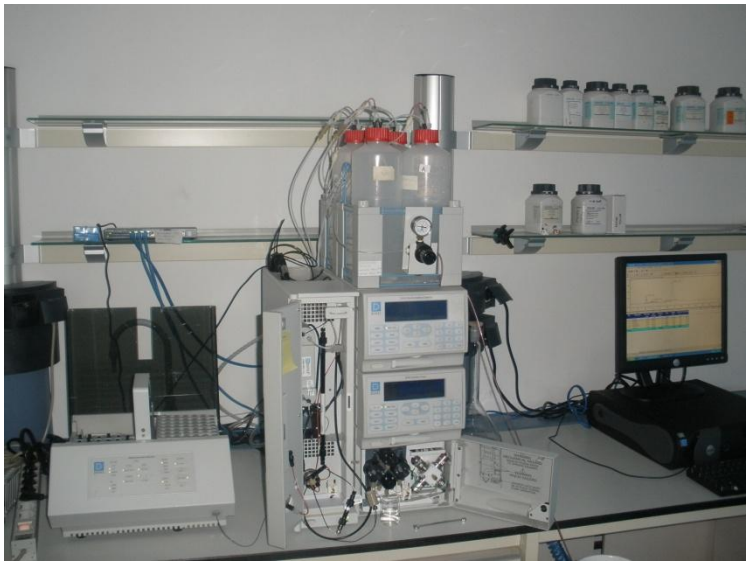

Figure 3.17. Ion chromatograph coupled to a conductimetric detector with postcolumn suppression and AS 40 autosampler (Dionex).

3.5.2 Metals quantification by Inductively Coupled Plasma-Mass Spectrometry (ICP-MS)

In order to determine the metals present on different types of samples (rainwater, black crusts etc.) a destructive analysis (in the case of black crusts) was done to determine the metallic composition and concentration in the selected samples.

The analytical procedure to quantify the metals on the samples involves: a microwave assisted acid extraction and subsequent, the elemental analysis by means of Inductively Coupled Plasma-Mass Spectrometry (ICP-MS).

3.5.2.1 Microwave assisted extraction

The acid digestion of the samples was carried out following the US Environmental Pollution Agency (USEPA) 3051A method [17] adapted and applied in previous research works by Carrero et al. [18-20]. The adapted method has proved to be very valuable since it has been customarily used in our research group to determine the metal content of different matrixes such as sediments, slag, mine wastes soils etc. The acid digestion protocol is useful to extract the following elements: Al, Sb, As, B, Ba, Be, Cd, Ca, Cr, Co, Cu, Fe, Pb, Mg, Mn, Hg, Mo, Ni, K, Se, Ag, Na, Sr, Ti, V and Zn.

The extraction of non-siliciclastic compounds was performed using a microwave assisted acid digestion in a Multiwave 3000 (Anton Paar, Graz, Austria) system provided with an 8XF-100 digestion rotor and 100 mL fluorocarbon polymer (PTFE) microwave vessels (see

Figure 3.18). Powdered 0.5 gr dried sample (constant weight verified using the Mettler-Toledo balance AJ150 model, ± 0.0001 g) were weighed in each Teflon vessel and subjected to acid digestion using 12 ml of 3:1 HNO_3 (69%) : HCl (36%). The acids were added and allowed to react for a few seconds before closing the vessels.

Figure 3.18. Multiwave 3000 microwave (Anton Paar, Graz, Austria) and Teflon vessels for digestion.

Then, vessels were introduced counterbalanced in the rotor, in each extraction three replicates from each sample and two blanks (Milli-Q water) were used in order to detect contaminations that could affect the analysis. Subsequently, the rotor was introduced into the microwave and samples were subjected to the method mentioned above. It consists on applying an initial ramp of sufficient power, to reach the temperature of 175^0 C during 5.5 min. Afterwards, the temperature was maintained between 170-180^0C during 4.5 min. After 10 minutes of heating, a third cooling step of 15 min was programmed in which the application of power ceases and the ventilation system is activated. After digestion and cooling, the vessels were removed from the rotor and they were opened carefully to wait until the acid vapor disappeared.

When reaching room temperature, the extracts of the vessels were filtered through Millex-HV 0.45 µm PVDF syringe filters (Merck® Millipore KGaA, Darmstadt, Germany) and quantitatively transferred to 50 mL pre-weighed polypropylene tubes. Small amounts of sample remaining in the vessels were collected with Milli-Q and they were transferred to the tubes after the filtration of these aliquots. After that, the tubes were weighted.

The extracts were kept in the refrigerator at 4^0C until the measurements.

3.5.2.2 Elemental analysis of the acid extracts by ICP-MS

Prior to the elemental measurements, the acid concentration of the acid extracts was reduced to less than 1% HNO_3 using Milli-Q water. In addition, a solution containing 10 $\mu g.L^{-1}$ of Be, Sc, Ge, In, Re and Bi was added as internal standard. The internal standards and ICP-MS calibration standards solutions were prepared from 1000 $mg.L^{-1}$ stock solutions of Alfa Aesar (Specpure®, Plasma standard solution, Germany) inside a class 100 clean room. All solutions were prepared using Milli-Q quality water. PL 20-200 µL and PL 500-5000 µL micropipettes (Eppendorf, Hamburg, Germany) with an calibration standards and samples dilutions were prepared using analytical balance model Mettler-Toledo XS205 (Colombus, OH, USA) with accuracy of ± 0.00001 g. The elemental analysis of the extracts was performed by ICP-MS (NexION 300, Perkin Elmer) in a class 100 clean room (see Figure 3.19). The argon used was supplied by Praxair (99.995%, Madrid, Spain).^{27}Al, ^{44}Ca, ^{88}Sr, ^{98}Mo, ^{114}Cd, ^{120}Sn, ^{121}Sb, ^{138}Ba, ^{184}W, ^{202}Hg and $^{206+207+208}Pb$ isotopes were determined in standard mode and ^{23}Na, ^{24}Mg, ^{39}K, ^{47}Ti, ^{51}V, ^{52}Cr, ^{55}Mn, ^{56}Fe, ^{59}Co, ^{60}Ni, ^{65}Cu, ^{66}Zn, ^{75}As, ^{78}Se, ^{111}Cd isotopes were determined in collision mode with He with in order to eliminate possible polyatomic interferences.

Figure 3.19. ICP-MS instrument (NexION 300, Perkin Elmer).

The plasma conditions such as argon flow of nebulizer, the torch position and the instrument lenses voltages were optimized before each measurement session aspirating a standard solution of 1ng/mL of Mg, Rh, In, Ba, Pb and U. The gas nebulizer flow was optimized obtaining a compromise between sensitivity and low oxides level (less than 2.5 % for the CeO/Ce ratio). The working conditions for the sample introduction and data acquisition are shown in Table 3.2. Finally, the data were acquired and analyzed for the

element quantitative analysis using the Elan 3.2 software (Perkin Elmer SCIEX™, Ontario, Canada).

Table 3.2. Experimental Conditions for ICP-MS analyses.

NebulizerFlow	0.90-1.00 L/min
Plasma Flow	18 L/min.
Auxiliar Flow	1.2 L/min.
RF Power	1600 W
HeliumFlow	4.0 mL/min
Dwell time	50 ms
Integration time	1000 ms
Scanning per replica	20
Replicas	3

3.6 Data treatment using chemometric tools

In some sections from this PhD Thesis, chemometric tools (multivariate statistics) were applied to treat the obtained quantitative data in order to extract additional information than the simple analytical data. The Unscrambler® 7.6 software [21] was used to perform the different chemometric treatments. Particularly, Correlation Analysis and Principal Component Analysis were used.

Thanks to the use of molecular techniques such as X-Ray Diffraction, Raman spectroscopy and Infrared Spectroscopy it was possible to know the nature of the soluble salts present in the analyzed samples. The correlation matrix obtained from the quantitative data (soluble cations and anions), must shown a high correlation between a cation and an anion if both are part of a crystallized salt in the sample under study. Therefore, the correlation analysis can be a good tool to confirm the molecular species identified with the analytical techniques. Moreover, when spectroscopic results are ambiguous, the correlation matrix can help to solve the doubts. Although in this work several halogen salts from the marine aerosol are expected in the samples; those salts have not a Raman response and the only method to detect at low concentrations is the correlation analysis.

To perform the correlation analysis, the quantitative data for the dissolved ions were introduced in units of nx mol/L M^{n+} (= to the old equivalents/L concentration) or mx mol/L X^{m-} just to guarantee the fulfillment of the electroneutrality condition:

$$\Sigma nx\,mol/L\ M^{n+} = \Sigma\ mx\ mol/L\ X^{m-}$$

Apart from the correlation analysis, Principal Component Analysisi (PCA) was also carried out. For example, PCA was used to see groupings of samples according to newly crystallized levels, types, etc. in different locations. Moreover the enrichment of rainwater by metals on different sampling sites was distinguished using PCA. This calculation was also carried out with Unscrambler® 7.6 software.

3.7 Chemical simulations through thermodynamic modelling

Additional to the chemometric calculations, chemical simulations through thermodynamic modelling were performed. These tools were useful to predict the crystallization of some soluble salts in porous materials, to model the probable chemical reactions that could be the responsible of the formation of specific decaying compounds, and also to confirm that specific molecular species can be formed under specific conditions.

For that purpose, the MEDUSA software [22] was used. As input data, the concentration values of the original species constituent of the building materials and/or original composition of crystals or minerals formed should be introduced. Then, according to the input, a modeling or prediction of the decay process is represented. In this work, the attack of marine aerosol (high input of chlorides and sulfates) on building materials was modeled. Thanks to the use of this software, it was possible to contrast the results obtained in the formation of double mix sulfates and nitrates salts by Raman, XRD, SEM-EDS and Infrared spectroscopy. Apart from this, in the Chapter 5, it was possible to predict the relations and the predominant compounds of the system Nitrite/Nitrate in the rainwater analyses.

3.8 References

[1] J. M. Madariaga, Analytical chemistry in the field of cultural heritage, Analytical Methods (2015) 7: 4848-4876.

[2] L. P. Choo-Smith, H. G. M. Edwards, H. P. Endtz, J. M. Kros, F. Heule, H. Barr, J. S. Jr. Robinson, H. A. Bruining, G. J. Puppels, Medical applications of Raman spectroscopy: from proof of principle to clinical implementation, Biopolymers (2002) 67: 1-9.

[3] L. T. Kerr, H. J. Byrne, B. M. Hennelly,Optimal choice of sample substrate and laser wavelength for Raman spectroscopy analysis of biological specimen, Analytical Methods (2015) 7: 5041-5052.

[4] M. Wojcieszak, A. Percot, S. Noinville, G. Gouadec, B. Mauchamp, P. Colomban, Origin of the variability of the mechanical properties of silk fibers: 4. Order/crystallinity along silkworm and spider fibers, Journal of Raman Spectroscopy (2014) 45: 895-902.

[5]] S. Upasen, P. Batocchi, F. Mauvy, A. Slodczyk, P. Colomban, Protonation and structural /chemical stability of $Ln_2NiO_4+\delta$ ceramics vs. H_2O/CO_2: High temperature/water pressure ageing tests, Journal of Alloys and Compounds (2015) 622: 1074-1085.

[6]T. Aguayo, C. M. Araya, T. M. Icaza, M. Campos-Vallette. A vibrational approach for the study of historical weighted and dyed silks, Journal of Molecular Structure (2014) 1075: 471-478.

[7] M. Maguregui, U. Knuutinen, I. Martinez-Arkarazo, A. Giakoumaki, K. Castro, J. M. Madariaga, Field Raman analysis to diagnose the conservation state of excavated walls and wall paintings in the archaeological site of Pompeii (Italy), Journal of Raman Spectroscopy (2012) 43: 1747-1753.

[8] M. C. Caggiani, P. Colomban, C. Valotteau, A. Mangone, P. Cambon, Mobile Raman spectroscopy analysis of ancient enameled glass masterpieces, Analytical Methods (2013) 5: 4345-4354.

[9] P. Colomban, The on-site/remote Raman analysis with mobile instruments: a review of drawbacks and success in cultural heritage studies and other associated fields, Journal of Raman Spectroscopy (2012) 43: 1529-1535.

[10] V. Matovic, S. Eric, D. Sreckovic-Batocanin, P. Colomban, A. Kremenovic, The influence of building materials on salt formation in rural environments, Environmental Earth Sciences (2014) 72: 1939-1951.

[11] N. Prieto-Taboada, O. Gomez-Laserna, I. Martinez-Arkarazo, M. A. Olazabal, J. M. Madariaga, Relevance of cross-section analysis in correct diagnosis of the state of conservation of building materials as evidenced by Spectroscopic imaging, Analytical Chemistry (2013) 85: 9501-9507.

[12] Ente Nazionale Italiano di Unificazione (UNI) UNI 11087: Natural and artificial stones. Water soluble salts determination, Dosaggio dei Sali Solubili, Milano, Italy (2003).

[13]K. Castro, M. Perez-Alonso, M. D. Rodriguez-Laso, L. A. Fernandez, J. M. Madariaga, On-line FT-Raman and dispersive Raman spectra database of artists´ materials (e-VISART database), Analytical & Bioanalytical Chemistry (2005) 382: 248-258.

[14] M. Maguregui, N. Prieto-Taboada, J. Trebolazabala, N. Goienaga, N. Arrieta, J. Aramendia, L. Gomez-Nubla, A. Sarmiento, M. Olivares, J. A. Carrero, I. Martinez-Arkarazo, K. Castro, G. Arana, M. A. Olazabal, L. A. Fernandez, J. M. Madariaga. in: CHEMCH 1st International Congress Chemistry for Cultural Heritage, Ravenna, 30th June–3rd July (2010).

[15] R. T. Downs, M. Hall-Wallace, A database of crystal structures published in the American mineralogist and the Canadian mineralogist and its use as a resource in the classroom. in: 18th General Meeting of the International Mineralogical Association (2002) pp. 128.

[16] N. Prieto-Taboada, O. Gomez-Laserna, I. Martinez-Arkarazo, M. A. Olazabal, J.M. Madariaga, Optimization of two methods based on ultrasound energy as alternative to European standards for soluble salts extraction from building materials, Ultrasonic Sonochemistry (2012) 19: 1260-1265.

[17] EPA Method 3051A, Microwave assisted acid digestion of sediments, sludges, soils and oils. United States Environmental Protection Agency (USEPA) (2007).

[18] J. A. Carrero, Evaluación del impacto del Tráfico Rodado en Suelos y Plantas de márgenes de carretera. PhD Thesis. University of the Basque Country (2011).

[19] J. A. Carrero, N. Goienaga, S. Fdez-Ortiz de Vallejuelo, G. Arana, J. M. Madariaga, Classification of archaeological pieces into their respective stratum by a chemometric model

based on the soil concentration of 25 selected elements, Spectrochimica Acta Part B (2010) 65: 279-286.

[20] J. A. Carrero, I. Arrizabalaga, J. Bustamante, N. Goienaga, G. Arana, J. M. Madariaga, Diagnosing the traffic impact on roadside soils through a multianalytical data analysis of the concentration profiles of traffic-related elements, Science of the Total Environment (2013) 458-460: 427-434.

[21] Camo Asa. The Unscrambler® 7.6, Trodheim, Norway (2005).

[22] I. Puigdomenech. MEDUSA (Make Equilibrium Diagrams Using Sophisticated Algorithms), Department of Inorganic Chemistry, The Royal Institute of Technology (KTH): Stockholm, Sweden (2009).

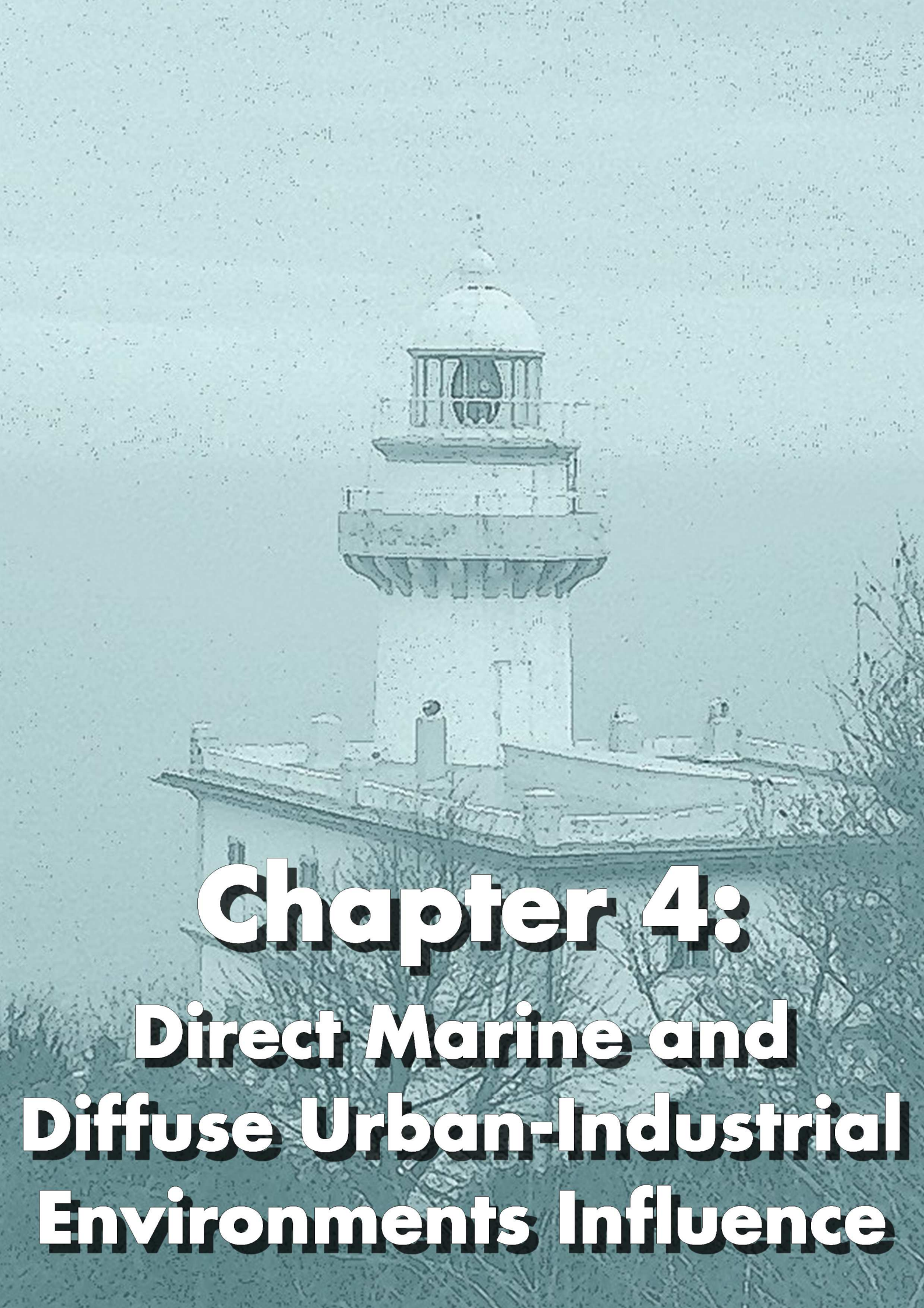

Chapter 4: Direct Marine and Diffuse Urban-Industrial Environments Influence

CHAPTER 4.

DIRECT MARINE AND DIFFUSE URBAN-INDUSTRIAL ENVIRONMENTS INFLUENCE

In this chapter, the negative influence of marine environment and additional possible contributions of other stressors, that can be transported by the wind coming from the close urban-industrial environment on the conservation state of an historical construction, Igueldo Lighthouse (San Sebastian, Basque Country, north of Spain), will be studied. Therefore, in this chapter the dry and/or wet depositions (coming from the marine aerosol) on exposed building materials will be evaluated.

Once salts and particles transported in the marine aerosol have been deposited on the pores of the building materials, and according to the microclimatic conditions, they can be dissolved and they can also undergo subsequent re-crystallization processes, leading to the pore fracture and material decay (dehydration/hydration cycles). In order to know if a specific salt or metal(loid)particle present in the surface as wet depositions comes from marine aerosol or from the influence of industries, road traffic, anthropogenic activities or even also from natural sources, it is necessary to determine which kind of airborne particulate matters are present in the atmosphere surrounding the construction under study.

The association between the surrounding environment and the construction can be achieved by developing a multianalytical methodology, based firstly on measurements conducted on the field (in situ analyses) and continuing with in-depth analyses in the laboratory. In this way, it is important to take into account the previous studies in the

literature about the influence of soluble salts in buildings and therefore the decay pathologies according to the materials which acts as matrix [1–7].

The specific environment which surrounds Igueldo Lighthouse is influenced by the sea and also suffers from diffuse pollution coming from urban-industrial areas. In this sense, it is important to define the decay sources that can affect negatively to the conservation state of the Igueldo Lighthouse construction. In Figure 4.1, a summary of all the anthropogenic and natural environmental stressors that can affect Igueldo Lighthouse building materials are presented. The location of the lighthouse in San Sebastian is relatively away from the influence of urban and industrial pollution. However, anthropogenic emissions (acid aerosols such as SO_x, NO_x and airborne particulate matter) coming from these sources placed quite far from the construction, can also have influence in its state of conservation in a diffuse way.

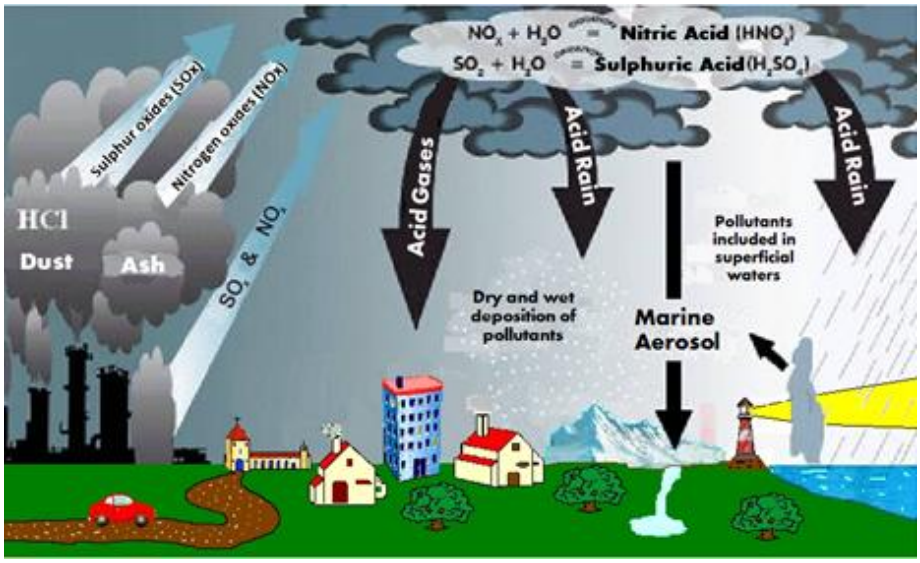

Figure 4.1. A representation of the influence of direct marine and diffuse urban-industrial environment on buildings close to the sea.

Buildings or constructions close to the sea, usually experiment dry and/or wet depositions of suspended particles and salts. Concretely, the most frequently salts found on building materials from constructions close to the sea are chlorides and sulfates. These kinds of salts, coming from the input of marine aerosol, can affect the integrity on different building materials, especially carbonaceous ones [8-10].

Regarding cementitious materials, chlorides can accelerate the corrosion of the steel and/or iron reinforcement promoting damage in the form of pitting, giving rise to breakdown of the oxide layer of the armature. Moreover, the sulfates present in the marine aerosol, are able to

penetrate the concrete mass [11] and react with the cement hydration product (mainly tricalcium silicate (Alite, C_3S), dicalcium silicate (Belite, C_2S) and tricalcium aluminate (C_3A)). The direct consequence is the formation of sulfates of different nature such as sodium sulfate, potassium, magnesium, calcium etc; which usually due to the hydration/dehydration cycles, promote the loss of material. For this reason, it is very important to improve the permeability properties of the concrete materials used in constructions close to the sea, because the higher permeability of a fluid, either liquid or gas, in these kinds of materials will ultimately depend on the porosity of the hydrated paste and aggregates. This permeability is very sensitive to the W/C (water/cement) ratio. For example, if a cement has an W/C= 0.8, its permeability will be almost 30 times higher than other with W/C=0.5. For cement/concrete and/or cementitious materials placed on marine environments, the W/C ratio should be very low [12].

In order to decide which material is more suitable to be used in constructions close to the sea, it is always necessary to carry out a study of the environmental impact which will be suffer the building. The correct choice of material will get the building life longer. In this way, cement resistant to the chlorides and sulfates attack is widely used nowadays.

In addition, according to the permeability and durability, pozzolanic materials such as silica fume are starting to be used as a preventive measure for these chlorides and sulfates attack coming from the marine aerosol, which is usually incorporated into the Portland cement, helping to improve their microstructure is usually used [13,14].

The global objective of this chapter was to apply a multianalytical methodology in order to characterize the composition of mortars, cements, limestones and sandstones from different parts of Igueldo Lighthouse (inner and outer areas (external terrace) and to assess possible deterioration processes that are taking place in these building materials. In this sense, the potential impact that Igueldo lighthouse is suffering due to its location is the impact of marine aerosol. Moreover, a possible additional impact of environmental stressors such as acid gases from a diffuse urban-industrial environment coming from San Sebastian city and the around industrial areas was not excluded.

4.1 Igueldo Lighthouse (San Sebastian, Basque Country, north of Spain)

Igueldo Lighthouse is located in San Sebastian (Basque Country, north of Spain) (see Figure 4.2). The evidence of a light signal in San Sebastian dated back to the 16th century. Originally the luminary was located in the castle, on the top of Mount Urgull, and its maintenance was

done by Confraternity of San Pedro which put to all the vessels that enjoy the light of the luminary, a tax that consisted in the two and a half percent of codfish brought from Terranova (common fishing zone of Basque fishermen in Canada).

Figure 4.2. Igueldo Lighthouse location in San Sebastian (Basque Country, north of Spain).

In the historical archives from 1625, a reference to a man responsible for guiding the vessels can be found.

"*Beside of the port or shell, a watchtower with one house, where a man with a firewood torch works during winter, is placed. This torch is used for guiding the vessels to the entrance in the noon part, where a noticeable majestry dock is placed. In it, more than a hundred vessels fit perfectly. Apart from that, another dock of high walls starts.*"[15].

Dr. L.Martinez de Isasti –Theologian (1565-1626)

In this way, coastal mountains were used for the construction of small towers, in order to use it as building for warn against enemy ships or to warn against the presence of fish stocks, and help to Basque fishermen to fish. Moreover, it was also used to communicate using fire or by using flags.

The first Igueldo Lighthouse was built in 1778 and it was placed at 184 meters of altitude, it had an outer perimeter of 32 meters, 20 meters of inner perimeter and it was 18 meters high. It also had two floors and a terrace on the top where the lighting mechanism was installed.

Taking into account the scarce installations of this type that existed in Europe at that time, Igueldo Lighthouse was considered the most important one in Europe.

However, since its construction, some disadvantages were observed, for example visibility problems due to the massive presence of fog. Furthermore, military actions carried out at that time were also the responsible of the loss of most of sandstone ashlars of the lighthouse. For all these reasons, over years, this first San Sebastian lighthouse was dropped out and forgotten. It was in 1912, when the *Monte Igueldo* Society put it into value as a tourist attraction, adding some decorative details, to make it more aesthetically attractive.

As San Sebastian needed a lighthouse that would elevate the category of the city, which was very important in that time, and taking advantage of the expansion which was taking place at the port of San Sebastian, it was decided to build a new lighthouse in 1855. Initially, it was thought to recover the lighthouse in its original location, but considering that its initial position caused problems, this option was rejected. For this reason, Manuel Peironcely was commissioned to design the new lighthouse. He built the new one at a lower altitude in the slope of Igueldo Mount, to avoid problems with fog. Therefore, the new Igueldo Lighthouse was placed at an altitude of 134 meters instead of 184 meters. During years, the new lighthouse has undergone many structural renovations. In 1911, it was decided to improve and renew its lighting. In 1918, the electrification project was performed. Later, in 1929, the installation was renewed and in 1934, the lighthouse inner rooms were coated with tiles (see Figure 4.3).

Figure 4.3. Historical photograph of Igueldo Lighthouse at the beginning of 20th century.

At the beginning, the original and last Igueldo Lighthouse, was composed of a single rectangular floor of 11.10m x 13.90m, with an inner courtyard of 3.3m x 6m. The tower was attached to the midpoint of the north façade and it was composed by a first cylindrical structure of 4m (outside diameter), that reached up to the height of the cornice that surrounded the building and to another second slightly frustoconical structure, topped by a quite flown cornice which is hold by supporting corbels. Up to the balcony position, the

lighthouse reaches 10.20 meters height. From there, the cylindrical tower and flashlight raise the focal plane at 13.5m above the ground (see Figure 4.4 left). It is noteworthy also that in subsequent reforms, the new floor was built quite successfully respecting the original architecture over the original floor (see Figure 4.4 right).

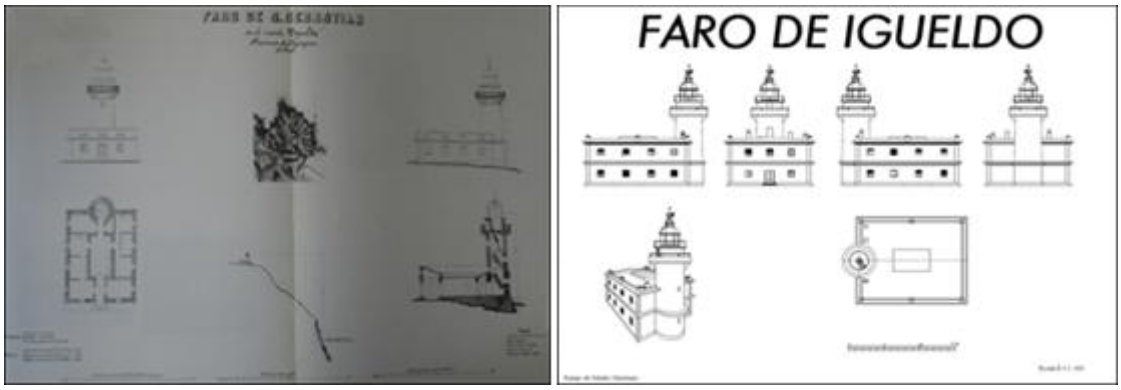

Figure 4.4. Initial (left) and current (right) main view and side view plans of Igueldo Lighthouse.

4.2 Materials used to construct the Igueldo Lighthouse

The Igueldo Lighthouse was built mainly using sandstone, initially composed by only one rectangular floor and thereafter adding a second floor with its façade covered by a narrow stone cornice, with moldings outlining in its two heights, and a terrace. In the façade oriented towards the sea, the tower stands over a cylindrically shaped plinth. Limited ornamentation was repeated at the flashlight base where white tastefully designed corbels support the oriel which surrounds the tower. The interior staircase with 54 steps also made of sandstone, allows the access to the outside.

In general terms, the original materials used to construct the lighthouse were collected in nearby areas such as local quarries. Therefore, the construction materials used could come from Igueldo quarries, because at that time almost all the material used in the surrounding buildings came from that quarry. The stones available in Igueldo quarry were sandstone and limestone, with massive presence of feldspars [16]. The sandstone coming from this quarry includes glauconite and it is also rich in detrital quartz, and other components such as potassium feldspar, plagioclase and glauconite grains, as a fundamental component of the frame. Igueldo quarry belongs to the "Flysch" ternary belonging of the Eocene [16].

The fact of knowing the stressors that can affect the conservation state of its building materials and also the origin of the original material used in the construction of the

lighthouse can give us a first idea of the types of pathologies that its materials can suffer. According to the Igueldo Lighthouse sandstone composition, this material can be susceptible to suffer dissolution, erosion and alveolization processes, changing its porosity and subsequent degradation.

4.3 Simulation of the preferential wind and rainwater direction for the correct sampling in the Igueldo Lighthouse

In order to extract reliable results with the applied analytical methodology, to perform an appropriate sampling is crucial. In this sense, it is necessary to know which the preferential directions of wind and rain are. In the rainwater, different kind of pollutants (e.g. acid aerosol and airborne particulate matter (APM)) can be incorporated. The wind push the rainwater to the building façade and wet depositions of those pollutants transported in the rain take place. Wind can also transport APM promoting a dry deposition of those metals and metalloids particles in the building materials. Both kind of depositions and wind can adversely affect the conservation state of the building materials and promote different kind of decay processes. The prediction of the wind behavior over a complex topographies is becoming a valuable tool for example in the evaluation of wind energy potential in a specific area, to predict fires behaviors on forest or for the study of pollutants dispersion and their impact on different buildings as in the present case [17].

To find out which areas of the lighthouse are the ones who can suffer the greatest impact of rain and wind, it is necessary to have the information about wind direction and speed. According to data provided by the Spanish Ministry [18], the three preferential wind directions in the area where the Igueldo lighthouse is located are north, northwest and south. Among these three directions, the northwest coincides with the preferential rain direction in the Igueldo area. For the simulation, the available rain and wind data belonging to 2010 (the year before the sampling) were introduced as initial data together with the Igueldo Lighthouse coordinates.

These rain and wind data belonging to 2010 (the year before the analyses) were introduced as initial data in the simulation software with the Igueldo Lighthouse coordinates. For that purpose, the Windstation simulation software was used [17]. This program is able to predict the streamlines based on the orography of the digital terrain model previously introduced in its software. In this way, the software develops mathematical iterations which are reflected in streamlines and flow speed, estimating different arrows whose length is directly

proportional to the wind speed. In our case the orography of Igueldo area is relatively complex (see Figure 4.5), because the lighthouse is located in a karstic area, full of cliffs, which includes additional variables that hinder the simulation.

Figure 4.5. Orography of the Igueldo Lighthouse surroundings.

The results obtained after the simulation is shown in Figure 4.6. The arrows in the figure indicate the preferential direction of wind and rain according to the site orography.

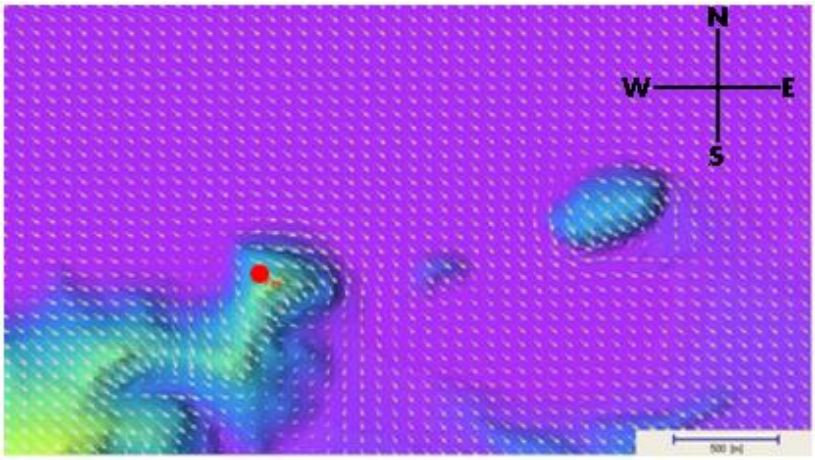

Figure 4.6. Results obtained after the simulation showing the preferential wind and rain directions in the Igueldo Lighthouse location.

Moreover, to calculate the rose of the winds, the values of wind speed and direction during 2010, which were measured by anemometers in Km/h units, were taken into consideration [17] (see Figure 4.7).

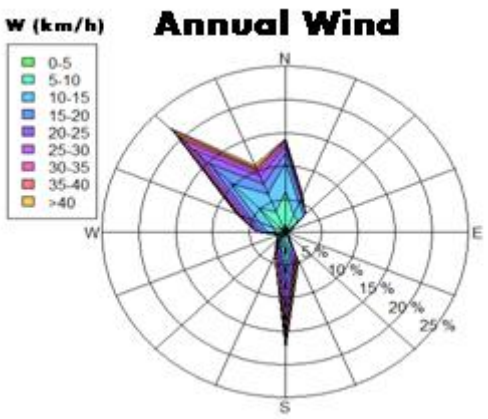

Figure 4.7. Rose of the wind at the Igueldo Lighthouse (2010).

Additionally, to the wind direction data, the pluviometric data can be also presented. In this way, the pluviometric data express the quantity of rain fallen which is expressed in milimeters (the water that can be accumulated in a 1 mm^2 horizontal and impermeable surface during the precipitation time). In the Figure 4.8, the pluviometric data added to the rose of the winds are presented. In this way, the preferential wind and rain direction is the N.W direction, with a high level of 10 mm of precipitations.

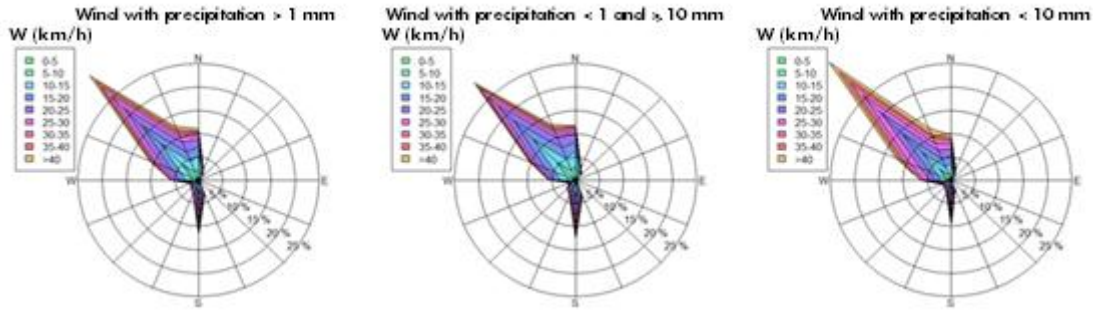

Figure 4.8. Rose of the winds together with the pluviometric data (direction and quantity).

After analyzing all the wind and rain data and considering the lighthouse location, it was concluded that the area most affected by these two climatic factors is the West area (see Figure 4.9). Once defined the preferential area of impact, an in-depth sampling of this area can be done, in order to assess if the impact of natural and anthropogenic environmental stressors transported by the rain and wind is taking place in this façade orientation.

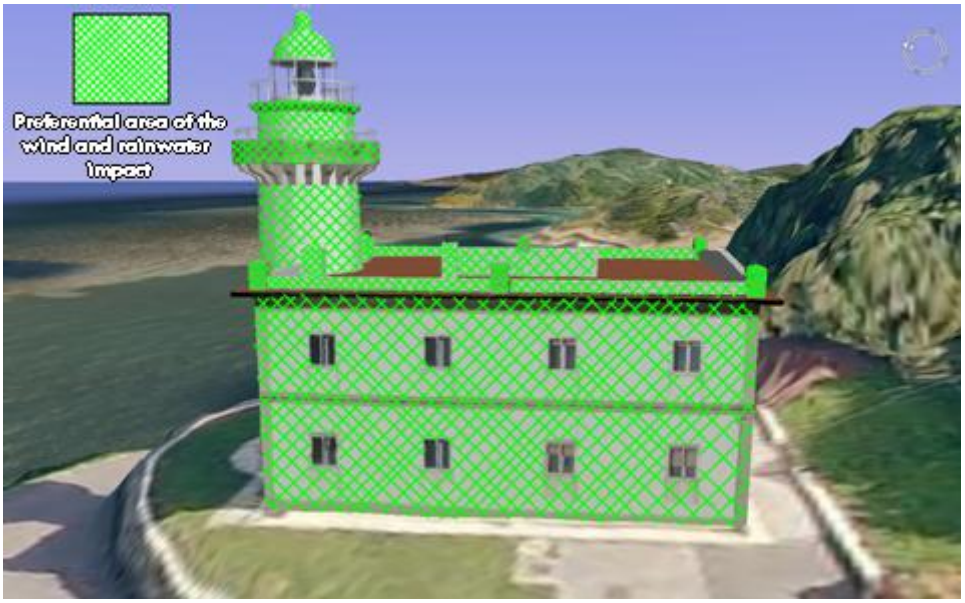

Figure 4.9. Preferential impact area of the wind and rain on the Igueldo Lighthouse.

As it will be explained in the following three scientific articles, different types of building materials were collected always taking into account the simulation carried out. In this way, samples from terrace and inner rooms were collected. Among the different materials, cementitious materials, mortar, sandstones, limestones, joint mortars and plasters were considered.

4.4 References

[1] B. Lubelli, R. P. J. Van Hees, C. J. W. P. Groot, The role of sea salts in the occurrence of different damage mechanisms and decay patterns on brick masonry, Construction & Building Materials (2004) 18:119–24.

[2] D. Camuffo, Physical weathering of stones, Science of the Total Environment (1995) 167:1–14.

[3] C. Cardell, F. Delalieux, K. Roumpopoulos, A. Moropoulou, F. Auger, R. Van Grieken, Salt-induced decay in calcareous stone monuments and buildings in a marine environment in SW France, Construction & Building Materials (2003) 17:165–79.

[4] V. Fassina, Neoformation decay products on the monument's surface due to marine spray and polluted atmosphere in relation to indoor and outdoor climate. In: Zezza F, editor. EC research workshop: origin, mechanisms and effects on degradation of monuments in marine and continental environments. Tecnomack(1996) p. 37–53.

[5]I. Martınez-Arkarazo, M. Angulo, L. Bartolome, N. Etxebarria, M. A. Olazabal, J. M. Madariaga, An integrated analytical approach to diagnose the conservation state of building materials of a palace house in the metropolitan Bilbao (Basque Country, North of Spain), Analytica Chimica Acta (2007)584:350–359.

[6] A. V. Turkington, E. Martin, H. A. Viles, B.J. Smith, Surface change and decay of sandstone samples exposed to a polluted urban atmosphere over a six-year period: Belfast, Northern Ireland, Building & Environment (2003) 38:1205–1216.

[7]P. Maravelaki-Kalaitzaki, G. Biscontin, Origin, characteristics and morphology of weathering crusts on Istria stone in Venice, Atmospheric Environment (1999) 33:1699-1709.

[8]K. Torfs, R. Van Grieken, F. Zezza, N. García, F. Macri, The cathedral of Bari, Italy: evaluation of environmental effects on stone decay phenomena, Studies in conservation, (1997) 42: 193-206.

[9]K. Torfs, R. Van Grieken,Chemical relations between atmospheric aerosols, deposition and stone decay layers on historic buildings at the mediterranean coast, Atmospheric Environment (1997)31: 2179-2192.

[10] F. Zezza, F. Macri, Marine aerosol and stone decay, Science of the Total Environment (1995) 167: 123-147.

[11] C. Yu, W. Sun, K. Scrivener, Degradation mechanism of slag blended mortars immersed in sodium sulfate solution, Cement and Concrete Research (2015) 72: 37-47.

[12] http://www.arquba.com/ [last acceded June 2015].

[13] S. Kawahara, T. Shima, Y. Suda, T. Saeki, Diffusion and binding of chloride ions in silica fume concrete, Konkurito Ronbunshu (2011) 64: 354-361.

[14]A. R. Hariharan, A. S. Santhi, G. M. Ganesh, International Journal of Civil and Structural Engineering (2011) 1: 695-706.

[15] L. Martinez de Isasti, Compendio Historial de Guipuzcoa (1625).

[16]I. Rodriguez-Maribona, M. Zalbide, F. Garmilla, F. Garcia, J. A. Ibanez, S. Garin, Conservation study of the stone material used in the Culture House of Almirante Oquendo, in San Sebastian, Materiales de Construcción (1999) 49: 19-30.

[17] A. M. G. Lopes, WindStation, a software for the simulation of atmospheric flows over complex topography, Environmental Modelling & Software (2003)18: 81–96.

[18] http://www.aemet.es [last acceded June 2015].

RESEARCH ARTICLE 1

Characterization and diagnosis of the conservation state of cementitious materials exposed to the open air in XIX century lighthouses located on the coast of the Basque Country: 'The case of Igueldo lighthouse, San Sebastian, North of Spain".

H. Morillas, M. Maguregui, O. Gómez-Laserna, J. Trebolazabala, J. M. Madariaga

Journal of Raman Spectroscopy (2012) 43: 1630–1636

Characterization and diagnosis of the conservation state of cementitious materials exposed to the open air in XIX century lighthouses located on the coast of the Basque Country: 'The case of Igueldo lighthouse, San Sebastian, North of Spain"

ABSTRACT

Non-invasive Raman spectroscopy for molecular analysis, assisted with other analytical techniques such as X-ray fluorescence for elemental analysis were applied to characterize possible pathologies on cement mortar and concrete (cementitious materials) from a historical 19th century lighthouse exposed to the open air, in Igueldo (San Sebastian, Basque Country, North of Spain). The spectroscopic observations were compared with quantitative concentration values of cations and anions extracted as soluble salts, treated by chemometric tools. The integrated analytical techniques were used to diagnose the influence of (1) marine aerosol, (2) seagull droppings and (3) original addition of sulfates to the cementitious materials, on the formation of decaying products such as chlorides, sulfates, nitrates, etc., that affect the integrity of the lighthouse outdoor area.

Keywords: Igueldo lighthouse; cementitious material; decaying; nitrates; sodium sulfate.

1. Introduction

During several decades, the impact of different environmental stressors, either anthropogenic or natural, have led to numerous deterioration processes of our Built Heritage materials, including those placed in lighthouses, causing several changes in the aesthetic appearance of the materials and affecting the integrity of all the building. Therefore, professionals from different fields, including scientists, are currently making great efforts to understand the mechanisms and consequences of different damages caused by these environmental stressors [1].

Considering the location of lighthouses, next to the sea, they can suffer the impact of marine aerosols, which usually transport chloride, sulfate and nitrate salts. The sea spray, composed primarily of seawater along with particles naturally generated by the action of wind on the seawater surface, introduces these ionic species into the atmosphere [2]. These ions present in the marine aerosol can be deposited on the surface of concrete. The consequence of this process is the formation of external efflorescence or even internal crystallizations of salts in the pores of cementitious materials. Examples of that can be the crystallization of different kinds of chloride salts and sodium, potassium, magnesium and calcium sulfates in the building materials which can lead to loss of its consistency. Other salts that can crystallize on or inside the building materials are the nitrates. These kinds of salt crystallizations are difficult to observe as they can be more easily dissolved by the effect of rainwater [3] than other salts such as chlorides, carbonates and sulfates. Next to Igueldo Lighthouse, there is not appreciable traffic density nor transit of ships, thus the possible impact of atmospheric NOx coming from marine or road traffic, polluted urban environment, etc., cannot be considered. For this reason, in this case, the most important nitrate source could be the ammonium nitrate (NH_4NO_3), that can be carried in infiltration waters and transported to the building materials through capillarity processes. This nitrate salt can be usually formed as a consequence of organic matter decomposition processes [4]. Ammonium nitrate can react easily with the carbonaceous composition of building materials (e.g. calcite ($CaCO_3$)) leading to the formation of their respective nitrate salt (e.g. nitrocalcite ($Ca(NO_3)_2 \cdot 4H_2O$)),[5] crystallizing inside the pores (sub-efflorescence) or on the surface of the building material (efflorescence)[6].

In recent years, the use of non-invasive techniques for the analysis of original and deterioration products of building materials has increased noticeably. In fact, the combination of noninvasive spectroscopic techniques that can offer both molecular and elemental composition is the most used analytical strategy. For instance, the use of Raman

spectroscopy and X-ray fluorescence (XRF) is a very useful and successful combination [7–10]. In this work, a combination of such non-destructive techniques (Raman and XRF) was applied to identify the possible presence of nitrate and sulfate salts in the outdoors terrace of Igueldo lighthouse (San Sebastian, Basque Country coast, north of Spain) exposed to the marine atmosphere. Moreover, to complete the spectroscopic results, samples of the different cementitious materials were subjected to the soluble salt test (ion chromatography was used to quantify the concentrations of soluble chlorides, sulfates, nitrates, etc.) using the method described elsewhere [4]. The concentration of dissolved anions and cations in the aqueous extracts was quantified by means of ion chromatography. Quantitative data were subjected to correlation analysis to explain better the possible links between those quantified anions and cations, coming from soluble salts, and also to compare the quantitative results with those obtained using Raman spectroscopy. Considering the location of the building, a possible link of the identified salts with the influence of the surrounding environment and possible stressors affecting those materials was also considered.

2. Experimental

2.1. Lighthouse description and sampling

The Igueldo lighthouse, located in San Sebastian (Basque Country, North of Spain), was built in 1855 (see Figure 1A and 1B). It stands 134 m above sea level and has suffered several restoration processes during its 156 years of life. The lighthouse has two floors and a terrace on the top of the construction. The main material used for the construction of its structure was sandstone. It is known that this stone comes from the Igueldo quarry, because all buildings constructed in that area and that time used materials from that location. Stones from Igueldo quarry are sandstone and limestone with high contents of feldspar [11]. In this work, six areas from the terrace of the lighthouse (see Figure 1C) were sampled (three from its structure; TE-1, TE-2, TE-3 and three from its floor; TF-1, TF-2, TF-3). From each area, three cement fragments with plaster remains and efflorescence in some cases were extracted (nine fragments from terrace structure (TE) and nine from terrace floor (TF)). The size of all samples ranges from 1 x 1 cm to 7 x 5 cm (see Figure 1D).

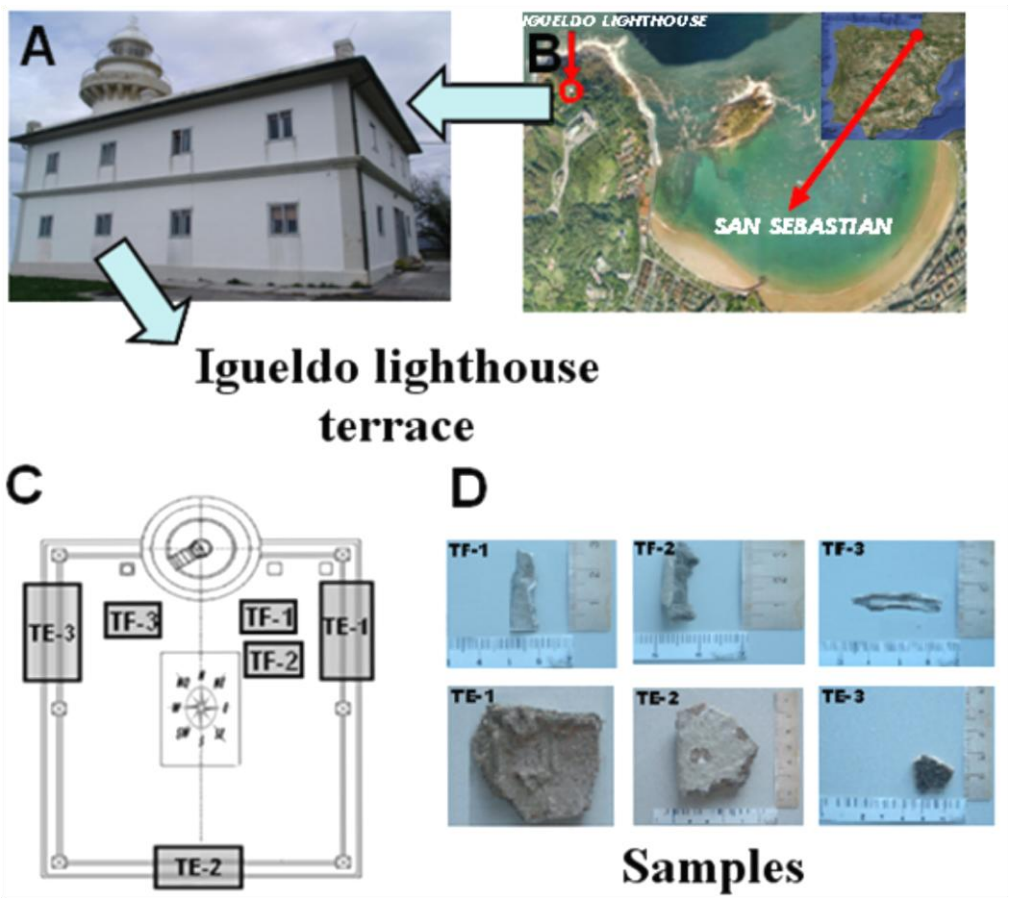

Figure 1. (A) General view of Igueldo lighthouse. (B) Location of the Igueldo Lighthouse in San Sebastian, Basque Country, North of Spain. (C) A plan of the terrace with the location of sampling areas from terrace structure (TE) and from terrace floor (TF). (D) Details for some of the analyzed samples from the six areas.

2.2. Instrumentation and methodology

For the mineralogical characterization of the samples, Raman spectroscopy was selected. Two Raman instruments were used, one portable spectrometer to guarantee the maximum presence of decaying compounds in the samples taken to the laboratory, and another laboratory instrument to obtain the maximum spectral information from samples at micrometric level. The portable Raman instrument was the innoRam™ (B&WTEK$_{INC.}$, Newark, USA) model which implements an excitation laser of 785nm (maximum output power of laser is 300 mW, but the user has the software capability to reduce it to 1%). The microprobe (around 0.1 mm of focus) can be used by hand or can be mounted on a manual X-Y-Z support with a micro-video camera to help in the focus on the desired area to perform the analysis (MICROBEAM S.A, Barcelona, Spain). The spectra were acquired in the 65–2500 cm^{-1} spectral range. The laboratory Raman spectrometer was a Renishaw RA100 Raman microprobe spectrometer (Renishaw, Gloucestershire, UK) which also implements a 785-nm excitation wavelength. The microscopic analysis was performed using 20x and 50x long-

range objective lenses mounted in the head of the Raman microprobe that also has a micro-video camera. Spectra were collected from 100 to 2200 cm^{-1} , although higher wavelength ranges were also considered in some measurements. The exposure time for each spectrum ranged from 5 to 20 s, and they were accumulated between five to ten times in order to improve the signal-to-noise ratio. Due to the fluorescence observed for some of the spots, the first and second derivatives were computed in order to unequivocally define a peak as well as the corresponding wavenumbers [12]. With both instruments, the laser power on the sample was attenuated to avoid thermal decomposition. Both Raman instruments were calibrated daily using the 520 cm^{-1} Raman band of a crystalline silicon chip. Spectral acquisition with the innoRam™ was performed using the BWSpec™ 3.26 software ($B\&WTEK_{INC}$), and Renishaw Wire 3.2 software was used with the RA100 spectrometer. The interpretation of all the Raman results was performed by comparing the acquired spectra with the spectra of pure standard compounds collected in the e-VISNICH dispersive Raman database [13], which contains Raman spectra of Natural, Industrial and Cultural Heritage compounds. Additionally, free available Raman databases (e.g. RRUFF[14]) were also considered for the assignation of Raman bands. The uric acid standard (crystalline, ≥99%) used in the Raman analysis was provided by Sigma-Aldrich (Milwaukee, WI, USA). Spectral interpretation and data treatment were carried out using GRAMS/AI 7.02 software (Thermo Fisher Scientific Inc., Waltham, USA).

For the elemental analysis, a Röntec (currently Bruker AXS, Berlin, Germany) ArtTax μ-XRF instrument was used. The instrument is provided with a molybdenum X-ray tube. Spectra were acquired at the maximum working voltage/current of 50 keV/700 mA during 500 s. The instrument includes a Xflash detector ($5mm^2$) and a CCD video camera that allows to focus on the sample (focussed area of 8 x 8 mm^2) by a motorized XYZ positioning unit controlled by the PC. The X-rays are collimated by a Tantalum collimator with a diameter of 650 mm. To determine elements with Z<20 (calcium), helium purging in the excitation and detection paths was used. However, lightweight elements below sodium (Z<11) cannot be identified. Instrument control and data-handling were performed using the Windowsbase ArtTax software 4.9.13.2 (Intax GmBH, Berlin, Germany).

The quantification of soluble salts, present in the samples of the lighthouse, was conducted by ion chromatography with conductivity detection after post-column ion suppression. Prior to the soluble salt quantification, an extraction of the soluble cations and anions was carried out using an ultrasound-based extraction method. All the samples were homogenized in an agate mortar and dried in an oven at 75 ^{o}C until constant weight. After that, powdered and dried samples were subjected to an ultrasound extraction procedure in

an ultrasound bath. 100 mg of powdered sample with 100 ml of Milli-Q quality water (Millipore, USA) was placed in an ultrasound bath during 100 min in order to extract soluble salts (anions and cations) from samples. Cations (K^+, Na^+, NH_4^+, Mg^{2+}, Ca^{2+}) and anions (F^-, Cl^-, NO_3^-, SO_4^{2-}) were quantified by means of a Dionex ICS 2500 ion chromatograph connected to a conductimetric detector (ED50 Dionex conductimetric detector) with post-column suppression (Dionex Corporation, Sunnyvaley, California, USA). The experimental conditions used for the quantification of these anions are described elsewhere [4].

3. Results

3.1. Molecular and elemental characterization: Raman spectroscopy and micro-X-ray fluorescence

Raman analysis of samples from the TE and floor showed that they were composed of a mixture of $CaCO_3$ (bands at 1085, 712 and 279 cm^{-1}), gypsum ($CaSO_4 \cdot 2H_2O$, bands at 1008, 1134, 414, 492, 619 and 669 cm^{-1}), bassanite ($CaSO_4 \cdot ½\ H_2O$, with its main band at 1015 cm^{-1}) and quartz (SiO_2) (main band at 464 cm^{-1}), containing also a minor percentage of aluminosilicates. In samples from TE-1, TE-2 and TE-3 areas, rutile (TiO_2) was also identified, showing bands at 443 and 609 cm^{-1}, together with additional bands at 1001 and 1031 cm^{-1} (see Figure 2). These two last bands can be related to polystyrene. TiO_2 and polystyrene can be considered additives in the mixture of some types of concretes. Usually, lightweight concrete includes both additives in its composition, as well as sodium and methyl silicate, calcium oxide and other minor components [15].

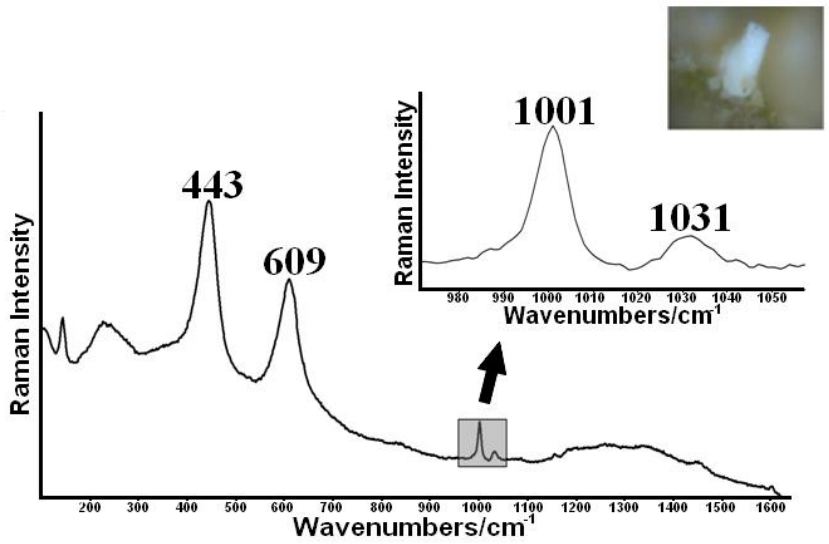

Figure 2. Raman spectrum of the lightweight concrete of terrace structure showing bands of rutile (TiO_2) and polystyrene.

As shown in Figure 3A, in most of the samples from TE-1, TE-2 and TE-3 areas, a band at 992 cm_1 was also identified. This band belongs to thenardite (Na_2SO_4). Besides this band, other bands at 1008 cm^{-1} and 1085 cm^{-1} were also identified, which can be related to $CaSO_4 \cdot 2H_2O$ and $CaCO_3$, respectively.

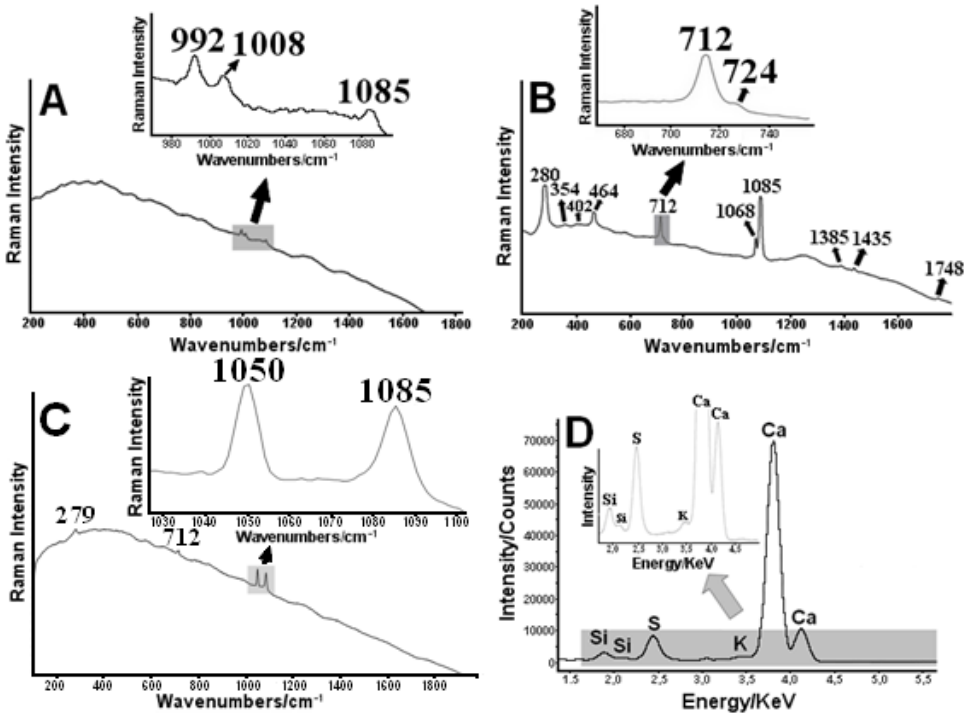

Figure 3. (A) Raman spectrum showing the presence of thenardite (Na_2SO_4, main band at 992 cm^{-1}), gypsum ($CaSO_4 \cdot 2H_2O$, main band at 1008 cm^{-1}) and calcite ($CaCO_3$, main band at 1085 cm^{-1}). (B) Raman spectrum showing the presence of nitratine ($NaNO_3$, main band at 1068 cm^{-1}). (C) Raman spectrum showing the presence of calcite (1085, 712 and 279 cm^{-1} bands) and a band at 1050 cm^{-1} belonging to the main band of niter (KNO_3, band width 1042–1058 cm^{-1}) and not to nitrocalcite ($Ca(NO_3) \cdot 4H_2O$, band width 1028–1072 cm^{-1}). (D) XRF spectrum showing the presence of calcium, potassium, silicon and sulphur as major elements in the terrace samples.

In all Raman spectra from the terrace areas, an additional band at 1068 cm^{-1} was also identified (see Figure 3B). This band can be related to nitratine ($NaNO_3$). Besides its main band at 1068 cm^{-1}, some of its secondary bands (724 cm^{-1} and 1385 cm^{-1}) were also identified (see Figure 3B). Sometimes, the band at 1068 cm^{-1} appeared together with the main band of $CaCO_3$ at 1085 cm^{-1}. Moreover, in most of the samples, secondary bands of $CaCO_3$ at 280, 712, 1435 and 1748 cm^{-1} were also observable as it is shown in Figure 3B. Additionally, in most spectra of the TE, typical Raman bands at 464, 402 and 354 cm^{-1} related to SiO_2 were also identified.

As mentioned above, there are numerous additives for concrete, Na_2O included among them. This oxide is difficult to detect by Raman spectroscopy due to its low Raman scattering. During the cement hardening, Na_2O is hydrated by the effect of water in the cement setting,

giving as a result the formation of sodium hydroxide (NaOH). NaOH can be easily transformed by atmospheric CO_2 into sodium carbonate (anhydrous or with hydration waters). If the concrete setting is complete, sodium carbonate should be the unique sodium compound of the porous matrix. However, this sodium carbonate can be attacked by atmospheric NO_x and/or infiltration waters carrying nitrate salts, giving as a result the formation of $NaNO_3$.

Apart from the main band of $NaNO_3$, a band at 1050 cm^{-1} belonging to a nitrate compound was detected in most of the samples (see Figure 3C). If we only look at the Raman band position (wavenumber at the maximum), this band can be assigned to niter (KNO_3) or to $Ca(NO_3)_2 \cdot 4H_2O$ if we take into account only the wavenumber at the maximum intensity of the band [5]. Figure 3C shows a detail of the nitrate (1050 cm^{-1}) and $CaCO_3$ (1085 cm^{-1}) bands present in one of the analyzed sample; both bands have nearly the same intensity ($I_{1050}/I_{1085} \approx 1$), but they show different band widths (18 cm^{-1} for $CaCO_3$ and 16 cm^{-1} for the nitrate compound respectively). In an early work on these kinds of building materials [16], we showed the band width of the main bands of $Ca(NO_3)_2 \cdot 4H_2O$ (1050 cm^{-1}) and $CaCO_3$ (1085 cm^{-1}), appearing in the same Raman spectrum with the same relative proportion ($I_{1050}/I_{1085} \approx 1$) than that observed in Figure 3C, which shown 44 and 18 cm^{-1} band width, respectively. Thus, the main band of nitrate in Figure 3C, having a band width of 16 cm^{-1}, must belong to KNO_3 and not to $Ca(NO_3)_2 \cdot 4H_2O$.

In order to verify the presence of potassium, an exhaustive point-by-point analysis of the samples was carried out by means of μ-XRF. As it can be observed in Figure 3D, the XRF analysis shows the presence of potassium, supporting the presence of KNO_3. However, the presence of minor quantities of $Ca(NO_3)_2 \cdot 4H_2O$ cannot be ruled out.

The identification of the soluble nitrate compounds, $NaNO_3$ and KNO_3 (and maybe $Ca(NO_3)_2 \cdot 4H_2O$), on the terrace could suggest a possible infiltration of nitrates through the cement cracks to the inner parts of the lighthouse. However, the great diversity of nitrate salts requires the identification of the source (or sources) of nitrate and its molecular form. The impact of atmospheric NO_x, in this case, can be ruled out as the main source for nitrate formation, because the lighthouse is located quite far from possible NO_x pollutant emission areas (industry, road traffic, etc.). Taking into account the location of the lighthouse on the coast, in front of a marine environment, the decomposition of organic matter coming from massive seagull droppings could be a possible source of nitrate. Concretely, there is a colony of those marine birds on the cliff, just below the lighthouse (see Figure 4A).

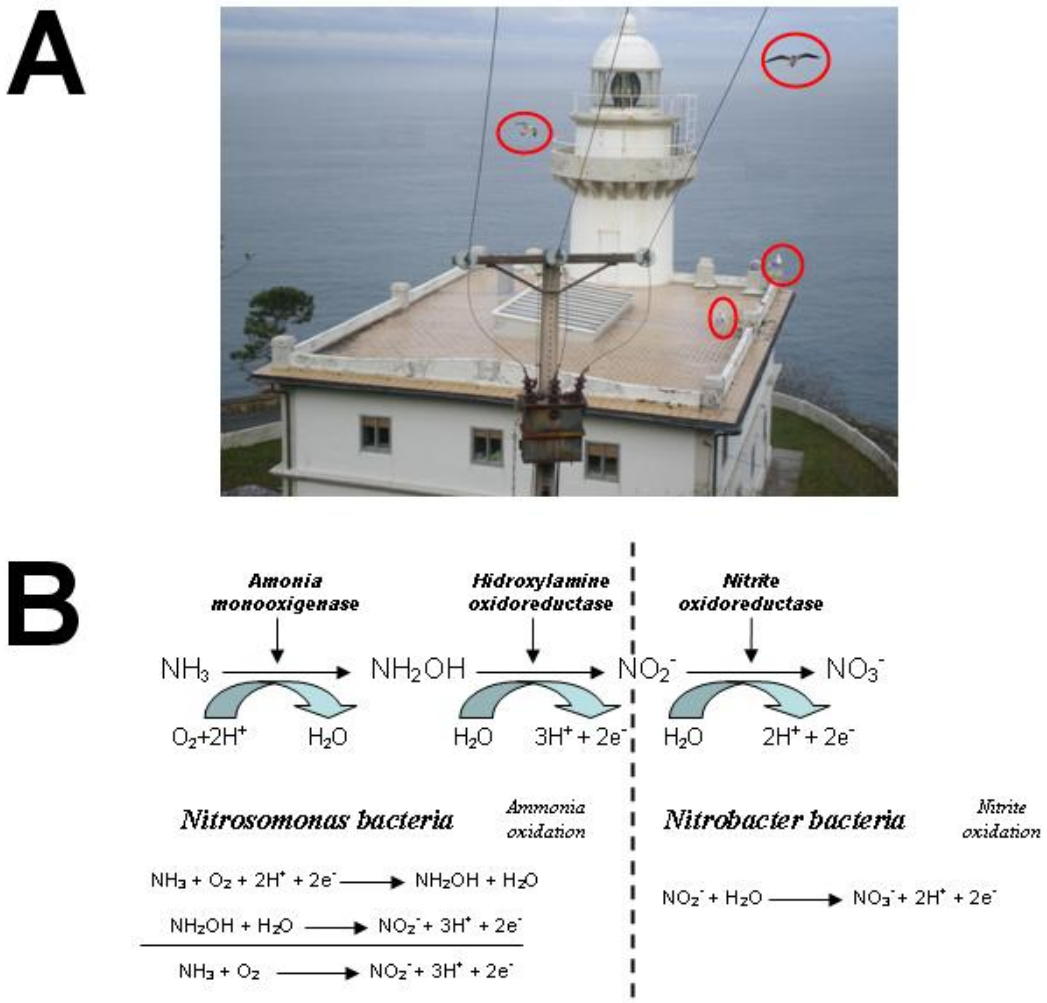

Figure 4. (A) A view of Igueldo lighthouse showing some seagulls over the terrace. (B) Reaction pathway explaining the nitrate formation (nitrification process produced by different bacteria) from ammonia.

Humans and animals excrete sodium chloride, which serves as nutrient for microorganisms such as bacteria which colonise the droppings, leading to the decomposition of the organic matter and to the subsequent nitrate formation. Nitrifying bacteria are responsible for this decomposition processes and usually live in marine environment and even in freshwater and/or wastewater [17,18]. Figure 4B shows the reaction pathway that takes place during the nitrification process performed in two steps carried out by Nitrosomonas and Nitrobacter bacteria, respectively, [19–23]; some authors point out that the optimum pH for the last step with Nitrobacter is 7.9 [24], the one we have in our exposed materials when rainwater comes in contact with the carbonate materials. Thus, the dropping of the seagulls could be one of the main sources of nitrogen to promote the final nitrate salts.

Considering this observation, droppings of seagulls were collected next to the terrace where cement samples were obtained. The analysis of these droppings performed with the two

Raman spectrometers considered in this work showed the presence of uric acid [25] as can be observed in Figure 5.

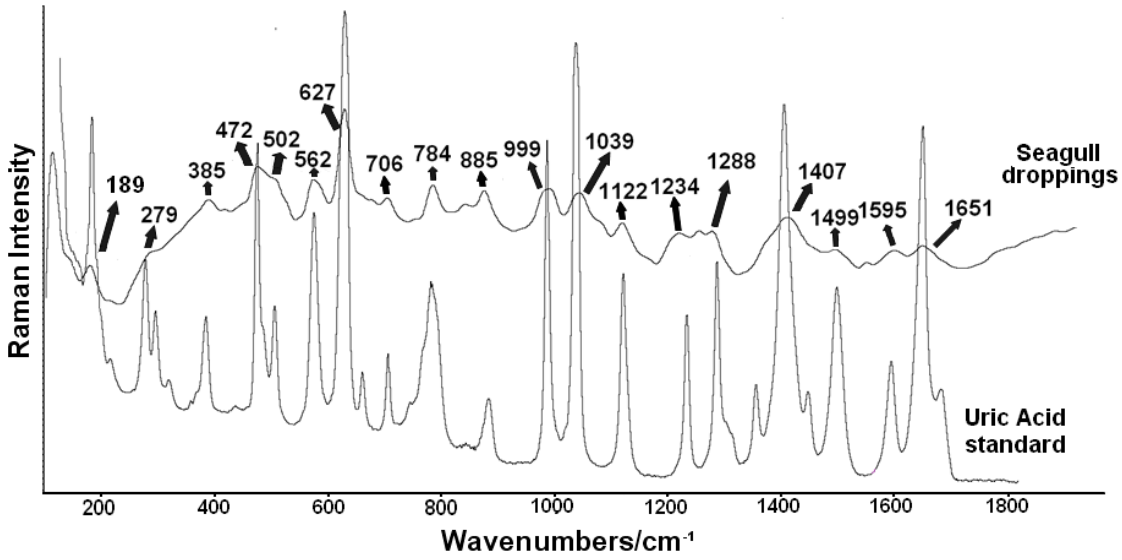

Figure 5. Raman spectrum of a seagull dropping sample, taken on to the terrace of the Igueldo lighthouse, superimposed to the Raman spectrum of a uric acid standard.

Uric acid could be the precursor of the nitrogen necessary to trigger all the explained reactions (see Figure 4B) assisted by the mentioned bacteria, giving as a result the formation of NH_4NO_3 in the terrace of the lighthouse. The NH_4NO_3 can react with the carbonate compounds (the acid ammonium and the base carbonate are non compatible acid–base species and hence they react) present in the original composition of the cementitious materials, giving as a result the crystallization of their respective nitrate salts, when the water evaporates (see Reactions 1 and 2). During this reaction, carbonate compounds are also transformed into bicarbonates (HCO_3^-) (see Reactions 1 and 2) and ammonia (NH_3) is formed.

$$Na_2CO_3\,(s) + 2\,NH_4NO_3\,(dis) \leftrightarrows 2\,NaNO_3\,(s) + HCO_3^- + NH_3\,(g) + NH_4^+ \quad \textbf{(1)}$$

$$K_2CO_3\,(s) + 2\,NH_4NO_3\,(dis) \leftrightarrows 2\,KNO_3\,(s) + HCO_3^- + NH_3\,(g) + NH_4^+ \quad \textbf{(2)}$$

The presence of $NaNO_3$ in the analyzed materials can have another source. In a marine environment, marine-originated "genuine" sea salt particles such as NaCl can be found [26]. However, "reacted sea-salt" particles such as $NaNO_3$ can also be found [27], promoted by the reaction of NaCl with atmospheric NO_x (mainly N_2O_5)[28] gaseous pollutants.

3.2. Quantification of soluble salts and correlation analysis

Figure 6A and 6B shows the box and whisker diagrams of total concentrations of quantified anions and cations from the nine samples of the TE and nine samples of the TF (B). Additionally, Tables 1 and 2 summarize the concentrations of all ions in mg·kg $^{-1}$ (ppm) units for the 18 samples.

Table 1. Anions concentrations (mg anion·kg^{-1} sample) of terrace structure and terrace floor samples.

Samples	F^-	Cl^-	NO_3^-	SO_4^{2-}	HCO_3^-
TE-1-1	< D.L	107 ± 29	306 ± 65	635±14	10161 ± 471
TE-1-2	< D.L	117 ± 29	299 ± 66	637 ± 15	10145 ± 462
TE-1-3	< D.L	123 ± 29	313 ± 66	646 ± 15	10102 ± 459
TE-2-1	< D.L	122 ± 29	317 ± 64	764 ± 15	8129 ± 423
TE-2-2	< D.L	115 ± 29	316 ± 66	759 ± 15	8168 ± 424
TE-2-3	< D.L	124 ± 29	340 ± 66	766 ± 15	8142 ± 421
TE-3-1	< D.L	176 ± 29	345 ± 65	569 ± 14	8663 ± 433
TE-3-2	< D.L	165 ± 29	306 ± 66	551 ± 14	8732 ± 432
TE-3-3	< D.L	174 ± 29	288 ± 65	582 ± 14	8714 ± 431
TF-1-1	< D.L	97 ± 28	277 ± 62	185 ± 12	6977 ± 422
TF-1-2	< D.L	90 ± 29	289 ± 65	192 ± 12	6969 ± 420
TF-1-3	< D.L	95 ± 28	272 ± 65	185 ± 12	6955 ± 421
TF-2-1	< D.L	81 ± 29	292 ± 66	194 ± 12	7512 ± 446
TF-2-2	< D.L	79 ± 29	282 ± 65	189 ± 12	7525 ± 444
TF-2-3	< D.L	83 ± 29	289 ± 65	200 ± 12	7492 ± 449
TF-3-1	< D.L	90 ± 29	297 ± 65	82 ± 12	6956 ± 412
TF-3-2	< D.L	84 ± 29	289 ± 66	78 ± 12	6968 ± 416
TF-3-3	< D.L	95 ± 29	282 ± 65	85 ± 12	6948 ± 417

< D.L: under Detection Limit

Detection Limits: F^- (0.19 ppm), Cl^- (0.08 ppm), NO_3^- (0.17 ppm), SO_4^- (0.03 ppm)

Table 2. Cations concentrations (mg cation·kg^{-1} sample) of terrace structure and terrace floor samples.

Samples	Na^+	NH_4^+	K^+	Mg^{2+}	Ca^{2+}
TE-1-1	958 ± 39	23 ± 9	943 ± 60	173 ± 17	9112 ± 453
TE-1-2	948 ± 39	22 ± 9	933 ± 61	176 ± 17	9119 ± 455
TE-1-3	947 ± 39	22 ± 9	928 ± 60	174 ± 17	9114 ± 455
TE-2-1	887 ± 38	22 ± 9	872 ± 59	146 ± 17	7404 ± 442
TE-2-2	903 ± 39	23 ± 9	868 ± 60	146 ± 17	7419 ± 448
TE-2-3	917 ± 39	23 ± 9	875 ± 60	146 ± 17	7412 ± 448
TE-3-1	910 ± 38	22 ± 9	842 ± 60	132 ± 17	7847 ± 445
TE-3-2	912 ± 39	23 ± 9	855 ± 60	127 ± 17	7837 ± 449
TE-3-3	913 ± 38	23 ± 9	858 ± 33	129 ± 23	7835 ± 424
TF-1-1	166 ± 35	21 ± 9	149 ± 55	104 ± 16	7096 ± 422
TF-1-2	171 ± 38	22 ± 9	157 ± 59	105 ± 17	7083 ± 447
TF-1-3	162 ± 37	22 ± 9	154 ± 58	105 ± 16	7065 ± 437
TF-2-1	298 ± 38	22 ± 9	157 ± 59	166 ± 17	7436 ± 449
TF-2-2	284 ± 37	22 ± 9	161 ± 58	164 ± 17	7445 ± 445
TF-2-3	282 ± 38	22 ± 9	157 ± 59	165 ± 17	7439 ± 447
TF-3-1	110 ± 37	22 ± 9	156 ± 58	107 ± 17	7029 ± 444
TF-3-2	105 ± 37	23 ± 9	157 ± 59	109 ± 17	7026 ± 447
TF-3-3	102 ± 38	22 ± 9	156 ± 58	107 ± 16	7023 ± 441

Detection Limits: Na^+ (0.09 ppm), NH_4^+ (0.02 ppm), K^+ (0.15 ppm), Mg^{2+} (0.04), Ca^{2+} (1.19 ppm)

In each box and whisker diagram, values for calcium are not included, because their order of magnitude is much higher than the values for the rest of ions (7837 mg·kg^{-1} median value and 8122 mg·kg^{-1} average value for TE samples, and 7083 mg·kg^{-1} median value and 7182 mg·kg^{-1} average value for TF samples). Additionally, values of concentrations for HCO_3^- of the TE and TF samples are not included in these diagrams. With the applied ion chromatographic method, it is not possible to obtain the concentration of HCO_3^- , because a mixture of CO_3^{2-} and HCO_3^- was used as eluent in the chromatographic system. Therefore, the values of HCO_3^- were obtained as the difference of cations sum and anions sum following the procedure shown elsewhere [4].

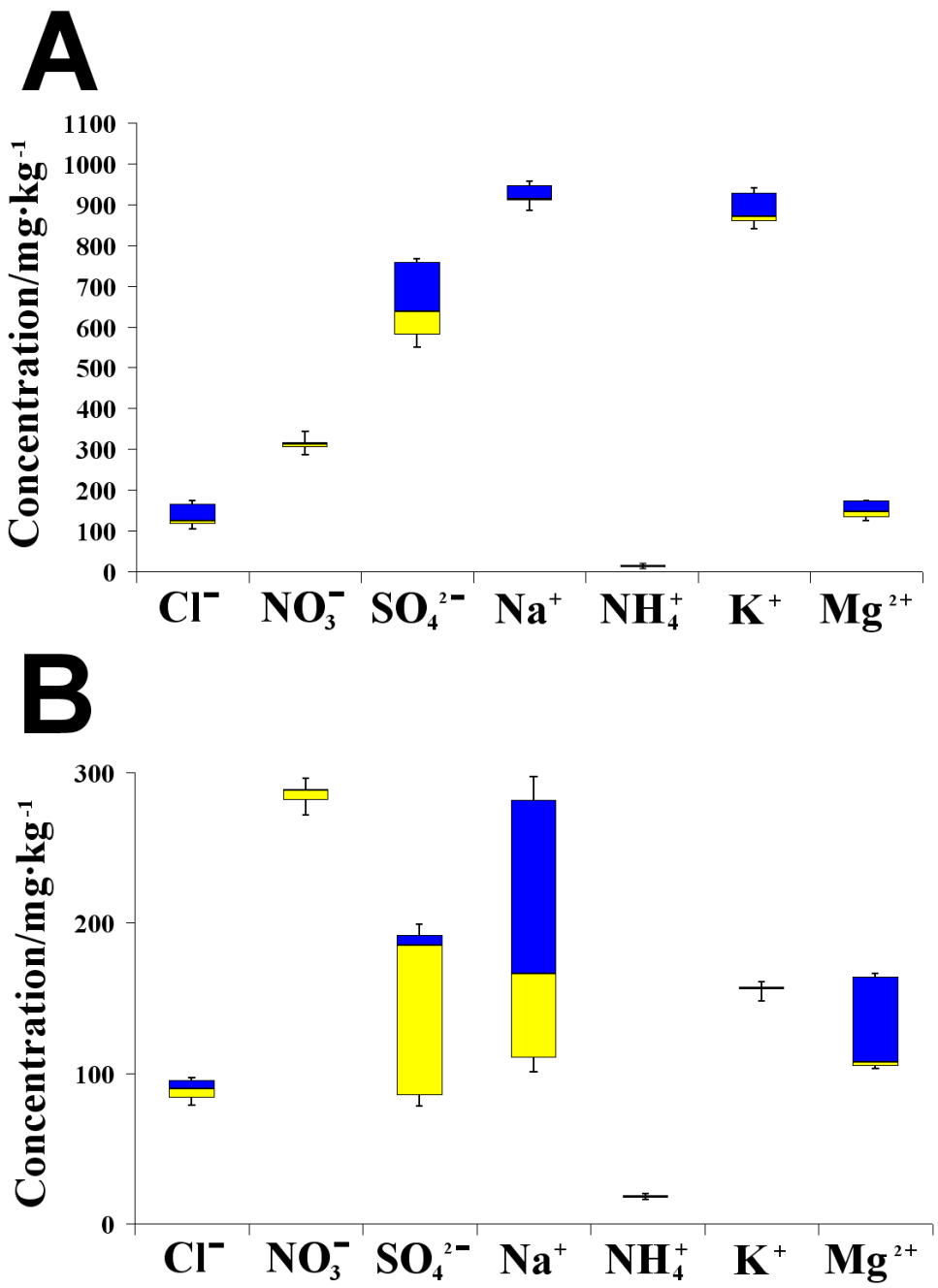

Figure 6. Box and whisker diagrams of soluble ions from the (A) terrace structure samples and (B) terrace floor samples.

Soluble salts analysis confirmed the presence of nitrate salts. The concentration of nitrates is higher in samples from the TE than in samples from the TF (see the median value in Figure 6A and B and each sample concentration value in Table 1 and Table 2). Additionally, one of the highest concentrations for anions belongs to chlorides (apart from sulfates, which most of them come from the original composition). These salts can be related with the influence of marine aerosol deposition (mainly NaCl). According to the cations, these data confirm the presence of potassium, also identified by means of XRF.

In order to observe possible links between different ions, correlation analysis was carried out using The Unscrambler 9.2® software. For this chemometric treatment, data were introduced in miliequivalents·kg^{-1} scale in order to balance the charges of each ion in the final calculation. Prior to that, it was assessed that the sum of cations fit with the sum of anions. The whole correlation matrix obtained can be observed in the Table 3.

Table 3. Correlation analysis matrix from terrace structure and floor samples of the lighthouse.

	Cl^-	NO_3^-	SO_4^{2-}	HCO_3^-	Na^+	NH_4^+	K^+	Mg^{2+}	Ca^{2+}
Cl^-	1.000								
NO_3^-	0.576	1.000							
SO_4^2	0.661	0.745	1.000						
HCO_3^-	0.531	0.482	0.766	1.000					
Na^+	0.752	0.725	0.967	0.865	1.000				
NH_4^+	0.159	0.262	0.279	0.265	0.318	1.000			
K^+	0.752	0.723	0.964	0.861	0.989	0.333	1.000		
Mg^{2+}	0.030	0.328	0.517	0.708	0.566	0.208	0.491	1.000	
Ca^{2+}	0.353	0.319	0.597	0.967	0.712	0.187	0.708	0.727	1.000

One of the highest correlations belongs to potassium and sodium (0.989). This highly positive correlation could suggest that both cations come from the same origin. Related to this, sodium and potassium also show high correlations with sulfate (0.967 and 0.964, respectively) and also with HCO_3^- (0.865 and 0.861, respectively). The correlations of both cations with HCO_3^- and sulfates could suggest that both elements were included as additives in the cementitious material mixture. In the concrete setting, sodium and potassium hydroxides (coming from their respective hydrated oxides) as additives react with CO_2 forming sodium and potassium carbonates, respectively. Neither of the carbonates was identified by Raman spectroscopy. In the presence of sulfates (from the mixture or the surrounding environment), carbonates can be transformed into their respective sulfates. In this case, sodium sulfate (as Na_2SO_4) was identified by means of Raman spectroscopy, but not potassium sulfate. This last sulfate is highly soluble. Considering that analyzed samples are exposed to the rainwater, it could be quite difficult to identify potassium sulfate crystallizations by means of Raman spectroscopy.

Additionally, sodium and potassium are also correlated with chloride (0.752 for both cations). The salts (NaCl and KCl) can be present in the samples due to the influence of marine aerosol. The mentioned cations (sodium and potassium) are also slightly correlated with nitrate (0.725 and 0.723, respectively). This correlation trend reinforces the

identification of $NaNO_3$ by means of Raman spectroscopy as well as the presence of KNO_3. Nevertheless, the absence of correlation (see Table 3) between calcium and nitrate could highly support that the main nitrate salt crystallized in the analyzed cementitious materials is KNO_3, instead of $Ca(NO_3)_2 \cdot 4H_2O$.

Finally, the correlation analysis also shows a link between soluble HCO_3^- and calcium (0.967), probably due to the acid attack on the original $CaCO_3$ present in the samples from the terrace. This $CaCO_3$ can react with the acid ammonium cation (NH_4^+), giving soluble Ca^{2+} and HCO_3^- ions, together with the gaseous NH_3 species, as final products:

$$CaCO_3\,(s) + NH_4^+ \leftrightarrows Ca^{2+} + HCO_3^- + NH_3\,(g) \quad \textbf{(3)}$$

Ammonium can originate from previously explained NH_4NO_3 formation or as a by-product of the $NaNO_3$ and KNO_3 formation (see Reactions 1 and 2). This observation could be reasonable if we take into account the low concentration values of ammonium quantified in the samples (see all the values in Table 1 and 2). These low values could be explained with the transformation of the initial NH_4^+ into NH_3 after the whole set of reactions (from Reaction 1 to 3).

4. Conclusions

The combination of two spectroscopic non-invasive techniques such as Raman spectroscopy and micro-XRF has been proved as a powerful strategy to characterize the mineralogical composition of cements and plasters containing efflorescence from the terrace of Igueldo lighthouse. The original composition of these cementitious materials belongs to a mixture of $CaCO_3$, silicates (mainly SiO_2 and additional aluminosilicates) and calcium sulfates with different number of hydration molecules ($CaSO_4 \cdot 2H_2O$ and $CaSO_4 \cdot ½\ H_2O$). This hydration difference between both calcium sulfate forms can be explained due to a dehydration process of the material. Moreover, the analyzed cementitious materials showed in their original composition additives such as titanium oxide. In some samples taken from the structure of the lighthouse terrace, titanium oxide and polystyrene were also identified. These additives are representative of lightweight cement, recently used in the cementitious material production, suggesting a possible restoration process executed in the past in this area of the lighthouse. Additionally, in some efflorescence, Na_2SO_4 and $NaNO_3$ were also identified. Both compounds are not included in the original formulation of these materials, thus they can be linked to deterioration of the original Na_2O additive incorporated to the original cement mixture. Raman evidence of the presence of KNO_3 was also obtained (potassium oxide was used originally as additive in the cementitious material), although the

presence of $Ca(NO_3)_2 \cdot 4H_2O$ cannot be discarded. The high variety of nitrates identified in these materials can suggest a massive infiltration of nitrate salts through their porous structure down to the internal parts of walls and rooms. One of the possible nitrate sources could be the decomposition of seagull droppings, which abound in the terrace of the lighthouse.

During this decomposition, NH_4NO_3 can be formed after the metabolism of Nitrifying bacteria. The obtained NH_4NO_3 could react (acid attack of ammonium) with different carbonates that can be present in the cementitious material (Na_2CO_3/$Na_2CO_3 \cdot 10H_2O$, K_2CO_3 and/or $CaCO_3$) giving as a result the formation of their respective nitrate salts ($NaNO_3$, KNO_3 and/or $Ca(NO_3)_2 \cdot 4H_2O$). The use of ion chromatography and its chemometric analysis allowed also confirming the presence of the sodium and potassium nitrate. Moreover, the concentration of some inorganic salts such as chlorides which are not detectable by Raman spectroscopy was also quantified. Their presence was logical if we take into account the influence of marine aerosol in these kinds of constructions. The correlation analysis carried out with the quantitative results also reinforced the observation of the Na_2SO_4 presence done by means of Raman spectroscopy. The possible sulfate source in those materials could be the dissolved calcium sulfate coming from their initial formulation (e.g. $CaSO_4 \cdot 2H_2O$, $CaSO_4 \cdot ½\ H_2O$, etc.). However, sulfates can also come from the surrounding marine aerosol. Moreover, correlation analysis also suggests the possible presence of potassium sulfate, sodium carbonate and potassium carbonate which could not be confirmed by Raman spectroscopy. Correlation analysis also suggests the presence of sodium and potassium chloride, which can come from marine aerosol depositions and subsequent recrystallization of them inside their porous matrix. As far as nitrate salts are concerned, the correlation analysis suggested the possible presence of $NaNO_3$ and KNO_3, excluding the presence of $Ca(NO_3)_2 \cdot 4H_2O$ due to the absence of correlation between the dissolved calcium and nitrate ions. Thanks to the use of Raman spectroscopy, assisted with other spectroscopic techniques such as micro-XRF and soluble salts quantification by means of ion chromatography, it was possible to identify different pathologies (nitrate salt formation as a consequence of possible infiltration coming from seagull droppings decomposition, marine aerosol influence, Na_2SO_4 efflorescence formation due to sulfate use in the mixture, etc.) affecting the cementitious materials located outside the Igueldo lighthouse.

5. References

[1] F. Veniale, M. Setti, S. Lodola, Diagnosing stone decay in built heritage. Facts and perspectives, Materiales de Construcción (2008) 58: 11-32.

[2] M. MacLeod, M. Scheringer, C. Gotz, K. Hungerbuhler, C. I. Davidson, T. M. Holsen, Handbook of Chemical Mass Transport in the Environment (2011) 135.

[3] P. Davini, Informatore del Marmista, Giorgio Zusi Editore, Verona, Italy (2005) 44: 16.

[4] M. Maguregui, A. Sarmiento, I. Martinez-Arkarazo, M. Angulo, K. Castro, G. Arana, N. Etxebarria, J. M. Madariaga, Analytical Diagnosis Methodology to Evaluate Nitrate Impact on Historical Building Materials, Analytical and Bioanalytical Chemistry (2008) 391: 1361-1370.

[5] A. Sarmiento, M. Maguregui, I. Martinez-Arkarazo, M. Angulo, K. Castro, M. A. Olazabal, L. A. Fernandez, M. D. Rodriguez-Laso, A. M. Mujika, J. Gomez, J. M. Madariaga, Raman Spectroscopy as a tool to diagnose the impacts of combustion and greenhouse acid gases on properties of Built Heritage, Journal of Raman Spectroscopy (2008) 39: 1042-1049.

[6] I. Martinez-Arkarazo, M. Angulo, L. Bartolome, N. Etxebarria, M. A. Olazabal, J. M. Madariaga, An Integrated Analytical Approach to Diagnose the Conservation State of Building Materials of a Palace House in the Metropolitan Bilbao (Basque Country, North of Spain), Analytica Chimica Acta (2007) 584: 350-359.

[7] L. K. Herrera, H. A. Videla, Surface analysis and materials characterization for the study of biodeterioration and weathering effects on cultural property, International Biodeterioration & Biodegradation (2009) 63: 813-822.

[8] M. Sawczak, A. Kaminska, G. Rabczuk, M. Ferretti, R. Jendrzejewski, G. Sliwinski, Complementary use of the Raman and XRF techniques for non-destructive analysis of historical paint layers, Applied Surface Science (2009) 255: 5542-5545.

[9] K. Castro, A. Sarmiento, I. Martinez-Arkarazo, J. M. Madariaga, L. A. Fernández, Green Copper pigment biodegradation in Cultural Heritage: From Malachite to Moolooite, thermodynamic modeling, X-ray fluorescence and Raman Evidence, Analytical Chemistry (2008) 80: 4103 – 4110.

[10] N. Prieto-Taboada, M. Maguregui, I. Martínez-Arkarazo, M. A. Olazabal, G. Arana, J. M. Madariaga, Spectroscopic evaluation of the environmental impact on black crusted modern

mortars in urban-industrial areas, Analytical & Bioanalytical Chemistry (2011) 399: 2949-2959.

[11] I. Rodriguez-Maribona, M. Zalbide, F. Garmilla, F. Garcia, J. A. Ibanez, S. Garin, Conservation study of the stone material used in the Culture House of Almirante Oquendo, in San Sebastian, Materiales de Construcción (1999) 49: 19-30.

[12] K. Castro, M. Pérez-Alonso, M. D. Rodríguez-Laso, J. M. Madariaga, Raman fibre optic approach to artwork dating, Spectrochimica Acta Part A (2004) 60: 2919-2924.

[13] M. Maguregui, N. Prieto-Taboada, J. Trebolazabala, N. Goienaga, N. Arrieta, J. Aramendia, L. Gomez-Nubla, A. Sarmiento, M. Olivares, J. A. Carrero, I. Martinez-Arkarazo, K. Castro, G. Arana, M. A. Olazabal, L. A. Fernandez, J. M. Madariaga, ChemCH 1st International Congress Chemistry for Cultural Heritage, Ravenna, 30th June–3rd July (2010).

[14] R. T. Downs, M. Wallace, A Database of Crystal Structures. Published in the American Mineralogist and The Canadian Mineralogist and Its Use as a Resource in the Classroom. 18th General Meeting of the International Mineralogical Association, 1–6 Sept (2002) Edinburgh, Scotland. Programme with Abstracts, page 128.

[15] Kokai Tokkyo Koho (1980) p. 5.

[16] N. Prieto-Taboada, O. Gómez-Laserna, I. Ibarrondo, I. Martinez- Arkarazo, M. A. Olazabal, J. M. Madariaga, Conference on Micro-Raman and Luminescence Studies in the Earth and Planetary Sciences (CORALS II), Madrid, 18th–20th May (2011).

[17] S. Safaeian, M. Amirsharifi, A. Esmaeili, L. Salimi, Effect of Metasystox-R on marine Nitrosomonas sp. as a nitrification inhibitor, Pakistan Journal of Biological Sciences (2008)11: 668-671.

[18] H. Dang, L. Jing, C. Rupery, L. Wang, L. Guo, Z. Zhang, M. G. Klotz, Diversity, abundance, and spatial distribution of sediment ammonia-oxidizing betaproteobacteria in response to environmental gradients and coastal eutrophication in Jiaozhou Bay, China, Applied Environmental Microbiology (2010) 76: 4691–4702.

[19] B. B. Colliver, T. Stephenson, Production of nitrogen oxide and dinitrogen oxide by autotrophic nitrifiers, Biotechnology Advances (2000) 18: 219-232.

[20] C. Fiencke, E. Spieck, E. Bock, Nitrifying Bacteria, Nitrogen Fixation in Agriculture, Forestry, Ecology, and the Environment (2005) 255-276.

[21] J. J. L. Cantera, L. Y. Stein, Interrelationship between nitrite reductase and ammonia-oxidizing metabolism in Nitrosomonas europaea, Archives of Microbiology (2007) 188: 349-354.

[22] T. Zhang, L. Ye, A. H. Y. Tong, M.-J. Shao, S. Lok, Ammonia-oxidizing archaea and ammonia-oxidizing bacteria in six full-scale wastewater treatment bioreactors, Applied Microbiology Biotechnology (2011) 91: 1215-1225.

[23] D. C. Rodriguez, O. Ramirez, G. Peñuela-Mesa, Behavior of nitifying and denitrifying bacteria in sequencing batch reactor for the removal of ammoniacal nitrogen and organic matter, Desalination (2011) 273: 447-452.

[24] C. Grunditz, G. Dalhammar, Development of nitrification inhibition assays using pure cultures of Nitrosomonas and Nitrobacter, Water Research (2001) 35: 433-440.

[25] V. R. Kodati, A. T. Tu, J. L. Turumin, Raman Spectroscopic identification of uric-acid-type kidney stone, Applied Spectroscopy (1990) 44: 1134-1136.

[26] A. Nadstazik, L. Falkowska, Selected ionic components of the marine aerosol over the Gulf of Gdańsk, Oceanologia (2001) 43: 23-37.

[27] I. Szalóki, C.-U. Ro, J. Osán, J. de Hoog, R. Van Grieken, X-Ray Spectrometry: Recent Technological Advances, (Eds: K. Tsuji, J. Injuk, R. Van Grieken), John Wiley & Sons, LTd, UK, (2004) pp. 569–592.

[28] D. I. Stewart, P. T. Griffiths, R. A. Cox, Reactive uptake coefficients for heterogeneous reaction of N2O5 with submicron aerosols of NaCl and natural sea salt, Atmospheric Chemistry & Physics (2004) 4: 1381-1388.

RESEARCH ARTICLE 2

Could marine aerosol contribute to deteriorate building materials from interior areas of lighthouses? An answer from the analytical chemistry point of view.

H. Morillas, M. Maguregui, O. Gómez-Laserna, J. Trebolazabala, J. M. Madariaga

Journal of Raman Spectroscopy (2013) 44: 1700–1710.

Could marine aerosol contribute to deteriorate building materials from interior areas of lighthouses? An answer from the analytical chemistry point of view

ABSTRACT

In this work, a multianalytical methodology based on a combination of spectroscopic techniques such as Raman spectroscopy and micro energy dispersive X-ray fluorescence spectroscopy, and soluble salt analysis by means of ion chromatography followed by a correlation analysis of these data was applied, in order to identify the nature of the deterioration compounds present in different building materials located on inner rooms from the ground floor of the Igueldo lighthouse (San Sebastian, Basque Country, North of Spain), and in order to prove if marine aerosol could contribute to cause deterioration processes in this kind of materials. The main deterioration compounds identified were sulfate and nitrate salts. Taking into consideration the positioning of some materials, a gypsum plaster covering them could be the sulfate source responsible of the crystallization process of a wide variety of sulfate salts. Nevertheless, in some areas were no gypsum plaster remains are present, ammonium sulfate crystallizations were identified. The presence of this kind of sulfate could suggest a possible sulfate input coming from the migration of ammonium sulfate (among other sulfate salts) carried on marine aerosol, which can be deposited on the facade of the lighthouse and migrate to its inner areas. The possible source of nitrates that could cause the crystallization of a wide variety of nitrate salts identified in this work could be the infiltration of ammonium nitrates coming from seagull droppings from outdoor to indoor areas.

Keywords: Lighthouses; marine aerosol; nitrates; sulfates; Raman spectroscopy

1. Introduction

Coastal environments are characterized by high levels of moisture and salts depositions coming from the so-called marine aerosol that is claimed by some professionals such as architects, restorers and so on, to be the principal source of deterioration of buildings located close to the sea. Such buildings can be also impacted by water infiltrations as well as by acid pollutants depositions (following either wet or dry processes). The main consequences of all these impacts can be the crystallization (e.g. sulfates, nitrates and chlorides) of alkaline and alkali-earth salts [1]. Since many years, lighthouses are considered important constructions from architectural, historical and cultural point of view. In the scientific literature, few references can be found about the characterization of original composition of the building materials from lighthouse, and even less regarding their deterioration processes [2]. In the literature, some works describe the negative influence of marine aerosol on building materials from constructions located near the coastal areas or next to the sea [3]. The marine aerosol, generated spontaneously is formed when the wind strikes over the surface of the ocean waves. Then, small bubbles discharge liquid particles in the air. These particles are impulsed at high speed and they are incorporated into the flowing air mass. They usually carry organic residue from the decomposition of algae, plankton and salts. The most abundant salt carried on marine aerosol is sodium chloride, but other salts such as sulfates and nitrates may also appear in notable quantities [4,5]. Besides, high load of other dissolved ions and suspended materials such as Ca^{2+}, K^{+}, Mg^{2+}, Fe^{3+}, Al^{3+}, Sr^{2+}, NH_4^{+}, HCO_3^{-} and Br^{-} can be deposited or can migrate to the surface of buildings located near the sea. Additionally, the 10% of marine aerosol is composed of organic matter [6,7] and occasionally, metals such as As, Ni, Cd, Pb, Ti, V, Cr, Mn, Cu, Mo, Rh and Hg as P.M 2.5 and P.M 10 airborne particulate matter can be transported by the marine aerosol [8]. These heavy metals as trace elements inside this naturally formed fog can come from combustion process originated because of maritime traffic, but also from industry and road traffic in coastal areas [9]. Therefore, buildings or constructions near the sea, or immersed in it, can experiment dry and wet depositions of different ionic species (salts). The wet deposition is the interaction of the suspended ionic species and pollutants incorporated in the rain, snow, fog or water vapour with the building material surface. On the contrary, in dry deposition, the acid aerosols and the airborne particulate matter depositions take place without the presence of the water. Particularly for buildings close to the sea, chloride and sulfate salts, which may affect the original composition of the buildings, cause different kinds of pathologies [10,11]. Due to the high load of chlorides and sulfates on marine aerosol, porous materials of lighthouses are supposed to be affected, mainly by sulfates and chloride salts deposition processes. On the one hand, the corrosive effect of

chlorides produce damages such as pitting on steel and iron structures and reaching through the concrete reinforcing bar, causing the breakdown of the passive oxide layer in the armour [12]. On the other hand, sulfate ions present in the marine aerosol are able to penetrate through the porous building materials, such as concrete, and react with it [13]. The direct consequence is the formation of sulfates of different nature, which could lead to losses in the consistency of the material together with other compounds present in the marine aerosol, like NaCl or $NaNO_3$. In addition, the most common soluble salts found in historical buildings often appear as efflorescences and subefflorescences. Among them, the most common ones are carbonates, sulfates, chlorides, nitrates with different numbers of crystallization waters. Examples of these crystallization processes can be calcite ($CaCO_3$) in patinas, gypsum ($CaSO_4 \cdot 2H_2O$), mirabilite ($Na_2SO_4 \cdot 10H_2O$), halite (NaCl), niter (KNO_3)[14]. The attack of soluble sulfate anions on cement mortar causes the formation of breakdown products like hydrated sulfates of calcium and aluminium, as ettringite [$Ca_6Al_2(SO_4)_3(OH)_{12} \cdot 26H_2O$], or of calcium-silicon, as thaumasite [$Ca_3Si(CO_3)(SO_4)(OH)_6 \cdot 12H_2O$][15]. For this reason, some works suggest to improve the permeability properties of concrete for buildings near the sea [16]. Permeability depends on the porosity of the cement paste that has been hydrated and aggregated. Thus, in the last years, cements resistant to the attack of chlorides and sulfates are being used in the construction of buildings located very close to the sea or immersed in it [17]. Taking into consideration the possible environmental stressors on specific building and the original components of the building materials included in it, it is possible to predict which kind of deterioration products are going to be formed in specific building materials, as a consequence of exposure to these stressors. This requires the chemical knowledge of the decaying processes as a function of the nature of original materials. In this work, a multianalytical methodology based on a combination of spectroscopic techniques such as Raman spectroscopy and micro energy dispersive X-ray fluorescence spectroscopy (μ-ED-XRF), and soluble salts analysis by means of ion chromatography followed by a correlation analysis of these data was applied in order to identify the nature of the deterioration compounds present in cement mortars, joint mortars of tiles, limestones and sandstones located on inner rooms from the ground floor of Igueldo lighthouse (San Sebastian, Basque Country, North of Spain); and in order to prove if marine aerosol could contribute to cause deterioration processes in this kind of materials. The lighthouse was built in 1855, it stands 134m above sea level, and it has two floors and a terrace. This multianalytical approach has shown its usefulness in such kind of diagnosis applied to explain the degradation of a mural painting due to water infiltrations containing ammonium nitrate [18]; to explain the degradation of bricks and mortars, affected by urban polluted atmospheres [19]; and to explain the degradation of a mural painting because of organic oxalic acid excreted by microorganisms [20], all of them are free from the influence

of marine aerosol. The chemical reactivity among original compounds used to erect the building and chemical species arriving at the surrounding of the lighthouse will be explained in terms of chemical models constructed following the methodology proposed elsewhere [21]. This type of chemical modelling has previously been used by the authors to explain the degradation of a mural painting due to water infiltrations containing ammonium nitrate [22] or the impact of NOx from ship engines dissolving the facades of a historical palace house due to the formation of soluble nitrate compounds [23].

2. Experimental

2.1. Sampling

Cement mortars, joint mortars of tiles and stones (limestone and carbonaceous stones) from Igueldo lighthouse (San Sebastian, Basque Country, North of Spain) were selected in order to study the original composition of these building materials from the lighthouse and their possible affections. All these samples were taken from indoor areas of the lighthouse ground floor. Concretely, samples of joint mortars, cement mortars and stones (carbonaceous sandstones and limestone) were taken from west areas of the lighthouse. In the North and East areas, joint mortars from tiles were collected. Joint mortars also present some efflorescences, which were sampled and included in the list of samples. Those cement mortars, joint mortars and stones that are almost detached and also efflorescences were collected using a scalpel. The rest of the samples were taken using a hammer and a chisel. The average size of the fragments never exceeded 2-3 cm (in some cases, the size of the sample was lower). Nine samples were analyzed: Joint Mortar-1, Sandstone-1, Sandstone-2, Sandstone-3, Limestone-1, Limestone-2, Cement mortar-1, Cement mortar-2 and Cement mortar-3.

2.2. Instrumentation

The analytical methodology applied can be divided in two steps. For the molecular analysis (original composition as well as determination of deterioration products), a Renishaw RA 100 portable Raman system (Renishaw, Gloucestershire, UK) coupled to a microprobe was used to collect the Raman spectra (785nm diode laser connected with a fibre-optics cable and a charge coupled device detector). The interpretation of all the Raman results was performed by comparing the acquired Raman spectra with Raman spectra of pure standard compounds collected in the e-VISNICH dispersive Raman database [24]. Additionally, free Raman databases (e.g. RRUFF[25]) were also considered for the assignation of Raman bands. For spectral treatment and analysis, Wire 2.0 (Renishaw) and GRAMS/32® (Galactic Industries) software were used. Once the compounds were identified, they were classified in

a first group as original compounds and in a second group compounds coming from the impact of marine aerosol, formed as a consequence of the impact of additional environmental stressors or caused as a consequence of the influence of specific compounds included in the original composition of the building materials. A given compound is said to be identified if it appeared at least five times in a different spectra.

The μ-ED-XRF ArtTax Röntec (currently Bruker, AXS, Berlin, Germany) was used to determine the elemental composition of cement mortar, joint mortars, sandstones and limestones. Spectra were acquired at the maximum working voltage/current of 50 keV/700 μA during 500 s. The instrument is composed of an X-ray tube with a Mo anode. The X-rays were collimated by a 0.65mm diameter tantalum collimator. The instrument has a special Xflash detector (5mm^2) and the measuring head of the instrument implements a charge-coupled device video camera that allows focusing on the sample (focussed are of 8 × 8mm^2) by a motorized XYZ positioning unit controlled by the computer. To determine elements with Z<11 (sodium), helium purging in the excitation and detection paths was used. The daily calibration of the instrument was made with a bronze reference standard (Bruker). Instrument control and data-handling were performed using the Windows-base ArtTax software 4.9.13.2 (Intax GmBH, Berlin, Germany).

Finally, the soluble salts analysis was carried out by ion chromatography with conductivity detection after post-column ion suppression. Prior to soluble salts quantification, an ultrasound-based extraction procedure was carried out for extraction of the soluble cations and anions. The experimental conditions used for the quantification of cations and anions are described elsewhere [26]. A Dionex ICS 2500 ion chromatography connected to a conductimetric detector (ED50 Dionex conductimetric detector) with post-column suppression (Dionex Corporation, Sunnyvale, California, USA) was used for the quantification of cations (K^+, Na^+, NH_4^+, Mg^{2+}, Ca^{2+}) and anions (F^-, Cl^-, NO_3^-, SO_4^{2-}).

3. Results and discussion

Raman spectroscopy and μ-ED-XRF analyses. To get an overview of the most relevant results obtained by Raman spectroscopy, Table 1 summarises the different compounds (original and deterioration compounds) detected in the different samples from building materials of indoor rooms from Igueldo lighthouse. In the case of walls oriented to the west, all the cement mortar samples analyzed showed a common mineralogical composition, which corresponded to a mixture of calcite ($CaCO_3$) and aragonite ($CaCO_3$) with minor proportions of quartz (α-SiO_2).

Table 1. Raman characteristic bands of the compounds (original and deterioration compounds) found in all the samples from Igueldo Lighthouse.

Molecular formula	Mineral name	Sample type	ν (cm^{-1})
$KAlSi_3O_8$	Adularia	Sandstone	282 m, 405 vw, 457 vw, 475 m, 512 vs
$CaCO_3$	Calcite	Sandstone, limestone, cement mortar and joint mortar	280 m , 712 m, 1085 vs, 1436 w
$CaSO_4{\cdot}2H_2O$	Gypsum	Limestone, cement mortar and joint mortar	413 m, 492 m, 619 m, 673 m, 1008 vs, 1132 m
$PbCO_3$	Cerussite	Cement mortar	674 vw , 837 vw , 1053 vs , 1207 m , 1240 m, 1331 s, 1480 w, 1660 w, 1861 m
$CaC_2O_4{\cdot}2H_2O$	Weddelite	Sandstone	504 m , 910 m, 1413 w, 1475 vs, 1626 w
$CaCO_3$	Aragonite	Sandstone, cement mortar and joint mortar	151 m, 205 m, 272 vw, 701 w , 1085 vs, 1102 m, 1201 vs, 1234 vs, 1303 vs, 1326 vs, 1520 w, 1617 w, 1762 w, 1857 m
SiO_2	Quartz	Sandstone and cement mortar	262 m, 355 m, 400 m, 464 vs, 694 w, 805 w, 1159 w
$Fe_2(SO_4)_3{\cdot}9H_2O$	(para)-coquimbite	Cement mortar	500 m, 600 w, 1025 vs, 1094 vw, 1176 vw, 1197 vw
K_2CO_3	Potash	Limestone	234 m , 680 w, 700 vw, 748 w, 1061 vs, 1145 vw, 1342 w, 1529 w
K_2SO_4	Arcanite	Limestone	455 m, 619 m, 988 vs, 1092 w, 1103 w, 1144 vw
$CaSO_4$	Anhidrite	Joint mortar	417 m, 500 m, 609 m, 627 m, 675 m, 1017 vs, 1112 w, 1130 m, 1160 w
$MgSO_4{\cdot}7H_2O$	Epsomite	Cement mortar and joint mortar	362 vw, 445 w, 462 w, 609 w, 985 vs, 1082 vw, 1145 vw
$Ba(NO_3)_2$	Nitrobarite	Cement mortar	200 w, 731 m, 1025 vw, 1046 vs, 1402 vw, 1631 vw,
$Na_2SO_4{\cdot}10H_2O$	Mirabilite	Cement mortar and joint mortar	450 w, 465 w, 621 m, 632 m, 647 m, 992 vs, 1101 m, 1132 m, 1152 m
$(NH_4)_2SO_4$	Mascagnite	Cement mortar	449 m, 614 w, 622 w, 974 vs, 1104 vw , 1417 vw
$CaSO_4{\cdot}½H_2O$	Bassanite	Cement mortar and joint mortar	429 m , 487 m , 627 m, 668 m, 1015 vs, 1128 m
TiO_2	Rutile	Joint mortar	449 vs, 609 vs
$NaNO_3$	Nitratine	Joint mortar	188 m, 414 vw, 518 vw, 533 vw, 722 s, 1067 vs, 1383 w, 1663 vw, 1775 vw
$MgSO_4{\cdot}6\ H_2O$	Hexahydrite	Cement mortar	249 w, 361 w, 442 w, 464 vw, 603 w, 982 vs, 1083 vw , 1148 vw
$MgSO_4{\cdot}4\ H_2O$	Starkeyite	Joint mortar	147 w, 232 w, 312 w, 462 m, 613 m, 1001 vs, 1084 vw, 1115 vw, 1155 vw, 1603 vw
KNO_3	Niter	Joint mortar	712 w, 1342 w, 1357 w, 1048 vs, 1777 vw

s: strong, m: medium, w: weak, vw: very weak; vs: very strong

In Figure 1A, a Raman spectrum representative of the original composition of cement mortars is shown (see details of the sampling area in Figure 1D). The presence of aragonite, together with the observation of small shells inside the porous matrix, can suggest a possible use of beach sand inside the global composition of the cementation mortar to construct the structure of the indoor walls of the lighthouse.

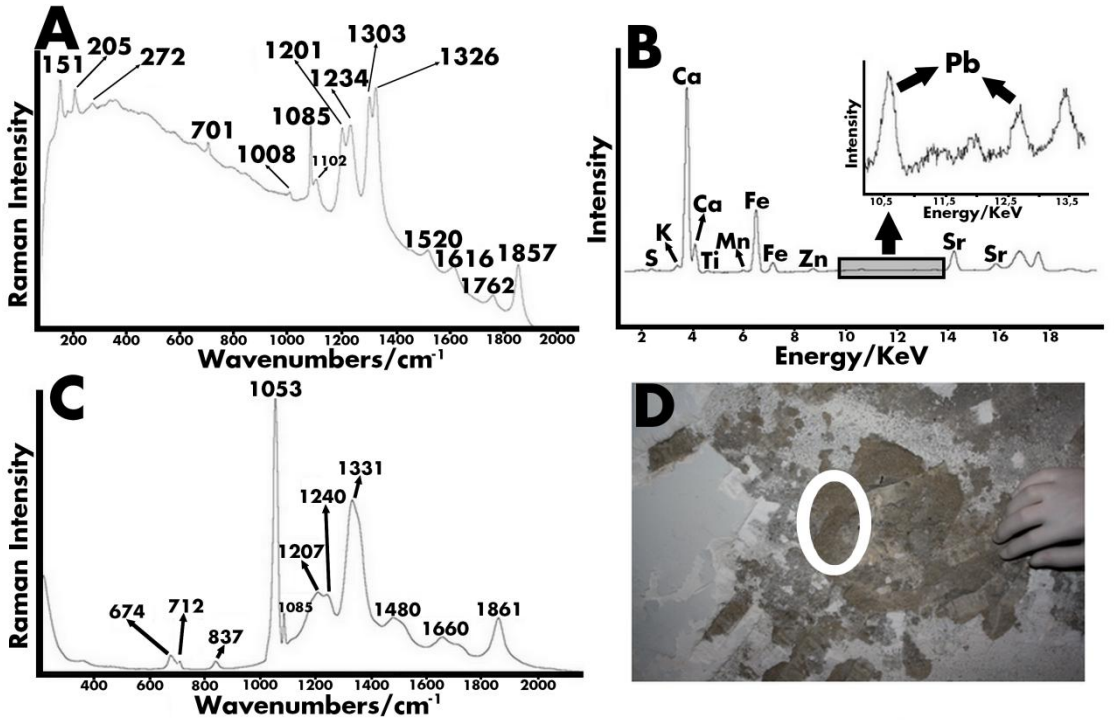

Figure 1. (A) Raman spectrum of cement mortar samples from west walls showing biogenic aragonite ($CaCO_3$, main Raman band at 1085 cm^{-1}) and gypsum ($CaSO_4 \cdot 2H_2O$, main Raman band at 1008 cm^{-1}); (B) μ-ED-XRF average spectrum acquired on different points from west walls cement mortar samples; (C) Raman spectrum of cerussite ($PbCO_3$) obtained on cement mortar samples from west walls; (D) general view of west walls where cement mortar samples were taken.

To define a specific component identified in the mortar as original, a historical knowledge of the additives used at the time of erecting the building (around 1865) is required. In those times, in the north of Spain, additives such as ferruginous sand (with SiO_2 and Fe_2O_3), but also fine grained Al_2O_3, TiO_2, BaO, Na_2O and K_2O white powders were added to get special properties to the mortars (mainly composed by CaO but also with small MgO and C quantities from the burning of grey calcite or dolomite of the nearby quarries) [27,28]. Additionally, the use of PbO in cement mortar as additive was very common [29]. It is necessary to understand the type of reactions that take place during the setting of cement mortar, to explain possible degradations that can be caused as a consequence of the influence of different factors. According to the additive type (mainly oxides) that are used in the setting, the corresponding carbonate can be formed, starting from the previous hydration process of the corresponding oxide, and its subsequent carbonation accelerated by the influence of atmospheric CO_2. For the CaO, K_2O, BaO and Na_2O additives, the reactions are the following:

$CaO\,(s) + H_2O \leftrightarrows Ca(OH)_2\,(s)$ **(1)**

$Ca(OH)_2\,(s) + CO_2\,(g) \leftrightarrows CaCO_3\,(s) + H_2O$ **(2)**

$K_2O\,(s) + H_2O \leftrightarrows KOH\,(s)$ **(3)**

$2\,KOH\,(s) + CO_2\,(g) \leftrightarrows K_2CO_3\,(s) + H_2O$ **(4)**

$BaO\,(s) + H_2O \leftrightarrows Ba(OH)_2\,(s)$ **(5)**

$Ba(OH)_2\,(s) + CO_2\,(g) \leftrightarrows BaCO_3\,(s) + H_2O$ **(6)**

$Na_2O\,(s) + H_2O \leftrightarrows 2NaOH\,(s)$ **(7)**

$2\,Na(OH)\,(s) + CO_2\,(g) \leftrightarrows Na_2CO_3 \cdot 10H_2O\,(s) + H_2O$ **(8)**

Apart from the molecular analysis, elemental analysis of cement mortar samples from the west wall was carried out by means of μ-ED-XRF. In all the samples, the elements identified were S, K, Ca, Ti, Mn, Fe, Zn, Sr and Pb (see Figure 1B). In different Raman measurements of cement mortar samples from west walls, the presence of a band at 1053 cm^{-1} was observed. This band can be associated with cerussite ($PbCO_3$) (see Figure 1C). Therefore, the identification of lead by means of μ-ED-XRF, and the presence of cerussite in the samples could suggest that in the original mixture of this cement mortar, lead oxide was included as an additive, which has been subsequently carbonated by the influence of CO_2.

As can be observed in Figure 1D, cement mortars from west walls were covered with a white plaster. This plaster appeared detached in some areas of the wall. The plaster was also analyzed using Raman spectroscopy, which allows identifying gypsum as its main component. In the cement mortar samples, gypsum ($CaSO_4 \cdot 2H_2O$) was systematically identified in many Raman measurements. This observation agrees with μ-ED-XRF results, because sulfur was identified in almost all the spots analyzed on cement mortar samples (see Figure 1B). Considering that the main component of the plaster covering cement mortars is gypsum, it can be said that the presence of this sulfate in cement mortar samples can be attributed to a migration of it from the plaster to the inner cement mortar. Dissolved sulfates from the plaster can react with the hydrated and carbonated calcium oxide from cement mortar to precipitate as gypsum. In some Raman measurements on cement mortar samples where gypsum plaster remains are not observable, a Raman band at 985 cm^{-1} together with the main band of gypsum was identified (see Figure 2A).

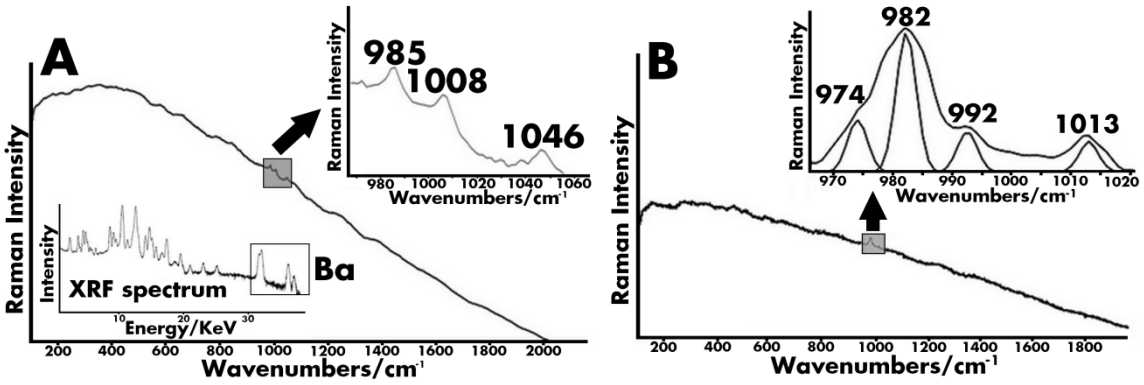

Figure 2. (A) On the top, 970–1060 cm^{-1} spectral range zoom showing the presence of epsomite ($MgSO_4 \bullet 7H_2O$, main band at 985 cm^{-1}), gypsum ($CaSO_4 \bullet 2H_2O$, main band at 1008 cm^{-1}) and nitrobarite [$Ba(NO_3)_2$], main band at 1046 cm^{-1}); and μ-ED-XRF spectrum of the same areas (bottom) from west wall cement mortar samples without gypsum plaster remains; (B) Raman spectrum acquired on cement mortar samples without gypsum plaster remains from west walls showing the presence of mascagnite [$(NH_4)_2SO_4$], main band at 974 cm^{-1}), hexahydrite ($MgSO_4 \bullet 6\ H_2O$, main band at 982 cm^{-1}), mirabilite ($Na_2SO_4 \bullet 10\ H_2O$, main band at 992 cm^{-1}) and bassanite ($CaSO_4 \bullet ½\ H_2O$, main band at 1013 cm^{-1}).

The band at 985 cm^{-1} can be assigned to epsomite ($MgSO_4 \cdot 7H_2O$). The formation of this type of magnesium sulfate and others with lower hydration waters ($MgSO_4 \cdot 6H_2O$, $MgSO_4 \cdot 5H_2O$, $MgSO_4 \cdot 4H_2O$, $MgSO_4$ etc.) is determined by the initial presence of MgO as an additive [27,28], which, during the setting of mortar, can be hydrated and the carbonated, to be transformed into $MgCO_3$. This magnesium carbonate, in the presence of a sulfate input, can be sulfated and transformed into magnesium sulfates; with different hydration/crystallization waters depending on the temperature and relative humidity present at the moment of the sulfation process [30].

Additionally, in some Raman measurements performed on the cement mortar samples from west wall, two Raman bands at 982 cm^{-1} and 1013 cm^{-1} were identified (see Figure 2B). The first band can be assigned to hexahydrite ($MgSO_4 \cdot 6H_2O$) and the second one to bassanite ($CaSO_4 \cdot ½H_2O$). Two shoulders near 982 cm^{-1} band can be observed in the Raman spectrum of Figure 2B. In order to separate these two shoulders, a curve-fitting procedure based on Laurentian and Gaussian algorithms was applied. Thanks to this deconvolution procedure, it was possible to extract both features centered on 992 and 974 cm^{-1}, respectively (see Figure 2B). These bands belong to the main bands of mirabilite ($Na_2SO_4 \cdot 10H_2O$) and mascagnite [$(NH_4)_2SO_4$], respectively. It is necessary to highlight the identification of ammonium sulfate crystallized in the cement mortar. Ammonium sulfate together with sea salts (e.g. chlorides) is a well-known component of the marine aerosol [31, 32]. The identification of this sulfate crystallized in the cement mortar could suggest a possible migration of ammonium sulfate from outdoors to indoors after a deposition process of the salt carried in the marine aerosol.

The deposited ammonium sulfate can penetrate, dissolve and migrate to suffer a recrystallization process in the inner parts of the wall.

In addition, Raman measurements performed on the cement mortar, an additional band at 1046 cm^{-1}, can be observed (see the band in Figure 2A). This band can be assigned to nitrobarite [$Ba(NO_3)_2$]. The measurements on this cement mortar samples by μ-ED-XRF indicate the presence of barium, in addition to other elements (see Figure 2A bottom), confirming the presence of barium nitrate. In previous works related to Igueldo lighthouse, it was demonstrated that the deposition of organic matter from marine birds have an important influence on the formation of nitrates [33]. These decomposition processes can be the main source of NH_4NO_3 infiltrations, which can migrate from outdoors through the inner walls of the lighthouse. Moreover, it is necessary to take into consideration that additives such as BaO, which are very common in the composition of mortars, have been probably used [34]. The aforementioned ammonium nitrate can react (see reaction 9) with the barium carbonate previously formed in the concrete setting (see reactions 5, 6).

$$BaCO_3\,(s) + 2\,NH_4NO_3\,(dis) \leftrightarrows Ba(NO_3)_2\,(s) + HCO_3^- + NH_3(g) + NH_4^+ \qquad \textbf{(9)}$$

In certain areas of the cement mortar of the west wall covered with a plaster, reddish-brown deposits were observed (see Figure 3A).

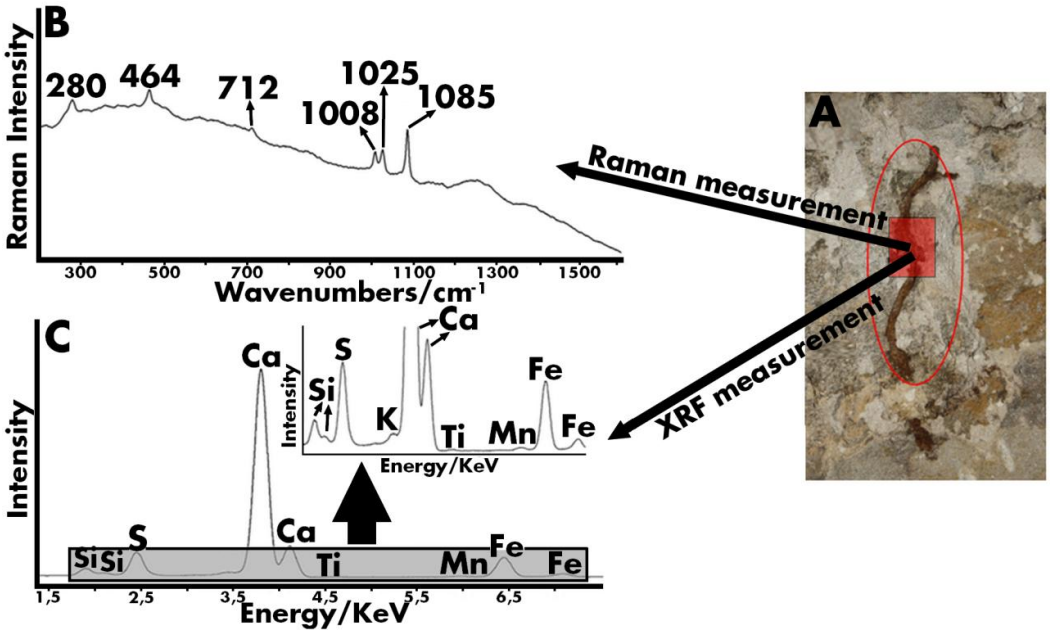

Figure 3. (A) General view of reddish-brown deposits on west walls; (B) Raman spectrum acquired on reddish brown deposits from west walls covered with plasters, showing the presence of calcite (CaCO3, main band at 1085 cm^{-1}), (para)coquimbite [$Fe(SO_4)_3 \bullet 9H_2O$] (main Raman band at 1025 cm^{1}), gypsum ($CaSO_4 \bullet 2H_2O$, main band at 1008 cm^{-1}) and quartz (SiO_2, main band at 464 cm^{-1}); (C) μ-ED-XRF spectrum showing the presence of Si, S, K, Ca, Ti, Mn and Fe on the reddish brown deposits from west walls.

Raman measurements performed on these deposits showed the main band of (para)coquimbite $Fe_2(SO_4)_3 \cdot 9\ H_2O$ at 1025 cm^{-1} . Near the inner west wall of the ground floor, the presences of the cracks were also identified. This observation indicates that the lighthouse has suffered physical stress. It is known that to remedy the presence of these cracks, some areas were underpinned with iron cramps. This practice is widely used to prevent the consequences of physical stress [35]. Salts carried by marine aerosol (mainly chlorides) can assist the iron cramps corrosion process acting as catalysts [36]. Chloride can react as catalyst in the oxidation process of iron cramps. This iron oxide from cramps can react with sulfates coming from the plaster or coming from outer filtrations. The presence of gypsum coming from the plaster in equilibrium with the dissolved sulfate ions coming from the plaster itself or from sulfates migration could ensure saturation conditions for a high sulfate source, which can react with the iron oxide to lead iron (III) sulfate nonahydrate (coquimbite or paracoquimbite), causing the fragmentation of the material. In all the Raman measurements from the reddish-brown deposit together with (para)coquimbite main band, the main Raman band of gypsum at 1008 cm^{-1} was also identified (see Figure 3B). This experimental observation could explain the proposed hypothesis to justify the formation of the iron (III) sulfate nonahydrate (gypsum, the source of sulfates). The same reactivity was previously identified on wall paintings including iron as iron (III) oxide red pigment (hematite) [37]. μ-ED-XRF measurements performed on these reddish-brown deposits showed the presence of calcium, iron and sulfur (see Figure 3C), indicating the probable presence of both sulfates (gypsum and iron (III) sulfate nonahydrate). In the limestone samples from the west walls of the lighthouse without gypsum plaster remains, calcite and gypsum was identified together with two additional Raman bands at 1061 and 988 cm^{-1}. These bands can be assigned to potash (K_2CO_3) and arcanite (K_2SO_4), respectively (see Figure 4).

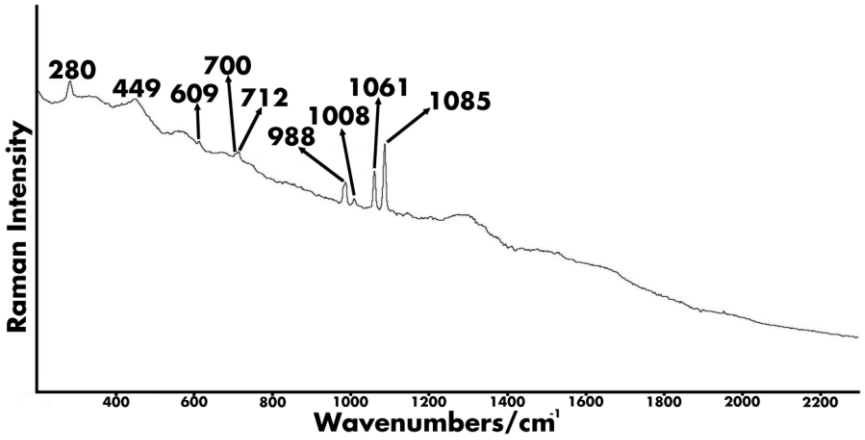

Figure 4. Raman spectrum acquired on limestone samples showing the presence of main bands of rutile (TiO_2, at 449 and 609 cm^{-1}), calcite ($CaCO_3$, at 1085, 712 and 280cm^{-1}), potash (K_2CO_3, at 1061 cm^{-1}), gypsum ($CaSO_4 \bullet 2H_2O$, at 1008 cm^{-1}) and arcanite (K_2SO_4, at 988 cm^{-1}).

The presence of potassium sulfate can be explained considering the reaction between dissolved sulfates from plaster over the limestone and potassium carbonate present in the limestone sample. In the bibliography, there are no references that explain the natural degradation of potash to arcanite in old buildings. As mentioned earlier, calcium and potassium carbonate can be considered as original components, considering the concrete setting (see reactions 1–4). Potassium carbonate is a highly soluble carbonate that can be dissolved and therefore react with solubilized sulfates in the limestone (see reactions 10–12), leaving only dissolved Ca^{2+} and HCO_3^- ions that migrate downstream or reprecipitate as $CaCO_3$ when water evaporates.

$$K_2CO_3\,(s) + H_2CO_3\,(dis) \leftrightarrows 2K^+ + 2HCO_3^- \quad \textbf{(10)}$$

$$CaSO_4 \cdot 2H_2O\,(s) \leftrightarrows CaSO_4\,(dis) \leftrightarrows Ca^{2+} + SO_4^{2-} \quad \textbf{(11)}$$

$$2K^+ + SO_4^{2-} \leftrightarrows K_2SO_4\,(s) \quad \textbf{(12)}$$

In the sandstone sample from the west walls of the lighthouse (see Figure 5A), adularia ($KAlSi_3O_8$) and quartz (α-SiO_2) were identified (see Figure 5B). The elemental analysis performed on samples from this area, confirmed the presence of potassium (see Figure 5C). This element can be related with the presence of potassium aluminium silicates, such as adularia (see Figure 5B). In the literature, there are some references that report the presence of aluminosilicates such as adularia, albite ($NaAlSi_3O_8$) and anorthite ($CaAl_2Si_2O_8$) in the sandstone used in Igueldo [38].

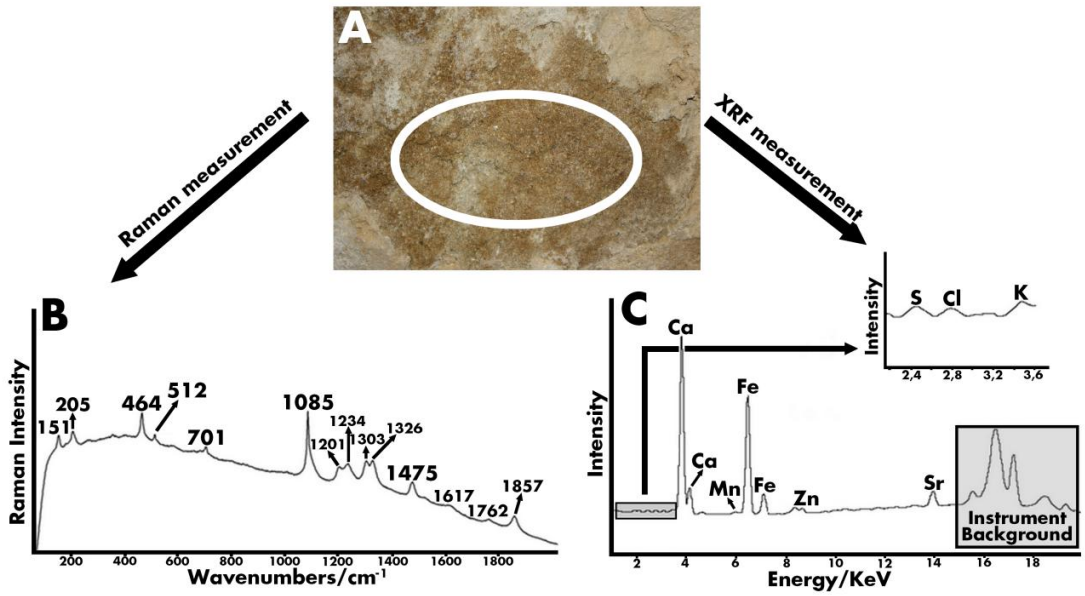

Figure 5. (A) General view of sandstone from west wall; (B) Raman spectrum from sandstone sample showing the presence of aragonite ($CaCO_3$, main band at 1085 cm^{-1}), quartz (SiO_2, main band at 464 cm^{-1}), adularia ($KAlSi_3O_8$, main band at 512 cm^{-1}) and weddellite ($CaC_2O_4 \cdot 2\,H_2O$, main band at 1475 cm^{-1}; (C) μ-ED-XRF average spectrum acquired on sandstone sample showing the presence of S, Cl, K, Ca, Mn, Fe, Zn and Sr in cement mortar samples.

In these samples, sulfate salts were not identified. Otherwise, in a high percentage of Raman measurements performed on the sandstone sample, weddellite ($CaC_2O_4{\cdot}2H_2O$) (main band at 1475 cm^1) was also identified (see Figure 5B). The presence of oxalates in this area may indicate a possible colonisation by different kind of microorganisms [39]. Several authors [40,41] discussed the possible formation of calcium oxalate resulting from the reaction of calcium carbonate with oxalic acid excreted by certain microorganisms. The North and East walls of the lighthouse are covered with tiles. In many areas, these tiles are cracked because of the influence of the cement mortar that joins the tiles to the wall (see Figure 6D1 and 6D2). Additionally, efflorescences emerge from the cement mortar, behind the tiles. In order to try to understand the deterioration process that is taking place in these walls, these efflorescence samples were analyzed. Raman analysis performed on these efflorescences showed the presence of calcite ($CaCO_3$) bands at 1085, 712 and 280 cm^{-1} and bands at 1152, 1132, 1101, 992, 647, 632, 621, 465 and 450 cm^{-1} assigned to mirabilite ($Na_2SO_4 \cdot 10H_2O$) (see Figure 6A). Thenardite and mirabilite crystallization on porous building materials, similar to cement mortars, is a common pathology cited by many authors [42,43]. The thenardite (Na_2SO_4), in normal conditions appears in environments with relative humidity lower than 75% and temperatures higher or equal to 32.4 °C [44]. At the moment of the sampling, the temperature was lower than 32.4 °C. Taking this into consideration, the main deterioration product detected can be assigned to mirabilite. The deterioration process that generate this kind of crystallized sulfate salts thorough the pores of the material leads to possible cracks and even breaks in the material due to the transition between mirabilite ($Na_2SO_4 \cdot 10H_2O$) and thenardite (Na_2SO_4). The differences on the numbers of hydration water during this transition promote increases and/or decreases in the volume of the crystallized sodium sulfates. Thus, in the case of Igueldo Lighthouse, the presence of these salts with constant change of volume can produce cracking phenomena and can lead to a breaking of the joint mortar of tiles from both mentioned areas [45] (see Figure 6D1).

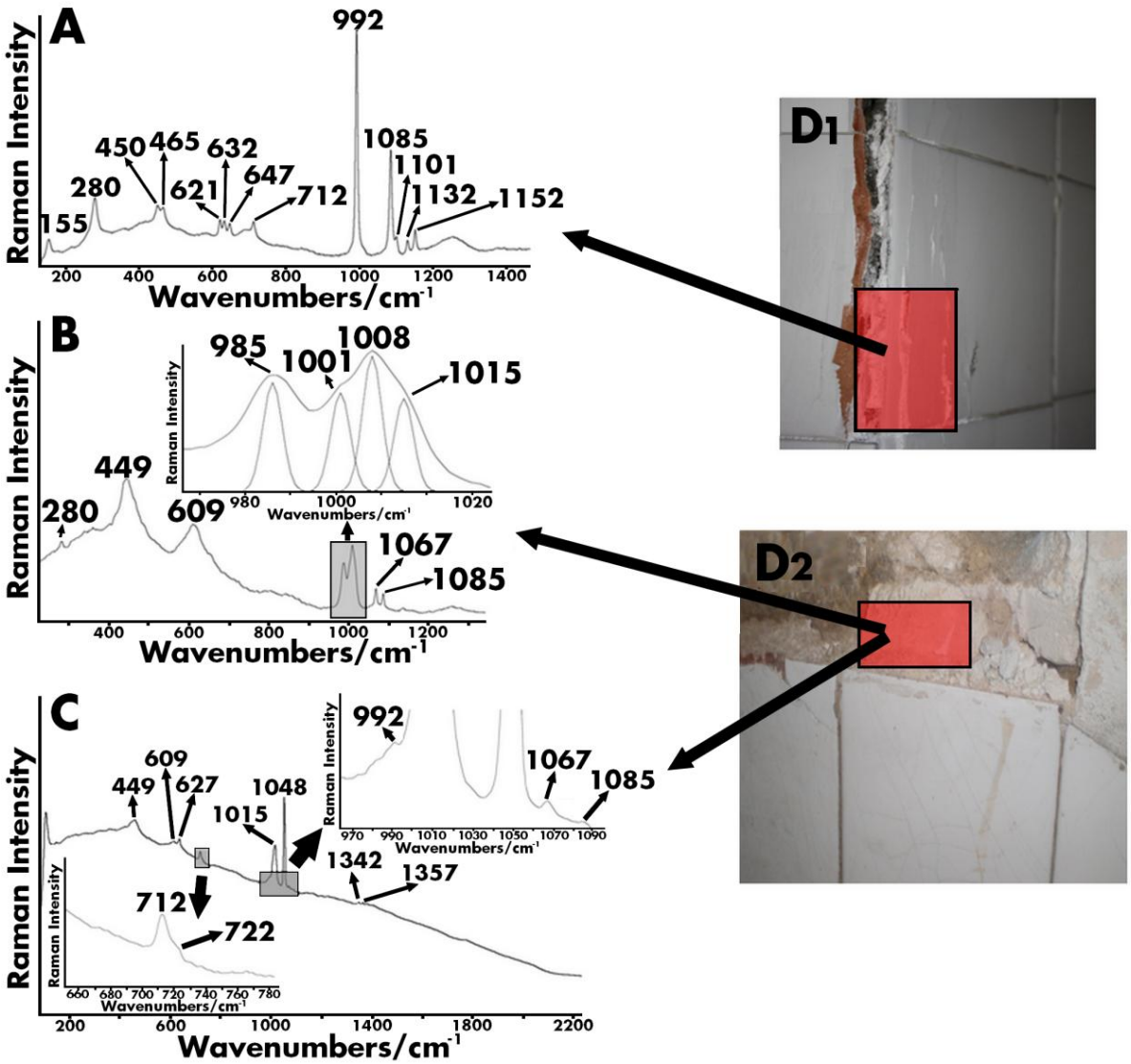

Figure 6. (A) Raman spectrum obtained from efflorescences behind the tiles and observable in D1 showing the presence of main bands of mirabilite ($Na_2SO_4 \cdot 10H_2O$) and calcite ($CaCO_3$); (B) Raman spectrum of cement mortars joining the cracked tiles showing the presence of rutile (TiO2 at 449 and 609 cm^{-1}), nitratine ($NaNO_3$, at 1067 cm^{-1}) and calcite ($CaCO_3$, at 1085 cm^{-1}). At the top of figure, Raman spectrum showing the presence of main bands of epsomite ($MgSO_4 \bullet 7H_2O$, at 985 cm^{-1}), starkeyite ($MgSO_4 \cdot 4H_2O$, at 1001 cm^{-1}), gypsum ($CaSO_4 \bullet 2H_2O$, at 1008 cm^{-1}) and bassanite ($CaSO_4 \cdot \frac{1}{2}H_2O$, at 1015 cm^{-1}); (C) Raman spectrum of cement mortars joining not altered tiles showing the presence also of main bands of rutile (449 and 609 cm^{-1}), bassanite (1015 cm^{-1}) and niter (1048 cm^{-1}). On top of Figure C, mirabilite at 992 cm^{-1}, nitratine at 1067 cm^{-1} and calcite at 1085 cm^{-1} can be observed. At the bottom of Figure C, bands at 712 and 722 cm^{-1} corresponding to the secondary bands of niter (KNO_3) and nitratine ($NaNO_3$), respectively, can be observed; (D1) General view of white powder (efflorescences) on the cracks of the tiles; (D2) General view of cement mortars joining the tiles.

The tiles lining the indoor areas were made in 1934. In those years, it was common to use cement clinker high in alkali, specifically mortars with NaOH. Thus, if NaOH is included in the composition, it is normal to identify natron (see also previous reactions 7, 8). Natron is a very soluble compound that can interact with sulfates resulting in the formation of mirabilite (see reactions 13–17).

$CaCO_3\,(s) + H_2CO_3\,(dis) \leftrightarrows Ca^{2+} + 2HCO_3^-$ **(13)**

$Na_2CO_3 \cdot 10H_2O\,(s) + H_2CO_3\,(dis) \leftrightarrows 2Na^+ + 2HCO_3^-$ **(14)**

$CaSO_4 \cdot 2H_2O\,(s) \leftrightarrows CaSO_4\,(dis) \leftrightarrows Ca^{2+} + SO_4^{2-}$ **(15)**

$2Na^{2+} + SO_4^{2-} \leftrightarrows Na_2SO_4\,(s)$ **(16)**

The calcite can precipitate again when the dissolved hydrogen carbonate from 14–15 reactions gets in contact with the dissolved Ca^{2+} from 16 (see reaction 17):

$Ca^{2+} + 2HCO_3^- \leftrightarrows CaCO_3\,(s) + H_2CO_3\,(dis)$ **(17)**

The source of sulfates in this casuistry can be internal or external. External sulfates can come from infiltrations carrying sulfates (e.g. marine aerosol). Internal sulfate sources can be sulfur-rich cement clinkers, contaminated aggregates, and so on. Cement mortar samples that join the tiles (joint mortars) to the wall were also analyzed. On the one hand, cement mortar samples that join the intact tiles without fractures were analyzed. On the other hand, cement mortar samples that join the fractured tiles with visible efflorescences were also analyzed. This sampling and subsequent characterization was performed in order to verify if sulfates are also crystallized on the original intact cement mortars which join the tiles. In the cement mortars where tiles are cracked, gypsum ($CaSO_4 \cdot 2H_2O$) was identified systematically in all the samples using Raman spectroscopy. Additionally, some spectra showed the presence of bands at 1015 and 1017 cm^{-1}. The first band can be assigned to bassanite ($CaSO_4 \cdot ½H_2O$) and the second one to anhydrite ($CaSO_4$). The presence of calcium sulfate with a lower number of hydration water may suggest a possible process of dehydration of gypsum present in the mortar. The main hypothesis to justify the presence of the three hydration forms of calcium sulfate could be a dissolution process of gypsum and a reprecipitation process into calcium sulfates with lower hydration water molecules as a function of available moisture. In additional Raman spectra, apart from gypsum, the presence of two shoulders near the main band of gypsum at 1008 cm^{-1} were also identified. In order to separate these shoulders in their respective individual bands, Gaussian and Laurentian algorithms based curve-fitting process was applied. With this deconvolution process, the presence of two bands centred at 1001 cm^{-1} and 1015 cm^{-1} were obtained (see top of Figure 6B). The band of 1001 cm^{-1} could be assigned to starkeyite ($MgSO_4 \cdot 4H_2O$) and the band at 1015 cm^{-1} corresponds to bassanite ($CaSO_4 \cdot ½H_2O$).

In the Raman spectra obtained from joint cement mortar samples where tiles do not show any crack and efflorescences, Raman bands at 449 cm^{-1} and 609 cm^{-1}, which can be assigned to rutile (TiO_2) were identified. The presence of rutile can be because of the use of this oxide as an additive [46]. Additionally, in the same sample, gypsum was also identified. Moreover

a band at 985 cm^{-1}, which can be assigned to epsomite ($MgSO_4 \cdot 7H_2O$) (see Figure 6B) was also identified. Therefore, it can be said that both cement mortars from not altered areas and cement mortars from areas with cracked tiles show sulfate salts crystallizations. Additionally, in cement samples from not altered areas, a Raman band at 1067 cm^{-1} that may be related to nitratine ($NaNO_3$) was also identified (see Figure 6B and 6C). The presence of this nitrate is very common, and it is caused by a nitration process of the sodium carbonate decahydrate (natron). Natron was used normally as an additive in construction for many years before the construction of the lighthouse Igueldo [47]. In some Raman spectra, apart from the band of nitratine, a band at 1048 cm^{-1} was also identified (see Figure 6C). Only having the main band at 1048 cm^{-1}, it is not possible to distinguish among niter (KNO_3) and nitrocalcite [$Ca(NO_3)_2 \cdot 4H_2O$]. However, medium/ weak bands at 712, 1342 and 1347 cm^{-1} (see Figure 6C bottom) are also present in the spectra confirming the presence of niter. The variety of nitrate salts crystallizations identified in the cement mortars joining the tiles suggest a possible migration of ammonium nitrate, which can easily react with sodium and potassium carbonates present in the cement mortars (see reactions 18 and 19). As was previously mentioned, ammonium nitrate can come from the decomposition of organic matter from seagull droppings present in the flat roof of the lighthouse [33].

$$Na_2CO_3 \cdot 10H_2O\,(s) + 2NH_4NO_3\,(dis) \leftrightarrows 2NaNO_3\,(s) + HCO_3^- + NH_3(g) + NH_4^+ + 10H_2O \quad \textbf{(18)}$$

$$K_2CO_3\,(s) + 2NH_4NO_3\,(dis) \leftrightarrows 2KNO_3\,(s) + HCO_3^- + NH_3(g) + NH_4^+ + 10H_2O \quad \textbf{(19)}$$

3.1.Quantification of dissolved anions and cations coming from soluble salts

In the Tables 2 and 3, the concentrations of solubilized anions and cations (gr ion·kg^{-1} sample) from all the building samples (joint mortars, sandstones, limestones and cement mortars) are respectively shown. The results are presented as an average of three replicate measurements.

Table 2. Concentrations of soluble anions (gr anion·kg^{-1} sample) of indoor rooms samples.

Samples	Cl^-	NO_3^-	SO_4^{2-}	HCO_3^-
Joint mortar-1	71.40 ± 8.30	14.30 ± 2.10	88.29 ± 0.14	198.00 ± 6.90
Sandstone-1	0.15 ± 0.08	< D.L	2.81 ± 0.27	11.23 ± 0.37
Sandstone-2	0.67 ± 0.07	0.27 ± 0.07	1.02 ± 0.08	4.60 ± 0.24
Sandstone-3	5.63 ± 0.10	3.99 ± 0.29	2.88 ± 0.87	5.40 ± 3.80
Limestone-1	0.39 ± 0.28	0.030 ± 0.001	0.54 ± 0.04	9.43 ± 0.81
Limestone-2	2.25 ± 0.24	1.61 ± 0.56	1.31 ± 0.56	8.47 ± 1.01
Cement mortar-1	7.20 ± 0.20	5.91 ± 0.02	12.34 ± 0.32	23.20 ± 2.20
Cement mortar -2	0.56 ± 0.03	0.031 ± 0.001	28.25 ± 0.14	63.00 ± 2.00
Cement mortar-3	0.48 ± 0.02	0.30 ± 0.02	53.80 ± 1.40	80.10 ± 4.60

< D.L: below Detection Limit

Table 3. Concentrations of soluble cations (gr cation·kg^{-1} sample) of indoor rooms samples.

Samples	Na^+	NH_4^+	K^+	Mg^{2+}	Ca^{2+}
Joint mortar-1	88.80 ± 0.24	< D.L	15.97 ± 1.97	61.44 ± 0.14	205.8 ± 1.6
Sandstone-1	2.57 ± 0.07	29.47 ± 0.13	2.03 ± 0.03	0.26 ± 0.01	9.31 ± 0.47
Sandstone-2	0.98 ± 0.21	30.13 ± 0.86	0.29 ± 0.11	0.72 ± 0.03	4.56 ± 0.06
Sandstone-3	3.18 ± 0.18	< D.L	0.56 ± 0.12	0.36 ± 0.02	13.80 ± 3.40
Limestone-1	0.26 ± 0.05	< D.L	0.76 ± 0.08	< D.L	9.37 ± 0.46
Limestone-2	1.41 ± 0.04	< D.L	0.42 ± 0.01	1.01 ± 0.07	10.80 ± 0.83
Cement mortar-1	1.65 ± 0.04	< D.L	0.37 ± 0.17	0.68 ± 0.14	45.90 ± 1.91
Cement mortar-2	2.05 ± 0.04	< D.L	0.62 ± 0.11	1.02 ± 0.14	88.15 ± 1.99
Cement mortar-3	1.11 ± 0.03	< D.L	0.90 ± 0.17	< D.L	132.6 ± 4.4

< D.L: below Detection Limit

In order to observe possible links between different ions, correlation analysis was carried out using The Unscrambler 9.2® software (Camo Process AS, Oslo, Norway). For this chemometric treatment, data were introduced in miliequivalents·kg^{-1} scale in order to balance the charges of each ion in the final calculation. Prior to that, it was assessed that the sum of cations fit with the sum of anions. The whole correlation matrix obtained can be observed in the Table 4.

Table 4. Correlation coefficients obtained from quantitative data of soluble salt analysis from building materials from indoor rooms of the lighthouse.

	Cl^-	NO_3^-	SO_4^{2-}	HCO_3^-	Na^+	NH_4^+	K^+	Mg^{2+}	Ca^{2+}
Cl^-	1.000								
NO_3^-	**0.937**	1.000							
SO_4^2	**0.804**	0.680	1.000						
HCO_3^-	**0.876**	0.752	**0.978**	1.000					
Na^+	**0.990**	**0.893**	**0.814**	**0.900**	1.000				
NH_4^+	-0.229	-0.332	-0.356	-0.329	-0.187	1.000			
K^+	**0.983**	**0.867**	**0.809**	**0.891**	**0.989**	-0.142	1.000		
Mg^{2+}	**0.989**	**0.890**	**0.814**	**0.901**	**0.999**	-0.189	**0.988**	1.000	
Ca^{2+}	0.764	0.663	**0.995**	**0.970**	0.780	-0.407	0.773	0.781	1.000

With the applied ion chromatographic method, it was not possible to obtain the concentration of HCO_3^-, because a mixture of CO_3^{2-} and HCO_3^- was used as eluent in the chromatographic system. Therefore, the values of HCO_3^- were obtained as the difference of cations sum and anions sum. For this subtraction, the quantitative data were transformed from mg·kg^{-1} into miliequivalents·kg^{-1}, in order to consider the charge of each cation and anion in the final subtraction. Details of the quantification of these anions are described elsewhere [18].

The most significant correlations between anions and cations take place between chlorides and sodium, potassium and magnesium (0.990, 0.983 and 0.989, respectively). These chlorides are usually present in the marine aerosol, but they are difficult to identify by Raman spectroscopy because of the low Raman scattering of chloride salts. Moreover, one of the highest correlations belongs to potassium and sodium (0.989). This highly positive correlation could suggest that both cations come from the same origin (marine aerosol). Other remarkable correlation takes place between sulfates with cations like sodium, potassium, calcium and magnesium (0.814, 0.809, 0.995 and 0.814, respectively). These correlations may be linked with the sulfation process caused by sulfates present in the original material surrounding material or coming from migrations from outside (e.g. marine aerosol).

Dissolved sulfates can react with the sodium, potassium, calcium and magnesium carbonates producing their respective sulfates. Correlation analysis agrees with Raman results, because sodium, potassium, calcium and magnesium sulfates were identified using this last spectroscopic technique. Apart from these observations, positive correlations were also observed between nitrates and sodium, potassium and magnesium (0.893, 0.867 and 0.890, respectively). Sodium nitrate and potassium nitrate were identified by Raman spectroscopy, but nitromagnesite was not identified. This compound has not been found in the analyzed samples, its presence cannot be rejected considering the high correlation between dissolved Mg^{2+} and NO_3^- ions. The low correlation between NO_3^- and HCO_3^- can be related with the formation of HCO_3^- as a consequence of CO_2 attack on the calcite mortars and subsequent reprecipitation of $CaCO_3$, that is, both anions have completely different routes of impact. Probably, this is also the reason for the low correlation between NO_3^- and Ca^{2+}. Finally, significant correlations were also observed between bicarbonates and sodium, potassium, calcium and magnesium (0.900, 0.891, 0.970 and 0.901, respectively). This observation could corroborate the presence of natron ($Na_2CO_3 \cdot 10H_2O$) and its respective product of nitrification; nitratine ($NaNO_3$). For potassium and calcium, the correlation analysis corroborates the presence of these carbonates as have been observed by Raman spectroscopy. Taking into account the correlation between bicarbonate and magnesium, it cannot be ruled out the presence of magnesium (bi)carbonate in the analyzed samples.

4. Conclusions

The multianalytical methodology based on non-invasive spectroscopic techniques such as Raman spectroscopy and μ-ED-XRF, together with soluble salts quantification by means of ion chromatography followed by data treatment (correlation analysis), allows to understand different pathologies that are affecting the building materials (cement mortars, joint mortars and stones) from inside rooms of Igueldo lighthouse ground floor. This methodology can be used as useful tool to predict the conservation state of the indoor areas of the lighthouse. In this work, portable analytical techniques (e.g. Raman and X-ray fluorescence spectrometers) were not considered. Nevertheless, a combination of field instrumentation [48, 49] with laboratory equipments can offer preliminary and sometimes concluding information about the conservation state of a specific construction or building. Moreover, portable spectrometers can be also used as screening tools to locate the most impacted areas, in order to perform a subsequent sampling to carry out and in depth characterization of the pathologies in the laboratory. In the building materials from Igueldo lighthouse, the most evident pathologies detected visually were cracks, material disintegration and so on, in areas covered with cement mortar. More evident is the cracking process of tiles from north and east inner areas. The formation of efflorescences appearing below the tiles and coming from the cement mortar joining them become tiles bent, causing their fracture. In all the analyzed samples, except sandstones, sulfate salts crystallizations were identified. In some areas of the inner rooms of the west wall of the lighthouse, the cement mortar is covered by a gypsum plaster, or remains of it can be observed. Solubilized sulfates coming from gypsum plaster can react with carbonates present in the building materials, causing sulfate salts crystallization on the surface (efflorescences) or inside the pores of the material (subefflorescences). In other areas from west wall not covered with gypsum plaster, sulfates were also identified in cement mortar. In this case mascagnite [$(NH_4)_2SO_4$], among other sulfates was identified in different Raman spectra. Ammonium sulfate is a typical sulfate salt that can be carried inside marine aerosol. Sulfates coming from marine aerosol can be deposited on the external façade of the lighthouse. These salts can migrate through the wall to inner parts following a dissolution-reprecipitation process. In this migration process, sulfates can also remain in solution on the wall and they can react with original carbonates present in the cement mortar, causing the formation of new sulfates (mirabilite, hexahydrite and calcium sulfates with different hydration waters). Additionally, chloride salts were also identified by means of soluble salt test and ion chromatography and its presence was corroborated using correlation analysis. Therefore, it is clear that sulfates and chlorides coming from marine aerosol are also impacting the inner areas of the lighthouse.

Apart from sulfates, nitrate salts (niter, nitratine and nitrobarite) were also identified on the inner walls of the lighthouse. Its presence can be attributed to the migration of the ammonium nitrate, formed through decomposed organic matter of seagull droppings present in the flat roof of the lighthouse [33]; the ammonium and nitrate ions can migrate to the inner areas of the lighthouse through crack in the roof and external walls, reaching the inner part of the wall and reacting with the carbonaceous material, giving rise to different kind of nitrate salts crystallizations. As a general conclusion, it can be said that migration of sulfates coming from marine aerosol and ammonium nitrate coming from seagull droppings are the main sources of salts affecting inner building materials of the lighthouse. Moreover, it is necessary to take into consideration the sulfate input coming from surrounding gypsum plaster to explain the formation of a wide variety of sulfate salts on building materials from internal rooms from Igueldo lighthouse.

5. References

[1] F. Oeztuerk, A. Zararsiz, V. A. Dutkiewicz, L. Husain, P. K. Hopke, G. Tuncel, Temporal variations and sources of Eastern Mediterranean aerosols based on a 9-year observation, Atmospheric Environment (2012) 61: 463-475.

[2] P. A. Warke, B. J. Smith, E. Lehane, Micro-environmental change as a trigger for granite decay in offshore Irish lighthouses: implications for the long-term preservation of operational historic buildings, Environmental Earth Sciences (2011) 63: 1415-1431.

[3] K. Torfs, R. Van Grieken, Chemical relations between atmospheric aerosols, deposition and stone decay layers on historic buildings at the mediterranean coast, Atmospheric Environment (1997) 31: 2179-2192.

[4] Y. Zhao, Y. Gao, Acidic species and chloride depletion in coarse aerosol particles in the US east coast, Science of the Total Environment (2008) 407: 541-547.

[5] S. S. Abdalmogith, R. M. Harrison, R. G. Derwent, Particulate sulphate and nitrate in southern England and Northern Ireland during 2002/3 and its formation in a photochemical trajectory model, Science of the Total Environment (2006) 368: 769-780.

[6] W. L. Chameides, A. W. Stelson, Aqueous-phase chemical processes in deliquescent sea-salt aerosols: A mechanism that couples the atmospheric cycles of S and sea salt, Journal of Geophysical Research (1992) 20: 565-580.

[7] H. Tervahattu, J. Juhanoja, V. Vaida, A. F. Tuck, J. V. Niemi, K. Kupiainen, M. Kulmala, H. Vehkamäki, Fatty acids on continental sulfate aerosol particles, Journal of Geophysical Research-Atmospheres (2005) 110: D06207.

[8] A. Arruti, I. Fernandez-Olmo, A. Irabien, Regional evaluation of particulate matter composition in an Atlantic coastal area (Cantabria region, northern Spain): Spatial variations in different urban and rural environments, Atmospheric Research (2011) 101: 280-293.

[9] E. T. Gomez, T. Sanfeliu, J. Rius, M. M. Jordan, Evolution, Sources and Distribution of Mineral Particles and Amorphous Phase of Atmospheric Aerosol in An Industrial and Mediterranean Coastal Area, Water Air & Soil Pollution (2005) 167: 311-330.

[10] K. Torfs, R. van Grieken, R. Zezza, N. García, F. Macri, The catedral of Bari: Italy, evaluation of environmental effects on stone decay phenomena, Studies in Conservation (1997) 42: 193-206.

[11] F. Zezza, F. Macri, Marine aerosol and stone decay, Science of the Total Environment (1995) 167: 123-143.

[12] V. Živica, Corrosion of reinforcement induced by environment containing chloride and carbon dioxide, Bulletin of Materials Science (2003) 26: 605-608.

[13] B. Mobasher, Simulation of Expansion in Blended Cement Based Materials Subjected to External Sulfate Attack, Transport Properties and Concrete Quality, Materials Science of Concrete, Eds. B. Mobasher, J. Skalny (2007) Special Volume: pp.157-171.

[14] A. Sarmiento, M. Maguregui, I. Martinez-Arkarazo, K. Castro, J. M. Madariaga, Raman spectroscopy as a tool to diagnose the impacts of combustion and greenhouse acid gases on properties of Built Heritage, Journal of Raman Spectroscopy (2008) 39: 1042-1049.

[15] V. Corinaldesi, G. Moriconi, F. Tittarelli, Thaumasite evidence for incorrect intervention in masonry restoration, Cement & Concrete Composites (2003) 25: 1157–1160.

[16] F. Li, Y. Chen, S. Long, J. Chen, Properties and microstructure of marine concrete with composite mineral admixture, Journal of Wuhan University of Technology-Materials Science (2009) 24: 497-501.

[17] K. Sotiriadis, E. Nikolopoulou, S. Tsivilis, Sulfate resistance of limestone cement concrete exposed to combined chloride and sulfate environment at low temperature, Cement & Concrete Composites (2012) 34: 903-910.

[18] M. Maguregui, A. Sarmiento, I. Martinez-Arkarazo, M. Angulo, K. Castro, G. Arana, N. Etxebarria, J. M. Madariaga, Analytical Diagnosis Methodology to Evaluate Nitrate Impact on Historical Building Materials, Analytical & Bioanalytical Chemistry (2008) 391: 1361-1370.

[19] M. Maguregui, A. Sarmiento, R. Escribano, I. Martinez-Arkarazo, K. Castro, J. M. Madariaga, Raman Spectroscopy after accelerated ageing tests to assess the origin of some decayed products found in real historical bricks affected by urban polluted atmospheres, Analytical & Bioanalytical Chemistry (2009) 395: 2119-2129.

[20] M. Maguregui, U. Knuutinen, J. Trebolazabala, H. Morillas, K. Castro, I. Martinez-Arkarazo, J. M. Madariaga, Use of in situ and confocal Raman spectroscopy to study the nature and distribution of carotenoids in brown patinas from a deteriorated wall painting in Marcus Lucretius House (Pompeii), Analytical & Bioanalytical Chemistry (2012) 402: 1529-1539.

[21] J. C. Raposo, J. Sanz, G. Borge, M. A. Olazabal, J. M. Madariaga, Development of a modified Bromley's Methodology for the estimation of ionic media effects on solution equilibria Part 3. Application to the construction of thermodynamic models, Fluid Phase Equilibria (1999)155: 1-19.

[22] M. Pérez-Alonso, K. Castro, M. Álvarez, J. M. Madariaga, Scientific analysis versus restorer's expertise for diagnosis prior to a restoration process: the case of Santa Maria Church (Hermo, Asturias, North of Spain), Analytica Chimica Acta (2004) 524: 379–389

[23] I. Martínez-Arkarazo, M. Angulo, L. Bartolomé, N. Etxebarria, M. A. Olazabal, J. M. Madariaga, An integrated Analytical Approach to Diagnose the Conservation State of Building Materials of a Palace House in the Metropolitan Bilbao (Basque Country, North of Spain), Analytica Chimica Acta (2007) 584: 350-359.

[24] M. Maguregui, N. Prieto-Taboada, J. Trebolazabala, N. Goienaga, N. Arrieta, J. Aramendia, L. Gomez-Nubla, A. Sarmiento, M. Olivares, J. A. Carrero, I. Martinez-Arkarazo, K. Castro, G. Arana, M. A. Olazabal, L. A. Fernandez, J. M. Madariaga, CHEMCH 1st International congress chemistry for cultural heritage, Ravenna (2010).

[25] R. T. Downs, M. Hall-Wallace, 18th General meeting of the international mineralogical association, Edinburgh, Scotland. Programme With Abstracts (2002) 128.

[26] N. Prieto-Taboada, O. Gómez-Laserna, I. Martinez-Arkarazo, M. A. Olazabal, J. M. Madariaga, Optimization of two methods based on ultrasound energy as alternative to European standards for soluble salts extraction from building materials, Ultrasonics Sonochemistry (2012) 19: 1260-1265.

[27] J. I. Alvarez, I. Navarro, P. J. García-Casado, Thermal, mineralogical, and chemical studies of the mortars used in the cathedral of Pamplona (Spain), Thermochimica Acta (2000) 365: 177-187.

[28] J. I. Alvarez, I. Navarro, A. Marti, P. J. García-Casado, A study of the ancient mortars in the north tower of Pamplona's San Cernin church, Cement & Concrete Research (2000) 30: 1413-1419.

[29] W. Nocun-Wczelik, G. Loj, Effect of PbO on setting and hardening of Portland cement, Cement-Wapno-Beton (2006) 11: 285-290.

[30] K. D. Grevel, J. Majzlan, Internally consistent thermodynamic data for magnesium sulfate hydrates, Geochimica et Cosmochimica Acta (2009) 73: 6805-6815.

[31] C. Leck, E. K. Bigg, Comparison of sources and nature of the tropical aerosol with the summer high Arctic aerosol, Tellus B (2008) 60*:* 118–126.

[32] B. Gantt, N. Meskhidze, The physical and chemical characteristics of marine organic aerosols: a review, Atmospheric Chemistry and Physics Discussions (2012) 12: 21779-21813.

[33] H. Morillas, M. Maguregui, O. Gómez-Laserna, J. Trebolazabala, J. M. Madariaga, Characterisation and diagnosis of the conservation state of cementitious materials exposed to the open air in XIX century lighthouses located on the coast of the Basque Country: "The case of Igueldo lighthouse, San Sebastian, North of Spain", Journal of Raman Spectroscopy (2012) 43: 1630-1636.

[34] R. Garcia, V. Rubio, I. Vegas, M. Frias, Random ionic mobility on blended cements exposed to aggressive environments, Journal of Hazardous Materials (2009) 168: 1602-1608.

[35] M. L'Heritier, P. Dillmann, P. Benoit, The use of ferrous alloys for the building of gothic churches. Role, origins and production of the metal, through the examples of Rouen and Troyes, Historical Metallurgy (2010) 44: 21-35.

[36] E. Malel, D. E. Shalev, Determining the Effect of Environmental Conditions on Iron Corrosion by Atomic Absorption, Journal of Chemical Education (2013) 90: 490-494.

[37] M. Maguregui, U. Knuutinen, I. Martinez-Arkarazo, K. Castro, J. M. Madariaga, Thermodynamic and spectroscopic speciation to explain the blackening process of hematite formed by atmospheric SO_2 impact: the case of Marcus Lucretius House (Pompeii), Analytical Chemistry (2011) 83: 3319-3326.

[38] I. Rodriguez-Maribona, M. Zalbide, F. Garmilla, F. Garcia, J. A. Ibanez, S. Garin, Conservation study of the stone material used in the Culture House of Almirante Oquendo, in San Sebastian, Materiales de Construcción (1999) 49: 19-30.

[39] M. Maguregui, U. Knuutinen, K. Castro, J. M. Madariaga, Raman spectroscopy as a tool to diagnose the impact and conservation state of Pompeian Second and Fourth style wall paintings exposed to diverse environments (House of Marcus Lucretius), Journal of Raman Spectroscopy (2010) 41: 1400-1409.

[40] K. M. Gierlus, O. Laskina, V. H. Grassian, Effect of the presence of oxalate on the cloud condensation nuclei activity of calcium-containing mineral dust aerosol, 239th ACS national meeting, San Francisco, CA, United States (2010).

[41] A. Zoppi, C. Lofrumento, N. F. C. Mendes, E. M. Castellucci, Metal oxalates in paints: a Raman investigation on the relative reactivities of different pigments to oxalic acid solutions, Analytical & Bioanalytical Chemistry (2010) 397: 841-849.

[42] M. Steiger, S. Asmussen, Crystallization of sodium sulfate phases in porous materials: the phase diagram Na_2SO_4-H_2O and the generation of stress, Geochimica et Cosmochimica Acta (2008) 72: 4291-4306.

[43] C. Rodriguez-Navarro, E. Doehne, E. Sebastian, How does sodium sulfate crystallize? Implications for the decay and testing of building materials, Cement & Concrete Research (2000) 30: 1527-1534.

[44] A. Hamilton, R. I. Menzies, Raman spectra of mirabilite, $Na_2SO_4 \cdot 10H_2O$ and the rediscovered metastable heptahydrate, $Na_2SO_4 \cdot 7H_2O$, Journal of Raman Spectroscopy (2009) 41: 1014-1020.

[45] M. Balonis, F. P. Glasser, The density of cement phases, Cement & Concrete Research (2009) 39: 733-739.

[46] S. S. Potgieter-Vermaak, J. H. Potgieter, M. Bellei, F. de Weerdt, P. van Grieken, The application of Raman spectrometry to the investigation of cement: Part II: A micro-Raman study of OPC, slag and fly ash, Cement & Concrete Research (2006) 36: 663-670.

[47] D. Jana, Concrete Petrography Past, Present and Future, 10th Euroseminar on microscopy applied to building materials, Scotland (2005).

[48] O. Gomez-Laserna, M. A. Olazabal, H. Morillas, N. Prieto-Taboada, I. Martinez-Arkarazo, G. Arana, J. M. Madariaga, In-situ spectroscopic assessment of the conservation state of building materials from a Palace house affected by infiltration water, Journal of Raman Spectroscopy (2013) 44: 1277-1284.

[49] P. Colomban, The on-site/remote Raman analysis with mobile instruments: a review of drawbacks and success in cultural heritage studies and other associated fields, Journal of Raman Spectroscopy (2012) 43: 1529-1535.

RESEARCH ARTICLE 3

The role of marine aerosol in the formation of (double) sulfate/nitrate salts in plasters.

H. Morillas, M. Maguregui, C. Paris, L. Bellot-Gurlet, P. Colomban, J. M. Madariaga

Microchemical Journal (2015) 123: 148–157.

The role of marine aerosol in the formation of (double) sulfate/nitrate salts in plasters

ABSTRACT

During decades the use of gypsum in different buildings has been very common, especially in the Atlantic lands of Europe. Decay compounds like salt crystallizations are ones of the principal deterioration factors of such historical buildings. In this study, gypsum-based plasters from different inner rooms of the Igueldo Lighthouse (San Sebastian, Spain), a building dated back to 1860 that has been subjected to several repairs within these years, were investigated in order to ascertain the main mineral phases produced during the weathering process. A combination of Raman spectroscopy, X-ray diffraction, infrared spectroscopy in ATR mode, SEM-EDS imaging and Raman imaging was successfully applied to study the distribution of different decay compounds in the gypsum-based matrix and to establish the decay reaction pathway which leads to the formation of the identified decay compounds. Additionally thermodynamic chemical modeling was also performed to explain the formation of specific decaying compounds. According to the location of Igueldo Lighthouse (just above a cliff, close to the sea), this building experiments a wide influence of the marine aerosol (Na^+, K^+, Mg^{2+}, Cl^- and NO_3^- input) and the influence of a high damp environment, giving rise to common efflorescence salts as well as to different mixed-calcium sulfates and mixed sulfate–nitrate salts, such as glauberite, syngenite, polyhalite and humberstonite. Dehydration process of gypsum from the plaster (leading to the presence of anhydrite and bassanite) was also identified.

Keywords: Gypsum, Marine aerosol, Sulfates, Nitrates, Raman imaging, SEM-EDS imaging.

1. Introduction

Gypsum ($CaSO_4 \cdot 2H_2O$) is one of the oldest materials used in construction. In the Neolithic period, with the development of fire based technologies, calcined gypsum plaster began to be developed, and it was used to assemble the pieces of masonry, seal the joints of the walls and to cover the walls of the houses, being progressively an alternative to the mud mortar. Since that time it began using regularly until nowadays, especially in the Atlantic lands of Europe. During production process, depending on the temperature and duration of the heating, gypsum converts to the hemihydrate (bassanite $CaSO_4 \cdot \frac{1}{2}H_2O$) or to an anhydrous form (anhydrite $CaSO_4$). Water partial pressure control is difficult and thus $CaSO_4$–H_2O system highly variable and phase equilibrium depends on grain size and thermal treatment kinetics. Recent studies have demonstrated that, under atmospheric pressure [1, 2], there are up to five compounds produced in this system, such as $CaSO_4 \cdot 2H_2O$ (gypsum, monoclinic), $CaSO_4 \cdot \frac{1}{2}H_2O$ (bassanite monoclinic/rhombohedral), γ-$CaSO_4$ (anhydrite I, or AI, cubic), β-$CaSO_4$ (anhydrite II, or AII, orthorhombic) and α-$CaSO_4$ (anhydrite III, or AIII, hexagonal). Depending on the pressure (neon gas as pressure-transmitting medium) and gradient, different mineral phases in the dehydration of the $CaSO_4$–H_2O system can suffer deformations in their structure [3, 4]. In the literature there are several studies that remark also the high influence of organic and inorganic additives which they have been used since the second half of the 20th century in order to control the hydration in gypsum setting/production [5–7]. Sometimes NaCl, $MgCl_2$, $CaCl_2$ solutions can dehydrate gypsum as a result of the lower water vapour pressure of these solutions, modifying its solubility [8]. The later compounds, together with nitrates and sulfates, are present in marine aerosol [9], besides of fatty acids [10]. Some authors point out that in marine aerosol a mixture of ions like Na^+, Ca^{2+}, Mg^{2+}, K^+, Cl^-, Br^-,I^-, Li^+, NO_3^- , NH_4^+, SO_4^{2-} and CO_3^{2-} are usually present along with structural water and other less common ions from anthropogenic sources (e.g., Ba^{2+}, Sr^{2+}, Pb^{2+}, VO^{2-}) [11–13]. In this way, in the marine aerosol composition, natural and anthropogenic ion inputs are present [14, 15]. There are studies that simulated the reactions between cations and anions in the complex Na^+, K^+, Ca^{2+}, Cl^-, SO_4^{2-}–H_2O system [16], which can occur in natural environment, promoting the formation of different type of sulfates. In the literature, several studies describe the formation of decay compounds in building materials as a consequence of the reactions between the original compounds and the ions transported in the marine aerosol. The main pathologies promoted due to these reactions are the formation of efflorescence, sub-efflorescence, loosing and detachment of the building materials, etc. [17–22]. Different decay compounds which have been detected inside the porous and/or over the gypsum surface or in presence of gypsum are listed in Table 1.

Table 1.- Mineral phases identified in plaster,

Mineral phase	Chemical formula	Reference
Bassanite	$CaSO_4 \cdot ½H_2O$	21
Anhydrite, types I, II and III	$CaSO_4$	1, 23
Glauberite	$CaNa_2(SO_4)_2$	24, 25
Thenardite	Na_2SO_4	26, 27
Mirabilite	$Na_2SO_4 \cdot 10H_2O$	28
Mascagnite	$(NH_4)_2SO_4$	21
Epsomite	$MgSO_4 \cdot 7H_2O$	29
(para) Coquimbite	$Fe_2(SO_4)_3 \cdot 9H_2O$	27
Syngenite	$K_2Ca(SO_4) \cdot H_2O$	29
Starkeyite	$MgSO_4 \cdot 4H_2O$	21
Hexahydrite	$MgSO_4 \cdot 6H_2O$	30
Eugsterite	$Na_4Ca(SO_4)_3 \cdot H_2O$	30
Darapskite	$Na_3(SO_4)(NO_3) \cdot H_2O$	31
Polyhalite	$K_2Ca_2Mg(SO_4)_4 \cdot 2H_2O$	32

Moreover, theoretical models based on density functional theory calculations of the structures and properties of compounds like anhydrite ($CaSO_4$), polyhalite ($K_2Ca_2Mg(SO_4)_4 \cdot 2H_2O$) and carnallite ($KMgCl_3 \cdot 6H_2O$) (the last two related with marine influence) have been studied [33]. Other authors, using techniques such as XRD and SEM-EDS have demonstrated the influence and direct relationship that exists in the formation of gypsum and glauberite with the marine aerosol; and their seasons' dependence/periodicity [34]. In this work, a combination of different analytical techniques, including Raman spectroscopy, X-ray diffraction and infrared spectroscopy in ATR mode have been used to identify different decay compounds formed on gypsum plasters from indoor areas of an historical building located in front of the sea, the Igueldo Lighthouse (Donostia-San Sebastian, north of Spain). Moreover, to complete and corroborate the point-by point spectroscopic results, SEM-EDS imaging and Raman imaging were used to map the distribution of the different decay compounds crystallized on gypsum-based plasters. Finally, thermodynamic calculations to complete the analytical statements taking into account the high influence of marine environment were carried out.

2. Materials and methods

2.1. Samplings

Plaster samples from the walls of the Lighthouse machine room, where the temperature conditions inside the room range between 27 °C (winter time) and 35 °C (summer time) with a wide range of relative humidity (>90%) were collected using a scalpel. The size of all of them never exceeded 2 × 2 cm^2. Plaster fragments were analyzed directly by means of point-by-point Raman spectroscopy. For the XRD, ATR-FTIR, SEM-EDS imaging and Raman imaging, the same samples were powdered.

2.2. Instrumentation

The SEM-EDS analyses were carried out using a EVO®40 Scanning Electron Microscope (Carl Zeiss NTS GmbH, Germany) coupled to an X-Max energy-dispersive X-ray spectrometer (Oxford Instruments, Abingdon, Oxfordshire, United Kingdom) for electron image acquisitions and elemental analysis (punctual and imaging). Although gypsum alone is not conductive, it was possible to obtain optimal results without carbon or gold coating. The SEM images were obtained at high vacuum employing an acceleration voltage of 30 kV and a 10–400 μm working distance. Different magnifications (reaching up to × 6800) were used for secondary electron images and an integration time of 50 s was employed to improve the signal-to-noise ratio. The EDS spectra were acquired and treated using the INCA software. Furthermore, a mapping of specific microscopic areas in the samples was possible, allowing the evaluation of the distribution of these elements over the sample.

ATR-FTIR spectra were recorded using a Bruker Equinox 55 spectrometer equipped with an extended KBr Beamsplitter and purged with dried air. A liquid nitrogen-cooled MCT detector or a Peltier-cooled DTGS Mid-IR detector was used. Two hundred scans were accumulated between 4000 and 600 cm^{-1} with a 4 cm^{-1} resolution with the help of an extended KBr Beamsplitter. A background was collected before each sample's spectra and additional atmospheric compensation was provided by Opus 6.5 Software. Few milligrams of sample powder are required for each measurement using an ATR diamond crystal accessory (Golden Gate®, Specac) which no require any additional sample preparation constraints. The obtained spectra were compared with the spectra of pure standard compounds contained in RRUFF [35] and in the e-VISART infrared databases [36].

The XRD analyses were performed with a PANalytical Xpert PRO powder diffractometer, equipped with a copper tube ($\lambda CuK_{\alpha 1}$ = 1.54060 Å, $\lambda CuK_{\alpha 2}$ = 1.54439 Å), vertical goniometer (Bragg–Brentano geometry), programmable divergence aperture, automatic interchange of

samples and secondary monochromator from graphite and PixCel detector. The measurement conditions were 40 kV and 40 mA, with an angular range (2θ) scanned from 5 to 70°. The X'pert HighScore (PANalytical) software in combination with the specific powder diffraction file database (International Centre for Diffraction Data-ICDD, Pennsylvania, USA) was used for the phase identification.

For micro-Raman spectra and Raman Imaging, a Senterra spectrometer (Bruker Optics, Karlsruhe, Germany) equipped with a Peltier-cooled charge-coupled device detector and × 10 and × 50 long working distance Olympus objectives was used to collect the Raman spectra excited under a 785 nm light from a diode laser. The Raman image acquisitions of specific areas of the plaster matrix were conducted using the Peak Pick Singular option. The interpretation of all the Raman results was performed by comparing the acquired Raman spectra with the Raman spectra of pure standard compounds collected in the e-VISNICH dispersive Raman database [37]. Additionally, free Raman databases (e.g. RRUFF [35]) were also considered for the assignation of unknown Raman bands. Different spectral analysis tools, OPUS© 7.0 (Bruker Optik GmbH, Ettlingen, Germany (2011)) for Raman Imaging; and Omnic 7.2 (Nicolet) and Wire 2.0 (Renishaw) for spectral treatment and assignation, were used.

Thermodynamic chemical modeling was also performed to explain the formation of specific decaying compounds, considering the composition of the plaster and the input of ions infiltrated in the material. For that purpose the MEDUSA [38] free academic program was used. This program implements its own Hydrochemical Equilibrium-Constant (HYDRA) database. This database was extended manually introducing the logarithm of the formation constant of specific mineralogical phases of interest [39]. Certain constants were obtained also from the Visual MINTEQ [40] database.

3. Results and discussion

3.1. Point-by-point Raman spectroscopy analyses

In the Raman spectra acquired on the gypsum plaster samples, different kind of sulfates and nitrates bands were distinguished. Most of the bands are centered between 960–1080 cm^{-1} as in Figure 1 is illustrated. This underlines the simultaneous presence of several sulfates such as syngenite ($K_2Ca(SO_4)_2 \cdot H_2O$, Raman band at 981 cm^{-1}), thenardite (Na_2SO_4, Raman band at 989 cm^{-1}), starkeyite ($MgSO_4 \cdot 4H_2O$, Raman band at 1001 cm^{-1}) and gypsum ($CaSO_4 \cdot 2H_2O$, Raman band 1008 cm^{-1}). In the same micronic spot (under x100 objective) nitrates such as niter (KNO_3, Raman band at 1048 cm^{-1}) and nitratine ($NaNO_3$, Raman band at 1067 cm^{-1}) were also identified (see Figure 1). Other compounds identified through Raman analyses include sulfates such as epsomite ($MgSO_4 \cdot 7H_2O$), hexahydrite ($MgSO_4 \cdot 6H_2O$), mirabilite ($Na_2SO_4 \cdot 10H_2O$), bassanite or gypsum hemihydrate ($CaSO_4 \cdot ½H_2O$) and anhydrite ($CaSO_4$).

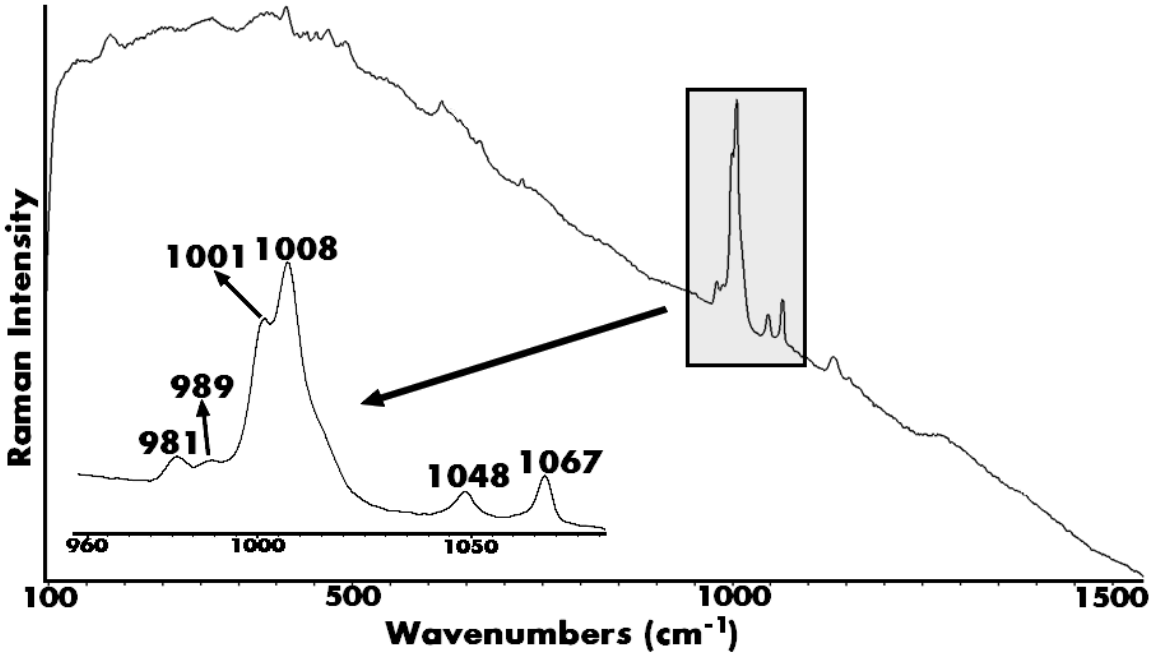

Figure 1. Raman spectrum showing bands of compounds present in the gypsum-based plaster.

3.2. X-ray diffraction and point-by-point Raman spectroscopy revision

To corroborate the Raman spectra assignation, X-ray powder diffraction (XRD) analyses were conducted on the collected samples. The acquired XRD spectra revealed the presence of different compounds, namely, quartz (SiO_2), gypsum ($CaSO_4 \cdot 2H_2O$), bassanite ($CaSO_4 \cdot ½H_2O$), polyhalite ($K_2Ca_2Mg(SO_4)_4 \cdot 2H_2O$), glauberite ($CaNa_2(SO_4)_2$), syngenite ($K_2Ca(SO_4)_2 \cdot H_2O$) and humberstonite ($K_3Na_7Mg_2(SO_4)_6(NO_3)_2 \cdot 6H_2O$) (see Figure 2). Considering that XRD hardly detect compounds which are below 5% in the sample and/or are amorphous [41], it is possible to say that the nitrates, sulfates and nitrate-sulfate salts detected are not in trace levels in the analyzed samples and these global analyses by XRD will take a general consideration of all phases. Taking into account these XRD results, the acquired Raman spectra were re-examined searching the possible presence of overlapped Raman signals. For example, in Figure 1, the signals at 981 and 1006 (shoulder in 1000 cm^{-1} region) cm^{-1} correspond to syngenite stretching mode; the bands at 989 and 1016 (shoulder in 1000 cm^{-1} region) cm^{-1} correspond to those of polyhalite; and the 1008 cm^{-1} peak to the main band of gypsum. Finally, the bands at 1013 (shoulder in 1000 cm^{-1} region), 1048 and 1067 cm^{-1} are clearly related with the stretching modes of humberstonite. Analyzing the whole spectrum shown in Figure 1, secondary bands of those mineral phases can be ascertained. For example, peaks at 183, 632 and 723 cm^{-1} belong to humberstonite; those at 414, 492, 669 and 1134 cm^{-1} belong to gypsum; and two weak bands at 436 and 652 cm^{-1} belong to polyhalite. Additionally, bands at 453, 469, 485, 618, 634, 1155, 1169 cm^{-1} belong to glauberite; and those at 441, 492, 642, 1139 cm^{-1} belong to syngenite.

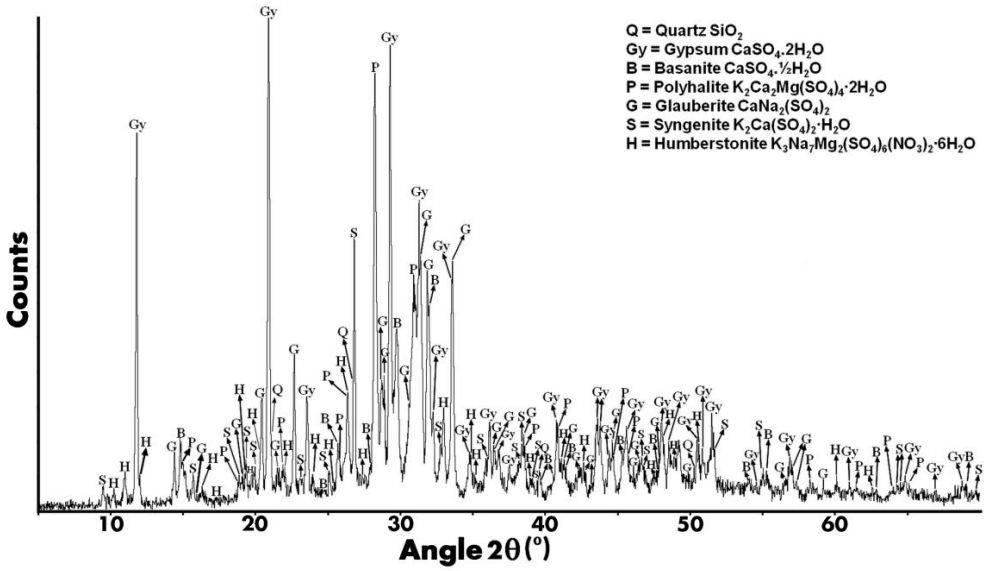

Figure 2. Representative XRD spectrum of gypsum-based plaster showing the different bands of quartz, gypsum, bassanite, polyhalite, glauberite, syngenite and humberstonite.

3.3. ATR-FTIR analyses

In order to search some complementary structural specificities of compounds, (i.e. the OH modes, or possibly less crystallized phases) gypsum plaster samples using ATR-FTIR were also analyzed. As an example, in Figure 3 (top left) a representative ATR-FTIR spectrum obtained from the gypsum plaster, showing very complex and broad IR bands can be observed. In order to resolve (separate) the overlapped IR bands and taking into consideration the hypothesis of the similarities between the band widths for all compounds, a curve-fitting process based on Gaussian and Laurentian algorithms was applied using Grams 32 software (Galactic, Thermo, USA) on three different regions which are common for all the collected IR spectra (Figure 3). With this spectral-treatment, it was possible to separate gypsum, bassanite, anhydrite, humberstonite, syngenite, polyhalite and glauberite IR bands. Therefore, the IR observations provide us complementary information about the hydration (OH modes) of different compounds because of the specific sensitivity of this technique to some structural features. Concretely, the IR bands between 3650 and 3200 cm^{-1} belong to OH stretching mode of crystalline water molecules of the hydrated compounds present in the samples. The band at 3602 cm^{-1} is related with bassanite. The ones at 3532 and 3403 cm^{-1} are related with the presence of gypsum, while the peak at 3474 cm^{-1} belongs to polyhalite [35]. The peaks at 3334 and 3248 cm^{-1} can be assigned to the presence of syngenite [35]. In an intermediate range, some bands are observable, like those at 1620 and 1683 cm^{-1}, related to the sulfate stretching mode of gypsum no water bending contribute to 1620–1660 cm^{-1} range, while the band at 1401 cm^{-1} could not be assigned to specific compound present in plaster matrix.

In the 1180–940 cm^{-1} range, after curve-fitting procedure different bands were identified. All the bands assigned in this area belong to the main bands of anhydrite (1095 cm^{-1}), gypsum (1105 cm^{-1}), glauberite (1083 cm^{-1}), polyhalite (1073 cm^{-1}) and humberstonite (1052 cm^{-1}) [35,42]. Apart of those IR signals, the band at 1005 cm^{-1} is related with the main band of syngenite, together with their secondary stretching bands at 1125 and 1111 cm^{-1}. The band at 1135 cm^{-1} could be related with both a secondary band of syngenite or polyhalite. The band at 986 cm^{-1} could belong to a secondary band of polyhalite or syngenite. Moreover, the bands at 1033, 1022 and 964 cm^{-1} were also observed but could not be assigned with those compounds.

Finally, in the third region, from 730–605 cm^{-1}, IR bands related with syngenite (675 and 645 cm^{-1}), polyhalite (656, 620 and 600 cm^{-1}), glauberite (630 and 605 cm^{-1}) and gypsum (668 cm^{-1}) were identified. Apart from this, two additional bands at 711 and 699 cm^{-1} were also observed, but it could not be assigned and related with the present compounds, which

could be related with secondary bands of some nitrates. This uncertainty was observed in practically all of the ATR-FTIR spectra collected from the samples, making difficult the unequivocal assignation of all the IR features to given compounds, especially in the case of compounds containing the nitrate anion.

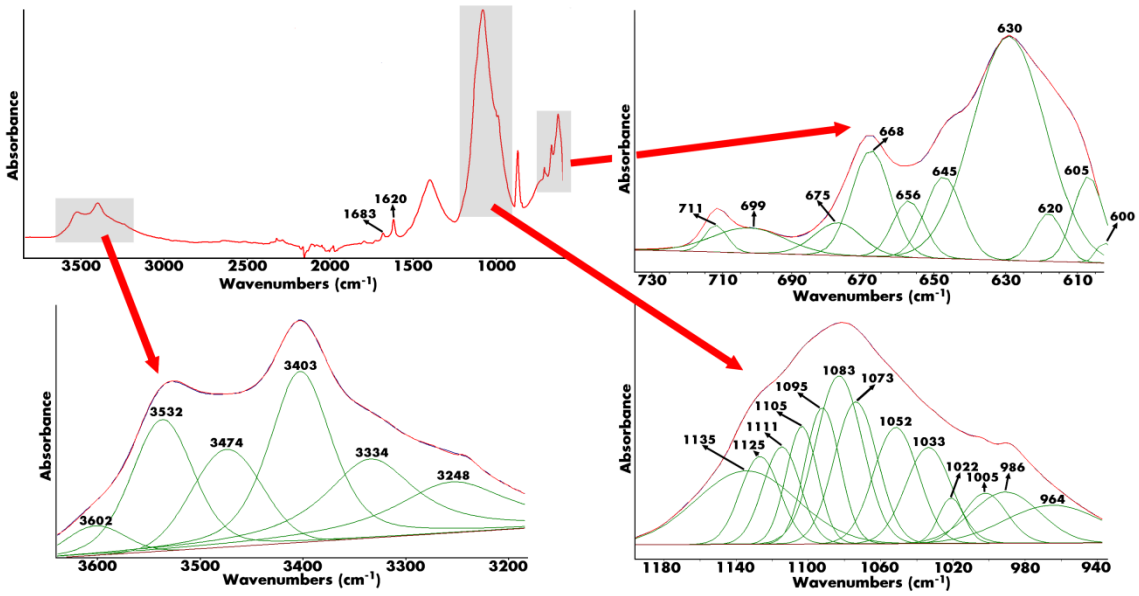

Figure 3. ATR-FTIR spectrum of a plaster sample with some enlargement and band decomposition of three informative spectral ranges.

3.4. Imaging by SEM-EDS and Raman spectroscopy

The molecular results described in the previous sections were confirmed using SEM-EDS (elemental analysis). Concretely, SEM-EDS imaging was applied in order to see the distribution of all the elements representative of each molecular phase identified using Raman, XRD and ATR-FTIR. In this way, in Figure 4, the distribution of K, O, S, Mg, Ca, Si, Na and Cl in a microscopic area (around 70 μm) of the plaster can be observed. Analyzing the elemental mappings, halite, quartz, syngenite and polyhalite can be distinguished. Therefore, with the elemental analyses, the presence of NaCl was verified (NaCl doesn't have Raman signature nor observable IR signal in the studied range due to its very ionic character). This example corroborates the good strategy using several techniques in order to obtain the most complete characterization.

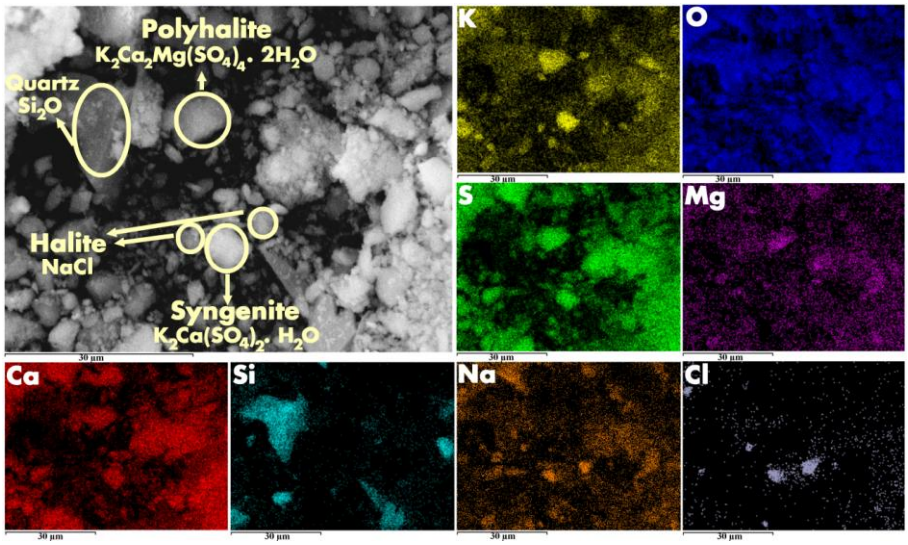

Figure 4. SEM-EDS imaging showing the presence and distribution of halite, quartz, syngenite and polyhalite

As it is going to describe in the following section, NaCl input coming from marine aerosol plays an important role in the formation of most of the new mineral phases. As can be observed in Figure 5, apart from halite, quartz, syngenite and polyhalite, glauberite distribution was also observed using SEM-EDS imaging. Additionally, in Figures 4 and 5, SEM-EDS imaging showed the distribution of Ca, S and O related with the gypsum ($CaSO_4 \cdot 2H_2O$) and also the distribution of Na, S and O was clearly observable in certain areas, suggesting the presence of thenardite or mirabilite ($NaSO_4$–$NaSO_4 \cdot 10H_2O$ system). This sodium sulfate system can also have an important influence in the decaying pathways affecting the matrix.

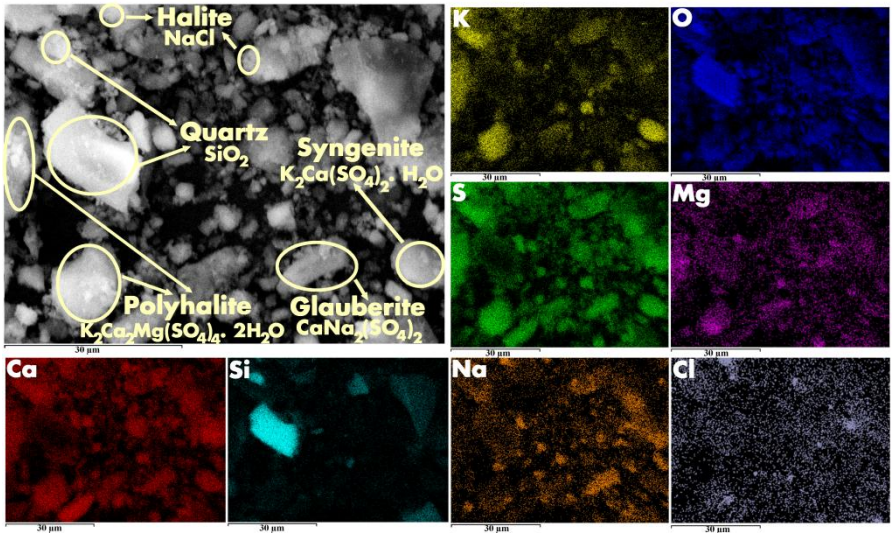

Figure 5. SEM-EDS imaging showing the presence and distribution of halite, quartz, syngenite, polyhalite and glauberite.

To confirm that the identified molecular phases are not crystallized in a punctual way, Raman imaging analysis were performed. As can be observed in Figure 6, the presence of glauberite ($CaNa_2(SO_4)_2$) with its main Raman band at 1001 cm^{-1} (see Figure 6A), polyhalite ($K_2Ca_2Mg(SO_4)_4 \cdot 2H_2O$) with its main Raman bands at 1016 and 989 cm^{-1} (see Figure 6B), gypsum ($CaSO_4 \cdot 2H_2O$) with its main Raman band at 1008 cm^{-1} (see Figure 6C), humberstonite ($K_3Na_7Mg_2(SO_4)_6(NO_3)_2 \cdot 6H_2O$) with its main Raman bands at 1013, 1048 and 1067 cm^{-1} (see Figure 6D) and syngenite ($K_2Ca(SO_4)_2 \cdot H_2O$) with its main Raman bands at 981 and 1006 cm^{-1} (see Figure 6E) were identified. Although the presence of anhydrite ($CaSO_4$) is clear, its Raman mapping was not added because it was difficult to mark exactly the peak at 1016 cm^{-1}. From the images, the heterogeneity and the wide presence of these compounds in the gypsum plaster must be concluded.

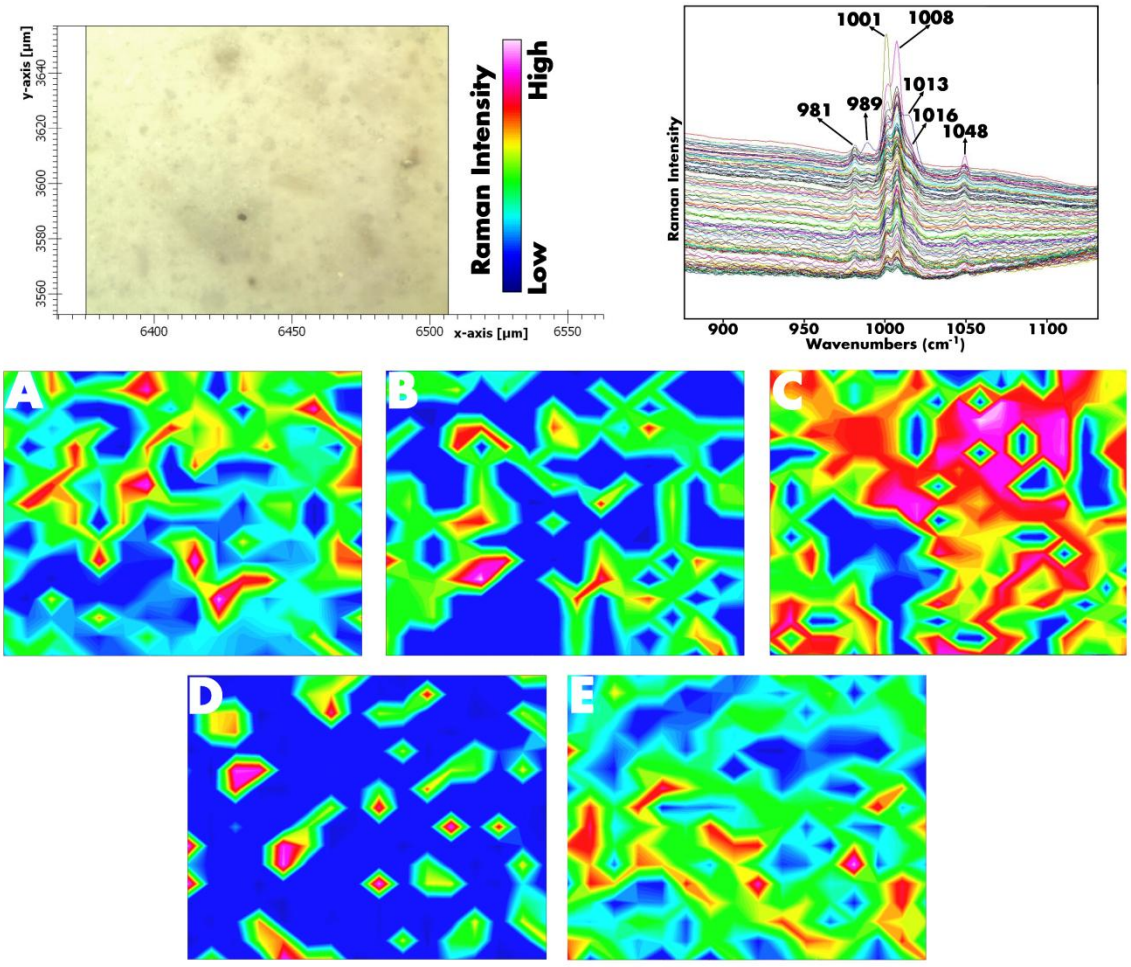

Figure 6. Raman imaging of a plaster sample showing the distribution of (A) glauberite (represented according to the 1001 cm^{-1} band), (B) polyhalite (represented according to the 989 cm^{-1} band), (C) gypsum (represented according to the 1008 cm^{-1} band), (D) humberstonite (represented according to the 1048 cm^{-1} band) and (E) syngenite (represented according to the 981 cm^{-1} band). The top left image shows the mapped area.

Table 2 summarizes all the compounds detected by the five analytical techniques used to characterize the samples. The whole set of analyses conducted by ATR-FTIR, Raman spectroscopy and XRD revealed a complex system of decay compounds. The combined use of XRD data with the Raman spectroscopy information has demonstrated to be an adequate analytical methodology to avoid inaccurate assignments and to detect all the compounds present in different proportions within the samples. The information given by ATR-FTIR itself is not enough to identify the different phases, due to the broad width of IR bands. Finally the use of SEM-EDS and Raman Imaging, complement the analytical information of the decay compounds present in plaster.

Table 2. Mineral phases identified in this work on/into the plaster matrix

Mineral phase	Chemical formula	Raman	XRD	ATR-FTIR	SEM-EDS	Raman imaging
Gypsum	$CaSO_4 \cdot 2H_2O$	**X**	**X**	**X**		**X**
Bassanite	$CaSO_4 \cdot ½H_2O$	**X**	**X**	**X**		**X**
Anhydrite, types I,II, III	$CaSO_4$	**X**		**X**		
Nitratine	$NaNO_3$	**X**				
Niter	KNO_3	**X**				
Thenardite	Na_2SO_4	**X**			**X**	
Mirabilite	$Na_2SO_4 \cdot 10H_2O$	**X**			**X**	
Mascagnite	$(NH_4)_2SO_4$	**X**				
Starkeyite	$MgSO_4 \cdot 4H_2O$	**X**				
Hexahydrite	$MgSO_4 \cdot 6H_2O$	**X**				
Epsomite	$MgSO_4 \cdot 7H_2O$	**X**				
Halite	NaCl		**X**		**X**	
Quartz	SiO_2	**X**	**X**		**X**	
Glauberite	$CaNa_2(SO_4)_2$	**X**	**X**	**X**	**X**	**X**
Polyhalite	$K_2Ca_2Mg(SO_4)_4 \cdot 2H_2O$	**X**	**X**	**X**	**X**	**X**
Syngenite	$K_2Ca(SO_4) \cdot H_2O$	**X**	**X**	**X**	**X**	**X**
Humberstonite	$K_3Na_7Mg_2(SO_4)_6(NO_3)_2 \cdot 6H_2O$	**X**	**X**	**X**		**X**
Total identified		**16**	**8**	**7**	**7**	**6**

3.5. Decay pathways and mechanisms

As seen in Table 2, a wide variety of decaying compounds were detected, containing ions like Na^+, K^+, Mg^{2+} and NO_3^-, apart from the Ca^{2+} and SO_4^{2-} coming from the plaster matrix. According to the previous studies performed in the Igueldo Lighthouse [20, 21], the deposition of high quantities of seagull drops were observed daily in the roof of the building. These drops are the responsible of the nitrate input in the building. Concretely, the ammonium is transformed into nitrates following a processes catalyzed by bacteria [20]. The non-transformed ammonium nitrate migrates downstream (to the walls of the inner rooms of the lighthouse) and it can react with the calcite based plaster, material also used in the Lighthouse construction. The acid ammonium ions react with the basic carbonate leading to the formation of niter (KNO_3) and nitratine ($NaNO_3$) [21].

The presence of the three Na^+, K^+ and NO_3^- ions seems to be related to the impact of marine aerosols that enters to the inner parts of the building through capillarity diffusion in the not well sealed walls of the lighthouse. The marine aerosol usually carries different inorganic compounds inside and/or dissolved ions like chlorides such as NaCl, KCl, $MgCl_2$, $CaCl_2$ [43]; nitrates such as $NaNO_3$ [44], $Ca(NO_3)_2$ [45], NH_4NO_3 and KNO_3 [46], $Mg(NO_3)_2$ [47]; sulfates such as Na_2SO_4 [48], $MgSO_4$ [49], $(NH_4)_2SO_4$ [50] and even mixed-cation with Na, Mg, K and Ca sulfates [51].

Moreover, as it has been described in the sampling section, plaster samples have been taken in a room where the average temperature depending on the season ranges between 27 and 35 °C. In this room all the machine system required for the proper functioning of the lighthouse is present. The complex systems of reactions that explain the decaying pathways occurring in the gypsum plaster of the inner areas of the Igueldo Lighthouse is summarized in Figure 7 and are explained below.

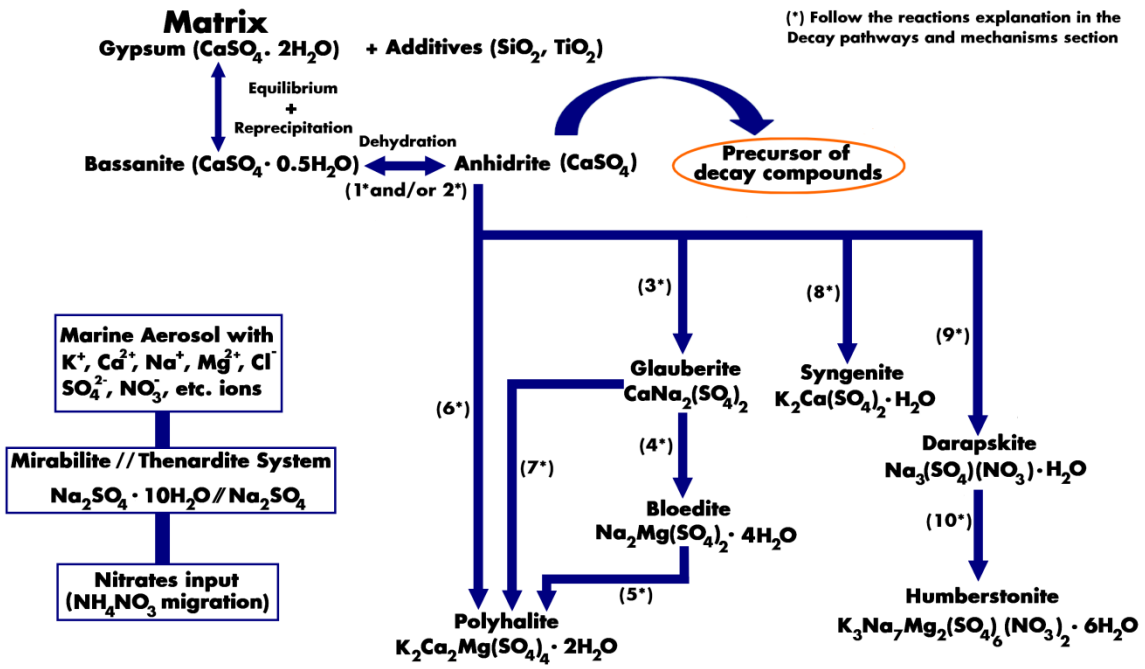

Figure 7. Decay pathway reactions diagram, showing the reactions which lead to the formation of glauberite, bloedite, polyhalite, syngenite, darapskite and humberstonite.

The first decaying step starts with the partial dissolution of gypsum when the water from outside enter the inside walls reaching to the gypsum based plasters. Gypsum is not an insoluble compounds, having an intrinsic solubility due to the presence of the dissolved $CaSO_4$ (dis) complex of the same stoichiometry than the solid phase. Then, this soluble complex [$CaSO_4$ (dis)] dissociates in free calcium (Ca^{2+}) and sulfate (SO_4^{2-}) ions if the water content in the porous material is enough. When this water starts evaporating, the saturation condition of bassanite ($CaSO_4 \cdot \frac{1}{2}H_2O$) is reached and this compound is precipitated. The whole set of interactions is summarized in Reaction 1:

$$CaSO_4 \cdot 2H_2O\ (s) \leftrightarrows CaSO_4\ (dis) \leftrightarrows Ca^{2+} + SO_4^{2-} + \tfrac{1}{2}\ H_2O\ (aq) \leftrightarrows CaSO_4 \cdot \tfrac{1}{2}\ H_2O\ (s) \quad \textbf{(1)}$$

When the temperature rises to the maximum (or simply with time), that water is completely evaporated and thus, anhydrite ($CaSO_4$) could be formed instead of bassanite, following Reaction 2:

$$CaSO_4 \cdot 2H_2O\ (s) \leftrightarrows CaSO_4\ (dis) \leftrightarrows Ca^{2+} + SO_4^{2-} \leftrightarrows CaSO_4\ (s) \quad \textbf{(2)}$$

As it was shown in a previous work, compounds such as thenardite (Na_2SO_4) and mirabilite ($Na_2SO_4 \cdot 10H_2O$) can be present in high quantities around this gypsum-based matrix if it suffers the impact of the marine aerosol [21]. Also the formation of other simple sulfates, like mascagnite ($(NH_4)_2SO_4$), epsomite ($MgSO_4 \cdot 7H_2O$) and starkeyite ($MgSO_4 \cdot 4H_2O$), was

explained [21]. However, in the present work we have identified a greater amount of mixed sulfates and their formation requires ascertaining the chemical reactions involved.

Some works in the literature mentioned that the precursor of many decay compounds, with large quantity of dissolved sulfates, is the anhydrite ($CaSO_4$) [52]. From anhydrite it is possible to find other compounds like glauberite ($CaNa_2(SO_4)_2$) [53]. There are studies about the influence of saline environment in the formation of glauberite [54] or the possibility to obtain glauberite in a system with anhydrite, thenardite and water at 25 °C [55]. However, the formation of a solid phase directly from another solid phase is not always a thermodynamic favored process.

In our case, the three forms of solid calcium sulfate (gypsum, bassanite and anhydrite), when enter in contact with water, dissolve partially due to the presence of the soluble $CaSO_4$ (dis) complex species, that dissociates to free calcium (Ca^{2+}) and sulfate (SO_4^{2-}) ions. If that water contains Na+ from the marine aerosol, Reaction 3 is thermodynamically favored, leading to the formation of glauberite:

$$Ca^{2+} + 2SO_4^{2-} + 2\ Na^{+} \rightarrow CaNa_2(SO_4)_2\,(s) \quad \textbf{(3)}$$

Glauberite has been proposed [56] as the precursor of the formation of other mixed sulfate compounds like polyhalite ($K_2Ca_2Mg(SO_4)_4 \cdot 2H2O$), that can also be formed through another intermediate compound such as bloedite ($Na_2Mg(SO_4)_2 \cdot 4H_2O$) (Reactions 4 and 5):

$$CaNa_2(SO_4)_2\,(s) + Mg^{2+} + 4H_2O \rightarrow Na_2Mg(SO_4)_2{\cdot}4H_2O\,(s) + Ca^{2+} \quad \textbf{(4)}$$

$$Na_2Mg(SO_4)_2 \cdot 4H_2O\,(s) + 2K^{+} + 2SO_4^{2-} \rightarrow K_2Ca_2Mg(SO_4)_4 \cdot 2H_2O\,(s) + 2H_2O \quad \textbf{(5)}$$

In this point, it is necessary to highlight that in the measurements performed in the gypsum plaster, it was not possible to find bloedite, but its presence should not be discarded. However, Reactions 4 and 5 starts from a solid phase, ending in another solid phase, a process that could not be completed due to passivation side-reactions. To overcome this problem, there are authors that suggest the direct formation of polyhalite from anhydrite impacted by a constant source of K^+ and Mg^{2+} coming from marine aerosol, in form of $MgSO_4$ and K_2SO_4, under less than 30 °C temperature conditions [57] (Reaction 6):

$$2CaSO_4 + 2K^{+} + Mg^{2+} + 2SO_4^{2-} + 2H_2O \rightarrow K_2Ca_2Mg(SO_4)_4{\cdot}2H_2O\,(s) \quad \textbf{(6)}$$

Apart from this, there is another work that mentions the possibility to obtain polyhalite from glauberite [58] but the reaction starts from two solid phases (Reaction 7):

$$CaNa_2(SO_4)_2\,(s) + 2K^{+} + CaMg(SO_4)_2\,(s) + 2H_2O \rightarrow K_2Ca_2Mg(SO_4)_4{\cdot}2H_2O\,(s) + 2Na^{+} \quad \textbf{(7)}$$

However, polyhalite can be formed from the dissolved calcium (Ca^{2+}) and sulfate (SO_4^{2-}) ions (dissociated from the soluble $CaSO_4$ (dis) complex) that enter in contact with dissolved K^+ and Mg^{2+} from the marine aerosol, following a similar reaction like 6. Even the formation of bloedite can be explained by the interaction (direct reaction) of SO_4^{2-} with Na^+ (from NaCl) and Mg^{2+} (from $MgCl_2$ or $MgSO_4$ or both) also from the marine aerosol.

The formation of syngenite ($K_2Ca(SO_4)_2 \cdot H_2O$) can be explained by the interaction of K^+ from the marine aerosol with the dissolved calcium (Ca^{2+}) and sulfate (SO_4^{2-}) ions (dissociated from the soluble $CaSO_4$ (dis) complex) from anhydrite, bassanite or gypsum (Reaction 8):

$$Ca^{2+} + 2\ SO_4^{2-} + 2K^+ + H_2O \rightarrow K_2Ca(SO_4)_2 \cdot H_2O\ (s) \quad \textbf{(8)}$$

In this case the role of dissolved K^+ coming from marine aerosol has high importance as it has been highlighted in other works [53, 59, 60]. Although the formation of polyhalite from syngenite is also possible at temperatures between 230 and 280°C [61], this must be discarded because that temperature range cannot be reached in the inner rooms of the lighthouse.

In order to understand better the chemical reactions leading to the formation of syngenite in the gypsum-based plaster, thermodynamic chemical modeling was used (see Figure 8). The possibility of formation of new sulfate in the plaster was searched through theoretical calculations using the MEDUSA software. To perform the chemical modeling several concentrations of the different components (ions) must be tested to see if the new solid phases are formed, or not. In a previous work [21], the soluble anions and cations were quantified in this gypsum plaster. According to those results, the Mg^{2+} and Na^+ concentrations were higher in this gypsum plaster than in the rest of the building materials analyzed. Considering this variability in the concentration range of the ions, two thermodynamic simulations were performed. One of them included the lower concentrations of both Na^+ and Mg^{2+} (1.16 M for Na^+ and 10 mM for Mg^{2+}) and the other simulation increased the concentration of both cations (5.80 M for Na^+ and 100 mM for Mg^{2+}) till a situation reached when evaporation is important.

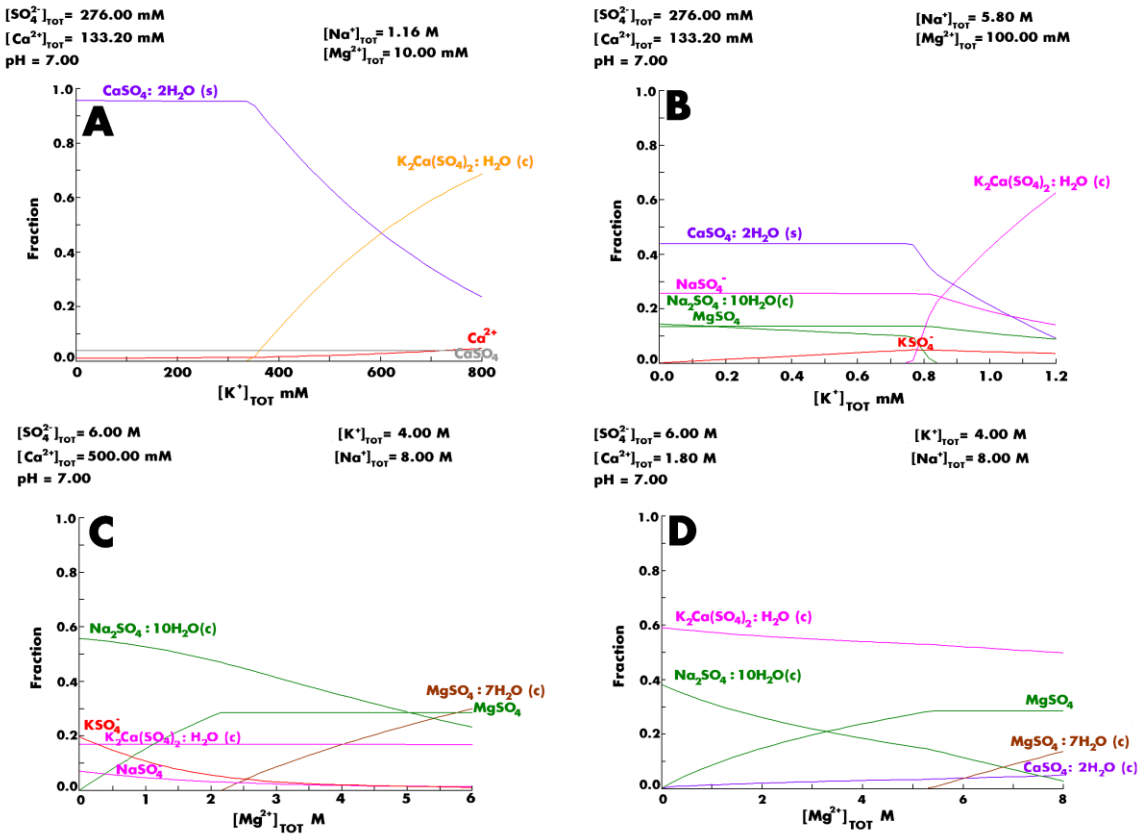

Figure 8. Mole Fraction diagrams showing the formation of syngenite and additional mineral phases in the gypsum-based plaster at high concentrations of sulfates and lower (A) or higher concentrations (B) of Na^+ and Mg^{2+} respectively. The (C) and (D) diagrams cover low concentrations of sulfates at higher or lower concentrations of Ca^{2+} respectively.

The thermodynamic simulation shown, at low concentration of both ions, the formation of syngenite ($K_2Ca(SO_4)_2 \cdot H_2O$) as the first mineralogical phase (see Figure 8A). Note that the concentration of K+ in this simulation ranges between 0 and 1.2 mM, because the experimental concentration of K^+ in the gypsum plaster was shown to be always lower than the Na^+ and Mg^{2+} ones [21]. As can be observed in Figure 8B, at higher concentrations of Na^+ (5.80 M), mirabilite ($Na_2SO_4 \cdot 10H_2O$) is the next phase be formed. Taking into consideration the concentration of soluble Na^+ identified in the gypsum plasters [21], the Na^+ concentration in this last simulation can be considered reasonable. According to the spectroscopic results, sodium sulfate was identified in many measurements performed on the gypsum plaster, but also in additional measurements performed in other building materials from the inner rooms of the Lighthouse [21]. It is necessary to remark that the anhydrous phase (thenardite, Na_2SO_4) was detected instead of mirabilite, as seen from laboratory Raman spectroscopy analyses. Considering the short range of temperature to transform one sodium sulfate form in the other, the dehydration process of the original

mirabilite should be considered during the transport and storage of the samples. In the simulations presented in Figure 8A and B, it can be observed that gypsum disappears, while both new sulfate phases are formed. Maybe for this reason, in some Raman spectra any gypsum traces were detected together with syngenite and thenardite.

Considering that sulfate ions are consumed when the new sulfate phases are formed, an additional situation in which the concentration of sulfate ions is not so high was necessary to be taken into account. The competition among phases can be seen in Figure 8C when the relative magnesium (Mg^{2+} input can come from marine aerosol) concentration increases. When the concentration of Mg^{2+} reaches to a certain level, the presence of mirabilite starts decreasing while epsomite ($MgSO_4 \cdot 7H_2O$) is formed, being syngenite nearly constant. When we considered the same situation (lower concentrations of sulfate ions), but at lower concentrations of Ca^{2+}, a similar tendency was observed, but in this case epsomite together with gypsum are formed (see Figure 8D). In our previous analysis performed on the plaster from the Igueldo lighthouse [21], the simultaneous presence of epsomite and gypsum was always detected in the Raman spectra. This thermodynamic simulation means that it is possible to observe the formation of epsomite in the gypsum plaster of Igueldo Lighthouse at relative high concentrations of Mg^{2+} and lower concentrations of dissolved SO_4^{2-} in the plaster. In this way, the magnesium coming from marine aerosol in form of sulfates or chlorides seems to have also an important role in the chemical decaying of the system.

Finally for the formation of the most complex mixed compound identified in this work, humberstonite ($K_3Na_7Mg_2(SO_4)_6(NO_3)_2 \cdot 6H_2O$), it seems to require firstly the formation of darapskite ($Na_3(SO_4)(NO_3) \cdot H_2O$) [52,62], by the input of dissolved Na^+ coming from marine aerosol and the input of nitrates from other sources, (seagull dropping and/or marine aerosol), as suggested elsewhere [20] on the dissolved $CaSO_4$(dis) complex species (Reaction 9):

$$CaSO_4\,(dis) + 3Na^+ + NO_3^- + H_2O \rightarrow Na_3(SO_4)(NO_3)\,.\,H_2O\,(s) + Ca^{2+} \quad \textbf{(9)}$$

After the formation of darapskite, this compound can be transformed, by the input of dissolved K^+ and Mg^{2+} from the marine environment, to humberstonite following Reaction 10:

$$2Na_3(SO_4)(NO_3).H_2O + 2Mg^{2+} + 3K^+ + Na^+ + 4SO_4^{2-} + 5H_2O \rightarrow K_3Na_7Mg_2(SO_4)_6(NO_3)_2.6H_2O \quad \textbf{(10)}$$

Other authors suggest the formation of humberstonite by repeated natural leaching of nitrates over sulfate bearing materials [42, 52, 63], as well as the consequence of the

reaction between dissolved sulfates coming from the plaster and sodium nitrate coming from the marine aerosol [9].

4. Conclusions

The principal source of deterioration affecting gypsum-based plasters of the interior areas of Igueldo Lighthouse is the marine aerosol (and rain charged with seawaters) which enters to the inner parts of the walls trough cracks and pores from the outside walls of the building. The reaction of the different ions of the marine aerosol with the dissolved calcium and sulfate ions present in the matrix leads to the formation of a wide variety of compounds, most of them well crystallized as revealed the XRD analyses.

The analytical methodology, combining XRD, SEM-EDS, ATR-FTIR and micro Raman spectroscopy (point-by-point and imaging), was required to identify the presence of the whole set of compounds summarized in Table 2. The combined use of Raman and XRD measurements identified most of the new complex compounds. Chloride salts were also identified by using XRD and SEM-EDS measurements on the samples from gypsum plasters, suggesting that the input of sodium and magnesium, also present in the new crystals, can come from the chlorides transported by the marine aerosol (e.g. NaCl, $MgCl_2$, KCl) [8].

Regarding the new salts crystallized in the plaster, it has been possible to assign the main Raman bands of the double sulfate–nitrate salt humberstonite ($K_3Na_7Mg_2(SO_4)_6(NO_3)_2 \cdot 6H_2O$). X-ray diffraction (XRD) and attenuated total reflectance infrared (ATR-FTIR) analyses confirmed the presence of humberstonite. Apart from this salt glauberite ($CaNa_2(SO_4)_2$), syngenite ($K_2Ca(SO_4)_2 \cdot H_2O$) and polyhalite ($K_2Ca_2Mg(SO_4)_4 \cdot 2H_2O$) were also identified by means of Raman spectroscopy. The presence of these salts was corroborated by means of XRD and ATR-FTIR. For instance, the efficiency of Raman scattering arises from the big intensity of the symmetric stretching mode of well defined molecular ions such as NO_3^-, CO_3^{2-}, SO_4^{2-}, etc., whatever the orientation of the analyzed crystal. Efflorescence salts usually form well defined crystals with anisotropic shape and thus bending mode intensity occurring in the 300–700 cm^{-1} range is very dependent of the analyzed spot. Furthermore bending modes have E or F character that implies many modes at very close wavenumbers. This implies overlapping of NO_3^- and SO_4^{2-} bending modes and their identification/use requires chemometric techniques. For all these reason the symmetric stretching bands are the most useful for phase identification if the instrument resolution is sufficient to separate the different peaks. The vibrational infrared spectra counterpart arises from the asymmetric stretching modes with generally F character, i.e. three bands. Thus the overlapping is important and phase identification is difficult.

Therefore, the combined use in these X-ray based and vibrational spectroscopic techniques was proven to be an adequate analytical methodology to avoid inaccurate assignments that can be done only using only one spectroscopic technique. Moreover, the use of the images from SEM-EDS and Raman allowed us to confirm the complex distribution of the new salts in the whole matrix.

Considering all the new mineral phases identified, a complete decaying pathway diagram, containing several reactions, was proposed. In this diagram, gypsum, bassanite and anhydrite are the precursors of the new crystalline phases, through its partial dissolution as the $CaSO_4$ (dis) complex species. The different calcium sulfates, in continuous contact with the marine environment and other surrounding sources of chemicals, like NH_4NO_3, experiment different reactions giving rise to new sulfates and double sulfate/nitrate salts. These compounds are primarily sub- and/or crypto-efflorescences which during time will affect the integrity and durability of the material (in this case gypsum) as well as the aesthetic appearance of the interior facades. In some areas of the rooms, the tiles covering some walls were being detached due to the formation of these new salts in the gypsum plaster placed under the tiles, which weaken its role as a joint mortar.

This more in-depth work on gypsum based materials, complements the previous works [20, 21] developed on other kind of building materials (carbonate and sandstone based materials) also from inside of the Igueldo Lighthouse (San Sebastian, Basque Country, north of Spain) where different kind of pathologies can be explained by the chemical reactivity between original materials and ions transported by the marine aerosol, with the contribution in this particular case of seagull dropping, as an extra source of ammonium and nitrate.

5. References

[1] N. Prieto-Taboada, O. Gomez-Laserna, I. Martinez-Arkarazo, M. A. Olazabal, J. M. Madariaga, Raman Spectra of the Different Phases in the $CaSO_4$–H_2O System, Analytical Chemistry (2014) 86: 10131-10137.

[2] A. N. Christensen, M. Olesen, Y. Cerenius, T. R. Jensen, Formation and Transformation of five different phases in the $CaSO_4$–H_2O System: Crystal Structure of the Subhydrate β-$CaSO_4 \cdot 0.5H_2O$ and Soluble Anhydrite $CaSO_4$, Chemistry of Materials (2008) 20: 2124-2132.

[3] P. W. Mirwald. Experimental study of the dehydration reactions gypsum-bassanite and bassanite-anhydrite at high pressure: Indication of anomalous behavior of H2O at high pressure in the temperature range of 50–300°C, Journal of Chemical Physics (2008) 128: 074502/1-074502/7.

[4] P. Comodi, A. Kurnosov, S. Nazzareni, L. Dubrovinsky, The dehydration process of gypsum under high pressure, Physics and Chemistry of Minerals (2012) 39: 65-71.

[5] M. Prisciandaro, A. Lancia, D. Musmarra, Calcium Sulfate Dihydrate Nucleation in the Presence of Calcium and Sodium Chloride Salts, Industrial & Engineering Chemistry Research (2001) 40: 2335–2339**.**

[6] M. Prisciandaro, A. Lancia, D. Musmarra, The Retarding Effect of Citric Acid on Calcium Sulfate Nucleation Kinetics**,** Industrial & Engineering Chemistry Research (2003) 42: 6647–6652.

[7] T. H. Chong, R. Sheikholeslami, Thermodynamics and kinetics for mixed calcium carbonate and calcium sulfate precipitation, Chemical Engineering Science (2001) 56: 5391-5400.

[8] S. B. Ahmed, M. M. Tlili, M. Amami, M. B. Amor, Gypsum Precipitation Kinetics and Solubility in the NaCl–$MgCl_2$–$CaSO_4$–H_2O System, Industrial & Engineering Chemistry Research (2014) 53: 9554–9560.

[9] A. U. Lewandowska, L. M. Falkowska, Sea salt in aerosols over the southern Baltic. Part 1. The generation and transportation of marine particles, Oceanologia (2013) 55: 279-298.

[10] L. Miñambres, E. Méndez, M. N. Sánchez, F. Castaño, F. J. Basterretxea, The effect of low solubility organic acids on the hygroscopicity of sodium halide aerosols, Atmospheric Chemistry & Physics (2014) 14: 11409-11425.

[11] J. Tursîc, B. Podkrajŝek, I. Grgić, P. Ctyroky, A. Berner, U. Dusek, R. Hitzenberger, Chemical composition and hygroscopic properties of size-segregated aerosol particles collected at the Adriatic coast of Slovenia, Chemosphere (2006) 63: 1193–1202.

[12] T. L. Guasco, L. A. Cuadra-Rodriguez, B. E. Pedler, A. P. Ault, D. B. Collins, D. Zhao, M. J. Kim, M. J. Ruppel, S. C. Wilson, R. S. Pomeroy, V. H. Grassian, F. Azam, T. H. Bertram, K. A. Prather, Transition Metal Associations with Primary Biological Particles in Sea Spray Aerosol Generated in a Wave Channel**,** Environmental Science & Technology (2014) 48: 1324–1333.

[13] L. Xia, Y. Gao, Chemical composition and size distributions of coastal aerosols observed on the US East Coast, Marine Chemistry (2010) 119: 77–90.

[14] M. Viana, J. Pey, X. Querol, A. Alastuey, F. de Leeuw, A. Lükewille, Natural sources of atmospheric aerosols influencing air quality across Europe, Science of the Total Environment (2014) 472: 825–833.

[15] S. C. Pryor, R. J. Barthelmie, J. T. Schoof, F. S. Binkowski, L. Delle Monache, R. Stull, Modelling the impact of sea-spray on particle concentrations in a coastal city, Science of the Total Environment (2008) 391:132-142.

[16] D. Freyer, W. Voigt, The measurement of sulfate mineral solubilities in the Na-K-Ca-Cl-SO4-H2O system at temperatures of 100, 150 and 200 ^{0}C, Geochimica et Cosmochimica Acta (2004) 68: 307-318.

[17] F. Zezza, F. Macri, Marine aerosol and stone decay, Science of the Total Environment (1995) 167:123-143.

[18] A. E. Charola, J. Pühringer, M. Steiger, Gypsum: a review of its role in the deterioration of building materials, Environmental Geology (2007) 52: 339-352.

[19] I. Martinez-Arkarazo, M. Angulo, L. Bartolome, N. Etxebarria, M. A. Olazabal, J. M. Madariaga, An integrated analytical approach to diagnose the conservation state of building materials of a palace house in the metropolitan Bilbao (Basque Country, North of Spain), Analytica Chimica Acta (2007) 584: 350-359.

[20] H. Morillas, M. Maguregui, O. Gómez-Laserna, J. Trebolazabala, J. M. Madariaga, Characterisation and diagnosis of the conservation state of cementitious materials exposed to the open air in XIX century lighthouses located on the coast of the Basque Country: 'The case of Igueldo lighthouse, San Sebastian, North of Spain", Journal of Raman Spectroscopy (2012) 43: 1630–1636.

[21] H. Morillas, M. Maguregui, O. Gómez-Laserna, J. Trebolazabala, J. M. Madariaga, Could marine aerosol contribute to deteriorate building materials from interior areas of lighthouses? An answer from the analytical chemistry point of view, Journal of Raman Spectroscopy (2013) 44: 1700–1710.

[22] N. Prieto-Taboada, I. Ibarrondo, O. Gomez-Laserna, I. Martinez-Arkarazo, M. A. Olazabal, J. M. Madariaga, Buildings as repositories of hazardous pollutants of anthropogenic origin, Journal of Hazardous Materials (2013) 248-249: 451-460.

[23] N. Prieto-Taboada, M. Maguregui, I. Martinez-Arkarazo, M. A. Olazabal, G. Arana, J. M. Madariaga, Spectroscopic evaluation of the environmental impact on black crusted modern mortars in urban-industrial areas, Analytical & Bioanalytical Chemistry (2011) 399: 2949-2959.

[24] L. Bityukova, Air pollution effect on the decay of carbonate building stones in old town of Tallinn, Water, Air, and Soil Pollution (2006) 172: 239–271.

[25] R. C. Clark, R. R. Hark, N. Salvado´, S. Butı´, T. Pradell, Spectroscopy study of mural paintings from the Pyrenean Church of Saint Eulàlia of Unha, Journal of Raman Spectroscopy (2010) 41: 1418–1424.

[26] T. Aguayo, E. Clavijo, F. Eisner, C. Ossa-Izquierdo, M. M. Campos-Vallette, Raman spectroscopy in the diagnosis of the wall painting *History of Concepción*, Chile, Journal of Raman Spectroscopy (2011) 42: 2143–2148.

[27] M. Maguregui, U. Knuutinen, I. Martinez-Arkarazo, A. Giakoumaki, K. Castro, J. M. Madariaga, Field Raman analysis to diagnose the conservation state of excavated walls and wall paintings in the archaeological site of Pompeii (Italy), Journal of Raman Spectroscopy (2012) 43: 1747–1753.

[28] A. Hamilton, R. I. Menzies, Raman spectra of mirabilite, $Na_2SO_4.10H_2O$ and the rediscovered metastable heptahydrate, $Na_2SO_4.7H_2O$, Journal of Raman Spectroscopy (2010) 41: 1014–1020.

[29] H. Morillas, M. Maguregui, J. Trebolazabala, J. M. Madariaga, Nature and origin of White efforescence on bricks, artificial stones, and joint mortars of modern houses evaluated by portable Raman spectroscopy and laboratory analyses, Spectrochimica Acta Part A: Molecular and Biomolecular Spectroscopy (2015) 136: 1195-1203.

[30] V. Matovic, S. Eric, D. Sreckovic-Batocanin, P. Colomban, A. Kremenovic, The influence of building materials on salt formation in rural environments, Environmental Earth Sciences (2014) 72: 1939-1951.

[31] V. P. Jentzsch, V. Ciobotâ, B. Kampe, P. Rösch, J. Popp, Origin of salt mixtures and mixed salts in atmospheric particulate matter, Journal of Raman Spectroscopy (2012) 43: 514–519.

[32] L. C. Prinsloo, Rock hyraces: A cause of San rock art deterioration?, Journal of Raman Spectroscopy (2007) 38: 496-503.

[33] P. F. Weck, E. Kim, C. F. Jové-Colón, D. C. Sassani, First-principles study of anhydrite, polyhalite and carnallite, Chemical Physics Letters (2014) 594: 1–5.

[34] G. Zhou, K. Tazaki, Seasonal variation of gypsum in aerosol and its effect on the acidity of wet precipitation on the Japan Sea side of Japan, Atmospheric Environment (1996) 30: 3301-3308.

[35] R. T. Downs, The RRUFF project: an integrated study of the chemistry, crystallography, Raman and infrared spectroscopy of minerals. Program and abstracts of the 19th general meeting of the international mineralogical association in Kobe, Japan, O03-13, (2006) http://rruff.info/index.php

[36] K. Castro, M. Perez, M. D. Rodriguez-Laso, J. M. Madariaga, FTIR spectra database of inorganic art materials, Analytical Chemistry (2003) 75: 214A-221A

[37] M. Maguregui, N. Prieto-Taboada, J. Trebolazabala, N. Goienaga, N. Arrieta, J. Aramendia, L. Gomez-Nubla, A. Sarmiento, M. Olivares, J. A. Carrero, I. Martinez-Arkarazo, K. Castro, G. Arana, M. A. Olazabal, L. A. Fernandez, J. M. Madariaga, CHEMCH 1st International congress chemistry for cultural heritage, Ravenna (2010).

[38] I. Puigdomenech, A. Zagorodni, M. Wang, M. Muhammed, Program Medusa MEDUSA (Make Equilibrium Diagrams Using Sophisticated Algoritms); The Royal Institute of Technology, Inorganic and Materials Chemistry, Stockholm, (2009) https://www.kth.se/en/che/medusa [last accessed, April 2015].

[39] http://www.iupac.org/index.php?id=410 [last accessed, April 2015].

[40] http://www.lwr.kth.se/English/OurSoftware/vminteq/ [last accessed, April 2015].

[41] B. Minčeva-Šukarova, A. İssi, A. Raškovska, O. Grupče, V. Tanevska, M. Yaygingöl, A. Kara, P. Colomban, Characterization of pottery from Republic of Macedonia. III A study of

the comparative mineralogical efficiency using micro-Raman mapping ang X-ray diffraction, Journal of. Raman Spectroscopy (2012) 43: 792-798.

[42] M. E. Mrose, J. J. Fahey, G. E. Eriksen, Mineralogical studies of the nitrate deposits of Chile. III. Humberstonite, $K_3Na_7Mg_2(SO_4)_6(NO_3)_2 \cdot 6H_2O$), a new saline mineral, The American Mineralogist (1970) 55: 1518-1533.

[43] J. H. Park, A. V. Ivanov, M. J. Molina, Effect of Relative Humidity on OH Uptake by Surfaces of Atmospheric Importance, Journal of Physical Chemistry A (2008) 112: 6968-6977.

[44] A. Laskin, M. J. Iedema, J. P. Cowin, Quantitative Time-Resolved Monitoring of Nitrate Formation in Sea Salt Particles Using a CCSEM/EDX Single Particle Analysis, Environmental Science & Technology (2002) 36: 4948-4955.

[45] S. M. Griffith, X. H. H. Huang, P. K. K. Louie, J. Z .Yu, Characterizing the thermodynamic and chemical composition factors controlling $PM_{2.5}$ nitrate: Insights gained from two years of online measurements in Hong Kong, Atmospheric Environment (2015) Available online at: DOI:10.1016/j.atmosenv.2015.02.009.

[46] L. Bencs, K. Ravindra, J. de Hoog, E. O. Rasoazanany, F. Deutsch, N. Bleux, P. Berghmans, E. Roekens, A. Krata, R. Van Grieken, Mass and ionic composition of atmospheric fine particles over Belgium and their relation with gaseous air pollutants, Journal of Environmental Monitoring (2008) 10: 1148-1157.

[47] E. Woods, K. D. Heylman, A. K. Gibson, A. P. Ashwell, S. R. Rossi, Effects of NO_y Aging on the Dehydration Dynamics of Model Sea Spray Aerosol**,** Journal of Physical Chemistry A (2013) 117: 4214–4222.

[48] I. N. Tang, A. C. Tridico, K. H. Fung, Thermodynamic and optical properties of sea salt aerosols, Journal of Geophysical Research [Atmospheres] (1997) 102(D19): 23269-23275.

[49] E. Woods, D. Chung, H. M. Lanney, B. A. Ashwell, Surface Morphology and Phase Transitions in Mixed NaCl/$MgSO_4$ Aerosol Particles, The Journal of Physical Chemistry A (2010) 114: 2837–2844.

[50] J. Nicolás, M. Chiari, J. Crespo, N. Galindo, F. Lucarelli, S. Nava, E. Yubero, Assessment of potential source regions of $PM_{2.5}$ components at a southwestern Mediterranean site, Tellus (2011) 63B: 96–106.

[51] M. Pòsfai, J. R. Anderson, P. R. Buseck, H. Sievering, Compositional variations of sea-salt-mode aerosol particles from the North Atlantic, Journal of Geophysical Research, [Atmospheres] (1995) 100(D11): 23063-23074.

[52] J. J. Pueyo, G. Chong, M. Vega, Mineralogía y evolución de las salmueras madres en el yacimiento de nitratos Pedro de Valdivia, Antofagasta, Chile, Revista geológica de Chile, (1998) 25: 03-15.

[53] P. V. Jentzsch, R. M. Bolanz, V. Ciobotâ, B. Kampe, P. Rösch, J. Majzlan, J. Popp, Raman spectroscopic study of calcium mixed salts of atmospheric importance, Vibrational Spectroscopy (2012) 61: 206-213.

[54] A. Chabas, R. A. Lefèvre, Chemistry and microscopy of atmospheric particulates at Delos (Cyclades-Greece), Atmospheric Environment (1999) 34: 225-238.

[55] D. Popovic, G. Stupar, J. Miladinovic, M. Todorovic, M. Zrilic, Solubility in the ternary system $CaSO_4$ + Na_2SO_4 + H_2O at 298.15 K, Russian Journal of Physical Chemistry A (2011) 85: 2349-2353.

[56] S. Collao, E. Arce, A. Andia, Mineralogy, chemistry and fluid inclusions in the nitrate ore deposits of Maria Elena, II region, Chile, Boletin de la Sociedad Chilena de Quimica (2002) 47: 181-190.

[57] T. M. Peryt, C. Pierre, S. P. Gryniv, Origin of Polyhalite deposits in the Zechstein (Upper Permian) Zdrada Platform (northern Poland), Sedimentology (1998) 45: 565-578.

[58] C. E. Harvie, J. H. Weare, L. A. Hardie, H. P. Eugster, Evaporation of seawater, calculated mineral sequences, Science (1980) 208: 498-500.

[59] J. T. Kloprogge, R .D. Schuiling, Z. Ding, L. Hickey, D. Wharton, R. L. Frost, Vibrational spectroscopic study of syngenite formed during the treatment of liquid manure with sulphuric acid, Vibrational Spectroscopy (2002) 28: 209-221.

[60] J. T. Kloprogge, Z. Ding, W. N. Martens, R. D. Schuiling, L .V. Duong, R. L. Frost, Thermal decomposition of syngenite, $K_2Ca(SO_4)_2.H_2O$, Thermochimica Acta (2004) 417: 143-155.

[61] J. Dankiewicz, K. Wieczorek-Ciurowa, Kinetic study of the thermal dehydration of syngenite $K_2Ca(SO_4)_2 \cdot H_2O$ under isothermal conditions, Journal of Thermal Analyses (1978) 13: 543-552.

[62] P. C. Burns, F. C. Hawthorne, The crystal structure of humberstonite, a mixed sulfate-nitrate mineral, The Canadian Mineralogist (1994) 32: 381-385.

[63] G. E. Ericksen, J. W. Hosterman, P. St. Amand, Chemistry, mineralogy and origin of the clay-hill nitrate deposits, Amargosa River Valley, Death Valley region, California, U. S. A, Chemical Geology (1988) 67: 85-102.

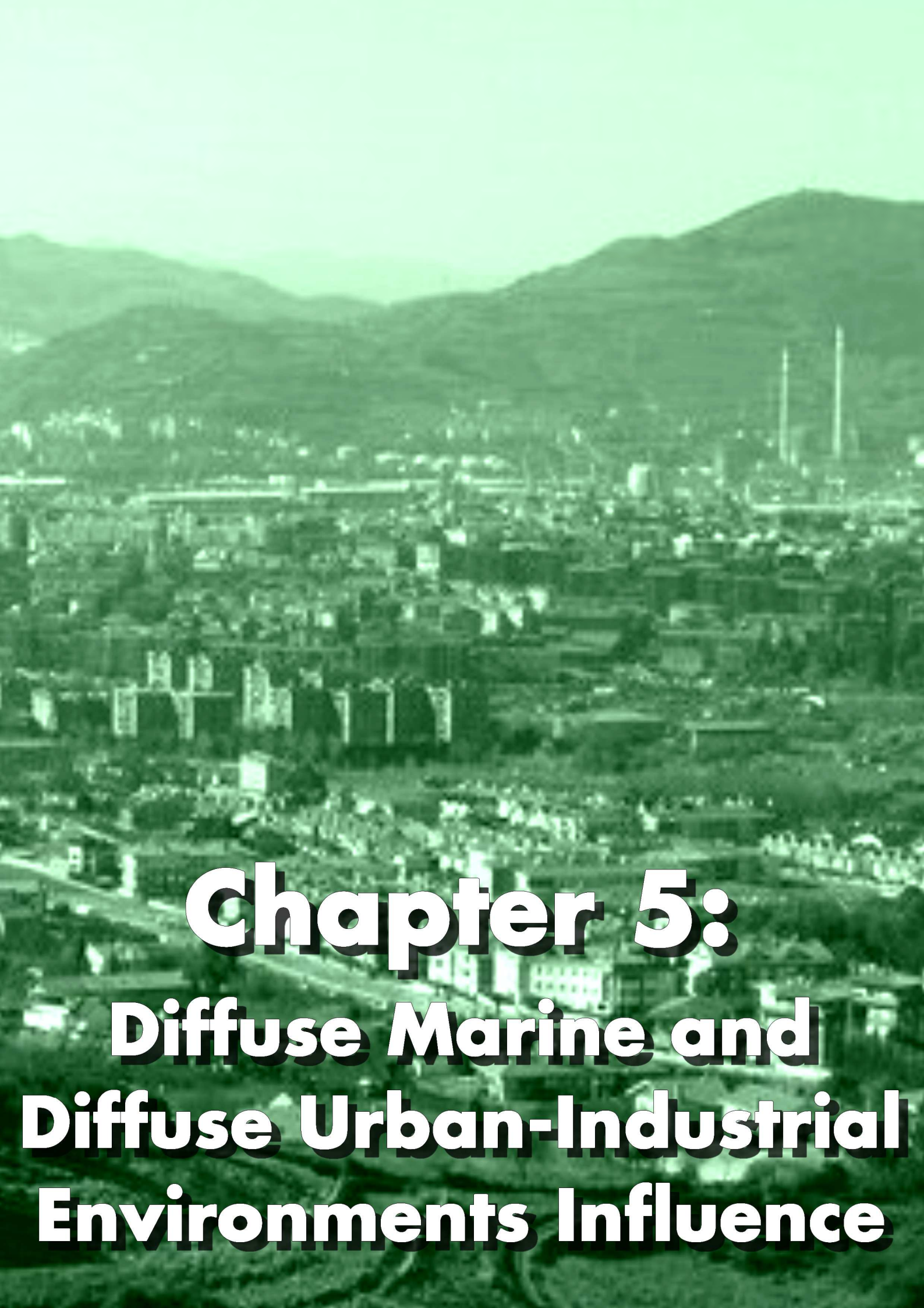

Chapter 5: Diffuse Marine and Diffuse Urban-Industrial Environments Influence

CHAPTER 5.

DIFFUSE MARINE AND DIFFUSE URBAN-INDUSTRIAL ENVIRONMENTS INFLUENCE

In this chapter, the diffuse influence of both marine environment and anthropogenic pollutants coming from an urban-industrial area will be evaluated on different kind of building materials used in detached houses from recent construction (Berango, Basque Country, north of Spain). In this case, the buildings under study are not immersed in marine nor urban-industrial environment, but the coast is placed around 2 Km and urban-industrial areas are also located at around 5-10 km to the buildings. Therefore, Primary and Secondary Marine Aerosol particles coming from the close marine environment, together with anthropogenic emissions (acid acids, metals, etc.) coming from the road traffic, industry, etc. can be transported by the effect of the wind. Therefore, the concentration of anions and metals in the rainwater from the area under study, will give an idea of the pollutants transported to this atmosphere, which could be present in a wet or dry deposition on the building materials under study.

In the literature, different case studies can be found dealing with the study of the pollution of environments similar like the one of Berango [1-3]. Berango is one of the 35 towns belonging to the Metropolitan Bilbao area, an economically and industrially important area from the north of Spain. In the past, many industrial activities were gathered in this area. Nowadays on the contrary, the number of industries has decreased considerably. However, Metropolitan Bilbao is still a highly industrialized area, especially important for the steel

industries, chemical plants producing acids and metallic compounds, metal processing and industrial port activities [4]. Moreover, this area also experiments high road traffic [5].

Some of the buildings located in the Metropolitan Bilbao and the surrounding areas show appreciable damages on their facade materials. Despite natural weathering parameters being the main factor accelerating the different materials decay processes [6], atmospheric contamination plays also an important role. The most relevant atmospheric pollutants that can affect the building materials can be the SO_x and NO_x gases that result in the formation of soluble salts such as sulfates [7–10] or nitrates [11] after the acidic attack of the corresponding acid rainwaters against the bricks, cementitious materials, artificial stones etc. In the particular case of carbonated materials, calcium sulfate (gypsum) is frequently formed as the final product [12, 13]. However, particulate matter usually including soot and carbonaceous particles, where heavy metals are trapped, as well as the marine aerosol typical from coastal areas, should be also considered in this case [14]. In the Figure 5.1, a general view of Berango can be observed.

Figure 5.1. A general view of Berango showing the coast at the back and also the near industry at the back-left of the photo.

5.1 Berango Building Materials and its Case Studies

In this chapter, two Case Studies will be presented. In the first one, a study about the nature and the possible origin of the efflorescences present in different building materials will be conducted. The detached houses under study, located in a residential area from the Metropolitan Bilbao (Basque Country, North of Spain), dated back to the 2002. All those constructions have two floors, a terrace and a garden. The main materials used for the construction of their facades are bricks, cementitious materials and artificial stones with

their respective joint mortars. In this way, three facades from the most impacted areas of three houses were finally selected to perform the study. In the House 1, its most impacted facade was made of bricks with joint mortars. The studied facade is in direct contact with the grass of the garden but protected from the main winds and rainfall. The facade studied in the House 2, made up of artificial stones, is also protected from the preferential winds and rainfall, but the garden in its back receives the rainwater, thus the water rich in ions from the garden can migrate to the wall under study. Moreover, on the other side of the wall, a tiled floor in where cement mortar was used can be observed. Finally, the wall from the House 3, made up of bricks together with their joint mortar, also has cement mortar in contact and the influence of infiltration waters coming from an annexe garden. The main difference with the previous walls under study is that this wall receives the impact of the preferential winds and rainfall.

For the second Case Study, rainwater samples from six different locations in the Metropolitan Bilbao, including Berango and La Galea (the third scenario which will be explained in the Chapter 6) (Basque Country, north of Spain) will be analyzed. In this case, the pH values, redox potential values, the anions concentrations and the metals concentrations present in these rainwater samples were determined. This study will allow us to evaluate if effectively, Berango could be considered an area affected by the marine aerosol and anthropogenic pollutants in a diffuse way. Apart from that, a correlation between the natural and anthropogenic stressors identified in the rainwater and its possible deposition on the cementitious building materials from a specific house of Berango will be also evaluated.

5.2 Building materials in modern constructions and their related pathologies

Artificial stone is a building material that characterizes a large part of the architectural heritage built between the 19th and the 21th centuries. There are several techniques developed in the 18th-19th centuries to obtain a material that simulated natural stone. For example, mix of sands, hill and pigments applied on wood bases or plaster worked to simulate ashlars of stone, or cast iron worked for appearing as stone. Between the end of the 19th century and the first half of the 20th century, artificial stone has been achieved in large part due to the rapid growth of Portland cement use. The introduction of Portland cement, in the first decades of the 19th century and the consequent progress of the respective technologies made possible the production and the spreading of the new material with very

low costs. The use of these techniques to produce artificial stone permitted the replacement of natural stone, a more expensive product and one that was difficult to procure given the distance to quarries and the cost and expenses of quarrying stone. European and North American manufacturing centers started to produce artificial stones by earthenware or cement and several mixes of modified gypsum plasters. These kind of artificial stones were patented as artificial marbles [15].

The pathologies that can be found on artificial stones can be variable, depending on the binding agent used for its manufacture (lime, sorel cement or Portland cement). The main pathology that can be found on artificial stones is the formation of cracks. Most of the times, the presence of this cracks depends on the quality of the used raw materials and also on the water content present in the material.

Regarding cement, its chemistry is quite complex, but in principle relies on the reaction of four main compounds derived from the clay or shale and limestone or chalk (tricalcium silicate, dicalcium silicate, tricalcium aluminate and tetracalcium alumino ferrite) with water. This hydration process leads to the formation of an alkali paste that slowly stiffens and hardens with the formation of crystalline products (ettringite, calcium silicate hydrate, tricalcium aluminate, calcium hydroxide) between the cement grains. Among cement, a wide variety of cements can be found: Portland cement (ordinary, rapid-hardening, ultra-high early strength, sulfate-resisting and low heat), Portland blast-furnace cement, white cement, masonry cement, super-sulfated cement and calcium aluminate (high alumina) cement.

One of the main pathologies on cements is the formation of sulfate salts. When sulfate salts (typically of calcium, magnesium and sodium) naturally present in the ground, groundwater and on the building materials themselves come into contact with cement-based mortars, a reaction occur between the sulfates and one of the main components of the cement, the tricalcium aluminate ($Ca_3Al_2O_6$) resulting in the formation of ettringite ($CaO{\cdot}Al_2O_3{\cdot}3CaSO_4{\cdot}32H_2O$) following the reaction:

$$Ca_3Al_2O_6 + 3\ CaSO_4{\cdot}2H_2O + 26\ H_2O \rightarrow 3\ CaO{\cdot}Al_2O_3{\cdot}3CaSO_4{\cdot}32H_2O \quad \textbf{(1)}$$

Moreover, if dissolved calcium and sulfate, coming even from different sources, get in contact with the cement, can promote also the formation of ettringite:

$$Ca_3Al_2O_6 + 3\ Ca^{2+} + 3\ SO_4^{2-} + 32\ H_2O \rightarrow 3\ CaO{\cdot}Al_2O_3{\cdot}3CaSO_4{\cdot}32H_2O \quad \textbf{(2)}$$

Ettringite takes large amounts of water, which results in expansion, leading to the breakdown and failure of the cementitious material. This effect can be minimized by reducing the amount of tricalcium aluminate in the cement [16].

If water evaporated from the surface of cement whose pore solution contains high amounts of alkali sulfates, a crystallization of these salts may take place in regions close to the surface (efflorescences). Under these conditions, the crystallization pressure generated in the process may act disruptively on the material. A particularly unfavorable situation may occur if sodium sulfate present in the pore solution is allowed to crystallize at temperature above 32 ºC and the formed anhydrous solid gets subsequently in contact with water (or additional amounts of the sulfate solution) at lower temperatures. Under these conditions re-crystallization of the anhydrous sodium sulfate (thenardite, Na_2SO_4) to its hydrated form (mirabilite, $Na_2SO_4 \cdot 10H_2O$) may take place [17]. This reaction is associated with an increase of the solid volume by 315.4%. The disruptive action on cement may be particularly enhanced if the existing temperature fluctuates around the above critical temperature, as under these conditions the conversion from thenardite to mirabilite and back, may repeat itself [18].

Apart from cement, clay has been widely used as a raw material in constructions and building materials since 8000 BC. For a long time, the degradation of this construction material has been a concern. In modern constructions, the main use of clay is represented in the use of bricks. The main pathology identified in this kind of materials is the salts formation. In brick walls, these salts can be formed due to the rising dampness coming from soils [19]. Another source of harmful salts is the sea spray, which is common in coastal areas in all parts of the world. The degradation caused by this salt spray has been widely studied through short-term test in the laboratory [20]. Efflorescence resulting by salt deposits has been observed in old clay ceramic facades and results in harmful types of damaging like exfoliations or spalling [21]. The modern urban atmospheres are also responsible of some degradations in bricks due to the reactivity of acid gases with alkaline compounds present in the bulk of the bricks [22]. Due to the severe action of the sea spray, this type of degradation has also been found in several recent buildings made up of bricks [23].

5.3 References

[1] E. Bernalte, C. Marin-Sanchez, E. Pinilla-Gil, F. Cereceda-Balic, V. Vidal-Cortez, An exploratory study of particulate PAHs in low-polluted urban and rural areas of southwest Spain: concentrations, source assignment, seasonal variation and correlations with other air pollutants, Water, Air & Soil Pollution (2012) 223: 5143-5154.

[2] W. Shao, Effectiveness of water protection policy in China: A case study of Jianxing, Science of the Total Environment (2010) 408: 690-701.

[3] D. Monaco, A. Riccio, E. Chianese, P. Adamo, S. Di Rosa, M. Fagnano, Chemical characterization and spatial distribution of PAHs and heavy hydrocarbons in rural sites of Campania Region, South Italy, Environmental Science & Pollution Research (2015) Ahead of Print. DOI 10.1007/s11356-015-4733-y

[4] I. Martínez-Arkarazo, M. Angulo, L. Bartolomé, N. Etxebarria, M. A. Olazabal, J. M. Madariaga, An integrated analytical approach to diagnose the conservation state of building materials of a palace house in the metropolitan Bilbao (Basque Country,North of Spain), Analytica Chimica Acta (2007) 584: 350–359.

[5] Labein Fundation, Action Plan for air quality in the region of the Bajo Nervion. Diagnosis of air pollution in the town of Getxo. Basque Goverment, Basque Country (2006).

[6] B. J. Colston, D. S. Watt, H. L. Munro, Environmentally induced stone decay: the cumulative effects of crystallization–hydration cycles on a Lincolnshire oopelsparite limestone, Journal of Cultural Heritage (2001) 2: 297–307.

[7] S. W. Massey, The effects of ozone and NO_x on the deterioration of calcareous stone, Science of the Total Environment (1999) 227: 109–121

[8] A. Charola, J. Pühringer, M. Steiger, Gypsum: a review of its role in the deterioration of building materials, Environmental Geology (2007) 52: 339–352.

[9] C. Grossi, A. Bonazza, P. Brimblecombe, I. Harris, C. Sabbioni, Predicting twenty-first century recession of architectural limestone in European cities, Environmental Geology (2008) 56: 455–461.

[10] E. Dotsika, D. Psomiadis, D. Poutoukis, B. Raco, P. Gamaletsos, Isotopic analysis for degradation diagnosis of calcite matrix in mortar, Analytical & Bioanalytical Chemistry (2009) 395: 2227–2234.

[11] M. Maguregui, A. Sarmiento, I. Martínez-Arkarazo, M. Angulo, K. Castro, G. Arana, N. Etxebarria, J. M. Madariaga, Analytical diagnosis methodology to evaluate nitrate impact on historical building materials, Analytical & Bioanalytical Chemistry (2008) 391: 1361 –1370.

[12] N. Bakaoukas, J. Kapolos, A. Koliadima, G. Karaiskakis, New gas chromatographic instrumentation for studying the action of sulfur dioxide on marbles, Journal of Chromatography A (2005) 1087: 169–176.

[13] Y. Bai, G. E. Thompson, S. Martinez-Ramirez, S. Brüeggerhoff, Mineralogical study of salt crusts formed on historic building stones, Science of the Total Environment (2003) 302: 247–251.

[14] A. Chabas, D. Jeannette, Weathering of marbles and granites in marine environment: petrophysical properties and special role of atmospheric salts, Environmental Geology (2001) 40: 359–368.

[15] T. Proudfoot, Artificial Stone. The Dictionary of Art, Grove's Dictionaries Inc., New York (1996).

[16] D. S. Watt, Building Pathology. Principles and Practice. Second Edition. Blackwell Publishing Oxford, UK (2007).

[17] M. A. Halliwell, N. J. Crammond, in: C. Sjostrom (Ed.), Durability of Building Materials and Components. E&FN Spon, London (1996) pp. 235-244.

[18] J. Skalny, J. Marchand, I. Odler. Sulfate Attack on Concrete, Spon Press, London, UK (2002).

[19] I. Rörig-Dalgaard, L. M. Ottosen. Diffusion and electromigration in clay bricks influenced by differences in the pore system resulting from firing, Construction Building Material (2012) 27: 390–397.

[20] Z. S. G. Silva, J. A. R. Simão, The role of salt fog on alteration of dimension stone, Construction & Building Material (2009) 23: 3321–3327.

[21] B. Lubelli, R. Hees, C. Groot. The role of sea salts in the occurrence of different damae mechanisms and decay patterns of brick masonry, Construction & Building Material (2004) 18: 119–124.

[22] M. Maguregui, A. Sarmiento, R. Escribano, I. Martínez-Arkarazo, K. Castro, J. M. Madariaga, Raman spectroscopy after accelerated ageing tests to assess the origin of some

decayed products found in real historical bricks affected by urban polluted atmospheres, Analytical & Bioanalytical Chemistry (2009) 395: 2119 –2129.

[23] B. Sena da Fonseca, J. A. R. Simao, C. Galhano, Effect of coastal environment in clay facing bricks and roof tiles. 1st Annual International Interdisciplinary Conference, AIIC (2013) Azores, Portugal, 432.

RESEARCH ARTICLE 4

Nature and origin of white efforescence on bricks, artificial stones, and joint mortars of modern houses evaluated by portable Raman spectroscopy and laboratory analyses.

H. Morillas, M. Maguregui, J. Trebolazabala, J. M. Madariaga

Spectrochimica Acta Part A: Molecular and Biomolecular Spectroscopy (2015) 136: 1195–1203.

Nature and origin of white efflorescence on bricks, artificial stones, and joint mortars of modern houses evaluated by portable Raman spectroscopy and laboratory analyses

ABSTRACT

Bricks and mortar currently constitute one of the most important building materials used in the construction of most modern facades. The deterioration of these materials is caused primarily by the impact of numerous external stressors, while poor manufacturing quality, particularly of mortars, can also contribute to this process. In this work, the non-invasive Raman spectroscopy technique was used to identify the recently formed deterioration compounds (primarily sulfates and nitrates) in bricks, artificial stones, and joint mortars from detached houses in the Bilbao metropolitan area (Basque Country, North of Spain), as well as to investigate the deterioration processes taking place in these materials. Additionally, to confirm and in some cases complement the results obtained with Raman spectroscopy, SEM-EDS and XRD measurements were also carried out.

Keywords: Portable Raman spectroscopy, Brick Mortar, Sulfates, Nitrates.

1. Introduction

Bricks and stones are two of the most durable building materials, which in most cases can be preserved for years and generally do not require any maintenance [1]. Owing to the industrial development in the nineteenth century, the use of bricks attained great importance and became a standard in the construction of homes. The durability of well-manufactured brick is comparable to that of stone-based materials, while the former has the advantage of being more easily shaped.

Mortar, a mixture of inorganic binders, sand, and water, has been in use since the time of the ancient Egyptians. Depending on the type of mortar and the components being joined, different additives can be used in the mixture [2].

Artificial stone is another material commonly used in construction, the generalized use of which dates from the nineteenth century. It consists primarily of a mixture of modern (usually a Portland type) cement, siliceous sand, gravel, and water. Depending on the proportion of each component in the mixture, the artificial stone can be produced with properties such as porosity, capillarity, and level of thermal insulation that differ from those of natural stones [3, 4]. Although there are buildings that over hundreds of years have nearly maintained their original aesthetic and mechanical features, there are several examples of impacts on the walls (both inside and outside) of such historical constructions [5–8], caused primarily by modern urban-industrial environments. Moreover, such environments particularly affect recently built facades, with significant degradations showing after only a few decades [9]. To slow down such degradations, new processes based on the use of coating materials have been proposed in recent years [10]. Building facades suffer from various degrees of exposure to heat, humidity, atmospheric acidic gases, and wind pressure as well from infiltration by aqueous solutions. Considering these sources of deterioration, several examples of building material degradation are commonly observed:

- Brick walls exhibiting soil and green plant growth from the ground level until a given height.
- The detachment of bricks above windows when the joint mortar reaches a high proportion of white efflorescence crystals.
- Planters enclosed in the facade exhibiting efflorescence after a few years of watering.

- The accumulation of white salts on facades when the surface is wetted with a salt solution (wind most likely moves ions dissolved in rainwater and the salts precipitate when the surface is wetted).
- The vertical displacement of white efflorescence caused by green grass on the street level.

In all of these cases, infiltration water carrying dissolved ions is the primary cause of the crystallization of salts. This takes place when the infiltration water reaches supersaturation and the thermodynamic characteristics of the media are adequate for the formation of a crystal nucleus. The crystallizations can occur at the surface (efflorescence) or within the porous structure of the building materials (subefflorescence). The impact of water infiltration (both crystallization and the dissolving of salts as a consequence of rainwater) over an extended period of time can contribute to the disintegration of building material [11]. On the other hand, mineralogical and chemical changes originating from salt mineralizations can induce structural changes by promoting cracks and disintegration [12] in joint mortar, bricks, and even artificial stones. Recently, laboratory simulations and accelerated weathering experiments that reproduce environmental attacks on samples of historical bricks have been carried out to establish the nature and formation mechanisms of such efflorescences [13]. Numerous studies can be found in the literature that span a wide range of useful analytical techniques used to identify the damage promoted by efflorescence and the soluble salts present in building materials [14,15]. Techniques such as optical microscopy, X-ray diffraction, electron scanning microscopy, and thermogravimetric analysis [16, 17] have been used to characterize the efflorescences as well as the chemical and mineralogical changes in building materials. Infrared and Raman spectroscopy can also now be used as an alternative analytical technique for this purpose [18], especially since the development of portable instrumentation to perform analyses in the field [19, 20].

In this work, a simple and non-destructive Raman spectrometer was used to perform a field analysis in which both the original and deterioration compounds present in facades from recently erected houses located in the metropolitan area of Bilbao (Basque Country, North of Spain) were characterized. To confirm and complement these in situ measurements, additional analyses were conducted in the laboratory using a benchtop Raman spectrometer as well as the SEM-EDS and XRD techniques. The primary materials used in the facades of the selected houses include bricks, artificial stones, and joint mortars. The facades were neither painted nor had a protection layer against rain or infiltration water.

2. Materials and methods

2.1. Description of the samples and locations

The studied facades were from houses built in 2002 and located in a residential zone of the Metropolitan area of Bilbao (Basque Country, Northern Spain, see Figure 1A). All of these homes have two floors, a terrace, and a garden. The primary materials used in the construction of their facades are bricks, artificial stones, and their respective joint mortars. A previous screening from different houses in the same residential area was performed using a portable Raman spectrometer. Three facades from the areas most by impacted by environmentally driven deterioration were selected to perform the study:

- House 1 has a southwest-oriented facade of exposed brick connected with joint mortar. This facade has direct contact with the green grass of the garden but is protected from the main winds and rainfall.

- House 2 has a southwest-oriented facade built from artificial stones supporting the garden, the soil of which meets the façade at the rear side of the home. The analyzed portion is protected from the main winds and rainfall, although the garden at the back of the home is exposed to the latter.

- House 3 has a northwest-oriented facade composed of exposed brick connected with joint mortar. The orientation of this façade exposes it to both the main winds and rainfall.

A schematic representation of the building pathologies identified in each of these detached houses can be viewed in Figure 1B. White efflorescence samples as well as some detached brick, artificial stone, and joint mortar samples were collected from the areas showing different Raman features during similar climatic conditions (absence of rain for 15 days, low temperature between 2 ^{o}C and 5 ^{o}C) in December 2012 and January 2013. The samples taken never exceeded 2 x 2 cm in size.

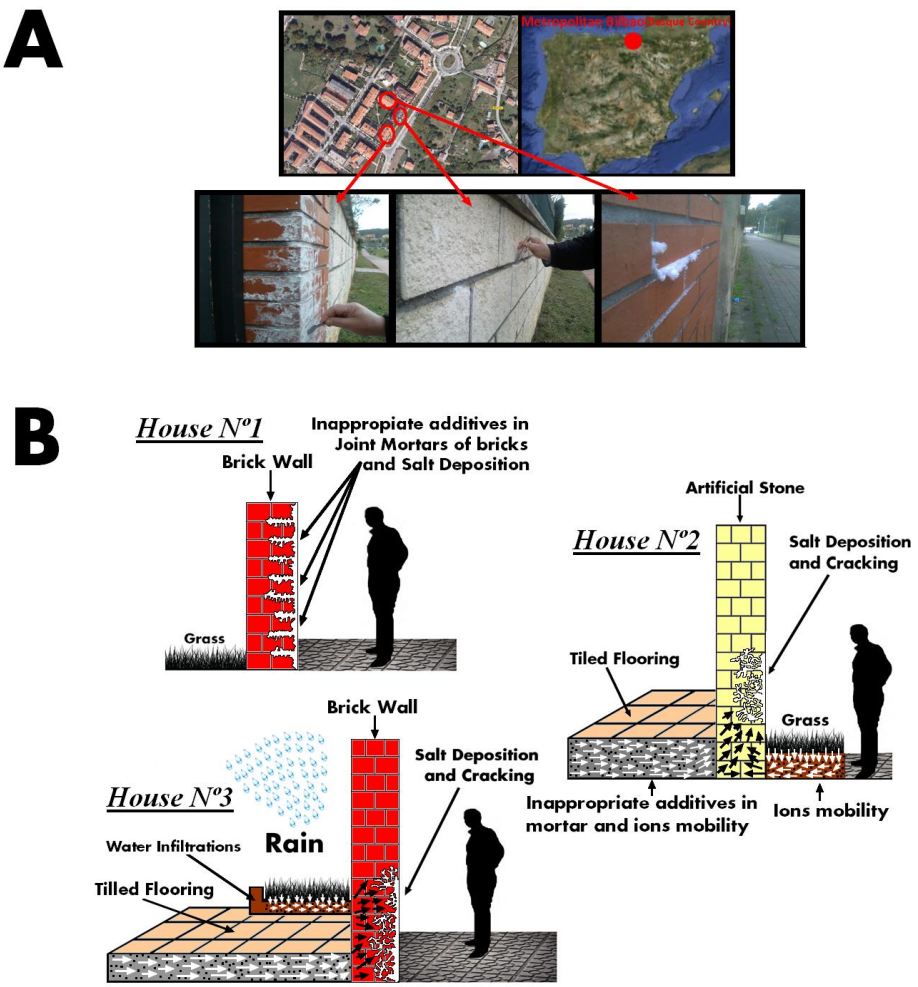

Figure. 1. (A) Location and details of the analyzed areas containing the detached houses (metropolitan Bilbao, North of Spain). (B) Schematic representation of the pathologies identified in the three detached houses considered in this work.

2.2. Instrumentation

Two Raman spectrometers were employed for the characterization of the samples: a portable spectrometer for the in situ or field analysis in which samples are screened without being removed and a benchtop spectrometer for an in-depth study to identify the maximum number of compounds in each sample. The portable innoRam™ (B&WTEK$_{INC.}$, Newark, USA) Raman spectrometer utilizes a 785 nm excitation laser and has a maximum output power of 300 mW. Variable attenuation of the output power was achieved through the implementation of filters, which allowed for the reduction of the output power down to 1% of the maximum. The spectra were typically collected using a wavelength range of 100–2200 cm^{-1}, although in some measurements larger ranges were used. The exposure time for each spectrum ranged from 2 to 10 s, and two to fifteen repeated acquisitions were averaged to improve the signal-to-noise ratio. The Raman microprobe (approximately 0.1

mm focal spot size) can be operated by hand or mounted on a manual X_Y_Z manipulator with a micro video camera to assist in the alignment (MICROBEAM S.A, Barcelona, Spain).

The laboratory-based measurements were carried out using a Renishaw RA100 Raman microprobe (Renishaw, Gloucestershire, UK), which also utilizes a 785 nm excitation laser. The microscopic analysis was performed using 20x and 50x long-range objective lenses mounted in the head of the Raman microprobe, which also has a micro-video camera. The spectra were typically collected from 100 to 3000 cm^{-1}, although larger wavelength ranges were also employed in some of the measurements. The exposure time for each spectrum ranged from 2 to 10 s, and ten to fifty repeated acquisitions were averaged to increase the signal-to-noise ratio. For both measurements, the laser power was attenuated to avoid thermal decomposition of the sample. Both Raman instruments were calibrated daily using the 520 cm^{-1} Raman band of a crystalline silicon chip. Spectral acquisition with the innoRam™ and RA100 spectrometers was performed using the BWSpec™ 3.26 software package ($B\&WTEK_{INC.}$) and the Renishaw Wire 3.2 software package, respectively. The Raman data were interpreted by comparing the acquired spectra with the spectra of pure standard compounds obtained from the e-VISNICH dispersive Raman database, which contains Raman spectra of natural, industrial and cultural heritage compounds, following a methodology described elsewhere [21]. Open access Raman spectral databases (e.g., RRUFF [22]) were also used in assigning some of the Raman bands. The spectral interpretation and data treatment were carried out using the GRAMS/AI 7.02 software package (Thermo Fisher Scientific Inc., Waltham, USA).

To corroborate some of the results, X-ray diffraction analyses were performed with a PANalytical Xpert PRO powder diffractometer equipped with a copper tube ($\lambda_{CuK\alpha media}$ = 1.5418 Å, $\lambda_{CuK\alpha1}$ = 1.54060 Å, $\lambda_{CuK\alpha2}$ = 1.54439 Å), vertical goniometer (Bragg–Brentano geometry), programmable divergence aperture, automatic sample changer, secondary graphite monochromator, and PixCel detector. The operating conditions for the Cu tube were 40 kV and 40 mA, and the angular range (2θ) was scanned between 5^0 and 70^0. The treatment of the diffractogram data and the identification of the mineral phases present was carried out with the X'pert HighScore (PANalytical) software package in combination with the Powder Diffraction File (PDF-2) database (International Centre for Diffraction Data – ICDD, Pennsylvania, USA).

For the acquisition of electron images and the determination of elemental compositions in the samples, SEM-EDS analyses were carried out using an EVO® 40 Scanning Electron Microscope (Carl Zeiss NTS GmbH, Germany) coupled to an X-Max Energy- Dispersive X-ray

spectroscopy system (Oxford Instruments, Abingdon, Oxfordshire, United Kingdom). The SEM images were obtained under high vacuum using an acceleration voltage of 20 kV and a working distance of 6–13 mm. The images were collected using a secondary electron detector at different magnifications (up to 10,000x). The elemental analysis was carried out using an 8.5 mm working distance, a 35° take-off angle, and an acceleration voltage of 20 KV. An integration time of 50 s was employed to achieve a good signal to noise ratio.

3. Results and discussions

3.1. House 1

The Raman analyses were conducted for two types of building materials used in this house. First, efflorescent samples present on bricks and the surface of the joint mortars of artificial stones were analyzed. The Raman spectra obtained from efflorescence on brick exhibited a band at 1049 cm^{-1} (see Figure 2A).

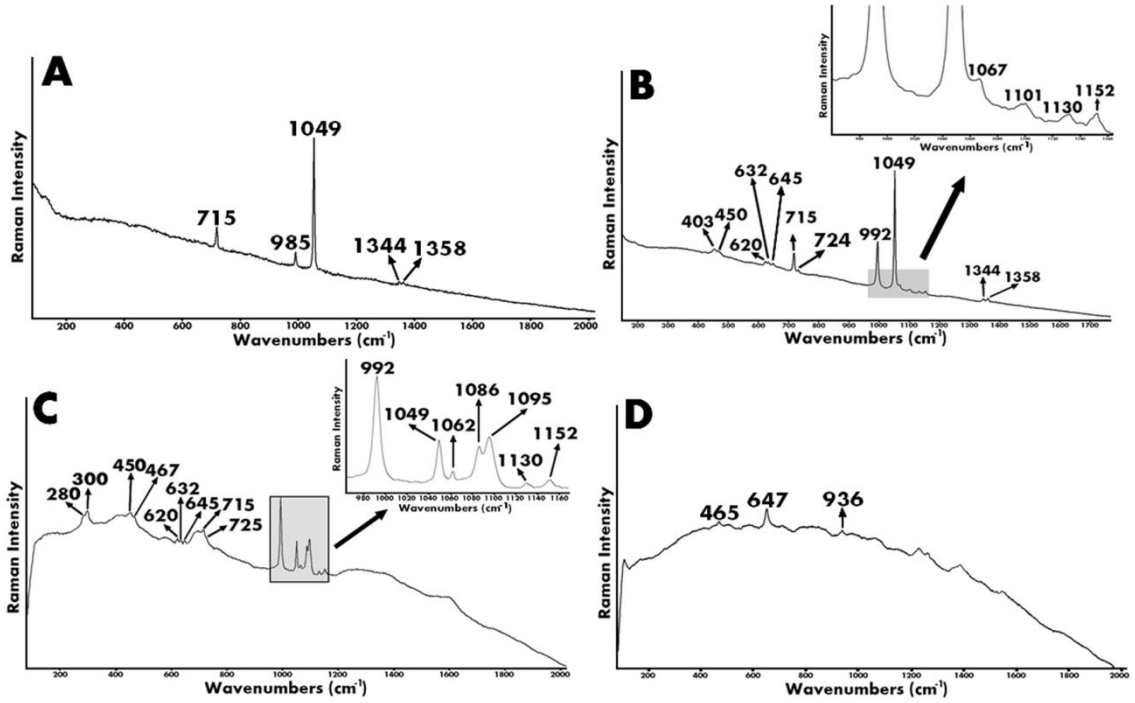

Figure. 2. (A) Raman spectrum of efflorescences in bricks indicating the presence of epsomite ($MgSO_4 \cdot 7H_2O$) and niter (KNO_3). (B) Raman spectrum of mortar showing bands of thenardite (Na_2SO_4), niter (KNO_3), and nitratine ($NaNO_3$). (C) Raman spectrum of efflorescences in mortar showing bands of thenardite (Na_2SO_4), niter (KNO_3), trona ($Na_3(HCO_3)(CO_3) \cdot 2H_2O$), calcite ($CaCO_3$), and dolomite ($MgCaCO_3$). (D) Raman spectrum of joint mortar showing the bands of quartz (SiO_2), pyrolusite (MnO_2), and anapaite ($Ca_2Fe^{2+}(PO_4)_2 \cdot 4\ H_2O$).

The band at 1049 cm^{-1} can be assigned to the ν_1 symmetric stretching mode of the NO_3^- group of niter (KNO_3) or nitrocalcite ($Ca(NO_3)_2 \cdot 4H_2O$) [20,23]. In certain Raman spectra, in addition to the bands at 1049 and 985 cm^{-1}, bands at 715, 1344, and 1358 cm^{-1} were also identified (see Figure 2A). The presence of these bands confirms that niter is the main nitrate salt crystallized in these samples. In addition to the nitrate Raman bands, a band at 985 cm^{-1} corresponding to the ν_1 symmetric stretching mode of the SO_4^{2-} group in epsomite ($MgSO_4 \cdot 7H_2O$), was also identified in these efflorescences (see Figure 2A). Epsomite has been identified in efflorescences on bricks in previous studies [24]. Furthermore, in several spectra acquired from the same efflorescences, a band at 992 cm^{-1} originating from thenardite (Na_2SO_4) was also identified, as discussed below.

The Raman analyses performed on efflorescences from the joint mortars revealed three main compounds, present either mixed together or alone. The in situ spectra displayed only the main bands of thenardite and niter at 992 and 1049 cm^{-1}, respectively. The main band at 992 cm^{-1} corresponds to the ν_1 symmetric stretching mode of the SO_4^{2-} group in thenardite. In the laboratory analyses, in addition to the main band of thenardite, bands originating from the sulfate group were also observed at 403, 450, 620, 632, 645, 992, 1101, 1130, and 1152 cm^{-1}. Moreover, the ν_4 anti-symmetric bending (715 cm^{-1}), ν_1 symmetric stretching (1049 cm^{-1}), and ν_3 anti-symmetric stretching modes (1344 and 1358 cm^{-1}) of the NO_3^- group of niter were also observed, together with the ν_4 anti-symmetric bending (724 cm^{-1}) and ν_1 symmetric stretching (1067 cm^{-1}) modes of the NO_3^- group of nitratine ($NaNO_3$) (see Figure 2B). Sodium nitrate has also been identified by Raman spectroscopy in previous studies on carbonate substrate-based mortars [25]. Sodium nitrate can appear as a deterioration product originating from trona ($Na_3(HCO_3)(CO_3) \cdot 2H_2O$), which can be present in the substrate material. Trona can be formed in the mortar setting, and upon air exposure this mixed carbonate–bicarbonate can be attacked by ammonium nitrate (most likely originating from nitrate salts transported by infiltration waters), leading to the formation of sodium nitrate through the following reaction:

$$3NH_4NO_3\,(dis) + Na_3(HCO_3)(CO_3) \cdot 2H_2O\,(s) \leftrightarrows 3NaNO_3\,(s) + 2HCO_3^- + NH_3(g) + 2NH_4^+ \quad \textbf{(1)}$$

In the Raman analysis performed on small dots resembling efflorescence located in the holes of the joint mortar samples, the main bands of thenardite and niter as well as a band at 1062 cm^{-1} belonging to trona were observed (see Figure 2C). The identification of trona in the joint mortar reinforces the hypothesis discussed above regarding nitratine formation. Additionally, peaks corresponding to the ν_1 symmetric stretching mode of the CO_3^{2-} group of calcite ($CaCO_3$) at 1086 cm^{-1} and the m1 symmetric stretching mode of the CO_3^{2-} group of

dolomite ($MgCa(CO_3)_2$) at 1095 cm^{-1} [26] were observed. Moreover, the signal-to-noise ratio of the spectra was high enough to allow secondary bands of these major compounds to be observed (see Figure 2C). In addition to the deterioration compounds located in the bulk of the joint mortars, the bending vibrations of the intra-tetrahedral O–Si–O angles from quartz (SiO_2) located at 465 cm^{-1} and the anti-symmetric stretching mode of the MnO_6 octaedra in pyrolusite (MnO_2) at 647 cm^{-1} were also identified (see Figure 2D). The presence of pyrolusite in the joint mortars was also confirmed via SEM-EDS and XRD analyses (see Figure 3A and B).

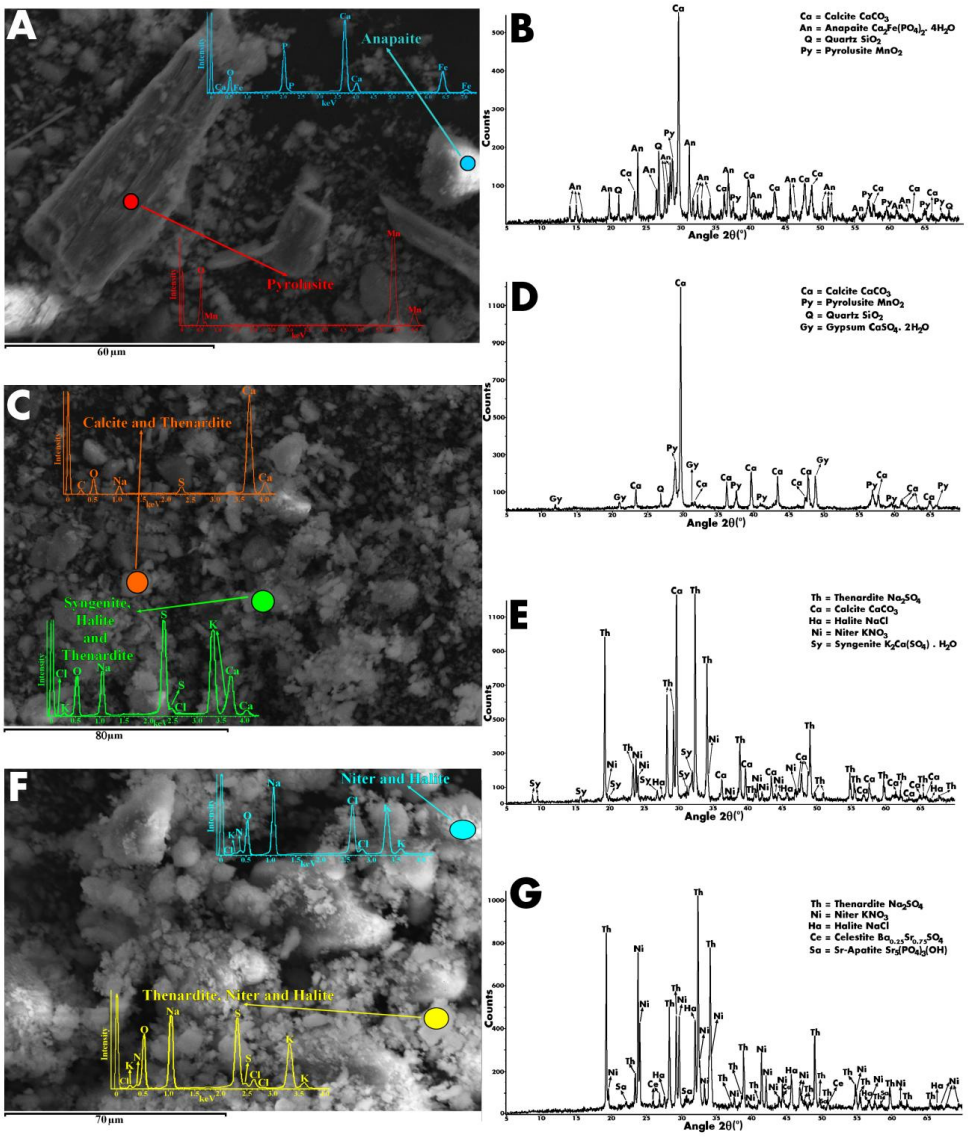

Figure. 3. (A) SEM-EDS results of joint mortar from House 1 showing pyrolusite and anapaite. (B) XRD diagram of joint mortars from House 1 showing calcite, anapaite, quartz and pyrolusite. (C) SEM-EDS of efflorescences from House 2 showing calcite, thenardite, syngenite, and halite. (D) XRD diagram of whitish patinas from House 2 showing calcite, anapaite, quartz, and pyrolusite. (E) XRD diagram of another patina from House 2 showing thenardite, calcite, niter, syngenite, and halite. (F) SEM-EDS of whitish patina from House 3 showing thenardite, niter, and halite. (G) XRD diagram of whitish patina from House 3 showing thenardite, niter, halite, celestite, and strontium apatite.

Some groups have also previously reported the presence of pyrolusite in mortars [27]. A band at 936 cm^{-1} that can be assigned to the m1 symmetric stretching mode of the PO_4^{3-} group of anapaite ($Ca_2Fe_2(PO_4)_2 \cdot 4H_2O$) (see Figure 3B) was also identified in the Raman measurements of the joint mortars. The presence of anapaite in the joint mortar was also confirmed via SEM-EDS and XRD (see Figure 3A and B). Although there is no mention of the use of anapaite as additive in the literature, it is well known that phosphates are commonly used to retard the setting of concrete [28, 29].

3.2. House 2

Several whitish patinas were identified on the artificial stones of the facade from House 2 (see Figure 4). To the best of our knowledge, there are no literature reports on the analysis of this type of material using Raman spectroscopy. In this work, the whitish patinas were characterized in situ as well as analyzed in the laboratory using the previously mentioned techniques. The Raman spectra of these patinas exhibited a band at 992 cm^{-1} belonging to the deterioration compound thenardite. Moreover, a band was identified at 647 cm^{-1} as corresponding to pyrolusite, which is present in the original material. Additionally, in some of the Raman spectra, bands at 578 and 643 cm^{-1} assignable to birnessite-type manganese oxides were also observed [30]. XRD measurements confirmed the presence of pyrolusite as well as that of calcite, quartz, and gypsum ($CaSO_4 \cdot 2H_2O$) (see Figure 3D). Additional sulfate compounds were clearly identified in the efflorescences from the whitish patina. For example, the spectrum in Figure 4A displays bands at 980, 1008, 1025, and 1086 cm^{-1} that correspond to the ν_1 symmetric stretching mode of the SO_4^{2-} group of syngenite ($K_2Ca(SO_4) \cdot H_2O$) and gypsum ($CaSO_4 \cdot 2H_2O$), to the ν_3 asymmetric stretching mode of the SO_4^{2-} group of (para)coquimbite ($Fe_2(SO_4)_3 \cdot 9H_2O$), and to the ν_1 symmetric stretching mode of the CO_3^{2-} group of calcium carbonate, respectively. In addition, a band at 280 cm^{-1} that can be assigned to calcite or aragonite is also present in the same spectrum (Figure 4A). Moreover, the appearance of another band at 711 cm^{-1} suggests that calcite is the main polymorph of calcium carbonate present in the sample.

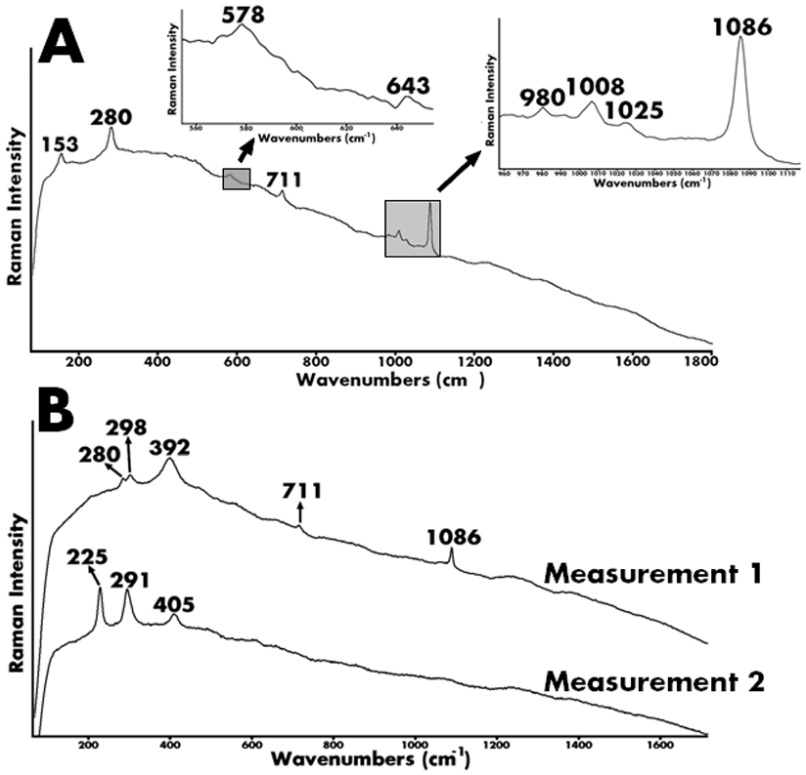

Figure. 4. (A) Raman spectrum of whitish patina on artificial stone showing bands of manganese oxide (MnO), syngenite ($K_2Ca(SO_4) \cdot H_2O$), gypsum ($CaSO_4 \cdot 2H_2O$), (para)coquimbite ($Fe_2(SO_4)_3 \cdot 9H_2O$) and calcite ($CaCO_3$). (B) *Measurement 1*: Raman spectrum of the same sample of artificial stone, showing bands belonging to limonite ($Fe_2O_4 \cdot H_2O$) and calcite ($CaCO_3$). *Measurement 2*: Raman spectrum of artificial stone showing bands of hematite (Fe_2O_3).

The Raman identification of (para)coquimbite was carried out based on the presence of its main band at 1025 cm^{-1}; however, it is difficult to affirm whether coquimbite, paracoquimbite polymorph, or a mixture of both is present in the sample on the basis of only this main band. (Para)coquimbite can be formed in these samples as a consequence of a sulfation process involving iron (III) oxides and oxyhidroxides [31]. Both iron oxyhidroxides (e.g., limonite ($Fe_2O_4 \cdot H_2O$) with main bands at 298 and 392 cm^{-1}) and iron (III) oxides (e.g., hematite (Fe_2O_3) with main bands at 225, 291, and 405 cm^{-1}) were identified in the sample (see Figure 4B). These iron oxides and hydroxides can react on an acidic and highly sulfated surface, resulting in the corresponding sulfates, which are known to be able to cause serious structural damages over time [32]. This type of reaction is made possible by the high amount of sulfates in solution on the surface of this material [33]. The XRD analysis performed on the same sample does not reveal the presence of (para)coquimbite. Because XRD can only detect compounds whose abundance is higher than the 5% of the total amount of the sample, (para)coquimbite may be a minor/trace component in this sample. On the contrary, compounds such as thenardite, calcite, niter, syngenite, and halite were clearly detected using this technique (see Figure 3E). The presence of halite (NaCl) and syngenite is

closely connected to the influence of marine aerosol [34]. The studied houses are located approximately 2 km from the sea; therefore, the influence of marine aerosol cannot be rejected. To corroborate the XRD data SEM-EDS analyses were also carried out, from which mineralization products containing Ca, C, Na, S, K, and Cl were detected (see Figure 3C). These results are in accordance with the XRD observations.

3.3. House 3

Raman measurements were carried out on the efflorescences from the joint mortars of the bricks used in the construction of House 3. These efflorescences appear as acicular crystals growing from the joint mortar when viewed using a microscope. It is worth noting that the samples were collected from the northwest-facing facade of the house, which experiences the least amount of sunlight. The Raman spectra revealed the presence of thenardite in the samples studied. In addition to the main band of this sodium sulfate located at 992 cm^{-1}, a small band at 975 cm^{-1} was also identified (see Figure 5A) as the ν_1 symmetric stretching mode of the SO_4^{2-} group of mascagnite ($(NH_4)_2SO_4$). This mineral is present neither in the original composition of the brick nor in the joint mortar and therefore can be considered a deterioration compound. House 3 has a garden that is connected to the portion of the façade where these efflorescences were identified. This arrangement enables infiltration waters to carry ammonium nitrate (NH_4NO_3) from the decomposition of the plants and green grass of the garden to the facade. The sulfate compounds included intentionally in the original facade composition can dissolve and react with the ammonium, resulting in the formation of ammonium sulfate. In this reaction, the cation partnered with the sulfate reacts with the nitrate ions carried in the infiltration waters to form the respective nitrate mineralization products. The described reaction pathway can be considered as:

$$CaSO_4 \cdot 2H_2O \rightarrow Ca^{2+} + SO_4^{2-} + 2H_2O \quad \textbf{(2)}$$

$$2NH_4NO_3 + CaCO_3 \rightarrow Ca(NO3)2 + HCO_3^- + NH_3(g) + NH_4^+ \quad \textbf{(3)}$$

$$2HCO_3^- + FeO \rightarrow FeCO_3 + 2H_2O \text{ or mixed carbonate} \quad \textbf{(4)}$$

$$2NH_4^+ + SO_4^{2-} \rightarrow (NH_4)_2SO_4 \quad \textbf{(5)}$$

Considering that for the in situ measurements, information from the joint mortar can also be obtained during the direct measurements of the efflorescences on the joint mortars from the brick, original joint mortar without any visual efflorescence was simultaneously characterized. The main components identified by Raman spectroscopy were calcite, quartz, and carbon, indicating that the joint mortar used is a calcareous mortar. In areas of the joint

mortar where efflorescence was visually identified, the typically observed bands of charcoal (C) at 1320 and 1595 cm^{-1}, and of thenardite at 450, 467, 620, 632, 645, 992, 1130, and 1152 cm^{-1} were obtained. Additionally, new bands at 166, 280, 718, and 1090 cm^{-1} were also identified. These bands can be assigned to ankerite ($CaFe(CO_3)_2$), which is a mixed carbonate of calcium and iron (see Figure 5B). The bands at 166 and 280 cm^{-1} correspond to the ionic translations and librations (restricted rotation) of the CO_3^{2-} group of ankerite, while the bands at 718 cm^{-1} and 1090 cm^{-1} correspond to the ν_4 anti-symmetric bending vibration and the m1 symmetric stretching vibration of the same moiety. The identification of mixed calcium and iron carbonate suggest that the reaction pathway outlined above is taking place in this sample (see reaction (4) in the previous reaction pathway). An additional analysis on other efflorescence samples taken from the joint mortar (see Figure 5C) revealed the presence of calcite (153, 280, 711, and 1086 cm^{-1}), epsomite (985 cm^{-1}), charcoal (1320 and 1595 cm^{-1}), and limonite (392 cm^{-1}). In the areas where acicular efflorescence was sampled, thenardite (450, 467, 620, 632, 645, 992, 1101, 1130, and 1152 cm^{-1}), niter (715, 1049, 1344, and 1358 cm^{-1}), nitratine (184, 724, 1067, and 1385 cm^{-1}) and trona (1062 cm^{-1}) were identified by the Raman spectra, as shown in Figure 5D.

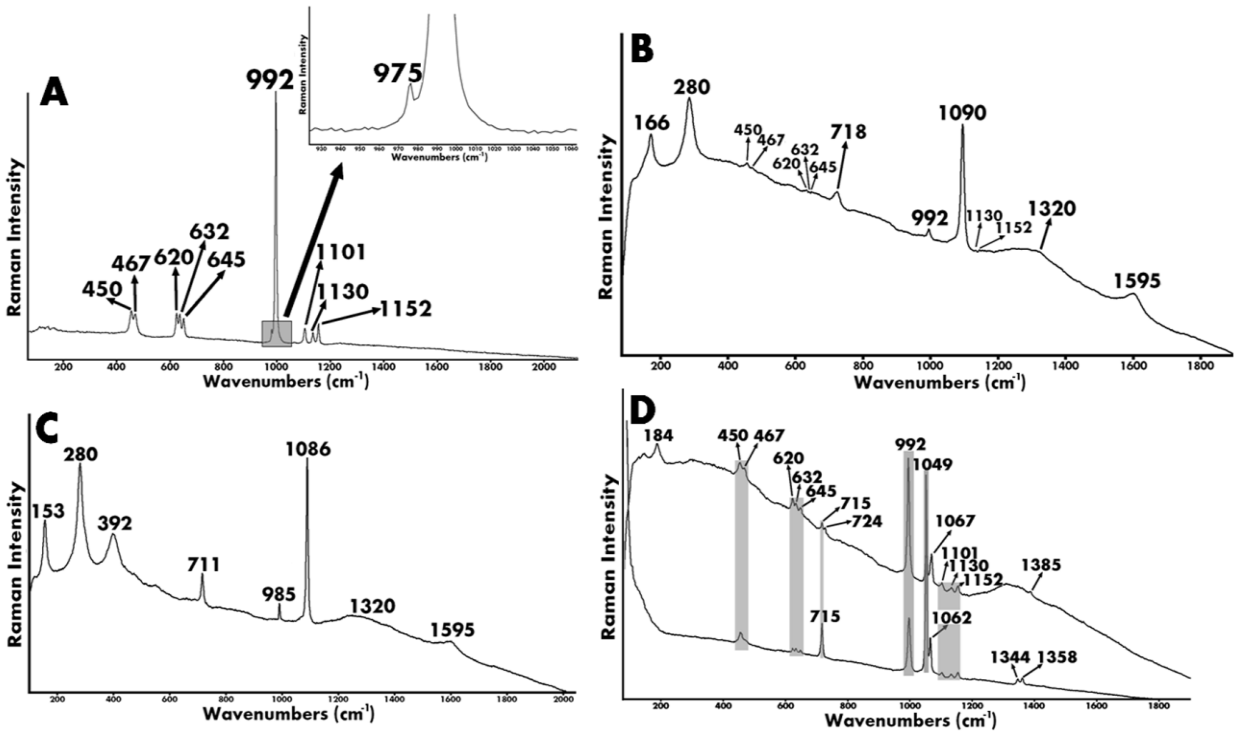

Figure. 5. (A) Raman spectrum of efflorescences on bricks showing bands of thenardite (Na_2SO_4) and a band at 975 cm^{-1} assigned to mascagnite ($(NH_4)_2SO_4$). (B) Raman spectrum of mortars showing bands of thenardite (Na_2SO_4), charcoal (C) and ankerite ($CaFe(CO_3)_2$). (C) Raman spectrum of calcite ($CaCO_3$), epsomite ($MgSO_4 \cdot 7\ H_2O$), charcoal (C), and limonite ($Fe_2O_4 \cdot H_2O$). (D) Raman spectrum of efflorescence showing bands of thenardite (Na_2SO_4), niter (KNO_3), nitratine ($NaNO_3$), and trona ($Na_3(HCO_3)(CO_3) \cdot 2H_2O$).

To confirm the presence of some of these compounds in these efflorescences, XRD and SEM-EDS analyses were also carried out. The XRD analysis of the efflorescences revealed the presence of thenardite, niter, halite, celestite ($Ba_{0.25}Sr_{0.75}SO_4$), and strontium apatite ($Sr_5(PO_4)_3OH$) (see Figure 3G). These XRD and SEM-EDS results complement those obtained by Raman spectroscopy because these compounds were not detected with the latter technique. It is therefore important to emphasize that the combined used of the three techniques employed is an adequate strategy for extracting the maximum information on the mineralization products present in recently formed efflorescences. The SEM-EDS measurements performed on these efflorescences revealed the presence of S, Na, N, K, and Cl (see Figure 3F), which confirms the crystallization of thenardite, niter, and halite. The analysis performed via SEM-EDS did not exhibit the presence of Ba, Sr, and P in the efflorescences. However, the fact that in contrast to XRD, SEMEDS is a microscopic analysis technique must be taken into account. It is likely that celestite and apatite were not present in the selected microscopic areas used in the EDS analysis; therefore, the elements mentioned above were not detected with EDS.

4. Conclusions

The principal source of deterioration affecting the building materials present in the modern houses studied in this work is the mineralization of salts. This type of crystallization is primarily external (efflorescence), which affects the integrity and durability of the materials as well as the aesthetic appearance of the facades. The data obtained from the analyses carried out mainly in situ and in the laboratory, gives an overview of the deterioration products that are present in bricks, artificial stones, and their joint mortars sampled from recently constructed houses. The Raman spectroscopy, XRD, and SEM-EDS results revealed the presence of thenardite (Na_2SO_4) in most of the efflorescences from all of the houses studied. Mirabilite ($Na_2SO_4 \cdot 10H_2O$) and thenardite (Na_2SO_4) formation on porous building materials such as mortar is a common pathology cited by many authors [35,36]. The identification of mirabilite or thenardite by Raman spectroscopy is rather difficult in general because their main spectral bands are quite close (approximately 989 cm^{-1} for mirabilite and approximately 992–993 cm^{-1} for thenardite) [37]. Nevertheless, in this work, well-resolved Raman spectra that also contained medium and small-intensity bands were obtained, allowing us to affirm that sodium sulfate is mainly crystallized as thenardite. The deterioration process that generates these types of crystallized sulfate salts inside the pores of the material leads to possible cracks and even breaks in the material during the transition from thenardite to mirabilite. The change in the number of waters of hydration during this transition causes increases and/or decreases in the volume of the crystallized sodium

sulfates. This change in volume promotes the expansion and contraction of the material in which these salts are crystallized, leading to fissures and cracks. According to the results presented in this work, we propose that the mortars used in the construction of these houses are composed of a mixture of additives such as K_2O, MgO, Na_2O, SiO_2, MnO_2, CaO, and Fe_2O_x. This conclusion can be explained by considering the original and deterioration products that have been identified. As many authors have noted, the majority of mortars generally contain these types of additives, and the difference between mortars is based on their proportions. For example, the resistance of mortars to deterioration varies according to these proportions; therefore, the proper mixture of the original components and additives must be selected according to the environment in which these building materials are going to be used. Figure 6 displays a schematic representation of the deterioration pathway identified in the analyzed building materials.

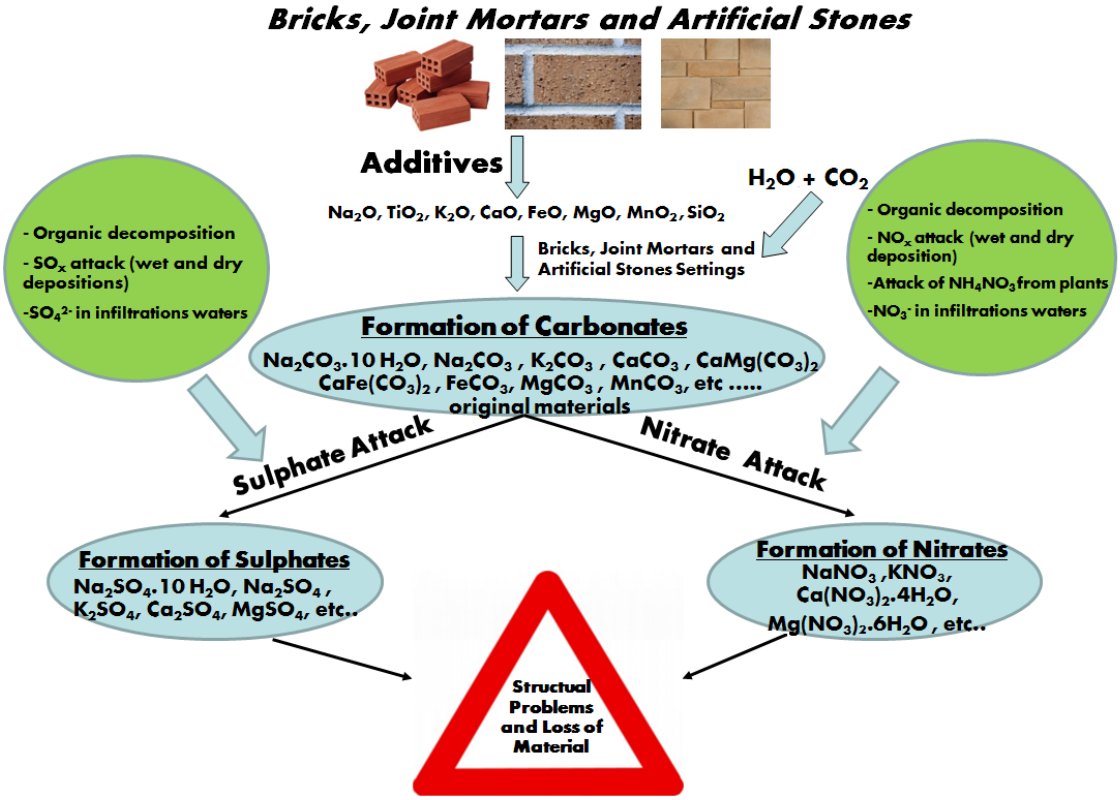

Figure. 6. Schematic representation of the deterioration pathway described in the text for the analyzed bricks, joint mortars, and artificial stones.

During the setting of the bricks and mortars, the additives (oxides) included in their composition can be carbonated by atmospheric CO_2, yielding the corresponding carbonates. These carbonates can be subsequently attacked by nitrate salts (typically ammonium nitrate) transported by infiltration waters, causing the formation of new nitrates salts on the surface (efflorescence) or inside the pores of the building material (sub-efflorescence). In addition to the identified nitrates, various types of sulfate salts were also detected. The joint mortar used in these constructions can contain a high load of sulfates, which can dissolve and subsequently dissociate in solution, facilitating the reaction of these ions with the cations from the dissociated salts carried in infiltration waters. This process is responsible for the formation of the corresponding sulfates (see Figure 6). Moreover, the presence of chlorides in the form of halite also suggests the possible influence of marine aerosol on the formation of these recently formed efflorescences. Considering that the homes are in close proximity to the coast (2 km), this hypothesis cannot be rejected. We have demonstrated that portable in situ Raman spectroscopy is a highly useful technique for the diagnosis of the discussed pathologies in building materials. A subsequent complementary Raman analysis of extracted samples in the laboratory yields the maximum amount of information, which is helpful for predicting the deterioration processes taking place in the considered building materials. Accompanying techniques such as SEM-EDS and XRD have also been proven to be very useful for the identification of compounds such as pyrolusite and anapaite. There have been no literature reports to date that describe deterioration prevention strategies executed on modern building materials, including those used in detached houses intended for use as private homes. Therefore, the discussion contained in this work regarding the original composition of building materials and the newly formed deterioration products will be helpful toward the proposal of prevention strategies that thwart or minimize the deterioration of these materials due to environmental impact.

5. References

[1] F. J. Alejandre, R. Villegas, Brick durability and conservation treatment of Santa Maria de Jesus chapel portal (Seville, Spain), Materiales de Construcción (2009) 59: 85–103.

[2] L. M. Snell, B. G. Snell, The early roots of cement, Concrete International (2000) 22: 83–85.

[3] R. Bustamante, J. Monjo, M. I. Sanchez de Rojas, Constructive Aspects of the Artificial Stone Veneer (arcosita "Butsems") of the South Facade of the Spanish Senate Palace, Materiales de Construcción (2012) 62: 309–318.

[4] M. Barsottelli, G. F. Cellai, F. Fratini, C. Manganelli Del Fa, The hygrometric behavior of some artificial stone materials used as elements of masonry walls, Materials and Structures (2001) 34: 211–216.

[5] M. Maguregui, A. Sarmiento, I. Martinez-Arkarazo, M. Angulo, K. Castro, G. Arana, N. Etxebarria, J. M. Madariaga, Analytical diagnosis methodology to evaluate nitrate impact on historical building materials, Analytical & Bioanalytical Chemistry (2008) 391: 1361–1370.

[6] F. Fratini, E. Pecchioni, L. Rovero, U. Tonietti, The earth in the architecture of the historical centre of Lamezia Terme (Italy): Characterization for restoration, Applied Clay Sciences (2011) 53: 509–516.

[7] K. Castro, M. Perez-Alonso, M. D. Rodriguez-Laso, J. M. Madariaga, Pigment analysis of a wallpaper from the early 19th century: *Les Monuments de Paris,* Journal of Raman Spectroscopy (2004) 35: 704–709.

[8] J. Ruedrich, M. Seidel, E. Rothert, S. Siegesmund, Length changes of sandstones caused by salt crystallization, Geological Society Special Publication Building Stone Decay: From Diagnosis to Conservation, E-Publishing Inc., London, (2007) pp. 199–209.

[9] N. Prieto-Taboada, M. Maguregui, I. Martinez-Arkarazo, M. A. Olazabal, G. Arana, J. M. Madariaga, Spectroscopic evaluation of the environmental impact on black crusted modern mortars in urban-industrial areas, Analytical & Bioanalytical Chemistry (2011) 399: 2949–2959.

[10] D. Kolokotsa, P. Maravelaki-Kalaitzaki, S. Papantoniou, E. Vangeloglou, M. Saliari, T. Karlessi, M. Santamouris, Development and analysis of mineral based coatings for buildings and urban structures, Solar Energy (2012) 86: 1648–1659.

[11] A. Broggi, E. Petrucci, M. P. Bracciale, M. L. Santarelli, FT-Raman spectroscopy for quantitative analysis of salt efflorescences, Journal of Raman Spectroscopy (2012) 43: 1560–1566.

[12] R. N. Yong, V. R. Ouhadi, Experimental study on instability of bases on natural and lime/cement-stabilized clayey soils, Applied Clay Sciences (2007) 35: 238–249.

[13] M. Maguregui, A. Sarmiento, R. Escribano, I. Martinez-Arkarazo, K. Castro, J. M. Madariaga, Raman Spectroscopy after accelerated ageing tests to assess the origin of some decayed products found in real historical bricks affected by urban polluted atmospheres, Analytical & Bioanalytical Chemistry (2009) 395: 2119-2129.

[14] J. I. Alvarez, I. Navarro, A. Marti, P. J. García-Casado, A study of the ancient mortars in the north tower of Pamplona's San Cernin church, Cement & Concrete Research (2000) 30: 1413-1419.

[15] G. Cultrone, I. Sidraba, E. Sebastian, Mineralogical and physical characterization of the bricks used in the construction of the "Triangul Bastion". Riga (Latvia), Applied Clay Sciences (2005) 28: 297–308.

[16] L. Rampazzi, R. Bugini, St. Lorenzo basilica in Milan: Integral approach to characterization of historical mortars, e-Preservation Science (2006) 3: 21–26.

[17] B. Ipekoglu, H. Boke, O. Cizer, Assessment of material use in relation to climate in historical buildings, Building and Environment (2007) 42: 970–978.

[18] M. Perez-Alonso, K. Castro, J. M. Madariaga, Vibrational spectroscopic techniques for the analysis of artefacts with historical, artistic and archaeological value, Current Analytical Chemistry (2006) 2: 89–100.

[19] P. Lopez-Arce, A. Zornoza-Indart, C. Vazquez-Calvo, M. Gomez-Heras, M. Alvarez de Buergo, R. Fort, Evaluation of Portable Raman for the Characterization of Salt Efflorescences at Petra, Jordan, Spectroscopy Letters (2011) 44: 505–510.

[20] H. Morillas, M. Maguregui, O. Gomez-Laserna, J. Trebolazabala, J. M. Madariaga, Characterisation and diagnosis of the conservation state of cementitious materials exposed to the open air in XIX century lighthouses located on the coast of the Basque Country: 'The case of Igueldo lighthouse, San Sebastian, North of Spain", Journal of Raman Spectroscopy (2012) 43: 1630–1636.

[21] M. Maguregui, N. Prieto-Taboada, J. Trebolazabala, N. Goienaga, N. Arrieta, J. Aramendia, L. Gomez-Nubla, A. Sarmiento, M. Olivares, J.A. Carrero, I. Martinez-Arkarazo, K. Castro, G. Arana, M.A. Olazabal, L.A. Fernandez, J.M. Madariaga. in: CHEMCH 1st International Congress Chemistry for Cultural Heritage, Ravenna, 30th June–3rd July, (2010).

[22] R. T. Downs, M. Hall-Wallace, A database of crystal structures published in the American mineralogist and the Canadian mineralogist and its use as a resource in the classroom. in: 18th General Meeting of the International Mineralogical Association, pp. 128, (2002).

[23] H. Morillas, M. Maguregui, O. Gomez-Laserna, J. Trebolazabala, J. M. Madariaga, Could marine aerosol contribute to deteriórate building materials from interior areas of lighthouses? An answer from the analytical chemistry point of view, Journal of Raman Spectroscopy (2013) 44: 1700–1710.

[24] M. Maguregui, U. Knuutinen, K. Castro, J. M. Madariaga, Raman spectroscopy as a tool to diagnose the impact and conservation state of Pompeian second and fourth style wall paintings exposed to diverse environments (House of Marcus Lucretius), Journal of Raman Spectroscopy (2010) 41: 1400–1409.

[25] A. Sarmiento, M. Maguregui, I. Martinez-Arkarazo, K. Castro, J. M. Madariaga, Raman spectroscopy as a tool to diagnose the impacts of combustion and greenhouse acid gases on properties of Built Heritage, Journal of Raman Spectroscopy (2008) 39: 1042-1049.

[26] F. Veniale, M. Setti, C. Rodriguez-Navarro, S. Lodola, W. Palestra, A. Busetto, Thaumasite as decay product of cement mortar in brick masonry of a church near Venice, Cement & Concrete Composites (2003) 25: 1123–1129.

[27] V. S. Ramachandran, J. J. Beaudoin, Handbook of Analytical Techniques in Concrete Science and Technology. Principles, Techniques and Applications, William Andrew Publishing, New York, (2001).

[28] B. E .I. Abdelrazig, J. H. Sharp, B. El-Jazairi, The microstructure and mechanical properties of mortars made from magnesia-phosphate cement, Cement & Concrete Research (1988) 18: 415–425.

[29] N. E. Hipedinger, A. N. Scian, E. F. Aglietti, Magnesia-phosphate bond for cold-setting cordierite-based refractories, Cement & Concrete Research (2002) 32: 675–682.

[30] C. Julien, M. Massot, R. Baddour-Hadjean, S. Franger, S. Bach, J. P. Pereira-Ramos, Raman spectra of birnessite manganese dioxides, Solid State Ionics (2003) 159: 345–356.

[31] M. Maguregui, U. Knuutinen, I. Martinez-Arkarazo, K. Castro, J. M. Madariaga, Thermodynamic and Spectroscopic Speciation to Explain the Blackening Process of Hematite Formed by Atmospheric SO_2 Impact: The Case of Marcus Lucretius House (Pompeii), Analytical Chemistry (2011) 83: 3319–3326.

[32] S. S. Potgieter-Vermaak, J. H. Potgieter, R. Van Grieken, The application of Raman spectrometry to investigate and characterize cement, Part I: A review, Cement & Concrete Research (2006) 36: 656-662.

[33] A. El-Turki, R. J. Ball, G. C. Allen, The influence of relative humidity on structural and chemical changes during carbonation of hydraulic lime, Cement & Concrete Research (2007) 37: 1233–1240.

[34] P. Vargas-Jentzsch, B. Kampe, V. Ciobotaˇ, P. Rosch, J. Popp, Inorganic salts in atmospheric particulate matter: Raman spectroscopy as an analytical tool, Spectrochimica Acta Part A: Molecular and Biomolecular Spectroscopy (2013) 115: 697–708.

[35] M. Steiger, S. Asmussen, Crystallization of sodium sulfate phases in porous materials: the phase diagram Na_2SO_4-H_2O and the generation of stress, Geochimica et Cosmochimica Acta (2008) 72: 4291-4306.

[36] C. Rodriguez-Navarro, E. Doehne, E. Sebastian, How does sodium sulfate crystallize? Implications for the decay and testing of building materials, Cement & Concrete Research (2000) 30: 1527-1534

[37] A. Hamilton, R. I. Menzies, Raman spectra of mirabilite, $Na_2SO_4{\cdot}10H_2O$ and the rediscovered metastable heptahydrate, $Na_2SO_4{\cdot}7H_2O$, Journal of Raman Spectroscopy (2009) 41: 1014-1020.

RESEARCH ARTICLE 5

The influence of rainwater composition on the conservation of cementitious building materials in the Metropolitan Bilbao (Basque Country, north of Spain).

H. Morillas, I. Marcaida, M. Maguregui, J. A. Carrero, J. M. Madariaga

Submitted to Science of the Total Environment in July (2015)

The influence of rainwater composition on the conservation of cementitious building materials in the Metropolitan Bilbao (Basque Country, north of Spain)

ABSTRACT

Rainwater is one of main pollution tracer around the world. There are many reasons that can explain the presence and high concentrations of certain metals and metalloids in the rainwater (traffic, marine port activities, industry, etc.). In this work, rainwater samples were collected at six different locations in the Metropolitan Bilbao (Basque Country, north of Spain) during November 2014. Heavy metals and metalloids concentrations were determined by means of ICP-MS and anions by ion chromatography. The pH and redox potential values on these samples were also assessed. According to the obtained results, different trends along the estuary of Bilbao have been observed. To corroborate some hypothesis, thermodynamic simulations and correlation analyses were also carried out using quantitative data. These trends are closely related to the surrounding pollution and marine influence. Finally, in order to ascertain the influence of the Metropolitan Bilbao rainwater on buildings materials, a recent construction was characterized. Using techniques such as SEM-EDS, Raman Spectroscopy and XRD, different types of sulfates and nitrates were observed.

Keywords*:* Rainwater, wet depositions, cementitious material, pollution, ion chromatography, ICP-MS, Raman spectroscopy.

1. Introduction

Rainwater composition plays an important role in scavenging soluble components from the atmosphere and it can also help to understand the relative contributions of different kind of atmospheric pollutants [1]. Although, more than 90% of the total amount of pollutants present in the atmosphere can be lixiviated by rainwater [2], the rainwater itself can carries high concentrations of metals and metalloids among others cations and anions such as ammonium, nitrites, nitrates, sulfates, chlorides etc. Furthermore, the main environmental problem related with the rainwater composition is its acidification. Acid rain is usually formed due to dissolution of acid aerosols (mainly SO_x and NO_x) coming from anthropogenic sources. This acid rain supposes one of the major global environmental problems due to its important impact on vegetation and aquatic environments [2]. The deposition of acid rain on constructions has negative influence in the conservation state of the building materials used on them [3]. Since the 20th century, Europe has experienced a strong industrialization and an extensive road traffic, which affected strongly surrounded environment and subsequently also the rainwater composition. For this reason, it is important to characterize the anthropogenic pollutants which can change the original composition of the initial rainwater. In this way, different research groups have analyzed rainwater composition of different areas, using ion chromatography and ICP-MS, in forest areas with haze [4], semi-urban areas [5], rural areas [6, 7] and industrial areas [7]. In this sense, many authors are trying to study the pollution levels based on the study of air composition, rainwater composition and depositions on geological samples [8]. Regarding rainwater analyses, they can be performed following different objectives. For example, depending of the air mass trajectories, the water vapor and subsequently rainwater can transport different compounds from biomass burning emissions during the pre-monsoon season like in Lijiang (China) [9]. Sometimes, it is necessary to know the composition of rainwater if the collected rainwater is used to drink [10]. In other cases, rainwater analyses can help to determine the presence of rare earth elements, as the study of Iwashita et al. in the suburban area of Tokyo [11]. There are also some studies about concentrations of heavy metals such as Cu, Cd, Zn and Pb by means of potentiometic stripping analyses (PSA) [12]. Other works, studied the variability of some anions in rainwater in Portugal by means of Ion Chromatography [13]. In this way, the industrial activities have high influence in the ongoing process of atmospheric and rainwater chemistry alteration [14]. Other works have focused their studies on the concentrations of anions, cations and pH variability in mountain areas without pollution [15]. In addition, there are also studies about nitrogen fractions and soluble organic compounds in rainwater from marine environments [16]. Other studies focused their

attention on the heavy metal concentration variability in the rainwater depending on the differences on air directions in coastal areas [17]. Moreover, other studies dealed with the differentiation of possible trends in rainwater heavy metals concentrations in areas influenced by marine aerosol against areas not influenced by it [18]. It is also important to highlight the influence of industry [19-21] and maritime traffic [22-24] to understand the reasons of the presence of certain contaminants as well as the different concentration levels of heavy metals and airborne particulate matter in general ($PM_{2.5}$ and PM_{10}), especially in areas influenced by industrial harbor activities.

In this work, rainwater samples from six different locations in Metropolitan Bilbao (Basque Country, north of Spain) during November 2014 were collected. Heavy metals concentrations were determined by means of ICP-MS. Anions were quantified using the ion chromatography technique and pH and Redox potential values were also determined. Finally, in order to assess the influence of certain pollutants transported by the rainwater from Metropolitan Bilbao, different analyses on cementitious building materials from a construction located in the area of Metropolitan Bilbao (Berango, north of Spain) were conducted by means of Raman spectroscopy and SEM-EDS.

2. Experimental

2.1. Sampling Locations

The sampling of rainwater on each location from Metropolitan Bilbao (Basque Country, north of Spain) was conducted at the same day (3rd November 2014) (see Figure 1).

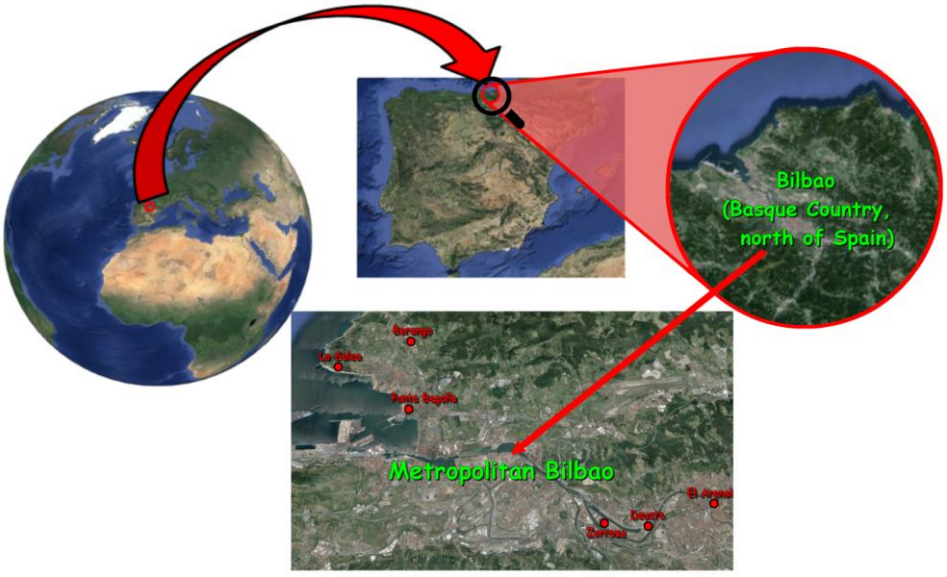

Figure 1. Sampling locations from Metropolitan Bilbao.

The first sampling point was *El Arenal*, located in the heart of Bilbao and in the upper part of the estuary. This sampling point can provide information about the heavy metals and acid aerosol level dissolved in rainwater in the heart of the city. Prior to these analyses, it is assumed that the high road traffic in this area can be a significant source of pollutants (e.g. airborne particulate matter (APM) and NO_x). Industrial activity should not have influence, because there is no industry that can contribute to increase the metallic particles and acid gases input.

The second sampling point was placed in *Deusto*, on the shore of the estuary. *Deusto* is also highly influenced by road traffic, like the *El Arenal* sampling area. The main difference with *El Arenal* sampling point is that *Deusto* can suffer diffuse influence of industrial activity, thus, this source can contribute to increase the APM and acid aerosol emissions.

The third sampling point chosen was *Zorroza*, on the banks of the estuary. In this area the main industrial activity of the Metropolitan Bilbao is located. These types of focal points can emit high concentration of acid gases and APM to the atmosphere. In contrast, road traffic should not be a pollutants emission source, because the number of vehicles in this area is minimal.

The fourth sampling point chosen for rainwater sampling was *Punta Begoña* in Getxo. Historically in this area high level of SO_2 emissions have been detected. The main pollutants emission source is the industrial port. Moreover, a high affluence of vehicles is registered in this area, because of the presence of Ereaga Beach and Algorta Sport Harbour.

The fifth sampling point chosen was a residential area in *Berango*. This area is located relatively close to the coast (2 km) and could also experiments the influence of diffuse marine aerosol and road traffic.

Finally the sixth sampling point chosen was the *Fortress of La Galea*, which is located in an area with low road traffic, but with a clear influence of the marine environment and the industrial port. Moreover the emissions from a petroleum refinery, a power generation plant producing liquid hydrocarbures as fuel and from the maritime traffic of the Bay of Abra (Port of Bilbao) increase the pollutants concentration levels in the rainwater of this area.

2.2. Material and sampling

All the rainwater samples from the six sampling points were collected using 2 litres PYREX® glass beaker (The Science Company, Denver, USA) and 800 ml SCHOTT DURAN glass beaker (DURAN Group GmbH, Wertheim/Main, Germany). Before the sampling, the new glass bakers were rinsed with Milli-Q water, in order to ensure the cleanliness of each container. After sampling, rainwater samples were filtered using 20ml BRAUN Omnifix® syringe and a MN Chromafil® Xtra PA-45/25 filter with 0.45 μm of pore size and 25 mm of diameter.
For the Berango cementitious building materials, the sampling was carried out using a little hammer, a chisel and scalpel. The average size of the extracted fragments never exceeded 2-3 cm^2 (in some cases, the size of the sample was lower).

2.3. Instrumentation

For the analysis of pH and redox potential of the rainwater samples, Crison microph 2000 (Crison Instruments S.A. Alella, Barcelona, Spain) instrument was used. For the daily calibration of the pH meter, two buffer solutions (pH 7.00 buffer solution (Crison pH 7.00 @ 25^0C buffer solution CRI9464.99) and pH 4.01 buffer solution (Crison pH 4.01 @ 25^0C buffer solution CRI9463.99)) were used. For the calibration of the conductimeter, a diary calibration using Hamilton Redox Bufer 475± 5mV (traceable to N.I.S.T and P.T.B (N.I.S.T: National Institute of Standards and Technology, USA and P.T.B: Physikalich-Technische Bundesanstalt, Germany) was used.

The quantification of metals and metalloids in rainwater samples was performed by means of an ICP-MS (NexION 300, Perkin Elmer) instrument in a class 100 clean room. The argon used was supplied by Praxair (99.995%, Madrid, Spain). Calibration standards were prepared by weight using an analytical balance model Mettler-Toledo XS205 (Colombus, OH, USA) with an accuracy of ± 0.00001 g from commercial solutions of 1000 mg/L supplied by Alfa Aesar (Specpure ®, Plasma standard solution, Germany). Sc, Ge, In, Re and Bi were used as internal standards and the following isotopes ^{7}Li, ^{107}Ag, ^{27}Al, ^{44}Ca, ^{88}Sr, ^{98}Mo, ^{114}Cd, ^{120}Sn, ^{121}Sb, ^{138}Ba, ^{184}W, ^{202}Hg and $^{206+207+208}$Pb were determined in standard mode and ^{23}Na, ^{24}Mg, ^{39}K, ^{47}Ti, ^{51}V, ^{52}Cr, ^{55}Mn, ^{56}Fe, ^{59}Co, ^{60}Ni, ^{65}Cu, ^{66}Zn, ^{75}As, ^{78}Se, ^{111}Cd isotopes were determined using a collision cell and an He flow, in order to eliminate possible polyatomic interferences.

Moreover, soluble salts analysis in rainwater samples was carried out using a Dionex ICS 2500 ion chromatograph connected to a conductimetric detector (ED50 Dionex conductimetric detector) with post-column suppression (Dionex Corporation, Sunnyvale, California, USA). The anions quantified were F^-, Cl^-, NO_2^-, NO_3^- and SO_4^{2-}. For their

separation, an Ion Pac AS11-HC (4x250 mm) column and anionic postcolumn Ion Pac GS11-HC (4x50mm) were used. As mobile phase 20mM Na_2CO_3-$NaHCO_3$ solution, 1.5 ml/min flow and 112mA of suppression voltage was used. The data acquisition and integration were carried out using Chromaleon 6.60–SPIa software (Dionex Corporation, Sunnyvaley, California, USA).

For the molecular characterization of cementitious materials from Berango building, two Raman spectrometers were employed. Firstly, a portable spectrometer for the in situ or field analyses in which the materials preliminary screening without being removed from the façade was used. After the preliminary analyses, samples were extracted in order to be measured using a benchtop spectrometer for an in-depth study, to identify the maximum number of compounds on each sample. The portable Raman spectrometer used was an innoRam™ model (B&WTEK$_{INC.}$, Newark, USA) which implements a 785 nm excitation laser and it has a maximum output power of 300 mW. Variable attenuation of the output power was achieved through the implementation of filters, which allowed for the reduction of the output power down to 1% of the maximum. The spectra were typically collected using a wavelength range of 100–2200 cm^{-1}, although in some measurements larger ranges were collected. The measurement time for each spectrum ranged from 1 to 10 s, and two to twenty repeated acquisitions were averaged to improve the signal-to-noise ratio. The Raman probe (down to 0.1 mm focal spot size) can be operated by hand or mounted on a micro-video camera to reduce the spot size.

The Raman measurements in the laboratory were carried out using a Renishaw RA100 Raman spectrometer (Renishaw, Gloucestershire, UK), which also includes a 785 nm excitation laser. The microscopic analyses were performed using 20x and 50x long-range objective lenses mounted in the video-camera where the Raman probe was connected. The spectra were typically collected from 100 to 3000 cm^{-1}, although larger wavelength ranges were also employed in some of the measurements. The exposure time for each spectrum ranged from 1 to 10 s, and ten to seventy repeated acquisitions were averaged to increase the signal-to-noise ratio. In this case also, the laser power was attenuated to avoid thermal decomposition of the sample. Both Raman instruments were calibrated daily using the 520 cm^{-1} Raman band of a crystalline silicon chip. Spectral acquisition with the innoRam™ and RA100 spectrometers were performed using the BWSpec™ 3.26 (B&WTEK$_{INC.}$) and the Renishaw Wire 3.2 software packages respectively. The Raman data were interpreted by comparing the acquired spectra with the spectra of pure standard compounds obtained from the e-VISNICH dispersive Raman database, which contains Raman spectra of natural, industrial and cultural heritage compounds, following a methodology described elsewhere

[25]. Open access Raman spectral databases (e.g., RRUFF [26]) were also used to assingn some of the Raman bands. The spectral interpretation and data treatment were carried out using the GRAMS/AI 7.02 software package (Thermo Fisher Scientific Inc., Waltham, USA).

The SEM-EDS analyses were carried out using a EVO®40 Scanning Electron Microscope (Carl Zeiss NTS GmbH, Germany) coupled to an X-Max Energy-Dispersive X-Ray spectrometer (Oxford Instruments, Abingdon, Oxfordshire, United Kingdom) for electron image acquisitions and elemental analysis (punctual and imaging). Although sometimes cementitious materials alone are not conductive, it was possible to acceptable optimal results without carbon or gold coating. The SEM images were obtained at high vacuum employing an acceleration voltage of 30 kV and a 10–400 μm working distance. Different magnifications (reaching up to ×6,800) were used for secondary electron images and an integration time of 50 s was employed to improve the signal-to-noise ratio. The EDS spectra were acquired and treated using the INCA software.

3. Results

The obtained pH and Redox potential values for the six sampling points are shown in Table 1.

Table 1. pH and Redox potential values from each rainwater sample.

Sampling Points	pH	Redox Potential (mV)
El Arenal	6.20 ± 0.03	182 ± 1
Deusto	6.50 ± 0.03	172 ± 2
Zorroza	6.85 ± 0.03	167 ± 1
Punta Begoña	7.12 ± 0.02	166 ± 2
Berango	6.45 ± 0.03	299 ± 2
La Galea	6.43 ± 0.03	322 ± 2

The carbon dioxide (CO_2) concentration on each sampling points should be constant, thus we should not expect pH variations among the sampling points. Unless basic particulate matter reacts with the rainwaters, the pH can vary slightly due to the influence of other acid gases such as NO_x and SO_x, which when are dissolved in rainwater, they give rise to nitrates and sulfates respectively. As seen the pH is constant for three sampling points (Deusto, Berango, La Galea; pH= 6.46 ± 0.5) (see also Figure 2). Only the most urban influenced sampling location has lower pH value. The differences in the pH values obtained, in Zorroza

and Punta Begoña are due to the neutralization of the mentioned acids by the suspended particles. For example, in Punta Begoña the rainwater pH obtained was 7.12; this could be due to such neutralization processes between the carbonate particulate matter emitted during the maritime port activity.

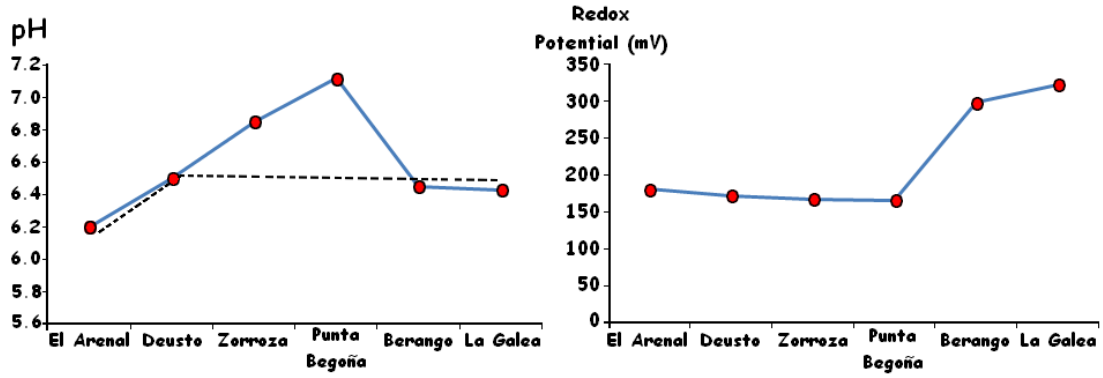

Figure 2. pH and Redox Potential tendency along the six analyzed rainwater samples.

The redox potential values show a lower redox potential in the estuary area, in comparison to the most outer sampling points (Berango and La Galea). This could have a relationship with the road traffic and the industrial activities. In these areas, the ozone concentration is influenced by the higher volume of road traffic, responsible of NO_x and VOC gases emissions and industrial emissions. In this sense, when the sampling point is further from the city (Punta Begoña), the ozone concentration would be lower and thus, the reduction potential of that area will be reduced, which is what it is observed in the analysis of collected rainwater samples.

3.1. Metals and metalloids concentrations in rainwater samples

The analysis of metals and metalloids in the atmosphere is of great interest, as certain heavy metals such as lead, nickel, cadmium and arsenic are common air pollutants which are mainly emitted by some industrial activities and during the burning of coal. Although their level in the environment is low, their deposition can cause serious consequences, such as their influence on the degradation of specific building materials included in constructions.

In this work, the concentrations of each metal and metalloid on each rainwater sample are presented as an average of three repetitive measurements on each sample (see the concentrations in Table 1 of Annexes). The Sr and Cu concentrations increase slightly or remain practically constant, while the rainwater analyzed is close to the coast. As can be seen in Figure 3, the highest Sr concentration was identified in Punta Begoña rainwater.

Both elements, Cu and Sr could have their origin in the port activity near the area. Marine aerosol can also contribute to increase the Sr concentration in rainwater [27].

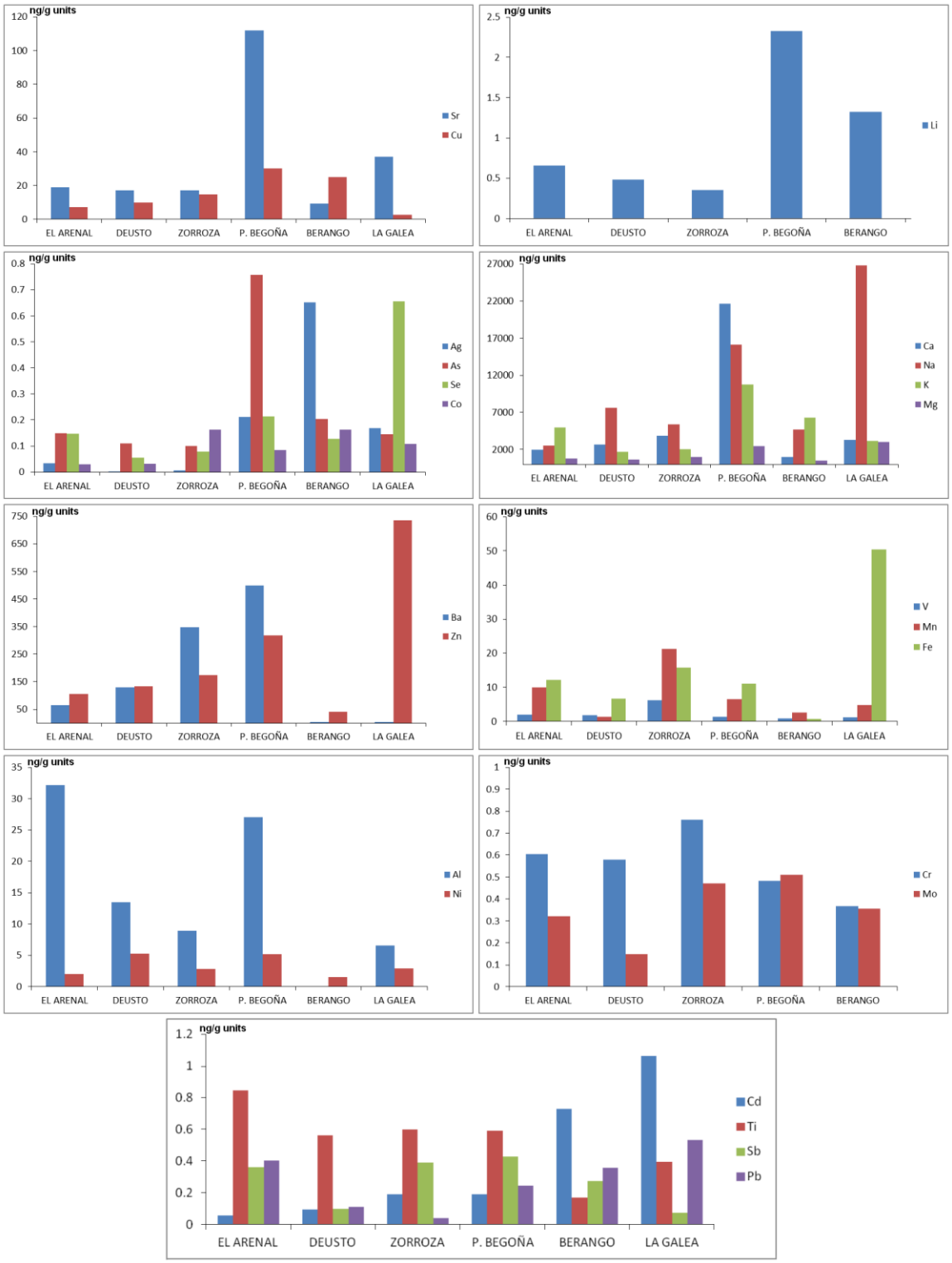

Figure 3. Bar charts showing metals and metalloids concentrations (ng/g units) on each rainwater sample.

Regarding lithium, the sampling point where a maximum concentration was obtained was Punta Begoña. It is necessary to highlight that the concentration of Li for La Galea rainwater in the Figure 2 was not included because a higher concentration comparing with other points (437 ppb) was obtained. This high value could be related with the impact of the port activity, which would also explain the maximum value obtained in Punta Begoña. For the Ag, As, Se and Co, low concentrations were detected. As can be seen in Figure 3, the concentrations of some of these metals and metalloids are especially high in the rainwater from Punta Begoña (As), Berango (Ag) and in the rainwater from La Galea (Se). The high presence of As in Punta Begoña rainwater, can be due to the influence of road traffic [28], which is very high in this area. Regarding cobalt, the concentration in Zorroza and Berango is very similar. This can be due to the road traffic also [29].

For the case of Na, Mg, K and Ca, the highest concentrations were determined in the rainwater sample from Punta Begoña. Even higher concentrations of sodium were detected in La Galea rainwater, which like Punta Begoña, it also undergo the direct influence of marine aerosol (located on a cliff in front of Bay of Abra). On the contrary, in the sampling points closer to Bilbao city center, the concentrations of sodium decrease (see Figure 3). The highest concentration of Ca was detected in Punta Begoña rainwater. Ca can be present in the atmosphere as calcium carbonate particles. This observation agrees with the neutralized pH determined in Punta Begoña rainwater, as an influence of a higher concentration of carbonates. As it has been mentioned before, this kind of particulate matter can come from the mineral phases transported from the port activity. Natural erosion and emission of calcareous stones from the surrounding location can also contribute to increase the calcium carbonate particles emitted in this area. Considering the correlation analysis performed with all the variables quantified in the rainwater samples, the correlation matrix has been calculated (see the results in Table 3 from Annexes). In this sense, a high correlation between calcium and strontium (0.98) was determined, which is an indicative of the presence of calcium carbonate coming from a calcareous rock, which usually contains noticeable amounts of strontium. Therefore, the presence of calcium carbonate particles from the atmosphere in the rainwater is evident. Moreover, the calcium carbonate particles can react in the atmosphere with the acid SO_2 (as H_2SO_4 after its incorporation to the rainfall or due to the humidity influence) and the other acids giving soluble calcium and bicarbonate.

Other metals such as Ba and Zn (see Figure 3) reach high concentrations for Punta Begoña and La Galea rainwaters respectively. Although in Punta Begoña, a high number of vehicles

is registered due to the diary affluence of tourist who visit the beach and sport harbor, probably these two metals come from the port activity.

The highest concentration of V and Mn has been detected in the rainwater from Zorroza. Although iron concentration is also high in this sampling point, the maximum concentration was registered in Punta Begoña. The high concentrations of V, Mn and Fe in Zorroza and Fe in Punta Begoña could be due to the emissions of these metals coming from a near company which produce rolled steel coils from scrap and prereduced iron operations. The highest concentration of V and Mn in Zorroza rather than in Punta Begoña could be explained because the wind direction is oriented to Zorroza, therefore the metallic particles can be transported to this sampling point. Considering the correlation analysis performed with all the variables quantified in the rainwater samples, the correlation matrix has been calculated (see the result in Table 3 from Annexes). In this sense, the coincident source of V and Mn was also confirmed because a high correlation was identified between both metals (0.93). In Punta Begoña rainwater, higher concentrations of Fe were quantified due to the Fe emissions as a consequence of the fuel oil combustion from ships which enter and leave the Bilbao Port [30].

Regarding Al and Ni, varying concentrations depending on the sampling area were observed. In Punta Begoña and El Arenal rainwater, higher concentration of these metals is present.

As can be seen in Figure 3, Cr and Mo concentrations in rainwater from all the sampling points are low. In Punta Begoña 0.5 ppb for both metals was determined a relatively low concentration. In this point, we have to highlight that for the case of La Galea, it was decided not to include in the bar chart because the concentrations of Cr and Mo were much higher than in the rest of sampling point (see Table 1 of Annexes). The higher concentration of both metals, in La Galea rainwater, could be due to the emissions coming from the port activity. Finally, the concentrations of Cd, Ti, Sb and Pb are quite low. The highest concentrations of Pb and Cd were registered in La Galea rainwater. This could be because of the surrounded industry and maritime traffic that are present in the Abra Bay.

3.2. Quantification of anions in rainwater samples

Figure 4 shows different bar charts representing the concentrations of each anion present in the six rainwater samples.

The analysis of chloride ion (Cl^-) mainly provides information about the influence of marine aerosol, because the sampling points on Metropolitan Bilbao are clearly influenced by the Cantabrian Sea. The marine aerosol, generated spontaneously, is formed when the wind strikes over the surface of the ocean waves. Then, small bubbles discharge liquid particles in the air. These particles are impulsed at high speed and they are incorporated into the flowing air mass [31]. The highest concentration of chlorides was registered in the Punta Begoña and La Galea rainwaters, which are the closest areas to the sea. Thus, due to their location, they are more exposed to sea spray. The other four sampling points show considerably lower chloride concentrations. These concentrations can be related with the chloride background which is maintained along the Nervion River (which varies depending on the day, season etc.). Regarding the correlation analysis (see Table 3 from Annexes), a high correlation was obtained between chloride and sodium (0.97) and chloride and magnesium (0.98). These observation points out that the main chlorides incorporated or lixiviated by the rainwater coming from marine aerosol are sodium and magnesium chlorides.

In view of the results of fluorides (see Figure 4), there is no clear trend in the observed results. As it can be seen, fluorides were detected in Zorroza and El Arenal rainwaters, while in Punta Begoña, La Galea and Deusto this anion was not detected.

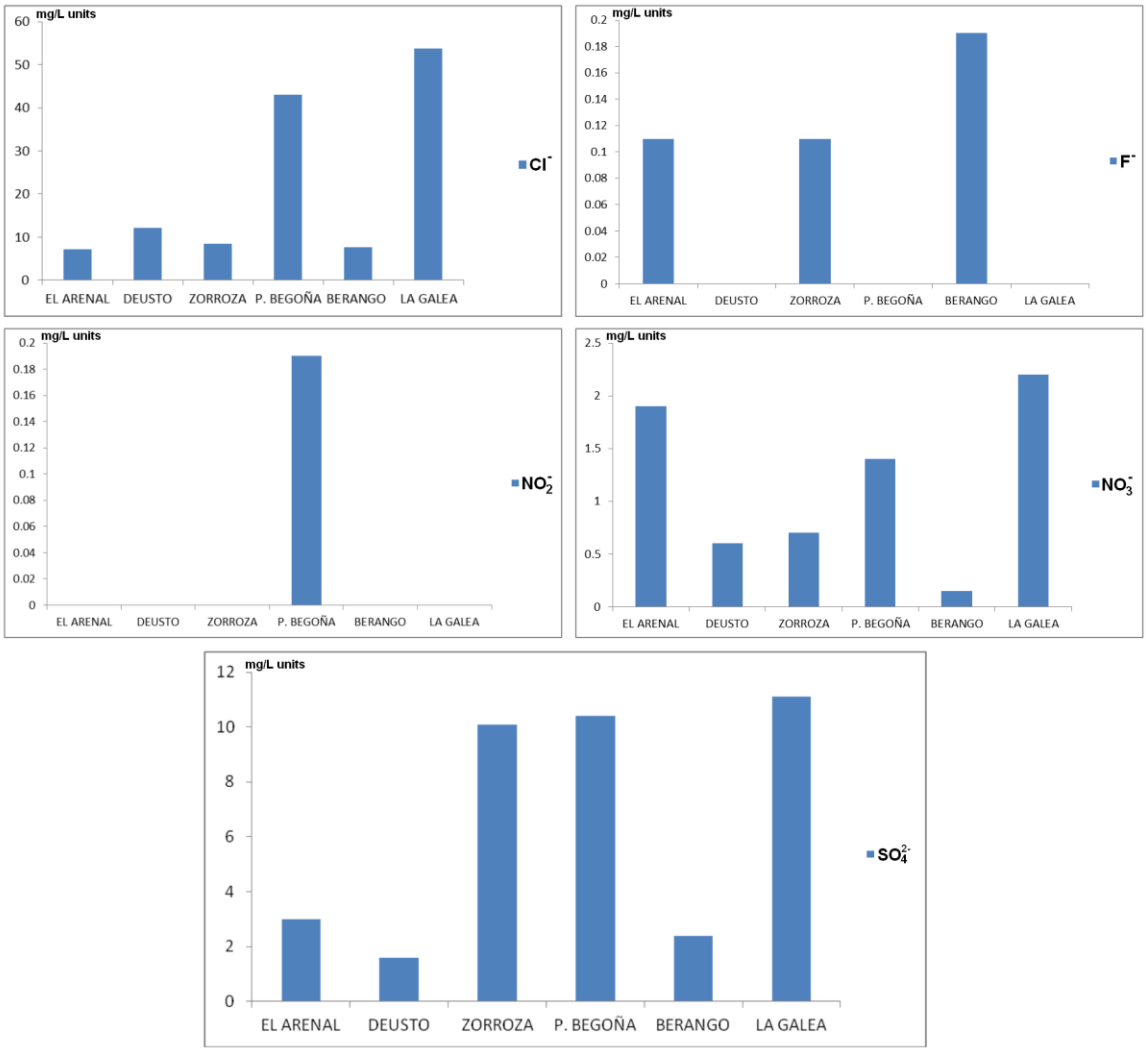

Figure 4. Bar charts showing the anions concentrations (mg/L units) in the rainwater from each sampling points.

The absence or presence of nitrite ions (NO_2^-) in rainwater indicates if the emitted nitrogen to the atmosphere has been totally oxidized or not. NO_x can be oxidized in the atmosphere, by the influence of ozone (O_3). In the NO_x (mainly as N_2O) emissions, the N is in +1 oxidation (N (I)) state. N_2O can be oxidized into nitrite (NO_2^-) in where N is in +3 oxidation state (N (III)). Finally, these nitrites can be oxidized to form nitrate ions (NO_3^-) in where N is in +5 oxidation state (N (V)). The presence of nitrites in rainwater indicates that all the nitrogen emitted into the atmosphere has not been completely oxidized. As we can see in Figure 4, nitrites only were detected in Punta Begoña, the sampling point outside from Bilbao city center. In the city center, higher concentrations of ozone can be registered. In Punta Begoña, the concentration of ozone is not so high, thus the entire emitted N (I) cannot be oxidized to nitrates. However, in all other areas, as they are located very near or in the city center, ozone (O_3) concentrations may be high enough so that all the NO_x emitted into the atmosphere is oxidized to nitrates.

Nitrates appear in all sampling areas where previously nitrites were not found (see Figure 4). However, in Punta Begoña, nitrates and nitrites were detected in the rainwater. Therefore, in this area, the emitted N (I), has been almost completely oxidized to N (V) (concentration of 1.4 ppm or 22.6 mM). However, a lower concentration (0.19 ppm or 4.13 uM) has not completely oxidized into N (V) and remains in the rainwater as Nitrogen (I) or nitrites. That is, the 12% of the total emitted N (I) is in the form of nitrite, and the remaining 88% is completely oxidized to nitrate. In order to understand this situation, a thermodynamic simulation of the described system (total nitrogen concentration of 27 µM) was done using the MEDUSA software (see Figure 5).

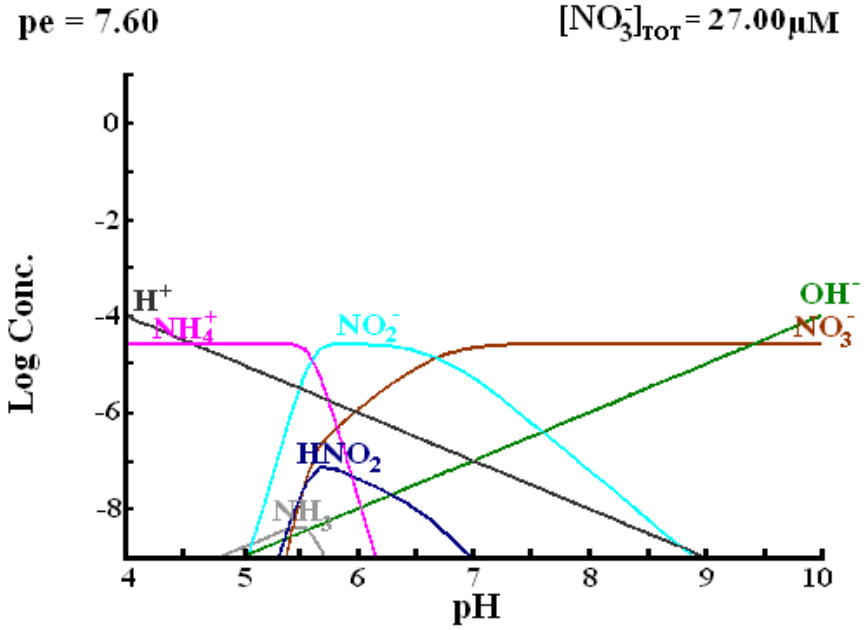

Figure 5. Thermodynamic modelling of the NO_2^-/NO_3^- system wich takes place in the rainwater from Punta Begoña sampling point.

As seen, at the pH value (7.12) of the rainwater (see Figure 5), the major specie is NO_3^-, but NO_2- is also present more or less in the same ratio observed experimentally in the rainwater. In this way, the thermodynamic simulation agree with the experimental evidences.

Regarding the SO_x gases emissions to the atmosphere, SO_2 is the main gas emitted in where SO_2 can be oxidized to the +6 oxidation state to form sulfates. This oxidation process in +4 oxidation state can also take place due to ozone (O_3). As can be seen in Figure 4, the maximum sulfates concentrations were determined in Punta Begoña, La Galea and Zorroza

sampling points, which are clearly influenced by industrial activity, as has been remarked throughout the manuscript.

For the case of Punta Begoña, these high concentrations are due to the SO_2 emissions coming from the port activity. In Zorroza, waste management companies can contribute to increase the SO_2 emissions which lead to sulfates. However Deusto, El Arenal and Berango, sulfates concentrations on rainwater are relatively low, as these areas are not exposed to any industrial activity, and therefore there is no a nearby source of SO_2 acid gas emissions. Apart from the SO2 input coming from anthropogenic activities, natural sources can also contribute to increase the sulphur concentration in rainwater. Concretely, a high correlation (0.72) was found between sulfates and chloride anions (see Table 3 from Annexes). This correlation could suggest that sulfates present in the rainwater can also come from the marine aerosol, like the chloride input.

3.3. Chemometric treatment of metals, metalloids and anions concentrations in rainwaters

In order to extract additional conclusions about the variability of the rainwater in the different sampling points, chemometric analyses based on Principal Component Analysis (PCA) were carried out with the metals, metalloids and anions concentrations in the rainwaters from the different sampling areas. These analyses were performed using the Unscrambler 7.2 software all the variables quantified in the rainwater samples.

In the score plot obtained after the Principal Component Analysis (PCA), three different groups can be observed (see Figure 6). The first one represents La Galea rainwater, a sampling point highly impact by the marine aerosol.

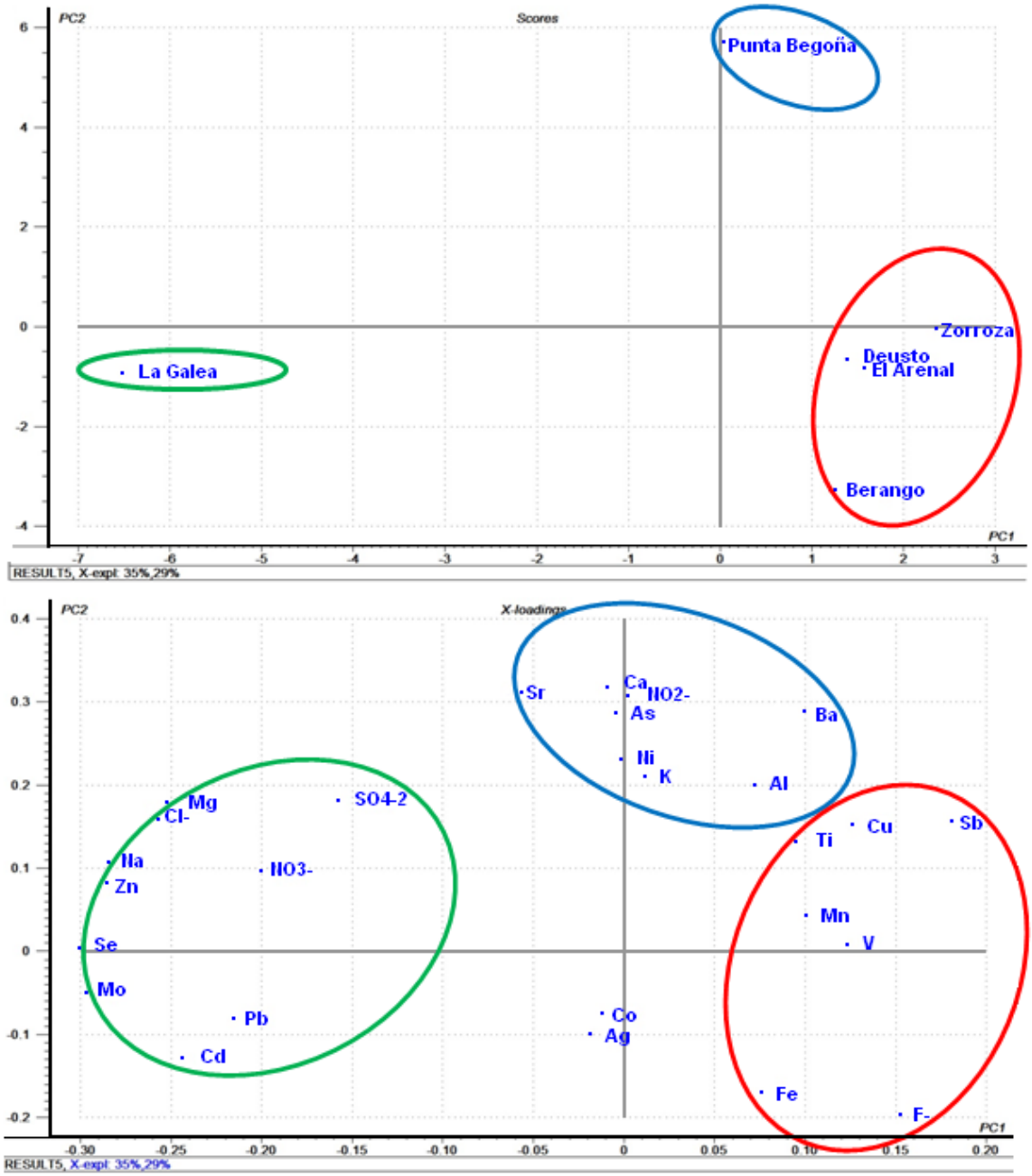

Figure 6. Scores (bottom) and loadings plots (top) obtained after the PCA analysis of the anions, metals and metalloids concentrations in rainwaters.

Having a look to the loadings plot, La Galea is defined by high concentrations of nitrates, sulfates, Mg, Na and Cl (see Figure 6). These anions and metalloids are the main components of the salts transported in the marine aerosol. This observation agrees with the correlation analysis results, because a high correlation was also determined between Na-Cl and Mg-Cl as it has been mentioned before. The sampling areas impacted by the urban-industrial emissions (El Arenal, Deusto, Zorroza and Berango) are grouped together (see Figure 6 bottom). In this case, this group and the elements according to the loadings plots are characterized by a higher presence of Fe, F, Mn, Sb, Cu, Ti and V. Finally, a third group,

representing the rainwater of Punta Begoña sampling location was defined (see Figure 6 bottom). In this case, the influence of the port activity can be clearly observed. As it has been mentioned before, nitrites (NO_2^-) were detected as well as metals such as As, Sr and Ba which their presence is also high as explained before (see loadings plot at the top of Figure 6).

3.4. Deposition of Airborne Particulate Matter and acid aerosols transported by rainwater and its influence on the conservation state of cementitious building materials

Considering the concentration of metals and anions from the rainwaters at each sampling point, Berango is one of the areas with fewer amounts of metals and dissolved anions. However, different pathologies were identified in the building materials (artificial stone and bricks) from detached houses from this area [32]. In this sense, in order to assess if the cementitious materials from another detached house of Berango, are suffering airborne particulate matter depositions and impact from the acid aerosols dissolved in the rainwater and deposited on the façades, a complete characterization of those materials has been conducted. In this sense, cementitious materials were taken from the façades oriented to the rainwater and wind direction.

3.5. Molecular characterization of Berango cementitious materials

Raman spectroscopy was useful to define different original compounds present on the original cementitious materials, such as hematite (Fe_2O_3, Raman bands at 219, 237, 288, 403, 488 and 606 cm^{-1}), limonite ($FeO(OH)\cdot nH_2O$, Raman bands at 239, 298, 394 and 552 cm^{-1}) and quartz (SiO_2, Raman bands at 262, 355, 394, 464, 695, 805 and 1159 cm^{-1}) (see Figure 7). These compounds act as additives in the cement setting [33]. As we can see in Figure 7A, the Raman analyses of the efflorescence from cement material reveals the presence of thenardite (Na_2SO_4 , Raman bands at 450,464, 620, 631, 646, 992, 1100, 1130 and 1151 cm^{-1}) and natrite (Na_2CO_3, Raman bands at 194, 700 and 1080 cm^{-1}). The thenardite-mirabilite system (Na_2SO_4-$Na_2SO_4\cdot 10H_2O$) is a common pathology in cementitious building materials [34-36]. Apart from these compounds, a very dangerous compound which can appear in the cement materials was observed. This compound was the ettringite ($Ca_6Al_2(OH)_{12}(SO_4)_3\cdot 26H_20$, Raman bands at 218, 361, 448, 544, 600, 648, 857, 890, 986 and 1061 cm^{-1}) (see Figure 7B). Prior to ettringite formation, thaumasite ($Ca_6Si_2(OH)_{12}(CO_3)_2(SO_4)_2\cdot 24H_2O$) is usually formed. The thaumasite is formed in cements as a consequence of a continuous sulfation process. In the cement setting, the sulfates react

with the cement compounds such as C3A (tricalcium aluminate) forming the ettringite and the hydrated calcium monosulphoaluminate ($Ca_4Al_2(OH)_{12}(SO_4)\cdot 6H_2O$) consuming the added sulfates in form of additive [37]. Nevertheless, ettringite can follow reacting with an excess of sulfates and with the carbonated cement in order to form the thaumasite. The formation of this compound give rise to the worst decay processes which can be find in the cement, because the presence of this compound promote volume changes causing the buiding wall collapse. Moreover if the thaumasite follow reacting with the hydrated calcium monosulphoaluminate, it can promote also the absolute loss of material [38, 39].

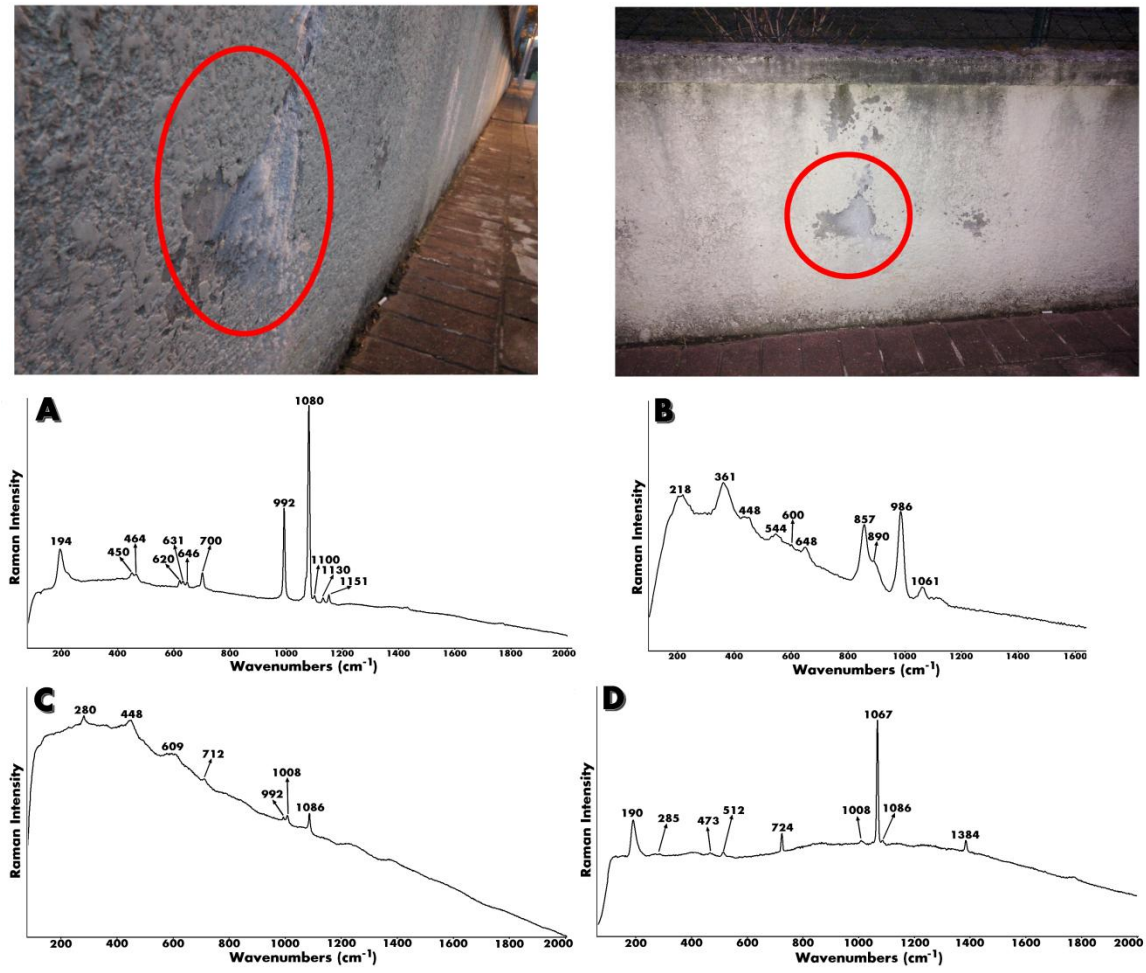

Figure 7. A) Raman spectrum showing the presence of thenardite (Na_2SO_4) and natrite (Na_2CO_3); B) Raman spectrum of ettringite ($Ca_6Al_2(OH)_{12}(SO_4)_3\cdot 26H_20$); C) Raman spectrum showing the presence of gypsum ($CaSO_4\cdot 2H_2O$), calcite ($CaCO_3$), thenardite (Na_2SO_4) and rutile (TiO_2) and D) Raman spectrum showing the presence of adularia ($KAlSi_3O_8$), calcite ($CaCO_3$), gypsum ($CaSO_4\cdot 2H_2O$) and nitratine ($NaNO_3$).

As it is described in previous works, high quantities of sulfate compounds can appear in cementitious materials [32]. The main sulfate usually identified on cementitious materials was the gypsum ($CaSO_4\cdot 2H_2O$). In this sense, as we can see in Figure 7C, among rutile (TiO_2,

Raman bands at 448 and 609 cm^{-1}) and calcite ($CaCO_3$, Raman bands at 280, 712 and 1086 cm^{-1}), gypsum ($CaSO_4 \cdot 2H_2O$, main Raman band at 1008 cm^{-1}) together with thenardite (Na_2SO_4, main Raman band at 992 cm^{-1}) were identified. Apart from that, gypsum ($CaSO_4 \cdot 2H_2O$, with its main Raman band at 1008 cm^{-1}) was also identified together with calcite ($CaCO_3$, with its main Raman band at 1086 cm^{-1}), adularia ($KAlSi_3O_8$, Raman bands at 285, 473 and 512 cm^{-1}) and nitratine ($NaNO_3$, Raman band at 190, 724, 1067 and 1384 cm^{-1}). The presence of nitratine on cementitious materials can suggests a continuous attack of nitrates [40], since nitrate salts are very soluble and sometimes difficult to identify its presence. Although the concentration of nitrates in the rainwater from Berango was low, the presence of nitratine could be a signal of possible wet depositions of NO_x coming from the atmosphere. Additionally, a possible nitrate salts input coming from infiltration waters cannot be rejected.

3.6. Elemental characterization of Berango cementitious materials

In order to complement the analyses carried out in cementitious materials by Raman spectroscopy, SEM-EDS point by point and imaging analyses were carried out. An example of these analyses is presented in Figure 8. Nitrogen was identified on the cementitious materials in more than 10 spectra (see Figure 8A and B). This observation can be related with the possible presence of nitrates, such as nitratine ($NaNO_3$) which was identified by Raman spectroscopy as it has been mentioned in the previous section. Sodium nitrate can be present in the building material as particulate matter coming from the salts included in the marine aerosol (see Figures 8A and 8B) [41] or can be formed in the material starting from the sodium carbonate in reaction with nitrate salts input coming from infiltration waters.

Among the nitrogen, other elements related also with the marine aerosol influence such as Cl were detected by EDS. Although Berango is not located next to the sea, the diffuse influence of the near marine environment is evident. Other elements such as sulphur and calcium, which could be related with the presence of some sulfate such as gypsum ($CaSO_4 \cdot 2H_2O$) which was also distinguished by Raman spectroscopy, were also identified by EDS. Moreover, the presence of K, Al, Si and O in EDS spectra, can be related with the presence of potassium aluminosilicates (e.g. KAl_3SiO_8) which were also identified by Raman spectroscopy. This kind of silicates can be original compounds of the cementitious material itself, but they can also be related with particulate matter depositions. Finally, the presence of Fe in the EDS spectra could be related with the different iron oxides used as additives in the characterized cementitious material, but their signal can also come from iron particles deposited on the surface of the cementitious materials.

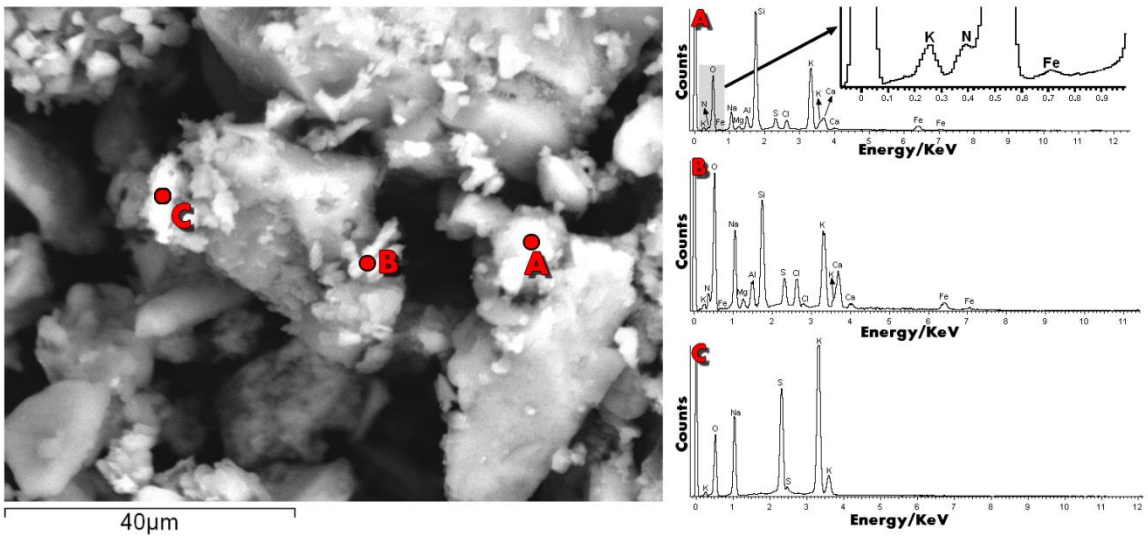

Figure 8. A microphotograph of the cementitious material acquired using the SEM (left) and different EDS spectra of different points inside this microscopic area (right).

Other microscopic areas from cementitious materials surface show the presence of K, Na, S and O (see Figure 8C). Considering that Cl was not present in the EDS spectrum, it cannot be said that NaCl is present in this microscopic area. Therefore, the most probable compound that could be present is a Aphthitalite ($K_3Na(SO_4)_2$). This compound was previously identified in efflorescences from cementitious materials [42]. The formation of these types of doble sulfate compounds could be related with a continuous sulfation process [43]. In this sense, although the concentration of sulfates in Berango rainwater was relatively low, a continuous deposition process of the acidified rainwater on the cementitious material can promote the formation of this type of compounds.

Apart from point-by-point EDS analyses, mappings were also acquired on different microscopic areas from the cementitious material (see Figure 9). In the mapping shown in Figure 9, a clear distribution of NaCl can be observed, showing again the clear influence of marine aerosol. Apart from the halite (NaCl) presence, fluor was also detected, distributed in different microscopic areas and not as punctual depositions (see Figure 9). This observation agrees with the data from Berango rainwater, where fluoride was the highest one among the six sampling points.

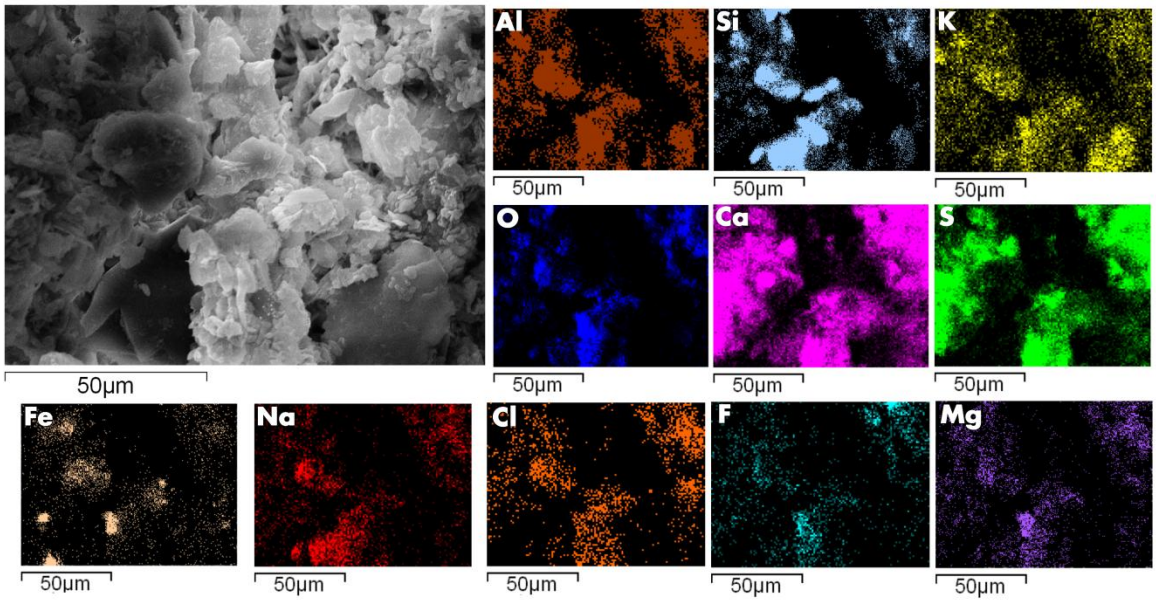

Figure 9. SEM-EDS mapping of cementitious building materials from a building in Berango.

Apart from that, elements like Ca, Al, S, O follow the same distribution in the EDS maps (see Figure 9). This could suggest a possible presence of ettringite $Ca_6Al_2(OH)_{12}(SO_4)_3{\cdot}26H_20$, also detected by Raman spectroscopy. Moreover, the presence of quartz (SiO_2) and adularia (KAl_3SiO_8) can be also distinguished at sight of the EDS mapping results (see Figure 9). Finally, remark the clear correlation between the distribution of S, O and Ca. This elemental distribution could be related to the presence of gypsum ($CaSO_4{\cdot}2H_2O$), a compound identified also by Raman spectroscopic analyses.

4. Conclusions

The results presented in this work show a high variability of metals, metalloids and anions concentrations among the six rainwater samples taken from different points inside Metropolitan Bilbao. In general terms, the acidity of the samples increases while we are approaching to the Bilbao city center, due to the higher presence of acid gases dissolved in the rainwaters and originated from the influence of road traffic and industrial emissions. The reduced presence of particulate matter promotes the rainwater neutralization. Moreover, taking into account the results obtained by ICP-MS, the heavy metals concentrations reveal an influence of the surrounded industry and maritime port. The road traffic has also a clear influence. For the anions results quantified by ion chromatography, they revealed the influence of marine aerosol (mainly chlorides and fluorides in some cases) and green houses acid gases (presence of sulfates, nitrates and nitrites).

The influence of the acid compounds and metals transported in the rainwater which can be deposited on the surface of the buildings was evaluated in a specific sampling point, Berango, where apart from rainwater, cementitious materials from a modern house were characterized, in order to extract conclusions about the influence of the rainwater composition on the conservation state of such building materials. Although the rainwater from Berango showed the lowest concentration of anions, metals and metalloids, a clear impact of acid pollutants and metallic airborne particulate matter that can be transported by rainwater and deposited on building materials is evident.

Therefore, the combined use of a molecular microscopic technique (Raman spectroscopy) and elemental technique (SEM-EDS) demonstrate that the building, placed in a diffuse marine and diffuse urban-industrial environment such as Berango area, can experiment a negative influence of acid aerosol and airborne particulate matter transported by rainwater in its conservation state. Thanks to Raman spectroscopy, it was possible to determine the presence of sulfate compounds such as ettringite, thenardite and gypsum which can be formed due to the sulfate input of the material itself, but also as an influence of SO_x wet depositions. Nitratine ($NaNO_3$) salt was also identified and its presence was reinforced with the N detection by means of EDS. This salt can be present on the cementitious materials as a dry deposition (airborne particulate matter coming from the marine aerosol).

SEM-EDS analyses (point by point and imaging) also revealed a clear influence of marine aerosol thanks to the identification of NaCl, the main salt transported by marine aerosol. Sulfate salts identified also by Raman spectroscopy (e.g. gypsum, thenardite, aphthilatite and ettringite) was corroborated also by this elemental technique.

The whole multianalytical methodology described in this work have allowed to understand the high influence of acid aerosols and metal and metalloids transported in the rainwater on the conservation state of cementitious building materials. Metals, metalloids and acid aerosols can be deposited on the surface of these materials following dry and wet depositions. Airborne particulate matter (e.g. calcium carbonate) can also react with the acid aerosols in the atmosphere promoting the formation of secondary particles (e.g. transformation of calcium carbonate particles in reaction with the acid form of the SO_2 aerosol included in the rainwater forming calcium sulfate as secondary particle). These particles, together with the primary ones can be also deposited on the materials following a dry deposition.

5. Annexes

Table 1. Metals and metalloids concentrations (ng/g) in rainwater samples.

	El Arenal	Deusto	Zorroza	Punta Begoña	Berango	La Galea
Li	0.657 ± 0.002	0.482 ± 0.05	0.35 ± 0.01	2.33 ± 0.06	1.33 ± 0.05	437 ± 7
Sr	19.0 ± 0.3	17.2 ± 0.2	17.1 ± 0.3	112 ± 2	9.3 ± 0.1	37 ± 1
Ag	0.034 ± 0,001	0.002 ± 0.008	0.006 ± 0.005	0.211 ± 0.006	0.652 ± 0.009	0.169 ± 0.009
As	0.15 ± 0.01	0.109 ± 0.008	0.10 ± 0.02	0.76 ± 0.02	0.20 ± 0.02	0.145 ± 0.009
Se	0.15 ± 0.07	0.06 ± 0.06	0.08 ± 0.07	0.21 ± 0.06	0.13 ± 0.09	0.6 ± 0.1
Ca	1969 ± 30	2689 ± 32	3830 ± 34	21620 ± 450	957 ± 16	3312 ± 70
Na	2550 ± 38	7586 ± 43	5401 ± 51	16110 ± 320	4674 ± 80	26765 ± 380
Mg	747 ± 13	666 ± 3	1013 ± 8	2466 ± 56	485 ± 11	3001 ± 50
K	4938 ± 89	1689 ± 12	2045 ± 11	10740 ± 240	6320 ± 91	3173 ± 68
Ba	65.1 ± 0.6	129 ± 1	347 ± 9	498.5 ± 2.9	3.5 ± 0.1	4.2 ± 0.3
Cu	7.17 ± 0.07	9.79 ± 0.08	14.6 ± 0.1	30 ± 1	25.1 ± 0.2	2.79 ± 0.04
Zn	105.3 ± 0.6	133.4 ± 1.5	174 ± 11	318 ± 10	41 ± 1	735 ± 12
V	1.89 ± 0.06	1.75 ± 0.05	6.2 ± 0.1	1.29 ± 0.03	0.82 ± 0.02	1.18 ± 0.03
Mn	9.9 ± 0.2	1.39 ± 0.03	21.2 ± 0.2	6.6 ± 0.2	2.61 ± 0.03	4.8 ± 0.1
Fe	12.2 ± 5.2	6.7 ± 2.6	15.7 ± 0.4	11 ± 3	0.6 ± 0.6	50.4 ±0.6
Co	0.030 ± 0.001	0.032 ± 0.002	0.162 ± 0.003	0.085 ± 0.005	0.163 ± 0.002	0.109 ± 0.003
Al	32.2 ± 0.5	13.45 ± 0.45	8.9 ± 0.4	27.0 ± 0.7	0.02 ± 0.74	6.5 ± 0.8
Mo	0.3 ± 0.1	0.15 ± 0.09	0.5 ± 0.1	0.51 ± 0.1	0.36 ± 0.03	63 ± 3
Sb	0.361 ± 0.003	0.09 ± 0.01	0.391 ± 0.009	0.427 ± 0.005	0.27 ± 0.02	0.0740 ± 0.0009
Pb	0.405 ± 0.003	0.11 ± 0.01	0.04 ± 0.01	0.243 ± 0.006	0.36 ± 0.03	0.53 ± 0.03
Cr	0.604 ± 0.013	0.6 ± 0.3	0.8 ± 0.4	0.48 ± 0.04	0.3 ± 0.15	11.1 ± 0.1
Ni	2.0 ± 0.3	5.3 ± 0.3	2.8 ± 0.1	5.2 ± 0.5	1.54 ± 0.52	2.9 ± 0.7
Cd	0.056 ± 0.002	0.095 ± 0.008	0.191 ± 0.004	0.19 ± 0.02	3.89 ± 0.06	1.06 ± 0.02
Ti	0.84 ± 0.03	0.56 ± 0.04	0.59 ± 0.03	0.6 ± 0.1	0.17 ± 0.02	0.39 ± 0.05

Table 2. Anions concentrations (mg/L) in rainwater samples.

	El Arenal	Deusto	Zorroza	Punta Begoña	Berango	La Galea
Cl^-	7.1 ± 0.1	12.13 ± 0.04	8.4 ± 0.1	43.0 ± 0.2	7,60 ± 0,05	53, 7 ± 0,1
NO_2^-	Not detected	Not detected	Not detected	0.19 ± 0.01	Not detected	Not detected
NO_3^-	1.9 ± 0.1	0.6 ± 0.1	0.70 ± 0.02	1.4 ± 0.1	0,15 ± 0,01	2,2 ± 0,1
SO_4^-	3.0 ± 0.1	1.58 ± 0.03	10.1 ± 0.1	10.4 ± 0.1	2,40 ± 0,04	11,1 ± 0,3
F^-	0.11 ± 0.02	Not detected	0.11 ± 0.02	Not detected	0,19 ± 0,02	Not detected

Table 3. Pearson correlation coefficients matrix of all the quantitative data obtained from rainwater samples

	Cl^-	NO_2^-	NO_3^-	SO_4^{2-}	F^-	pH	REDOX	V	Mn	Fe	Co	Li	Sr	Ag	As	Se	Ba	Cu	Zn	Ca	Na	K	Mg	Al	Mo	Sb	Pb	Cr	Ni	Cd	Ti
Cl^-	1.00																														
NO_2^-	0.50	1.00																													
NO_3^-	0.64	0.15	1.00																												
SO_4^{2-}	**0.72**	0.43	0.46	1.00																											
F^-	-0.70	-0.42	-0.50	-0.41	1.00																										
pH	0.33	0.78	-0.19	0.62	-0.31	1.00																									
REDOX	0.36	-0.35	0.13	0.07	0.20	-0.42	1.00																								
V	-0.37	-0.22	-0.21	0.33	0.18	0.32	-0.48	1.00																							
Mn	-0.26	-0.08	0.03	0.46	0.26	0.31	-0.43	**0.93**	1.00																						
Fe	-0.39	-0.20	-0.62	-0.36	0.83	-0.15	0.49	-0.19	-0.18	1.00																					
Co	-0.01	-0.10	-0.42	0.39	0.52	0.32	0.43	0.36	0.36	0.64	1.00																				
Li	**0.75**	-0.20	0.64	0.51	-0.42	-0.24	0.71	-0.25	-0.20	-0.25	0.10	1.00																			
Sr	0.68	**0.97**	0.34	0.56	-0.56	0.73	-0.25	-0.25	-0.09	-0.33	-0.13	0.03	1.00																		
Ag	-0.01	0.06	-0.41	-0.20	0.55	-0.05	0.65	-0.50	-0.44	**0.91**	0.55	-0.02	-0.02	1.00																	
As	0.49	**0.99**	0.13	0.38	-0.33	0.72	-0.25	-0.31	-0.15	-0.08	-0.05	-0.19	**0.95**	0.19	1.00																
Se	**0.85**	0.00	**0.72**	0.58	-0.43	-0.14	0.69	-0.35	-0.22	-0.23	0.08	**0.97**	0.22	0.06	0.02	1.00															
Ba	0.17	0.78	-0.08	0.52	-0.31	**0.93**	-0.70	0.42	0.46	-0.33	0.07	-0.41	**0.72**	-0.30	0.70	-0.30	1.00														
Cu	-0.04	0.70	-0.52	0.05	0.25	0.68	-0.18	-0.11	-0.06	0.50	0.38	-0.56	0.53	0.57	**0.74**	-0.41	0.58	1.00													
Zn	**0.91**	0.13	0.71	**0.72**	-0.63	0.08	0.48	-0.19	-0.11	-0.44	0.05	**0.93**	0.35	-0.15	0.11	**0.95**	-0.07	-0.39	1.00												
Ca	0.54	**0.99**	0.19	0.52	-0.49	0.82	-0.39	-0.13	-0.01	-0.29	-0.09	-0.15	**0.98**	-0.03	**0.97**	0.04	0.83	0.64	0.20	1.00											
Na	**0.97**	0.30	0.60	0.69	-0.69	0.21	0.48	-0.33	-0.27	-0.37	0.05	**0.86**	0.50	-0.02	0.29	**0.91**	0.02	-0.19	**0.97**	0.35	1.00										
K	0.33	0.86	0.10	0.19	0.00	0.48	-0.06	-0.46	-0.22	0.23	0.03	-0.23	**0.79**	0.46	**0.92**	0.00	0.46	0.78	-0.03	0.79	0.13	1.00									
Mg	**0.98**	0.49	0.69	0.82	-0.67	0.37	0.30	-0.22	-0.08	-0.44	0.04	0.74	0.68	-0.09	0.48	**0.84**	0.25	-0.07	**0.92**	0.55	**0.95**	0.31	1.00								
Al	0.03	0.49	0.51	-0.02	-0.30	0.08	-0.66	-0.08	0.12	-0.55	-0.73	-0.32	0.48	-0.50	0.45	-0.18	0.40	0.01	-0.13	0.48	-0.15	0.41	0.08	1.00							
Mo	0.75	-0.20	0.64	0.51	-0.42	-0.24	0.71	-0.25	-0.20	-0.25	0.10	**1.00**	0.03	-0.02	-0.19	**0.97**	-0.41	-0.56	**0.93**	-0.15	**0.86**	-0.24	0.74	-0.32	1.00						
Sb	-0.27	0.50	-0.10	0.19	0.39	0.49	-0.54	0.38	0.60	0.16	0.20	-0.63	0.37	0.03	0.50	-0.48	0.66	0.61	-0.45	0.48	-0.45	0.57	-0.16	0.48	-0.63	1.00					
Pb	0.48	-0.10	0.63	0.06	0.02	-0.54	0.75	-0.67	-0.44	0.15	-0.08	0.66	0.03	0.37	-0.01	0.75	-0.61	-0.29	0.52	-0.15	0.49	0.22	0.44	0.01	0.66	-0.31	1.00				
Cr	0.74	-0.21	0.64	0.52	-0.42	-0.24	0.69	-0.22	-0.17	-0.27	0.10	**1.00**	0.02	-0.05	-0.20	0.97	-0.40	-0.58	**0.93**	-0.16	**0.86**	-0.26	0.74	-0.32	1.00	-0.63	0.65	1.00			
Ni	0.37	0.59	0.00	0.17	-0.83	0.57	-0.52	-0.08	-0.24	-0.62	-0.46	-0.11	0.60	-0.43	0.50	-0.09	0.59	0.18	0.16	0.63	0.30	0.16	0.32	0.30	-0.11	-0.13	-0.46	-0.11	1.00		
Cd	-0.15	-0.24	-0.47	-0.29	0.65	-0.24	0.74	-0.39	-0.39	**0.94**	0.61	0.05	-0.31	**0.95**	-0.11	0.05	-0.50	0.36	-0.17	-0.32	-0.09	0.17	-0.23	-0.68	0.05	-0.13	0.36	0.03	-0.57	1.00	
Ti	-0.16	0.14	0.46	0.02	-0.28	-0.01	-0.77	0.33	0.44	-0.72	-0.67	-0.29	0.16	-0.82	0.05	-0.25	0.35	-0.31	-0.14	0.18	-0.26	-0.06	-0.06	**0.86**	-0.28	0.38	-0.23	-0.27	0.24	-0.87	1.00

6. References

[1] H.Wang, G. Han, Chemical composition of rainwater and anthropogenic influences in Chengdu, Southwest China, Atmospheric Research (2011) 99: 190-196.

[2] A. H. J. Gromping, P. Ostapczuk, H. Emons, Wet Deposition in Germany: Long–term trends and the contribution of heavy metals, Chemosphere (1997) 34: 2227–2236.

[3] A. H. Bravo, A. R. Soto, E. R. Sosa, A. P. Sanchez, J. A. L. Alarcon, J. Kahl, B. Ruiz, Effect of acid rain on building materials of the El Tajin archaeological zone in Veracruz, Mexico, Environmental Pollution (2006) 144: 655-660.

[4] S. Norela, M. S. Saidah, M. Mahmud, Chemical composition of the haze in Malaysia 2005, Atmospheric Environment (2013) 77: 1005-1010.

[5] F. O. M. Alahmr, M. Othman, N. B. A. Wahid, A. A. Halim, M. T. Latif, Compositions of dust fall around semi-urban areas in Malaysia, Aerosol and Air Quality Research (2012) 12: 629-642.

[6] Y. L. Zhang, X. Q. Lee, F. Cao, D. K. Huang, Seasonal variation and sources of low molecular weight organic acids in precipitation in the rural area of Anshun, Chinese Science Bulletin (2011) 56: 1005-1010.

[7] P. Ostapczuk, E. Pobozy, A. Baade, H. Emons, Ion-chromatographic monitoring of main components of rain water in industrial and rural sites in Germany, Fresenius Environmental Bulletin (2002) 11: 326-331.

[8] A. Attar, Global environment: water, air and geochemical cycles, International Journal of Environmental Studies (2013) 70: 155-156.

[9] N. Zhang, J. Cao, Y. He, S. Xiao. Chemical composition of rainwater at Lijiang on the Southeast Tibetan Plateau: influences from various air mass sources, Journal of Atmospheric Chemistry (2014) 71: 157-174.

[10] H. Malassa, F. Al-Rimawi, M. Al-Khatib, M. Al-Qutob, Determination of trace heavy metals in harvested rainwater used for drinking in Hebron (south West Bank, Palestine) by ICP-MS, Environmental Monitoring and Assessment (2014) 186: 6985-6992.

[11] M. Iwashita, A. Saito, M. Arai, Y. Furusho, T. Shimamura, Determination of rare earth elements in rainwater collected in suburban Tokyo, Geochemical Journal (2011) 45: 187-197.

[12] M. R. F. Cerqueira, M. A. C. Matos, D. Lowinsohn, R. C. Matos, Optimization and determination of dissolved trace metals (Cu, Cd, Zn and Pb) in rainwater by potentiometric stripping at a southeaster site of Brazil, Sustainable Environment Research (2014) 24: 13-21.

[13] P. S. M. Santos, M. Otero, E. B. H. Santos, A. C. Duarte, Chemical composition of rainwater at a coastal town on the southwest of Europe: What changes in 20 years?, Science of The Total Environment (2011) 409: 3548-3553.

[14] L. B. L. S. Lara, P. Artaxo, L. A. Martinelli, R. L. Victoria, P. B. Camargo, A. Krusche, G. P. Ayers, E. S. B. Ferraz, M. V. Ballester, Chemical composition of rainwater and anthropogenic influences in the Piracicaba River Basin, Southeast Brazil, Atmospheric Environment (2001) 35: 4937–4945.

[15] H. Niu, Y. He, X. X. Lu, J. Shen, J. Du, T. Zhang, T. Pu, H. Xin, L. Chang, Chemical composition of rainwater in the Yulong Snow Mountain region, Southwestern China, Atmospheric Research (2014) 144: 195-206.

[16] A. Gioda, O. L. Mayol-Bracero, G. J. Reyes-Rodriguez, G. Santos-Figueroa, J. L. Collett, Water-soluble organic and nitrogen levels in cloud and rainwater in a background marine environment under influence of different air masses, Journal of Atmospheric Chemistry (2008) 61: 85-99.

[17] M. Koulousaris, M. Aloupi, M. O. Angelidis, Total metal concentrations in atmospheric precipitation from the northern Aegean Sea, Water, Air, & Soil Pollution (2009) 201: 389-403.

[18] B. Srinivas, M. R. Kumar, A. R. Kumar, R. S. N. Sastry, Rainwater chemistry and quality in and around twin cities of Hyderabad and Secunderabad, Andhra Pradesh, India, Journal of Applied Geochemistry (2012) 14: 83-88.

[19] A. Ummugulsum, A. Kadir, Emission inventory of primary air pollutants in 2010 from industrial processes in Turkey, Science of the Total Environment (2014) 488-489: 369-381.

[20] L. Jong-Myoung, L. Jin-Hong, M. Jong-Hwa, C. Yong-Sam, K. Ki-Hyun, Airborne PM_{10} and metals from multifarious sources in an industrial complex area, Atmospheric Research (2010) 96: 53-64.

[21] M. L. Figueiredo, A. Monteiro, M. Lopes, J. Ferreira, C. Borrego, Air quality assessment of Estarreja, an urban industrialized area, in a coastal region of Portugal, Environmental Monitoring and Assessment (2013) 185: 5847-5860.

[22] Z. Minjiang, Z. Yan, M. Weichun, F. Qingyan, Y. Xin, L. Chunlei, Z. Bin, Y. Qi, C. Limin, Characteristics and ship traffic source identification of air pollutants in China's largest port, Atmospheric Environment (2013) 64: 277-286.

[23] D. Muellerd, S. Uibel, M. Takemura, D. Klingelhoefer, D. A. Groneberg, Ships, ports and particulate air pollution-an analysis of recent studies, Journal of Occupational Medicine and Toxicology (2011) 6: 31.

[24] D. Contini, A. Gambaro, F. Belosi, S. De Pieri, W. R. L. Cairns, A. Donateo, E. Zanotto, M. Citron, The direct influence of ship traffic on atmospheric $PM_{2.5}$, PM_{10} and PAH in Venice, Journal of Environmental Management (2011) 92: 2119-2129.

[25] M. Maguregui, N. Prieto-Taboada, J. Trebolazabala, N. Goienaga, N. Arrieta, J. Aramendia, L. Gomez-Nubla, A. Sarmiento, M. Olivares, J. A. Carrero, I. Martinez-Arkarazo, K. Castro, G. Arana, M. A. Olazabal, L. A. Fernandez, J. M. Madariaga. in: CHEMCH 1st International Congress Chemistry for Cultural Heritage, Ravenna, 30th June–3rd July (2010).

[26] R. T. Downs, M. Hall-Wallace, A database of crystal structures published in the American mineralogist and the Canadian mineralogist and its use as a resource in the classroom. in: 18th General Meeting of the International Mineralogical Association (2002) pp. 128.

[27] F. Culkin, Chemical oceanography, The Major Constituents of Sea Water, Academic Press, London, New York (1965), pp. 121–161.

[28] G. B. Luilo, O. C. Othman, A. Mrutu, Arsenic: a toxic trace element of public health concern in urban roadside soils in Dar es Salaam City, Journal of Materials and Environmental Science (2014) 5: 1742:1749.

[29] P. G. Obara, C. E. Obara, C. L. Roberts, C. H. Young, C. D. Williams, Influence of vehicular traffic on a major trunk road on rural air quality in UK, Microchemical Journal (2011), 99: 344-351.

[30] A. Sorooshian, Z. Wang, M. M. Coggon, H. H. Jonsson, B. Ervens, Observations of sharp oxalate reductions in Stratocumulus clouds at variable altitudes: Organic acid and metal

measurements during the 2011 E-PEACE campaign, Environmental Science & Technology (2013) 47: 7747-7756.

[31] C. D. O'Dowd, G. de Leeuw, Marine aerosol production: a review of the current knowledge, Philosophical Transactions of the Royal Society A, (2007) 365: 1753–1774.

[32] H. Morillas, M. Maguregui, J. Trebolazabala, J. M. Madariaga, Nature and origin of white efflorescence on bricks, artificial stones, and joint mortars of modern houses evaluated by portable Raman spectroscopy and laboratory analyses, Spectrochimica Acta Part A: Molecular and Biomolecular Spectroscopy (2015) 136: 1195-1203.

[33] S. Chandra, Waste Materials Used in Concrete Manufacturing, Elsevier (William Andrew Inc. U.S.A.) (1996), 672.

[34] H. Morillas, M. Maguregui, O. Gómez-Laserna, J. Trebolazabala, J. M. Madariaga, Could marine aerosol contribute to deteriorate building materials from interior areas of lighthouses? An answer from the analytical chemistry point of view, Journal of Raman Spectroscopy (2013) 44: 1700–1710.

[35] -Arkarazo, A. Giakoumaki, K. Castro, J. M. Madariaga, Field Raman analysis to diagnose the conservation state of excavated walls and wall paintings in the archaeological site of Pompeii (Italy), Journal of Raman Spectroscopy (2012) 43: 1747–1753.

[36] V. Matovic, S. Eric, D. Sreckovic-Batocanin, P. Colomban, A. Kremenovic, The influence of building materials on salt formation in rural environments, Environmental Earth Sciences (2014) 72: 1939-1951.

[37] F. Bart , C. Cau-dit-Coumes, F. Frizon, S. Lorente, Cement-Based Materials for Nuclear Waste Storage, Springer (New York, U.S.A) (2013).

[38] S. Sahu, D. L. Exline, M.P. Nelson, Identification of thaumasite in concrete by Raman chemical imaging, Cement and Concrete Composites (2002) 24: 347-350.

[39] H. Brocken, T. G. Nijland, White efflorescence on brick masonry and concrete masonry blocks, with special emphasis on sulfate efflorescence on concrete blocks, Construction Building Materials (2004) 18: 315-323.

[40] H. Morillas, M. Maguregui, O. Gómez-Laserna, J. Trebolazabala, J. M. Madariaga, Characterisation and diagnosis of the conservation state of cementitious materials exposed to the open air in XIX century lighthouses located on the coast of the Basque Country: 'The case of Igueldo lighthouse, San Sebastian, North of Spain, Journal of Raman Spectroscopy (2012) 43: 1630-1636.

[41] D. Gupta, H. Kim, G. Park, X. Li, H. J. Eom, C. U. Ro, Hygroscopic properties of NaCl and $NaNO_3$ mixture particles as reacted inorganic sea-salt aerosol surrogates, Atmospheric Chemistry and Physics, (2015) 15: 3379-3393.

[42] V. Matovic, N. Vaskovic, S. Eric, D. Sreckovic-Batocanin, Interaction between binding materials-the cause of damage to gabbro stone on the monument to the unknown soldier (Serbia), Environmental Earth Sciences (2010) 60: 1153-1164.

[43] H. Morillas, M. Maguregui, C. Paris, L. Bellot-Gurlet, P. Colomban, J. M. Madariaga, The role of marine aerosol in the formation of (double) sulfate / nitrate salts in plasters, Microchemical Journal (2015) 123: 148-157.

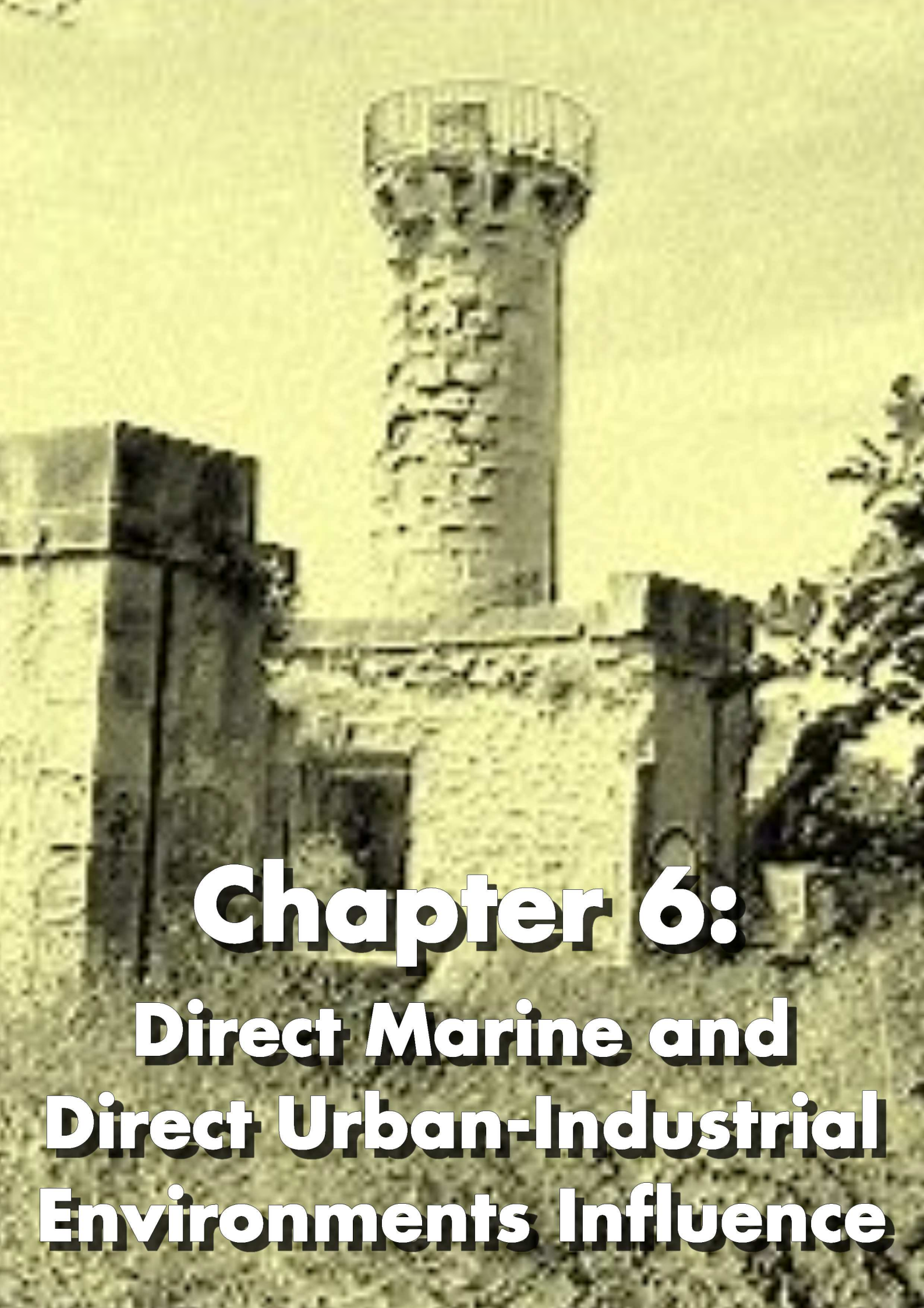

Chapter 6:
Direct Marine and Direct Urban-Industrial Environments Influence

CHAPTER 6.

DIRECT MARINE AND DIRECT URBAN-INDUSTRIAL ENVIRONMENTS INFLUENCE

In this chapter, the direct influence of both marine aerosol and environmental stressors coming from urban-industrial environments on a specific construction will be evaluated. The selected building was La Galea Fortress (Getxo, Basque Country, north of Spain). As it will be explained in the research articles, this building undergo the direct influence of the Primary and Secondary Marine Aerosol particles, crustal particles, acid aerosol depositions, metallic airborne particulate matter depositions, etc. As it can be observed in Figure 6.1, many industries (e.g. steel industries) and the port of Bilbao are placed in front of the fortress. Apart from this, as it can be also observed in the Figure 6.1, La Galea Fortress is located just on a cliff (50 m high) in the coast.

Figure 6.1. Views from La Galea Fortress, showing the location, directly influenced by the marine aerosol and an urban-industrial area.

6.1 La Galea Fortress

The actual La Galea Fortress was called La Galea Castle by the authorities at the time of its construction, like that appears in most of the existing references, but also occasionally it was named as Prince Castle, as it is written in historical archives from 1744 [1]. The initial origin of this location dates back to the middle of the 18th century.

The Lordship of Bizkaia ordered to build a fortress due to the special geo-strategic characteristics of Punta Galea, being a suitable location to ensure the defense of Bilbao´s Abra Bay, and also to ensure the defense of nearby coastal towns. Since the 16th century, some references can be found in where they referred to the used of this construction as a watchtower. The creation of this lookout point was done as a preventive measure against the threat of naval attacks. From this location, it was possible to control the port of Bilbao, making crossfire with batteries disposed on the opposite area (Zierbena, Portugalete, Basque Country). During that time there were many conflicts with British troops. The plan of defense against the fear of an English landing included several measures. Among them, the implementation of a new defensive structure at the entrance of Abra Bay can be highlighted. At that moment, La Galea Fortress raised up.

La Galea Fortress was built in 1742 [2, 3] between April and December and it kept a similarity with the currently existing fortress. It was designed by the engineer Jaime Sycre and the work was executed under the supervision of stonemasons and carpenters like Juan Pagoeta, Lorenzo Orueta and Francisco Dañobeitia. The construction was completed finished at the end of 1742.

In 1782 inside the fortress, the first lighthouse installation was laid down. This lighthouse was a pioneer construction in the Biscay coast, after Igueldo Lighthouse (construction under study also in this PhD Thesis). This first lighthouse was replaced in the mid-19th century by another completely different with a new layout, ignoring why or how it disappeared the previous lighthouse. The new building was designed by the engineer Francisco Antonio Echanove. During history, the Fortress has suffered different collateral damages. In 1795, during the Convention War, the Fortress was occupied by French troops, and in 1825 the British troops destroyed it. After this war, the fortress suffered a progressive abandonment and the loss of its military role.

During the Second Carlist War (1873-1876) the lighthouse, was intentionally turned off as a measure of strength. The second lighthouse in La Galea keeps the current octagonal building

and its circular tower, together with other complementary buildings, such as the two wells for water storage. Later, at the end of the War, in 1880, a building next to the lighthouse, destined to house the person acting as the lighthouse keeper was erected. Nowadays, together with the tower, it is one of the most representative buildings of the whole fortress despite its poor conservation state.

When this last lighthouse was opened, several technical disadvantages were detected and over time they were accentuated. On the one hand, its high altitude was practically invisible for the ships when heavy fog was accumulated in the area. On the other hand, due to the industry development in the estuary, the light from the lighthouse was confused with the glow of Altos Hornos. Considering this situation, it was decided to build another lighthouse on a new site, about 600 meters at the north of the first one. The 1st of May 1905 [4] was the last day of use of La Galea Ligthouse. After that, the Fortress was abandoned, a situation that was prorogated until the mid-20th century, coinciding with the return of the fortress to the municipal property in 1947. At that time, it was decided to reuse all the construction as a restaurant. During 1955-1957 years, the restorations of the place began. Restoration works only were conducted in the indoor areas of the lighthouse keeper house. Additionally, a new building was constructed annexed to the remains of the fortress. After years of use as a restaurant, the fortress was abandoned. Nowadays, the fortress is almost in ruins. The roofs of the fortress have disappeared and the sandstone from the fortress shows a very bad conservation state, specially the one of the tower. Additionally, some of the stairs from the inner area of the tower have been lost.

6.2 La Galea Fortress Architecture

Nowadays, the Fortress has a polygonal shaped plant (a dodecahedron), almost perfectly symmetric showing approximately an area of just over 3.700 m^2, with 1.700 m^2 of moat. The perimeter is delimited by a rampart with two distinct sectors in their section and type. The rampart forehead is opened to the sea and the perimeter is executed with a double lining. In one layer has a masonry wall executed with local materials and fixed with a very compact calcareous mortar, except in the corners and at the vertex which are sandstone ashlars. While, on the other layer has a lining executed in sandstone ashlar blocks with fairly regular size, the interior rampart walls are made of clay, grass and abundant gravel without any mortar. For the construction of the fortress moat, a hole of 7 meters high and two meters width was opened.

Figure 6.2. A general view of La Galea Fortress and its surrounding environment.

6.2.1 Entrance arch

The entrance of the fortress was located on the South-southeast orientation. It is built using sandstone ashlars. The entrance has an arch appearance that opens inwardly in a wide vault. Its outside dimensions are 1.80 meters wide and 2.12 meter high; while the interior size is 4.38 x 2.50 meters (see Figure 6.3).

Figure 6.3. La Galea Fortress entranced arch.

At the top of the entrance arch, the front wall appears with small access as completely smooth truncated pyramid, without any decoration excepting the stones themselves. This facade originally had a small slightly protruding stone, that nowadays it is almost completely lost. On the inside of this structure the voids of the wooden bar designed to strengthen the closing of the door is still preserved, although none of these elements (bar and door) have been not preserved until today.

6.2.2 La Galea Fortress Tower

Inside the enclosure, it can identify a total of three buildings linked historically with the tower. The first one is the Lighthouse Tower, being the oldest. The second one belongs to a building used to house the lighthouse keeper. Finally, a small building, the one constructed in the 20th century is also preserved nowadays (see Figure 6.4). The tower is a building with

circular and cylindrical ground and performed with sandstone blocks. The diameter of the tower base is 3.30 meters reaching 2.95 meters at the top, being the walls thickness 0.60 meters. Its total height is 10.85 meters (originally with flashlight, the tower reached a full wingspan of 12.35 meters). At the top, the tower is topped by a projecting cornice which bears on a series of monolithic limestone corbels and currently is crowned by a balcony with iron railings. As referred in the chronicles of that time, originally this building was completely whitewashed and white painted. Today nothing remains of it except a few white scraps on the ground floor. Inside the tower, several vains to provide illumination to the narrow and steep spiral staircase that allows the ascent to the top of the building were destined. This staircase was performed by large sandstone blocks, and now has lost in two different sections several steps. To this staircase accessed from a lintel vain opened at the base and whose jambs appear slightly chamfered, where his initial gap (95 cm wide and 1.74 cm high) narrowing slightly until being reduced to 77 cm. In its base, this tower is surrounded by a single building octagonal floor executed in a similar way to the tower by sandstone ashlars. The only decoration is presented in the cornice and plinth area with a horizontal band performed by limestone blocks which protrude slightly from the facade line and chromatically contrasting with the rest of the wall by its whitish color. Furthermore the tower has four openings vains and the dimensions are of 8.60 meters each side and a height until the cornice of 4.05 m. Nowadays is formed by a formwork bricks, cement and a cement mortar layer with large stones volumes which in the mid-1950s were replaced to the original cover.

Figure 6.4. La Galea Fortress Tower with its octogonal base (left), through a covered walkway connects to the lighthouse keeper house (right).

6.2.3 Surrounding environment

In order to determine if La Galea site suffers the influence of acid aerosols and airborne particulate matter emissions, available data from a meteorological station located just 600 meters far from La Galea Fortress were evaluated. These data are registered by the Department of Environment and Territorial Policy of the Basque Government [5]. From Figure 6.5 to 6.12 the concentration of CO, O_3, NO, NO_2, NO_x and SO_2 acid aerosols in the atmosphere of La Galea site and the concentrations of PM_{10} and $PM_{2.5}$ airborne particulate matter are represented from January 2012 to June 2015, the period in which this PhD Thesis was developed. Apart from the concentrations of these pollutants, the percentage of relative humidity (%RH) is also presented in Figure 6.13.

According to the CO concentrations (µg/m^3), the values during the considered period are quite similar except the value of September 2014, which reached the concentration of 20.94 µg/m^3.

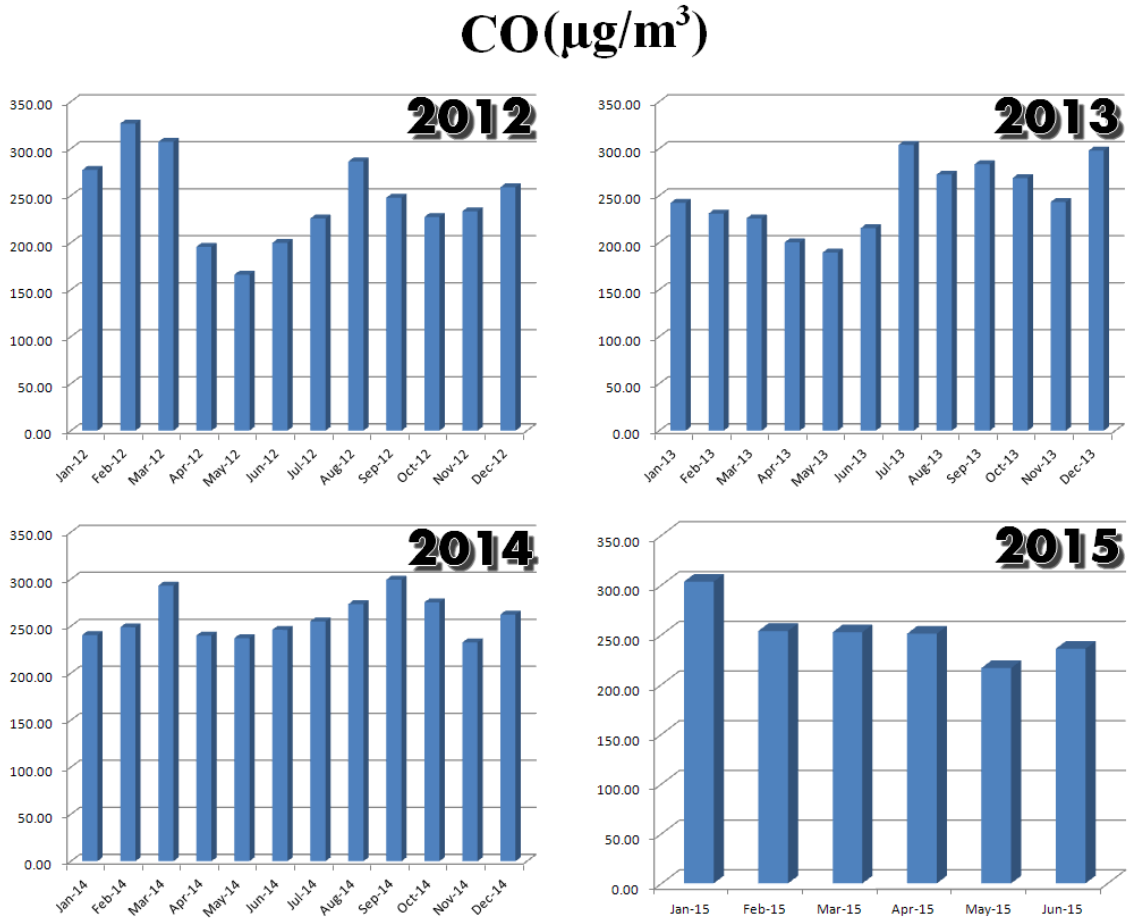

Figure 6.5. CO concentrations (µg/m^3) from January 2012 to June 2015.

The problem of this environmental stressor resides in its ability for the carbonation process of some building materials (e.g. cements). As it has been explained in the Chapter 1, the carbonation process promotes the formation of White Crusts (formation of calcium carbonate, $CaCO_3$) among others types of decay products with the formation of carbonates.

Regarding ozone (O_3) concentrations (see Figure 6.6), the spring season (February-June) from 2012-2014 shows the highest values. The ozone acts as an oxidizer in the atmosphere, being able to oxidize NO_x, NO, NO_2 acid gases emitted to the atmosphere, giving rise to N_2O_5, which can react with the rainwater giving as a result the formation of nitric acid.

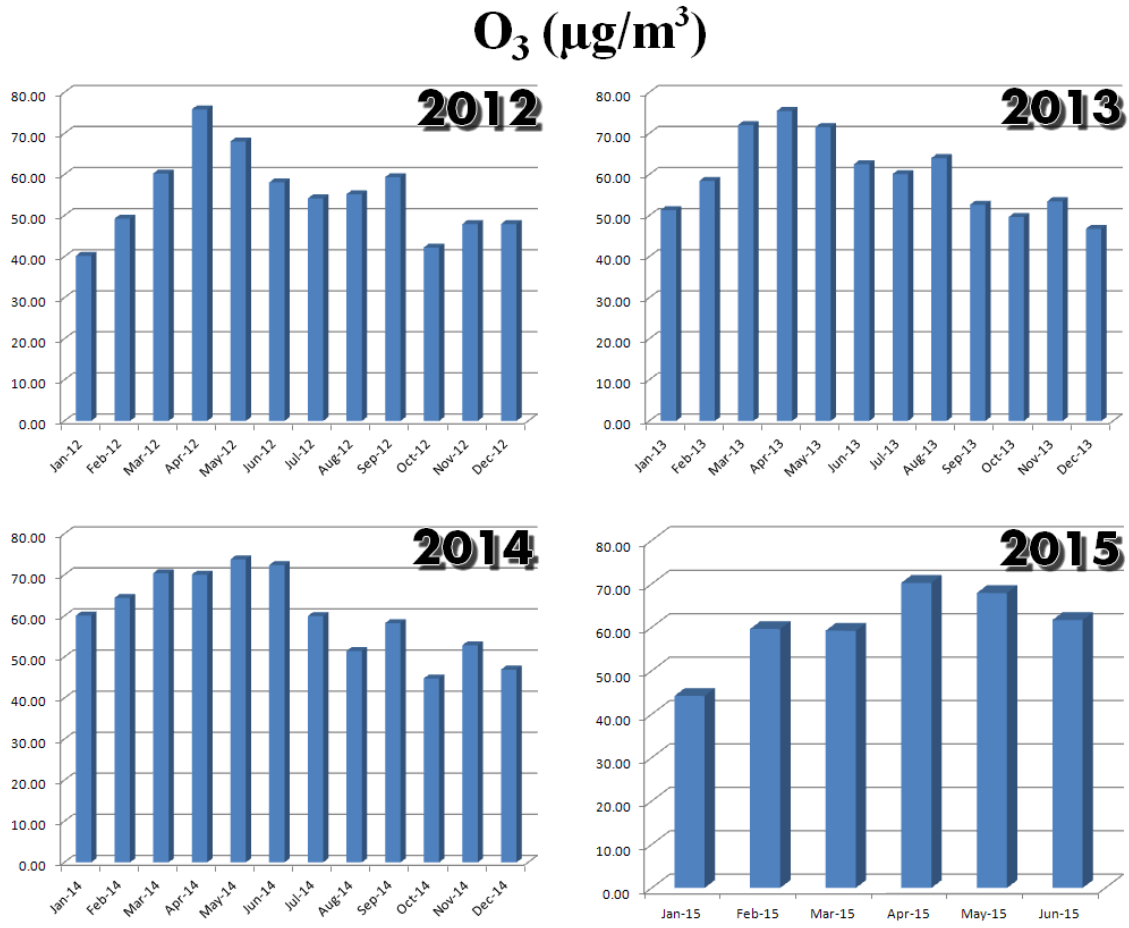

Figure 6.6. O_3 concentrations (µg/m^3) from January 2012 to June 2015.

In the Figure 6.7- 6.9 the values of NO, NO_2 and NO_x (µg/m^3) respectively are represented. In this case, the higher values of NO correspond to the autumn and winter season, observing that in all the years the highest value takes place in January and December. For the case of NO_2 and NO_x, similar trends can be observe, the high values of NO_2 an NO_x are observed systematically during the autumn and winter seasons from 2012 to June 2015.

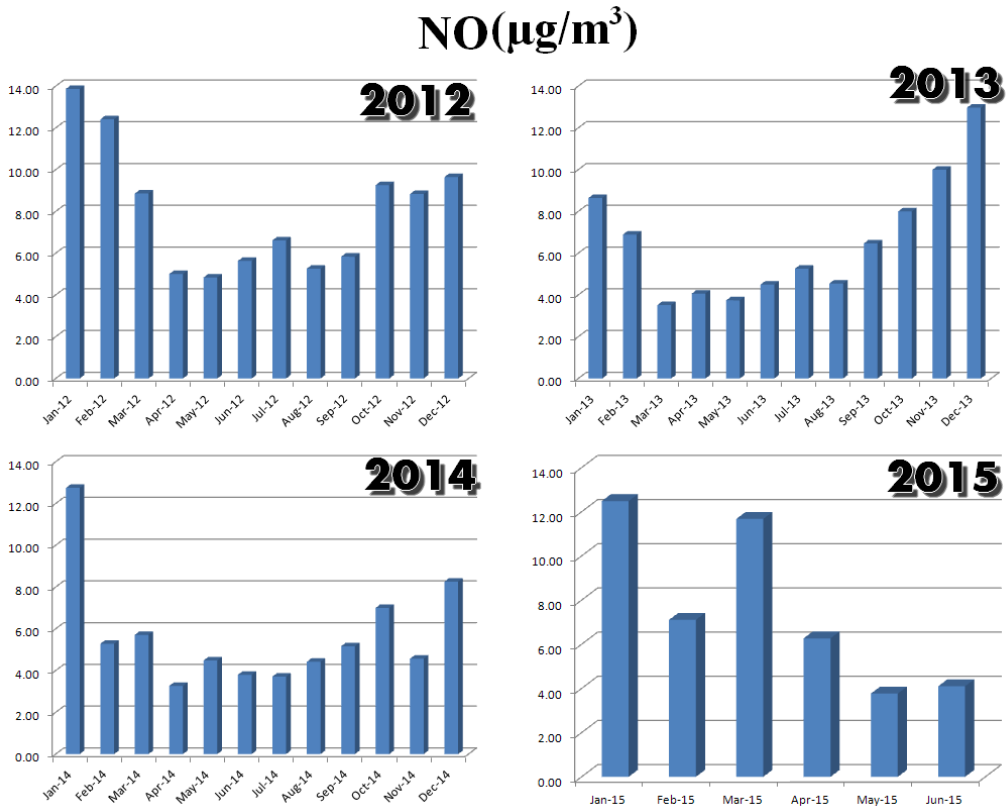

Figure 6.7. NO concentrations (µg/m³) from January 2012 to June 2015.

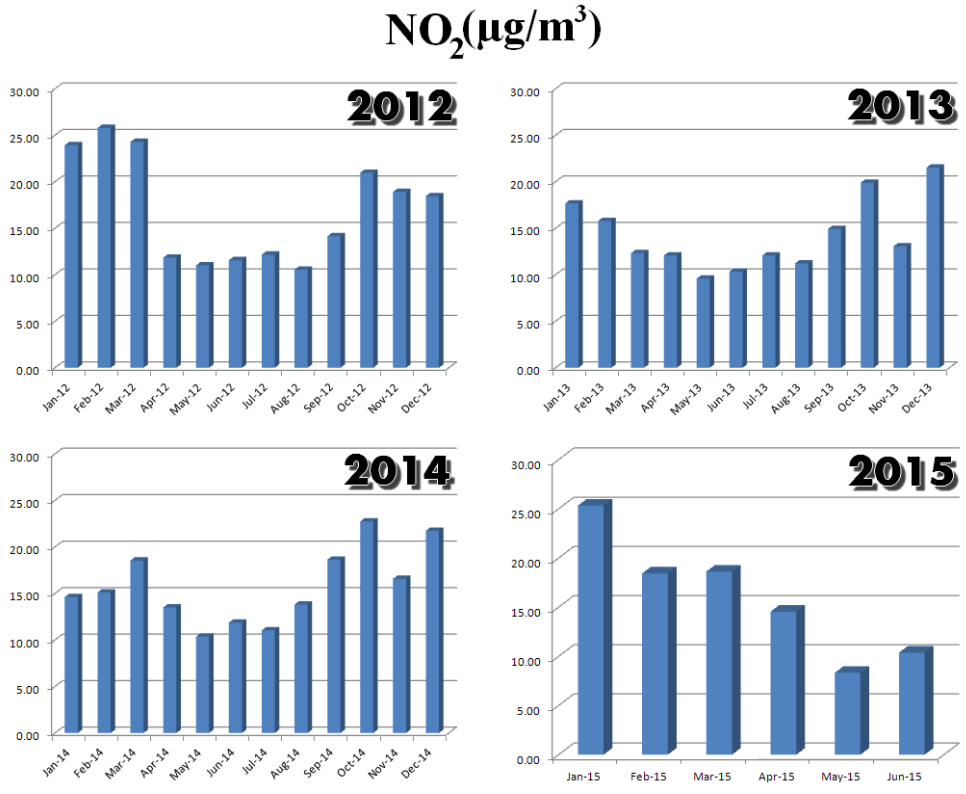

Figure 6.8. NO_2 concentrations (µg/m³) from January 2012 to June 2015.

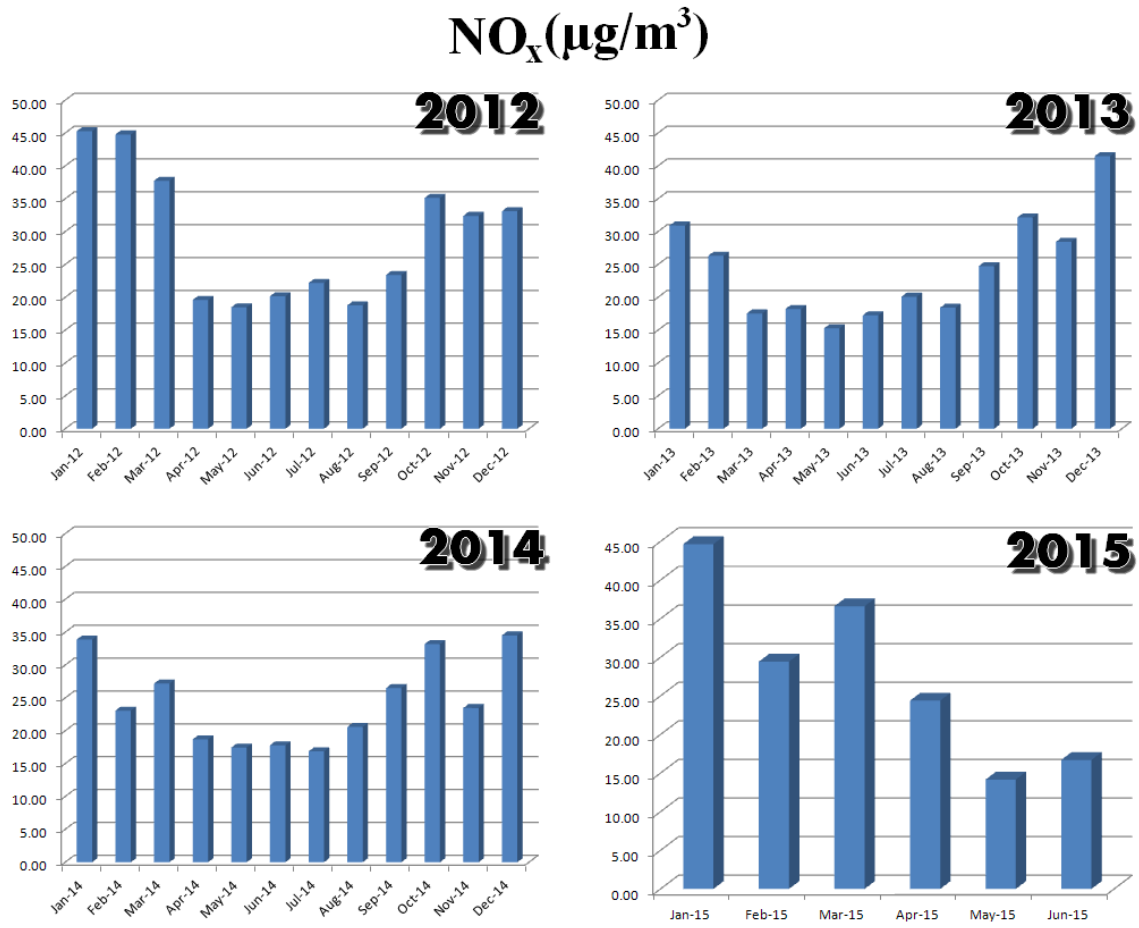

Figure 6.9. NO_x concentrations (µg/m³) from January 2012 to June 2015.

The NO, NO_2 and NO_X from the atmosphere can react with the original material (usually carbonaceous materials or materials with high load of carbonates) following reactions 1 to 3. If we assume that the precursor of the reactions is the NO, it can react in the atmosphere with oxygen (or ozone) giving rise to the NO_2. After that, and in presence of rainwater, the NO_2 is transformed into HNO_3; the oxidized form, and NO (g) the reduced one (reaction 2), which can be deposited on the building material, reacting with the carbonates present to give rise to the subsequent nitrates (reaction 3). These newly formed nitrates are more soluble than the original carbonates, thus material loss could take place.

$$3NO\ (g) + 3/2\ O_2\ (g) \leftrightarrows 3\ NO_2\ (g) \quad \textbf{(1)}$$

$$3NO_2\ (g) + H_2O \leftrightarrows 2HNO_3 + NO\ (g) \quad \textbf{(2)}$$

$$2mHNO_3 + M_2(CO_3)_m \leftrightarrows 2M(NO_3)_m \cdot nH_2O + mCO_2\ (g) + (m\text{-}n)H_2O \quad \textbf{(3)}$$

In the Figure 6.10 the concentrations of SO_2 (µg/m³) are represented. In this case, there were no data available for June 2015, probably because the instrument was temporary out of work. The SO_2 concentrations were quite similar, and no clear trends can be observed. This is probably due to the primary source (industries at work) of this pollutant.

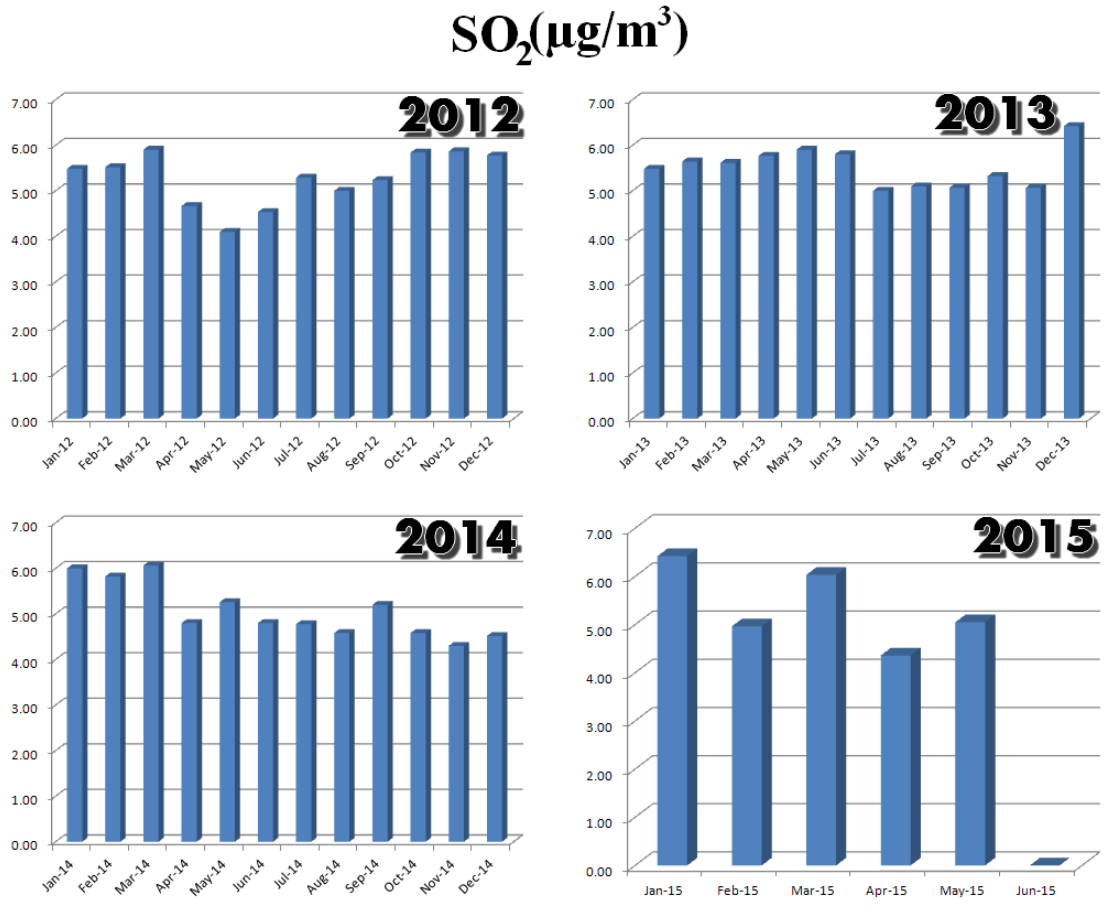

Figure 6.10. SO_2 concentrations (µg/m³) from January 2012 to June 2015.

SO_2, like NO, NO_2, NO_x can react with the material promoting the formation of sulfates. In a first step SO_2 can react with the oxygen (or ozone) giving rise to SO_3 (see reaction 4). Then, the SO_3 can react with the environment water giving rise the sulfuric acid (reaction 5) that can react with the carbonaceous material obtaining the subsequently sulfate (reaction 6). Sulfates are more soluble than carbonates, thus like in the case of nitrates, material loss can take place in the affected building material.

$$SO_2\,(g) + \tfrac{1}{2}\,O_2\,(g) \leftrightarrows SO_3\,(g) \qquad \textbf{(4)}$$

$$SO_3\,(g) + H_2O \leftrightarrows H_2SO_4 \qquad \textbf{(5)}$$

$$mH_2SO_4 + M_2(CO_3)_m \leftrightarrows M_2(SO_4)_m \cdot nH_2O + (m\text{-}n)H_2O + mCO_2\,(g) \qquad \textbf{(6)}$$

Finally, in the Figures 6.11 and 6.12 the concentrations of PM_{10} and $PM_{2.5}$ ($\mu g/m^3$) respectively can be observed. For the case of PM_{10} the data were collected from 2012 until today and for $PM_{2.5}$ the data were collected only from 2014 until today. In this case again, no clear tendencies are observable. The high value of $PM_{2.5}$ in September 2014 was referred as to the temperature inversion we suffered in those days.

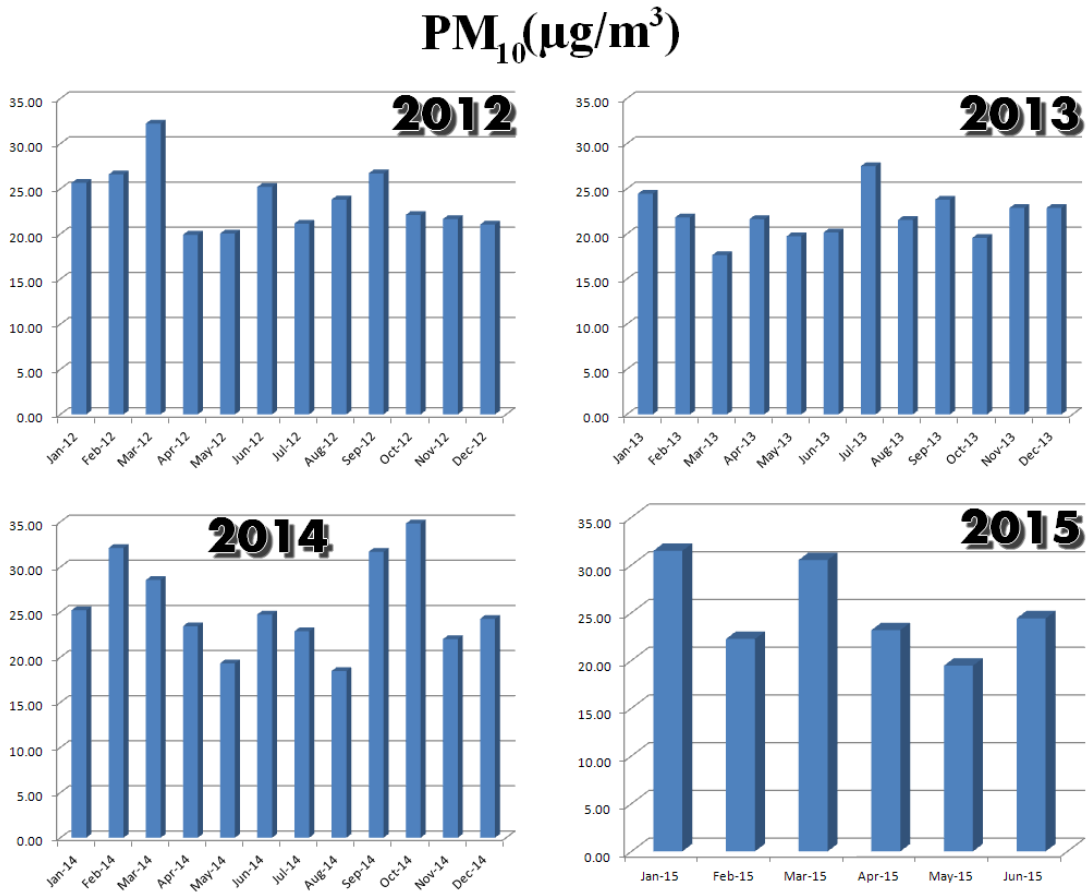

Figure 6.11. PM_{10} concentrations ($\mu g/m^3$) from January 2012 to June 2015.

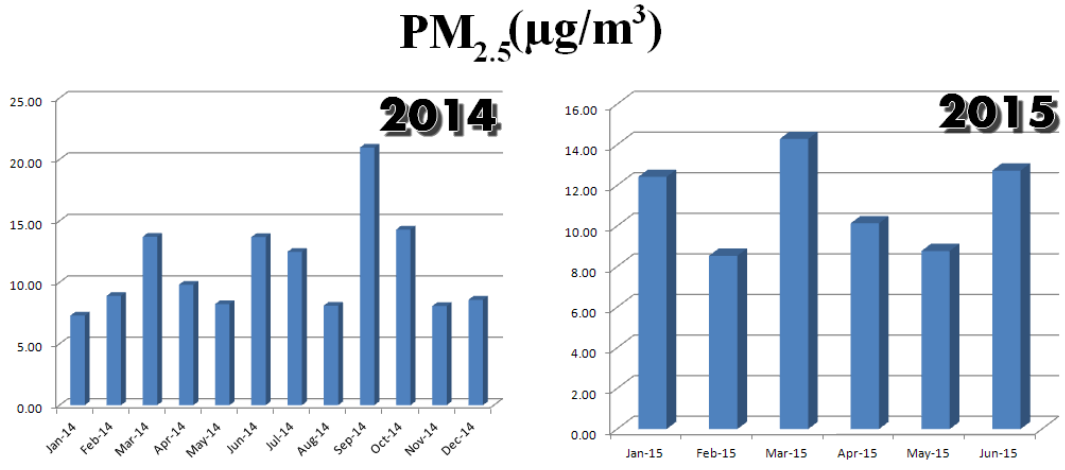

Figure 6.12. $PM_{2.5}$ concentrations ($\mu g/m^3$) from January 2012 to June 2015..

If the wind carries the airborne particulate matter to the sandstone walls, they can hit the material surface favoring day by day the loss of material. Moreover, these particles can be trapped not only in the building material itself, but also in new formations on the surface of the materials (e.g. black crusts)

Finally, in the Figure 6.13, the relative humidity percentage (%RH) of La Galea site is presented. The average value through the represented years (from 2012 until June 2015) is 76.56 %. As it will be explained later, the %RH values are very important, for the development of certain chemical reactions, as well as for the biological colonization processes over the building surfaces.

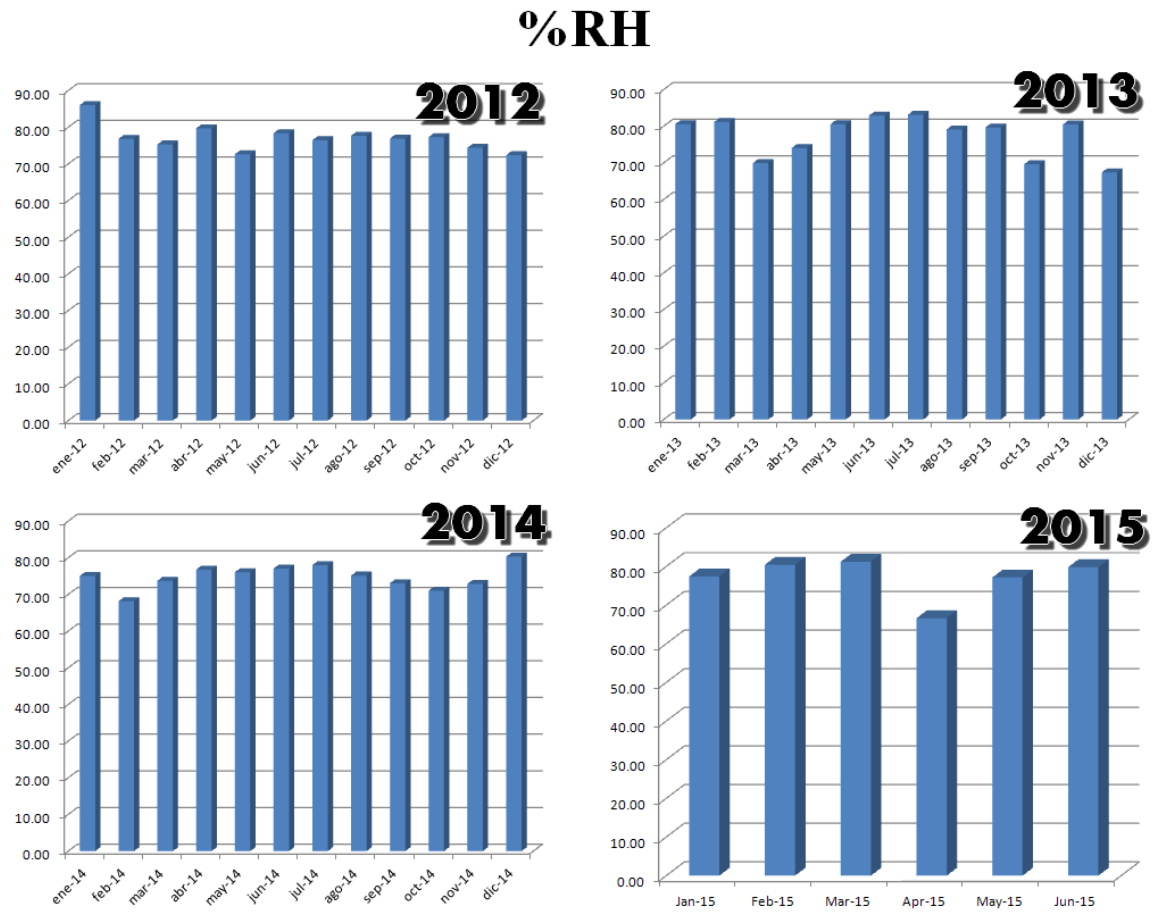

Figure 6.13. Relative Humidity %RH from January 2012 to June 2015.

6.3 References

[1] Junta de 8 de julio 1744 y Junta de 16 de octubre de 1749. Acuerdos de Diputación y Juntas Generales. AJO 100, AJO 104. 1742-1744.

[2] S. Gumuzio, Getxo Municipal Archives (1987) 141.

[3] J. M. Beascoechea, Getxo Municipal Archives (1992) 230.

[4] M. A. Sánchez Terry (1987) 44-46.

[5]http://www.ingurumena.ejgv.euskadi.net/r49-3614/es/aa17aCalidadAireWar/estacion/mapa?locale=es [last accessed July 2015]

RESEARCH ARTICLE 6

Characterization of the main colonizer and biogenic pigments present in the red biofilm from La Galea Fortress sandstone by means of microscopic observations and Raman Imaging.

H. Morillas, M. Maguregui, I. Marcaida, J. Trebolazabala, I. Salcedo, J. M. Madariaga

Microchemical Journal (2015) 121: 48-55

Characterization of the main colonizer and biogenic pigments present in the red biofilm from La Galea Fortress sandstone by means of microscopic observations and Raman imaging

ABSTRACT

This work aims to understand the nature of the main colonizer and the composition of the biogenic compounds present in a reddish biofilm located on the sandstone from the Northwest side of La Galea Fortress (Getxo, North of Spain). For that purpose, microscopic observations of the main colonizer and the biofilm were conducted using Phase Contrast Microscope and a Scanning Electron microscope. These observations allowed identifying the *Trentepohlia* algae as the main colonizer responsible for the reddish biofilm formation. In order to determine the composition of the organic compounds present in the *Trentepohlia* algae and those excreted by them, point-by-point and Raman imaging using confocal Raman microscope were applied. These analyses allowed identifying not only β-carotene as the main biogenic pigment but also additional carotenoids such as bacterioruberin. Moreover, the identification of scytonemin suggests the presence of cyanobacteria on the biofilm.

Keywords: Trentepohlia algae, SEM, Raman imaging, Carotenoids, Scytonemin, Bacterioruberin.

1. Introduction

The main objective of the all the researchers and professionals working with items belonging to the Cultural Heritage is to try to preserve the history around monuments and historic buildings with more relevance. For centuries, sandstone has been one of the most used materials to construct historical buildings. This material exposed to the open air (atmosphere) can suffer biological colonization. One of the main consequences of this biological growing is the formation of biofilms [1]. In the literature many authors pointed out that the biodeterioration process can promote physical and mechanical stress, chemical changes in the composition of stone substrates and esthetical changes in the facades of constructions [2]. The micro-organisms that promote these kinds of biodeterioration processes generally are algae, bacteria, cyanobacteria, fungi, mosses, lichens, higher plants, etc. [3–6]. The first responsible for stone deterioration are the phototropic microorganisms. In some cases, after the growing of these kinds of microorganism, harmful invasions by mosses and vascular plants can be unchained [7]. The invasion by vascular plants is the most critical step in the destruction of monuments, constructions, buildings, etc. made of sandstone [8]. The pioneering microorganisms such as cyanobacteria and algae are able to produce biofilms that retain water and entrap dust, soil particles, spores and seeds; and in some critical cases, they are also responsible of crack and fissure formation [9].

Another factor to consider is the facade orientation of the building where the colonization is placed. Normally, these microorganisms (autotrophs and phototrophs) colonize the north or nortwest facades of buildings made of sandstones, in which the orientation is more influenced by the rain and wind [10].

In some particular cases, microorganisms colonizing in stone and other building material surfaces can act as a bioprotection for the material itself. These biological biofilms can act as a protective barrier against environmental stressors [11]. In the literature there are many works dealing with the bioprotection and related applications to extend the life of historical buildings [12, 13].

Regarding the colonizers, some microorganisms can grow in hostile environments. For this reason, the probability of biological growing depends on several factors. One of the main factors could be the environmental conditions on which a specific type of microorganism may grow [14]. In this way, the relative humidity percentage (% RH) is one of the main environmental factors considered in the growing of microorganisms on stone surfaces [15].

The physicochemical parameters of the substrate have also high influence on the microorganisms growing and biofilm formation process. Depending on the physical parameters of the rock, i.e., permeability, porosity and also on the conservation state of the stone (i.e. small cracks, fissures, too abraded stones) different organisms can grow [16]. The nutrients for the colonizers can come from the stone substrate itself [17] and also from airborne particulate matter deposition coming from the atmosphere (i.e. crustal particulate matter coming from the erosion of surrounding stones, airborne particulate matter carried by marine aerosol).

In the literature there are numerous works about the problem of microorganism colonizations in different types of materials. Sometimes, marble and limestone can be intensely bio-erosioned by different phenomena like epilithic and endolithic forms of sponges. This observation has been ascertained by using X-ray diffraction for matrix characterization and SEM for the identification of sponges [18]. In other cases, hot spring travertine material biocolonizations were characterized using FEG-SEM, SEM-EDS and Raman spectroscopy [19]. In other works, the influence of biocolonizations on ceramic was also studied, observing the growth rate for different colonizers using Phase Contrast Microscopy and monitoring the ceramic bioreceptivity by 2D scanning for the colonizer surface using a Pulse-Amplitude Modulated Fluorometer and quantifying the emitted fluorescence by different colonizers [7].

According to the growing of algae biofilms in sandstones placed on constructions, studies that carried out measures over sandstone colonized sub-surface in order to see the moisture movements and conditions using 2D electrical resistivity tomography (ERT) and observing that some biofilms can act as bioprotector against different stressors [11] can be found in the literature.

The main objective of this work is to characterize the nature of the main colonizer responsible for the reddish biofilm formation in the sandstone from La Galea Fortress (Getxo, North of Spain). For this purpose, microscopic observations using Phase Contrast microscope and SEM were conducted. Moreover, an in-depth characterization of the biogenic pigments present on the biofilm was conducted by means of micro-Raman spectroscopy using point-by-point and imaging analysis strategies. Finally, and in order to observe if the composition of the sandstone from this fortress can be a good substrate for the colonizers responsible for the biofilm formation, an elemental and molecular characterization of the sandstone which supports the biofilm was conducted using SEM-EDS and micro-Raman spectroscopy.

2. Materials and methods

2.1. La Galea Fortress and the surrounding climatology

La Galea Fortress is located in the cliff overlooking the Bay of Agra, in Getxo (north of Spain) and about 80m above sea level. The Fortress is an 18th century military building and took the place of an old watchtower that already existed in the 16th century (Figure 1A). It has masonry and ashlar walls, 14 embrasures for cannons (originally they were 18) and it is surrounded by a moat on the land side. The building hosted several storehouses to keep arsenals, as well as installations for the troops. The most important part of the fortress is the principal tower (Figure 1A, B, C). The tower of the military fortresses was the most important part of this kind of fortifications, where the soldiers observed possible threats. When its military function was discarded at the end of the 19th century, it was used as a lighthouse, until the middle of the 20th century.

The climatic conditions of the location where La Galea fortress is immersed are the following: average temperature of 18.3 °C, average minimum temperature of 7 °C and average maximum temperature of 20.3 °C. Moreover, the annual precipitations are around 1200 mm in which at least, during 128 days rainfall above 1 mm are recorded. The annual average relative humidity is around 76%, but in some periods the humidity reaches 90% or higher values. The annual sunshine hours are 1532 and the average wind speed is 5.6 kts, where the most common directions of wind are to the north-northwest and south-southeast components [20].

Figure 1. (A) General view of La Galea Fortress, (B) red biofilm colonizing the sandstone from the Northwest side of the Fortress tower and (C) general view of the Northwest side of the tower showing the red biofilm on the sandstone blocks.

2.2. Sampling procedure

The conservation state of the sandstone from the fortress tower is very poor, especially the South-southeast side of the tower (Figure 2A and 2B). Alveolization and disintegration phenomena are clearly visible. In some area, certain sandstone blocks are almost disappearing (see details of the disintegration and losing of the sandstone in Figure 2A, 2B). The towerside of the fortress that only shows red biofilms is the Northwest facade. This is the only orientation which shows that sandstone blocks are in a good state of conservation (Figure 1B, C). In the literature, many authors point out that these kinds of colonizations normally occur facing north and northwest and in areas with high moisture content [21]. In this facade, several sandstone fragments with red biofilms were collected. To carry out the sampling, the samples were taken using a little hammer and a chisel and the average size of the fragments never exceeded 2–3 cm.

Figure 2A and 2B. South-southeast side of tower showing its bad state of conservation.

2.3. Instrumentation

A Nikon Eclipse 80i PCM (Phase Contrast microscope) provided with 20×, 40×, and 60× objective lenses was used to obtain microphotographs of the red biofilm. For the preparative process of the sample, special tweezers were used to sample the main colonizer from the red biofilm, under the view of a microscope. After the extraction of the main colonizer, it was placed on a slide and a drop of oil was also added to avoid spherical aberration with the highest numerical aperture lenses, promoted by the different indexes of refraction of the specimen and the objective lenses.

Microscopic images with a Scanning Electron Microscope (SEM) of the red biofilms to determine the structural anatomy of the main colonizer and the biogenic excretions included in these biofilms using an EVO®40 SEM (Carl Zeiss STS, Germany) were also obtained. For the image acquisition, samples were coated with gold in order to ensure their conductivity and therefore, to obtain better microscopic images. The SEM images were acquired at high vacuum employing an acceleration voltage of 30 kV. It was reached up to 10,000× magnification using a secondary electron detector. In order to determine the elemental composition of the sandstone, the X-Max Energy-Dispersive X-ray spectrometer

(Oxford Instruments, Abingdon, Oxfordshire, United Kingdom) coupled to the SEM was used. In order to ensure the conductivity of the biofilm and sandstone surfaces, and to improve the image resolution acquired with the SEM, samples were coated with gold.

The red biofilm and the sandstone were also analyzed using a confocal Raman microscope (Renishaw, Gloucestershire, UK). The spectrometer is coupled to a DMLM Leica microscope which includes 20×, 50×, and 100× long range objective lenses. The instrument implements several lasers, but in this work the 785 and 514 nm excitation lasers were used. The spectrometer was daily calibrated by using the 520 cm^{-1} Raman band of a silicon chip. The information obtained with both lasers was combined in order to obtain the maximum spectral information. In order to avoid thermal photodecomposition of organic compounds present in the red biofilm, the nominal power of the lasers never exceeded 1 mW. Data acquisition was carried out using Wire 3.2 software package (Renishaw). Spectra were acquired between 100 and 4000 cm^{-1} (1 cm^{-1} spectral resolution) and several scans were accumulated for each spectrum in order to improve the signal-to-noise ratio (5–15 s, 10–30 accumulations).

Apart from the point-by-point Raman analyses, Raman image acquisitions of specific areas of the red biofilms on sandstone samples were conducted using the StreamLine Plus by Renishaw and the 514 nm excitation laser. After performing a baseline correction, the spectra were filtered for a wavenumber region that corresponds to the fingerprint area of the compounds under study. In order to construct the images of the different distributions, the Wire 3.2 software (Renishaw) was used, that implements different options for Raman Imaging. Different areas of the red biofilm were mapped according to the Signal to Baseline option, setting a different color to the main Raman band belonging to each identified compound in the selected area.

3. Results and discussion

3.1. Molecular and elemental characterization of the sandstone using Raman spectroscopy and SEM-EDS

For the characterization of the molecular composition of the sandstone matrix using Raman spectroscopy, the 785 nm excitation laser was used. This laser offered the best spectral results for this kind of matrix. The main components of the sandstone which act as a support for the colonization are iron (III) oxides (hematite (Fe_2O_3), main bands at 225, 292, 410, 495 and 611 cm^{-1}) and oxyhydroxides. Among the last ones, different polymorphs were identified (e.g. limonite ($FeO(OH).\ nH_2O$), main bands at 240, 298, 393, 477 and 548 cm^{-1}, and lepidocrocite (γ-FeO(OH), main bands at 212, 246, 304, 343, 373, 522 and 648 cm^{-1})). Another main constituent of La Galea Fortress is the quartz (α-SiO_2), main bands at 262, 355, 400, 464, 694, 805, and 1159 cm^{-1}.

Apart from quartz, additional silicates were also identified, such as orthoclase, adularia, ($KAlSi_3O_8$) with its main bands at 282, 405, 457, 475 and 512 cm^{-1}. Finally in specific spectra, charcoal (C) was also identified, thanks to the presence of its main broad bands at 1320 and 1595 cm^{-1} (Figure 3A, B).

Apart from the molecular characterization, as it was previously commented, elemental characterization of the sandstone was also conducted using energy dispersive X-ray spectrometry (EDS). In Figure 3C, the microphotograph obtained with the SEM where the EDS measurements were performed can be observed. The sandstone matrix is composed by C, O, Mg, Al, Si, Fe, K and Ca (Figure 3D, E, F). The presence of Ca and C could suggest that the sandstone of La Galea Fortress is a calcarenite type sandstone, a specific type of sandstone that includes calcium carbonate as cementing in its original composition. The C line can also be related with the presence of charcoal, identified in this matrix by means of Raman spectroscopy. Fe and O can be related with iron (III) oxides and oxyhydroxides such as hematite and limonite and lepidocrocite, identified by means of Raman spectroscopy. The presence of K, Al, Si and O can be related with adularia, identified by Raman spectroscopy. The presence of silicon in the EDS spectrum can be also related with quartz, identified also by means of Raman spectroscopy.

In the EDS spectra acquired from the La Galea Fortress sandstone, Na was also present. This element can come from the original composition of the matrix, but it can be also related with halite (NaCl) crystallizations and depositions in this building material. Concretely, chlorine is present in almost all the EDS spectra acquired. As an example, the spectrum showed in

Figure 3E can be mentioned. In this spectrum, the intensity of the Na and Cl lines is much higher than the intensity of the lines of the rest of the elements coming from the sandstone matrix. Therefore, the measurement linked with the EDS spectrum in Figure 3E can be related with a deposited NaCl particle or with a new NaCl crystallization (Figure 3C). Some of the elements present in the sandstone matrix such as Ca, Mg and Na can act as macronutrients for the colonizers present in the sandstone. Moreover, elements such as Fe and Cl, also present in the sandstone, can be considered as micronutrients for the correct growing of colonizer such as *Enteromorpha intermedia* algae [22] or different Fe-reducing bacteria such as *Geobacter metallireducens* and *Geothrix diplococcus* present in feldspars orthoclases [23]. Therefore, the sandstone itself together with the influence of the surrounding atmosphere (temperature, % RH, etc.) can be considered a good substrate for the growing of certain microorganisms [24].

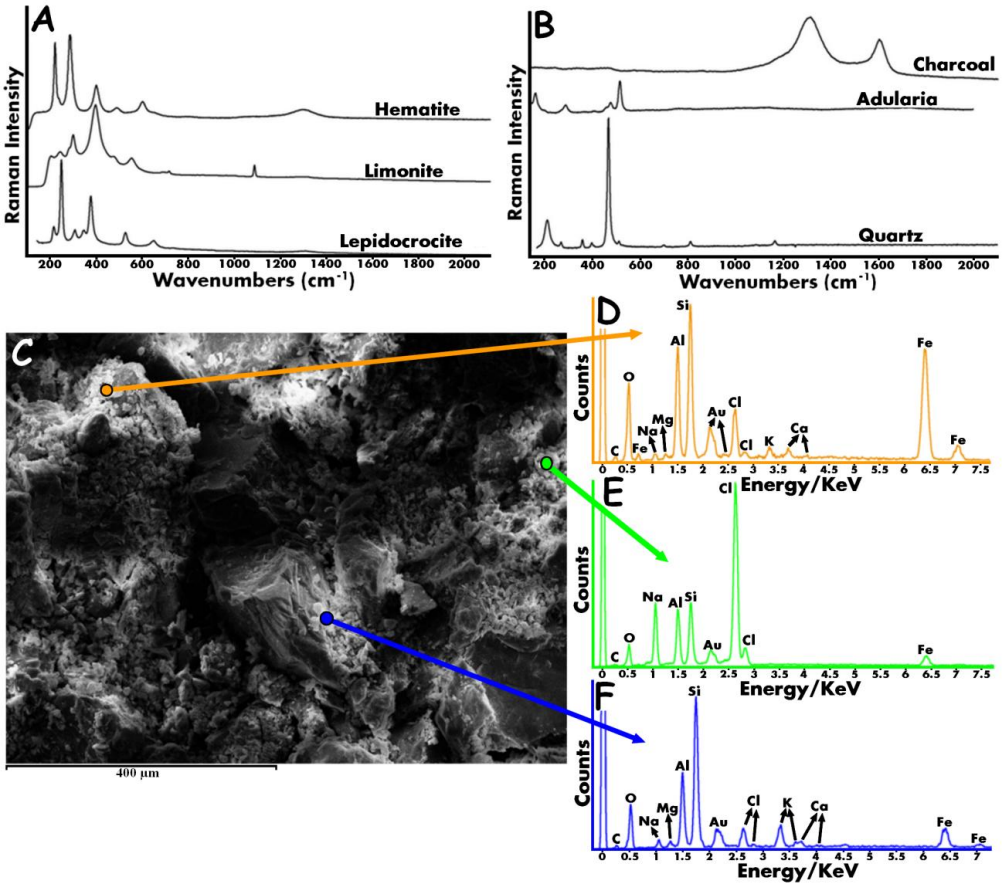

Figure 3. Raman spectra acquired on the sandstone showing (A) hematite (Fe_2O_3), limonite ($FeO(OH)\cdot nH_2O$) and lepidocrocite (γ-$FeO(OH)$), (B) charcoal, adularia ($KAlSi_3O_8$) and quartz (SiO_2), (C) sandstone matrix morphology under SEM, (D) sandstone matrix EDS spectrum showing the presence of C, O, Fe, Na, Mg, Al, Si, Au, Cl, K and Ca, (E) sandstone matrix EDS spectrum showing the presence of C, O, Na, Al, Si, Au, Cl, and Fe, and (F) Sandstone matrix EDS spectrum showing the presence of C, O, Na, Mg, Al, Si, Au, Cl, K.

3.2. Microscopic observations to determine the nature of the main colonizer of the red biofilm

For the characterization of the structural anatomy of the main colonizer extracted from the surface of the red biofilm, microphotographies with the Phase Contrast Microscope (PCM) using 20×, 40×, and 60× objective lenses were obtained. In Figure 4A, B, D, the different parts of the main colonizer of the red biofilm can be observed. The obtained microphotographs showed the characteristic long filaments and short chains of large cells of algae. As can be observed, inside the filaments, regular and irregularly shaped cells embedded in clear mucilage and mostly filled with discrete orange oil droplets of varying size can be observed (Figure 4E, F). These kinds of filaments are representative of algae from the genus *Trentepohlia* [25].

According to the literature, *Trentepohlia* algae are one of the main biodeteriogen on building materials from historical buildings in different areas and countries worldwide. In the literature, the typical atmospheric conditions in where *Trentepohlia* algae are growing are described and they belong to an annual Relative Humidity (RH) of 72–90%, an annual average precipitation of 1200–1900 mm and an annual average temperature around 12–17 °C [25, 26]. These atmospheric conditions are quite similar to those of the La Galea Fortress (see La Galea Fortress and the surrounding climatology Section).

As examples, in China, its presence has been found on rocks throughout a valley [25], in funerary sculptures from Argentina [26], in limestone monuments from Mexico [27], and in wall paintings colonizations from Italy [28]. Only one case of *Trentepohlia* sandstone colonization is referred in the literature, concretely in a Buddhist temple in Cambodia [29]. According to the environmental conditions (temperature, relative humidity percentage, etc.) and latitude, the Cambodia scenario is very different compared with the one of the La Galea Fortress. *Trentepohlia* algae colonization produces physical degradation (e.g. material disintegration, erosion) of the monuments and discoloration of the colonized surface, due to pigment production as an adaptation to increase the resistance of the colonizers against environmental stress [26, 27].

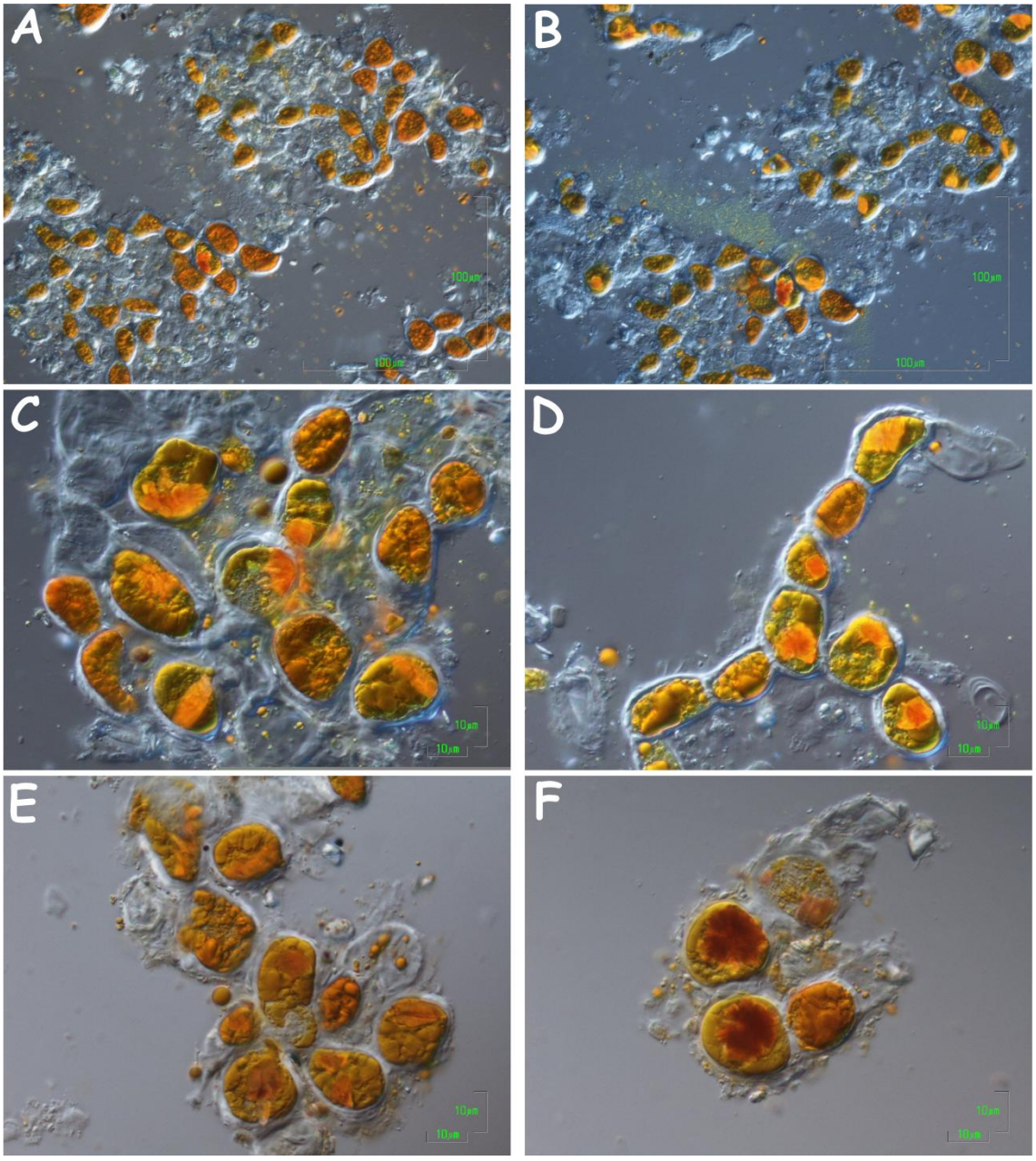

Figure 4. (A) and (B) General view of the colonies of *Trentepohlia*. (C) and (D) Physiognomy of *Trentepohlia* showing its long filaments and short chains of large cells. (E) and (F) Red and orange crystals inside the shaped cells embedded in clear mucilage of *Trentepohlia*.

In order to characterize better *Trentepohlia* algae and to observe the interaction of *Trentepohlia* with the sandstone matrix, additional microphotographs were acquired with a Scanning Electron Microscope (SEM) with different magnifications (Figure 5A, B, C).

As can be observed in Figure 5D, the colonization over the sandstone is very heterogeneous. In the same figure, details of the filaments and hiphae penetrating the sandstone can be appreciated. According to several authors, hiphae and filament penetration can cause loss of material [30, 31] and can be related with photosynthetic system between the algae and

cyanobacteria or parasitic fungi [32]. Moreover, a large quantity of crystals can be observed on the algae (Figure 5E) and inside their globular cells (Figure 5F).

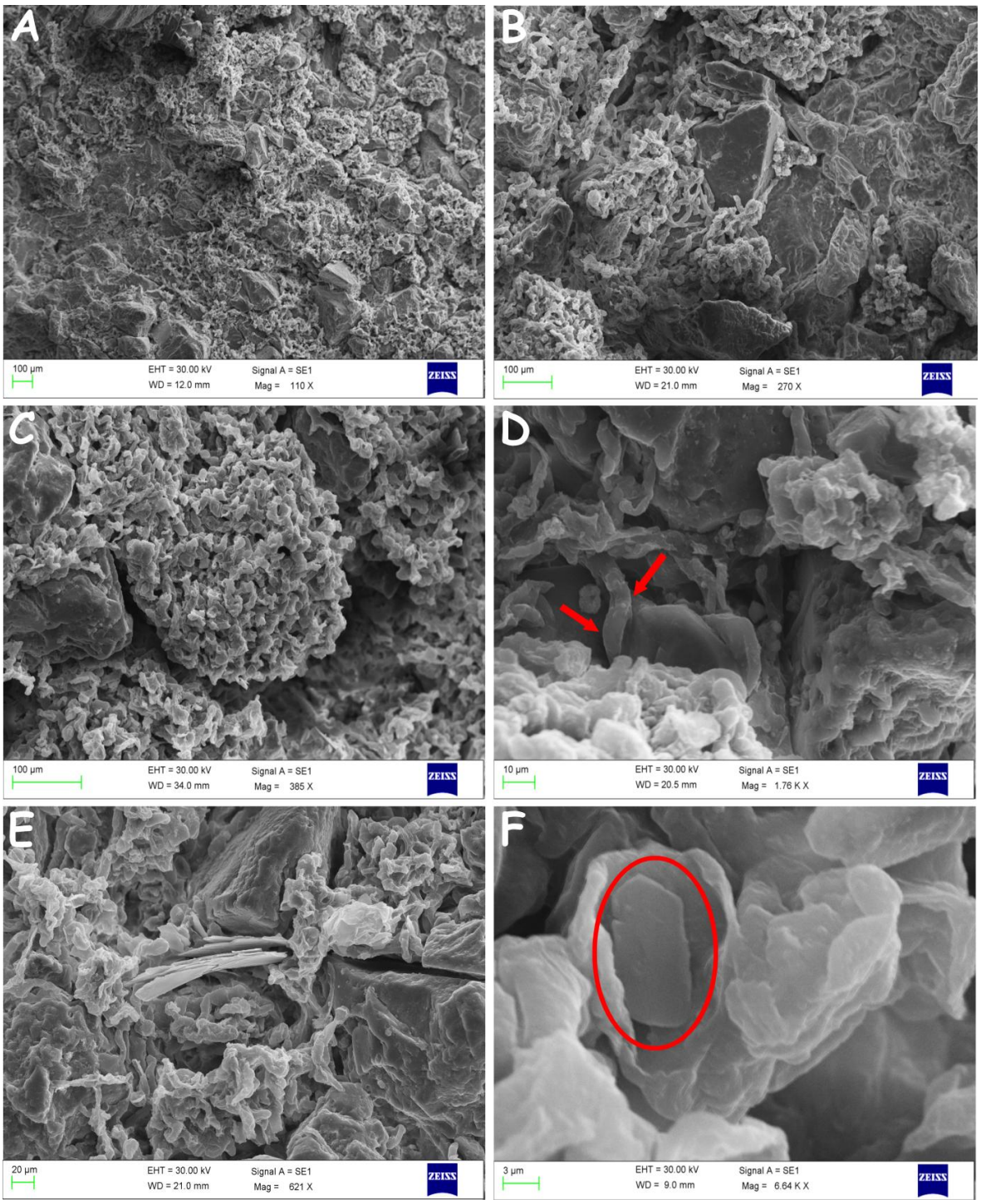

Figure 5. Microphotographs obtained using SEM. (A) and (B) General view of *Trentepohlia* colonization over sandstone. (C) General view of *Trentepohlia's* external physiognomy. (D) Hyphae penetrating the surface of the sandstone. (E) Crystallizations on the biofilm. (F) Crystals formed into the globular cells of the *Trentepohlia* algae.

3.3. Point-by-point and Raman imaging on red biofilms

In order to know what types of biogenic compounds are present in the reddish colored biofilm, different measurements were performed by micro-Raman spectroscopy using the 512 nm excitation laser. Considering that most of the organic compounds present on the structure of the microorganisms and those excreted by them have unsaturations, the 512 nm laser can be a good option to achieve the Resonance Raman effect. This effect allows magnifying certain bands and also reveals some vibrational modes which cannot be observable with the 785 nm laser. In almost all the measurements performed β-carotene (Figure 6), showing its characteristic bands at 519, 790, 855, 873, 879, 961, 1006, 1136, 1157, 1192, 1213, 1255, 1269, 1281, 1354, 1390, 1446, 1526, 1571 and 1597 cm^{-1} were identified. Moreover, thanks to the use of 512 nm excitation laser, certain vibrational modes such as overtones and combination tones of β-carotene were also revealed at 2012, 2159, 2313, 2349, 2476, 2522, 2672, 2707 and 3024 cm^{-1}. The main excreted pigment by red algae is β-carotene [33]. *Trentepohlia* algae filaments contain cells filled with carotenoid pigments, which are accumulated as a response to the light exposition, acting as a shield against photodecomposition and nitrogen deficiency [28]. These carotenoid pigments are observably crystallized in the globular cells (as examples see Figs. 4C, D, E, F and 5F). These crystals are accumulated in the chloroplasts, to prevent the photodamage of the chlorophyll [25–29, 34]. The formation of β-carotene crystals (orange-red) masks the real green color of the photosynthetic pigments of the algae, chlorophyll, giving as a result a red colored biofilm, instead of a green colored colonization. Apart from β-carotene, astaxanthine was also identified in *Trentepohlia* algae [34]. The algae also excrete this biogenic pigment to protect itself against UV-radiation. In the red biofilm of the La Galea Fortress, it was not possible to identify Raman bands related with astaxanthine. Taken into account the northwest orientation of the tower, where the algae has grown up, high intensity light, sunlight and deficiency of nutrients should be excluded as stressor promoting the formation of β-carotene crystals. Thus, salinity [35] and maybe greenhouse gasses from the nearby power station and refinery plants should be considered as the precursor of the β-carotene crystal synthesis [36]. Other spectra acquired on the red biofilm, showed bands related with scytonemin at 496, 576, 660, 678, 753, 1096, 1171, 1285, 1324, 1383, 1435, 1554, 1598 and 1631 cm^{-1} (Figure 6).

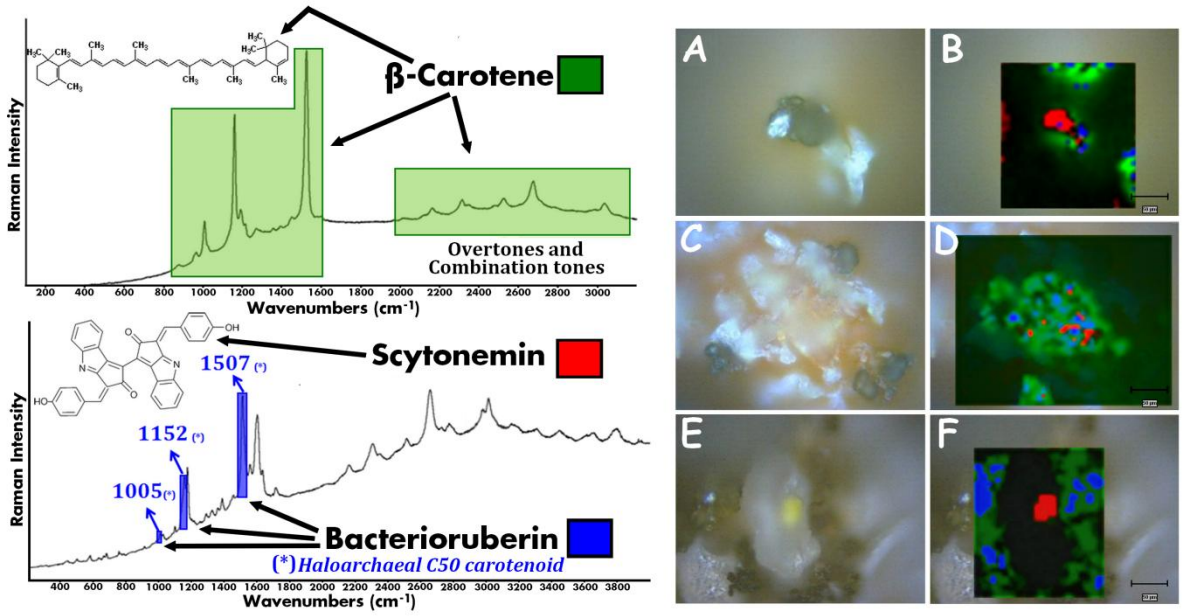

Figure 6. Raman spectra showing bands related with the three main biogenic pigments (β-carotene, scytonemin and haloarchaeal C50 carotenoid) identified on the biofilm and some examples of their distribution on the biofilm.

The identification of scytonemin could suggest that among *Trentepohlia*, other colonizers such as cyanobacteria could be also present in the red biofilm. This yellow-brown pigment is usually present in the extracellular sheaths of cyanobacteria. Some authors suggest that the most probable cyanobacteria present with the family of *Trentepohliaceae* are *Chroococcus and Nostoc* [28]. In the literature, there are examples of the relation between cyanobacteria and photosynthetic systems [37]. In some cases, cyanobacteria and red algae (e.g. *Trentepohlia*) form supramolecular assemblies called phycobilisomes. An example of this kind of assemblies *Gloeocapsa* can be mentioned [38]. These assemblies can act as light-harvesting complexes [39]. The presence and the survival of cyanobacteria in terrestrial environment depends largely on the synthesis of a specialized set of protective biochemicals in response to different stressors like desiccation with high-energy radiation insulation, extreme pH variations, changes of temperature and pressure and also high concentrations of toxic heavy metals particles [40]. Apart from these biogenic pigments, in some areas of the red biofilm, Raman bands at 1005, 1152 and 1507 cm^{-1} were identified (Figure 6 bottom left). These Raman bands could belong to haloarchaeal C50 carotenoids (e.g. bacterioruberin). In the same Raman spectrum (bottom spectrum of Figure 6), different combination bands and overtones related with carotenoids at 2120–2820 cm^{-1} were also present. Finally two bands between 2900–3100 cm^{-1} assigned to CH_2 and CH_3 stretching modes suggest the presence of proteins and/or lipids [41]. According to literature apart from β-carotene, other antioxidants such as L-ascorbic (vitamin C) acid and antioxidants

and lipids such as tocopherols (vitamin E) are present in *Trentepohlia* cells [42]. The last ones, in other types of algae, are also related with protection against exposure to light and in some cases against nitrogen stress [43]. Taking into account the location of the La Galea Fortress, which is surrounded by maritime traffic and industry this hypothesis cannot be ruled out. In order to map the distribution of the main biogenic pigments excreted by *Trentepohlia* algae and possible cyanobacteria, Raman imaging was used. In the literature, no work can be found showing the distribution of β-carotene, bacterioruberin and scytonemin in the same biofilm. In Figure 6B, D, F some examples of Raman images acquired on the red biofilm can be observed. The black areas in the Raman images correspond to areas where none of the main bands of these three compounds appear. The black areas in the Raman maps of Figure 6 can be quartz, iron oxides and oxyhydroxides, aluminosilicates or charcoal (see matrix composition of Figure 3), that is, compounds related with the sandstone substrate. The green color corresponds to β-carotene, the red color to scytonemin and the blue color to bacterioruberin. It is important to highlight that in the acquired Raman images, β-carotene (green color in Figure 6) is the major and predominant compound, thus it can be said that the main biogenic pigment that offers the reddish color to the biofilm is the β-carotene. For the case of scytonemin (red color in Figure 6) its distribution is very heterogeneous and punctual without remarkable trends. In all the Raman images acquired, bacterioruberin is distributed on the surface together with β-carotene. On the contrary, in most of the Raman images acquired, scytonemin is localized or accumulated separately from both carotenoids.

4. Conclusions

In this work, a multianalytical methodology based on the use of microscopic observations (PCM and SEM) and micro-Raman analysis (point-by-point and imaging) was used in order to characterize the nature of the main colonizer and the biogenic pigment on the red colonization or biofilm from the northwest face of the tower of the La Galea Fortress. Apart from that, an elemental and molecular characterization of the sandstone acting as the support of the colonization was also carried out. Thanks to the use of the Phase Contrast Microscope (PCM), it was possible to determine that the main colonizer of the red biofilm is the *Trentepohlia* alga. With these microscopic observations, it was possible to observe the short chains of cells and globular body's oily organic crystal fillings. In order to corroborate these statements, additional observations of the red biofilm using the Scanning Electron Microscopy (SEM) were performed. These observations helped us to understand better the distribution of *Trentepohlia* over the substrate and its interaction with the matrix. It was also observed how the alga penetrates into the matrix using its filaments and hiphae, revealing also organic crystal growths on the globular bodies, thereby confirming what it was, as previously seen by PCM. The use of point-by-point micro-Raman spectroscopy on the substrate revealed that the main components of the sandstone are quartz, iron oxides (limonite, hematite, lepidocrocite), aluminosilicates (adularia, ortoclasa) and charcoal. In order to complete these results, additional SEM-EDS analyses of the sandstone were also conducted observing the presence of elements like C, O, Fe, Na, Mg, Al, Si, Cl, K and Ca. Some of these elements can act as macro- (Ca, Mg and Na) and micro-nutrients (Fe and Cl) of *Trentepohlia* algae. According to the literature [26–28] it is not very common to find *Trentepohlia* algae colonization over sandstone, except in one scenario described in Cambodia [29]. According to the composition of the red biofilm, the point-by-point Raman analyses revealed the presence of three main compounds: β-carotene, scytonemin and haloarchaeal C50 carotenoid. Moreover, Raman band related with lipids and/or proteins were also distinguished. Finally Raman imaging allowed us to map the distribution of carotenoids such as β-carotene and bacterioruberin, and other organic pigments such as scytonemin on the red biofilm from the La Galea Fortress. The selection of appropriate excitation laser wavelength (514 nm) helped us to distinguish additional Raman bands (weak Raman bands inside carotenoids fingerprints, overtones, combination tones, etc.), due to the Resonance Raman effect achieved. The presence of different kinds of biogenic pigments suggests that *Trentepohlia* alga is suffering an intense stress which is the responsible of these biological pigment excretions. Considering that the colonization is placed in the northwest façade of the tower, the sunlight cannot be considered as the main

stressor. Nevertheless, additional stressors such as salinity (buildings close to the sea) and also the surrounding acid atmosphere (i.e. SO_x and NO_x acid aerosols) can be considered as potential stressors which can trigger the excretion of the identified biogenic pigments. Even though the main colonizer promotes the formation of a red colored biofilm on the surface of the sandstone, originating an esthetical change from this northwest facade of the tower, it is necessary to remark that the conservation state of the sandstone blocks of this orientation, where the red biofilm is present, is better comparing with the rest of the orientations. Therefore, a possible bioprotection action of the biofilm with respect to the sandstone can be assumed.

5. References

[1] H. Hu, S. Ding, Y. Katayama, A. Kusumi, S. X. Li, R. P. de Vries, J. Wang, X. Z. Yu, J. D. Gu, Occurrence of Aspergillus allahabadii on sandstone at Bayon temple, Angkor Thom, Cambodia, International Biodeterioration & Biodegradation (2013) 76: 112–117.

[2] A. A. Gorbushina, J. Heyrman, T. Dornieden, M. Gonzalez-Delvalle, W. E. Krumbein, L. Laiz, K. Petersen, C. Sáiz-Jimenez, J. Swings, Bacterial and fungal diversity and biodeterioration problems in mural painting environments of St. Martins church (Greene-Kreiensen, Germany), International Biodeterioration & Biodegradation (2004) 53: 13–24.

[3] T. Varnali, H. G. M. Edwards, Iron-scytonemin complexes: DFT calculations on new UV protectants for terrestrial cyanobacteria and astrobiological implications, Astrobiology (2010) 10: 711–716.

[4] S. Görs, R. Schumann, N. Häubner, U. Karsten, Fungal and algal biomass in biofilms on artificial surfaces quantified by ergosterol and chlorophyll a as biomarkers, International Biodeterioration & Biodegradation (2007) 60: 50–59.

[5] M. Maguregui, U. Knuutinen, J. Trebolazabala, H. Morillas, K. Castro, I. Martinez-Arkarazo, J. M. Madariaga, Use of in situ and confocal Raman spectroscopy to study the nature and distribution of carotenoids in brown patinas from a deteriorated wall painting in Marcus Lucretius House (Pompeii), Analytical & Bioanalytical Chemistry (2012) 402: 1529–1539.

[6] C. C. Gaylarde, O. Ortega-Morales, Microbial colonisation of historic building in Latin America, Heritage Microbiology and Science Royal Society of Chemistry, E-Publishing Inc., Cambridge, UK, (2008) 39–44.

[7] M. C. Portillo, M. F. Gazulla, E. Sanchez, J. M. Gonzalez, A procedure to evaluate the resistance to biological colonization as a characteristic for product quality of ceramic roofing tiles, Journal of the European Ceramic Society (2011) 31: 351–359.

[8] G. Gómez-Alarcón, M. Muñoz, X. Ariño, J. J. Ortega-Calvo, Microbial communities in weathered sandstones: the case of Carrascosa del Campo church, Spain, Science of the Total Environment (1995) 167: 249–254.

[9] M. Hoppert, C. Flies, W. Pohl, B. Guenzi, J. Schneider, Colonization strategies of lithobiontic microorganisms on carbonate rocks, Environmental Geology (2006) 46: 421–428.

[10] C. Adamson, S. McCabe, P. A. Warke, D. McAllister, B. J. Smith, The influence of aspect on the biological colonization of stone in Northern Ireland, International Biodeterioration & Biodegradation (2013) 84: 357–366.

[11] N. A. Cutler, H. A. Viles, S. Ahmad, S. McCabe, B. J. Smith, Algal greening and the conservation of stone heritage structures, Science of the Total Environment (2013) 442: 152–164.

[12] X. Ariño, J. J. Ortega-Calvo, A. Gomez-Bolea, C. Saiz-Jimenez, Lichen colonization of the Roman pavement at Baelo Claudia (Cadiz, Spain): Biodeterioration vs bioprotection, Science of the Total Environment (1995) 167: 353–363.

[13] M. Ramirez, M. Hernandez-Mariné, E. Novelo, M. Roldan, Cyanobacteria containing biofilms from a Mayan monument in Palenque, Mexico, Biofouling (2010) 26: 399–409.

[14] S. Sanchez-Moral, L. Luque, S. Cuezva, V. Soler, D. Benavente, L. Laiz, J. M. Gonzalez, C. Saiz-Jimenez, Deterioration of building materials in Roman catacombs: The influence of visitors, Science of the Total Environment (2005) 349: 260–276.

[15] A. Jain, S. Bhadauria, V. Kumar, R. S. Chauhan, Biodeterioration of sandstone under the influence of different humidity levels in laboratory conditions, Building & Environment (2009) 44: 1276–1284.

[16] M. Garcia-Valles, M. Vendrell-Saz, J. Molera, F. Blazquez, Interaction of rock and atmosphere. Patinas on Mediterranean monuments, Environmental Geology (1998) 36: 137–149.

[17] C. M. Duarte, J. Dachs, M. Llabres, P. Alonso-Laita, J. M. Gasol, A. Tovar-Sanchez, S. Sanudo-Wilhemy, S. Agusti, Aerosol inputs enhance new production in the subtropical northeast Atlantic, Journal of Geophysical Research-Biogeosciences (2006) 11: 1–8.

[18] P. Aloise, M. Ricca, M. F. La Russa, S. A. Ruffolo, C. M. Belfiore, G. Padeletti, G. M. Crisci, Diagnostic analysis of stone materials from underwater excavations: the case study of the Roman archaeological site of Baia (Naples, Italy), Applied Physics A: Materials Science & Processing (2014) 114: 655–662.

[19] S. E. Jorge-Villar, L. G. Benning, H. G. M. Edwards, AMASE team, Raman and SEM analysis of a biocolonised hot spring travertine terrace in Svalbard, Norway, Geochemical Transactions (2007) 8: 8.

[20] EUSKALMET: basque meteorology agency [Internet] [last accessed on 9th October 2014] © EUSKALMET — Directorate of Attention to Emergencies and Meteorology — Eusko Jaurlaritza—Basque Government, (2011). (Available from http://www.euskalmet.euskadi.net/s075853x/eu/meteorologia/home.apl?e=8).

[21] B. O. Ortega-Morales, C. Gaylarde, A. Anaya-Hernandez, M. J. Chan-Bacab, S. C. De la Rosa-García, D. Arano-Recio, J. Montero-M, Orientation affects Trentepohlia-dominated biofilms on Mayan monuments of the Rio Bec style, International Biodeterioration & Biodegradation (2013) 84: 351–356.

[22] S. S. Sagar, Mineral Nutritive Status of Enteromorpha intermedia bliding: A fresh water green algae, International Research Journal of Pharmaceutical & Applied Sciences (2013) 3: 143–147.

[23] J. R. Rogers, P. C. Bennett, W. J. Choi, Feldspars as a source of nutrients for microorganisms, American Mineralogist (1998) 83: 1532–1540.

[24] F. Bartoli, A. Casanova Municchia, Y. Futagami, H. Kashiwadani, K. H. Moon, G. Caneva, Biological colonization patterns on the ruins of Angkor temples (Cambodia) in the biodeterioration vs bioprotection debate, International Biodeterioration & Biodegradation (2014) 96: 157–165.

[25] G. Liu, Q. Zhang, H. Zhu, Z. Hu, Massive Trentepohlia-Bloom in Glacier Valley of Mt.Gongga, China, and a New Variety of Trentepohlia (Chlorophyta), PLoS One (2012) 7: e37725.

[26] P. Guiamet, M. Crespo, P. Lavin, B. Ponce, C. Gaylarde, S. Gómez de Saravia, Biodeterioration of funeral sculptures in La Recoleta Cemetery, Buenos Aires, Argentina: Pre-and post-intervention studies, Colloids and Surface B: Biointerfaces (2013) 101: 337-342.

[27] P. Gaylarde, G. Englert, O. Ortega-Morales, C. C. Gaylarde, Lichen-like colonies of pure Trentepohlia on limestones monuments, International Biodeterioration & Biodegradation (2006) 58: 119–123.

[28] L. Zucconi, M. Gagliardi, D. Isola, S. Onofri, M. C. Andaloro, C. Pelosi, P. Pogliani, L. Selbmann, Biodeterioration agents in or on the wall paintings of the Holy Saviour´s cave (Vallerano, Italy), International Biodeterioration & Biodegradation (2012) 70: 40–46.

[29] C. C. Gaylarde, C. Hérnandez-Rodríguez, Y. E. Navarro-Noya, O. Ortega-Morales, Microbial Biofilms on the Sandstone Monuments of the Angkor Wat Complex, Cambodia, Current Microbiology (2012) 64: 85–92.

[30] N. Schiavon, T. De Caro, A. Kiros, A. T. Caldeira, I. E. Parisi, C. Riccucci, G. E. Gigante, A multianalytical approach to investigate stone biodeterioration at a UNESCO world heritage site: the volcanic rock-hewn churches of Lalibela, Northern Ethiopia, Applied Physics A: Materials Science Processing (2013) 113: 843–854.

[31] S. E. Favero-Longo, C. Gazzano, M. Girlanda, D. Castelli, M. Tretiach, C. Baiocchi, R. Piervittori, Physical and chemical deterioration of Silicate and Carbonate rocks by Meristematic Microcolonial Fungi and Endolithic Lichens (Chaetothyriomycetidae), Geomicrobiology Journal (2011) 28: 732–744.

[32] M. Hernández-Mariné, E. Clavero, M. Roldán, Microscopy methods applied to research on cyanobacteria, Limnetica (2004) 23: 179–186.

[33] L. Chen, L. Zhang, W. Zhang, T. Liu, Comparative analysis of growth and carotenoid accumulation of Trentepohlia arborum in aerial, subaerial, and aquatic cultivation, Journal of Applied Phycology (2014) 27: 1079-1087.

[34] A. A. Voytsekhovich, G. P. Kashevarov, Pigment content of photosynthetic apparatus of green algae (Chlorophyta)-the photobionts of lichens, International Journal of Algae (2010) 12: 282–292.

[35] E. A. Shalaby, S. M. M. Shanab, V. Singh, Salt stress enhancement of antioxidant and antiviral efficiency of Spirulina platensis, Journal of Medicinal Plants Research (2010) 4: 2622–2632.

[36] R. G. Guevara-González, I. Torres-Pacheco, E. Rico-García, R. V. Ocampo-Velázquez, A. Mercado-Luna, R. Castañeda-Miranda, L. O. Solís-Sánchez, D. Alaniz-Lumbreras, R. Gómez-Loenzo, G. Herrera-Ruíz, G. M. Soto-Zarazúa, β-carotene Production Under Greenhouse Conditions. Beta Carotene 59 – 91, Nova Science Publisher New York, (2009) 59–91.

[37] N. Keshari, S. B. Adhikary, Characterization of cyanobacteria isolated from biofilms on stone monuments at Santiniketan, India, Biofouling (2013) 29: 525–536.

[38] Y. Saga, H. Tamiaki, Fluorescence spectroscopy of single photosynthetic light-harvesting supramolecular systems, Cell Biochemistry & Biophysics (2004) 40: 149–165.

[39] V. Jurado, A. Z. Miller, S. Cuezva, A. Fernandez-Cortes, D. Benavente, M. A. Rogerio-Candelera, J. Reyes, J. C. Cañaveras, S. Sanchez-Moral, C. Saiz-Jimenez, Recolonization of mortars by endolithic organisms on the walls of San Roque church in Campeche (Mexico): A case of tertiary bioreceptivity, Construction & Building Materials (2014) 53: 348–359.

[40] M. J. Cocero, S. Ferrero, Crystallization of β-carotene by a GAS process in batch Effect of operating conditions, The Journal of Supercritical Fluids (2002) 22: 237–245.

[41] L. C. Prinsloo, W. Du Plooy, C. Van der Merwe, Raman spectroscopic study of the epicuticular wax layer of mature mango (Mangifera indica) fruit, Journal of Raman Spectroscopy (2004) 35: 561–567.

[42] K. Abe, N. Nishimura, M. Hirano, Simultaneous production of β-carotene, vitamin E and vitamin C by the aerial microalga Trentepohlia aurea, Journal of Applied Phycology (1999) 11: 331–336.

[43] T. Leya, A. Rahn, C. Lutz, D. Remias, Response of arctic snow and permafrost algae to high light and nitrogen stress by changes in pigment composition and applied aspects for biotechnology, FEMS Microbiology Ecology (2009) 67: 432–443.

RESEARCH ARTICLE 7

Characterization of Primary Marine Aerosol particles and Secondary Marine Aerosol particles and anthropogenic particulate matter through the development of a home-made passive sampler and evaluation of their impact on Built Heritage.

H. Morillas, M. Maguregui, C. Garcia-Florentino, I. Marcaida, J. M. Madariaga

Submitted to Water Research in September (2015)

Characterization of Primary Marine Aerosol particles and Secondary Marine Aerosol particles and anthropogenic particulate matter through the development of a home-made passive sampler and evaluation of their impact on Built Heritage

ABSTRACT

Dry deposition is one of the most dangerous processes that take place in the environment. Usually this process is related with the industrial/urban fog or even marine aerosol in the coastal areas. Particularly, marine aerosol transports different types of salts which can be deposited on building materials by dry deposition promoting different decay pathways.

In this work, an analytical methodology based on Raman Spectroscopy and SEM-EDS (point-by-point and imaging) was applied. For that purpose, firstly evaporated seawater (presence of Primary Marine Aerosol (PMA)) was analyzed. After that, using a home-made passive sampler, different suspended particles coming from marine aerosol (transformed particles in the atmosphere (Secondary Marine Aerosol (SMA)) and metallic airborne particulate matter coming from anthropogenic sources, were analyzed. Finally in order to observe if the SMA particles and metallic particles identified in the home-made passive sampler can be deposited on a building, sandstone samples from La Galea Fortress (Getxo, north of Spain) located in front of the sea and in the place where the passive sampler was mounted, were analyzed.

Keywords: Dry deposition, marine aerosol, Raman spectroscopy, SEM-EDS, sulfate, nitrate, chloride.

1. Introduction

Many studies dealing with the characterization of the materials including historical buildings close to the sea conclude that marine aerosol exerts high influence on their conservation state [1-10]. To understand the formation of marine aerosol, it is previously necessary to know which the main soluble compounds present in seawater are. As many authors point out, the main ions that are present in seawater are (from a higher to lower percentage) chloride (Cl^-), sodium (Na^+) sulfate (SO_4^{2-}), magnesium (Mg^{2+}), calcium (Ca^{2+}), potassium (K^+), bicarbonate (HCO_3^-), bromide (Br^-), borate ($H_2BO_3^-$) and strontium (Sr^{2+}) [11,12]. The marine aerosol comprises primary (PMA) and secondary aerosol (SMA) particles. The primary aerosol production results from the interaction of wind on the ocean surface resulting in the mechanical production of marine aerosol. The marine aerosol is made up of inorganic sea salts and organic matter and is produced via the bubble-bursting process, typically resulting from whitecap generation, producing film and jet drops and giving as a result the formation of sea-spray particles in the range of the submicrometre size, up to a few micrometers. The secondary aerosol production follows two sub-steps: (i) new particles formation via the nucleation of stable clusters of 0.5–1 nm size (once formed, these clusters can grow to larger sizes via condensation processes) and (ii) they also can grow via heterogeneous reactions and aqueous phase oxidations of dissolved gases in the existing aerosol particles [13-15]. Apart from salts, marine aerosol also transports trace metal and nutrients from the oceans to the atmosphere through wet and dry depositions [16].

Considering that most of the suspended particles present have a size lower than 10 μm, techniques which allow high magnifications are necessary for their characterization. Nanometer-sized structures and aerosol particles are often characterized by the use of transmission electron microscopy (TEM) equipped with a variety of analyzers such as bright field and dark field imaging, selected area electron diffraction (SAED), electron energy loss spectroscopy (EELS) and energy dispersive spectrometry (EDS) [17,18]. Apart from this, other techniques able to detect and quantify the mixed marine aerosol with particulate matter are used. For example in order to characterize small clusters present in marine aerosol a combination of SEM-EDS with TEM-EDS and STXM-NEXAFS can be used [19]. Apart from the elemental characterization, other technique that can be use to characterize the molecular composition of airborne marine aerosol is Raman micro-spectroscopy [20]. Other authors also use FTIR for the molecular characterization of inorganic and organic compounds in aerosol samples collected using Teflon filters [21, 22]. A combined use of FTIR and Raman spectroscopy is also a good alternative to perform a complete molecular

characterization [23]. Regarding the organic compounds, presents in marine aerosol, GC/MS is widely used [24].

Nowadays, different sampling methods for the aerosol particles trapping and analysis can be found. In general terms, these sampling methods are expensive and require maintenance [25]. As an example of those kinds of sampling methods, cascade impact can be mentioned. With this kind of sampling methods, airborne particulate matter can be separate according to their size (e.g. PM_{10}, $PM_{2.5}$). In this case, a pump must be used to impulse the air to the sampler. The first "low cost" aerosol sampler was described in 2001 [26, 27]. It was small, lightweight, cheap, easy to operate, but very efficient. After the sampling (from hours to months), the sampler was covered and brought to the lab.

According to the inorganic compounds in the suspended particles of marine aerosol, the presence of NaCl, KCl, SiO_2, Fe_2O_3, Na_2SO_4, K_2SO_4, $CaCO_3$, and $CaSO_4$ is widely known. The most abundant particle that can be found are carbonaceous and $(NH_4)_2SO_4/NH_4HSO_4$-containing particles, followed by mineral (e.g., aluminosilicate, SiO_2, $CaCO_3$), sea salt (NaCl etc.), K-rich particles (e.g., K_2SO_4 and KCl), Fe-rich particles, fly ash, and transition or heavy-metal-containing (e.g., $ZnSO_4$, $ZnCl_2$, $PbSO_4$) particles [28]. Apart from them, nitrates such as $Mg(NO_3)_2$, KNO_3, $NaNO_3$ can be also present [29]. Among the other compounds above mentioned, marine aerosol carries also high load of sulfates mainly in form of magnesium sulfate or magnesium mixed sulfates [30, 31].

The effect that marine aerosol exerts on the environment is high. Thus, buildings that are close or immersed on the coastal, can suffer the effects of marine aerosol in the form of dry deposition. These dry marine aerosol depositions promote different decaying processes on the building materials [2, 4, 6]. For example, the inorganic salts mentioned above can migrate to the inner parts of building material through their pores promoting new salts formations or crystallizations inside (sub-efflorescences) or outside the porous material with its consequently material degradation [32,33].

In this work, a home-made passive sampler was designed for direct airborne particulate trapping coming from a marine and a direct urban-industrial environment. The trapped particles were characterized using SEM-EDS and Raman micro-spectroscopy. Apart from that, inorganic salts that can be formed from the direct evaporation of the sea water of the environment were also characterized, in order to determine which can be the composition of the primary marine aerosol (PMA) particles that can be transformed in the atmosphere into the secondary marine aerosol particles (SMA), that are going to be the resultant particles trapped in the home-made passive sampler. Finally, a correlation between the

composition of the trapped particles and those deposited on the surface of the sandstone from La Galea Fortress (Getxo, Basque Country, north of Spain), located in front of the sea will be establish, in order to evaluate the negative consequences that this kind of dry depositions can cause on the conservation state of a building material such as the sandstone.

2. Experimental

2.1. Samplings

To determine the composition of the salts present in the seawater, a seawater sample from the Abra Bay (Getxo, north of Spain) was collected. This seawater was evaporated at open air (22^0C) adding 1 ml of seawater over an aluminium pin stub covered by a carbon conductive tape. Secondly, a home-made passive sampler valid to collect airborne particulate matter from the atmosphere and particles coming from the marine aerosol was developed (see Figure 1). In Figure 1 A, the drawing of the home-made passive sampler is presented. All the structure of the passive sampler was fixed in the South-southeast side (just in an open window for protect it of the rainfalls) of the tower of La Galea Fortress (Getxo, north of Spain) (which is going to be the building under study) using silicone (see Figure 1 B and C). Finally in order to test, the influence of the surrounding marine environment and the possible dry depositions that can suffer this historical building located close to the sea, different sandstone samples were analyzed. These sandstones samples were collected also from the South-southeast face of the tower using a scalpel and the size of all of them never exceeded 2×2 cm^2. The sampling area is located just on a cliff in front of the coast. In the surrounding, different industries (a petrochemical refinery, a power generation plant) and high ships traffic due to the Port of Bilbao activity located in front of the building which can contribute to the airborne particulate matter emissions are placed

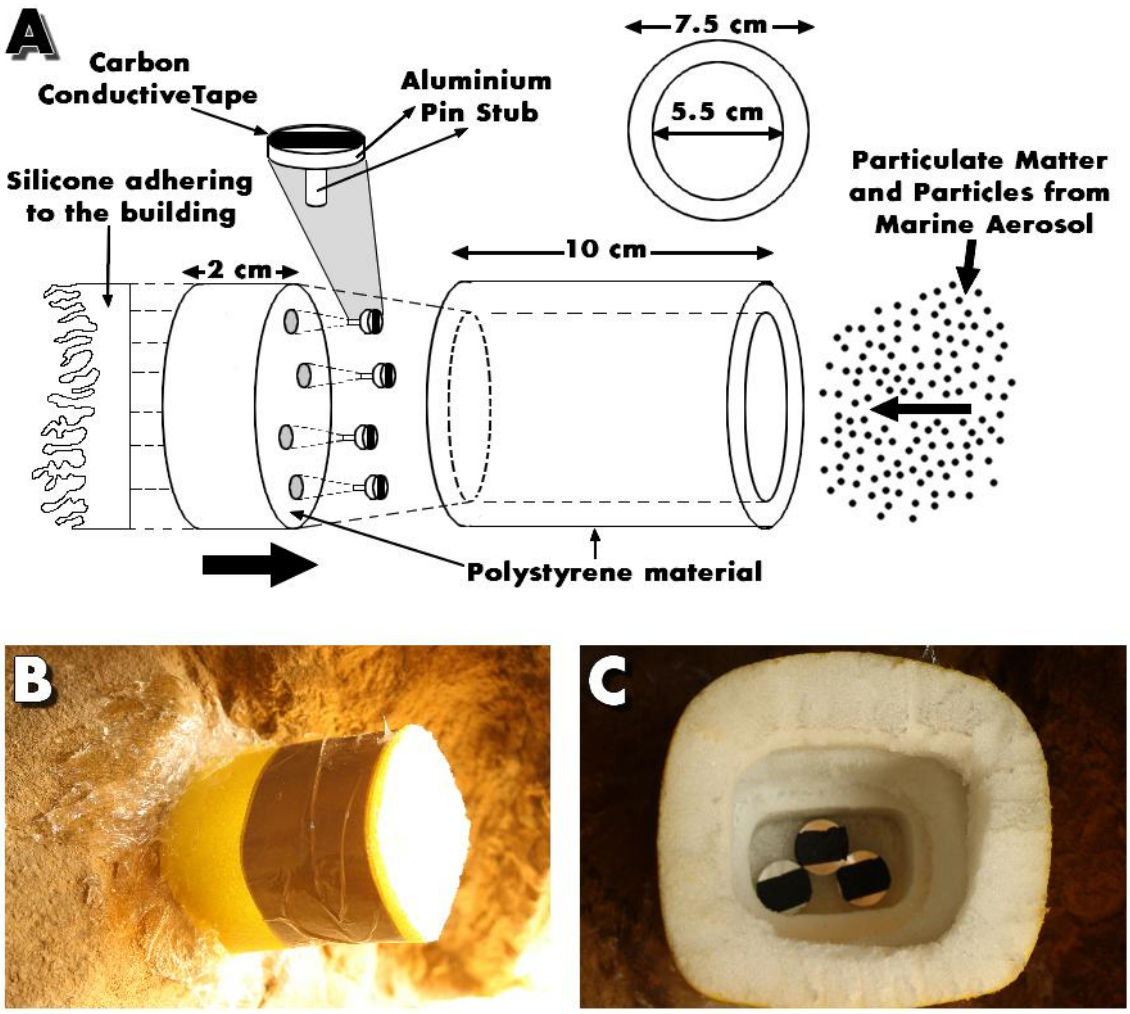

Figure 1. A) Drawing of the home-made passive sampler and B) and C) passive sampler fixed with silicone in the South-southeast side of the tower of La Galea Fortress.

2.2. Instrumental

The SEM-EDS analyses were carried out using a EVO®40 Scanning Electron Microscope (Carl Zeiss NTS GmbH, Germany) coupled to an X-Max Energy-Dispersive X-ray spectrometer (Oxford Instruments, Abingdon, Oxfordshire, United Kingdom) for electron image acquisitions and elemental analysis (punctual and imaging). Although sometimes, deposited particles alone are not conductive, it was possible to obtain optimal results without carbon or gold coating. The SEM images were obtained at high vacuum employing an acceleration voltage of 30 kV and a 10–400 μm working distance. Different magnifications (reaching up to ×6,800) were used for secondary electron images and an integration time of 50 s was employed to improve the signal-to-noise ratio. The EDS spectra were acquired and treated using the INCA software. Furthermore, a mapping of specific microscopic areas in the samples was possible, allowing the evaluation of the distribution of these elements over the sample.

For the micro-Raman analyses, the inVia Renishaw confocal Raman microspectrometer (Renishaw, Gloucestershire, UK) coupled to a DMLM Leica microscope with 5×, 20×, 50×, and 100× long range lens. Excitation lasers (785 and 514 nm; nominal laser power 350 mW and 50 mW respectively) and different magnification lens (50× and 100×, mainly) were used to perform the measurements. The spectrometer was daily calibrated by using the 520 cm^{-1} Raman band of a silicon chip. Lasers were set at low power (not more than 1 mW at the sample) in order to avoid thermal decomposition. Data acquisition was carried out using the Wire 3.2 software package (Renishaw). Spectra were acquired between 100 and 3000 cm^{-1} and several scans were accumulated for each spectrum in order to improve the signal-to-noise ratio. The interpretation of all the Raman results was performed by comparing the acquired Raman spectra with Raman spectra of pure standard compounds collected in the e-VISNICH dispersive Raman database [34]. Additionally, free Raman databases (e.g. RRUFF [35]) were also considered for the assignation of Raman bands.

3. Results

3.1. Evaporated Seawater Characterization

The evaporated seawater from the Abra Bay was analyzed over an aluminium pin stub covered by carbon conductive tape. For Raman analyses the pin stub was mounted on standard plasticine to maintain it stable.

Firstly, for the analyses of evaporated seawater, Raman spectroscopy was carried out in order to try to extract the major information about the possible evaporites present in the first cycle of dry depositions (primary marine aerosols (PMA)). In the Figure 2, different Raman spectra are presented. For example, in Figure 2 A, kainite $KMg(SO_4)Cl{\cdot}3H_2O$, with its bands at 450, 630, 1023 and 1040 and 1196 cm^{-1} can be observed; according to the literature, this compound has been identified in seawater evaporation and synthesized also in the laboratory [36, 37]. In the Figure 2 B, langbeinite $K_2Mg_2(SO_4)_3$, with its bands at 457, 466, 626, 1053, 1123, 1134 and 1245 cm^{-1} can be observed. This double sulfate has been also previously described in other works [38]. Hanksite $KNa_{22}(SO_4)_9(CO_3)_2Cl$ was also detected as evaporite by Raman spectroscopy (see Figure 2 C), showing its bands at 456, 629, 960 (shoulder), 988, 1080 and 1114 cm^{-1}. This mixed compound has been detected in different water evaporates from sediments [39]. Apart from these double salts, pure gypsum $CaSO_4{\cdot}2H_2O$ Raman spectra with its bands at 414, 493, 620, 670, 1008 and 1135 cm^{-1} was also observed (see Figure 2 D). At this point it is necessary to highlight that although the

Raman spectra of polyhalite ($K_2Ca_2Mg(SO_4)_4 \cdot 2H_2O$) and carnallite ($KMgCl_3 \cdot 6H_2O$) were not detected, it is widely known that these compounds can be also present as PMA in the evaporated seawater [40, 41].

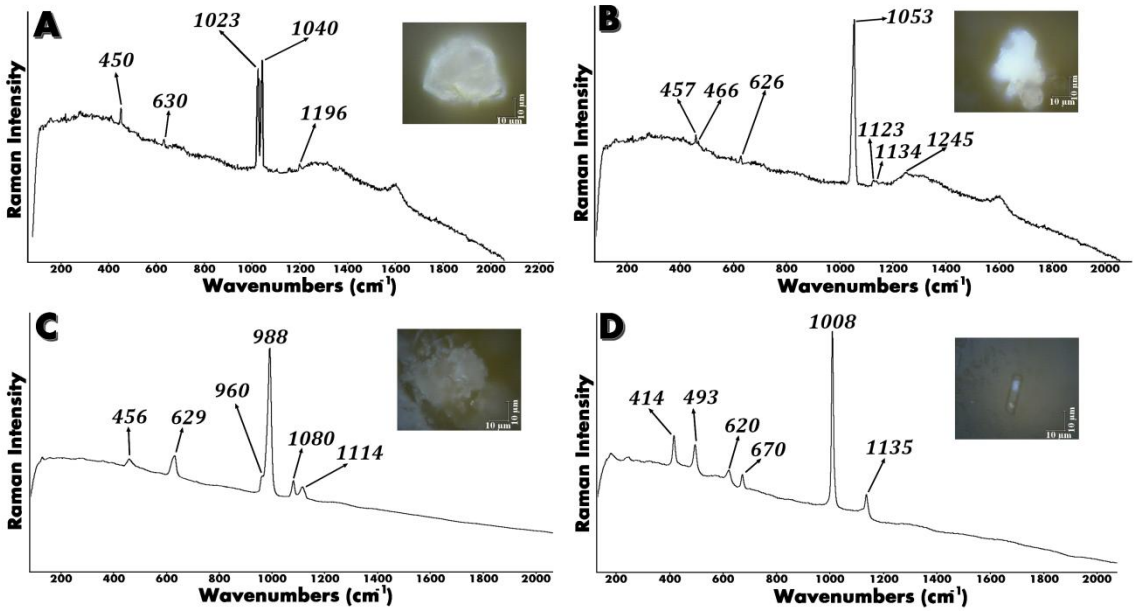

Figure 2. Raman spectra of evaporite minerals A) Kainite ($KMg(SO_4)Cl \cdot 3H_2O$), B) Langbeinite ($K_2Mg_2(SO_4)_3$), C) Hanksite ($KNa_{22}(SO_4)_9(CO_3)_2Cl$) and D) Gypsum ($CaSO_4 \cdot 2H_2O$).

In order to extract more information about the PMAs present in the evaporation process of seawater, different SEM-EDS (point-by-point and mappings) analyses were carried out. In Figure 3, different evaporated particles can be observed. According to the maps on Figure 3 A, B, C and D, the Na and Cl distributions are clearly superimposed, suggesting the presence of halite (NaCl). Apart from halite, in certain areas, a similar elemental distribution of K and Cl is also observable, pointing out to the presence of sylvite (KCl). Both minerals, halite and sylvite, cannot be observed by Raman spectroscopy, because they are band Raman scatterers due to their very ionic character. This example corroborates the good strategy of using both elemental and molecular techniques in order to obtain the most complete characterization. Analyzing more in depth the mappings of Figure 3, for example in the surroundings and inner areas of halite particles, just in the center of the main particle, a similar distribution of K, Mg, S and O can be observed (see Figure 3A). This observation could be related with the possible presence of langbeinite (($K_2Mg_2(SO_4)_3$), observed also by Raman spectroscopy). Apart from this, in the Figure 3A, little particles (aprox. 5 μm) surrounding the halite particle (aprox. 85 μm) with the similar elemental distribution of Ca, S and O can be also observed. These elements distributions can be related with the presence of gypsum ($CaSO_4 \cdot 2H_2O$, observed also by Raman spectroscopy) or anhydrite ($CaSO_4$).

According to the literature, anhydrite is also presented as evaporite mineral [42]. For the figure 3B, C and D similar elemental distributions trends can be observed. In these cases, around the halite (NaCl), K, Mg, O, (in some cases Ca and even Cl) and S are related, suggesting a possible presence of polyhalite ($K_2Ca_2Mg(SO_4)_4 \cdot 2H_2O$), carnallite ($KMgCl_3 \cdot 3H_2O$), kieserite ($MgSO_4 \cdot H_2O$) and epsomite ($MgSO_4 \cdot 7H_2O$). Polyhalite is closely related with the marine aerosol and has also high influence on the conservation state of buildings as has been described in the literature [9]. Moreover, carnallite, kieserite and epsomite, have been also described as evaporites [43-45]. Among these compounds, we could not discard the possible presence of $MgCl_2$ or even $CaCl_2$.

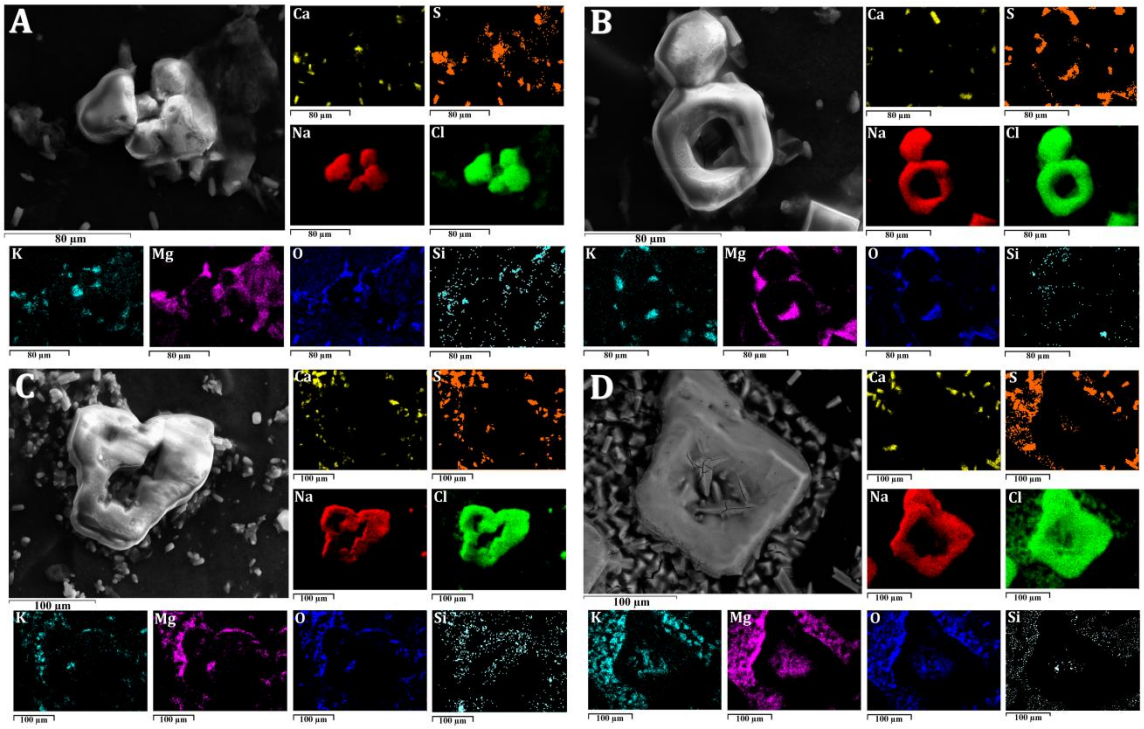

Figure 3. Different elemental distributions of seawater evaporites.

3.2. Deposited Marine salts and airborne particulate matter on the Home-made Passive Sampler

Raman spectroscopy was used for the molecular characterization of the compounds deposited (secondary marine aerosol, SMA) on the developed home-made passive sampler (see Figure 1). Figure 4 A shows a pure particle of gypsum (observing its main band at 1008 cm^{-1} and also all the secondary bands). According to the Raman results of the evaporites from seawater, gypsum can be considered one of the PMA compounds that can be transported in the marine aerosol without change in its composition to be deposited on the surface of buildings later on.

In the Figure 4 B and 4 C, two particles of pure nitromagnesite ($Mg(NO_3)_2 \cdot 6H_2O$, main band at 1059 cm^{-1}) and nitratine ($NaNO_3$, main band at 1067 cm^{-1}) can be observed. In both cases, apart from their strong bands, their medium and also weak bands are observable.

These both nitrate particles, can be formed in the atmosphere by reactions between sea salts coming from marine aerosol and several gaseous nitrogen acids such as HNO_3, N_2O_5, NO_2 and $ClONO_2$ frequently present in the modern atmospheres. Among the nitrogen species, HNO_3 is reported to be the most important in the nitrate formation from sea salts in the marine atmosphere [46]. In addition, the Henry constant of HNO_3 is higher than the other nitrogen species, and evaporation of nitrate from the particles to HNO_3 in the gas phase and its subsequent transport to coarse sea salt particles are well-established experimentally [47, 48]. Moreover, HNO_3 may react with salts from marine aerosol (NaCl, MgCl or even $CaCl_2$) or crustal particles ($CaCO_3$) in the atmosphere giving rise nitrates such as nitratine ($NaNO_3$), nitromagnesite ($Mg(NO_3)_2 \cdot 6H_2O$) and nitrocalcite ($Ca(NO_3)_2 \cdot 4H_2O$) [49]. Although there is a clear presence of nitrates, comparing with the organic compounds, nitrates are typically a smaller fraction of the marine aerosol [50].

In Figure 4 D and E, the Raman spectrum of mascagnite ($(NH_4)_2(SO_4)$), with its main band at 974 cm^{-1} and the Raman spectrum of Rutile (TiO_2) (main bands at 449 and 611 cm^{-1}) with nitrammite ($(NH_4(NO_3)$, main band at 1040 cm^{-1}) can be observed respectively. In the literature there are many works that describe how ammonia is released to the atmosphere as a result of the decomposition of vegetation, in the use of fertilizer, coming from the biomass burning, decay of waste products from domestic and wild animals and from seas and oceans. Total ammonia ($NH_3 + NH_4^+$) is the sum of both, the gaseous and aerosol forms and in many conditions gaseous ammonia is predominant [49]. When the equilibrium favors aerosol forms, the major species are ammonium bisulfate, ammonium sulfate, and ammonium nitrate, depending on the conditions. Seinfeld [51] reported that generally ammonia occurs in the form of $(NH_4)_2SO_4$ in the atmosphere, but it can also be found in the form of NH_4NO_3 [52]. Without discriminating the natural source for the case of Figure 4 E, with the presence of rutile together with nitrammite, this mixture could also suggest an anthropogenic source. According to the literature, there exist different applications of this compounds mixture, such as catalytic reactions [53].

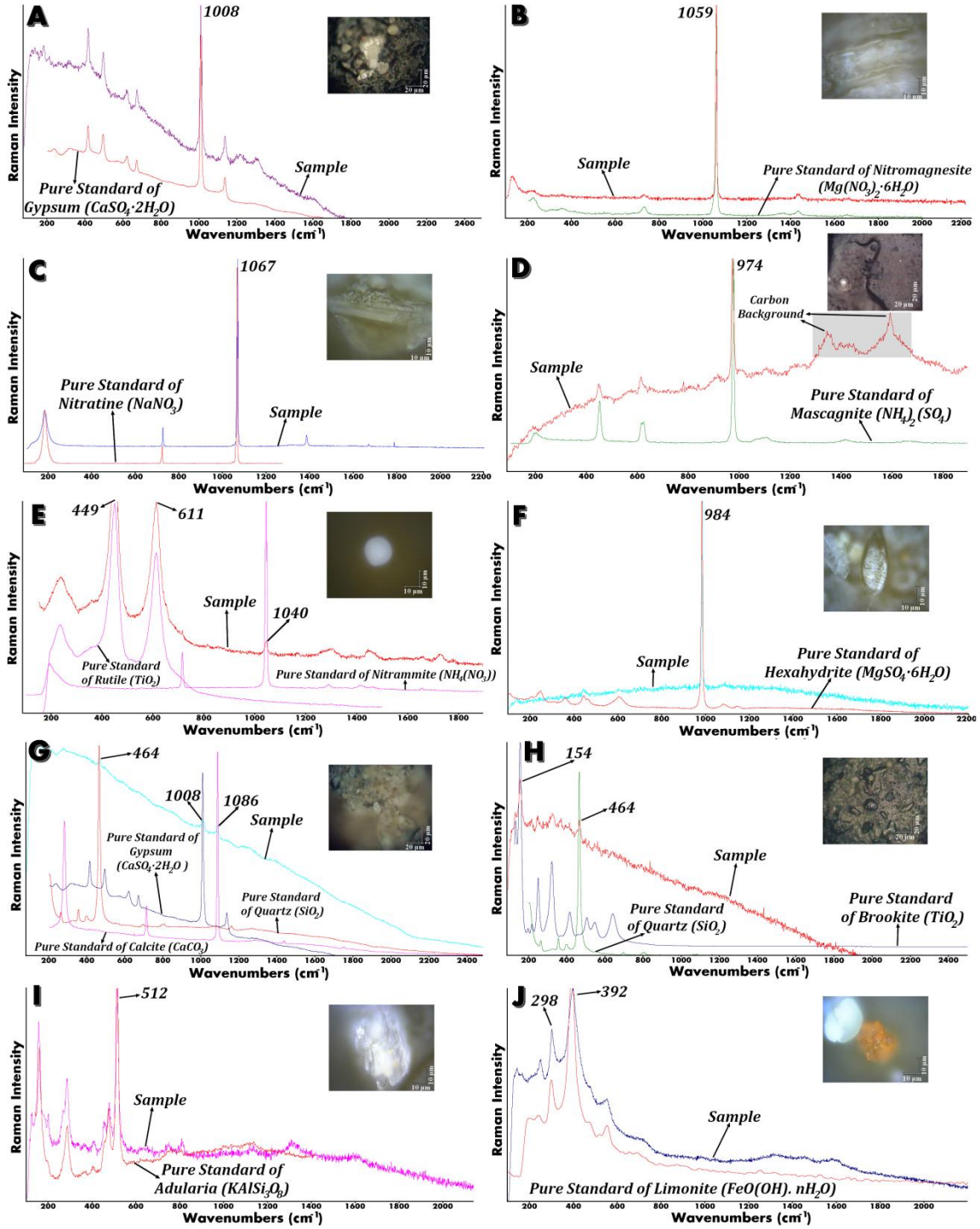

Figure 4. Different Raman spectra obtained in the trapped particles on the home-made passive sampler showing the presence of A) Gypsum ($CaSO_4 \cdot 2H_20$), B) Nitromagnesite ($Mg(NO_3)_2 \cdot 6H_2O$, C) Nitratine ($NaNO_3$), D) Mascagnite ($(NH_4)_2(SO_4)$), E) Rutile (TiO_2) and Nitrammite ($NH_4(NO_3)$), F) Hexahydrite ($MgSO_4 \cdot 6H_2O$), G) Calcite ($CaCO_3$), Gypsum ($CaSO_4 \cdot 2H_2O$) and Quartz (SiO_2), H) Brookite (TiO_2) and Quartz (SiO_2), I) Adularia ($KAlSi_3O_8$) and J) Limonite ($FeO(OH) \cdot nH_2O$).

Following with the Raman spectra, Figure 4 F shows the presence of hexahydrite ($MgSO_4 \cdot 6H_2O$), with its main Raman band at 984 cm^{-1}. The presence of magnesium sulfates such as hexahydrite and epsomite ($MgSO_4 \cdot 7H_2O$) in marine aerosol is widely known [54, 55].

In Figure 4 G, the Raman spectrum of gypsum ($CaSO_4 \cdot 2H_2O$) with its main band at 1008 cm^{-1}, quartz (SiO_2) with its main band at 464 cm^{-1} and calcite ($CaCO_3$) with its main band at 1086 cm^{-1} can be observed. Quartz and calcite particles cannot be related with particles coming from marine aerosol. They are related with suspended dust or crustal particles coming from the erosion of calcareous and siliceous rocks from the surrounding environment. In the same way, in the Figure 4 H, the Raman spectrum of brookite (TiO_2) and quartz (SiO_2) showing its main bands at 154 and 464 cm^{-1} respectively can be observed. In this way, two polymorphs of TiO_2 were identified: rutile and brookite, both coming from anthropogenic emissions.

Finally in Figures 4 I and 4 J, the Raman spectra of adularia ($KAlSi_3O_8$, main band at 512 cm^{-1}) and limonite ($(FeO(OH) \cdot nH_2O)$, main bands at 298 and 392 cm^{-1}) can be observed respectively.

Among the Raman spectra observed in all the Figure 4, other compounds such as epsomite ($MgSO_4 \cdot 7H_2O$, with its main band at 985 cm^{-1}), starkeyite ($MgSO_4 \cdot 4H_2O$, with its main band at 1001 cm^{-1}), hematite (Fe_2O_3, with its main bands at 225, 292, 410, 495 and 611 cm^{-1}), lepidocrocite (γ-FeO(OH), with its main bands at 212, 246, 304, 343, 373, 522 and 648 cm^{-1} and lead oxide (PbO, with its main band at 148 cm^{-1}) were observed in the Raman analyses carried out over the pin stub from the home-made passive sampler.

In the marine aerosol, apart from suspended salts which act as Secondary Marine Aerosol particles (SMA) after the reaction between the Primary Marine Aerosols (PMA) and the NO_x, SO_x etc. present in the atmosphere, other types of airborne particulate matters, that can have others anthropogenic sources can coexist together with the suspended salts. Apart from the described compounds identified by the Raman spectra obtained on the home made passive sampler, different particles were deposited. In Figure 5 A, a spherical particle of 7 μm approximately composed mainly by Ce and La was detected. This particle is closely related with additives used in the combustion of diesel motors in ships [56]. In the Figure 5 B an acicular particle of 120 μm approximately composed by Fe and Cl is present. Moreover, in the Figure 5 C, an aggregate particle composed mainly by Bi and Th was also detected. In this case, the emitted particle is related with the addition of selective catalytic engine fuel additives in the biodiesels used in some ships [57]. In the Figure 5 D, the deposited particle

is composed by K, Al , Si and O being related with some aluminosilicate, probably adularia $KAlSi_3O_8$, which was also detected by Raman micro-spectroscopy.

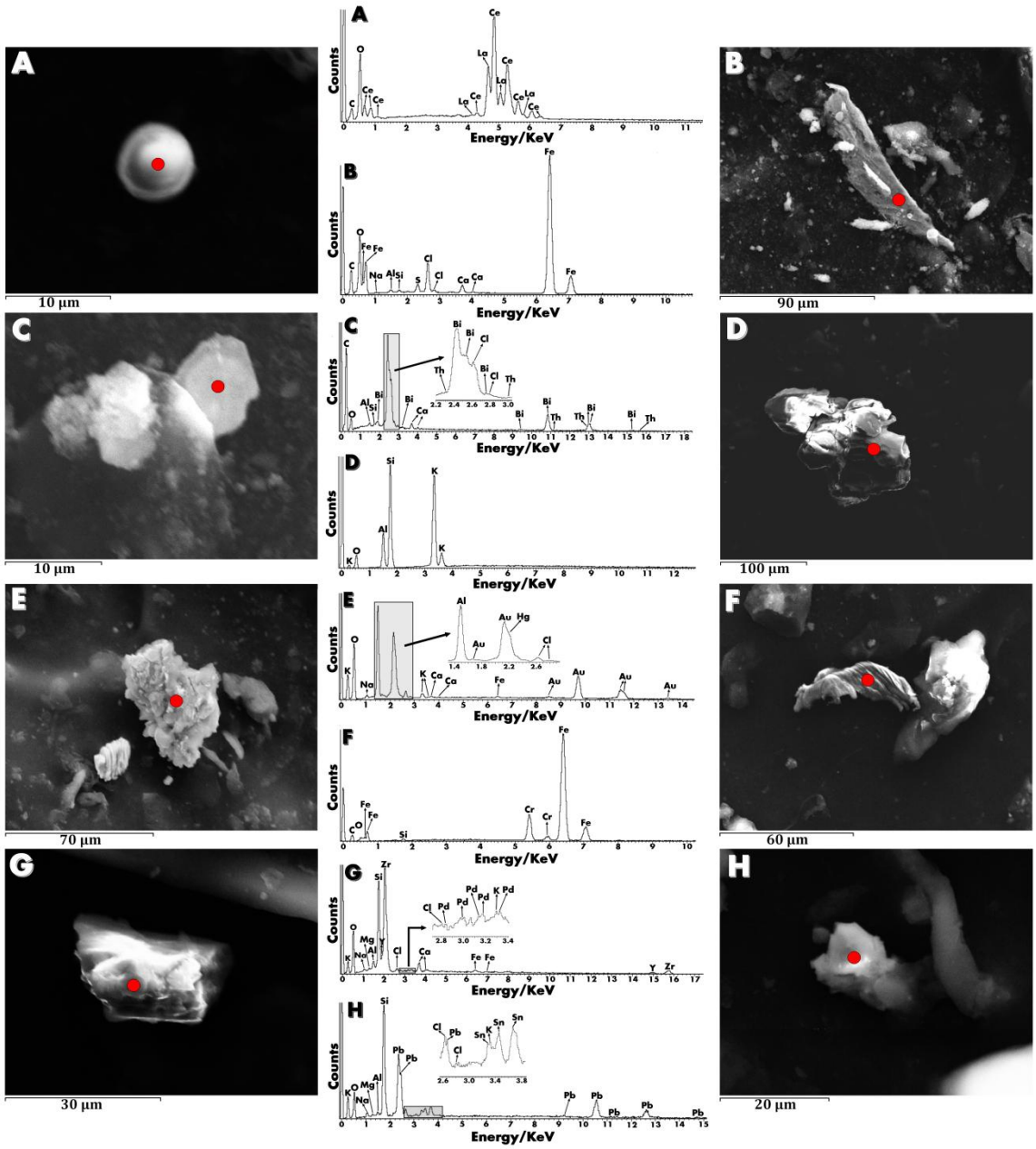

Figure 5. A) Spherical particle composed mainly by Ce and La, B) Irregular particle composed mainly by Fe and Cl, C) Aggregate particle composed mainly by Bi and Th, D) Aggregate aluminosilicate particle composed by K, Al, Si and O, E) Aggregate particle composed mainly by Au, Al and Hg, F) Aggregate particle composed mainly by Cr and Fe, G) Aggregate particle composed mainly by Zr, Si, Pd and Y among other elements and H) Aggregate composed particle by Si, Pb and Sn.

In the Figure 5 E, a particle composed mainly by Au, Al and Hg is observed. In this case, this elemental composition could be related with particle emissions coming from the power generation plant which is relatively close to the sampling area [58]. Moreover as it can be seen in the Figure 5 F, a particle constituted mainly by Cr and Fe is observed. This elemental composition is closely related with the diesel engines emissions, which although diesel engines are recognized for their fuel efficiency, robustness and durability, they emit two dangerous pollutants, NO_x and soot. In this soot emitted, iron chromate can be observed as component of the soot [59].

In the Figure 5 G, a particle of approximately 25 μm composed mainly by Zr, Si, Pd and Y among other trace elements is presented. In this case, this particle can be related with the use of additives as catalyzer in the fuel to minimize the PAH, CO, or even NOx emissions from different transport ways such as ships [60]. Finally in the Figure 5 H a particle of approximately 10 μm composed mainly by Pb and Sn is observed. The probable source of this type of particle is the fuel oil combustion emission of ships and according to the literature the size of these particles can be considered as PM_{10} [62]. As it can be observed, there is a clear influence of the particles emitted due to the ships traffic in the sampling area. At this point we have to highlight that along the Abra Bay all the ships coming from around the world, enter and leave the Bilbao port for a sea route just in front of the sampling area. As can be supposed, the sum of the marine aerosol and the pollutants coming from the surrounded port and even the power plant and industries that are close to the sampling area can have a high negative influence on the atmosphere due to acid aerosols and metallic particulate matter emissions.

Moreover, among the particles observed in Figure 5, an example of exhaustive SEM-EDS analyses of the deposited particles on the home made passive sampler is presented. In this way, in the Figure 6, three sampled points are presented. In the Figure 6 A, the analysis carried out on the biggest particle (approximately 30 μm) is mainly composed by K and Cl which is related with the presence of KCl coming from the marine aerosol. In the same way, the presence of Na and Cl observed in the Figure 6 B suggest the presence of NaCl which is the main component present in the marine aerosol. Among these two components, a third one can be observed in the Figure 6 C, where the similar maps of N, Na and O suggests the presence of $NaNO_3$, observed also by Raman spectroscopy (see Figure 4C). This compound, as we have explained before is present also in the marine aerosol and it is the result of the reaction between the HNO_3 present in the atmosphere and the NaCl.

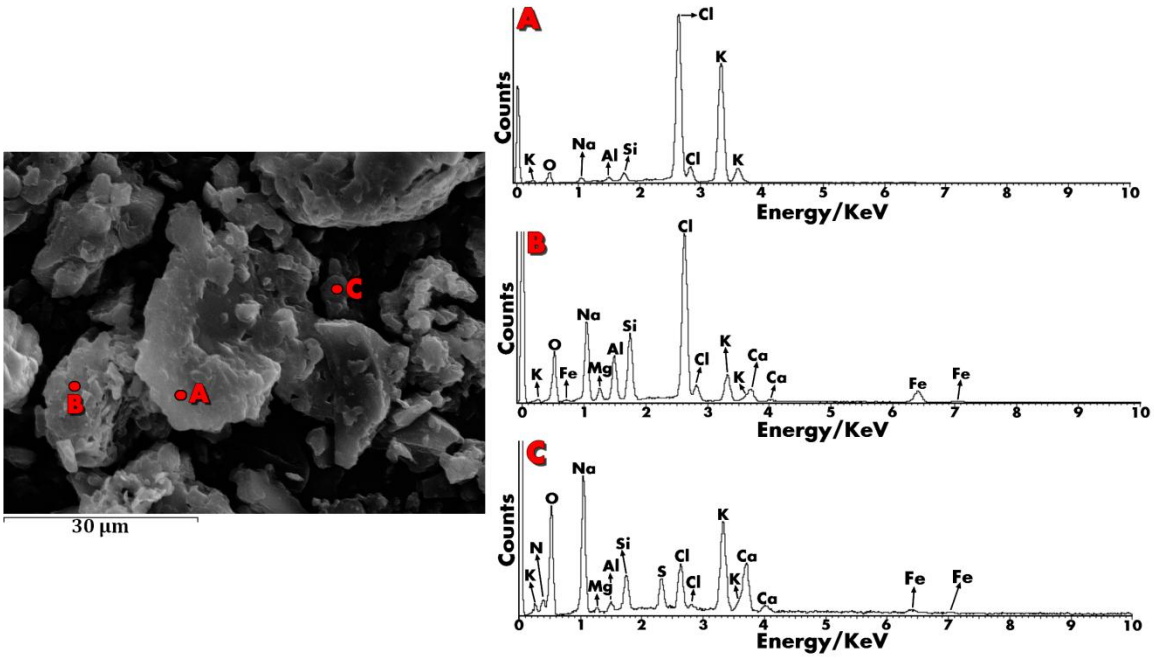

Figure 6. SEM-EDS point-by-point analyses showing the presence of A) possible KCl coming from the marine aerosol, B) possible NaCl coming from the marine aerosol among other elements and C) possible presence of $NaNO_3$, (presence of N, Na and O) as a secondary marine aerosol particle among othe elements.

3.3. Dry Depositions over La Galea Fortress sandstone

In order to demonstrate the influence of the dry deposition of secondary marine aerosol (SMA) particles on the conservation state of the sandstone from La Galea Fortress, sandstone samples from the tower were analyzed. As it can see in Figure 7, this building which dated back to 1742, is just on a cliff with the direct exposure to the marine aerosol and the emissions of surrounded industry and ships traffic (see Figures 7 A and B). It is necessary to remark that La Galea Fortress tower is in a very poor conservation state, since the tower is suffering a losing process of its sandstone (see Figures 7 C and D).

Figure 7. Location and views from La Galea Fortress, showing A) and B) the direct influence of the marine aerosol, surrounded industry and ships traffic C) and D) evidences of the poor conservation state of La Galea Fortress tower.

To observe the dry deposition process on the sandstone material, which is mainly composed by quartz (SiO_2), aluminosilicates such as adularia ($KAlSi_3O_8$), ferric oxides such as limonite ($FeO(OH).\ nH_2O$) and hematite (Fe_2O_3), oxyhydroxides such as lepidocrocite (γ-FeO(OH)) and charcoal (C) as it was described in previous works [7], Raman spectroscopy was applied on the superficial area of different small pieces of the sandstone blocks from the South-southeast tower side (see Figure 8).

In the Figure 8 A, the Raman spectrum of nitratine ($NaNO_3$), with its main Raman band at 724, 1067 and 1384 cm^{-1} can be observed. This compound was previously detected in the Raman spectra obtained in the deposited salts on the home made passive sampler. Undoubtedly being a punctual presence of this compound the only source of this nitrate must to be a dry deposition coming from the marine aerosol. For the Figure 8 B, the presence a band at 985 cm^{-1} (among the band at 280 and 1086 cm^{-1} belonging to calcite ($CaCO_3$)) suggests the presence of epsomite ($MgSO_4 \cdot 7H_2O$). This magnesium sulfate was also detected in the deposited particles on the home-made passive sampler together with other magnesium sulfate (hexahydrite). Magnesium sulfates cannot be formed due to the reaction between magnesium carbonates and wet deposition of SO_2 from the atmosphere, since these kinds of carbonates are not present in the sandstone, suggests again a dry deposition process of these secondary marine aerosol particles.

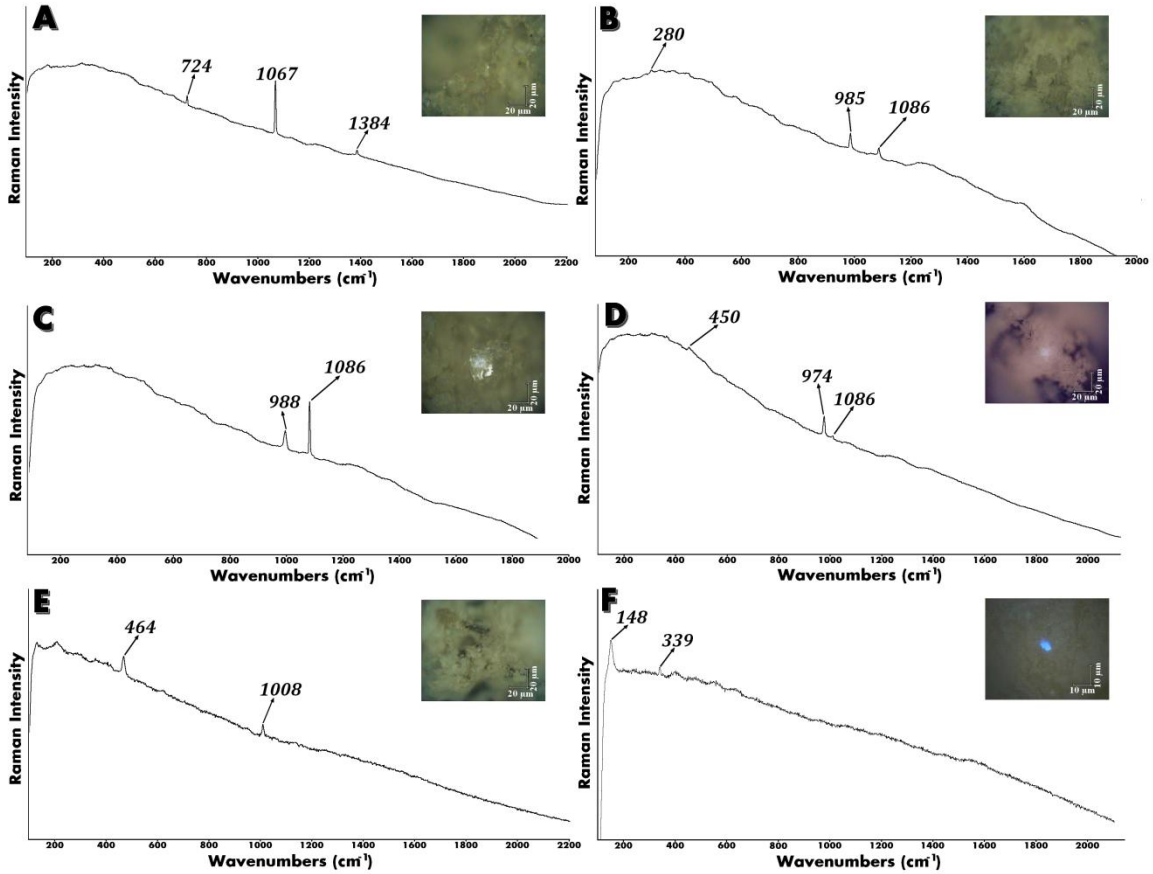

Figure 8. Different dry Depositions over the sandstone showing the presence of A) Nitratine ($NaNO_3$ with its main Raman band at 1067 cm^{-1}, B) Epsomite ($MgSO_4 \cdot 7H_2O$, with its main Raman band at 985 cm^{-1}) and Calcite ($CaCO_3$, with its main Raman bands at 1086 cm^{-1}), C) Arcanite (K_2SO_4, with its main Raman band at 988 cm^{-1}) and Calcite ($CaCO_3$, with its Raman bands at 1086 cm^{-1}), D) Mascagnite ($(NH_4)_2SO_4$, with its main Raman band at 974 cm^{-1}) and Calcite ($CaCO_3$, with its Raman bands at 1086 cm^{-1}), E) Gypsum ($CaSO_4 \cdot 2H_2O$, with its Raman bands at 1008 cm^{-1}), and quartz (SiO_2 with its main Raman band at 464 cm^{-1}) and F) Lead oxide with (PbO with its main Raman band at 148 cm^{-1}).

In the Figure 8 C, a Raman band at 988 cm^{-1} belonging to arcanite (K_2SO_4), among the presence of Calcite with its main Raman at 1086 cm^{-1} can be observed. Although, this potassium sulfate was not detected on the home made passive sampler, it is widely known that this salt is present in marine aerosol and it can be formed at an specific relative humidity percentage (% RH) value of 62% [62]. Although the average of relative humidity in this area is around 76%, in some periods the % RH can go down until these required magnitudes.

Figure 8 D shows a Raman band at 974 cm^{-1} (among the presence of Calcite with its main Raman band at 1086 cm^{-1}) belonging to mascagnite ($(NH_4)_2SO_4$), together with the band at 974 cm^{-1}, a band at 450 cm^{-1} which belong to a secondary band of mascagnite was also detected. In this case, this sulfate was previously detected on the home-made passive sampler, and the fact of being in the sandstone material is a clear signal of dry deposition.

This sulfate, during time can be dangerous for the integrity of the material, because it can promote the loss of material [3, 5].

Moreover in the Figure 8 E, Raman bands at 464 and 1008 cm^{-1} belonging to quartz (SiO_2) and gypsum ($CaSO_4 \cdot 2H_2O$) respectively were also detected. In this case, the quartz is an original component of the sandstone, but the gypsum presence can be related with two different sources. On the one hand, the gypsum can be formed due to the reaction between the calcite from the sandstone and the SO_x present in the atmosphere [63]. On the other hand this gypsum can come also from the dry deposition as it is described in previous works [64].

Finally as it can be seen in the Figure 8F, bands at 148 and 339 cm^{-1} belonging to lead oxide (PbO) can be observed. As it has been described in the results from the home made passive sampler section, these types of particles can be found suspended in the atmosphere and therefore they can be deposited on the building materials following a dry deposition.

Apart from the molecular analysis, additional SEM-EDS elemental mappings from La Galea Fortress tower sandstone were carried out in order to complete the information about the dry deposition processes that are taking place in this historical building. Analyzing the elemental distribution of the EDS mapping (see Figure 9), halite (NaCl), quartz (SiO_2), sylvite (KCl), arcanite (K_2SO_4) and nitratine ($NaNO_3$) distributions can be distinguished. Therefore, with the elemental analyses, the presence of NaCl and KCl was verified. Moreover the presence of the same elemental distribution of N, Na and O could suggest the presence of $NaNO_3$, observed also by Raman spectroscopy. In the same way, the elemental distribution of K, S and O could suggest the presence of K_2SO_4, observed also by Raman spectroscopy. Moreover in different points, a similar elemental distribution of Ca, S and O can be observed. In this case, this elemental distribution could be related with the presence of gypsum ($CaSO_4 \cdot 2H_2O$) detected also by Raman spectroscopy.

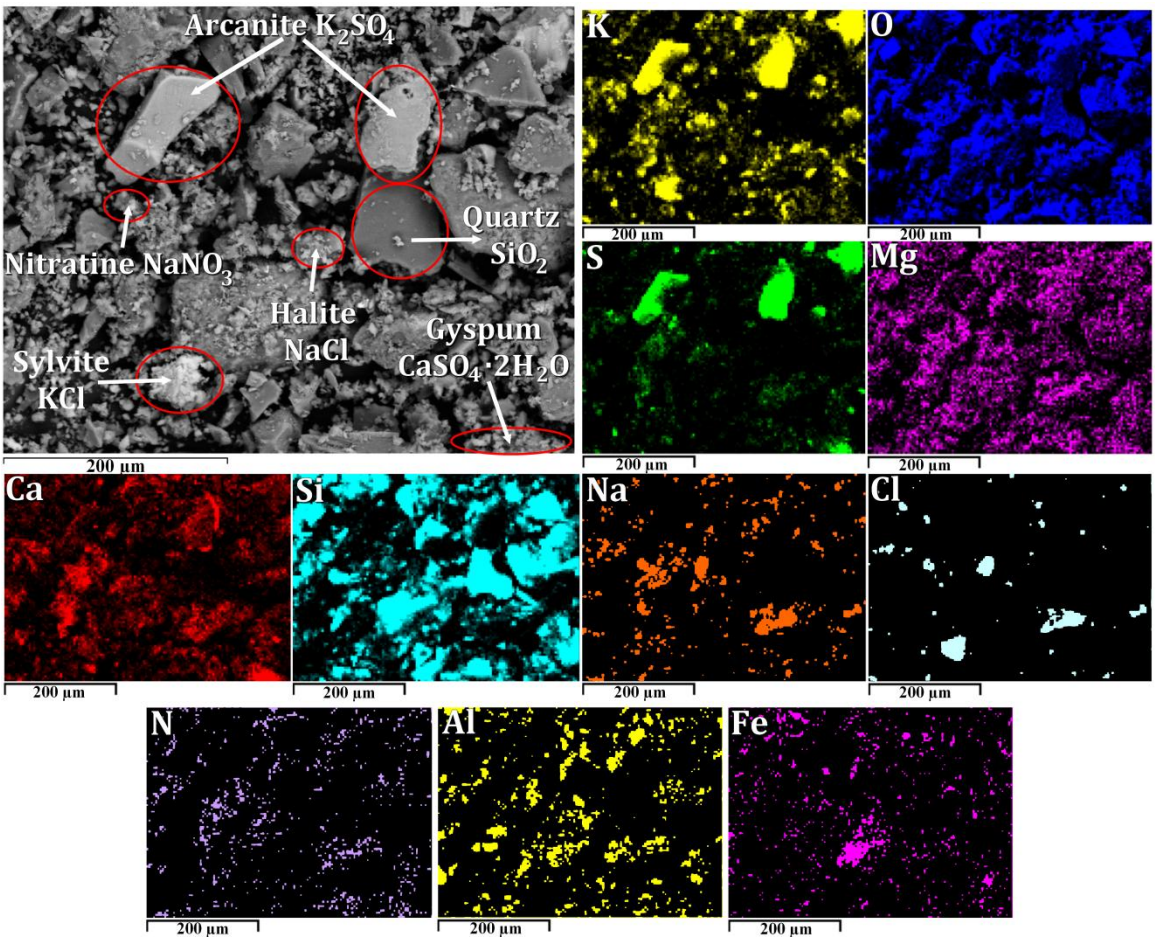

Figure 9. SEM-EDS mapping showing the distribution of the different elements present in the sandstone matrix.

4. Conclusions

The analytical methodology used in this work combining Raman spectroscopy and SEM-EDS (point-by-point and imaging) has been proved as a powerful strategy to characterize the composition of airborne particulate matter. The analyses carried out over the evaporated seawater from the Abra Bay revealed the majority presence of halite together with other compounds such as kainite ($KMg(SO_4)Cl \cdot 3H_2O$), langbeinite ($K_2Mg_2(SO_4)_3$, hanksite ($KNa_{22}(SO_4)_9(CO_3)_2Cl$) and gypsum ($CaSO_4 \cdot 2H_2O$). These compounds can be considered as Primary Marine Aerosol (PMA) particles and they can be formed in the first step of the marine aerosol formation due to its nearly saturation condition as the seawater droplets evaporate.

Thanks to the cheap and easy to handle home-made passive sampler developed, different kind of inorganic salts such as gypsum ($CaSO_4 \cdot 2H_20$), nitromagnesite ($Mg(NO_3)_2 \cdot 6H_2O$), nitratine ($NaNO_3$), mascagnite ($(NH_4)_2(SO_4)$), epsomite ($MgSO_4 \cdot 7H_2O$), hexahydrite

($MgSO_4 \cdot 6H_2O$), calcite ($CaCO_3$), among others such as quartz (SiO_2), brookite (TiO_2), quartz (SiO_2), adularia ($KAlSi_3O_8$), limonite ($FeO(OH) \cdot nH_2O$) and an aggregate particle composed by rutile (TiO_2) and nitrammite (NH_4NO_3) were detected by Raman spectroscopy. The majority of these compounds (except gypsum) can be consider components of the Secondary Marine Aerosol (SMA), which can be formed throughout different chemical reactions between the PMA formed when the wind strikes on the ocean waves and the NO_x and SO_x present in the atmosphere giving rise these types of compounds. Moreover, using punctual SEM-EDS measurements, different anthropogenic airborne particulate matter depositions on the homemade passive sampler were detected, containing different metal and metalloids particles related mainly with the additives used in the combustion fuel of ships motors (mainly diesel acting as catalyzer), particles related with the emissions from the nearby power plant and closely industries. Examples of that were aggregate particles including Ce, La; Bi and Th; Au, Al, Hg; Zr, Si, Sc, Pd and Y; Si, Pb and Sn, among others.

Finally in order to observe the possible dry depositions that can take place in the environment, sandstone samples from La Galea Fortress were analyzed. Thanks to the use of Raman spectroscopy, nitratine ($NaNO_3$), epsomite ($MgSO_4 \cdot 7H_2O$), arcanite (K_2SO_4), mascagnite ($(NH_4)_2SO_4$), lead oxide (PbO) among calcite ($CaCO_3$) and gypsum ($CaSO_4 \cdot 2H_2O$) were observed over the surface of the sandstone. Some of these compounds observed in the sandstone were previously detected on the home-made passive sampler such as mascagnite, nitratine, epsomite, calcite, gypsum and particles composed by Pb. Although arcanite and epsomite were not detected on the passive sampler, both sulfates could be also related with dry depositions. To complement the Raman identification of the deposited compounds, the SEM-EDS imaging revealed the presence of K_2SO_4, NaCl, KCl or $NaNO_3$ previously observed on the home-made passive sampler depositions.

All the salts identified coming from the dry deposition can be dissolved and they can react with the minor percentage of calcite ($CaCO_3$) present in the sandstone, giving as a result new compounds, which can be more soluble than the original calcite, accelerating then the losing material process of the sandstone. In this sense, special attention must pay to the correct explanation of the reactivity that give rise to the formation of sulfate and nitrate salts. As it has been proven in this work, sulfates and nitrates cannot only be formed in the building material following a reaction between the carbonate from the material itself and the acid aerosols deposited following a wet deposition or inclusion of salts coming from infiltration waters; the sulfate, nitrate and chloride salts can also be present in the material as deposited airborne particulate matter following a dry deposition.

5. References

[1] H. Morillas, M. Maguregui, O. Gómez-Laserna, J. Trebolazabala, J. M. Madariaga, Characterisation and diagnosis of the conservation state of cementitious materials exposed to the open air in XIX century lighthouses located on the coast of the Basque Country: 'The case of Igueldo lighthouse, San Sebastian, North of Spain, Journal of Raman Spectroscopy (2012) 43: 1630-1636.

[2] N. A. Stefanis, P. Theoulakis, C. Pilinis, Dry deposition effect of marine aerosol to the building stone of the medieval city of Rhodes, Greece, Building and Environment (2009) 44: 260–270.

[3] H. Morillas, M. Maguregui, O. Gómez-Laserna, J. Trebolazabala, J. M. Madariaga, Could marine aerosol contribute to deteriorate building materials from interior areas of lighthouses? An answer from the analytical chemistry point of view, Journal of Raman Spectroscopy (2013) 44: 1700–1710.

[4] M. Urosevic, E. Sebastián-Pardo, C. Cardel, Rough and polished travertine building stone decay evaluated by a marine aerosol ageing test, Construction and Building Materials (2010) 24: 1438–1448.

[5] H. Morillas, M. Maguregui, J. Trebolazabala, J. M. Madariaga, Nature and origin of white efflorescence on bricks, artificial stones, and joint mortars of modern houses evaluated by portable Raman spectroscopy and laboratory analyses, Spectrochimica Acta Part A: Molecular and Biomolecular Spectroscopy (2015) 136: 1195-1203.

[6] F. Zezza, F. Macri, Marine aerosol and stone decay, Science of the Total Environment (1995) 167: 123-43.

[7] H. Morillas, M. Maguregui, I. Marcaida, J. Trebolazabala, I. Salcedo, J. M. Madariaga, Characterization of the main colonizer and biogenic pigments present in the red biofilm from La Galea Fortress sandstone by means of microscopic observations and Raman Imaging, Microchemical Journal (2015) 121: 48–55.

[8] K. Torfs, R. Van Grieken, Chemical relations between atmospheric aerosols, deposition and stone decay layers on historic buildings at the Mediterranean coast, Atmospheric Environment (1997) 31: 2179-2192.

[9] H. Morillas, M. Maguregui, C. Paris, L. Bellot-Gurlet, P. Colomban, J. M. Madariaga, The role of marine aerosol in the formation of (double) sulphate/nitrate salts in plasters, Microchemical Journal (2015) 123: 148-157.

[10] I. Martinez-Arkarazo, M. Angulo, L. Bartolomé, N. Etxebarria, M. A. Olazabal, J. M. Madariaga, An integrated analytical approach to diagnose the conservation state of building materials of a palace house in the metropolitan Bilbao (Basque Country, North of Spain), Analytica Chimica Acta (2007) 584: 350-359.

[11] F. Culkin, Chemical oceanography, The Major Constituents of Sea Water, Academic Press, London, New York (1965) 121–161.

[12] D. Dyrssen, L. G. Sillen, Alkalinity and Total Carbonate in Sea Water—A Plea for p-t-Independent Data, Tellus, (1967) 19: 113–121.

[13] C. D. O'Dowd, M. Geever, M. K. Hill, S. G. Jennings, M. H. Smith, New particle formation: spatial scales and nucleation rates in the coastal environment, Geophysical Research Letters (1998) 25: 1661–1664.

[14] C. D. O'Dowd, T. Hoffmann, Coastal new particle formation: a review of the current state-of-the-art, Environmental Chemistry (2005) 2: 245–255.

[15] C. D. O´Dowd, G. de Leeuw, Marine aerosol production: a review of the current knowledge, Philosophical Transactions of the Royal Society A (2007) 365: 1753–1774.

[16] A. Baker, K. Weston, S. Kelly, M. Voss, P. Streu, J. N. Cape, Dry and wet deposition of nutrients from the tropical Atlantic atmosphere: links to primary productivity and nitrogen fixation, Deep Sea Research Part I: Oceanographic Research Papers (2007) 54: 1704-1720.

[17] Y. Chen, N. Shah, F. E. Huggins, G. P. Huffman, Microanalysis of ambient particles from Lexington, KY, by electron microscopy, Atmospheric Environment (2006) 40: 651–663.

[18] M. Pósfai, A. Gelencser, *R.* Simonics, K. Arato, J. Li, P. V. Hobbs, P. R. Buseck *(*2004*)*, Atmospheric tar balls: Particles from biomass and biofuel burning, Journal of Geophysical Research: Atmospheres (2004) 109: D06213.

[19] A. P. Ault, R. C. Moffet, J. Baltrusaitis, D. B. Collins, M. J. Ruppel, L. A. Cuadra-Rodríguez, D. Zhao, T. L. Guasco, C. J. Ebben, F. M. Geiger, T. H. Bertram, K. A. Prather, V. H. Grassian, Size-dependent changes in sea spray aerosol composition and properties with different seawater conditions, Environmental Science and Technology (2013) 47: 5603-5612.

[20] C. Deng, S. D. Brooks, G. Vidaurre, D. C. O. Thornton, Using Raman microspectroscopy to determine chemical composition and mixing state of airborne marine aerosols over the Pacific Ocean, Aerosol Science and Technology (2014) 48: 193-206.

[21] C. Coury, A. M. A. Dilner, A method to quantify organic functional groups and inorganic compounds in ambient aerosols using attenuated total reflectance FTIR Spectroscopy and multivariate chemometric techniques, Atmospheric Environment (2008) 42: 5923-5932.

[22] H. Shaka, N. A. Saliba, Concentration measurements and chemical composition of PM10-2.5 and PM2.5 at a coastal site in Beirut, Lebanon, Atmospheric Environment (2004) 38: 523-531.

[23] J. S. Gaffney, N. A. Marley, K. J. Smith, Characterization of fine mode atmospheric aerosols by Raman microscopy and diffuse reflectance FTIR, The Journal of Physical Chemistry A (2015) 119: 4524–4532.

[24] K. Kawamura, F. Sakaguchi, Molecular distributions of water soluble dicarboxylic acids in marine aerosols over the Pacific Ocean including tropics, Journal of Geophysical Research, Atmospheres (1999) 104: 3501-3509.

[25] J. Wagner, D. Leith, Field tests of a passive aerosol sampler, Aerosol Science (2001) 32: 33-48.

[26] J. Wagner, D. Leith, Passive aerosol sampler I: Principle of operation, Aerosol Science and Technology (2001) 34: 186-192.

[27] J. Wagner, D. Leith, Passive aerosol sampler Part II: wind tunnel experiments, Aerosol Science and Technology (2001) 34: 193-201.

[28] H. Geng, S. Kang, H. J. Jung M. Choël, H. Kim, C. U. Ro, Characterization of individual submicrometer aerosol particles collected in Incheon, Korea, by quantitative transmission electron microscopy energy-dispersive X-ray spectrometry, Journal of Geophysical Research: Atmospheres (2010) 115: D15306.

[29] C. U. Ro, K. Y. Oh, H. Kim, Y. P. Kim, C. B. Lee, K. H. Kim, C. H. Kang, J. Osan, J. de Hoog, A. Worobiec, R. Van Grieken, Single particle analysis of aerosols at Cheju Island, Korea, using Low-Z Electron Probe X-ray microanalysis: A direct proof of nitrate formation from sea salts, Environmental Science & Technology (2001) 35: 4487-4494.

[30] S. Maskey, H. Geng, Y-C. Song, H. Hwang, Y-J. Yoon, K-H, Ahn, C-U. Ro, Attenuated Total Reflection Fourier Transform-Infrared Imaging Techniques, Environmental Science & Technology (2011) 45: 6275-6282.

[31] L-Y. Zhao, Y-H. Zhang, Z-F. Wei, H. Cheng, X-H. Li, Magnesium Sulfate Aerosols Studied by FTIR Spectroscopy: Hygroscopic Properties, Supersaturated Structures, and Implications for Seawater Aerosols, Journal of Physical Chemistry A (2006) 110: 951-958.

[32] Y. Zhao, Y. Gao, Acidic species and chloride depletion in coarse aerosol particles in the US east coast, Science of the Total Environment (2008) 407: 541-547.

[33] S. S. Abdalmogith, R. M. Harrison, R. G. Derwent, Particulate sulphate and nitrate in Southern England and Northern Ireland during 2002/3 and its formation in a photochemical trajectory model, Science of the Total Environment (2006) 368: 769-780.

[34] M. Maguregui, N. Prieto-Taboada, J. Trebolazabala, N. Goienaga, N. Arrieta, J.Aramendia, L. Gomez-Nubla, A. Sarmiento, M. Olivares, J.A. Carrero, I. Martinez-Arkarazo, K. Castro, G. Arana, M.A. Olazabal, L.A. Fernandez, J.M. Madariaga. in: CHEMCH 1st International Congress Chemistry for Cultural Heritage, Ravenna, 30th June–3rd July, (2010).

[35] R.T. Downs, M. Hall-Wallace, A database of crystal structures published in the American mineralogist and the Canadian mineralogist and its use as a resource in the classroom. in: 18th General Meeting of the International Mineralogical Association, 2002, pp. 128.

[36] R. H. Dave, P. K. Ghosh, Efficient Recovery of Potassium Chloride from Liquid Effluent Generated during preparation of Schoenite from Kainite mixed salt and its reuse in production of potassium sulfate, Industrial & Engineering Chemistry Research (2006) 45: 1551-1556.

[37] M. G. Siemann, M. Schramm, Henry´s and non-Henry´s law behavior of Br in simple marine systems, Geochimica et Cosmochimica Acta (2002) 66: 1387-1399.

[38] D. W. Lewis, D. McConchie, Chemical Sediments, Practical Sedimentology, Springer-Verlag, (New York, USA) (1994), 186-201.

[39] H. Kasedde, J. B. Kirabira, M. U. Babler, A. Tilliander, S. Jonsson, Characterization of brines and evaporites of Lake Katwe, Uganda, Journal of African Earth Sciences (2014) 91: 55-65.

[40] A. Katz, A. Starinsky, Geochemical History of the Dead Sea, Aquatic Geochemistry (2009) 15: 159-194.

[41] C. E. Harvie, J. H. Weare, L. A. Hardie, H. P. Eugster, Evaporation of seawater: calculated mineral sequences, Science (1980) 208: 498-500.

[42] G. Testa, S. Lugli, Gypsum–anhydrite transformations in Messinian evaporites of central Tuscany (Italy), Sedimentary Geology (2000) 130: 249–268.

[43] H. Zimmermann, Tertiary seawater chemistry-implications from primary fluid inclusions in marine halite, American Journal of Science (2000) 300: 723-767.

[44] R. Sinha, B. C. Raymahashay, Evaporite mineralogy and geochemical evolution of the Sambhar Salt Lake, Rajasthan, India, Sedimentary Geology (2004) 166: 59-71.

[45] P. Gamazo, S. A. Bea, M. W. Saaltink, J. Carrera, C. Ayora, Modeling the interaction between evaporation and chemical composition in a natural saline system, Journal of Hydrology (2011) 401: 154-164.

[46] B. Wang, A. Laskin, Reaction between water-soluble organic acids and nitrates in atmospheric aerosols: Recycling of nitric acid and formation or organic salts, Journal of Geophysical Research: Atmospheres (2014) 119: 3335-3351.

[47] G. A. Poskrebyshev, P. Neta, R. E. Huie, Equilibrium constant of the reaction OH^-+ HNO_3 ⇆ H_20 +NO_3^- in aqueous solution, Journal of Geophysical Research (2001) 106: 4995-5004.

[48] N. K. Richards-Henderson, K. M. Callahan, P. Nissenson, N. Nishino, D. J. Tobias, B. J. Finlayson-Pitts, Production of gas phase NO2 and halogens from the photolysis of this water films containing nitrate, chloride and bromide ions at room temperature, Physical Chemistry Chemical Physics (2013) 15: 17636-17646.

[49] A. Mihajlidi-Zelić, D. Dordević, D. Relić, I. Tošić, L. Ignjatović, M. A. Stortini, A. Gambaro, Water-soluble inorganic ions in urban aerosols of the continental part of Balkans (Belgrade) during the summer – autumn (2008), Open Chemistry (2015) 13: 245–256.

[50] K. L. Hayden, A. M. Macdonald, W. Gong, D. Toom-Sauntry, K. G. Anlauf, A. Leithead, S-M. Li, W. R. Leaitch, K. Noone, Cloud processing of nitrate, Journal of Geophysical Research (2008) 113: D1820.

[51] J. H. Seinfeld, Atmospheric Chemistry and Physics of Air Pollution, Wiley, New York (USA) (1986), 1203.

[52] J. P. Putaud, R. Van Dingenen, A. Dell' Acqua, F. Raes, E. Matta, S. Decesari, M. C. Facchini, S. Fuzzi, Size-segregated aerosol mass closure and chemical composition in Monte Cimone (I) during MINATROC, Atmospheric Chemistry & Physics (2004) 4: 889-902.

[53] S. Livraghi, M. R. Chierotti, E. Giamello, G. Magnacca, M. C. Paganini, G. Cappelletti, C. L. Bianchi, Nitrogen-Doped Titanium Dioxide Active in Photocatalytic Reactions with Visible Light: A Multi-Technique Characterization of Differently Prepared Materials, Journal of Physical Chemistry C (2008) 112: 17244-17252.

[54] S. Silvergren, U. Wideqvist, J. Ström, S. Sjogren, B. Svenningsson, Hygroscopic growth and cloud forming potential of Arctic aerosol based on observed chemical and physical characteristics (a 1year study 2007–2008), Journal of Geophysical Research: Atmospheres (2014) 119: 14080–14097.

[55] I-M. Chou, R. R. Seal, Determination of epsomite-hexahydrite equilibria by the humidity-buffer technique at 0.1 MPa with implications for phase equilibria in the system $MgSO_4 \cdot H_2O$, Astrobiology (2003) 3: 619-630.

[56] H. Muroyama, H. Asajima, S. Hano, T. Matsui, K. Eguchi, Effect of an additive in a CeO2-based oxide on catalytic soot combustion, Applied Catalysis A: General (2015) 489: 235-240

[57] M. Elkadi, A. Pillay, J. Manuel, M. Z. Khan, S. Stephen, A. Molki, Sustainability study on Heavy metal uptake in Neem biodiesel using selective catalytic preparation and Hyphenated Mass Spectrometry, Sustainability (2014) 6: 2413-2423.

[58] F. S. Depoi, D. Pozebon, W. D. Kalkreuth, Chemical characterization of feed coals and combustion by products from Brazilian power plants, International Jounal of Coal Geology (2008) 76: 227-236.

[59] E.D. Banús, M. A. Ulla, E. E. Miró, V. G. Milt, Co,Ba,K/ZrO2 coated onto metallic foam (AISI 314) as a structured catalyst for soot combustion: Catalytic activity and stability, Applied Catalysis A: General (2011) 393: 9-16.

[60] F. Klingstedt, A. K. Neyestanaki, L-E. Lindfors, T. Salmi, T. Heikkila, E. Laine, An investigation of the activity and stability of Pd and Pd-Zr modified Y-zeolite catalysts for the removal of PAH, CO, CH4 and NOx emissions, Applied Catalysis A: General (2003) 239: 229-240.

[61] J. Pey, N. Perez, J. Cortes, A. Alastuey, X. Querol, Chemical fingerprint and impact of shipping emissions over a western Mediterranean metropolis: Primary and aged contributions, Science of the Total Environment (2013) 463-464: 497-507.

[62] S. W. Campbell, M. C. Evans, N. D. Poor, Predictions of size-resolved aerosol concentrations of ammonium, chloride and nitrate at a bayside site using EQUISOLV II, Atmospheric Environment (2002) 36: 4299-4307.

[63] C. M. Belfiore, D. Barca, A. Bonazza, V. Comité, M. F. Russa, A. Pezzino, S. A. Ruffolo, C. Sabbioni, Application of spectrometric analysis to the identification of pollution sources causing cultural heritage damage, Environmental Science and Pollution Research (2013) 20: 8848-8859.

[64] R. Kumar, A. Rani, K. M. Kumari, S. S. Srivastava, Atmospheric dry deposition to marble and red stone, Journal of Atmospheric Chemistry (2005) 50: 243-261.

RESEARCH ARTICLE 8

Evaluation of the influence of natural and anthropogenic stressors coming from a marine urban-industrial environment on the deterioration process of La Galea Fortress sandstone (Getxo, north of Spain).

H. Morillas, M. Maguregui, I. Marcaida, C. Garcia-Florentino, J. A. Carrero, J. M. Madariaga

Submitted to Analytical Chemistry in July (2015)

Evaluation of the influence of natural and anthropogenic stressors coming from a marine urban-industrial environment on the deterioration process of La Galea Fortress sandstone (Getxo, north of Spain)

ABSTRACT

The sandstone used in the construction of the tower and the entrance arch of La Galea Fortress (Getxo, north of Spain) shows a very bad preservation state. The location of this historic building is one of the possible reasons for its poor conservation state. A high percentage of sandstone has been lost, especially in the stone blocks from the tower. The fortress is located just on a cliff and close to the sea, and it experiments the direct influence of marine aerosol and also the impact of acid gases (SO_x and NO_x) coming from the ship engines (maritime traffic) near the building. This environment seems to be very harmful for the preservation of the sandstone used in it, promoting different pathologies (disintegration, alveolization, cracking or erosion blistering, salts crystallization on the pores and efflorescences). In this work, a multianalytical methodology based on the use of elemental techniques such as HH-ED-XRF, μ-ED-XRF, SEM-EDS and ICP-MS combined with molecular techniques such as Raman spectroscopy and XRD was applied in order to characterize the nature of the sandstone, to evaluate the pathologies related with sandstone losing and also to characterize the nature of the salts included in the superficial efflorescences. Concretely, in this last case compounds such as nitrates and sulfates have been detected.

Keywords: Marine aerosol, sandstone, nitrates, sulfates, Raman spectroscopy.

1. Introduction

Historical buildings are constituted by numerous materials such as stones [1], cements [2] , bricks [3], binding agents [4], ceramics [5], wood [6], metals [7], plastics [8], etc. Sandstone is a rock type usually included in different kind of constructions. It is a sedimentary and dendritic rock with variable colors and containing clasts of sand size. Its sand grains may be composed of minerals such as quartz and feldspars. The oxides of iron, manganese and other impurities are the ones which provide different tonalities to the sandstone [9, 10]. The binding agent of sandstone can be the quartz (silica) [11], clay [12], or even calcium carbonate [13, 14]. Depending on the binding agent, the sandstone can has higher or lower durability. In this sense, if quartz is present in the sandstone as binder agent, it gives higher durability than calcite acting as binder [15]. The sandstone which contains calcium carbonate as binder agent is called calcarenite, which is easier to be dissolved and consequently disintegrated. For this reason, its porosity makes itself particularly sensitive to the physical, chemical and biological agents [16]. Therefore, if calcarenite rather than sandstone with quartz as binding agent is used in a construction, it can suffer a higher deterioration process. Moreover, depending on the environmental stressors (acid pollutants, salts, airborne particulate matter etc.) that can impact on this material, the deterioration rate can increase [17].

The critical factor in the deterioration of calcarenite is the solubility of calcium carbonate, which is low in pure water but increases as the percentage of water dissolved carbon dioxide increases. The rainfall of unpolluted areas can gradually give rise to the dissolution of calcium carbonate due to its background acidity. Under this phenomenon, building materials can crumble and become even more porous accelerating their decay processes [18-19]. Although the calcium carbonate content of calcarenite is always less than 40%, this carbonate percentage is enough to react with acidic environmental pollutant agents [20-22]. Thus, in moderately polluted areas, rainwater causes progressively the dissolution of calcium carbonate. The rainwater pH value in this kind of environments is around 4-6. This is the pH value at which calcite dissolution process starts [23]. Considering this phenomenon, calcarenite would become gradually more porous, thereby accelerating its deterioration [24] and can be also accelerated even if there are acid pollutants in the atmosphere [25].

In this way, it is important to highlight that the durability of the natural sandstone does not only depend on the environmental stressor, it also depends on the mineralogy of the rock [26, 27]. For this reason there are works that studied the durability of rocks according to the

pore system, which affect the movement of fluids inside the rock, accelerating its physical, chemical and biological deterioration [28, 29].

Apart from the porosity, other factors are involved in the sandstone disintegration or losing process of sandstone. The first one corresponds to salts dissolved in infiltration waters, which can penetrate through the pores of the sandstone and crystallize inside them (sub-efflorescences). Sometimes salts can also crystallize on the surface (efflorescence) [30, 31]. The second one, acid gases such as CO_2, SO_x, NO_x, etc. which can be deposited on the surface of the material according to a dry deposition or, in most cases following a wet deposition (incorporation of the acid gases in the rain and subsequent deposition as acid) are other environmental stressors that can modify the original composition of the sandstone. These gases would transform into their respective acids, causing the reaction between them and the original sandstone promoting the crystallization of new soluble salts [32]. These salts can be rain washed and after several cycles of decaying the result is the losing material.

Apart from acid gases, airborne particulate matter (APM) coming from different sources can be deposited on the surface of the sandstone generating crusts or patinas on this materials. The APM origin could be both natural and anthropogenic. The natural APM can come from the erosion of natural rocks from the surrounding environment, and the anthropic ones can be emitted from urban-industrial sources [33, 34], maritime traffic [22] and road traffic [35].

Natural environmental factors also play an important role in the loss of material in sandstones. The permanent action of wind can transport detrital material from other building materials, promoting the development of tiny crusts. Over time and by the action of wind, these thin crusts promote the appearance of small depressions, usually in the central region of the sandstone surface, being the area from where water can penetrate easier, and the first susceptible area to be degraded. Subsequently as the arenization and alveolization processes advance, the concavity of surfaces increases with the ability to absorb water causing an increase of losing material and alveolization [36].

Additionally, the loss of material of sandstone caused by freeze-thaw phenomena also often causes fractures on the material. The pore structure of the stone plays an important role in its resistance to freeze-thaw. Fine pores are much more susceptible to be frozen than those with larger pores [37]. The cooling/heating and wetting/drying phenomena cause thermal expansion in the sandstone, because they generate internal tensions. In a well-connected pore system, the effect of freeze-thaw caused by volume increase is lower than in a low-connected pore system [38].

Moreover, the location of the buildings is very important for the conservation state of the materials used in it. One of the most dangerous environments is the coastal one, with the direct influence of marine aerosol [39, 40]. In this way, marine aerosol transports different salts. The most abundant salt carried on marine aerosol is sodium chloride, but other salts such as sulfates and nitrates may also appear in notable quantities. Besides, high load of other dissolved ions and suspended materials such as Ca^{2+}, K^{+}, Mg^{2+}, Fe^{3+}, Al^{3+}, Sr^{2+}, NH_4^{+}, HCO_3^{-} and Br^{-} can be deposited or can migrate to the surface of buildings located near the sea promoting new salts formations with its consequently material degradation [41,42]. These salts can react with the calcium carbonate from the sandstone promoting the formation of new compounds. Usually these compounds (sulfates and nitrates) are more soluble than calcium carbonate. Therefore, these new salts can be dissolved by the influence of the rainwater, promoting losing material in the sandstone block [43].

In this work, a multianalytical methodology based on a combination of elemental (hand-held energy dispersive X-Ray Fluorescence, micro energy dispersive X-Ray Fluorescence, SEM-EDS and ICP-MS) and molecular (micro-Raman spectroscopy and X-Ray Diffraction) spectroscopic techniques was applied in order to determine the original composition of La Galea Fortress sandstone and possible decay compounds that can be present on it. Apart from the influence of the anthropogenic emissions (acid gases, airborne particulate matter) and salts included in the original composition of building materials close to the sandstone, natural environmental factors (marine aerosol, winds, etc.) are going to be also considered as potential responsible of the poor conservation state of the sandstone used on the tower and on the entrance arch of this construction. Additionally, an elemental and molecular characterization was also applied to determine the nature of the white crusts formed on the entrance arch of the Fortress.

2. Materials and Methods

2.1. La Galea Fortress description and location

La Galea Fortress is located in the cliff overlooking the bay of Abra, in Getxo (Biscay, Basque Country, north of Spain) and about 50 m above the sea level. Additional description about its history and environmental conditions of the place where it is located can be found elsewhere [44]. It is necessary to remark that the average wind speed is 5.6 kts, where the two preferential wind directions are the South-southeast (SSE) and the Weast-northweast (WNW) [45].

Figure 1. Different views of La Galea Fortress, Getxo, north of Spain.

2.2. Samplings

Different sandstone samples from La Galea Fortress (Getxo, Basque Country, north of Spain) were selected in order to study the original composition of this building material and their possible affections. Taking into consideration the two preferential wind directions (SSE and WNW), sandstone samples from the SSE (SSE-SAN) and NW (NW-SAN) orientations of La Galea Fortress tower were extracted (see Figure 2). Considering the good conservation state of the sandstone from the NW orientation where a reddish biolfilm is present, it was decided to sample the sandstone from this orientation, close to the WNW orientation, in order to observe if elemental or molecular differences can be found between the sandstone of the SSE and the NW which could explain the good conservations state of the NW sandstone. Apart from that, sandstone samples from the entrance arch of the fortress (EA-SAN) were also taken (see Figure 2).

Coming back to the tower of the fortress, in its SSE orientation, the hole left by an old window was closed using cement. In order to observe the possible influence of this cement on the conservation state of the sandstone from this orientation, a cement sample was extracted (SSE-CEM) from this location. An additional cement sample was also taken from the entrance arch of the fortress (EA-CEM). This cement was incorporated less than 15 years ago, in order to fix the metallic door to the arch. Finally, a sample from the limestone in the upper part of the arch dome (EA-LIM) was also taken for its characterization (see Figure 2). Regarding the pathologies visually observable in the fortress, white formations

(crust and stalactites) from the inner part of the entrance arch and white-greyish crust near the cement from the entrance arch (EA-CRU) and efflorescences from the tower were also taken (see Figure 2). To sample this salts a scalpel was used. Finally, to extract all the sandstone, limestone, cement and crust samples from the entrance arch and the tower, a hammer and a chisel were used. The average size of all the fragments never exceeded 2-3 cm (in some cases the size of the sample was lower).

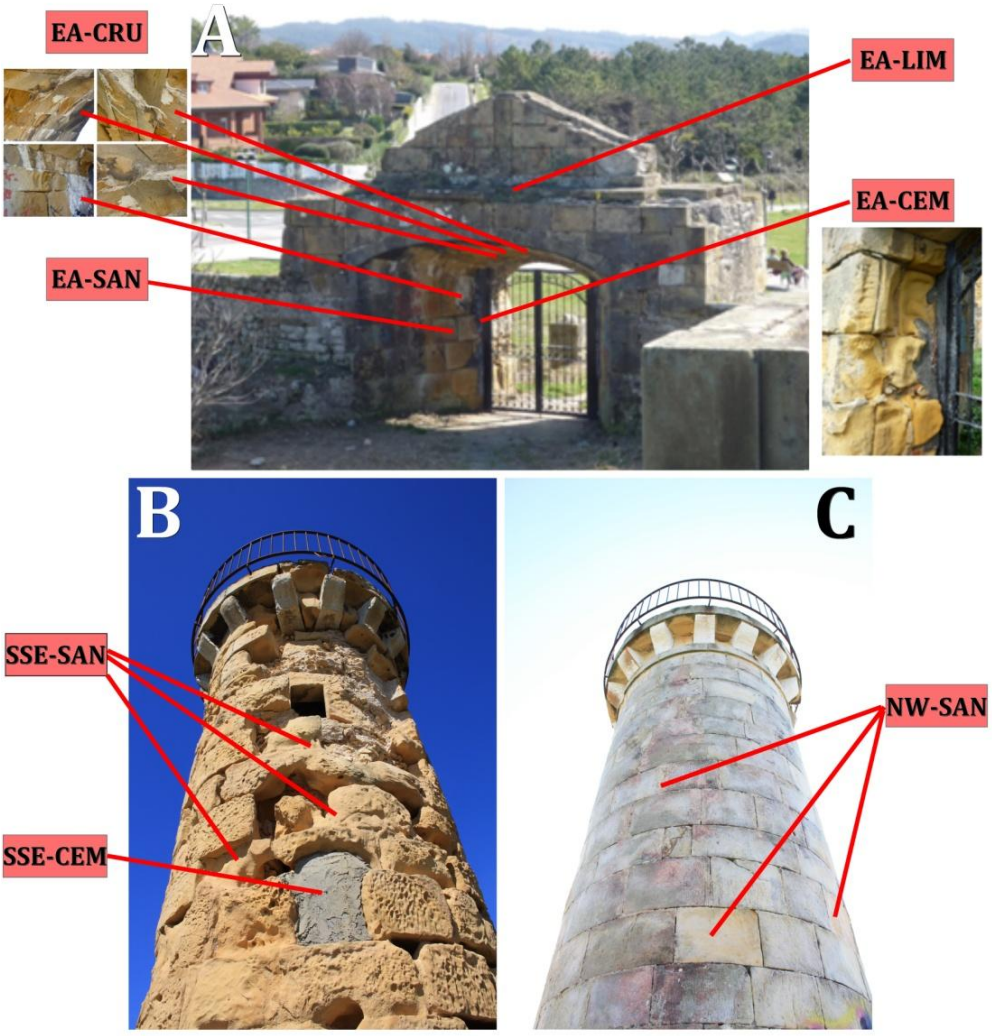

Figure 2. Locations of the samples taken in the entrance arch (A), in the South-southeast (B) and Northweast orientations of the tower (C) of La Galea Fortress.

2.3. Instrumentation

For this work, different analytical instruments were used. For the molecular analysis (original composition as well as determination of deterioration products) a Renishaw RA 100 portable Raman system (Renishaw, *Gloucestershire, UK)* coupled to a microprobe was used to collect the Raman spectra (785 nm diode laser connected with a fibre-optics cable and a CCD detector). In order to interpret all of the Raman results, the acquired Raman spectra were compared with Raman spectra of pure standard compounds collected in the e-VISNICH dispersive Raman database [46] and with free Raman databases (e.g. RRUFF [47]) for the assignation of Raman bands. For spectral treatment and analysis, Wire 2.0 (Renishaw) and OMNIC® Version 7.2 software Thermo Nicolet (Madison, WI, USA) were used. Once the compounds were identified, they were classified in a first group as original compounds and in a second group as deterioration compounds. A given compound is said to be identified if it appeared at least five times in different spectra from the same sample.

Besides the Raman analysis, for the molecular composition, XRD analyses were carried out using a powder diffractometer PANalytical Xpert PRO instrument equipped with a copper tube ($\lambda_{CuK\alpha media}$= 1.5418 Å, $\lambda_{CuK\alpha1}$= 1.54060 Å, $\lambda_{CuK\alpha2}$= 1.54439 Å), a vertical goniometer (Bragg-Brentano geometry), a programmable divergence aperture, an automatic interchange of samples, a secondary monochromator of graphite and a PixCel detector. The measurement conditions were 40 kV and 40 mA, with an angular range (2θ) scanned between 5 and 70°. Moreover, a specific software X`pert HighScore (PANalytical) in combination with the specific powder diffraction file database (International Centre for Diffraction Data - ICDD, Pennsylvania, USA) was used for the data treatment of the diffractograms and the identification of the mineral phases present.

For the elemental characterization of the sandstone and in some cases for the characterization of white crusts from the entrance arch, different X-Ray Fluorescence spectrometers were used. For the first elemental screening of La Galea Fortress sandstone, an XMET5100 (Oxford Instruments, UK) hand-held energy dispersive X-Ray Fluorescence spectrometer (HH-ED-XRF) was used. The instrument is equipped with a Rh tube working at a maximum voltage of 45 KV. The size of the emitted X-Ray beam is 9 mm. The analyzer includes a silicon drift detector (SDD) of high resolution that is able to provide an energetic resolution of 150 eV (calculated for the Mn K_α line at -20 ˚C) which allows acquiring spectra with 20 eV resolutions. The analyzer contains a PDA to control the spectrometer and also to save the spectral and quantitative information. In order to determine possible contributions from detector materials and possible contaminations of the XRF analyzer window, 20

repetitive spectra of an instrumental blank (a PTFE block) were acquired before each measurements batch. The PTFE block was cleaned before its use in a 20% nitric acid bath during 24 hours. Before its use, it was rinsed in Milli-Q water and dried. For the repetitive measurements, the same spectral conditions (voltage, current, filter and test time) as those used for the analysis of the sandstone were considered. To determine the presence of the heaviest elements (Z > Ti), the spectra were acquired during 50 seconds (real time) and the voltage and current of the X-Ray tube was set at 40 kV and 15 μA respectively. Additionally, to remove the "pinches" Bremsstrahlung and 3rd Generation peaks, a 500 μm Al filter was used. In order to improve the detection of the lighter elements (Z < Ti), additional measurements were performed without the Al filter and at lower voltage (13 kV) and higher current (40 μA). The test time in this case was 35 seconds for each measurement. All the collected spectra were transferred from the PDA of the instrument to a computer in .txt files

For the laboratory ED-XRF measurements, two micro energy dispersive X-Ray Fluorescence spectrometers (μ-ED-XRF) were used. For the measurements in the millimeter scale, the M4 Tornado (Bruker Nano GmbH, Berlin, Germany) μ-ED-XRF instrument was used. With this instrument, punctual measurements, line scans and HyperMaps from La Galea sandstone samples were acquired. The X-Ray tube implemented in this instrument is a micro-focus side window Rh tube powered by a low-power HV generator and cooled by air. Thanks to the implemented collimator, spot sizes of 1 mm were measured. The X-ray tube can work at a maximum voltage of 50 kV and at a maximum current of 700 μA, which were the conditions considered for the spectra acquisition in this work. The detection of the fluorescence radiation was performed by an XFlash® silicon drift detector with 30mm^2 sensitive area and energy resolution of 145eV for Mn-Kα. In order to improve the detection of the lightest elements (Z>11), filters were not used and measurements were acquired under vacuum (20 bar). To achieve the vacuum, a diaphragm pump MV 10 N VARIO-B was used. The live time used for each punctual measurement was 200 seconds. For the focusing of the area under study, two video-microscopes were used, one of them to explore the sample under a low magnification (1 cm^2 areas), and the other one to perform the final focusing (1 mm^2 areas). Apart from punctual measurements and line scans, HyperMaps were also acquired. The elemental maps showed in this work were obtained after a previous assignation of the elements, deconvolution and application of Fundamental Parameters based-method to obtain the maps regarding the quantitative information of each element on each point from the mapped area. The spectral data acquisition and treatment was performed using the M4 TORNADO software and the quantification was done thanks to the M-Quant software package

Additional elemental maps from la Galea sandstone were also acquired using a lower lateral resolution (650 μm) thanks to the use of a lower diameter collimator implemented in a second μ-ED-XRF instrument, the portable ARTAX μ-ED-XRF from Röntec (currently Bruker Nano GmbH, Berlin, Germany). In this case, each elemental map is constructed according to the net areas of XRF lines. This spectrometer implements a low-power metal-ceramic-type MCBM 50 X-Ray tube with molybdenum target as excitation source. The molybdenum anode spot size in the instrument is 70 x 50 μm, and it can be used at a maximum voltage of 50 kV and at a maximum current of 700 μA (maximum power of 35 W). The radiation-protecting tube housing is equipped with an electrical shutter and safety functions externally controlled by a PC. The X-Ray Fluorescence radiation is detected by means of an electro-thermally cooled Xflash® detector, which is a silicon drift detector with high-speed low-noise electronics. The detector has an active area of 5 mm^2 and a 8 μm-thick Dura-beryllium window. The geometry between primary beam, sample, and detector is fixed at 0°/40° relative to the perpendicular of the sample surface. The X-Rays were collimated by a tantalum collimator with a diameter of 0.65 mm and the beam diameter in the sample surface is around 200 mm^2. An integrated CCD camera provides an image of the sample region under investigation (8 mm x 8 mm). In the vibration-damped swivel arm from the instrument, a motor-driven XYZ positioning stage is directly mounted, which consists of three equal modules with a maximum travel of 50 mm in each direction. This motor unit allows focusing on different parts of the sample. For the mapping of La Galea Fortress sandstone the maximum voltage and current were used and 800 seconds of test time for each analyzed point. The spot size of each measured point was reduced up to 650 μm thanks to a mechanical collimator. In this case, measurements were performed at air. Instrument control and data-handling were performed using the Windows-base ARTAX software 4.9.13.2 (Intax GmBH, Berlin, Germany). In order to improve the representation of the elements distribution on the sandstone samples, the elemental maps presented in this work were constructed using the Surfer® 10 software (Golden Software, LLC, USA).

In order to improve the detection of lighter elements (C, O, N, Na and Mg) on the sandstone samples, SEM-EDS analyses were also carried out. For those analyses, an EVO®40 Scanning Electron Microscope (Carl Zeiss NTS GmbH, Germany) coupled to an X-Max Energy-Dispersive X-ray spectroscopy equipment (Oxford Instruments, Abingdon, Oxfordshire, United Kingdom) and it was used for electron image acquisitions and elemental composition determinations (punctual and quantitative mapping) of the sandstone samples. As sandstone samples are not conductive, all the analyzed samples were coated with gold in order to improve the microscopic images. The SEM images were obtained at high vacuum

employing an acceleration voltage of 30 kV and a 10–400 μm working distance. To take the images, different magnifications (reaching up to 6,800×) were used by a secondary electron detector whereas an integration time of 50 s was employed to improve the signal to noise ratio. The EDS spectra were acquired and treated using the INCA software. The SEM-EDS spectra processed by the INCA program, permits the elemental analysis of selected areas previously seen by SEM. Furthermore, a mapping of specific microscopic areas in the samples was possible, allowing the evaluation of the distribution of these elements over the sample.

ICP-MS was used to quantify the trace elements, and also major and minor elements present in the sandstone. In this case, an acid digestion was performed, using 0.5 gr of dried sandstone sample and acid treatment with 12 ml of 3:1 HNO_3 (69%) : HCl (36%). Prior to the elemental measurements, the acid concentration of the acid extracts was reduced to less than 1% HNO_3 using Milli-Q water. In addition, a solution containing 10 $\mu g.L^{-1}$ of Be, Sc, Ge, In, Re and Bi was added as internal standard. The internal standards and ICP-MS calibration standards solutions were prepared from 1000 $mg.L^{-1}$ stock solutions of Alfa Aesar (Specpure®, Plasma standard solution, Germany) inside a class 100 clean room. All solutions were prepared using Milli-Q quality water. PL 20-200 μL and PL 500-5000 μL micropipettes (Eppendorf, Hamburg, Germany) with an calibration standards and samples dilutions were prepared using analytical balance model Mettler-Toledo XS205 (Colombus, OH, USA) with accuracy of ± 0.00001 g. The elemental analysis of the extracts was performed by ICP-MS (NexION 300, Perkin Elmer) in a class 100 clean room. The argon used was supplied by Praxair (99.995%, Madrid, Spain). ^{27}Al, ^{44}Ca, ^{88}Sr, ^{98}Mo, ^{114}Cd, ^{120}Sn, ^{121}Sb, ^{138}Ba, ^{184}W, ^{202}Hg and, ^{206}Pb+^{207}Pb+^{208}Pb isotopes were determined in standard mode and ^{23}Na, ^{24}Mg, ^{39}K, ^{47}Ti, ^{51}V, ^{52}Cr, ^{55}Mn, ^{56}Fe, ^{59}Co, ^{60}Ni, ^{65}Cu, ^{66}Zn, ^{75}As, ^{111}Cd isotopes were determined in collision mode with He with in order to eliminate possible polyatomic interferences. The plasma conditions such as argon flow of nebulizer, the torch position and the instrument lenses voltages were optimized before each measurement session aspirating a standard solution of 1ng/mL of Mg, Rh, In, Ba, Pb and U. The gas nebulizer flow was optimized obtaining a compromise between sensitivity and low oxides level (less than 2.5 % for the CeO/Ce ratio). Finally, the data were acquired and analyzed for the element quantitative analysis using the Elan 3.2 software (Perkin Elmer SCIEXTM, Ontario, Canada).

3. Results and Discussion

3.1. Characterization of La Galea Fortress sandstone

As it has been mentioned in the introduction, the sandstone from the entrance arch and the tower of La Galea Fortress show a poor conservation state. Different kinds of pathologies are visible on the sandstone: disintegrations or losing material, alveolizations, crackings, etc., especially in the tower. However, all the sandstone blocks from the tower do not show these pathologies. As can be observed in Figure 3 top, the most affected orientation is the South-southeast (SSE), where a high percentage of the sandstone has been lost (see Figure 2). In this orientation, the hole left by an old window was closed using modern cement. Apart from that, the North-northeast and the North orientations show a high amount of efflorescences (salts crystallized on the surface) on the sandstone (see Figure 3 top). On the contrary, the sandstone from the Northwest orientation, where a reddish biofilm is present (biogenic pigments excreted by Trentepohlia algae as the main colonizer on the biofilm) [44] shows a good conservation state (see Figure 3 top).

According to the available meteorological data, the two preferential directions of wind in Punta Galea, the place where the fortress is located, are South-southeast (SSE) and West-northwest (WNW)[45]. Taking into account this information, the SSE orientation of the fortress which shows the worst conservation state (SSE), matches with one of the preferential wind direction. Considering that the wind can assist erosion, alveolization, etc. deterioration processes of the sandstone, this natural factor among other natural and anthropogenic factors, must be taken into consideration to explain the bad conservation state of the sandstone from the SSE orientation of the tower. On the contrary, the sandstone from the WNW orientation, which also presents reddish patinas, shows a good conservation state. Therefore, these organic biofilms could act as protective layer against the erosion of the sandstone.

In order to extend these visual observations and to consider all the natural and anthropogenic factors that can have influence in the poor conservation state of the sandstone, elemental and molecular characterizations of this material from the SSE and NW orientations of the tower and additional analyses on the sandstone from the entrance arch of the fortress were conducted.

3.2. Elemental characterization of the sandstone

The in situ analyses performed with the hand-held energy dispersive X-Ray Fluorescence spectrometer (HH-ED-XRF) showed the presence of the same elements (Al, Si, S, K, Ca, Ti, Mn, Fe, Cu, Zn, Pb, Rb, Sr and Zr) in the external and inner areas of the sandstone from both orientations of the tower (SSE and NW). To identify additional minor and trace elements which were not able to detect by means of the non-invasive ED-XRF technique, elemental quantification of the sandstone from both orientations of the tower and from the entrance arch was conducted using ICP-MS. The concentration of major, minor and trace elements quantified by ICP-MS are presented in the Table 1 as average of three replicate samples from each location. Comparing the HH-ED-XRF non-invasive results and the ICP-MS destructive results, it can be said that apart from the most lighter elements, which cannot be detected using the hand-held instrument (Na and Mg), the HH-ED-XRF instrument is able to detect all the major and minor elements present on the sandstone, except V, Cr, Ni, As and Ba. These elements concentrations are under 9 $mg \cdot Kg^{-1}$ (see Table 1). On the contrary, the HH-ED-XRF instrument is able to detect the concentration of Cu which is between 3.3-4.5 $mg \cdot Kg^{-1}$, depending on the sample type. ICP-MS was also useful to determine the presence of Co, Sn, Mo and Sb in the sandstone at trace levels (see Table 1). Elements like Ag and Hg were under the limit of detection of the ICP-MS method in all the samples (see Table 1). Finally, by means of ICP-MS, W and Tl were only detected in the sandstone from the NW orientation and Cd in the sandstone from the SSE (see Table 1). Having a look to the trace elements detected by ICP-MS in the sandstone, it must be remarked that the concentration of lead is higher than the one that can be found in a natural sandstone (around 10 $mg \cdot Kg^{-1}$) [48]. This higher concentration could be related with an additional input of lead coming from the airborne particulate emissions of the port activity and other anthropogenic sources.

Regarding the measurements performed with the HH-ED-XRF instrument (more than 30 for each orientation and side), in all of them in the inner areas of the sandstones, a weak signal at 9.2 keV was detected (see Figures 3B and 3D). This signal is very low, and it is almost lost in the backgrounds of all the spectra from the external areas. This peak can be related with the K-alpha lines of Ga. It is reported that the average concentration of Ga in sandstones as trace element is usually around 1-15 ppm [48]. However, in the spectra acquired on the external areas, it was not possible to detect its L lines, thus it cannot be rejected that the signal at 9.2 keV could belong to an artifact.

Regarding Pb and As and due to the lack of a proper deconvolution algorithm in the software available to treat XRF spectra acquired on site, it was not possible to confirm the presence/absence of As in the sandstone tower (see Figures 3B and 3D). Additionally, the L-alpha and L-beta lines of Au at 9.7 and 11.4 keV respectively present in the spectra, belong to the gold present in the detector (see Figures 3B and 3D). The net area of both peaks in the spectra from sandstone do not exceed the ones obtained in the repetitive measurements of the instrumental blank, thus it can be affirm that Au is not present in the XRF measurements or it is under the limit of detection. The same happens with the K-alpha line of Sn detected around 25 keV in all the spectra, this signal also come from the set up of the instrument, because the net area on all the spectra do not exceed the net area of Sn determined on the repetitive measurements of the instrumental blank.

Table 1. Concentration of the elements in $mg \cdot Kg^{-1}$ and method RSD (Relative Standard Deviation) obtained by ICP-MS for the sandstone of the entrance arch (S-EA), South-southeast (S-SSE-T) and Northwest (S-NW-T) orientations of the tower from La Galea Fortress.

Elements	S-EA	S-SSE-T	S-NW-T	RSD (%)
Al	11224 ± 1150	9647 ± 283	7123 ± 755	7
Fe	15498 ± 1517	9448 ± 379	13156 ± 1372	6
Ca	11670 ± 1687	15058 ± 1351	13241 ± 1905	11
Na	1634 ± 134	3679 ± 173	3292 ± 116	10
Mg	1351 ± 73	1179 ± 90	1087 ± 62	10
K	450 ± 10	470 ± 57	422 ± 59	9
Zn	49 ± 2	120 ± 3	25 ± 2	4
Pb	16.7 ± 1.0	39.0 ± 0.2	46.5 ± 0.7	3
Li	11.90 ± 0.23	13.28 ± 0.08	5.72 ± 0.41	3
Ti	17 ± 1	15.4 ± 0.1	12 ± 2	9
Sr	12.8 ± 0.7	9.54 ± 0.60	6.42 ± 0.06	4
Mn	11.57 ± 0.07	6.2 ± 0.2	13 ± 1	5
V	8.9 ± 0.2	7.1 ± 0.4	5.0 ± 0.5	6
Cr	7.2 ± 0.2	6.4 ± 0.2	9.2 ± 0.7	5
Ba	6.2 ± 0.2	7.34 ± 0.05	5.1 ± 0.5	5
Cu	4.53 ± 0.02	4.46 ± 0.08	3.30 ± 0.05	1
Ni	4.4 ± 0.1	3.7 ± 0.2	7.1 ± 1.0	7
As	3.95 ± 0.08	1.83 ± 0.07	2.0 ± 0.2	5
Sn	0.47 ± 0.01	0.46 ± 0.01	0.51 ± 0.03	4
Co	0.46 ± 0.01	0.65 ± 0.02	0.71 ± 0.03	3
Mo	0.141 ± 0.001	0.06 ± 0.01	0.16 ± 0.03	10
Sb	0.34 ± 0.02	0.24 ± 0.02	0.203 ± 0.003	5
Ag	<LOD	<LOD	<LOD	1
W	<LOD	<LOD	0.06 ± 0.06	10
Hg	<LOD	<LOD	<LOD	1
Tl	<LOD	<LOD	0.126 ± 0.002	1
Cd	<LOD	0.121 ± 0.005	<LOD	2

LOD: Limit of Detection

The net areas of Si, the main element of the sandstone, on the repetitive HH-ED-XRF measurements from the sandstone of the NW orientation are higher (see Figure 3C) than in the measurements on the SSE orientation. Considering that the sandstone from this orientation do not show disintegration and losing material phenomena, the higher area of Si could suggest that less material has been lost in this orientation. On the contrary, the net area of Cu, Zn and Pb on each spectrum is higher for the measurements performed on the SSE orientations (see Figure 3B). This observation agrees with the ICP-MS results, since the concentration of these metals was high in the samples from this orientation. These results could suggest a higher input of these metals on the sandstone from the SSE orientation. Nevertheless, this difference could also be attributed to the heterogeneous distribution of these metals in the sandstone as it will be explained later. Regarding the spectral differences between the measurements performed on the external and inner areas of the sandstone blocks from both orientations, the tendencies are coincident for both orientations. The net areas of Ca and S for the measurements of the external areas are higher than those of internal areas (see Figures 3A and 3C). This observation can be related with possible depositions of calcium carbonate particles in the external surface of the sandstone blocks. Moreover, the higher S net area in the external parts could be related with the deposition of calcium sulfate as airborne particulate matter or formed as a consequence of the reaction between the calcium carbonate on the sandstone and wet depositions of SO_2 (as H_2SO_4 when it is incorporated in the rainwater) coming from the industries and maritime port close to La Galea Fortress.

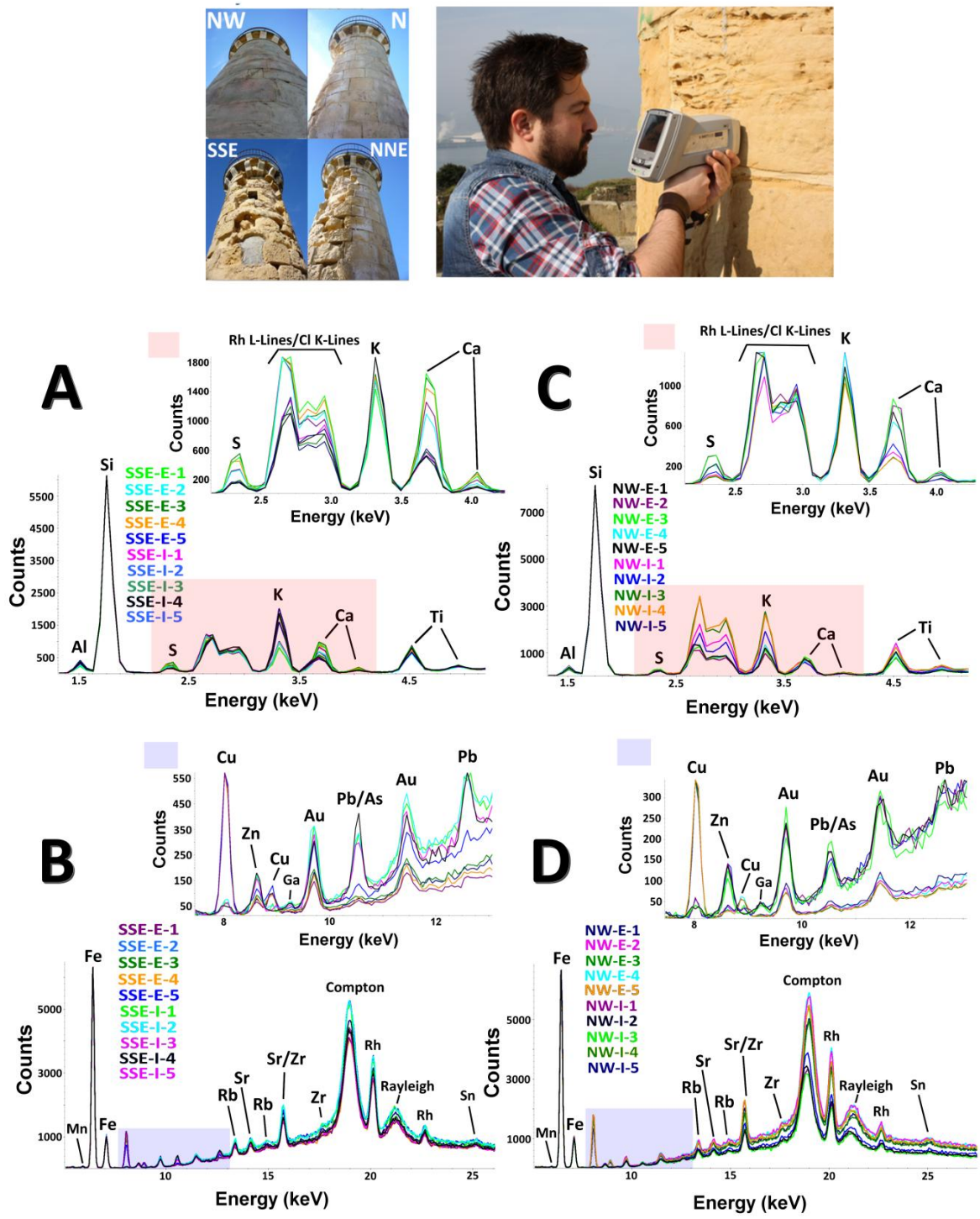

Figure 3. A general view of all the orientations of La Galea Fortress tower and a detail of the in situ measurement process with the hand-held ED-XRF instrument (top). Some XRF spectra as an example of all the measurements performed for the lightest elements on the sandstone from (A) the SSE (external and inner areas) and (B) for the heaviest elements on the sandstone from the SSE (external and inner areas), (C) XRF spectra as an example of all the measurements performed for the lightest elements on the sandstone from NW (external and inner areas), and (D) XRF spectra as an example of all the measurements performed for the heaviest elements on the sandstone from NW (external and inner areas).

In order to confirm if the concentration of all the elements quantified by means of ICP-MS and detected by means of HH-ED-XRF in the sandstone of La Galea Fortress are homogeneously distributed through the stone, line scans and mappings were conducted in a sandstone fragment (around 6 x 5 cm) from the SSE orientation of La Galea Fortress tower. The measurements were performed on the external part of the sandstone in contact with the atmosphere. In the Figure 4, the results obtained for the line scan are presented. In this line, 51 points (1 mm of lateral resolution) were measured.

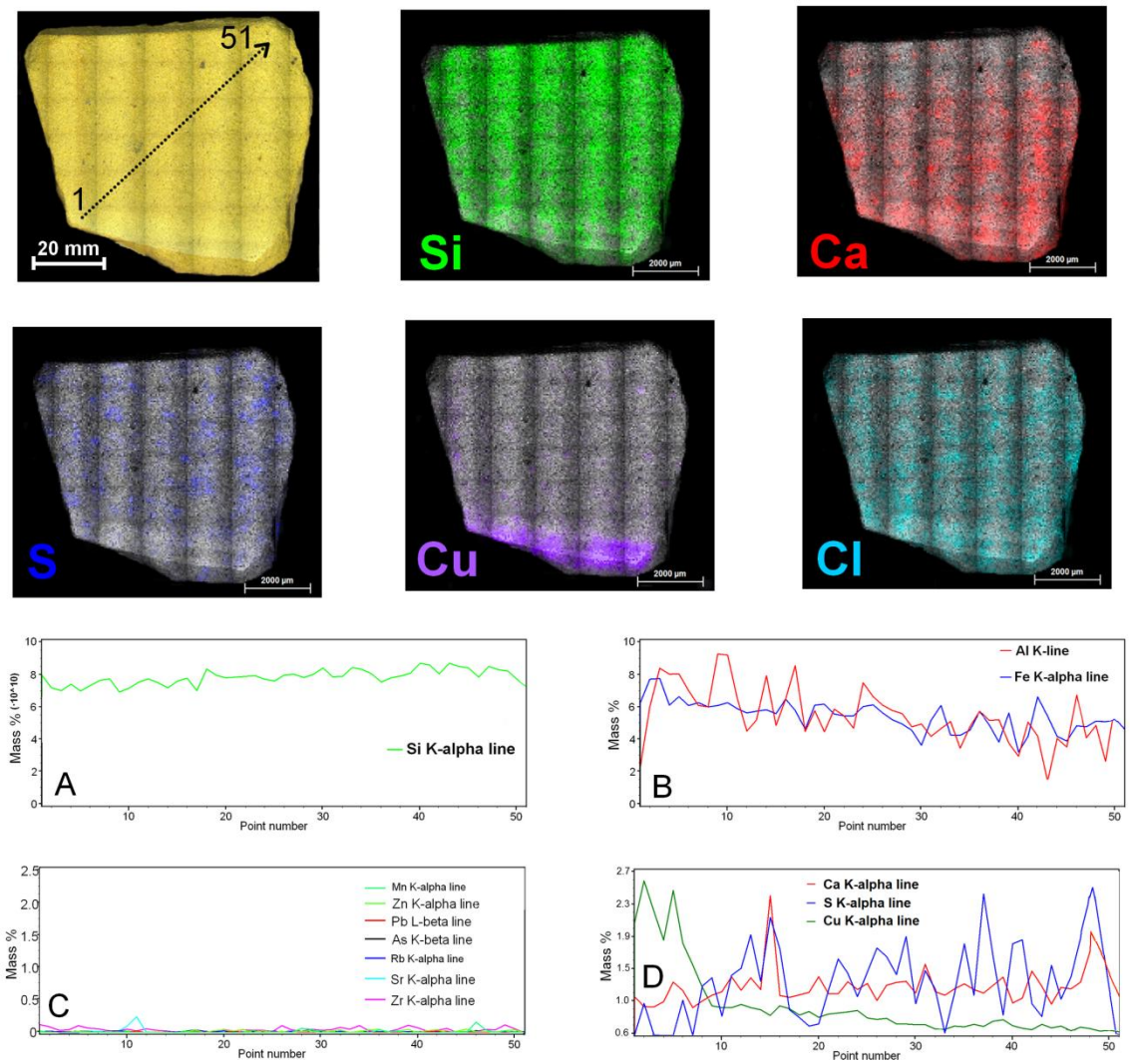

Figure 4. Visible image of a sandstone fragment from the SSE orientation of the tower (top left) in where the elemental HyperMaps (see some examples on the Figure) and line scan were performed (see the line marked on the top left) and the concentrations of some elements obtained on through the 51 on the line in mass percentage (A, B, C and D).

Si, Fe and Al, major elements on the sandstone, are homogeneously distributed through the stone (see Figures 4A and 4B). On the contrary, the concentrations of trace elements such as Mn, Zn, Pb, As, Rb, Sr and Zr and other minor elements such as S and Ca show ups and downs in the concentration through the sandstone, depending on the measured point (see Figures 4C and 4D). Regarding Cu, its concentration distribution could be considered more or less constant through the sandstone, but a maximum of it, its presence is centered at the lower left part of the sandstone (see Figure 4D). In order to go deeper in the distribution of Ca, S, Cu and other elements, HyperMaps of the whole sandstone fragments were acquired at 1 mm of lateral resolution (see the distribution of some elements present in the sandstone fragment on the Figure 4). Regarding Ca, it can be observed how this element is distributed through the entire sandstone surface, while sulfur is located in punctual areas which match with the location of Ca, suggesting the presence of calcium sulfate in those points and reinforcing the ED-XRF in situ observations. This observation was also reinforced with the line scan performed on the sandstone fragments, since the ups and downs in the concentration of Ca and S are coincident (see Figure 4D).

In the Figure 5, additional elemental maps obtained with a lower lateral resolution (650 μm) and from a smaller area (around 2.5 x 0.8 cm) are present. In this case, it is also evident that calcium is highly distributed in the sandstone, more or less in a homogeneous way. Nevertheless, a "hot-spot" can also be observed. The map of S in the same area (see Figure 5) does not match with the Ca distribution. The mappings at 650 μm spot size were performed without vacuum, thus probably in the areas where the concentration of S is zero, the instrument is not able to detect its signal (see the low S signal in the accumulated spectrum for all the mapped area in Figure 5). Consequently, no correlations between Ca and S can be observed. Si and Fe show more homogeneous distributions in the mappings with both lateral resolutions (see Figures 4 and 5). This observation agrees with the line scan, since a more or less homogenous concentration of these elements was identified in all the 51 analyzed points. With the mappings performed at a higher lateral resolution, the presence of some "hot-spots" for Sr, Rb, Pb, Mn, Ti, Ni, Zn and Cu can be observed (see Figure 5). Regarding this more heterogeneous distributions of some elements in the sandstone, it is necessary to mention that in the in situ measurements performed with the HH-ED-XRF instrument, the net areas of copper on each spectrum show higher values on the external measurements than on the internal areas of the sandstone (see Figure 3). For zinc and lead, the tendency is the opposite, higher values of net areas were observed on the inner measurements. These observations are closely related with the heterogeneous distribution of Cu, Zn and Pb. All these elements are present in the sandstone as trace elements

(concentrations lower than 100 ppm), thus considering that their distribution is not homogeneous, depending on the measured area a higher or lower concentration of them can be obtained. This observation can be also reinforced with the Cu HyperMap from the Figure 4. This element is highly distributed in the lower part of the sandstone that is why in the line scan, the concentration of the first point (see the line position on the visible image from the top left on Figure 4) at the bottom left of the image was higher than in the rest of the points from the line (see the concentrations variation through the line in the Figure 4D). Therefore, depending which area of the sandstone you measure with the HH-ED-XRF instrument, you can obtain a more intense signal coming from Cu, due to the heterogeneous distribution of this element in the stone. The higher concentration of Cu in the lower areas of the sandstone does not imply necessarily that the sandstone is being enriched with copper depositions coming from anthropogenic emissions of the nearby industry, but this new input of metals on the sandstone cannot be rejected.

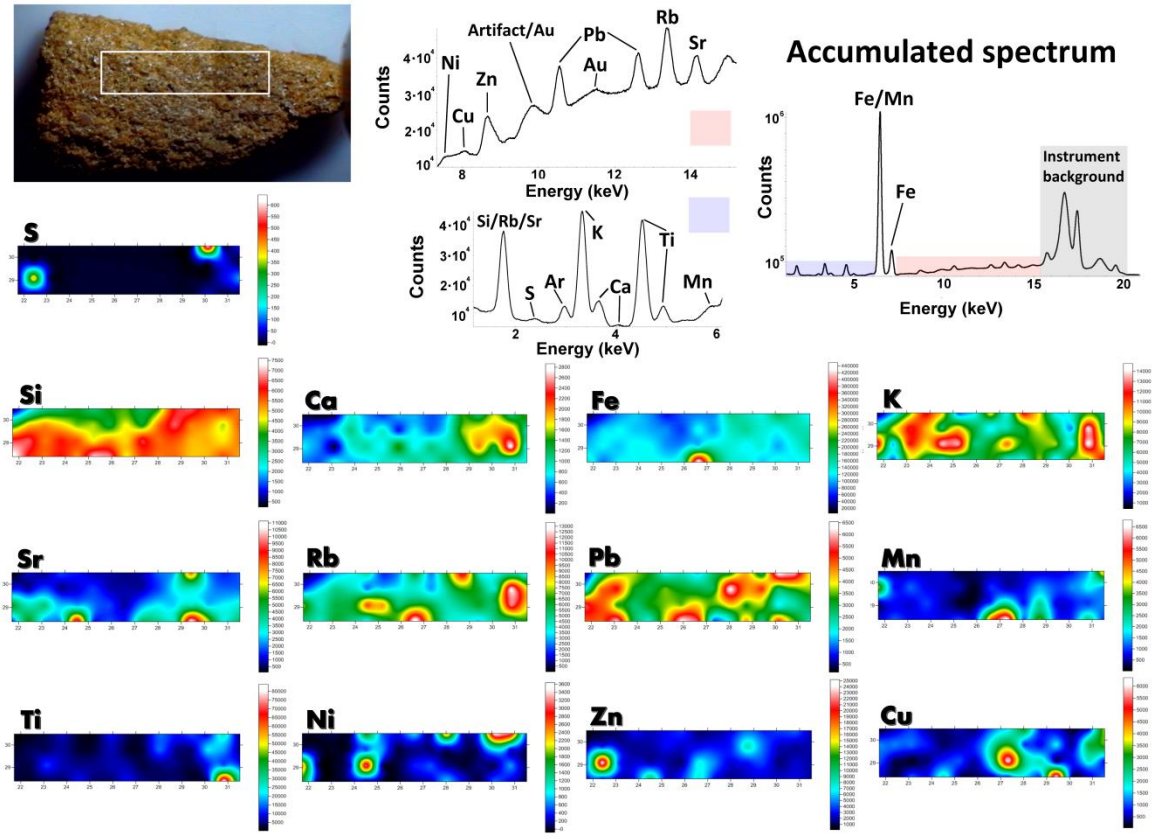

Figure 5. Elemental maps of the sandstone selected area and the accumulated spectrum obtained from all the points measured on the selected surface.

Regarding the lightest elements, with the measurements performed with the HH-ED-XRF instrument, it is quite difficult to determine if chloride is present in the sandstone, because the L-Lines of Rh anode from the tube interfere in the detection of the K-Lines of Cl. Only in some repetitive measurements from the sandstone of SSE external parts, the net area of the line at 2.6 keV from Cl is higher than in the measurements performed on the instrumental blank, suggesting the possible presence of Cl. In the laboratory and using the μ-ED-XRF measurements under vacuum, it was possible to detect the presence of Cl (see the Cl map in the Figure 4) randomly distributed through all the sandstone. This observation suggests that chloride salts coming from the marine aerosol are being deposited on this building material.

In order to extract more conclusions about the presence and distribution of the lightest elements and additional heaviest elements in the sandstone, the ED-XRF results were complemented with additional measurements using the SEM-EDS technique (see Figure 6). In the microscopic maps (more than 200 x 200 μm) Si and O show the same elemental distribution and their maps represent the main component of the sandstone, the quartz (SiO_2). Additionally, K, Al, Si and O also show a coincident distribution suggesting the presence of aluminosilicates such as adularia ($KAlSi_3O_8$) as original components of the sandstone. In certain microscopic areas, Fe and O also show a similar distribution, giving an idea about a possible presence of iron oxides or oxyhidroxides such as hematite, limonite, lepidocrocite or goethite, which can be original components of the sandstone. The coincident distribution of Ti and O in the microscopic analysis can also be related with titanium oxide. In order to determine which is the iron oxide or oxyhidroxide and which is/are the polymorphic phases of titanium oxide present, additional molecular analyses must be done (see the following sections).

Regarding the compounds which cannot be attributed to the original composition of the sandstone, a clear distribution of Na and Cl, attributed to halite (NaCl) was identified. Apart from that, in some areas, similar distributions of K and Cl attributed to sylvite (KCl) and Na, N and O related with nitratine ($NaNO_3$) presence were detected (see Figure 6). The presence of halite, sylvite and nitratine are closely related with the influence of marine aerosol, because these salts are usually transported in the marine aerosol and they can be deposited on the surface of the building materials. Although the presence of sylvite is in less quantity than halite in the marine aerosol, it is well-known that KCl can be also present in marine aerosol [49]. Additionally, Ca, S and O show a coincident distribution, pointing out the presence of calcium sulfate in the sandstone and agreeing with the ED-XRF results. Apart from this, in certain areas the elemental distribution of Mg, S and O is similar, and it could be

related with the presence of magnesium sulfates (e.g. starkeyite or epsomite). All this observations are going to be confirmed later using molecular analyses.

Thus, for the elements Na, N, and O similar distribution in some areas that can be attributed to nitratine ($NaNO_3$) can be observed. As we have mentioned above, the marine aerosol carries suspended this salt.

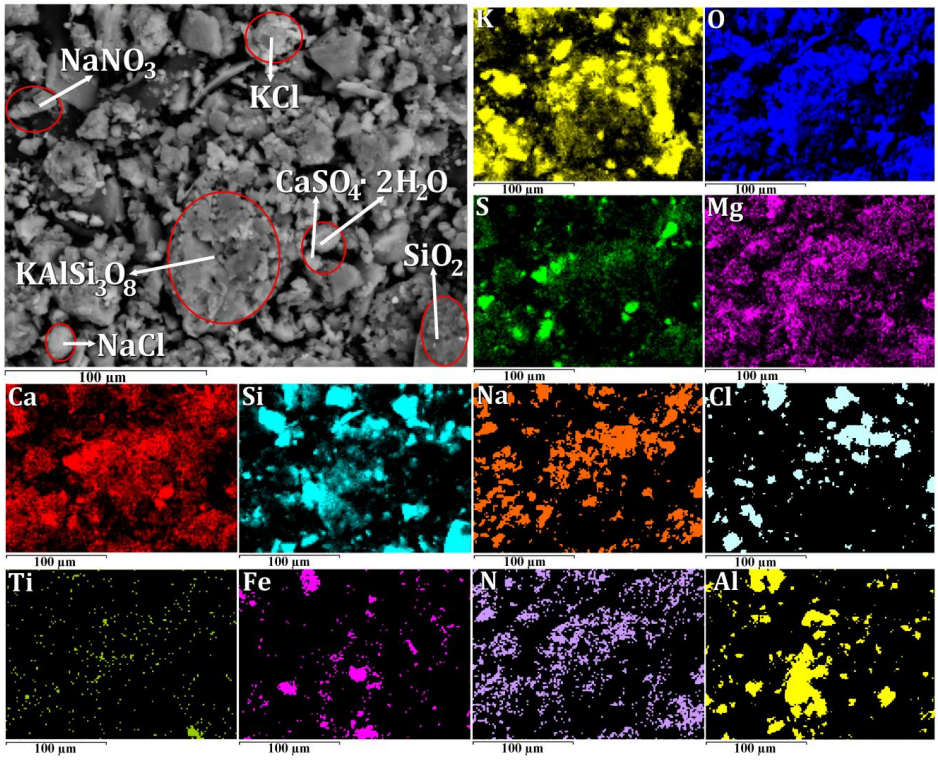

Figure 6. SEM-EDS imaging showing coincident distributions which point out the presence of quartz (SiO_2), adularia ($KAlSi_3O_8$), iron oxides, titanium oxide (TiO_2), calcium sulfates, magnesium sulfates, sylvite (KCl), halite (NaCl), and nitratine ($NaNO_3$).

3.3. Molecular characterization of the sandstone

In the present work, an in-depth molecular characterization of La Galea Fortress sandstone was conducted, in order to complement the preliminary analysis of this material conducted in a previous work [44]. In the Table 2, a summary of the main mineral phases identified by means of micro-Raman spectroscopy (μ–RS) on the sandstone from La Galea Fortress can be observed (see also related Raman spectra in Figure 7). Raman analyses were complemented with additional analyses using X-Ray Diffraction (see Figure 8). With both techniques, quartz (SiO_2) was the main mineral phase identified on the sandstone. Apart from that, aluminosilicates (e.g. adularia, $KAlSi_3O_8$), hematite (α-Fe_2O_3) and iron oxyhydroxides such as limonite [$FeO(OH)\cdot nH_2O$], goethite ($FeO(OH)$) and lepidocrocite [γ-$FeO(OH)$] were also

identified using both techniques (see also Figure 8A). Coal was also identified in several Raman spectra from the sandstone samples. Using X-Ray Diffraction, it was possible to identify two additional original silicates from the sandstone: kaolinite ($Al_2Si_2O_5(OH)_4$) (see Figure 8A and C) and illite [$(K,H_3O)(Al,Mg,Fe)_2(Si,Al)_4O_{10}[(OH)_2,(H_2O)]$] (see Figure 8C), which were not identified by means of μ–RS. This last technique was also useful to identify the presence of rutile (TiO_2). Ti was identified using elemental techniques at trace levels in the sandstone [50].

Table 2. Summary of the main original mineral phases and deterioration compounds identified by micro-Raman spectroscopy on the sandstone samples from La Galea Fortress.

Molecular formula	Mineral name	Original (OC) or Deterioration Compunds (DC)	ν (cm^{-1})
$KAlSi_3O_8$	Adularia	OC	282, 405, 457, 475 and 512
α-Fe_2O_3	Hematite	OC	225, 292, 410, 495 and 611
$FeO(OH)\cdot nH_2O$	Limonite	OC	240, 298, 393, 477 and 548
γ-FeO(OH)	Lepidocrocite	OC	212, 246, 304, 343, 373, 522 and 648
C	Coal	OC	1320 and 1595
TiO_2	Rutile	OC	244, 440 and 606
$CaSO_4\cdot 2H_2O$	Gypsum	DC	413, 492, 619, 673, 1008 and 1133
$CaSO_4$	Soluble Anhydrite	DC	1025
Na_2SO_4	Thenardite	DC	450, 464, 620, 631, 646, 992,1100,1130 and 1151
$MgSO_4\cdot 4H_2O$	Starkeyite	DC	147,232, 312, 462, 613, 1001, 1084, 1115, 1155 and 1603
$MgSO_4\cdot 7H_2O$	Epsomite	DC	362, 445, 462, 609, 985, 1082 and 1145
$(NH_4)_2SO_4$	Mascagnite	DC	975
KNO_3	Niter	DC	715, 1048, 1344, 1358 and 1777
$Ca(NO_3)_2\cdot 4H_2O$	Nitrocalcite	DC	715, 1342, 1357, 1048 and 1777

In most of the Raman measurements (see Figure 7A) and also on the X-Ray difractograms (see Figure 8B) performed on all the sandstone samples, calcite ($CaCO_3$) was identified. This observation agrees with the elemental results, since a high distribution of calcium was identified in the sandstone samples. This calcium carbonate present on the sandstone can have natural origin, since it can acts as cementing agent [14], but an additional input of calcite can be present on the sandstone coming from the dry deposition of calcium carbonate as airborne particulate matter coming from the erosion of calcareous rocks.

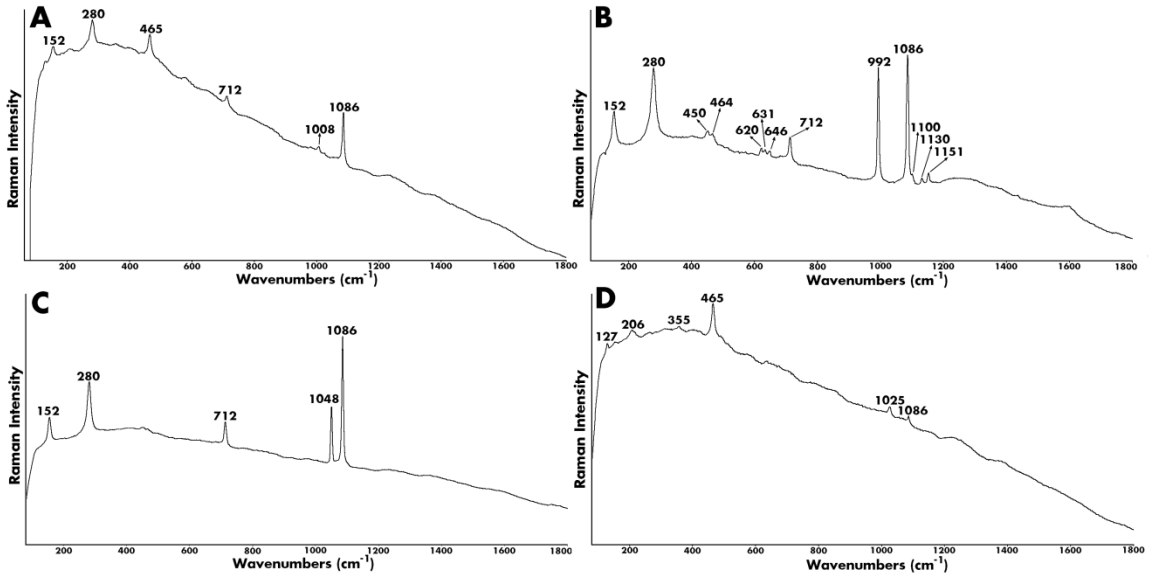

Figure 7. (A) Raman spectrum acquired on the sandstone samples showing the bands of calcite ($CaCO_3$) and gypsum ($CaSO_4{\cdot}2H_2O$). (B) Raman spectrum acquired on the efflorescences from the sandstone close to the cement mortar from the entrance arch showing the bands of calcite, thenardite (Na_2SO_4); (C) Raman spectrum acquired on the sandstone samples showing the bands of calcite ($CaCO_3$) and niter (KNO_3) and (D) Raman spectrum acquired on the joint mortar from sandstone samples showing the bands of calcite ($CaCO_3$), quartz (α-SiO_2) and soluble anhydrite ($CaSO_4$).

The presence of calcite in this sandstone becomes this material more susceptible to be deteriorated, since the calcium carbonate present in the sandstone composition can react with different acid aerosols and/or with the salts penetrating the material giving rise to more soluble compounds than calcite. This kind of transformation was confirmed with both molecular techniques used, since gypsum ($CaSO_4{\cdot}2H_2O$) was identified in all the sandstone samples with and without visual affections (alveolizations, disintegrations, etc.) (see Figures 7A, 8C and 8D). As it has been mentioned in the results related with the elemental characterization, sulfates can be formed as a consequence of the reactions between the calcite from the sandstone with the acid SO_2 emissions transported by the rainwater. For the case of gypsum, the sulfation process of calcite present in sandstone occurs through Reactions 1 and 2.

$$CaCO_{3\,(s)} + H_2CO_{3\,(dis)} \leftrightarrows Ca^{2+} + 2HCO_3^- \qquad \text{(Reaction 1)}$$

$$2Ca^{2+} + SO_4^{2-} \leftrightarrows CaSO_{4\,(dis)} \underset{\leftrightarrows}{} CaSO_4 \cdot 2H_2O_{(s)} \qquad \text{(Reaction 2)}$$

Gypsum can be also present in the sandstone as secondary particulates (gypsum formed as a consequence of the reaction between the natural calcium carbonate particles and the acid SO_2 in the atmosphere). Gypsum formed on the sandstone can be dissolved more easily than calcite by the rainwater action.

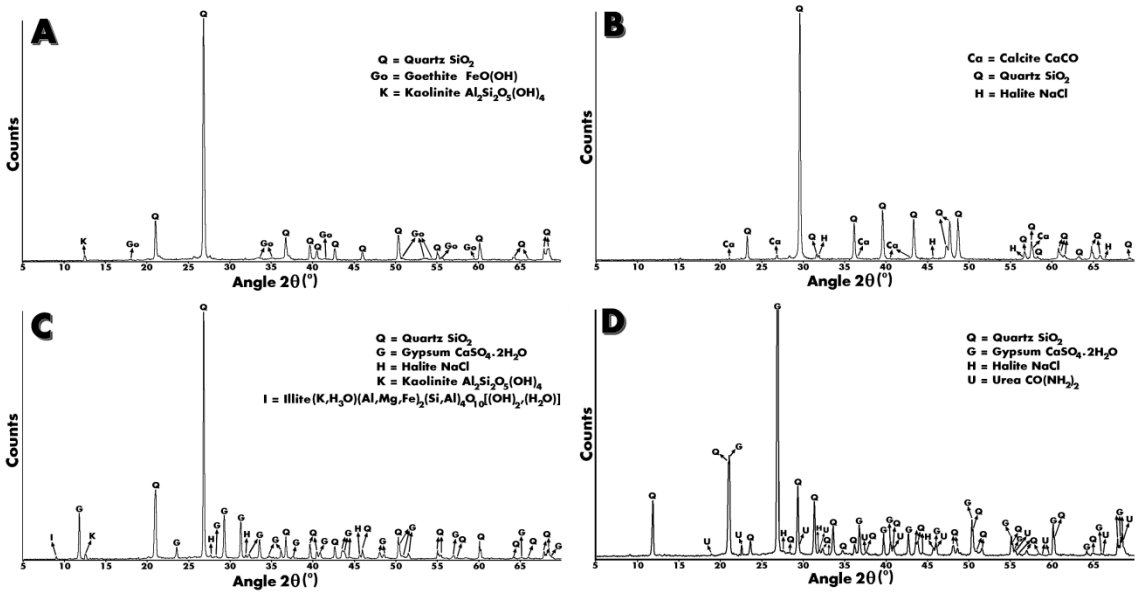

Figure 8. Representative XRD spectrum from the sandstone of La Galea Fortress showing the different bands of (A) quartz, goethite, kaolinite (B) calcite, quartz, and halite (C) quartz, gypsum, halite, kaolinite and illite (D) the different bands of quartz, gypsum, halite and urea.

Apart from the sulfur input as SO_2 coming from anthropogenic emissions, additional input of sulfate salts that can react with the calcite from the sandstone must be considered. The sandstone annexed to the cement inserted in both, the entrance arch and the SSE orientation of the tower, showed efflorescences in its surface. It is well-known that in the composition of cement mortars, sulfates are usually included. These salts can be dissolved and mobilized into the sandstone, reacting with the calcite present in it. In the areas close to the cement mortar included in both locations of the fortress, the sandstone has lost a high percentage of material and clear alveolizations are also observable. The micro-Raman analyses performed on the efflorescences showed the presence of calcite ($CaCO_3$, Raman bands at 152, 280, 712 and 1086 cm^{-1}) and thenardite (Na_2SO_4, Raman bands at 450, 464, 620, 631, 646, 992, 1100, 1130 and 1151 cm^{-1}) (see Figure 7B). The formation of sodium sulfate in cements is a fairly common pathology [51]. Usually cements include a considerable concentration of alkaline cations (such as sodium) which can react with sulfates which are present in the original cement mixture, giving rise to new crystallizations of sodium sulfates. Sodium sulfate can be present in its anhydrous (thenardite, Na_2SO_4) or in its totally hydrated (mirabilite, $Na_2SO_4 \cdot 10H_2O$) form. However an intermediate hydrated phase (heptahydrate, $Na_2SO_4 \cdot 7H_2O$) has been also described [52]. When the cement samples were taken (January and February 2014), the weather was dry and with a considerable high temperature for that time of year (around 20 °C). This may means that at the sampling moment, the sodium sulfate was dehydrated or in the transit to the laboratory

its dehydration process occurred. The dehydration process takes place at a relative humidity lower than 75% and 20°C. The problem in the precipitation of such salts is that they can be hydrated and dehydrated depending on temperature and relative humidity. The volume of the hydrated and dehydrated sodium sulfate is different, thus these hydration/dehydration cycles produce contraction and expansion phenomena in the porous structure of the sandstone where they crystallize, promoting crackings, disintegrations, etc. pathologies in the sandstone.

The cement mortar that joins together the sandstone block could be an additional source of sulfate salts that can migrate to the sandstone. The analyses performed by Raman spectroscopy on this joint mortars revealed the presence of calcite ($CaCO_3$, main band at 1086 cm^{-1}) and gypsum ($CaSO_4 \cdot 2H_2O$, main band at 1008 cm^{-1}), together with a band at 1025 cm^{-1} which can be related with the soluble anhydrite or AIII, a metastable compound [53] (see Figure 7D).

Regarding the influence of salts coming from the marine aerosol which can be deposited on the sandstone, halite (NaCl) was identified by means of XRD (see Figures 8B, 8C and 8D). This salt was identified not only in the external areas, but also in the inner areas of the sandstone. Therefore, this salt can be deposited on the inner areas of the sandstone from the upper part of the tower which is opened. Additionally, the massive crackings, fissures and holes, especially in the SSE orientation could permit the entrance of this salt to the inner areas. Moreover, as it can be observed in the Figure 8D, in a specific sandstone fragment where a black deposit or crust is observable, apart from quartz, gypsum and halite, urea ($CO(NH_2)_2$) was identified. The presence of urea can be attributed to an anthropogenic source. Its origin can reside in the bird droppings. In this dropping, the urea can be transformed into nitrate following a process catalyzed by different nitrifying bacteria [40].

Thanks to Raman spectroscopy, it was possible to identify the nitratine ($NaNO_3$), with its main band at 1067 cm^{-1} (see Figure 9B) in the sandstone from the SSE orientation of the tower. This salt can be deposited on the material coming from marine aerosol [54-56]. Apart from nitratine, niter (KNO_3) was also identified thanks to the presence of its strong band at 1048 cm^{-1} and its secondary bands at 1344 and 1358 cm^{-1} (see Figure 9B). In the same spectrum were niter and nitratine have been identified, thenardite (Na_2SO_4, main band at 992 cm^{-1} among the secondary bands) was also detected (see Figure 9B). The presence of this salt on the sandstone without visual efflorescences suggests that this sulfate can be present in the material crystallized on its pores. This observation confirms once more the influence of the alkali sulfates coming from the cement in the formation of soluble salts on

the sandstone. Apart from thenardite, epsomite ($MgSO_4 \cdot 7H_2O$, main band at 985 cm^{-1}) was also identified in the same Raman spectrum (see Figure 9B). Marine aerosol can carry magnesium sulfates with different hydration degrees. These sulfates can be deposited on the surface of the building materials as airborne particulate matter [54, 55]. Apart from epsomite, starkeyite ($MgSO_4 \cdot 4H_2O$) was also found in the sandstone samples (main Raman band at 1001 cm^{-1}, see Figure 9C). Finally, samples from the interior of the tower (SSE) were analyzed. As we can see in Figure 9D, bands at 975 and 1086 cm-1 belonging to mascagnite ($(NH_4)_2SO_4$) and calcite ($CaCO_3$), respectively were observed. In this case, the presence of this ammonium sulfate is attributed also to the influence of marine aerosol that by a dry deposition (there is open window) or wet deposition can deposit on sandstone. The deposited ammonium sulfate can penetrate, dissolve and migrate to suffer a recrystallization process in the inner parts of tower.

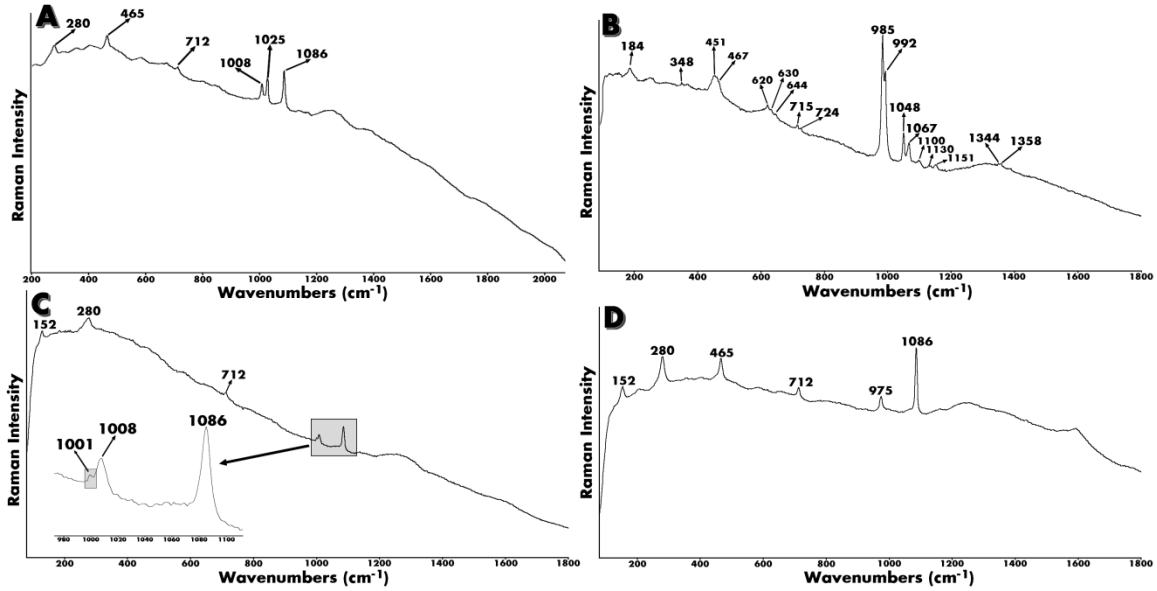

Figure 9. Raman spectra acquired on the sandstone from the SSE orientation of the tower showing the presence of (A) gypsum ($CaSO_4 \cdot 2H_2O$), calcite and soluble anhydrite ($CaSO_4$); (B) epsomite ($MgSO_4 \cdot 7H_2O$), thenardite (Na_2SO_4), niter (KNO_3) and nitratine ($NaNO_3$); (C) calcite ($CaCO_3$), gypsum ($CaSO_4 \cdot 2H_2O$) and starkeyite ($MgSO_4 \cdot 4H_2O$) and (D) calcite ($CaCO_3$), quartz (α-SiO_2) and mascagnite ($(NH_4)_2SO_4$).

3.4. Characterization of white formations from the entrance arch of La Galea Fortress

In the inner part of the dome of the entrance arch, different white formations can be observed (see Figure 2). In some cases, the white formations acquire the appearance of crusts, but in some cases they appear as stalactites (see Figure 2). These white formations were analyzed by Raman and SEM-EDS. The white crusts and stalactites offered coincident results. The elements detected using EDS in both formations were Ca, C, and O (see Figure 10B). Additional aggregate particles composed by Na, Al, Mg and Si, which can be related with the presence of aluminosilicates and particles from marine aerosol (Na and Mg) origin deposited on the formations were also identified (see Figure 10A).

The Raman analyses performed revealed that the white formations are constituted by calcite. At the top of the cornice from the external part of the dome from the arch, limestone mortar (calcite was determined in the mortar by Raman spectroscopy) was used to stabilize the arch structure. Therefore, the white formations may have been formed due to the dissolution of the calcite coming from the limestone and a subsequent migration and re-precipitation in the inner parts of the dome of the entrance arch.

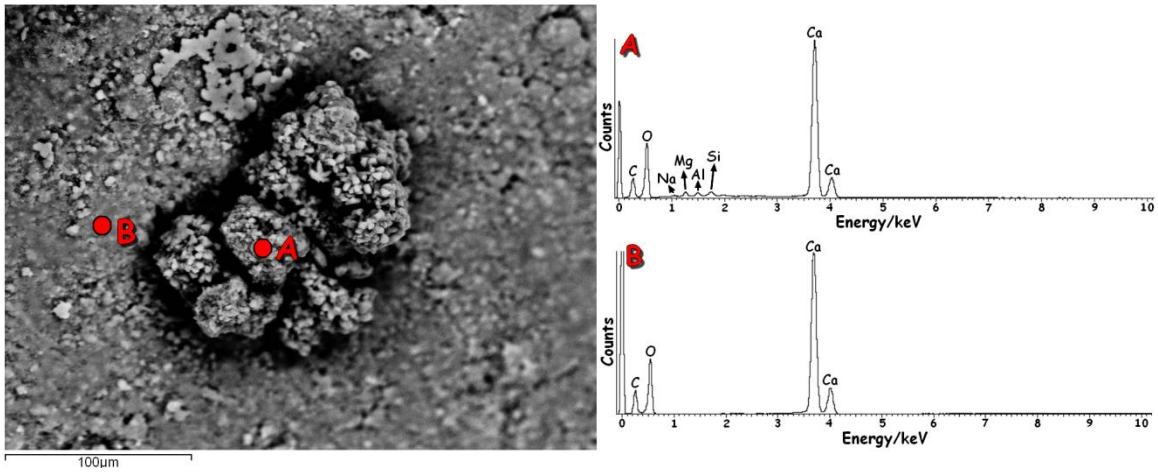

Figure 10. A) EDS spectrum showing the presence of aggregate particles on the white crusts from the entrance arch showing the presence of C, O, Na, Mg, Al, Si and Ca, B) EDS spectrum showing the presence of C, O, and Ca related with the presence of calcite as main component of the white crusts.

Apart from calcite, a band at 1049 cm^{-1} which can be related with nitrocalcite ($Ca(NO_3)_2{\cdot}4H_2O$) or niter (KNO_3) was also detected using Raman spectroscopy. Nitrate salts which can be present in the white formations can be formed due to the migration of ammonium nitrate (NH_4NO_3) from the outside upper part of the dome, where too much vegetation can be observe. The ammonium nitrate can react with carbonates giving as a

result the crystallization of their respective nitrate salt. In this case considering that the main carbonate is calcium carbonate, the most probable nitrate that can be present in the white formations is the nitrocalcite (see in Reaction 3). During this reaction, carbonate compounds are also transformed into bicarbonates (HCO_3^-) and ammonia (NH_3) is formed.

$$CaCO_{3(s)} + 2NH_4NO_{3(dis)} + 4H_2O \leftrightarrows Ca(NO_3)_2{\cdot}4H_2O_{(s)} + HCO_3^- + NH_{3\,(g)} + NH_4^+ \quad \text{(Reaction 3)}$$

In grayish crust near the cement from the entrance arch, apart from calcite, quartz and gypsum were identified by Raman spectroscopy. Considering the proximity of the cement to the grayish crusts, in this case the source of sulfates can come from the cement itself. Furthermore, in some Raman measurement, an additional band at 1025 cm^{-1} related with the soluble anhydrite was also identified.

4. Conclusions

Thanks to the multianalytical methodology applied based on elemental (punctual and imaging) and molecular analytical techniques (punctual analyses), it was possible to perform an in-depth characterization of the sandstone of the entrance arch and the tower from La Galea Fortress. Apart from quartz as original component of the sandstone, other kind of aluminosilicates and silicates (adularia, kaolinite and illite), hematite and iron oxides and oxyhidroxides were also identified. The in situ and laboratory ED-XRF analyses indicated that calcium is highly distributed in the sandstone. The calcium concentration higher than 1 % identified on the sandstone using ICP-MS suggests the presence of calcium carbonate in the original composition of the stone, which was confirmed by means of micro-Raman spectroscopy and XRD. The presence of calcite in the sandstone becomes this material more susceptible against the attack of atmospheric acid aerosols such as SO_2. Regarding sulfur presence, an irregular distribution of this elemental was observed through all the sandstone thanks to μ-ED-XRF mappings. The molecular techniques revealed a repetitive presence of gypsum in the sandstone. Therefore, this salt is the main source of sulfur in the sandstone. The reaction between calcium carbonate and the acid SO_2 aerosol deposited following a wet process give rise to the formation of gypsum, a more soluble compound, which can be dissolved more easily than calcium carbonate, promoting the losing material in this kind of stone.

Apart from the anthropogenic emissions of SO_2, an additional input of sulfates can be present in the sandstone due to the influence of cements rich in sulfates included in both, the tower and the entrance arch of the fortress. The sulfates from the cement can be

dissolved and they can migrate to the annex sandstone reacting with the carbonates present in the stone. Related with this, sodium sulfate (thenardite), a typical alkali sulfate that can be crystallized in cements, was identified in the sandstone from the tower and from the entrance arch. Marine aerosol can also contribute to increase the input of sulfates in the material but following a wet deposition of sulfate particles. Related with this observation, two kinds of magnesium sulfates (epsomite and starkeyite) and ammonium sulfate (mascagnite) were identified in the sandstone.

By means of μ-ED-XRF imaging and SEM-EDS, it was also possible to observe how chloride, coming also from the marine aerosol, is highly distributed on the sandstone. In addition, in most of the XRD spectra, sodium chloride (NaCl) and a less percentage of sylvite (KCl) were detected. Among this, in certain areas similar distribution of Na, N and O was also observed suggesting the possible presence of sodium nitrate (nitratine) coming from marine aerosol depositions. This observation was corroborated using Raman spectroscopy, since nitratine ($NaNO_3$) was identified.

Apart from alveolization, disintegration problems and losing material on the sandstone from the entrance arch and the tower of La Galea Fortress, an additional pathology related with the presence of white and grayish crust and stalactites on the entrance arch was visually detected. The main component of these formations is the calcite. However, nitrates were also identified in some grayish crusts. In this case, the source of calcite come from the limestone placed in the external part at the top, to reinforce the dome of the arch. The calcium carbonate from the limestone is being dissolved and it is re-precipitating again in the inner parts of the dome of the entrance arch. Additionally, the contribution of nitrates could come from the vegetation at the top of the arch.

5. References

[1] R. Dreesen, M. Dusar, Historical building stones in the province of Limburg (NE Belgium): role of petrography in provenance and durability assessment, Materials Characterization (2004) 53: 273-287.

[2] T. Schmid, P. Dariz, Determination and imaging of binder remnants and aggregates in historic cement stone by Raman spectroscopy, Journal of Raman Spectroscopy (2013) 44: 882-891.

[3] M. Maguregui, A. Sarmiento, R. Escribano, I. Martinez-Arkarazo, K. Castro, J. M. Madariaga, Raman spectroscopy after accelerated ageing tests to assess the origin of some decayed products found in real historical bricks affected by urban polluted atmospheres, Analytical and Bioanalytical Chemistry (2009) 395: 2119-2129.

[4] L. Anania, A. Badala, G. D'Agata, Bond behavior of standard and reinforced anchorage between CFRP sheet and natural calcareous stone, Applied Mechanics and Materials (2014) 446-447: 1091-1098.

[5] L. Medeghini, P. P. Lottici, C. De Vito, S. Mignardi, D. Bersani, Micro-Raman spectroscopy and ancient ceramics: applications and problems, Journal of Raman Spectroscopy (2014) 45: 1244-1250.

[6] R. Ortiz, M. Parraga, J. Navarrete, I. Carrasco, E. Vega, M. Ortiz, P. Herrera, J. A. Jurgens, B. W. Held, R. A. Blanchette, Investigations of Biodeterioration by Fungi in Historic Wooden Churches of Chiloe, Chile, Microbial Ecology (2014) 67: 568-575.

[7] F. O. Palacios, R. S. Angelica, T. A. B. C. Sanjad, The metal alloys from the XIX century and weathering action in the Mercado do Ver-o-Peso building, northern Brazil: Identification with the usage of laboratory analysis, Materials Characterization (2014) 96: 225-233.

[8] E. Angelini, S. Grassini, S. Corbellini, M. Parvis, M. Piantanida, A multidisciplinary approach for the conservation of a building of the seventeenth century, Applied Physics A: Materials Science & Processing (2010) 100: 763-769.

[9] F. Balsamo, F. H. R. Bezerra, M. M. Vieira, F. Storti, Structural control on the formation of iron-oxide concretions and Liesegang bands in faulted, poorly lithified Cenozoic sandstones, Geological Society of America Bulletin (2013) 125: 913-931.

[10] N. J. F. Blamey, K. Azmy, U. Brand, Provenance and burial history of cement in sandstones of the Northbrook Formation (Carboniferous), western Newfoundland, Canada: A geochemical investigation, Sedimentary Geology (2014) 299: 30-41.

[11] C. Fischer, S. Waldmann, H. von Eynatten, Spatial variation in quartz cement type and concentration: An example from the Heidelberg formation (Teufelsmauer outcrops), Upper Cretaceous Subhercynian Basin, Germany, Sedimentary Geology (2013) 291: 48-61.

[12] F. Bourdelle, T. Parra, O. Beyssac, C. Chopin, O. Vidal, Clay minerals as geo-thermometer: a comparative study based on high spatial resolution analyses of illite and chlorite in Gulf Coast sandstones (Texas, U.S.A), American Mineralogist (2013) 98: 914-926.

[13] R. Sankaran, N. Sobhi ASTER mapping of limestone formations and study of caves,springs and depressions in parts of Sultanate of Oman, Environmental Earth Science (2014) 71: 133–146.

[14] Q. Yongan, W. Min, Z. Wei, L. Da, Calcite cements in burrows and their influence on reservoir property of the Donghe sandstone, Tarim Basin, China, Journal of Earth Science (2012) 23: 129-141.

[15] S. Siegesmund, A. Török, Building Stones. Stone in Architecture. Properties, Durability. 5th Edition, Springer (New York) (2014) pag 82.

[16] S. Bugani, M. Camaiti, L. Morselli, E. Casteele, K. Janssens, Investigating morphological changes in treated vs. untreated stone building materials by x-ray micro-CT, Analytical and Bioanalytical Chemistry (2008) 391: 1343-1350.

[17] A. V. Turkington, E. Martin, H. A. Viles, B. J. Smith, Surface change and decay of sandstone samples exposed to a polluted urban atmosphere over a six-year period: Belfast, Northern Ireland, Building & Environment (2003) 38: 1205–1216.

[18] A. Samaouali, L. Laanab, Y. Geraud, A. Nounah, M. Boukalouch, Experimental study of chemical deterioration of Chellah monument stones, Physical & Chemical News (2008) 44: 103-106.

[19] R. J. Schaffer, The weathering of natural building stones, Building Research Special Report, London (1932) n.18.

[20] F. Garcia-Garmilla, I. Rodriguez-Maribona, M. Cano, M. Zalbide, J. A. Ibanez-Gomez, E. Osa-Chans, S. Garin, An analytical comparison of two comercial consolidating products

applied to eocene sandstones from 16th and 19th century monuments in San Sebastian, northern Spain, Materiales de Construcción (2002) 52: 5-17.

[21] M. J. Campos-Sunol, A. Dominguez-Vidal, M. J. Ayora-Canada, M. J. Torre-Lopez, Renaissance patinas in Ubeda (Spain): mineralogic, petrographic and spectroscopic study, Analytical and Bioanalytical Chemistry (2008) 391: 1039-1048.

[22] I. Martinez-Arkarazo, M. Angulo, L. Bartolome, N. Etxebarria, M. A. Olazabal, J. M. Madariaga, An integrated analytical approach to diagnose the conservation state of building materials of a palace house in the metropolitan Bilbao (Basque Country, North of Spain), Analytica Chimica Acta (2007) 584: 350-359.

[23] A. Charola, Acid Rain Effects on Stone Monuments, Journal of Chemical Education (1987) 64: 436-437.

[24] G. F. Andriani, N. Walsh, The effects of wetting and drying, and marine salt crystallization on calcarenite rocks used as building material on historic monuments, Building Stone Decay (2007) 271(Geological Society Special Publication), 179-188.

[25] L. Bergamonti, I. Alfieri, M. Franzò, A. Lorenzi, A. Montenero, G. Predieri, M. Raganato, A. Calia, L. Lazzarini, D. Bersani, P. P. Lottici, Synthesis and characterization of nanocrystalline TiO_2 with application as photoactive coating on stones, Environmental Science & Pollution Research (2014) 21: 13264–13277.

[26] A. Török, B. Vásárhelyi, The influence of fabric and water content on selected rock mechanical parameters of travertine, examples from Hungary, Engineering Geology (2010) 115: 237–245.

[27] E. Molina, G. Cultrone, E. Sebastian, F. J. Alonso, Evaluation of stone durability using a combination of ultrasound, mechanical and accelerated aging tests, Journal of Geophysics and Engineering (2013) 10: 035003-035021.

[28] M. Maguregui, U. Knuutinen, J. Trebolazabala, H. Morillas, K. Castro, I. Martinez-Arkarazo, J. M. Madariaga Use of in situ and confocal Raman spectroscopy to study the nature and distribution of carotenoids in brown patinas from a deteriorated wall painting in Marcus Lucretius House (Pompeii), Analytical & Bioanalytical Chemistry (2012) 402: 1529-1539.

[29] E. Molina, G. Cultrone, E. Sebastian, F. J. Alonso, L. Carrizo, J. Gisbert, O. Buj, The pore system of sedimentary rocks as a key factor in the durability of building materials, Engineering Geology (2011) 118: 110–121.

[30] M. Maguregui, A. Sarmiento, I. Martinez-Arkarazo, M. Angulo, K. Castro, G. Arana, N. Etxebarria, J. M. Madariaga, Analytical diagnosis methodology to evaluate nitrate impact on historical building materials, Analytical and Bioanalytical Chemistry (2008) 391: 1361-1370.

[31] O. Gomez-Laserna, M. A. Olazabal, H. Morillas, N. Prieto-Taboada, I. Martinez-Arkarazo, G. Arana, J. M. Madariaga, In-situ spectroscopic assessment of the conservation state of building materials from a Palace house affected by infiltration water, Journal of Raman Spectroscopy (2013) 44: 1277-1284.

[32] A. Sarmiento, M. Maguregui, I. Martinez-Arkarazo, M. Angulo, K. Castro, M. A. Olazabal, L. A. Fernandez, M. D. Rodriguez-Laso, A. M. Mujika, J. Gomez, J. M. Madariaga, Raman spectroscopy as a tool to diagnose the impact of combustión and greenhouse acid gases on properties of Built Heritage, Journal of Raman Spectroscopy (2008) 39: 1042-1049.

[33] N. Prieto-Taboada, M. Maguregui, I. Martinez-Arkarazo, M.A. Olazabal, G.Arana, J. M. Madariaga, Spectroscopic evaluation of the environmental impact on black crusted modern mortars in urban-industrial areas, Analytical and Bioanalytical Chemistry (2011) 399: 2949-2959.

[34] N. Prieto-Taboada, O. Gomez-Laserna, I. Martinez-Arkarazo, M. A. Olazabal, J. M. Madariaga, Relevance of Cross-Section Analysis in Correct Diagnosis of the State of Conservation of Building Materials As Evidenced by Spectroscopic Imaging, Analytical Chemistry (2013) 85: 9501-9507.

[35] J. A. Carrero, N. Goienaga, M. Olivares, I. Martinez-Arkarazo, G. Arana, J. M. Madariaga, Raman spectroscopy assisted with XRF and chemical simulation to assess the synergic impacts of guardrails and traffic pollutants on urban soils, Journal of Raman Spectroscopy (2012) 43: 1498-1503.

[36] M. Hoyos, S. Sanchez-Moral, E. Sanz-Rubio, J. C. Canaveras, Alteration causes and processes in the stone material from the pavement in Baelo Claudia archeological site, Cadiz/Spain, Materiales de Construcción, (1999) 49: 5-18.

[37] M. H. Ghobadi, R. Babazadeh, An investigation on the effect of accelerated weathering on strength and durability of Tertiary sandstones (Qazvin province, Iran), Environmental Earth Sciences (2015) 73: 4237–4250.

[38] V. Cardenes, F.J. Mateos, S. Fernandez-Lorenzo, Analysis of the correlations between freeze-thaw and salt crystallization tests, Environmental Earth Sciences (2014) 71: 1123-1134.

[39] H. Morillas, M. Maguregui, O. Gómez-Laserna, J. Trebolazabala, J. M. Madariaga, Could marine aerosol contribute to deteriorate building materials from interior areas of lighthouses? An answer from the analytical chemistry point of view, Journal of Raman Spectroscopy (2013) 44: 1700–1710.

[40] H. Morillas, M. Maguregui, O. Gómez-Laserna, J. Trebolazabala, J. M. Madariaga, Characterisation and diagnosis of the conservation state of cementitious materials exposed to the open air in XIX century lighthouses located on the coast of the Basque Country: The case of Igueldo lighthouse, San Sebastian, North of Spain, Journal of Raman Spectroscopy (2012) 43: 1630-1636.

[41] Y. Zhao, Y. Gao, Acidic species and chloride depletion in coarse aerosol particles in the US east coast, Science of the Total Environment (2008) 407: 541-547.

[42] S. S. Abdalmogith, R. M. Harrison, R. G. Derwent, Particulate sulphate and nitrate in Southern England and Northern Ireland during 2002/3 and its formation in a photochemical trajectory model, Science of the Total Environment (2006) 368: 769-780.

[43] E. Franzoni, E. Sassoni, Correlation between microstructural characteristics and weight loss of natural stones exposed to simulated acid rain, Science of the Total Environment (2011) 412-413: 278-285.

[44] H. Morillas, M. Maguregui, I. Marcaida, J. Trebolazabala, I. Salcedo, J. M. Madariaga, Characterization of the main colonizer and biogenic pigments present in the red biofilm from La Galea Fortress sandstone by means of microscopic observations and Raman Imaging, Microchemical Journal (2015) 121: 48–55.

[45] http://es.windfinder.com/windstats/windstatistic_punta_galea_getxo.htm [last accessed July 2015].

[46] M. Maguregui, N. Prieto-Taboada, J. Trebolazabala, N. Goienaga, N. Arrieta, J. Aramendia, L. Gomez-Nubla, A. Sarmiento, M. Olivares, J. A. Carrero, I. Martinez-Arkarazo, K. Castro, G. Arana, M. A. Olazabal, L. A. Fernandez, J. M. Madariaga, *CHEMCH 1st International Congress Chemistry for Cultural Heritage*, Ravenna (2010).

[47] R. T. Downs, M. Hall-Wallace, 18th General Meeting of the International Mineralogical Association, Edinburgh, Scotland. Programme With Abstracts (2002) 128.

[48] M. Fleischer, Chemical Composition of Sandstone, Data of Geochemistry, U.S. Government Printing Office, (Washington D.C, U.S.A) 6th Edition (1973) Pag S13

[49] H. Geng, S. Kang, H. J. Jung, M. Choël, H. Kim, C. U. Ro, Characterization of individual submicrometer aerosol particles collected in Incheon, Korea, by quantitative transmission electron microscopy energy-dispersive X-ray spectrometry, Journal of Geophysical Research: Atmospheres (2010) 115: D15306.

[50] N. Okay, T. Zack, A. I. Okay, M. Barth, Sinistral transport along the Trans-European suture zone: detrital ziron-rutile geochronology and sandstone petrography from the Carboniferous flysch of the Pontides, Geogological Magazine (2011) 148: 380-403.

[51] H. Morillas, M. Maguregui, J. Trebolazabala, J. M. Madariaga, Nature and origin of white efflorescence on bricks, artificial stones, and joint mortars of modern houses evaluated by portable Raman spectroscopy and laboratory analyses, Spectrochimica Acta Part A: Molecular and Biomolecular Spectroscopy (2015) 136: 1195-1203.

[52] A. Hamilton, R. I. Menzies, Raman spectra of mirabilite, $Na_2SO_4.10H_2O$ and the rediscovered metastable heptahydrate, $Na_2SO_4.7H_2O$, Journal of Raman Spectroscopy (2010) 41: 1014–1020.

[53] N. Prieto-Taboada, O. Gomez-Laserna, I. Martinez-Arkarazo, M. A. Olazabal, J. M. Madariaga, Raman spectra of the different phases in the $CaSO_4$-H_2O system, Analytical Chemistry (2014) 86: 10131-10137.

[54] L-Y. Zhao, Y-H. Zhang, Z-F. Wei, H. Cheng, X-H. Li, Magnesium Sulfate Aerosols Studied by FTIR Spectroscopy: Hygroscopic Properties, Supersaturated Structures, and Implications for Seawater Aerosols, Journal of Physical Chemistry A (2006) 110: 951-958.

[55] S. Maskey, H. Geng, Y-C. Song, H. Hwang, Y-J. Yoon, K-H, Ahn, C-U. Ro, Attenuated Total Reflection Fourier Transform-Infrared Imaging Techniques, Environmental Science & Technology (2011) 45: 6275-6282.

[56] C. U. Ro, K. Y. Oh, H. Kim, Y. P. Kim, C. B. Lee, K. H. Kim, C. H. Kang, J. Osan, J. de Hoog, A. Worobiec, R. Van Grieken, Single particle analysis of aerosols at Cheju Island, Korea, using Low-Z Electron Probe X-ray microanalysis: A direct proof of nitrate formation from sea salts, Environmental Science & Technology (2001) 35: 4487-4494.

RESEARCH ARTICLE 9

In situ screening and imaging techniques applied to the characterization of the Black Crusts formed on the sandstone from the lighthouse keeper house of La Galea Fortress (Getxo, north of Spain).

H. Morillas, M. Maguregui, C. Garcia-Florentino, J. A. Carrero, I. Salcedo, J. M. Madariaga

Submitted to Environmental Science & Technology in July (2015)

In situ screening and imaging techniques applied to the characterization of the Black Crusts formed on the sandstone from the lighthouse keeper house of La Galea Fortress (Getxo, north of Spain)

ABSTRACT

Black crust in buildings can be formed as a result of different kind of chemical and physical reactions between the stone surface and environmental factors (e.g. acid aerosols emitted to the atmosphere, airborne particulate matter, etc.). Moreover, biological colonizations can also be present on them. This kind of pathology is widely present in limestones, but fewer are the case study dealing with the characterization of black crusts on sandstones. Considering the complex composition of the black crust, a proper analytical methodology must be design and applied in order to perform and in-depth characterization of these kinds of crusts. In this work, a previous in situ screening of the elemental composition of the black crusts formed on the sandstone from an old building used to house the lighthouse keeper from La Galea Fortress was performed using a hand-held energy dispersive X-Ray Fluorescence spectrometer. After this preliminary study, samples of black crusts were taken in order to characterize them in the laboratory using molecular techniques (Raman spectroscopy and XRD) and elemental techniques (ICP-MS, SEM-EDS and micro energy dispersive X-Ray Fluorescence). With the last two elemental techniques, imaging analyses were performed at different lateral resolutions in order to observe the distribution of the metals and other kind of particles trapped in the black crust samples. Additionally, a biological colonization found beneath the black crusts was also characterized using Phase Contrast microscopy.

Keywords*:* Black crust, sandstone, cyanobacteria, Raman spectroscopy, XRD, ICP-MS, SEM-EDS, μ-ED-XRF imaging.

1. Introduction

On the surface of building materials included in constructions, different kind of crusts can be found. Among them, grayish or black crusts can be mentioned. Usually these kinds of crusts appear in the areas less exposed to the rainfalls. The chemical composition of them can vary greatly depending on the building material where they grow up (e.g. marble, limestone, sandstone, etc.), the geographical location of the building and the environment where the building is located. In this sense, the chemical composition of the black crusts on a building located in an urban and/or industrial environment [1], against those located in a coastal [2], rural environment [3] or volcanic environment [4] can vary greatly. The anthropogenic emissions coming from maritime traffic [5, 6], industries [7] or road traffic [8] can also have influence in the composition of black crust.

The matrix of black crusts is made up of gypsum ($CaSO_4 \cdot 2H_2O$). In the calcareous materials (e.g. limestone which main component is calcium carbonate), gypsum can be formed between the reaction of the calcium carbonate from the material itself and wet depositions of the SO_2 present in the atmosphere [9]. Considering that the concentration of this acid aerosol is higher in the urban-industrial environments, it is supposed that the black crust formations will be found principally in more polluted environments [10]. The formation of gypsum crusts and by extension black crusts are not so easy found for the case of sandstones. However, these kind of crust have been identified in calcarenite sandstones (calcium carbonate acting as cementing agent in the stone) or even in calcium-carbonate free sandstones [10]. Apart from gypsum, different kind of airborne particulate matter can be trapped on its structure. Among these particles, natural particles emitted to the atmosphere and coming from the erosion of the surrounding siliceous and calcareous stones can be deposited on the gypsum crust. Apart from that, metallic particles emitted from anthropogenic sources on urban-industrial emissions (e.g. road traffic, industry, maritime traffic etc.) [11-13] can also be trapped in its structure. Moreover, in the buildings placed in marine environments, salts transported by the marine aerosol can also be trapped in the gypsum matrix.

In the black crusts, the responsible of its grayish/black color are the carbon particles (shoot) trapped in the gypsum matrix [14]. Additionally, organic carbon and organic pollutants such as polycyclic aromatic hydrocarbons, triterpenoid hydrocarbons, etc. can also be present in the black crusts [15, 16].

Although black crust is a well-known pathology in construction, in some cases, these kinds of crusts can act as protective layer of porous building materials or as barriers against the environmental stressors, which can react with the original material, promoting its degradation [17]. However, in some cases, these crusts can also have a destructive effect on the material, promoting for example exfoliations in the original stone [18]. Apart from possible physical damages on the material, black crusts usually give rise to aesthetical problems. During a restoration process of a specific building, construction, monument, etc. in where black crusts are present, it can be decided to remove these unsightly patinas. Two possible situations could happen if these crusts are removed from its support or stone matrix. On the one hand, a quick formation of a new gypsum crust on the stone could take place, slowing down its deterioration process [19]. The formation of this new crust depends on numerous factors such as possible wetting-drying or freeze-thaw cycles that can undergo the stone [20] among others. On the other hand, the removal of the black crusts acting as a protective layer of the porous stone could make this material very unstable [21] in a short period of time, promoting its quick deterioration (e.g. losing material).

According to literature, several works can be found dealing with the chemical variations of black crusts compositions through times, depending on the changes in the pollution levels (acid gases emission and particulate matter) of the atmosphere where the black crusts are present [12, 22]. Moreover there are some studies which determine if the gypsum present in the black crust comes from a natural origin or if it is formed due to the influence of wet SO_2 depositions from the atmosphere. In those works, sulfur and oxygen isotopes analyses were conducted [2].

Generally, the analytical methodologies applied up to now to characterize the composition of black crusts, compromise a combination of different elemental and molecular techniques. Several examples of multianalytical methodologies can be found in the literature. Among others, the combined use of SEM-EDS with FTIR on the characterization of black crusts on granites [23]; ion chromatography applied together with SEM-EDS in the analysis of black crust formed on dolomitic rocks in a building of Milan [24]; FT-IR and SEM-EDS combined with LA-ICP-MS in black crusts formed on buildings from Milan and Florence and monument from Rome [12]; XRD, SEM, TG/DTA together with ICP-OES, ICP-MS and INAA analyses on black crusts formed on sandstones from buildings in Kraków [10]; FT-IR imaging combined with SEM-EDS and LA-ICP-MS analyses on black crusts formed on building from Seville [25]; optical microscopy, XRF, XRF, SEM, SEM-EDX, SEM-WDS, LA-ICP-MS, ion chromatography and GC-MS techniques applied to characterize the black crusts from the Cologne, Altenberg and Xanten cathedrals [26] etc., mutianalytical methodologies can be mentioned.

In this work an analytical strategy based on the use of different spectroscopic techniques was applied to characterize the composition of the black crusts present in the sandstone from an old building used to house the lighthouse keeper from La Galea Fortress. On the one hand, a preliminary screening of the black crusts was conducted using a hand-held energy dispersive X-Ray Fluorescence spectrometer (HH-ED-XRF). After that, samples of black crust were taken in order to characterize them in the laboratory using molecular techniques (Raman spectroscopy and XRD) and elemental techniques (ICP-MS, SEM-EDS and micro energy dispersive X-Ray Fluorescence (μ-ED-XRF)). With the last two elemental techniques, imaging analyses were performed at different lateral resolutions in order to observe the distribution of the metals and other kind of particles trapped in the black crust samples. Additionally, Phase Contrast microscopy was used to determine the nature of the main colonizer from the biological colonization found underneath the black crusts.

2. Experimental

2.1. La Galea site description and surrounded climatology

La Galea Fortress is located in the cliff overlooking the bay of Agra, in Getxo (Biscay, Basque Country, north of Spain) and about 50 m above the sea level (see Figure 1). In its origins (18^{th} century), this construction acted as a fortress. This fortress undergoes two destructions and after that, in the year 1782, the fortress was reused as a lighthouse. The first lighthouse was substituted by a second one. In the year 1880, the lighthouse keeper house, where the black crust objects of research are place, was constructed. Additional description about the history of this construction and environmental conditions of the place where it is located can be found elsewhere [27].

2.2. Samplings

Black crusts on the sandstone from the lighthouse keeper house are only present in the South-southeast (SSE) and Southwest (SW) orientations. The SSE orientation matches with one preferential direction of the wind in La Galea Fortress. In the NW orientation of the lighthouse keeper house, very close to the second preferential direction of the wind (North-northwest), black crust remains cannot be found. In the Figure 1, a complete view of the house under study, and the three areas where the in situ measurements and sampling was conducted, can be observed. In the SW orientation, one sample was extracted from the frame of the door (BC1). Two additional samples were extracted from the SSE orientation, one of them from the frame of the door (BC2) and the other sample was a compound sample formed by a mixture of two fragments from both the frame of both windows of the SSE

orientation (BC3). All the samples were extracted using a scalpel and the size of the black crust fragments never exceeded 2-3 cm.

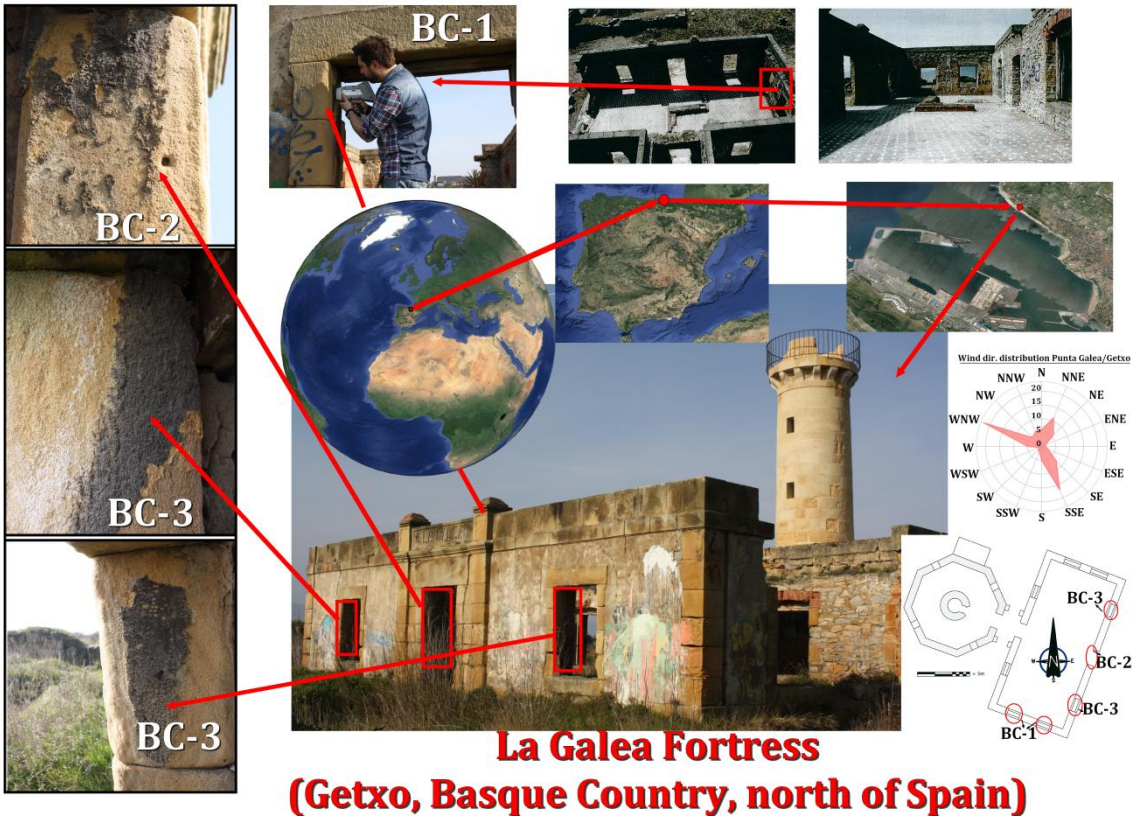

Figure 1. General view of the location of La Galea Fortress and different views of the lighthouse keeper house and the areas on it (BC1 is oriented to the Southwest and BC2 + BC3 are oriented to the South-southeast) were black crusts over the sandstone were in situ measured and extracted.

2.3. Instrumentation

For the molecular characterization of the black crust matrix, a portable innoRam™ ($B_{\&}WTEK_{INC.}$, Newark, USA) Raman spectrometer was used in the laboratory. This portable Raman spectrometer utilizes a 785 nm excitation laser and has a maximum output power of 300 mW. Variable attenuation of the output power was achieved through the implementation of filters, which allowed reducing the output power down to 1% of the maximum power of the laser. The measurements were conducted in the microscopic scale thanks to the coupling of the Raman probe to the BAC151B video microscope sampling system ($B_{\&}WTEK_{INC.}$, Newark, USA), which allows to couple different magnification objective lens. In this case, the measurements were performed using the 50x objective lens. The spectra were typically collected using a wavelength range of 100–2200 cm^{-1}, although in

some measurements larger ranges were used. The exposure time for each spectrum ranged from 2 to 10 s, and two to fifteen repeated acquisitions were averaged to improve the signal-to-noise ratio. Apart from micro-Raman measurements, XRD analyses were performed with a powder diffractometer PANalytical Xpert PRO, equipped with a copper tube ($\lambda_{CuK\alpha media}$= 1.5418 Å, $\lambda_{CuK\alpha1}$= 1.54060 Å, $\lambda_{CuK\alpha2}$= 1.54439 Å), vertical goniometer (Bragg-Brentano geometry), programmable divergence aperture, automatic interchange of samples, secondary monochromator from graphite and PixCel detector. The measurement conditions were 40 kV and 40 mA, with an angular range (2θ) scanned between 5 and 70°. For the data treatment of the diffractograms and the identification of the mineral phases present, the specific software X`pert HighScore (PANalytical) in combination with the specific powder diffraction file database (International Centre for Diffraction Data - ICDD, Pennsylvania, USA) was used.

The preliminary elemental screening of the black crust was carried out using an XMET5100 (Oxford Instruments, UK) hand-held energy dispersive X-Ray Fluorescence spectrometer (HH-ED-XRF). The instrument is equipped with a Rh tube working at a maximum voltage of 45 KV. The size of the emitted X-Ray beam is 9 mm. The analyzer includes a silicon drift detector (SDD) of high resolution that is able to provide an energetic resolution of 150 eV (calculated for the Mn K_α line at -20 ˚C) which allows to acquire spectra with 20 eV resolution. The analyzer contains a PDA to control the spectrometer and also to save the spectral and quantitative information. In order to determine possible contributions from detector materials and possible contaminations of the XRF analyzer window, 20 repetitive spectra of an instrumental blank (a PTFE block) were acquired before each measurements batch. The PTFE block was cleaned before its use in a 20% nitric acid bath during 24 hours. Before its use, it was rinsed in Milli-Q water and dried. For the repetitive measurements, the same spectral conditions (voltage, current, filter and test time) as those used for the analysis of the sandstone were considered. To determine the presence of the heaviest elements (Z > Ti), and the voltage and current of the X-Ray tube was set at 40 kV and 15 μA respectively and the spectra were acquired during 200 seconds (real time) in order to improve the limit of detection for the identification of trace elements. Additionally, to remove the “pinches” Bremsstrahlung and 3rd Generation peaks, a 500 μm Al filter was used. In order to improve the detection of the lighter elements (Z < Ti), additional measurements were performed without the Al filter and at lower voltage (13 kV) and higher current (40 μA). The test time in this case was 140 seconds for each measurement. All the collected spectra were transferred from the PDA of the instrument to a computer in .txt files

For the characterization of the black crusts in the laboratory at millimeter scale, the M4 TORNADO (Bruker Nano GmbH, Berlin, Germany) micro energy dispersive X-Ray Fluorescence spectrometers (μ-ED-XRF) was used. With this instrument, punctual measurements from the black crusts samples were obtained. The X-Ray tube implemented in this instrument is a micro-focus side window Rh tube powered by a low-power HV generator and cooled by air. Thanks to the collimator implemented, spot sizes of 1 mm were measured. The X-ray tube can work at a maximum voltage of 50 kV and at a maximum current of 700 μA, which were the considered conditions for the spectra acquisition in this work. The detection of the fluorescence radiation was performed by an XFlash® silicon drift detector with 30mm^2 sensitive areas and energy resolution of 145eV for Mn-Kα. In order to improve the detection of the lightest elements (Z>11), filters were not used and measurements were acquired under vacuum (20 bar). To achieve the vacuum, a diaphragm pump MV 10 N VARIO-B was used. The live time used for each punctual measurement was 200 seconds. For the focusing of the area under study, two video-microscopes were used, one of them to explore the sample under a low magnification (1 cm^2 areas), and the other one to perform the final focusing (1 mm^2 areas). The spectral data acquisition and treatment was performed using the M4 TORNADO software and the quantification was done thanks to the M-Quant software package.

For the study of elements distribution on the black crust samples, elemental imaging was conducted using an additional μ-ED-XRF instrument, the portable ARTAX μ-ED-XRF from Röntec (currently Bruker Nano GmbH, Berlin, Germany). The elemental maps were obtained using 650 μm of lateral resolution thanks to the use of a lower diameter collimator. Each elemental map was constructed according to the net areas of XRF lines. The spectrometer implements a low-power metal-ceramic-type MCBM 50 X-Ray tube with molybdenum target as excitation source. The molybdenum can be used at a maximum voltage of 50 kV and at a maximum current of 700 μA (maximum power of 35 W). The radiation-protecting tube housing is equipped with an electrical shutter and safety functions externally controlled by a PC. The X-Ray Fluorescence radiation is detected by means of an electro-thermally cooled Xflash® detector, which is a silicon drift detector with high-speed low-noise electronics. The detector has an active area of 5 mm^2 and a 8 μm-thick Dura-beryllium window. The geometry between primary beam, sample, and detector is fixed at 0°/40° relative to the perpendicular of the sample surface. The X-Rays were collimated by a tantalum collimator with a diameter of 0.65 mm and the beam diameter in the sample surface is around 200 mm^2. An integrated CCD camera provides an image of the sample region under investigation (8 mm x 8 mm). In the vibration-damped swivel arm from the instrument, a motor-driven

XYZ positioning stage is directly mounted, which consists of three equal modules with a maximum travel of 50 mm in each direction. This motor unit allows focusing on different parts of the sample. For the mappings and for each analyzed point, the maximum voltage and current and 800 seconds of test time were used. In this case, measurements were performed at air. Instrument control and data-handling were performed using the Windows-base ARTAX software 4.9.13.2 (Intax GmBH, Berlin, Germany). In order to improve the representation of the elements distribution on the black crusts samples, the elemental maps presented in this work were constructed using the Surfer® 10 software (Golden Software, LLC, USA).

In order to characterize the particles trapped in the black crust samples, a scanning electron microscope coupled to an energy dispersive X-Ray spectrometer (SEM-EDS) was used. The SEM used was an EVO®40 Scanning Electron Microscope (Carl Zeiss NTS GmbH, Germany) and the EDS was an X-Max Energy-Dispersive X-ray spectrometer (Oxford Instruments, Abingdon, Oxfordshire, United Kingdom). In order to improve the images acquired with the SEM, some samples were coated with gold. These images were obtained at high vacuum employing an acceleration voltage of 30 kV and a 10–400 μm working distance. To take the images, different magnifications (reaching up to 6,800×) were used by a secondary electron detector whereas an integration time of 50 s was employed to improve the signal to noise ratio. The EDS spectra were acquired and treated using the INCA software. This software allows to analyze selected areas previously seen by SEM. Furthermore, a mapping of specific microscopic areas in the samples was possible, allowing the evaluation of the distribution of these elements over the samples.

ICP-MS was also used to quantify the major, minor and trace elements present in the black crust samples. Prior to the elemental measurements, acid digestions of the black crusts samples were carried out. For that purpose, black crust were crushed in an agate mortar and dried until constant weight. 0.5 gr of dried black crust samples were digested in a microwave oven using 12 ml of 3:1 HNO_3 (69%) : HCl (36%) mixture. The acid concentration of the obtained acid extracts was reduced to less than 1% HNO_3 using Milli-Q water. In addition, a solution containing 10 μg.L-1 of Be, Sc, Ge, In, Re and Bi was added as internal standard. The internal standards and ICP-MS calibration standards solutions were prepared from 1000 mg.L-1 stock solutions of Alfa Aesar (Specpure®, Plasma standard solution, Germany) inside a class 100 clean room. All solutions were prepared using Milli-Q quality water. PL 20-200 μL and PL 500-5000 μL micropipettes (Eppendorf, Hamburg, Germany) with an calibration standards and samples dilutions were prepared using analytical balance model Mettler-Toledo XS205 (Colombus, OH, USA) with accuracy of ±

0.00001 g. The elemental analysis of the extracts was performed by ICP-MS (NexION 300, Perkin Elmer) in a class 100 clean room. The argon used was supplied by Praxair (99.995%, Madrid, Spain). ^{27}Al, ^{44}Ca, ^{88}Sr, ^{98}Mo, ^{114}Cd, ^{120}Sn, ^{121}Sb, ^{138}Ba, ^{184}W, ^{202}Hg and, ^{206}Pb+^{207}Pb+^{208}Pb isotopes were determined in standard mode and ^{23}Na, ^{24}Mg, ^{39}K, ^{47}Ti, ^{51}V, ^{52}Cr, ^{55}Mn, ^{56}Fe, ^{59}Co, ^{60}Ni, ^{65}Cu, ^{66}Zn, ^{75}As, ^{111}Cd isotopes were determined in collision mode with He with in order to eliminate possible polyatomic interferences. The plasma conditions such as argon flow of nebulizer, the torch position and the instrument lenses voltages were optimized before each measurement session aspirating a standard solution of 1ng/mL of Mg, Rh, In, Ba, Pb and U. The gas nebulizer flow was optimized obtaining a compromise between sensitivity and low oxides level (less than 2.5 % for the CeO/Ce ratio). Finally, the data were acquired and analyzed for the element quantitative analysis using the Elan 3.2 software (Perkin Elmer SCIEXTM, Ontario, Canada).

To determine the nature of the main colonizer of the colonization underneath the black crust and on the sandstone, microscopic observations were carried out using a Nikon Eclipse 80i PCM (Phase Contrast microscope) provided with 20×, 40×, and 60× objective lenses. For the preparative process of the sample, special tweezers were used to sample the main colonizer from the biological patina, under the view of a microscope. After the extraction of the main colonizer, it was placed on a slide and a drop of oil was also added to avoid spherical aberration with the highest numerical aperture lenses, promoted by the different indexes of refraction of the specimen and the objective lenses.

3. Results and Discussion

3.1. In situ elemental screening of black crusts

All the black crusts present in the lighthouse keeper house are placed in the most protected areas from the rain, that is, in the frames of the doors and windows from both orientations (SW and SSE). Usually, dark coloured crusts tend to be formed in areas protected from the rain. However, these areas are also exposed to the high pollution sources (maritime port and industries) located near the building, allowing the deposition of particles that are incorporated or trapped into the growing crust. In order to evaluate if metals are accumulated in black crusts from both orientations, a rapid screening with a hand-held energy dispersive X-Ray Fluorescence spectrometer (HH-ED-XRF) was conducted. In the Figure 2, a summary of the results obtained using this device is presented. In the bar charts of Figure 2, only 5 measurements, among the 15, performed on each black crust area are presented to simplify the visualization of the results. Spectral data were normalized in order to compare the elemental measurements performed on the three measured areas. For the

lighter elements (Al, Si, P, S and Cl), the net area of each element was normalized against the Ca K-alpha1 line net area at 3.69 keV. The S presence in the XRF measurements (see Figure 2 E) confirms that these black crusts are made up of a sulfate crust. Moreover, the normalized area of Al and Si is more or less constant in the three measured areas (BC1, BC2 and BC3) (see Figure 2 A). The presence of Al and Si in the black crusts suggests that aluminosilicate particles are deposited or trapped in the black crust matrix. This observation will be confirmed with additional measurements in the laboratory. P is also present in all the acquired spectra (see Figure 2 E), suggesting the presence of phosphates in the black crusts. Moreover, the normalized values of P are more or less constant in the black crusts from both orientations. Considering that a Rh X-Ray tube was used for the measurements, it is to be expected that this element L-lines cause interference on the Cl K-lines. The software available to perform the spectral information acquired with the hand-held instrument is not able to perform signal deconvolutions. Therefore, in order to distinguish the contribution of Rh L-lines of the tube from the contribution of Cl K-lines, the average net area of Rh L-alpha1 line normalized against the Ca K-Alpha1 from different repetitive measurements (more than 10) of the instrumental blank (a Teflon block) was subtracted to the net areas of Cl K-alpha1 line normalized against the Ca K-Alpha1. In some measurements, the normalized value of Cl K-alpha1 area was the same of the normalized value of Rh L-alpha1 area. Therefore, due to this interference, in these measurements, the Cl presence cannot be ascertained. However, in some measured areas of the black crusts, this subtraction was higher than zero, confirming the possible presence of Cl in the black crusts (see Figure 2 A), which was later confirmed with XRD technique.

For the heavier elements [$Z \geq 20$ (Ca)], the net areas of their K-alpha lines were normalized against the net area of the Rh Compton line, to correct possible matrix effects and variations on the positioning of the measuring interface. As can be observed in Figure 2 B, the values of the normalized areas of Ca, Fe, Sr and Rb K-alpha lines in the black crust from the SW orientation (BC1) and those from the SSE orientations (BC2 and BC3) are more or less in the same order of magnitude. In all the black crusts from both orientations different metals, such as Ti, Cr, Mn, Ni, Cu, Zn and Pb were also detected. Therefore, with the in situ elemental screening of the black crust, it can be concluded that different kind of metals are trapped in the black crust matrix. One of the sources of emission of these metallic particles can be the sea port of Bilbao located in front of La Galea Fortress in the SW orientation (see Figure 1). Moreover, in this orientation, additional industries that can contribute to metallic particle emissions are also located.

Having a look to the bar chart of Figure 2 C and D and spectra from Figure 2 F, a clear difference in the values of Zn K-alpha line (8.6 keV), Pb L-beta line (12.6 keV), Ti K-alpha line (4.5 keV), Cr K-alpha line (5.4 keV), Mn K-alpha line (5.9 keV), Ni K-alpha line (7.4 keV), Cu K-alpha line (8.0 keV), and Br/As K-alpha (around 11.8 keV) normalized areas are observable. The values are higher for the BC2 and BC3 black crust areas from the SSE orientation, than for the BC1 black crust areas from the SW orientations. This trend suggests that the metallic particles emitted by different anthropogenic sources are mainly transported to the SSE orientation, thanks to the influence of one of the preferential wind direction in La Galea. The presence of Ti, Cr, Mn and Pb particles in the SSE orientation in La Galea Fortress was confirmed in a previous works thanks to the sampling of particulate matter from the atmosphere of La Galea area using a home-made passive sampler.

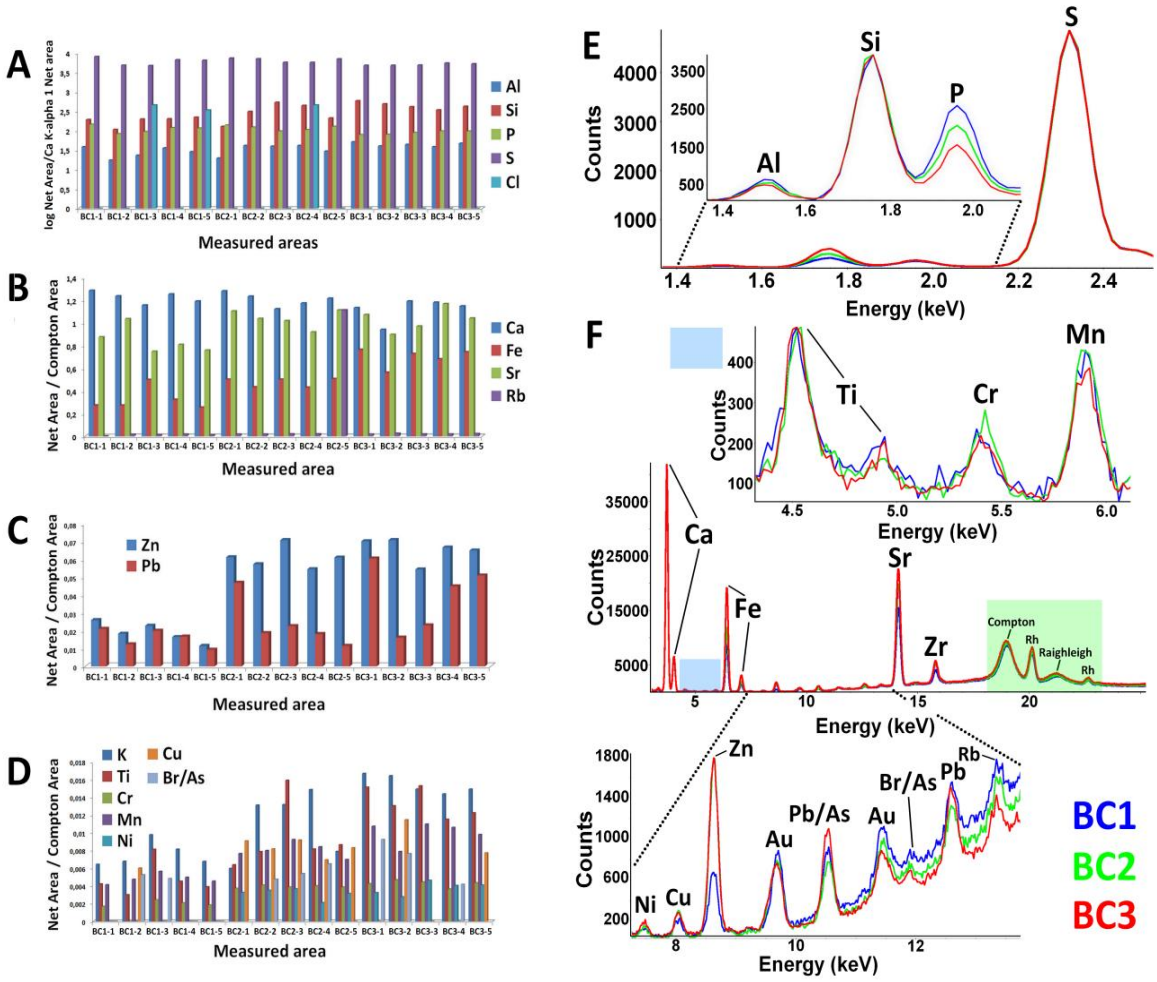

Figure 2. (A, B, C, D) Bar charts showing the normalized areas of all the elements found in the black crust from the lighthouse keeper house (BC1 on the SW orientation and BC2 and BC3 on the SSE orientation), (E) One representative spectrum from each black crust analyzed showing the presence of the lightest elements and (F) One representative spectrum from each black crust analyzed showing the presence of the heaviest elements.

3.2. Characterization of black crusts in the laboratory

3.2.1. Black crusts morphology and biological colonizations

The black crusts taken from both orientations are cauliflower-like black crusts with globular or framboidal morphology [17, 28] (see Figure 3 G). In the Figure 3 H, the stratigraphy of the extracted samples is represented. As it is well-known, the first step in the growing of black crusts on the surface of stones is the formation of a gypsum crust. According to our previous in-depth study of La Galea Fortress sandstone, this kind of stone contains around 10000 mg/Kg of calcium carbonate, thus this low percentage of calcium carbonate could act as the starting nucleus of gypsum formation, since calcium carbonate could be transformed into this sulfate due to the atmospheric SO_2 influence. Surrounding the areas of some of the analyzed black crusts, gypsum efflorescences were also identified (see those efflorescences on BC3 from the Figure 1); thus, this observation evidences that gypsum crusts could be formed on the surface of this sandstone. Moreover, the joint mortar that joins together different sandstone blocks could be another source of sulfates which could migrate to the porous matrix of this sandstone.

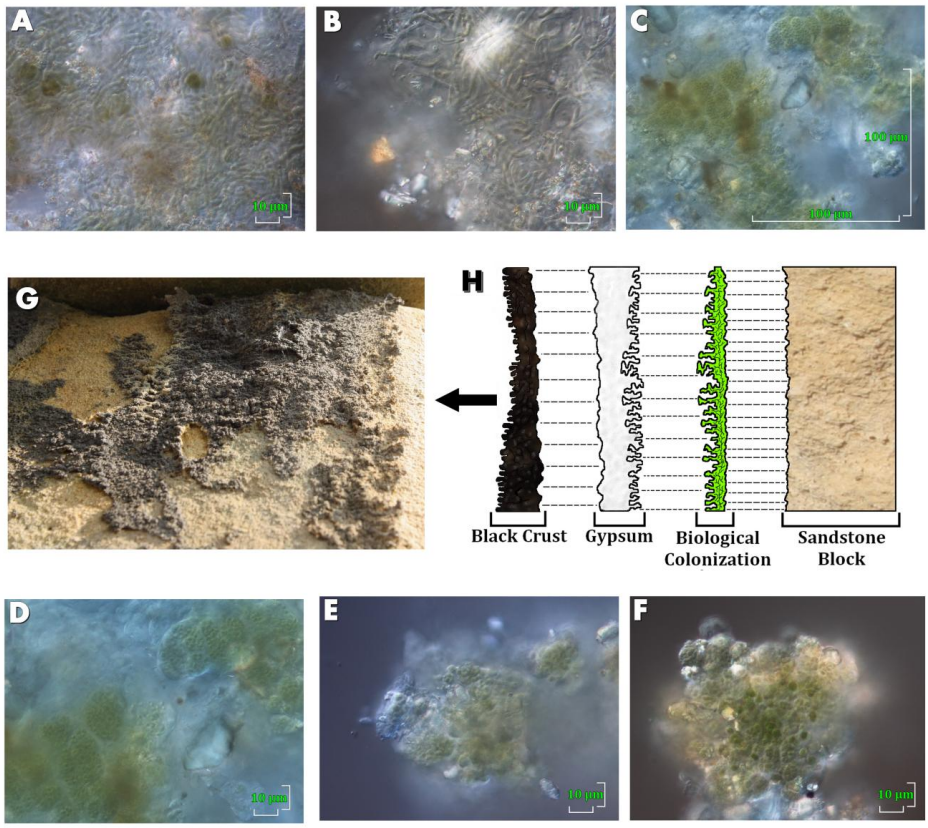

Figure 3. A detail of the black crust from the SSE orientation (BC2) (G) and the stratigraphy of all the extracted black crusts samples from both orientations (H), together with the micro-photographies of the samples extracted from the biological colonizations beneath the black crust samples from both orientations (A-F).

In the extracted black crust samples, biological patinas, biofilms or biological colonizations were visually observed beneath the crust and close to the sandstone (see Figure 3 H). Different microphotographs were acquired from the samples extracted from the biological patina using a Phase Contrast Microscope (see Figure 3 A-F). The microscopic observations suggest that the main colonizers on the biological patinas beneath the black crusts are combined communities of cyanobacteria and green algae. Concretely, the green algae present in the biofilms belong to the genera *Stichococcus* (Figure 3 A and B) and the identified cyanobacteria are from the Genus *Aphanothece* (see Figure 3 F). This kind of cyanobacteria/green algae communities can be found in stone surfaces from building underside of flaking scales and on the freshly exposed stone [29]. Therefore, in this case, the biological colonization could be developed before the gypsum crust growing or also after this mineral crust formation, thanks to the presence of cracks between the gypsum crust and the sandstone.

3.2.2. Elemental and molecular characterization of black crusts

In the Figure 4 A, B and C, microscopic images of the BC2 black crust extracted from the SSE orientation are presented as an example of the representative morphology of all the sampled black crusts. These microscopic images under the SEM confirm that the black crust morphology is globular or framboidal. The elemental analyses performed on the acicular crystals from the black crusts using the EDS coupled to the SEM (see Figure 4 C) showed the presence of Ca, S and O (see Figure 4 F). The X-Ray Diffraction (XRD) analyses performed on those black crust samples confirmed this observation, since the major component of the black crusts identified with this technique was gypsum ($CaSO_4 \cdot 2H_2O$). Raman results also agree with XRD observations, because gypsum (bands at 414, 493, 620, 670, 1008 and 1135 cm^{-1}) was also identified in all the Raman spectra acquired. Apart from that, using XRD, bassanite ($CaSO_4 \cdot 1/2\ H_2O$) and quartz (α-SiO_2) were also identified (see Figure 4 D). This last silicate was also identified by Raman spectroscopy (main band at 465 cm^{-1}). Silicon was also identified using EDS (see Figure 4 F and G). Additionally, with Raman spectroscopy in most of the spectra acquired on the black crust, the D and G-bands of carbon were also identified at 1311 and 1599 cm^{-1} respectively (see Figure 4 E). This carbon is the responsible of the blackened colour of the gypsum crusts. The presence of carbon was also confirmed by means of EDS (see Figure F and G).

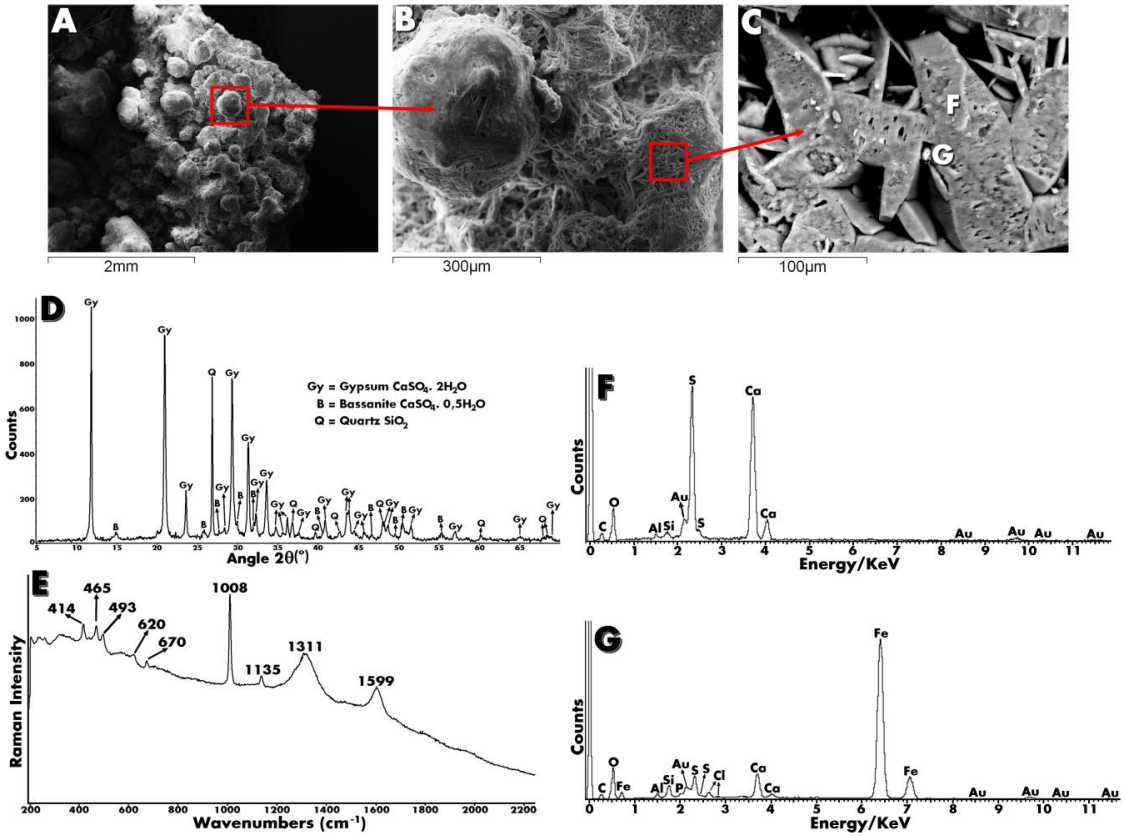

Figure 4. (A, B and and C) Morphology of the studied black crust, (D) XRD spectrum showing the presence of gypsum, bassanite and quartz, (E) Raman spectrum showing the presence of gypsum, quartz and charcoal, (F) EDS spectrum showing the presence of Ca, S and O belonging to gypsum, and Si, Al and C belonging to possible quartz, aluminosilicate and charcoal and (G) EDS spectrum showing the presence of Fe, Al, Si, Cl, Ca, S, O and P.

Considering that the limit of detections of the energy dispersive spectrometer coupled to the SEM for some metals that can be trapped or accumulated in the black crusts is not good enough, in order to confirm their presence, elemental maps from specific areas of the black crusts were acquired using a micro energy dispersive X-Ray Fluorescence spectrometer (μ-ED-XRF). In the Figure 5 an example of the elemental mappings obtained from the sample fragment of BC2 sampling area (SSE orientation) are presented. The imaging analyses were performed at air, therefore elements with Z > 15 (Si) cannot be detected. The elements identified in the mapping were Si, Cl, S, K, Ca, Ti, V, Cr, Mn, Fe, Ni, Cu, Zn, Pb, As, Br, Rb, Sr and Ba. In the Figure 5, all the elemental maps are represented according to the most intense line of each element and the one which do not interfere with other elements. The map of Si is not present due to the low intensity of its K-alpha line in the spectra. For As and Br, their K-beta and K-alpha lines, which have interference one to each other, were only detected. Therefore, the elemental maps of these elements are only showed as indicative and not as conclusive results. Nevertheless, as it will be explained later, the presence of Br as trace element in the black crusts was confirmed using an additional μ-ED-XRF

spectrometer and the application of a more suitable deconvolution process on the spectra acquired. According to the obtained elemental maps, the one for Ca and S is quite coincident, confirming the gypsum crust on the black crust sample (see Figure 5). Sr, as Rb are also highly distributed in the black crust. In this case, the black crust can be enriched with Sr coming from marine aerosol [30]. The distribution of Cl, Br, K, Mn, V, Fe, Zn and Cr in the mapped area is more or less coincident. The first two elements are present in sea salts transported by the marine aerosol (chlorides and bromides). The concentration of chlorides is much higher in the marine aerosol than the one for bromides [31, 32]. The deposition of chloride salts was also confirmed in previous studies developed in La Galea Fortress. In those works, aggregate particles of Fe and Cr were identified, suggesting that both metals are emitted from the same industrial source. In this case also, the elemental distribution of Fe and Cr is completely coincident (see Figure 5). In the areas where lower presence of Cl, Br, K, Mn, Fe, Zn and Cr can be observed, Ba is highly accumulated. This metal can be emitted to the atmosphere as particulate matter coming from the road traffic [33, 34]. Concretely, Ba together with Zn and Ti, are considered tyre wear particles. Ba, usually as barium sulfate, can also come from the brake wear, including abrasion of brake lining material and brake discs, caused by grinding of brake pad constituents or volatilization and condensation of brake pad material [35].

The distribution of Pb, Ti, Cu and Ni is more punctual than for the rest of the elements. The first two elements were widely identified also in the airborne particulate matter from La Galea atmosphere. These metals can come from the Bilbao port and thermal power station emissions. Additionally, Cu and Ni, like Zn, can come from industrial emissions, but also from road dust and vehicles emissions (exhaust emissions) [35].

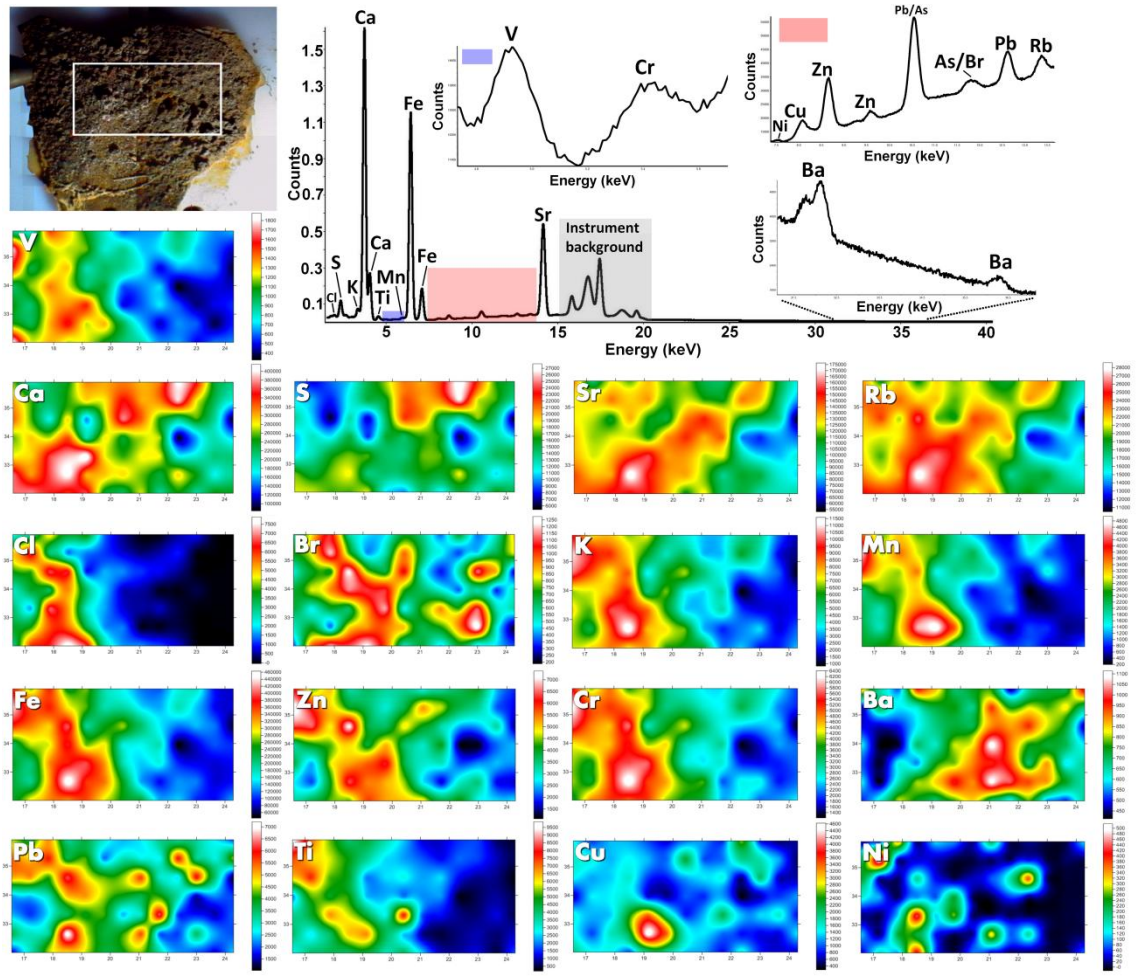

Figure 5. Accumulated spectrum obtained from the mapped area of the black crusts BC2 from the SSE orientation and maps of distribution for each element identified on the selected area.

Having this global information about the presence and distribution of different metals in the black crust and taking into account the irregularities in the morphology of these kind of crusts, additional punctual μ-ED-XRF measurements were conducted in the flattest surface and in the globular forms of several fragments from black crust area BC2 from the SSE orientation (see results on Figure 6). Ten repetitive measurements were performed on each area using a lateral resolution of 1 mm, in order to obtain conclusions on bigger areas (not so microscopic areas). Although a FP (Fundamental Parameter) based method was applied to approach the concentration of each element on the measurement areas, considering a possible matrix effect and the possible heterogeneous nature of the black crusts, in this work the net counts offered by the data treatment software were considered. In order to normalize the data, the net counts of K-lines from each detected element were normalized against the K-alpha line of Rh from the tube (see results in Figure 6).

In both analyzed areas (see microscopic details of the measured areas on the flattest surface vs. framboidal/globular forms in Figure 6) the same elements were identified. However, in the globular or framboidal forms, Cr, which was not identified in the flattest surface, was

also detected. The normalized counts of Ca and S are higher in the flattest surface of the black crust than in the framboidal/globular forms, representing the more compact gypsum matrix growing on the surface of the sandstone. The normalized counts of elements like Al, K, Ti, Mn, Fe, Zr, Ni and Rb are similar in both areas of the black crusts. However, the normalized counts of Si, Cl, Zn, Cu, Sr, Br, Y, V and Cr are higher in the framboidal/globular forms. On the contrary, the normalized counts of Pb and As are higher in the flattest surface of the black crusts.

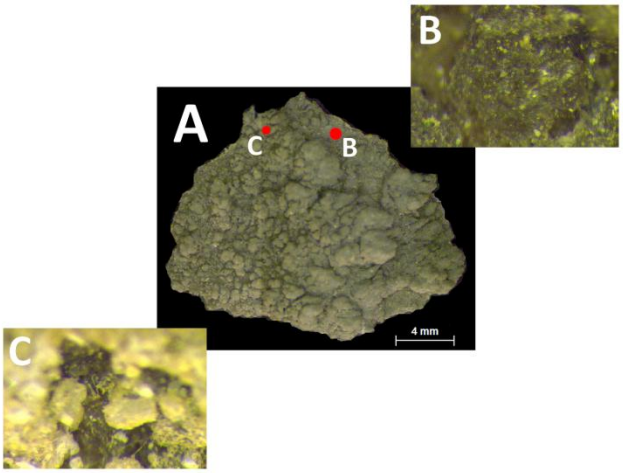

Elements	Flattest surface	Globular/Framboidal forms
Si	0.1203 ± 0.0287	0.2342 ± 0.0407
Al	0.0157 ± 0.0023	0.0193 ± 0.0035
S	2.2227 ± 0.0342	1.7148 ± 0.0397
Cl	0.0214 ± 0.0104	0.1071 ± 0.0605
K	0.0524 ± 0.0096	0.0595 ± 0.0064
Ca	8.0013 ± 0.5810	6.7254 ± 0.3867
Ti	0.0429 ± 0.0106	0.0421 ± 0.0156
Mn	0.0114 ± 0.0015	0.0147 ± 0.0057
Fe	1.7178 ± 0.5299	1.7959 ± 0.6041
Zn	0.0462 ± 0.0090	0.0717 ± 0.0264
Cu	0.0075 ± 0.0023	0.0150 ± 0.0066
Pb	0.0728 ± 0.0090	0.0295 ± 0.0110
As	0.0263 ± 0.0077	0.0098 ± 0.0047
Sr	1.1653 ± 0.1175	1.9206 ± 0.2492
Zr	0.0092 ± 0.0012	0.0066 ± 0.0010
Ni	0.0030 ± 0.0017	0.0039 ± 0.0012
Br	0.0056 ± 0.0007	0.0182 ± 0.0006
Rb	0.0116 ± 0.0013	0.0142 ± 0.0011
Y	0.0002 ± 0.0001	0.0047 ± 0.0012
V	0.0003 ± 0.0001	0.0023 ± 0.0009
Cr	Non-detected	0.0059 ± 0.0018

Figure 6. (A) Optical image of one of the black crusts from the BC2 sampling area (B) an example of the microscopic appearance of the flattest areas of the black crust (C) an example of the microscopic appearance of the globular or framboidal areas of the black crust. On the right of the image, the normalized counts for each detected element together with the related standard deviation (SD) of the repetitive measurements on each area can be observed.

In order to obtain an average concentration of the elements present in all the black crust fragments extracted from BC1 (SW orientation), BC2 (SSE orientation) and BC3 (SSE orientations) samplings areas, an acid digestion of the black crust fragments followed by a quantification using ICP-MS was conducted. In the Table S1 from the Supplementary Material, the concentration of all the elements identified by ICP-MS in the acid extracts from the black crust are presented as an average of three repetitive samples from each sampling area in $mg \cdot Kg^{-1}$ units. According to the average concentration of each element on each sampling area (see Figure 7), the black crusts from both orientations show more or less constant concentrations of Al, Na, Mg, Ca, Sb and Se. The concentrations of most of the metals (Fe, Sn, Ba, Pb, Ti, Mn, Co, Cu, Zn, As, Cd, V, Cr and Ni) present in the black crusts from the SSE orientations (BC2 and BC3) are higher, than the ones from the black crusts of the SW orientation (BC1). This tendency agrees with the preliminary observations performed with the HH-ED-XRF device. In this sense, one of the preferential wind directions, the SSE, could transport the metallic particles emitted by the maritime port and nearby industry to the SSE orientation of the building. Therefore, a higher accumulation of these metals is

observable in the black crusts from the SSE orientation. On the contrary, the concentrations of K and Sr on the black crusts from the SW orientation (BC1) are higher (see Figure 7). Sr input in the black crust can be related with the influence of marine aerosol.

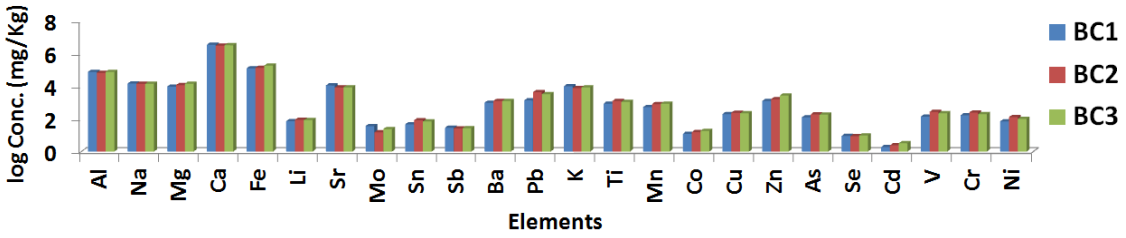

Figure 7. Bar diagram showing the average concentration ($mg \cdot Kg^{-1}$) in logarithmic scale for the three replicate samples of black crusts from each sampling area.

In order to determine possible correlations between the metals identified on the black crusts, the Pearson correlation coefficients were calculated using the quantitative data obtained with the ICP-MS (see the correlation matrix in the Table S2 from the Supplementary Material section). Among other correlations, Pb-Sn (0.96) and Fe-Cr (0.90) correlations must be highlighted. In a previous work, airborne particulate matter was sampled in the location of La Galea Fortress. In that sampling, aggregate particles of Pb + Sn and Fe + Cr deposited on the passive sampler were identified. The high correlations obtained for both pairs of metals in the black crust reinforce the conclusion about a possible common origin of emission of each metal pair.

In order to characterize the individual or aggregated particles that are trapped and accumulated in the black crusts from La Galea, SEM-EDS analyses were performed. As can be seen in Figure 8, a different particulate matters (Figure 8 A-F) are trapped in the black crusts. The sizes of these visually identified particles never exceed 10 μm, thus in this case most of the particulate matters trapped on the black crusts from La Galea location belong to PM_{10}.

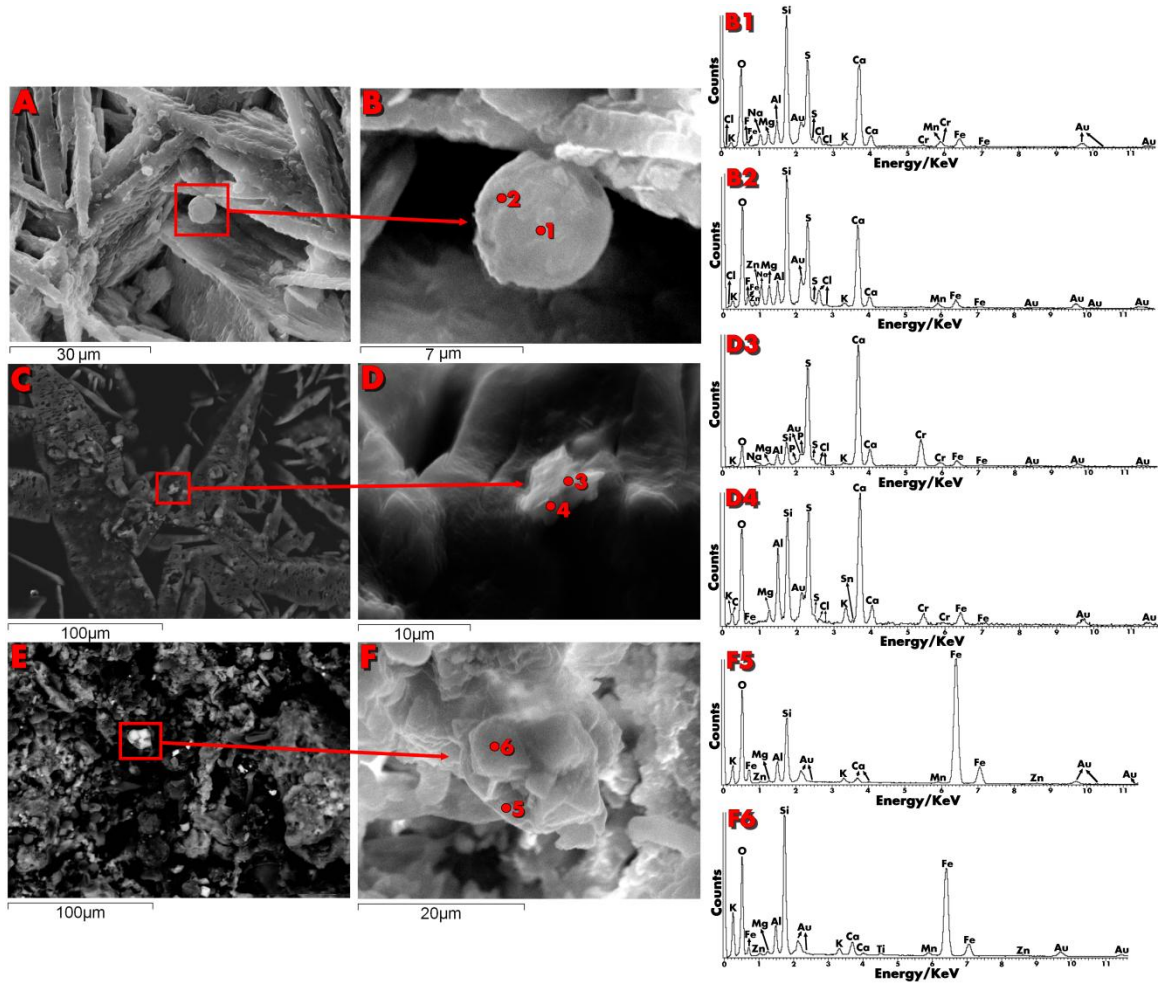

Figure 8. A) General view of an spherical particle trapped in the gypsum matrix, B) A view of the particle in (A) using a higher magnification, B_1, B_2) EDS spectra of the composition of the spherical particle, C) General view of an aggregate particle trapped in the black crust, D) A view of the particle in (C) using a higher magnification, D_1, D_2) EDS spectra of the composition of the particle in (C) and (D), E) General view of an additional aggregate particle, F) A view of the particle in (E) using a higher magnification, F_5, F_6) EDS spectra of the particle in (E) and (F).

The replicate EDS analyses (see Figure 8 B1 and B2) performed on spherical particles such as the one showed in Figure 8 A and B, showed the repetitive presence of Cl, K, O, F, Fe, Na, Mg, Al, S and Ca. Nevertheless, depending of the measured microscopic area, additional elements such as Si, Zn, Mn and Cr were observed. Therefore, a microscopic heterogeneous composition can be found in this kind of spherical particles.

According to the literature, some authors point out that atmospheric SO_2 can be superficially absorbed on sub-spherical fly ash particles made up of Al, Si and Fe; the same elements that the ones identified in the spherical particle from Figure 8 A and B. The S absorbed in this particles play a significant catalytic role in the black crust formation [36, 37]. Apart from Cl, the F detected in the spherical particle could also be related with emissions coming from the

marine aerosol. The additional metals (Fe, Zn and Cr) identified in the spherical particle can be related with the steelworks industries, which are placed in the Bay of Agra, close to La Galea Fortress.

The EDS analyses performed on the aggregate particle from the Figure 8 C and D showed the presence of K, O, Na, Mg, Al, Si, P, S, Cl, Ca, Cr and Fe. The presence of P could be closely related with the fuel combustion of the ships that circulate close to the construction. Apart from phosphorous, elements like Al, Ca, Na, Mg, K, Fe, S and also Li, Ti, V, Cr, Mn, Co, Ni, Cu, Zn, As, Se, Rb, Sr, Cd, Sn Sb, Ba, La, Ce and Hf as minor and minor/trace levels could be also related with the fuel combustion [38, 39]. In additional EDS measurements performed on the aggregated particle from the Figure 8 C and D (see D4 EDS spectrum of Figure 8), Sn was also detected in the particle. Sn can also be related with the steel industry and also with the road traffic. In an additional aggregated particle, bigger (around 20 μm) than the previous one (see Figure 8 E and F), apart from the elements identified in the previous particles, the presence of Ti in the particle must me remarked (see EDS spectrum of the Figure 8 F6). These elements can be closely related with the fuel combustion of ships from the Bilbao Port.

In additional particles trapped in the gypsum matrix from the black crust, the presence of nitrogen with additional elements was clearly observed using EDS (see Figure 9). In the same spectra, Na was also detected. Considering that in a previous work in where airborne particulate matter was sampled and analyzed, particles containing sodium nitrate were identified; it is possible that those particles that are present in the atmosphere can be deposited on the black crust matrix. Additional sodium nitrate particles were also detected in the sandstone from La Galea Fortress. As it was pointed out in our previous work, sodium nitrate can be formed in the atmosphere, due to the reaction between sodium chloride particles and NO_x acid aerosol present in the atmosphere [5, 37]. Therefore, the identification of this nitrate not only in the black crust matrix, but also in the sandstone itself point out that the transformation process of sodium chloride particles is evident and it is not an isolated example of the deposition of this kind of Secondary Marine Aerosol Particles (SMAP) formed in the atmosphere and deposited in the porous matrixes.

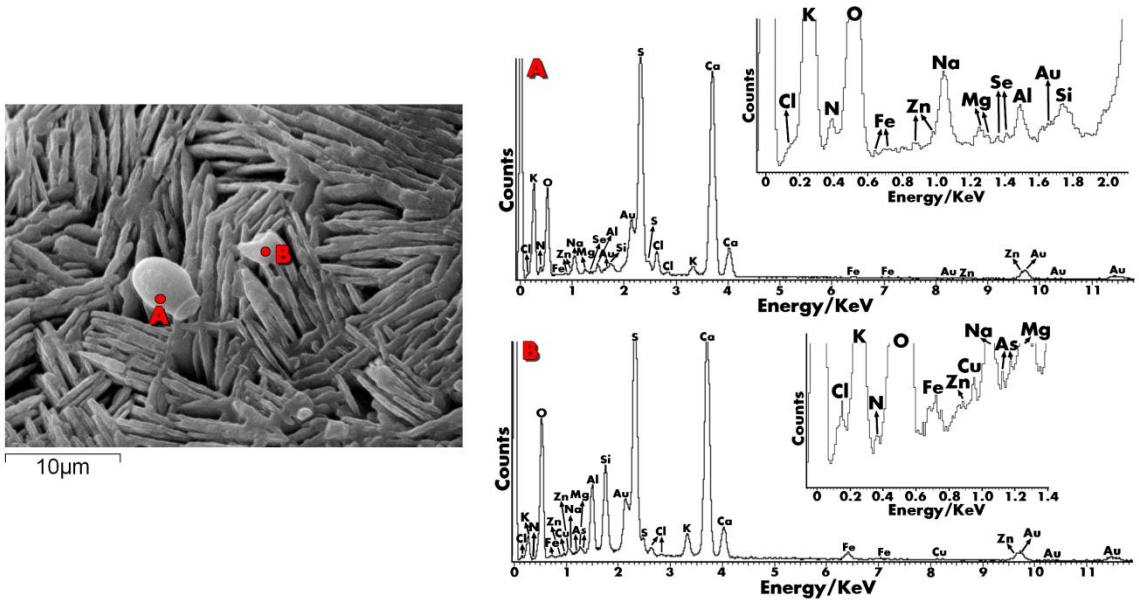

Figure 9. A) EDS spectrum of the heterogeneous particle composed by N, Cl, K, O, Fe, Zn, Na, Mg, Se, Al, Si, S and Ca B) EDS spectrum of the semi spherical particle composed by N, Cl, K, O, Fe, Zn, Cu, Se, Na, As, Mg, Al, Si, S and Ca.

Apart from N and Na, other elements were also identified in this kind of particles such as Cl, K, O, Fe, Zn, Cu, Na, As, Mg, Al, Si, S and Ca. This result evidence that together with SMAP, airborne particles emitted by different anthropogenic sources containing metals (Fe, Zn, Cu and As in this case) can be aggregated and deposited. Remarkable is also the presence of Se in this kind of particles. According to the ICP-MS results (see Figure 7), Se was identified in low concentrations. This Se can be present in the black crust coming from the combustion of the fuels of the ships from the Bilbao Port [39].

Considering that most of the particles visualized under the SEM microscope are aggregated particles, which contain different elements, it was decided to perform EDS imaging on one of those representative particles in order to see all the elements distribution. The particle under study was a 10 μm particle (PM_{10}) (see Figure 10). The EDS imaging study revealed the presence of O, Al, Si, Cr, Fe, Mn, Ni, S, Ti, C, Cu and Ca on the particle. The Ca and S maps are coincident in a specific area, which correspond with the gypsum matrix of the black crust. Apart from that, as it can be observed in Figure 10, S is also present in the particle. Si also was highly distributed in the black crust matrix, suggesting the presence of quartz (α-SiO_2), which was also identified using Raman spectroscopy and XRD as it has been mentioned at the beginning of this work. Additionally, some areas of the Si and Al mappings are coincident, pointing out the presence of aluminosilicates in the black crust matrix (evidence also observed by Raman and XRD). Regarding the metals present in the spherical particle, Cr, Fe, Mn, Ni, Ti and Cu were detected (see Figure 10). This spherical particle is a good example to illustrate how the individual airborne particles do not only include a

specific metal in its composition. Having a look to the distribution maps, once again Fe and Cr appear together, reinforcing the observation made thanks to the correlation analysis which point out to a common origin of both metals. As it has been mentioned through all this work, the metals distributed in this particle can come from the combustion of the fuel used in the ships from Bilbao Port and also from industries near from La Galea.

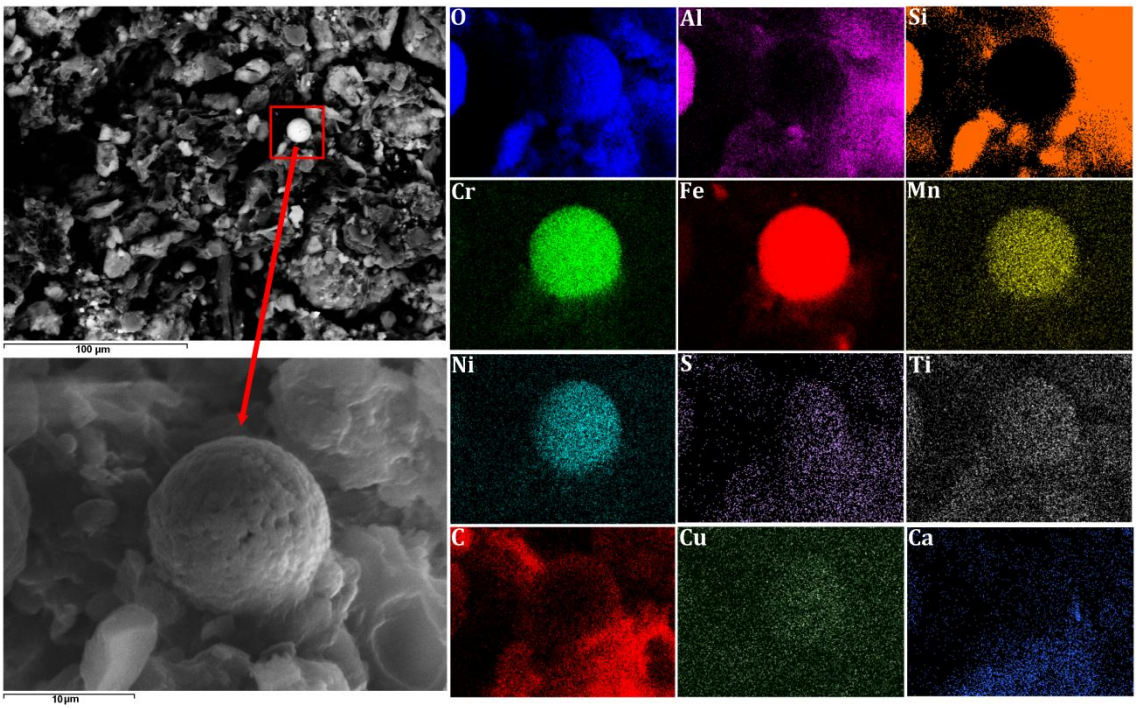

Figure 10. SEM-EDS mapping showing the distribution of O, Al, Si, Cr, Fe, Mn, Ni, S, Ti, C, Cu and Ca in a 10 µm diameter spherical particle (PM10) trapped on the black crust matrix.

4. Conclusions

Thanks to the multianalytical methodology applied, an exhaustive characterization of the composition of black crusts present in the sandstone from the SW and SSE orientations of the lighthouse keeper house from the actual La Galea Fortress was performed. All the black crusts located on this building are cauliflower-like black crusts with globular or framboidal morphologies. The presence of gypsum crust together with silicates (α-quartz and aluminosilicates) depositions and carbon particles trapped was also assessed using SEM-EDS and a combination of two molecular techniques (Raman spectroscopy and XRD).

Apart from the black crust itself, next to the sandstone and beneath the black crust, a biological colonization including cyanobacteria and green algae communities, is present. The cyanobacteria present belong to the Genus *Aphanothece* and the green algae to the *Stichococcus g*enera. Thanks to the preliminary screening with the HH-ED-XRF instrument, it was possible to asses that the normalized areas from the metals identified in the black

crusts (Fe, Zn, Pb, Ti, Cr, Mn, Ni and Cu) were higher in the black crust areas from the SSE orientation. This observation was later confirmed in the laboratory using a destructive technique such as ICP-MS. The influence of marine aerosol was also clearly proven since the presence of Cl and Br were identified. Moreover, the elemental distribution of both elements in the black crusts is coincident, suggesting the same origin for both elements. Apart from that, the distribution of Fe and Cr in the black crust was more or less similar, suggesting also a common source of emission for both metals. Thanks to the correlation analysis performed with the ICP-MS quantitative data, a high correlation between both metals was also obtained, confirming this previous observation. This trend was also observed in previous work where airborne particulate matters (aggregated particles of Fe and Cr) from the atmosphere of La Galea site were sampled. .

The distinguished elemental characterization of both, the flattest surface or the background of the black crust, and the globular/ framboidal formations at the millimeter scale allowed to asses that the normalized signals arising from some metals (e.g. Zn, Cu, Y, V, Cr, etc.) is higher in the globular/ framboidal formations than in the flattest surface or background of the black crusts. However, it is necessary to remark that the normalized signals of Pb and As in the background of the black crust were higher than the ones in the globular/framboidal formations placed in the surface of the black crust background. Additionally, using the quantitative data obtained by means of ICP-MS, a high correlation between Pb and Sn was identified, confirming that aggregate particles of Pb and Sn present in the atmosphere could be deposited and trapped in the black crust matrix.

The analysis of individual particles trapped on the black crust confirm that most of them are PM_{10} (10 μm size particles) and they are made up of a wide variety of elements. Apart from the direct influence of marine aerosol (Na and Cl in the particles), S was also identified in some particles. All the metals detected using the HH-ED-XRF and additional μ-ED-XRF analyses were identified in the laboratory as constituents of the particulate matter. Some of these metallic particles can come from emissions of the vehicle exhaust, emissions from the fuel combustion of the ships from Bilbao Port and also from the surrounding industries. Apart from that, N together with Na was also detected in the trapped particles, confirming that the sodium nitrate particles that can be formed in the atmosphere as Secondary Marine Aerosol particles (reaction between NaCl particles and the NO_x from the atmosphere) can be deposited and also trapped in the black crusts.

All the results extracted evidence that black crusts can be formed on sandstone with a minor percentage of calcium carbonate. Moreover, the HH-ED-XRF spectrometer has been proven

as a promising tool to extract results without taking any sample, which can be conclusive enough. In this case, the black crusts from the lighthouse keeper house from La Galea Fortress act as collector of the emitted metallic airborne particulate matter and Primary/Secondary Marine Aerosol particles. Moreover, according to all the results extracted with all the elemental applied techniques (hand-held and laboratory ED-XRF instruments and ICP-MS), the black crusts from the SSE orientation showed higher metals concentrations. Therefore, it can be concluded that the preferential SSE wind direction transport metallic particles to the black crusts located on this orientation to a greater extent than to the ones from the SW orientation.

5. Supplementary Material

Table S1. Concentration of the elements in mg·Kg^{-1} and method RSD (Relative Standard Deviation) obtained by ICP-MS for the black crusts from BC1 (SW orientation), BC2 (SSE orientation) and BC3 (SSE orientations) samplings areas

Elements	BC1	BC2	BC3	RSD (%)
Al	76444 ± 854	67286 ± 1175	96622 ± 2266	6
Na	14717 ± 456	15929 ± 155	14410 ± 1239	11
Mg	9633 ± 84	11990 ± 24	14353 ± 313	5
Ca	3598698 ± 51815	3154765 ± 51851	3274416 ± 78992	8
Fe	126174 ± 7365	103786 ± 13	186439 ± 3862	6
Li	72.24 ± 0.86	89.73 ± 0.24	85 ± 1	2
Sr	11327 ± 68	8489 ± 21	8722 ± 16	3
Mo	36.62 ± 0.24	15.08 ± 0.07	23.86 ± 0.64	4
Sn	46.78 ± 0.28	82.90 ± 0.52	70.27 ± 0.22	5
Sb	28.52 ± 0.16	16.60 ± 0.05	14.27 ± 0.56	10
Ba	992 ± 2	1094 ± 5	1241 ± 7	4
Pb	1369 ± 20	4342 ± 27	3269 ± 11	5
K	10158 ± 88	7811 ± 31	8617 ± 50	6
Ti	864 ± 13	471 ± 1	484.05 ± 0.58	2
Mn	537 ± 3	806 ± 5	868 ± 14	4
Co	12.34 ± 0.08	12.63 ± 0.04	18.65 ± 0.10	5
Cu	199.60 ± 0.67	154.45 ± 0.77	218.07 ± 0.45	3
Zn	1266 ± 7	1554 ± 16	2723 ± 11	5
As	125.36 ± 0.89	189.54 ± 0.63	185.06 ± 0.60	4
Se	9.09 ± 0.06	6.49 ± 0.09	9.78 ± 0.24	10
Cd	1.92 ± 0.02	2.42 ± 0.01	3.22 ± 0.01	6
V	139.14 ± 0.65	273 ± 1	161.74 ± 0.71	4
Cr	167.01 ± 0.55	248 ± 3	190 ± 12	3
Ni	70 ± 1	129.56 ± 0.70	98 ± 2	6
W	0.47 ± 0.04	0.874 ± 0.004	2 ± 1	3
Tl	<LOD	<LOD	<LOD	1

LOD: Limit of Detection

Table S2. Pearson correlation coefficients matrix of all the quantitative data obtained from ICP-MS analyses.

	Al	Na	Mg	Ca	Fe	Li	Sr	Mo	Sn	Sb	Ba	W	Tl	Pb	K	Ti	Mn	Co	Cu	Zn	As	Se	Cd	V	Cr	Ni
Al	1.00																									
Na	0.53	1.00																								
Mg	0.74	0.62	1.00																							
Ca	0.86	0.28	0.65	1.00																						
Fe	0.50	0.11	0.58	0.22	1.00																					
Li	-0.20	-0.19	0.21	-0.18	0.24	1.00																				
Sr	0.01	0.07	-0.53	0.04	-0.56	-0.74	1.00																			
Mo	-0.26	-0.13	-0.72	-0.34	-0.47	-0.33	0.76	1.00																		
Sn	-0.07	-0.11	0.46	0.03	0.33	0.73	-0.94	-0.85	1.00																	
Sb	-0.37	-0.40	-0.81	-0.19	-0.68	-0.57	0.87	0.75	-0.77	1.00																
Ba	0.47	0.30	0.76	0.17	0.77	0.50	-0.67	-0.54	0.45	-0.84	1.00															
W	-0.39	-0.43	-0.22	-0.53	0.18	0.77	-0.41	0.14	0.29	-0.18	0.36	1.00														
Tl	-0.01	0.25	-0.23	0.11	-0.82	-0.33	0.65	0.46	-0.51	0.54	-0.45	-0.23	1.00													
Pb	-0.01	-0.07	0.52	0.13	0.32	0.74	-0.89	-0.88	0.96	-0.76	0.49	0.26	-0.47	1.00												
K	-0.03	0.14	-0.51	-0.09	-0.47	-0.49	0.92	0.85	-0.92	0.76	-0.49	-0.15	0.60	-0.84	1.00											
Ti	0.19	0.16	0.58	0.33	0.12	0.79	-0.62	-0.58	0.70	-0.64	0.50	0.29	-0.32	0.81	-0.45	1.00										
Mn	-0.13	-0.12	0.28	-0.27	0.41	0.91	-0.83	-0.32	0.73	-0.69	0.66	0.81	-0.41	0.67	-0.62	0.60	1.00									
Co	0.18	0.18	0.37	-0.17	0.57	0.63	-0.42	0.02	0.20	-0.53	0.78	0.73	-0.24	0.19	-0.11	0.38	0.76	1.00								
Cu	0.21	0.26	-0.01	-0.18	0.27	-0.02	0.32	0.66	-0.56	0.11	0.34	0.40	0.18	-0.54	0.55	-0.22	0.11	0.70	1.00							
Zn	0.26	0.17	0.43	-0.09	0.63	0.62	-0.56	-0.15	0.34	-0.65	0.84	0.69	-0.32	0.30	-0.32	0.38	0.82	0.95	0.57	1.00						
As	-0.18	-0.09	-0.66	-0.08	-0.65	-0.71	0.97	0.73	-0.89	0.94	-0.78	-0.38	0.62	-0.84	0.88	-0.64	-0.83	-0.53	0.19	-0.67	1.00					
Se	0.54	0.80	0.34	0.26	0.14	-0.58	0.55	0.28	-0.68	0.10	0.13	-0.47	0.31	-0.60	0.60	-0.31	-0.52	0.09	0.57	-0.06	0.40	1.00				
Cd	0.18	0.16	0.46	-0.14	0.64	0.68	-0.73	-0.33	0.53	-0.78	0.86	0.66	-0.44	0.49	-0.51	0.45	0.89	0.88	0.37	0.96	-0.81	-0.14	1.00			
V	-0.19	-0.23	0.24	0.11	-0.02	0.43	-0.66	-0.87	0.83	-0.45	0.32	-0.04	-0.36	0.87	-0.76	0.56	0.30	-0.30	-0.87	-0.17	-0.54	-0.68	0.05	1.00		
Cr	-0.49	-0.52	-0.27	-0.49	0.90	0.83	-0.53	0.21	0.51	-0.21	0.21	0.93	-0.28	0.44	-0.34	0.37	0.83	0.53	0.07	0.54	-0.46	-0.73	0.58	0.23	1.00	
Ni	-0.21	-0.13	-0.66	-0.37	-0.34	-0.19	0.68	0.97	-0.77	0.66	-0.30	0.33	0.46	-0.79	0.82	-0.46	-0.19	0.25	0.77	0.06	0.64	0.33	-0.14	-0.85	0.11	1.00

6. References

[1] N. Prieto-Taboada, M. Maguregui, I. Martinez-Arkarazo, M. A. Olazabal, G. Arana, J. M. Madariaga, Spectroscopic evaluation of the environmental impact on black crusted modern mortars in urban-industrial areas, Analytical & Bioanalytical Chemistry (2011) 399: 2949-2959.

[2] T. Rivas, S. Pozo, M. Paz, Sulfur and oxigen isotope analysis to identify sources of sulfur in gypsum-rich black crusts developed on granites, Science of the Total Environment (2014) 482-483: 137-147.

[3] A. Török, T. Licha, K. Simon, S. Siegesmund, Urban and rural limestone weathering; the contribution of dust to black crust formation, Environmental Earth Sciences (2011) 63: 675-693.

[4] D. Barca, C. M. Belfiore, G. M. Crisci, M. F. La Russa, A. Pezzino, S. A. Ruffolo, A new methodological approach for the chemical characterization of black crusts on building stones: a case study from the Catania city centre (Sicily, Italy), Journal of Analytical Atomic Spectrometry (2011) 26: 1000-1011.

[5] I. Martinez-Arkarazo, M. Angulo, L. Bartolome, N. Etxebarria, M. A. Olazabal, J. M. Madariaga, An integrated analytical approach to diagnose the conservation state of building materials of a palace house in the metropolitan Bilbao (Basque Country, North of Spain), Analytica Chimica Acta (2007) 584: 350-359.

[6] N. Prieto-Taboada, I. Ibarrondo, O. Gomez-Laserna, I. Martinez-Arkarazo, M. A. Olazabal, J. M. Madariaga, Buildings as repositories of hazardous pollutants of anthropogenic origin, Journal of Hazardous Materials (2013) 248-249: 451-460.

[7] P. Ausset, F. Bannery, M. Del Monte, R. A. Lefevre, Recording of pre-industrial atmospheric environment by ancient crusts on stone monuments, Atmospheric Environment (1998) 32: 2859-2863.

[8] C. Rodriguez-Navarro, E. Sebastian, Role of particulate matter from vehicle exhaust on porous building stones (limestone) sulfation, Science of the Total Environment (1996) 187: 79-91.

[9] A. Sarmiento, M. Maguregui, I. Martinez-Arkarazo, M. Angulo, K. Castro, M. A. Olazabal, L. A. Fernandez, M. D. Rodriguez-Laso, A. M. Mujika, J. Gomez, J. M. Madariaga, Raman

spectroscopy as a tool to diagnose the impact of combustion and greenhouse acid gases on properties of Built Heritage, Journal of Raman Spectroscopy (2008) 39: 1042-1049.

[10] M. Marszałek, Z. Alexandrowicz, G. Rzepa, Composition of weathering crusts on sandstones from natural outcrops and architectonic elements in an urban environment, Environmental Science & Pollution Research (2014) 21: 14023-14036.

[11] I. Ozga, N. Ghedini, C. Giosuè, C. Sabbioni, F. Tittarelli, A. Bonazza, Assessment of air pollutant sources in the deposit on monuments by multivariate analysis. Science of the Total Environment (2014) 490: 776-784.

[12] D. Barca, V. Comite, C. M. Belfiore, A. Bonazza, M. F. La Russa, S. A. Ruffolo, G. M. Crisci, A. Pezzino, C. Sabbioni, Impact of air pollution in deterioration of carbonate building materials in Italian urban environments, Applied Geochemistry (2014) 48: 122-131.

[13] C. M. Belfiore, D. Barca, A. Bonazza, V. Comité, M. F. La Russa, A. Pezzino, S. A. Ruffolo, C. Sabbioni, Application of spectrometric analysis to the identification of pollution sources causing cultural heritage damage, Environmental Science & Pollution Research (2013) 20: 8848-8859.

[14] A. Bonazza, P. Brimblecombe, C. M. Grossi, C. Sabbioni, Carbon in Black Crusts from the Tower of London, Environmental Science & Technology (2007) 41: 4199-4204.

[15] C. Saiz-Jimenez, B. Hermosin, Black crusts in the European built environment, Corrosion Reviews (2004) 22: 381-393.

[16] N. Ghedini, C. Sabbioni, A. Bonazza, G. Gobbi, Chemical-Thermal Quantitative Methodology for Carbon Speciation in Damage Layers on Building Surfaces, Environmental Science & Technologies (2006) 40: 939-944.

[17] A. Török, Surface strength and mineralogy of weathering crusts on limestone buildings in Budapest, Building & Environment (2003) 38: 1185-1192.

[18] H. Zhang, M. Shi, W. Shen, Z. Li, B. Zhang, R. Liu, R. Zhang, Damage or protection? The role of smoked crust on sandstones from Yungang Grottoes, Journal of Archaeological Science (2013) 40: 935-942.

[19] B. J. Smith, A. Török, J. J. McAllister, J. Megarry, Observations on the factors influencing stability of building stones following contour scaling: a case study of the oolitic limestones from Budapest, Hungary, Building & Environment (2003) 38: 1173-1183.

[20] B. J. Smith, A. V. Turkington, P. A. Warke, P. A. M. Basheer, J. J. McAlister, J. Meenly, J. M. Curran, Modelling the rapid retreat of building sandstones. A case study from polluted maritime environment, Natural Stones, Weathering Phenomena, Conservation Strategies and Case Studies, Geological Society (London, U.K) Special Publications (2002) 205: 339-354.

[21] A. Török, Oolitic limestone in polluted atmospheric environment in Budapest: weathering phenomena and alterations in physical properties, Natural Stones, Weathering Phenomena, Conservation Strategies and Case Studies, Geological Society (London, U.K.) Special Publications (2002) 205: 363-379.

[22] M. F. La Russa, C. M. Belfiore, V. Comité, D. Barca, A. Bonazza, S. A. Ruffolo, G. M. Crisci, A. Pezzino, Geochemical study of black crusts as a diagnostic tool in cultural heritage, Applied Physics A: Materials Science and Processing (2013) 113: 1151–1162.

[23] J. S. Pozo-Antonio, M. P. Fiorucci, A. Ramil, A. J. López, T. Rivas, Evaluation of the effectiveness of laser crust removal on granites by means of hyperspectral imaging techniques, Applied Surface Science (2015) 347: 832-838.

[24] P. Fermo, R. Gonzalez-Turrión, M. Rosa, A. Omegna, A new approach to assess the chemical composition of poder deposits damaging the stone surfaces of historical monuments, Environmental Science & Pollution Research (2015) 22: 6262-6270.

[25] S. A. Ruffolo, V. Comite, M. F. La Russa, C. M. Belfiore, D. Barca, A. Bonazza, G. M. Crisci, A. Pezzino, C. Sabbioni, An analysis of the black crusts from the Seville Cathedral: A challenge to deepen the understanding of the relationships among microstructure, microchemical features and pollution sources, Science of the Total Environment (2015) 502: 157-166.

[26] B. Graue, S. Siegesmund, P. Oyhantcabal, R. Naumann, T. Licha, K. Simon, The effect of air pollution on stone decay: the decay of the Drachenfels trachyte in industrial, urban, and rural environments-a case study of the Cologne, Altenberg and Xanten cathedrals, Environmental Earth Sciences (2013) 69: 1095-1124.

[27] H. Morillas, M. Maguregui, I. Marcaida, J. Trebolazabala, I. Salcedo, J. M. Madariaga, Characterization of the main colonizer and biogenic pigments present in the red biofilm from La Galea Fortress sandstone by means of microscopic observations and Raman Imaging, Microchemical Journal (2015) 121: 48–55.

[28] A. Török, Black crusts on travertine: factors controlling development and stability, Environmental Geology (2008) 56: 583-597.

[29] A. Török, S. Siegesmund, C. Müller, A. Hüpers, M. Hoppert, T. Weiss, Differences in texture, physical properties and microbiology of weathering crust and host rock: a case study of the porous limestone of Budapest (Hungary) Building Stone Decay: From Diagnosis to Conservation, Geological Society (London, U.K.), Special Publications (2007) 271: 261-276.

[30] C. E. Whipkey, R. C. Capo, O. A. Chadwick, B. W. Stewart, The importance of sea spray to the cation budget of a coastal Hawaiian soil: a strontium isotope approach, Chemical Geology (2000) 168: 37-48.

[31] F. Culkin, Chemical oceanography, The Major Constituents of Sea Water, Academic Press, London, New York (1965) 121–161.

[32] D. Dyrssen, L. G. Sillen, Alkalinity and Total Carbonate in Sea Water. A Plea for p-t-Independent Data, Tellus (1967) 19: 113–121.

[33] J. A. Carrero, I. Arrizabalaga, J. Bustamante, N. Goienaga, G. Arana, J. M. Madariaga, Diagnosing the traffic impact on roadside soils through a multianalytical data analysis of the concentration profiles of traffic-related elements, Science of the Total Environment (2013) 458-460: 427-434.

[34] J. A. Carrero, N. Goienaga, M. Olivares, I. Martinez-Arkarazo, G. Arana, J. M. Madariaga, Raman spectroscopy assisted with XRF and chemical simulation to assess the synergic impacts of guardrails and traffic pollutants on urban soils, Journal of Raman Spectroscopy (2012) 43: 1498-1503.

[35] P. Pant, R. M. Harrison, Estimation of the contribution of road traffic emissions to particulate matter concentrations from field measurements: A review, Atmospheric Environment (2013) 77: 78-97.

[36] A. J. Hutchinson, J. B. Johnson, G. E. Thompson, G. C. Wood, P. W. Sage, M. J. Cooke, The role of fly-ash particulate material and oxide catalysts in stone degradation, Atmospheric Environment. Part A. General Topics (1992) 26: 2795–2803.

[37] G. Montana, L. Randazzo, P. Mazzoleni, Natural and anthropogenic sources of total suspended particulate and their contribution to the formation of black crusts on building stone materials of Catania (Sicily), Environmental Earth Science (2012) 67: 1097–1110.

[38] S. M. Almeida, C. A. Pio, M. C. Freitas, M. A. Reis, M. A. Trancoso, Source apportionment of fine and coarse particulate matter in a sub-urban area at the Western European Coast, Atmospheric Environment (2005) 39: 3127–3138.

[39] J. Pey, N. Perez, J. Cortes, A. Alastuey, X. Querol, Chemical fingerprint and impact of shipping emissions over a western Mediterranean metropolis: Primary and aged contributions, Science of the Total Environment (2013) 463-464: 497-507.

Chapter 7:
Integrated Discussion and Future Works

CHAPTER 7.

INTEGRATED DISCUSSION AND FUTURE WORKS

In this chapter of the present PhD manuscript an integrated discussion is presented, leading to the general conclusions of the research work.

The analytical methodologies applied on each Case Study (the three studied scenarios) offer the required information (elemental and molecular) about the original composition and decaying products of the different analyzed building materials. The used methodology was divided in two parts. In a first step, preliminary analyses were conducted in some cases using non-invasive portable/hand-held instruments (ED-XRF and Raman spectroscopy). After that, the analyses were extended in the laboratory using elemental (SEM-EDS, μ-ED-XRF point by point and μ-ED-XRF imaging analyses) and molecular (micro-Raman spectroscopy, infrared spectroscopy and XRD punctual and imaging analyses in some cases) techniques. Apart from that, the quantification of soluble salts and acid-extractable metal(oid)s was also conducted using ion chromatography and ICP-MS respectively. This combination of analytical tools offered a deep overview of the conservation state of the materials under study, thanks to the characterization of their related pathologies.

Apart from the experimental results, and in order to extract additional conclusions, chemometric treatments (e.g. correlation analysis) of the quantitative data (ions and metal(oid)s concentrations) were conducted. These kind of data treatments allowed to observe which ions and/or metal(oid)s are correlated with others. For example, a high correlation between ions confirms the existence of a specific salt crystallized in the material (e.g. a high correlation between Na^+ and Cl^- suggests the presence of NaCl coming from the marine aerosol). Moreover, correlations between specific metals could suggest that both

metals deposited on the material were emitted from the same source. Therefore, this kind of data treatments could be useful to confirm the experimental evidences.

Apart from that, the simulation of chemical reactions through thermodynamic modellings allowed to explain the decaying pathways proposed according to the experimental obtained results. This tool is very useful to confirm for example if a specific soluble salt (or double salt) can be formed on a specific building material under realistic conditions marked by the environment where the construction is placed (e.g. SO_2 concentrations from the atmosphere, etc.).

All these analytical tools were applied to characterize the original composition and the pathologies that can be formed due to the influence of different kind of marine environments on a wide variety of building materials (sandstones, limestones, bricks, plasters, cementitious materials, etc.) placed in three constructions from the Basque Country (north of Spain). The three buildings are influenced respectively by (a) a direct marine and diffuse urban-industrial environment, (b) a diffuse marine and a diffuse urban-industrial environment and (c) a direct marine and a direct urban-industrial environment.

Most of the environmental stressors (natural and/or anthropogenic) present in this kind of environments can be deposited on the building materials following wet and/or dry depositions. Considering that acid aerosols (e.g. SO_2) can be incorporated in the rainwater to suffer a subsequent wet deposition (SO_2 transformation into H_2SO_4), in some cases study from this work, the anions and metal(oid)s concentrations of the rainwaters, from the area where the constructions are located, were determined.

As an example of direct marine and diffuse urban-industrial influenced environments, the Igueldo Lighthouse construction (San Sebastian, Basque Country, north of Spain) was studied. In a first step, the building materials (cementitious materials, limestones and sandstones) from the outdoor terrace floor were characterized. Apart from the possible influence of Secondary Marine Aerosol (chlorides and sulfates presence), the sulfate input included in the original cementitious materials can also contribute to observe new sulfate crystallizations (dissolution and re-precipitation process). Remarkable is the presence of nitrates. In this case, the outdoor terrace of the lighthouse is daily full of seagull's droppings. These droppings are an important source of ammonium nitrate due to the transformation process of the urea from the droppings, induced by the microbial activity. The ammonium nitrate in solution can react with the original components of the materials, giving as a result the respective nitrate salts.

In the indoor rooms of the lighthouse, the most evident pathology identified was the cracking process of the tiles from the north and east walls of the inner rooms. The responsible of those cracks is the formation of sulfate salts as efflorescences on the cement mortar that fix the tiles to the wall. The sulfates included in the cement mortar itself could be dissolved by water infiltrations, and they can re-crystallize on the surface of the cement mortar as other species, promoting the cracking of the tiles fixed on the top of this mortar. Another remarkable result could be the repetitive identification of mascagnite [$(NH_4)_2SO_4$]; this sulfate included in the Secondary Marine Aerosol could be deposited on the external parts of the building (this conclusion was also extracted in the analyses performed on La Galea Fortress). After that, it can be dissolved and migrate as NH_4^+ and SO_4^{2-} to the inner areas of the building, to suffer a subsequent re-precipitation as another metal sulfate salt. Another evidence of the migration and re-precipitation of particles coming from the marine aerosol is the identification of sodium chloride on the inner rooms of the lighthouse. Additionally, nitrate salts were also identified on the building materials from the inner areas of the lighthouse, suggesting that the ammonium nitrate coming from the seagull's droppings can migrate to the inner areas of the lighthouse, reacting with the original materials.

It is necessary to remark that in the gypsum plaster samples from the indoor rooms of the lighthouse, a wide variety of salts were identified. Apart from chlorides coming from the Primary Marine Aerosol Particles deposition, additional sulfate salts such as glauberite, syngenite and polyhalite, and humberstonite, a double sulfate nitrate salt were identified using Raman spectroscopy, infrared spectroscopy and XRD. Therefore, with this case study, it was proven that the application of combined spectroscopic techniques is an adequate analytical methodology able to avoid inaccurate or uncertain assignments that can be done only using one spectroscopic technique. Moreover imaging analyses (SEM-EDS and Raman) allowed to confirm that the presence of this complex mixture of single and double soluble salts was not punctual in the gypsum plaster. Moreover, thermodynamic simulations were also useful to confirm the proposed decaying pathway which leads to the formation of specific salts in these gypsum plasters.

To evaluate the influence of a diffuse marine and a diffuse urban-industrial environment on building materials, different detached houses from Berango (Basque Country, north of Spain) were selected. In this case study, bricks, artificial stones and their joint mortars were characterized. The main pathology identified on those materials was the formation of efflorescences. The main salt identified on those efflorescences was thenardite (Na_2SO_4). The alkali compounds (e.g. Na_2O) included in the joint mortars together with sulfates

presence give rise to this kind of salts crystallizations. The thenardite can be re-hydrated and transformed into mirabilite ($Na_2SO_4 \cdot 10H_2O$). The hydration and dehydration cycles of these salts give rise to expansion and contraction of the material in which these salts are crystallized, leading to fissures and cracks.

In a general way, the efflorescences present on the detached houses were formed by a synergic effect between the ions in infiltrations waters and the additives used for the building constructions. From the conclusions of this PhD it should be emphasized how important is to use adequate additives for the setting of materials, because during time some of them can be solubilized, due to the reaction with the surrounding environment, and migrate throughout the material promoting loss of material and efflorescence formations.

Although these houses are placed 2 Km far from the coastal area, the identification of halite also suggests the nfluence of marine aerosol in a diffuse way on the formation of these recent efflorescences. This will take more a longer time period to be observed, but the nature of efflorescences seems to be similar to those detected in other building with a direct influence of marine aerosol.

Apart from that, rainwater samples from different points along Metropolitan Bilbao, including Berango, were also studied, in order to evaluate the influence of the rainwater in the conservation state of another detached house from Berango which is influenced by the wet depositions (placed in the rains preferential orientation) observing different decay compounds related with the cement degradation.

Finally, La Galea Fortress located in Getxo (Basque Country, north of Spain) was selected as the third construction to evaluate the influence of a direct marine and a direct urban-industrial environment on building materials. Comparing the concentration of sulfates and nitrates in La Galea site, the concentration of these anions is higher than in the rest of the locations where rainwater was sampled and characterized. This observation, together with the available data about acid aerosol emission confirm that La Galea is, among the third locations considered in this work, the most polluted one. We must highlight that the dissolved concentration of many metals (e.g. Zn, Pb, etc.) in the rainwater from La Galea is also high, suggesting that higher emissions of metallic airborne particulate matters are present in this atmosphere. Apart from that, the results obtained from La Galea rainwater offered the highest concentrations of chlorides, confirming the direct influence of the marine aerosol.

The principal material used in La Galea Fortress was the sandstone. Concretely, the sandstone from the tower of the fortress shows the worst conservation state. Regarding all the orientations of the tower, the worst preserved area in the South-southeast (SSE) orientation in where alveolizations, cracks, etc. pathologies are observable. This orientation matches with one of the preferential wind direction. However, the sandstone from the Northweast (NW) orientation, which is close to the second preferential wind directions (the North-northwest), shows a good conservation state. In this area, a reddish biofilm or biopatina is present. Thanks to microscopic observations, it was possible to asses that the main colonizer in this biological patina is the Trentepohlia algae. The good conservation state of the sandstone in this area suggests that this alga can act as bioprotector of the NW tower face. Apart from the characterization of the main biological colonizer, a complete characterization of the biogenic pigments excreted by the colonizer was conducted using point by point and Raman imaging analyses.

In a second study in La Galea site, the wide varieties of particles on the Primary Marine Aerosol (PMA) were characterized. Apart from that, Secondary Marine Aerosol particles (SMAP) present in the atmosphere of La Galea were sampled. For that purpose, a home-made passive sampler was designed and constructed. This passive sampler was applied successfully since a wide variety of SMAP were collected and characterized. With this case study it was possible to prove how the PMA particles transform their composition in the atmosphere due to their reaction with the acid aerosols present in the atmosphere (NO_x, SO_x, CO_2 etc.). Apart from that, crustal particles and metallic airborne particulate matter were also sampled and characterized elemental and molecularly.

In order to evaluate if the crustal particles, SMAP and metallic airborne particulate matter are impacting in the sandstone from La Galea Fortress, a previous characterization of the sandstone material from the tower and the entrance arch of La Galea Fortress was conducted using the whole analytical methodology. Using molecular techniques it was possible to asses that calcium carbonate is present in the original composition of the sandstone. This carbonate percentage becomes this material more susceptible for being impacted by the acid aerosols following a wet deposition. In this sense, gypsum was constantly identified in the sandstone matrix. Moreover, thanks to μ-ED-XRF mappings, the random distribution of sulfur, which matches in some areas with the calcium distribution, was ascertained. The newly formed gypsum on the sandstone can be dissolved easily than the sandstone itself, promoting the loss of material. Apart from the anthropogenic emissions of SO_2, an additional input of sulfates can be present in the sandstone due to the influence of cements rich in sulfates included in both, the tower and the entrance arch of the fortress.

The sulfates from the cement can be dissolved and they can migrate to the annex sandstone reacting with the carbonates present in the stone. Related with this, sodium sulfate (thenardite), a typical alkali sulfate that can be crystallized in cements, was identified in the sandstone from the tower and from the entrance arch. Marine aerosol can also contribute to increase the input of sulfates in the material but following a wet deposition of sulfate particles; from this observation, two kinds of magnesium sulfates (epsomite and starkeyite) and ammonium sulfate (mascagnite) were identified in the sandstone. Some of these sulfates were identified also in the home-made passive sampler. Therefore, the identification of these compounds evidences that the SMAP can be deposited on La Galea Fortress sandstone following a wet deposition. Additionally, $NaNO_3$, an additional SMAP was also identified on the sandstone surface as airborne particulate matter.

These kinds of PMAP and SMAP can be also trapped in a specific crust, usually formed in the areas protected by the rainwater, the black crust. These kinds of crusts are also present in La Galea Fortress, particularly, in the lighthouse keeper house. During the history of this construction, its use was changed and in a certain period of time this construction was remodeled into a lighthouse. All the black crust formations are placed in the SSE orientation and in the SW orientation. The first orientation matches with one of the preferential direction of the wind. Apart from the gypsum crust, a biological colonization formed by a cyanobacteria and green algae community was also characterized. Regarding the metals trapped on the black crusts, thanks to the preliminary screening with the HH-ED-XRF instrument, it was possible to asses that the concentration of all the metals identified in the black crusts (Fe, Zn, Pb, Ti, Cr, Mn, Ni and Cu) was higher in the black crust areas from the SSE orientation. This observation was later confirmed in the laboratory using a destructive technique such as ICP-MS. The influence of marine aerosol was also clearly proven since the presence of Cl and Br were identified. Moreover, the elemental distribution of both elements in the black crusts is coincident, suggesting the same origin for both elements. Apart from that, the distribution of Fe and Cr in the black crust was more or less similar, suggesting once more a common source of emission for both metals. Thanks to the correlation analysis performed with the ICP-MS quantitative data, a high correlation between both metals was also obtained, confirming this previous observation. This trend was also observed in airborne particulate from the atmosphere of La Galea site, since aggregate particles of Fe and Cr were sampled from the atmosphere using the home-made passive sampler.

Remarkable is also the higher accumulation of metals (except Pb and As) in the framboidal formations of the black crusts. Moreover, the analyses of individual particles trapped on the black crust confirm that most of them are PM_{10} and they are made up of a wide variety of

elements. Apart from the direct influence of marine aerosol (Na and Cl in the particles), S was also identified in some of them. N together with Na was also detected in the trapped particles, confirming that the sodium nitrate particles that can be formed in the atmosphere as a SMAP (reaction between NaCl particles and the NO_2 from the atmosphere) can be deposited and trapped in the black crusts.

The knowledge obtained in the present PhD work allows understanding the decay compounds, from the analytical chemistry point of view, that different building materials can experiment in different locations close or immersed in marine environments. This PhD manuscript can also help to design possible strategies in the restoration processes that can be developed on buildings close to the sea.

All the constructions considered in the Case Studies presented in this PhD Thesis are located at a certain altitude above sea level. In future works, a new Case Study including a construction located at sea level (zero altitude) will be considered. In this case, the direct and horizontal influence of marine aerosol on the construction will be evaluated. The construction representative of this casuistry will be the Punta Begoña Galleries, situated also in Getxo (Basque Country, north of Spain) and located very close to La Galea Fortress (less than 4 Km). In this case, the Galleries also experiment the influence of the anthropogenic emissions coming from the Bilbao Port and the surrounding urban-industrial area. The main difference regarding La Galea Fortress is that in this case, Punta Begoña Galeries undergo the direct influence of the road traffic, since the place where the Galleries are erected is a tourist area (a roundabout and a parking in placed just in front of the Galleries). Moreover, in this future Case Study, the characterization of the original composition and possible pathologies that can be present on additional building materials which were not considered in this PhD Thesis will be included (e.g. concrete, ceramic, etc.).

Apart from the evaluation of the influence of natural environmental stressors coming from the marine environment and anthropogenic emissions coming from road traffic and urban-industrial area on the conservation state of the construction, the removal of pollutants and degradation compounds from the facades of this construction will be considered. As it has been pointed out in this PhD Thesis, the construction materials can act as repository of hazardous compounds (e.g. metals). Therefore, special precautions should be taken during their manipulation. Moreover, considering that the future construction under study is close to the sources of anthropogenic emissions, it is expected that the accumulation of hazardous compounds will be higher in its building materials. Considering that a multidisciplinary project involving scientist of different fields (chemist, geologist, architects, archaeologists,

etc.) devoted to the characterization of the materials, to the evaluation of the conservation state of the building and to apply value enhancement actions on the building considering also the surrounding landscape; the removal of pollutants is an important task previous to any restoration to guarantee human and environmental safety. In this way, considering the huge amounts of cleaning products used in the treatments of facades, it is important to find a low cost cleaning system according to green chemistry and human health principles. In this sense, previous studies of our research group on carbonate based materials have pointed out agar hydrogels as a promising solution for removal of pollutants or even cleaning o the facades, as they have the capability of trapping both surface attached (crusts, metal leaching patinas, efflorescences, etc.) and more in depth penetrating pollutants. Therefore, agar hydrogels will be tested in the building materials (e.g. hydraulic mortars and first generation reinforced concretes) included in these Galleries, in order to remove the pollutants, crystallized salts and additional crusts present in this construction.

Apart from that, after the removal of pollutants, correcting actions should be carried out in order to avoid the damage to progress. Nowadays, the consolidation with nanoparticles of calcium hydroxide is one of the most used technologies for this purpose. However, taking into account the composition of the materials included in Punta Begoña Galleries, other alternatives based on different compounds such as nanoparticles of calcium oxalate are going to be studied. Calcium oxalate has been pointed out in previous research projects conducted by our research group as a good alternative, since it forms colorless protective superficial micro-layers with a high chemical stability under acid environments. Moreover, the application of oxalate as nanoparticles may improve the consolidation efficiency. However, as the correcting actions require a previous application of the removing system, this future task is completely conditioned to the results obtained during the phase of pollutants removal from the facades.

Additionally, future works will be also conducted in a building of recent construction placed in the Technological and Scientific Park of Biscay (Zamudio, Basque Country, north of Spain). In the Northwest façade of this building, a reddish biopatina or biofilm can be observed. The aesthetical appearance of this biological colonization is quite similar to the one of La Galea Fortress. Moreover, the orientation of the building where this colonization has been grown is the same than in La Galea Fortress. Therefore, in a future work, a in depth study of this biological patina and the building material beneath will be performed, in order to establish a possible correlation between the casuistry of La Galea Fortress and the one in this modern building. Moreover, additional studies will be performed in the biological patina on both, La Galea Fortress and in the modern building from the Technological Park.

These last studies will be focused on the evaluation of the possible pollutants accumulation on this kind of naturally formed patinas. Particularly, the evaluation of possible metallic airborne particulate matter accumulations, on the reddish biopatinas of both buildings, coming from the anthropogenic emissions of the surrounding environments of each construction will be evaluated.

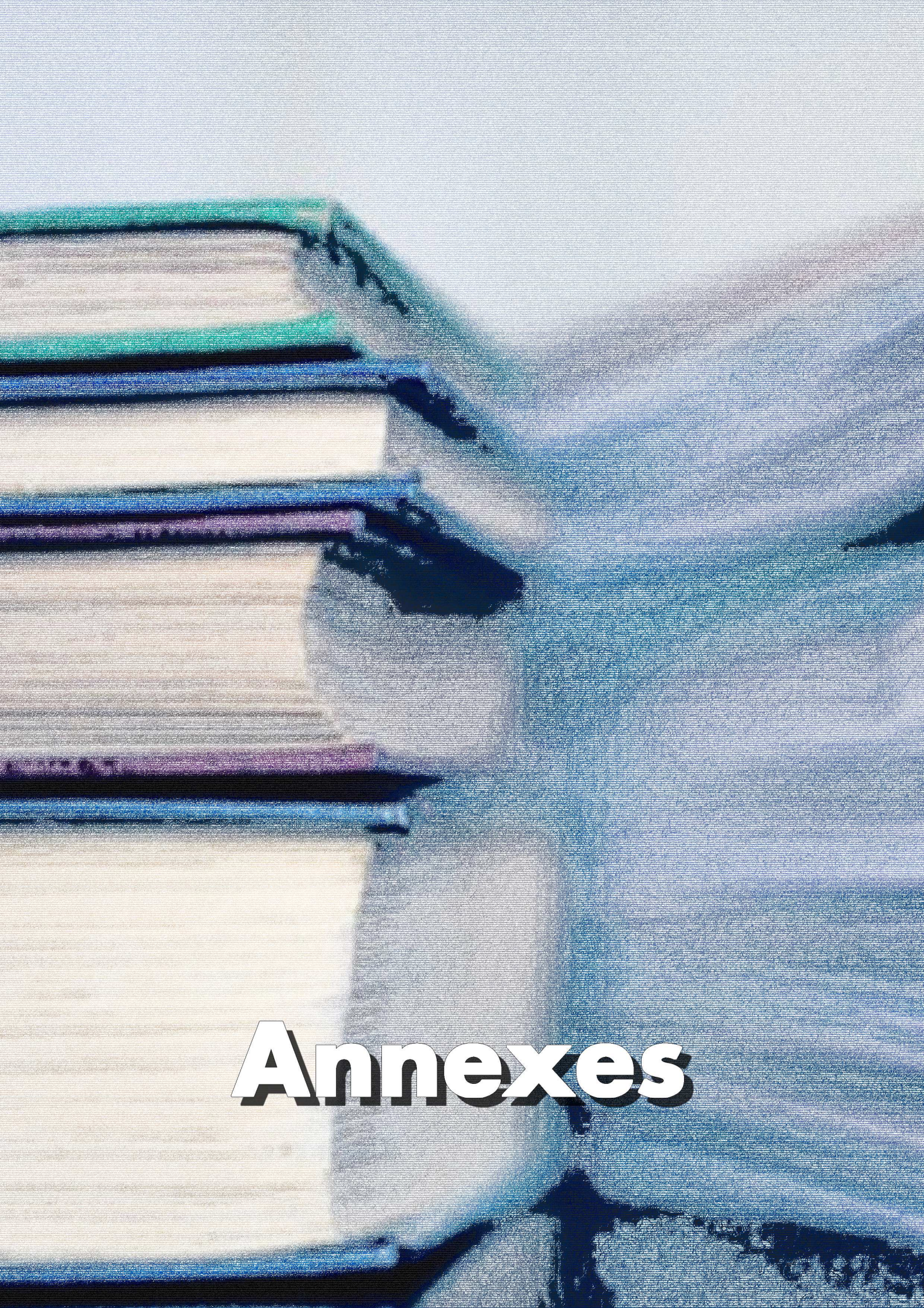

Annexes

ANNEXES

Scientific Publications

1. H. Morillas, M. Maguregui, O. Gómez-Laserna, J. Trebolazabala, J. M. Madariaga, Characterisation and diagnosis of the conservation state of cementitious materials exposed to the open air in XIX century lighthouses located on the coast of the Basque Country: 'The case of Igueldo lighthouse, San Sebastian, North of Spain", Journal of Raman Spectroscopy (2012) 43: 1630–1636.

2. H. Morillas, M. Maguregui, O. Gómez-Laserna, J. Trebolazabala, J. M. Madariaga, Could marine aerosol contribute to deteriorate building materials from interior areas of lighthouses? An answer from the analytical chemistry point of view, Journal of Raman Spectroscopy (2013) 44: 1700–1710.

3. H. Morillas, M. Maguregui, J. Trebolazabala, J. M. Madariaga, Nature and origin of White efforescence on bricks, artificial stones, and joint mortars of modern houses evaluated by portable Raman spectroscopy and laboratory analyses, Spectrochimica Acta Part A: Molecular and Biomolecular Spectroscopy (2015) 136: 1195-1203.

4. H. Morillas, M. Maguregui, I. Marcaida, J. Trebolazabala, I. Salcedo, J. M. Madariaga, Characterization of the main colonizer and biogenic pigments present in the red biofilm from La Galea Fortress sandstone by means of microscopic observations and Raman Imaging, Microchemical Journal (2015) 121: 48–55.

5. H. Morillas, M. Maguregui, C. Paris, L. Bellot-Gurlet, P. Colomban, J. M. Madariaga, The role of marine aerosol in the formation of (double) sulfate/nitrate salts in plasters. Microchemical Journal (2015) 123: 148-157.

Communications to International Congresses

Héctor Morillas, Olivia Gómez-Laserna, Maite Maguregui and Juan Manuel Madariaga, Raman, FT-IR and XRF for the characterization and diagnosis of mortars and concrete degradation processes from XIX century lighthouses located on the coast of the Basque Country: "The case of Igueldo Lighthouse, San Sebastian", 6th International Congress on the Application of Raman Spectroscopy in Art and Archaeology (RAA2011), Parma (Italy) (2011) (POSTER PRESENTATION).

Héctor Morillas, Maite Maguregui, Josu Trebolazabala, Isabel Salcedo and Juan Manuel Madariaga, Study of red biopatina composition on sandstone from a historical war Fort in La Galea (Biscay, north of Spain) by means of single point focusing Raman analysis and Raman Imaging combined with microscopic observation, 7th International Congress on the Application of Raman Spectroscopy in Art and Archaeology (RAA2013), Ljubljana (Slovenia) (2013) (POSTER PRESENTATION).

Héctor Morillas, Javier García-Galán, Maite Maguregui, Olivia Gómez-Laserna, Josu Trebolazabala, and Juan Manuel Madariaga, Analytical Methodology to diagnose the impact of different environmental stressors in historical buildings close to the sea, 6th International Congress "Science and Technology for the Safeguard of Cultural Heritage in the Mediterranean Basin, Athens (Greece) (2013) (ORAL PRESENTATION).

Héctor Morillas, Iker Marcaida, Maite Maguregui, Iker Arrizabalaga and Juan Manuel Madariaga, SEM-EDS, XRD and Raman spectroscopy applied to the characterization of black crust formation on sandstone from La Galea Fortress, TECHNART 2015 – Non-destructive and microanalytical techniques in art and cultural heritage, Catania, (Italy) (2015) (POSTER PRESENTATION).

Héctor Morillas, Maite Maguregui, Celine Paris, Ludovic Bellot-Gurlet, Philippe Colomban and Juan Manuel Madariaga, The role of chlorides and nitrates from marine aerosol in the formation of sulphate and double sulphate nitrate salts in gypsum plasters from inner areas of Igueldo Lighthouse (San Sebastian, Basque Country, north of Spain, 8th International Congress on the Application of Raman Spectroscopy in Art and Archaeology (RAA2015), Wroclaw (Poland) 2015. (POSTER PRESENTATION).

Marine aerosol is a chemical complex system formed by inorganic salts and organic matter, together with airborne particulate matter from the surrounding environment. The primary particles transported in the marine aerosol (PMA) can experiment different chemical reactions in the atmosphere, promoting the so-called Secondary Marine Aerosol (SMA) particles. These kinds of particles, together with the natural crustal or mineral particles and the metallic airborne particulate matter emitted by anthropogenic sources (road traffic, industry, etc.) can be deposited on building materials from a specific construction following dry deposition processes. Apart from that, the acid aerosols (e.g. CO_2, SO_2, NO_x, etc.) present in modern urban-industrial environments, coming also from anthropogenic sources, could be deposited in the buildings following dry or a wet deposition mechanisms. The interactions of these natural and anthropogenic stressors with building materials can promote different kind of pathologies.

In this PhD work, the negative influence of different marine environments (direct or diffuse influence), with or without the influence of an urban-industrial area (direct or diffuse), on the conservation state of two historical constructions and some newly built houses from the Basque Country (north of Spain) was evaluated. These constructions include a wide variety of building materials (sandstones, limestones, artificial stones, bricks, plasters, cementitious materials, etc.). The analytical methodology applied for this purpose involved, in some case studies, the use of non-invasive portable/hand-held spectroscopic technique (ED-XRF and Raman spectroscopy) able to perform an in situ screening in order to extract preliminary results. After that, non-invasive spectroscopic techniques (micro-Raman spectroscopy, FT-IR, XRD, m-ED-XRF, SEM-EDS), together with destructive techniques (ICP-MS and ion chromatographic), thermodynamic modellings and chemometric tools was also applied to extract the final conclusions about the pathologies identified on the constructions under study in relation with the specific marine environment where they are located.

Thanks to the use of these analytical tools, it was possible to characterize different deterioration processes caused mainly by the influence of marine aerosol (wet and dry deposition), infiltration waters, birds droppings, salts migrations, atmospheric acid gases impact, biological colonizations, etc. Moreover, the characterization of the PMA particles and SMA particles was conducted, thanks to the development of a home-made passive sampler in the last case. Additionally, the deposition of this kind of particles on sandstone, following dry deposition processes, was also confirmed.

UPV EHU